

DISSERTATION

INDEPENDENT MEASUREMENT OF THE T2K NEAR DETECTOR CONSTRAINT
USING THE OFF-AXIS PI-ZERO DETECTOR

Submitted by

Matthew Gregory Hogan

Department of Physics

In partial fulfillment of the requirements

For the Degree of Doctor of Philosophy

Colorado State University

Fort Collins, Colorado

Fall 2019

Doctoral Committee:

Advisor: Walter Toki

Robert Wilson

Norman Buchanan

Wen Zhou

Copyright by Matthew Gregory Hogan 2019

All Rights Reserved

ABSTRACT

INDEPENDENT MEASUREMENT OF THE T2K NEAR DETECTOR CONSTRAINT USING THE OFF-AXIS PI-ZERO DETECTOR

The Tokai to Kamioka (T2K) experiment is a long-baseline neutrino oscillation experiment hosted in Japan in search for electron neutrino appearance in a high purity muon neutrino beam. In order to constrain the systematic uncertainties in the oscillation analysis, a dedicated near detector (ND) complex called ND280 is located 280 meters from the neutrino production source in line of the beam. To date, the Fine Grain Detector (FGD) in ND280 has provided the ND constraint using a binned maximum likelihood estimate fit. This thesis describes the effort to validate the ND constraint using the same framework, but with an independent data set from the ND280 Pi-Zero Detector (PØD). Expanding on previously developed PØD selections, new selections have been developed to select neutrino and antineutrino events in one and multiple track topologies on water and carbon. These selections are shown to have similar sensitivity to the T2K flux and cross section systematic uncertainties. Using the same parameterization as the official ND constraint result, a hypothesis test was conducted between the PØD-only and FGD-only data fit results. A p-value of 0.2865 was obtained indicating the two data sets are likely describing the same population of neutrinos and their interactions in T2K.

ACKNOWLEDGEMENTS

I would like to first thank Elliott Forney for making a publicly accessible L^AT_EX template available at <https://github.com/idfah/csuthesis>. I also thank the T2K Beam and Near Detector Flux Task Force and the T2K collaboration for supporting this analysis. I give thanks to my loving wife Hannah who has supported me through my graduate career. I want to acknowledge the support from my family and friends. I could not have made it this far without them.

I acknowledge the support of the United States Department of Energy under Grant Contracts DEFG0293ER40788 and DESC0017740 to support my research. I also acknowledge my advisers Robert Wilson and Walter Toki for supporting me with grant proposals and guiding me on my journey through graduate school.

Contents

ABSTRACT	ii
ACKNOWLEDGEMENTS	iii
Contents	iv
List of Tables	vii
List of Figures	ix
Chapter 1 Introduction	1
1.1 Introduction to Neutrinos	1
1.2 Tokai to Kamioka Experiment	26
1.3 Summary	52
Chapter 2 BANFF Likelihood	53
2.1 Introduction to Conditional PDFs and Likelihoods	54
2.2 BANFF Fit Test Statistic	55
Chapter 3 The PØD Selections and Samples	61
3.1 Global Reconstruction	62
3.2 The PØD Selection Cuts	63
3.3 Selection Kinematics	70
3.4 Summary of Selections	91

Chapter 4	The BANFF Fit Model Parameters	94
4.1	Fit Binning	94
4.2	Penalty Terms and Systematic Uncertainties	98
4.3	Chapter Summary	133
Chapter 5	Fitter Validation	136
5.1	Asimov Data Fit	136
5.2	Fake Data	147
5.3	Validation Summary	152
Chapter 6	Fitter Results	154
6.1	Prefit Sample Distributions	154
6.2	Postfit Results	155
6.3	Summary	195
Chapter 7	Discussion	197
7.1	Potential Impacts on the T2K Oscillation Analysis	198
7.2	Analysis Improvements	198
7.3	Future Prospects	204
Bibliography	208
Appendix A	Contributions to the PØD CC- π Analysis	217
A.1	Particle Identification Tools	218
A.2	Momentum Reconstruction	222
Appendix B	The PØD-Only Bin Normalization Parameters	228
Appendix C	Toy Experiment Variations	247
Appendix D	Cross Section Parameters Variations	274

Appendix E Log-Likelihood Sample Scans	291
Appendix F Log-Likelihood Penalty Scans	305
Appendix G The PØD-Only Postfit Parameters	317

List of Tables

1.1	Sensitivity of Different Oscillation Experiments	20
1.2	Global Best Fit for the Oscillation Parameters	23
1.3	PØD Water Target Mass Composition	44
2.1	Parameters that Affect the Analysis Bins	57
3.1	The PØD Water Target Fiducial Volume and Veto Corridor Definitions	66
3.2	T2K Data-Taking Periods and Collected POT Used in the Analysis	70
3.3	Enumeration of NEUT Interaction Modes	72
4.1	Flux Binning and Uncertainties	101
4.2	List of Detector Systematics in the Analysis	109
4.3	Eigenvalues of the Sample Covariance	125
4.4	Cross Section Model Fit Parameters in the BANFF Fit	132
5.1	Event Rate Table for Asimov Set	139
6.1	Neutrino-Nucleon Exposure on Target Elements	183
7.1	Neutrino-Nucleon Exposure on Target Elements in a Run 2 - 8 PØD+FGD Joint Fit	206
A.1	Selection Statistics for the PØD CC- 1π Analysis	221
B.1	Observable Normalization Fit Bins	228

D.1	Event Rate Variations Per Cross Section Parameter Variation	275
G.1	Prefit and Postfit Parameters with Errors	318

List of Figures

1.1	The Elementary Particles of the Standard Model of Particle Physics	3
1.2	The CC and NC $\nu_e e^- \rightarrow \nu_e e^-$ Interaction	6
1.3	Helicity of the Neutrino	7
1.4	A Schematic of θ in $\nu_e e^-$ Scattering	11
1.5	A ν_μ -Induced CCQE Interaction	12
1.6	Illustration of a Mixing Matrix in Two Dimensions	16
1.7	Survival and Disappearance Probability	18
1.8	Semi-logarithmic Plot of the Two Flavor Survival Probability	19
1.9	Neutrino Mass Hierarchy Problem and MNSP Representation	22
1.10	The Matter and Energy Content of the Universe	25
1.11	Birds Eye View of the T2K experiment on the Japanese Archipelago	27
1.12	The Unoscillated ν_μ Flux at Super-Kamiokande	28
1.13	Bird's Eye View of the J-PARC Laboratory	29
1.14	Schematics of the J-PARC Accelerators	30
1.15	The Neutrino Beamline at J-PARC	31
1.16	Photographs of the T2K Target Station	32
1.17	Accumulated Protons on Target for T2K	33
1.18	Schematic of the INGRID Detector	36
1.19	Photographs of the T2K MPPC	37
1.20	The T2K On-Axis Beam Profile	37

1.21	The INGRID Detector Event Rate	38
1.22	Schematic of the Off-Axis Near Detector ND280	40
1.23	The ND280 Detector Magnetic Field Measurement	41
1.24	Schematic of the PØD	43
1.25	Cross Section of a PØD Scintillating Bar	44
1.26	Cut-Away Drawing of a TPC Volume in ND280	46
1.27	Diagram of the Super-Kamiokande Detector	47
1.28	Representative T2K Events in Super-Kamiokande	48
1.29	Predicted and Best Fit Measurements for the T2K Flux at SK	49
1.30	Predicted CCInc Cross Section at T2K Energies	50
3.1	The PØD ν_μ and $\bar{\nu}_\mu$ CC-0 π Selection Kinematics	62
3.2	Frequently Used Legends in the Analysis	72
3.3	Reconstructed Kinematics of the ν_μ in FHC Mode CC 1-Track Selection Categorized by CCQE and Non-CCQE Interactions	74
3.4	Reconstructed Kinematics of the ν_μ in FHC Mode CC 1-Track Selection Categorized by the True Particle Matched to the Main Track	75
3.5	Reconstructed Vertex Z Position of the ν_μ in FHC Mode CC 1-Track Selection .	76
3.6	Efficiency and Purity of the ν_μ in FHC Mode CC 1-Track Selection	76
3.7	True Kinematics of the ν_μ in FHC Mode CC 1-Track Selection	77
3.8	Reconstructed Kinematics of the ν_μ in FHC Mode CC N-Tracks Selection Categorized by CCQE and Non-CCQE Interactions	78
3.9	Reconstructed Kinematics of the ν_μ in FHC Mode CC N-Tracks Selection Categorized by the True Particle Matched to the Main Track	79
3.10	Reconstructed Vertex Z Position of the ν_μ in FHC Mode CC N-Tracks Selection Categorized by the True Target Nucleus	79
3.11	Efficiency and Purity of the ν_μ in FHC Mode CC N-Tracks Selection	80
3.12	True Kinematics of the ν_μ in FHC Mode CC N-Tracks Selection	81

3.13	Reconstructed Kinematics of the $\bar{\nu}_\mu$ in RHC Mode CC 1-Track Selection Categorized by CCQE and Non-CCQE Interactions	82
3.14	Reconstructed Kinematics of the $\bar{\nu}_\mu$ in RHC Mode CC 1-Track Selection Categorized by the True Particle Matched to the Main Track	83
3.15	Efficiency and Purity of the $\bar{\nu}_\mu$ in RHC Mode CC 1-Track Selection	83
3.16	True Kinematics of the $\bar{\nu}_\mu$ in RHC Mode CC 1-Track Selection	84
3.17	Reconstructed Kinematics of the $\bar{\nu}_\mu$ in RHC Mode CC N-Tracks Selection Categorized by CCQE and Non-CCQE Interactions	85
3.18	Reconstructed Kinematics of the $\bar{\nu}_\mu$ in RHC Mode CC N-Tracks Selection Categorized by the True Particle Matched to the Main Track	85
3.19	Efficiency and Purity of the $\bar{\nu}_\mu$ in RHC Mode CC N-Tracks Selection	86
3.20	True Kinematics of the $\bar{\nu}_\mu$ in RHC Mode CC N-Tracks Selection	87
3.21	Reconstructed Kinematics of the ν_μ Background in RHC Mode CC 1-Track Selection Categorized by CCQE and Non-CCQE Interactions	88
3.22	Reconstructed Kinematics of the ν_μ Background in RHC Mode CC 1-Track Selection Categorized by the True Particle Matched to the Main Track	88
3.23	Efficiency and Purity of the ν_μ Background in RHC Mode CC 1-Track Selection	89
3.24	True Kinematics of the ν_μ Background in RHC Mode CC 1-Track Selection	90
3.25	Reconstructed Kinematics of the ν_μ Background in RHC Mode CC N-Tracks Selection Categorized by CCQE and Non-CCQE Interactions	90
3.26	Reconstructed Kinematics of the ν_μ Background in RHC Mode CC N-Tracks Selection Categorized by the True Particle Matched to the Main Track	91
3.27	Efficiency and Purity of the ν_μ Background in RHC Mode CC N-Tracks Selection	92
3.28	True Kinematics of the ν_μ Background in RHC Mode CC N-Tracks Selection	93
4.1	Main Track Momentum Resolution for the ν_μ in FHC Mode CC 1-Track Sample	96
4.2	Main Track Angular Residuals for the ν_μ in FHC Mode CC 1-Track Sample	97
4.3	The BANFF Prefit Flux Covariance Matrix	100

4.4	Neutrino Flux Prediction at SK and Flux Bin Edges	100
4.5	Vertex Distribution Showing Evidence of PØD Bulging	111
4.6	Bin Normalizations Edges for the ν_μ in FHC Mode Samples	118
4.7	Bin Normalization Edges for the $\bar{\nu}_\mu$ in RHC Mode Samples	119
4.8	Bin Normalizations for the ν_μ Background in RHC Mode Samples	120
4.9	Event Variations in Observable Normalization Bins	121
4.10	Detector Penalty Covariance Matrix	123
4.11	Principal Component for the Sample Variance	125
4.12	Cross Section Parameters Prefit Covariance and Correlation Matrices	134
5.1	Complete Prefit Correlation Matrix for the BANFF Fit.	137
5.2	Test Statistic Scans for Variations of Fit Parameters in the Asimov Set	141
5.3	Asimov Fit Results for the Flux at ND280	142
5.4	Asimov Fit Results for the Flux at Super-K	143
5.5	Asimov Fit Results for the Bin Normalization Parameters	144
5.6	Asimov Fit Results for the Cross Section and FSI Parameters	145
5.7	Complete Postfit Correlation Matrix for the Asimov Data Fit	146
5.8	Flux and Cross Section Postfit Correlation Matrix for the Asimov Data Fit . . .	146
5.9	Neutrino Flux in the High Energy Neutrino Flux Variation Fake Data Set . . .	148
5.10	Postfit Parameters for the High Energy ν_μ in FHC Flux Fake Data fit	150
5.11	Lepton Candidate Momentum in the Single Pion Event Rate Variation Fake Data Set	151
5.12	Postfit Parameters for the C_A^5 Fake Data Fit	153
6.1	Data and Prefit Legend	155
6.2	Prefit for the Water-In ν_μ in FHC CC 1-Track Sample	156
6.3	Prefit for the Water-In ν_μ in FHC CC N-Tracks Sample	157
6.4	Prefit for the Water-In $\bar{\nu}_\mu$ in RHC CC 1-Track Sample	158

6.5	Prefit for the Water-In $\bar{\nu}_\mu$ in RHC CC N-Tracks Sample	159
6.6	Prefit for the Water-In ν_μ in RHC CC 1-Track Sample	160
6.7	Prefit for the Water-In ν_μ in RHC CC N-Tracks Sample	161
6.8	Prefit for the Water-Out ν_μ in FHC CC 1-Track Sample	162
6.9	Prefit for the Water-Out ν_μ in FHC CC N-Tracks Sample	163
6.10	Prefit for the Water-Out $\bar{\nu}_\mu$ in RHC CC 1-Track Sample	164
6.11	Prefit for the Water-Out $\bar{\nu}_\mu$ in RHC CC N-Tracks Sample	165
6.12	Prefit for the Water-Out ν_μ in RHC CC 1-Track Sample	166
6.13	Prefit for the Water-Out ν_μ in RHC CC N-Tracks Sample	167
6.14	Postfit for the Water-In ν_μ in FHC CC 1-Track Sample	170
6.15	Postfit for the Water-In ν_μ in FHC CC N-Tracks Sample	171
6.16	Postfit for the Water-In $\bar{\nu}_\mu$ in RHC CC 1-Track Sample	172
6.17	Postfit for the Water-In $\bar{\nu}_\mu$ in RHC CC 1-Track Sample	173
6.18	Postfit for the Water-In ν_μ in RHC CC 1-Track Sample	174
6.19	Postfit for the Water-In ν_μ in RHC CC N-Tracks Sample	175
6.20	Postfit for the Water-Out ν_μ in FHC CC 1-Track Sample	176
6.21	Postfit for the Water-Out ν_μ in FHC CC N-Tracks Sample	177
6.22	Postfit for the Water-Out $\bar{\nu}_\mu$ in RHC CC 1-Track Sample	178
6.23	Postfit for the Water-Out $\bar{\nu}_\mu$ in RHC CC N-Tracks Sample	179
6.24	Postfit for the Water-Out ν_μ in RHC CC 1-Track Sample	180
6.25	Postfit for the Water-Out ν_μ in RHC CC N-Tracks Sample	181
6.26	Legend Used to Compare PØD-only and FGD-only Fit Results	182
6.27	Postfit ND280 Flux Parameters for the PØD-only BANFF Fit	186
6.28	Postfit SK Flux Parameters for the PØD-only BANFF Fit	187
6.29	Postfit Cross Section Parameters for the PØD-only BANFF Fit	188
6.30	Prefit and Postfit Bin Normalization Parameters	189
6.31	The 2p2h Shape Mirrored Spline	190

6.32 Postfit Correlation Matrix	191
6.33 Prefit and Post Flux and Cross Section Parameter Correlations	192
6.34 Prefit and Post Flux and Cross Section Parameter Correlations	193
6.35 P-Value for the PØD vs FGD ND Constraint	195
7.1 Cross-Validation Curve for the BANFF Fit Regularization Strength.	200
7.2 The Lasso vs Elastic Net Constraint	203
A.1 Topological Features Developed for CC-1 π Analysis	220
A.2 Momentum Calibration for PØD Fully Contained Muon Tracks	226
A.3 Resolution Function for PØD Fully Contained Muon Tracks	227
E.1 Corrected 2p2h Shape Location Scans	304

Chapter 1

Introduction

Chose trop vue n'est chère tenue

A thing too much seen is little prized – French proverb

1.1 Introduction to Neutrinos

The history of the neutrino can be traced back to the electron energy spectrum observed in neutron β -decay. While measurements of the α - and γ -decay of atomic nuclei showed discrete spectral lines, the electron (β particle) exhibited a continuous energy spectrum. Experimentally, there were two observed particles in each decay process and classical physics dictated that the outgoing daughter particles should have discrete energies. The fact that the β -decay spectrum was very different posed a fundamental problem for physicists in the mid-1910s, which was that energy was not conserved. Two solutions were postulated: either the “energy conservation law is only valid statistically in such a process [...] or an additional undetectable new particle [...] carrying away the additional energy and spin [...] is emitted” [87]. The latter solution was proposed by Wolfgang Pauli in a letter dated 4 December, 1930, to a group of physicists meeting in Tübingen, modern Germany, where he

first proposed the neutrino¹. Pauli's solution also predicted that the undetected neutrino would have half-integer spin, a quantum mechanical property of matter, since the observed particles in β -decay did not conserve angular momentum. The existence of the neutrino and validation of Pauli's predictions would not be experimentally verified for another 20 years.

The neutrino was first observed in 1953 by Clyde Cowan and Frederick Reines using a nuclear reactor in South Carolina, United States of America. Since then, three types or “flavors” of neutrinos and antineutrinos have been observed using accelerators and also from unique sources like the Sun and a supernova. Neutrino physics continues to be an active area of fundamental research since the neutrino is a truly unique probe to subatomic processes. For instance they are observed to originate from the depths of the Sun's core (over 10^7 degrees Kelvin) where fusion occurs.

Neutrinos rarely interact with normal matter, meaning that they travel essentially unimpeded towards one's particle detector. The rarity of such interactions can be illustrated by the fact that over a typical human lifetime, only one solar neutrino interaction with an individual is expected out of the 7.0×10^{10} neutrinos/cm²/sec incident on the Earth². So this begs the question: how does one detect a neutrino? The short answer is that one requires a large enough flux of neutrinos passing through a large dense volume of matter just to detect a single neutrino with today's technology.

Scientists continue to be interested in neutrinos due to the unusual properties they exhibit. One of the more recent and surprising aspects of neutrinos is their ability to undergo “flavor oscillations” where a neutrino of definite flavor (type) is created and later observed as a different flavor. The impact of differences between neutrino and antineutrino oscillations

¹In W Pauli's December 1930 letter, he referred to his proposed particle as the “neutron”, and not the neutrino. It would be Enrico Fermi who would coin the particle as a “neutrino” meaning in Italian *little neutral one*.

²To give some perspective to this number, this means 70 billion neutrinos are traveling every second through an area similar to one's own thumb nail.

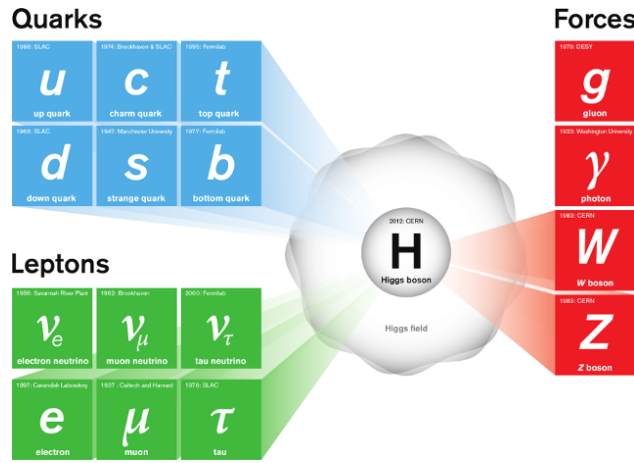


Figure 1.1: The Standard Model of particle physics consists of six quarks (up, down, strange, charm, bottom, and top), six leptons (electron, muon, tau, electron neutrino, muon neutrino, and tau neutrino), four force propagating bosons (gluon, photon, W, and Z), and the Higgs boson. The quarks, electron, muon, tau, W, and Z all gain mass through the Higgs field. The focus of this thesis are the neutrinos which are classified according to their charged, more massive lepton cousins. Image taken from [13].

could help explain the observed matter-antimatter asymmetry in the Universe which one of the most profound mysteries in physics today.

1.1.1 Neutrinos in the Standard Model

The Standard Model (SM) of particle physics is the theory of elementary or fundamental particle constituents and the forces between them. These forces are the electromagnetic, the weak, and the strong. String theory, which is not yet tested, attempts to incorporate the gravitational force. The SM forces and the gravitational force constitute the four *known* fundamental forces of the Universe. Each force in the SM has at least one “force carrier” particle that mediates the interactions between the matter particles. The force carriers are formally called “gauge bosons”, which indicates that they are particles with integer ($0, 1, 2, \dots$) spin that mediate the interaction. The weak nuclear gauge bosons, the charged W^\pm and the neutral Z, couple to neutrinos as well as the other fermions, particles with half-integer ($\frac{1}{2}, \frac{3}{2}, \frac{5}{2}, \dots$) spin, in the SM. All of the elementary particles of the SM are shown in Figure 1.1 on page 3.

Neutrinos in the SM are electrically neutral, massless particles categorized into three generations based on their charged, more massive lepton cousins. In the SM, the three neutrinos and the three antineutrinos are the only spin $1/2$ particles that experience only weak interactions. The neutrino and its associated charged cousin of the same flavor pair into a “weak isospin doublet” in the SM. These doublets are locally gauge invariant under a $SU(2) \otimes U(1)$ symmetry which leads to the postulated existence of the photon, the W^\pm and Z bosons. They are necessary to enable local gauge invariance³.

What follows is a brief introduction to weak interactions. This is followed by a exploration on the nature of neutrino handedness. Then this is proceeded by a discussion on neutrino scattering with matter.

1.1.1.1 Weak Interactions

The name “weak force” comes from the fact that this force is much weaker than the electromagnetic and strong nuclear forces. This is due to the weak mediating bosons, the W^\pm and Z , being massive particles unlike the massless gluon (g) and photon (γ). The W^\pm/Z have masses of $80/90 \text{ GeV}/c^2$, which is more massive than all the other elementary particles except for the top quark.

For weak interactions to occur at energies far below the rest mass (also called “off-shell”) of the W^\pm and Z , the interaction time must be infinitesimally small as dictated by the Heisenberg Uncertainty Principle

$$\Delta E \Delta t \gtrsim \hbar \quad (1.1)$$

³A gauge theory describes ways to measure physical forces or fields through interactions between elementary particles. The electric or magnetic fields for example can only be probed by charged particles. In the realm of quantum field theories, fields are postulated to permeate everywhere and it is excitations of these fields that produce experimental observables. Fields are constructed using the Lagrangian formalism and altered using gauge transformations. If altering the Lagrangian in some way does not affect the observables, this is referred to as a gauge invariance. Local gauge invariance means that under the constraints of the experiment, certain gauge transformations do not affect the observables. The allowed locally gauge invariant transformations require knowledge of its underlying Lie, or symmetry, group. With the weak isospin doublets, the Lie groups are $SU(2) \otimes U(1)$ where $SU(2)$ is the special unitary group of 2×2 unitary matrices, and $U(1)$ is the unitary (circle) group consisting of complex numbers of magnitude 1.

where ΔE is the energy of the particle and Δt is the time during which the particle exists. As an example, consider a neutrino emitting a Z-boson as shown in Figure 1.2a on page 6. If the energy of the neutrino is 1 GeV, the lifetime of the Z boson is about 10^{-25} seconds according to (1.1). In general, the probability that a massive particle of mass M will be created from the collision of two particles is given by a relativistic Breit–Wigner distribution

$$f(M) \propto \frac{1}{(M^2 - M_0^2)^2 c^4 + M_0^2 \Gamma^2}, \quad (1.2)$$

where M_0 is the rest mass and Γ is the decay width of the particle. For $M \ll M_0$, the probability of creating that particle will be infinitesimally small. Therefore to observe a single weak interaction requires a large number of weakly interacting particles.

Weak interactions are classified into two classes: charged current (CC) and neutral current (NC). The CC interaction involves a charged W boson and changes the incident neutrino into an electrically charged lepton of flavor l as shown Figure 1.2a on page 6. It is through the CC interaction where the flavor of the neutrino is inferred from the charged lepton. For instance, an electron type neutrino, ν_e , is inferred to have interacted with matter if an electron is observed. The same is not true for NC interactions, since those interactions are flavor agnostic. The NC interaction involves a neutral Z boson and does not change the neutrino's flavor as shown in Figure 1.2b on page 6.

1.1.1.2 Chirality: How Neutrinos are Left Handed

Neutrinos are observed to have their spin direction vectors σ opposite to their momentum \mathbf{P} and this is reversed for antineutrinos. This property is called helicity and is given by

$$\mathcal{H} = \frac{\sigma \cdot \mathbf{P}}{|\mathbf{P}|}. \quad (1.3)$$

Although neutrino detection is difficult, the neutrino helicity is readily inferred from the daughter muon's helicity in pion decay, $\pi^+ \rightarrow \mu^+ \nu_\mu$. The μ^+ has negative helicity ($\mathcal{H} = -1$)

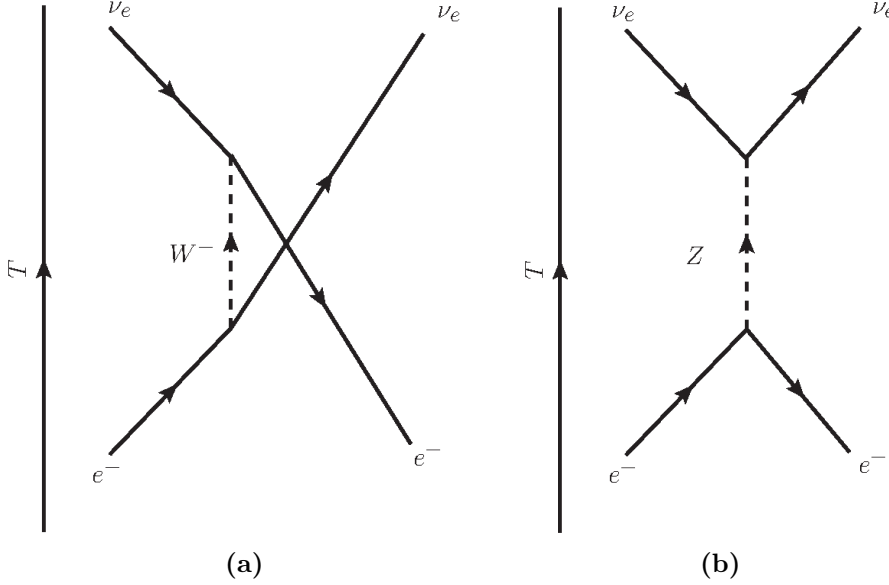


Figure 1.2: The CC and NC $\nu_e e^- \rightarrow \nu_e e^-$ interaction

and to conserve spin, the neutrino's helicity must also be negative as shown in Figure 1.3 on page 7. The antineutrino's helicity is positive (+1) as shown in Figure 1.3 on page 7 through use of the charge (C) conjugation and parity (P) transformations. A C conjugation is a linear transformation that transforms all particles into their corresponding antiparticles while the P transformation inverts all spatial coordinates. Thus neutrinos are referred to as *left-handed* (LH) particles while antineutrinos are referred to as *right-handed* (RH) particles. It turns out that helicity is a useful quantum number to describe neutrinos and coincides with a property called chirality. To understand chirality and its relationship to helicity requires an analysis of the Dirac Lagrangian and Dirac equation.

The Dirac Lagrangian for a free particle field $\psi(x)$ with half-integer spin can be written as

$$\mathcal{L} = \bar{\psi}(x) \left[\frac{i\hbar}{2} \sum_{\mu=0}^3 \gamma^\mu (\vec{\partial}_\mu - \vec{\partial}_\mu) - mc \right] \psi(x), \quad (1.4)$$

where $\psi(x)$ is a four-component vector (spinor) describing a particle field and γ^μ are a set of four 4x4 matrices. The adjoint field $\bar{\psi}(x)$ is defined as

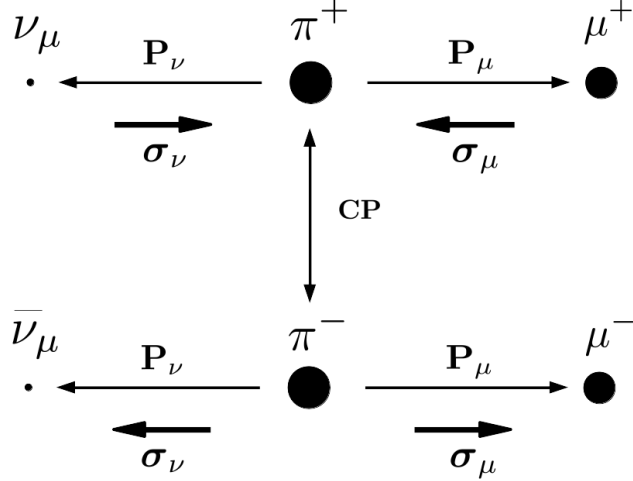


Figure 1.3: The helicity of the neutrino as inferred from pion decay. Since a pion at rest has zero (0) angular momentum, the system of daughter particles must have also net zero angular momentum. By measuring the muon's helicity, the helicity of neutrino is inferred. A neutrino (antineutrino) is a left-handed (right-handed) helicity particle since its spin is anti-parallel (parallel) to its momentum.

$$\bar{\psi}(x) \equiv \psi^\dagger(x) \gamma^0, \quad (1.5)$$

where \dagger denotes the conjugate and transpose operations. The $\overrightarrow{\partial}_\mu$ operator is a four-vector defined as

$$\partial_0 = \frac{1}{c} \frac{\partial}{\partial t}, \partial_1 = \frac{\partial}{\partial x}, \partial_2 = \frac{\partial}{\partial y}, \partial_3 = \frac{\partial}{\partial z}, \quad (1.6)$$

that acts only to the right while $\overleftarrow{\partial}_\mu$ only acts to the left (i.e. $\overleftarrow{\psi} \overrightarrow{\partial}_\mu = \partial_\mu \overleftarrow{\psi}$). The γ^μ matrices are not unique and different representations are more appropriate for different kinematic regimes. The field equations are extracted from the Lagrangian using the Euler-Lagrange procedure. In general for a set of M fields, the field equations are given by

$$\partial_\mu \frac{\partial \mathcal{L}}{\partial (\partial_\mu \psi_r)} - \frac{\partial \mathcal{L}}{\partial \psi_r} = 0 \quad (r = 0, 1, 2, \dots, M-1, M). \quad (1.7)$$

For the Dirac Lagrangian, the field equation for ψ is given by

$$\partial_\mu \frac{\partial \mathcal{L}}{\partial (\partial_\mu \bar{\psi})} - \frac{\partial \mathcal{L}}{\partial \bar{\psi}} = 0, \quad (1.8)$$

which yields the Dirac equation

$$\left[i\hbar \sum_{\mu=0}^3 \gamma^\mu \partial_\mu - mc \right] \psi(x) = 0. \quad (1.9)$$

The representation of the γ^μ matrices that is useful to describe neutrinos is the *Chiral representation* (also called the *Weyl representation*) where

$$\gamma^0 = \begin{bmatrix} 0 & I_2 \\ I_2 & 0 \end{bmatrix}, \gamma^1 = \begin{bmatrix} 0 & \sigma_x \\ -\sigma_x & 0 \end{bmatrix}, \gamma^2 = \begin{bmatrix} 0 & \sigma_y \\ -\sigma_y & 0 \end{bmatrix}, \gamma^3 = \begin{bmatrix} 0 & \sigma_z \\ -\sigma_z & 0 \end{bmatrix}, \quad (1.10)$$

I_2 is the 2×2 identity matrix, $\sigma_{x,y,z}$ are the Pauli Spin matrices given by

$$\sigma_x = \sigma_1 = \begin{pmatrix} 0 & 1 \\ 1 & 0 \end{pmatrix}, \quad \sigma_y = \sigma_2 = \begin{pmatrix} 0 & -i \\ i & 0 \end{pmatrix}, \quad \sigma_z = \sigma_3 = \begin{pmatrix} 1 & 0 \\ 0 & -1 \end{pmatrix}.$$

Using the Chiral representation, the chirality matrix, γ^5 (the fifth gamma matrix), is defined as

$$\gamma^5 = i\gamma^0\gamma^1\gamma^2\gamma^3 = \begin{bmatrix} -I_2 & 0 \\ 0 & I_2 \end{bmatrix}, \quad (1.11)$$

which is diagonal as well as Hermitian, meaning that its eigenvalues are real and observable. Let the eigenfunctions of the chirality matrix be denoted with subscripts P and M such that the eigenvalue equations are

$$\begin{aligned} \gamma^5 \psi_P &= +1 \psi_P, \\ \gamma^5 \psi_M &= -1 \psi_M. \end{aligned} \quad (1.12)$$

The field equation solutions to (1.9) can be decomposed into ψ_P and ψ_M projections using two chiral projection operators $\hat{O}_{P,M}$ where

$$\psi = (\hat{O}_P + \hat{O}_M) \psi = \psi_P + \psi_M. \quad (1.13)$$

The chiral operators are explicitly given by

$$\begin{aligned}\hat{O}_M &= \frac{1}{2} (I_4 - \gamma^5) = \begin{pmatrix} 0 & 0 \\ 0 & I_2 \end{pmatrix}, \\ \hat{O}_P &= \frac{1}{2} (I_4 + \gamma^5) = \begin{pmatrix} I_2 & 0 \\ 0 & 0 \end{pmatrix},\end{aligned}\tag{1.14}$$

where I_4 is the 4×4 identity matrix. Taken together (1.13) and (1.14) indicate the free neutrino field is a vector ψ minus axial vector $\gamma^5\psi$, also referred to as V-A, under P transformations. This feature is what allows for the weak force to violate P-symmetry and CP-symmetry. Referring back to (1.4) and (1.7), the Dirac equation becomes a set of coupled equations

$$\begin{aligned}i\hbar \sum_{\mu=0}^3 \gamma^\mu \partial_\mu \psi_P &= mc\psi_M \\ i\hbar \sum_{\mu=0}^3 \gamma^\mu \partial_\mu \psi_M &= mc\psi_P,\end{aligned}\tag{1.15}$$

where dynamics are set by the mass.

Since the chiral projection operators are decompositions of the identity matrix, the simplest nontrivial solution to ψ is

$$\psi = \begin{pmatrix} \chi_P \\ \chi_M \end{pmatrix}\tag{1.16}$$

where χ represents two-component spinors. Using 1.16 the Dirac equation in (1.15) can again be rewritten as

$$\begin{aligned}i\hbar \left[\frac{1}{c} \frac{\partial}{\partial t} + \boldsymbol{\sigma} \cdot \boldsymbol{\nabla} \right] \chi_P &= -mc\chi_M \\ i\hbar \left[\frac{1}{c} \frac{\partial}{\partial t} - \boldsymbol{\sigma} \cdot \boldsymbol{\nabla} \right] \chi_M &= -mc\chi_P,\end{aligned}\tag{1.17}$$

where

$$\boldsymbol{\sigma} \cdot \boldsymbol{\nabla} = \sigma_x \frac{\partial}{\partial x} + \sigma_y \frac{\partial}{\partial y} + \sigma_z \frac{\partial}{\partial z}.\tag{1.18}$$

In the limiting case of vanishing mass ($m \rightarrow 0$), as is in the SM, the free particle field equations in (1.17) decouple into

$$\begin{aligned} \left(\frac{E}{c} + \boldsymbol{\sigma} \cdot \mathbf{P} \right) \chi_P &= 0, \\ \left(\frac{E}{c} - \boldsymbol{\sigma} \cdot \mathbf{P} \right) \chi_M &= 0, \end{aligned} \tag{1.19}$$

where the differential operators have been evaluated as the particle's energy E and momentum three-vector \mathbf{P} . For massless neutrinos, χ_P and hence ψ_P , describe particles of negative energy $E = -|\mathbf{P}|c$ which in the context of quantum field theory are interpreted as antiparticles traveling backwards in time. Conversely, ψ_M have positive energy $E = |\mathbf{P}|c$ and which means they are particles traveling forward in time.

If one also multiplies (1.15) by $\gamma^5\gamma^0$ and uses the fact that the spin operator $\boldsymbol{\sigma}$ is given by

$$\boldsymbol{\sigma} = i(\gamma^2\gamma^3, \gamma^3\gamma^1, \gamma^1\gamma^2) = \gamma^0\gamma^k\gamma^5 \quad (k = 1, 2, 3), \tag{1.20}$$

each decoupled equation becomes

$$\frac{\boldsymbol{\sigma} \cdot \mathbf{P}}{|\mathbf{P}|} \psi_{P,M} = \gamma^5 \psi_{P,M} = \pm \psi_{P,M}, \tag{1.21}$$

where one recognizes that the helicity and chiral states are the same for $m \rightarrow 0$ only. Thus the labels M and P actually are identical to the LH and RH helicity labels, respectively. Using the results above, a neutrino is always observed as a LH particle while the antineutrino is always observed as a RH antiparticle.

The observation of only LH neutrinos and RH antineutrinos is an important feature in the SM. However, since neutrinos are known to have mass, given that neutrinos oscillate, it is theoretically possible to observe a RH neutrino and a LH antineutrino. That would require boosting to a highly relativistic reference frame with respect to the laboratory.

1.1.1.3 Neutrino Scattering with Matter

Charged current (CC) neutrino interactions on nuclear particles are the interactions investigated in this thesis. These interactions produce an outgoing charged lepton and a variety

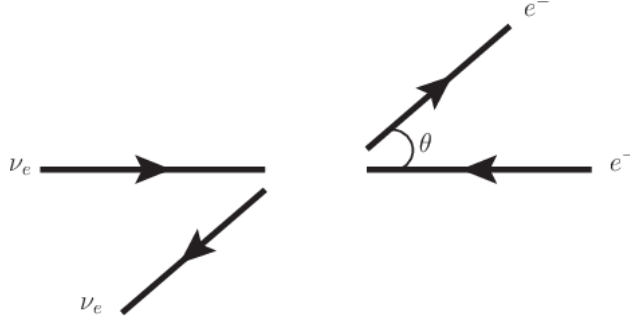


Figure 1.4: A schematic of θ in $\nu_e e^-$ scattering. The same diagram is used to describe $\bar{\nu}_e + e^-$ scattering with $\nu_e \rightarrow \bar{\nu}_e$.

of hadronic states. While interactions with valence electrons are possible, they are far less common in large, subatomic particle detectors. However, the physics of neutrino-electron scattering is very similar to neutrino-nucleus scattering.

Consider neutrino-electron scattering, the cross section for $\nu_e e^-$ is given by

$$\frac{d\sigma}{d\Omega} = \left(\frac{G_F \hbar c}{2\pi} \right)^2 s, \quad (1.22)$$

where G_F is the Fermi constant and s is the center of mass energy squared. Due to the V-A nature of the weak force, neutrinos couple to LH particles and to RH antiparticles. The outgoing particles are isotropically distributed in the center-of-mass frame since the initial and final spin state of the system is $J = 0$. Compare (1.22) with the cross section for $\bar{\nu}_e e^-$

$$\frac{d\sigma}{d\Omega} = \left(\frac{G_F \hbar c}{4\pi} \right)^2 (1 - \cos \theta)^2 s, \quad (1.23)$$

where θ is the observed scattering angle of the electron as shown in Figure 1.4 on page 11. Since the total spin of the $\bar{\nu}_e e^-$ system is $J = 1$ with z-projection $J_z = 1$, the antineutrino is preferentially forward scattered. Integrating over all angles, the cross sections are related to each other by

$$\sigma(\bar{\nu}_e e^-) = \frac{1}{3} \sigma(\nu_e e^-).$$

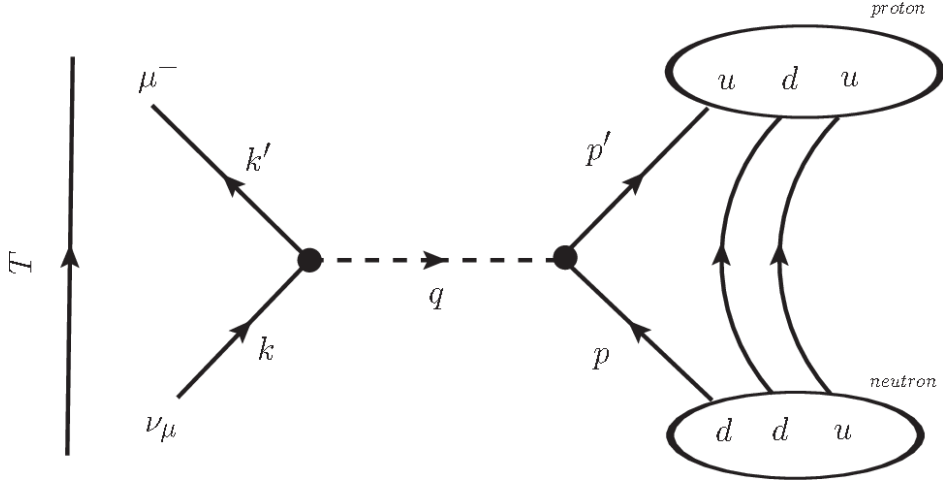


Figure 1.5: A ν_μ -induced CCQE interaction.

The factor $1/3$ arises from the fact that angular momentum conservation forbids the $J_z = -1$ and 0 states for $\bar{\nu}_e e^-$ scattering. The same $1/3$ factor arises between $\nu_\mu d \rightarrow \mu^- u$ and $\bar{\nu}_\mu u \rightarrow \mu^+ d$ scattering.

In neutrino-nuclear scattering, the simple picture of free quarks must be replaced with the reality of the nuclear medium. Interactions with a single quark are still possible, but nuclear effects can alter the products of the interactions. The kinematics of the particles involved can be altered as well depending on the initial state of the nucleus. Distinctions must be made in neutrino physics between observables from primary interactions like $\nu_e + e^-$ and nuclear “final state interactions” (FSI).

There are three neutrino-nuclear scattering classes presented in this thesis: quasi-elastic (CCQE), deep inelastic scattering (CC-DIS), and single pion production (CC- 1π). The ν CCQE interaction refers to the process where an incoming neutrino and neutron (udd) scatter to produce a charged lepton and proton (uud) as shown in Figure 1.5 on page 12. For $\bar{\nu}$ CCQE, the proton is converted to a neutron instead. The CCQE interaction is the lowest energy CC interaction with a nucleon and has approximate mass conservation between the proton-neutron states ($\Delta m = 1.29 \text{ MeV}/c^2$). The CC-DIS interaction is a high energy transfer process that shatters the nucleus apart. Finally, CC- 1π interactions refer to processes where a post-FSI charged pion is experimentally observed presumably from the decay of

resonance state like the $\Delta(1232)$ baryon. These interactions are not well understood currently since they occur in the transition between CCQE and CC-DIS interaction modes.

1.1.2 Neutrino Oscillations

Neutrino oscillations is the physical process of a neutrino produced with a particular, definite flavor and later observed as a different flavor. This phenomenon was first observed as a deficit of neutrinos for a number of atmospheric and solar neutrino experiments. The deficit also seemed more pronounced for atmospheric neutrinos as the distance from their source increased. For neutrino oscillations to occur, at most one neutrino can be massless. This observation firmly established that the SM is incorrect with its assumption of massless neutrinos.

The first indication of neutrino oscillations was from the Ray Davis Homestake Mine experiment [30] which began operation in the 1960s. Ray Davis was an expert chemist and designed a radiochemical experiment to measure the flux of neutrinos from the sun. The purpose of this experiment was to test John Bahcall's prediction of the fusion rate in the Sun and neutrino flux from it as well. Davis' experiment would need to operate for many years to collect enough statistics due to the expected low capture rate. Measurements continued into the 1980s and showed that the flux of neutrinos was about one-third the expected rate and this became known as the “Solar Neutrino Problem.” The primary explanations were either that the solar model was incorrect or the neutrino capture cross section was incorrect. The Sudbury Neutrino Observatory (SNO) was able to resolve this problem by making a model-independent measurement of the solar neutrino flux. The SNO experiment observed a ν_e CC-to-NC ratio of 0.301 ± 0.033 , which confirmed that only about 30% of neutrinos arrive as ν_e flavors on Earth. In other words, the majority of neutrinos arrive as the wrong flavor [87].

Another outstanding problem emerged with measurements of atmospheric neutrinos, which are the muon and electron types. Atmospheric neutrinos are produced when high

energy cosmic rays strike atmospheric particles. These cosmic ray collisions generate mostly pions and kaons that decay into neutrinos. When trying to measure the ν_μ/ν_e ratio, there was another significant deficit. This was particularly apparent for the Super-Kamiokande (SK) experiment, which is a 50 kt tank of pure water lined with thousands of photomultiplier tubes designed to observe solar and atmospheric neutrinos. It was the first experiment to perform a neutrino oscillation analysis that successfully explained the deficit.

The observation of neutrino oscillations is a relatively new discovery. Bruno Pontecorvo [62] first proposed such a mechanism in 1957 between neutrinos and antineutrinos much like known neutral K-mesons oscillations. However, oscillations between flavored neutrinos was not expected since it requires the neutrino to have mass. The reasons why are explained in the next subsection.

1.1.2.1 Two Flavor Derivation of Neutrino Oscillations

The phenomenon of neutrino oscillations can be described with elementary, non-relativistic quantum mechanics using the Schrödinger Equation

$$-\frac{\hbar}{i} \frac{d}{dt} |\nu(\mathbf{r}, t)\rangle = \hat{H} |\nu(\mathbf{r}, t)\rangle, \quad (1.24)$$

where \hat{H} is the Hamiltonian for the physical system. Here we consider massive neutrinos of mass m_j in its rest frame (free particle). The Hamiltonian is diagonal in this case, which acting on $|\nu_j\rangle$ results in the eigenvalue equation

$$\hat{H} |\nu_j(\mathbf{r}, t)\rangle = E_j |\nu_j(\mathbf{r}, t)\rangle, \quad (1.25)$$

where E_j is the energy of the neutrino $|\nu_j\rangle$. Substituting (1.25) into (1.24) and solving for $|\nu(\mathbf{r}, t)\rangle$, one obtains

$$|\nu_j(\mathbf{r}, t)\rangle = e^{-iE_j t/\hbar} |\nu_j(\mathbf{r}, t=0)\rangle, \quad (1.26)$$

where $|\nu_j(\mathbf{r}, t = 0)\rangle$ is created with momentum \mathbf{p} at the origin $\mathbf{r} = 0$. The time-independent solution to (1.24) is a plane-wave given by

$$|\nu_j(\mathbf{r}, t = 0)\rangle = e^{i\mathbf{p} \cdot \mathbf{r}/\hbar} |\nu_j\rangle. \quad (1.27)$$

Before being able to describe neutrino oscillations, the basis states must be defined. For this example, consider that there are only two eigenstates, labeled ν_1 and ν_2 , in the “mass” basis with definite mass m_1 and m_2 , respectively. However, experiments can produce neutrinos, as well as probe them, only in a definite flavor state, denoted by a Greek letter subscript. Let the generated neutrino, which is a linear superposition of mass states 1 and 2, have momentum \mathbf{p} and flavor α . Since both mass eigenstates share the same momentum \mathbf{p} (but not energy!), the exponential term in (1.27) is an overall phase that will cancel out later. One can postulate a linear transformation, U , between the basis states given by

$$\begin{bmatrix} \nu_\alpha \\ \nu_\beta \end{bmatrix} = \begin{bmatrix} U_{11} & U_{12} \\ U_{21} & U_{22} \end{bmatrix} \begin{bmatrix} \nu_1 \\ \nu_2 \end{bmatrix} \quad (1.28)$$

This linear transformation must be a unitary matrix ($U^{-1} = U^\dagger$, \dagger = transpose conjugate) since the states $\nu_{1,2}$ constitute a complete orthonormal basis in the mass basis. With this unitary property, U can be written as a rotation matrix

$$\begin{bmatrix} \nu_\alpha \\ \nu_\beta \end{bmatrix} = \begin{bmatrix} \cos(\theta) & \sin(\theta) \\ -\sin(\theta) & \cos(\theta) \end{bmatrix} \begin{bmatrix} \nu_1 \\ \nu_2 \end{bmatrix}, \quad (1.29)$$

where θ is the angle between the two bases. One can imagine this transformation between bases as shown in Figure 1.6 on page 16. The probability of creating a neutrino of flavor α and later observing it as flavor $\beta \neq \alpha$ at time $t = T > 0$ is given by

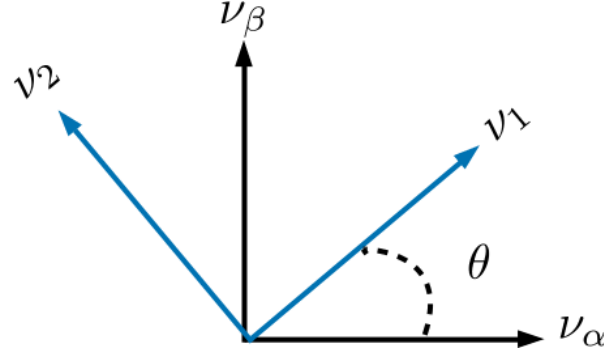


Figure 1.6: Illustration of a mixing matrix in two dimension.

$$\begin{aligned}
 \mathcal{P}(\nu_\alpha \rightarrow \nu_\beta) &= |\langle \nu_\alpha(t=0) | \nu_\beta(t=T) \rangle|^2 \\
 &= |\{\cos(\theta) \langle \nu_1(t=0) | + \sin(\theta) \langle \nu_2(t=0) |\} \\
 &\quad \times \{-\sin(\theta) |\nu_1(t=T)\rangle + \cos(\theta) |\nu_2(t=T)\rangle\}|^2.
 \end{aligned} \tag{1.30}$$

Evaluating all inner products and simplifying terms in (1.30) results in the following equation

$$\mathcal{P}(\nu_\alpha \rightarrow \nu_\beta) = \sin^2(2\theta) \sin^2\left(\frac{E_1 - E_2}{2\hbar} T\right). \tag{1.31}$$

The terminology of “neutrino oscillations” should be more apparent now since (1.31) demonstrates that the probability changes sinusoidally as a function of time T . This equation is not, however, terribly useful in the laboratory frame since it is hard to design an experiment where the travel time an individual neutrino is actually measured. Since neutrinos are nearly massless, they travel very close to the speed of light. Therefore time T is replaced with L/c where L is the distance between the neutrino origin and detection. One can also approximate the energy of the mass eigenstate as

$$\begin{aligned}
E_j &= \left(m_j^2 c^4 + p_j^2 c^2 \right)^{\frac{1}{2}} = p_j c \left(1 + \frac{m_j^2 c^2}{p_j^2} \right)^{\frac{1}{2}} \\
&\approx p_j c \left(1 + \frac{m_j^2 c^2}{2p_j^2} + \mathcal{O} \left(\frac{m_j c}{p_j} \right)^4 \right) \\
&\approx E_\nu + \frac{m_j^2 c^4}{2E_\nu},
\end{aligned} \tag{1.32}$$

where for oscillation experiments $p_j \gg m_j c$ and $p_j c \approx E_\nu$ where E_ν is the neutrino energy as measured in the laboratory. Substituting these assumptions in (1.31), the oscillation probability is given by

$$\mathcal{P}(\nu_\alpha \rightarrow \nu_\beta) = \sin^2(2\theta) \sin^2 \left(\frac{\Delta m^2 c^3}{4\hbar} \frac{L}{E_\nu} \right), \tag{1.33}$$

where $\Delta m^2 = m_2^2 - m_1^2$ is the mass-squared difference between the mass states.

For a moment consider evaluating all the physical constants in natural units ($c = \hbar = 1$), the Δm^2 in eV², L in km, and E_ν in GeV. The oscillation probability from between states ν_α to ν_β is given by

$$\mathcal{P}(\nu_\alpha \rightarrow \nu_\beta) = \sin^2(2\theta) \sin^2 \left(1.27 \frac{\Delta m^2}{[\text{eV}^2]} \frac{L/E_\nu}{[\text{km}/\text{GeV}]} \right) \text{ [natural units]} \tag{1.34}$$

which more clearly illustrates the physics of neutrino oscillations. The oscillation probability has an amplitude of $\sin^2(2\theta)$ and varies with frequency inversely proportional to Δm^2 as shown in Figure 1.7 on page 18. Since L and E_ν are the only controllable parameters for an oscillation experiment, probing θ or Δm^2 can be difficult unless the experiment can probe a large range of L/E_ν as shown in Figure 1.8 on page 19.

1.1.2.2 Three Flavor Oscillations

In the general case of oscillations using a $n \times n$ mixing matrix, the unitary transformation can be written as a rotation matrix with $\frac{n}{2}(n-1)$ weak mixing angles with $\frac{1}{2}(n-2)(n-1)$ Charge-Parity (CP) violating phases. In addition, oscillations are dictated by a total of $n-1$

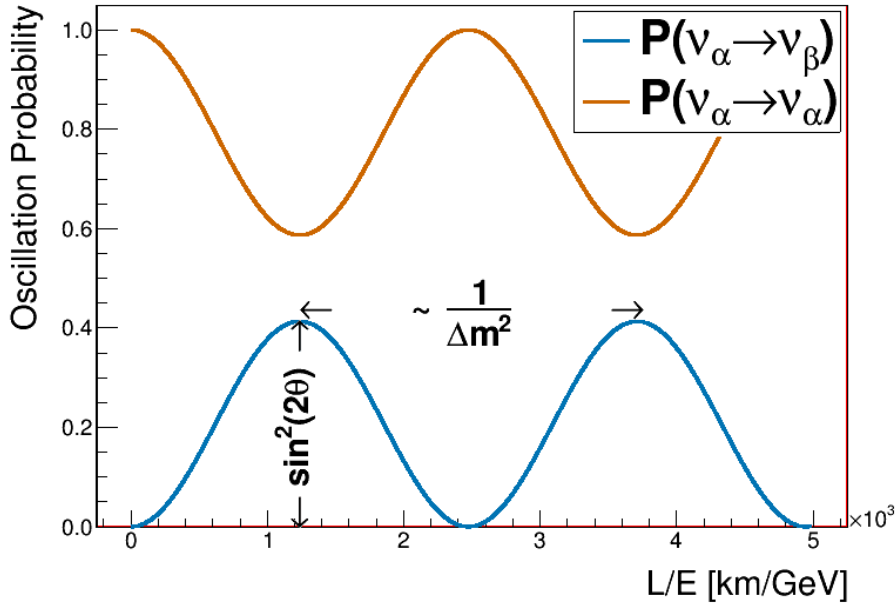


Figure 1.7: Two flavor oscillation probability as a function L/E is shown using $\theta = 20^\circ$ and $\Delta m^2 = 10^{-3} \text{ eV}^2/c^4$. The spacing between adjacent peaks/troughs is proportional to the inverse of Δm^2 . Note that $\mathcal{P}(\nu_\alpha \rightarrow \nu_\alpha) = 1 - \mathcal{P}(\nu_\alpha \rightarrow \nu_\beta)$ since the oscillation probability must always sum to 1.

mass-squared splittings [87]. This all assumes that neutrinos obey the Dirac Equation, or that they are not their own antiparticles. The favored mixing model is a 3×3 matrix since there are three known neutrino flavors, ν_e , ν_μ , and ν_τ . This means that there are three (3) mixing angles, one (1) CP violating phase, and three (3) mass-squared splittings.

The most frequently used matrix parameterization is the MNSP (MNSP: Maki-Nakagawa-Sakata-Pontecorvo) matrix. Pontecorvo is credited with first conceiving of neutrino oscillations, albeit between neutrino and antineutrinos [61]. It was Maki, Nakagawa, and Sakata who conceived of the parameterization based on the ideas of Pontecorvo [57]. The MNSP matrix is decomposed into separate rotation matrices as given by (1.35)

$$U_{\text{MNSP}} = \underbrace{\begin{bmatrix} 1 & 0 & 0 \\ 0 & c_{32} & s_{32} \\ 0 & -s_{32} & c_{32} \end{bmatrix}}_{U_{32}=U_{\text{atm}}} \times \underbrace{\begin{bmatrix} c_{31} & 0 & s_{31}e^{i\delta_{\text{CP}}} \\ 0 & 1 & 0 \\ -s_{31}e^{-i\delta_{\text{CP}}} & 0 & c_{31} \end{bmatrix}}_{U_{31}=U_{\text{rea}}} \times \underbrace{\begin{bmatrix} c_{21} & s_{21} & 0 \\ -s_{21} & c_{21} & 0 \\ 0 & 0 & 1 \end{bmatrix}}_{U_{21}=U_{\text{sol}}}, \quad (1.35)$$

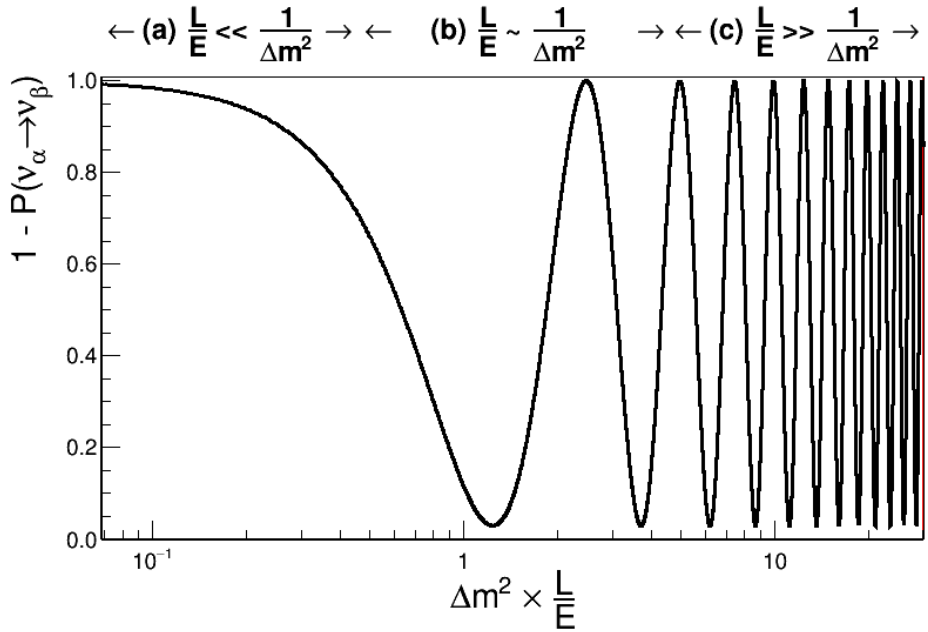


Figure 1.8: Semi-logarithmic plot of the survival probability of flavor α ($1 - \mathcal{P}(\nu_\alpha \rightarrow \nu_\beta) = \mathcal{P}(\nu_\alpha \rightarrow \nu_\alpha)$) over a wide range of L/E values for $\theta = 40^\circ$. The arrows above the plot coarsely denote three possible cases: (a) no oscillations ($L/E \ll 1/\Delta m^2$); (b) sensitivity to oscillations ($L/E \sim 1/\Delta m^2$); (c) only average measurement ($L/E \gg 1/\Delta m^2$). Image originally inspired by reference [71].

where

$$c_{ij} = \cos \theta_{ij}, \quad s_{ij} = \sin \theta_{ij}, \quad (1.36)$$

and δ_{CP} represents the CP violating phase. Each rotation matrix U_{ij} represents the different sources for neutrino oscillations experiments with “atm”, “rea”, and “sol” representing atmospheric ν ’s, nuclear reactor ν ’s, and solar ν ’s, respectively. The sensitivity of neutrino oscillations for different sources is given in Table 1.1 on page 20.

If neutrinos are their own antiparticles, they are not described by the Dirac Equation but instead are described the Majorana Equation. This adds two (in general $n - 1$) more CP violating Majorana phases, α and β , to the MNSP matrix

Source	Species	Baseline [km]	Mean Energy [GeV]	$\min(\Delta m^2) [\text{eV}^2]$
Reactor	$\bar{\nu}_e$	1	$\sim 10^{-3}$	$\sim 10^{-3}$
Reactor	$\bar{\nu}_e$	100	$\sim 10^{-3}$	$\sim 10^{-5}$
Accelerator	$\nu_\mu, \bar{\nu}_\mu$	1	~ 1	~ 1
Accelerator	$\nu_\mu, \bar{\nu}_\mu$	10^3	~ 1	$\sim 10^{-3}$
Atmospheric ν 's	$\nu_{e,\mu}, \bar{\nu}_{\mu,e}$	10^4	~ 1	$\sim 10^{-4}$
Sun	ν_e	1.5×10^8	$\sim 10^{-3}$	$\sim 10^{-11}$

Table 1.1: Sensitivity of different oscillation experiments originally published in reference [77].

$$U_{\text{MNSP}} \rightarrow U_{\text{MNSP}} \times \overbrace{\begin{bmatrix} 1 & 0 & 0 \\ 0 & e^{i\alpha} & 0 \\ 0 & 0 & e^{i\beta} \end{bmatrix}}^{U_{\text{Majorana}}}. \quad (1.37)$$

Unfortunately, neutrino oscillations are not able to probe the Majorana phases since the Majorana matrix is diagonal. The question of as to whether neutrinos are Majorana ($\nu = \bar{\nu}$) or Dirac ($\nu \neq \bar{\nu}$) particles is an open question that is being explored by neutrino-less double beta decay experiments [70].

The full three flavor oscillation probability is given by

$$\begin{aligned} \mathcal{P}(\nu_\alpha \rightarrow \nu_\beta) = & \delta_{\alpha\beta} - 4 \sum_{j=1}^3 \left[\sum_{i>j}^3 \text{Re}(K_{\alpha\beta,ij}) \sin^2(\phi_{ij}) \right] \\ & + 4 \sum_{j=1}^3 \left[\sum_{i>j}^3 \text{Im}(K_{\alpha\beta,ij}) \sin(\phi_{ij}) \cos(\phi_{ij}) \right], \end{aligned} \quad (1.38)$$

where

$$K_{\alpha\beta,ij} = U_{\alpha i} U_{\beta i}^* U_{\alpha j}^* U_{\beta j} \quad (1.39)$$

encapsulates the MNSP matrix elements and

$$\phi_{ij} = \frac{\Delta m_{ij}^2 c^3}{4\hbar} \frac{L}{E_\nu}. \quad (1.40)$$

Since CP violation means that $\mathcal{P}(\nu_\alpha \rightarrow \nu_{\beta \neq \alpha}) \neq \mathcal{P}(\bar{\nu}_\alpha \rightarrow \bar{\nu}_{\beta \neq \alpha})$, CP violating terms must be odd function of δ_{CP} . Consider the following two examples, muon neutrino survival and muon neutrino to electron neutrino appearance.

Muon Neutrino Survival The probability of a muon type neutrinos (antineutrinos) surviving is given by

$$\begin{aligned}\mathcal{P}\left(\overset{(-)}{\nu}_\mu \rightarrow \overset{(-)}{\nu}_\mu\right) &= 1 - 4s_{23}^2 c_{13}^2 \left(V_{\cos \delta_{\text{CP}}}\right) \sin^2 \phi_{31} \\ &\quad - 4s_{23}^2 c_{13}^2 \left(Z_{\cos \delta_{\text{CP}}}\right) \sin^2 \phi_{32} \\ &\quad - 4 \left(V_{\cos \delta_{\text{CP}}}\right) \left(Z_{\cos \delta_{\text{CP}}}\right) \sin^2 \phi_{21},\end{aligned}\tag{1.41}$$

where

$$V_{\cos \delta_{\text{CP}}} = s_{12}^2 c_{23}^2 + s_{13}^2 s_{23}^2 c_{12}^2 + 2s_{12}s_{13}s_{23}c_{12}c_{23} \cos \delta_{\text{CP}},\tag{1.42}$$

$$Z_{\cos \delta_{\text{CP}}} = c_{12}^2 c_{23}^2 + s_{13}^2 s_{23}^2 s_{12}^2 - 2s_{12}s_{13}s_{23}c_{12}c_{23} \cos \delta_{\text{CP}},\tag{1.43}$$

and $\overset{(-)}{\nu}_\mu$ represents either ν_μ or $\bar{\nu}_\mu$. If a definitive measurement of $\mathcal{P}(\nu_\mu \rightarrow \nu_\mu) \neq \mathcal{P}(\bar{\nu}_\mu \rightarrow \bar{\nu}_\mu)$ in vacuum occurs, it implies that the combined C, P and time (CPT) symmetry is violated⁴.

Electron Neutrino Appearance The previous subsection briefly explored the muon disappearance probability, which is not tested as a channel for CP violation. Electron neutrino appearance, however, does provide insight into CP violation in the lepton sector. The appearance probability of electron neutrino types from muon neutrino types is given by

⁴When going to through matter however, the oscillation probability is affected. This is explained more in Section 1.1.2.3.

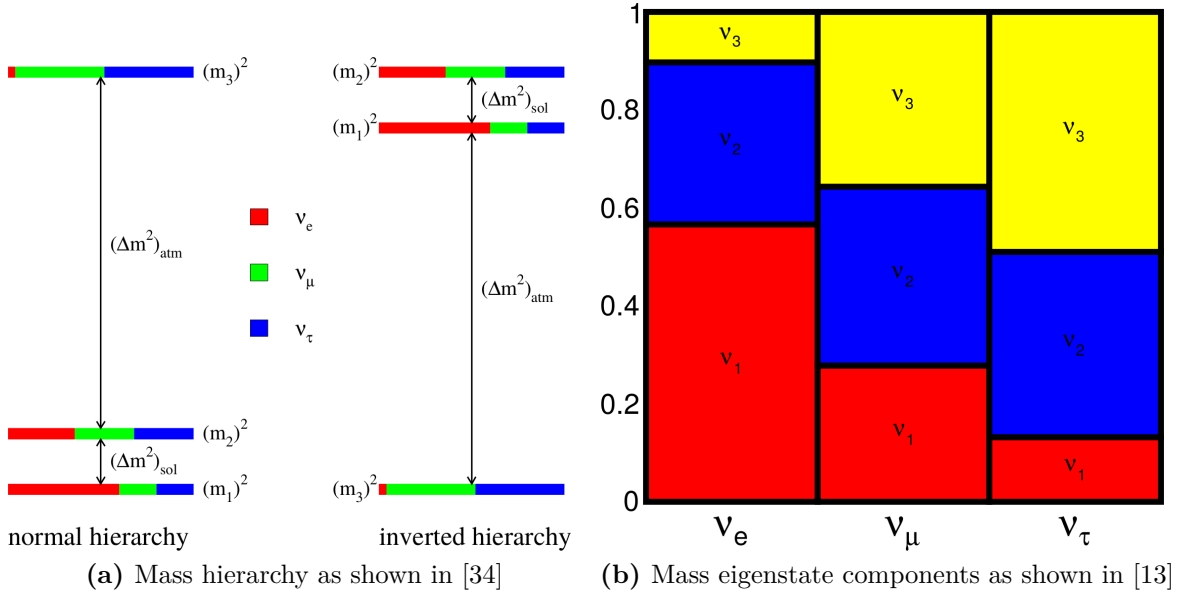


Figure 1.9: Neutrino mass hierarchy problem and MNSP representation. Left: the mass hierarchy problem is shown. The colored bars for each mass eigenstate correspond to the approximate flavor content of the neutrino. For example, state “2” has about equal three portions of all three flavors. Right: the mass eigenstate components of each flavor eigenstate. This is a complementary demonstration of the MNSP matrix.

$$\begin{aligned}
 \mathcal{P} \left(\overset{(-)}{\nu}_\mu \rightarrow \overset{(-)}{\nu}_e \right) = & 4 c_{13}^2 s_{13}^2 s_{23}^2 \sin^2 \phi_{31} \\
 & + 8 \left(X_{\cos \delta_{\text{CP}}} \right) \cos \phi_{23} \sin \phi_{31} \sin \phi_{21} \\
 & - \underbrace{8 \left(Y_{\sin \delta_{\text{CP}}} \right)}_{\text{CP violating}} \sin \phi_{32} \sin \phi_{31} \sin \phi_{21} \\
 & + 4 \left(Z_{\cos \delta_{\text{CP}}} \right) s_{12}^2 c_{13}^2 \sin^2 \phi_{21}, \tag{1.44}
 \end{aligned}$$

where

$$X_{\cos \delta_{\text{CP}}} = c_{13}^2 s_{12} s_{13} s_{23} (c_{12} c_{23} \cos \delta_{\text{CP}} - s_{12} s_{13}), \tag{1.45}$$

$$Y_{\sin \delta_{\text{CP}}} = \frac{1}{8} \sin (2\theta_{12}) \sin (2\theta_{13}) \sin (2\theta_{23}) c_{13} \sin \delta_{\text{CP}}, \tag{1.46}$$

and (+) represents the sign change from neutrinos to antineutrinos. The CP violating term (1.46) is also known as the Jarlskog Invariant and is a measure of CP violation independent

Parameter	Normal Hierarchy	Inverted Hierarchy	Units
Δm_{32}^2	2.51 ± 0.05	-2.56 ± 0.04	10^{-3} eV 2
Δm_{21}^2		7.53 ± 0.18	10^{-5} eV 2
$\sin^2(\theta_{21})$		$0.307^{+0.013}_{-0.012}$	1
$\sin^2(\theta_{32})$	$\begin{cases} 0.417^{+0.025}_{-0.028} & \theta_{32} \in (0, \frac{\pi}{2}) \\ 0.597^{+0.024}_{-0.030} & \theta_{32} \in (\frac{\pi}{2}, \frac{\pi}{4}) \end{cases}$	$\begin{cases} 0.421^{+0.033}_{-0.025} & \theta_{32} \in (0, \frac{\pi}{2}) \\ 0.592^{+0.023}_{-0.030} & \theta_{32} \in (\frac{\pi}{2}, \frac{\pi}{4}) \end{cases}$	1
$\sin^2(\theta_{31})$		2.12 ± 0.08	10^{-2}
δ_{CP}	217^{+40}_{-28}	280^{+25}_{-28}	degrees

Table 1.2: Global best fit for the oscillation parameters. All values except for δ_{CP} are combined values from the Particle Data Group and δ_{CP} is from the 2018 NuFit analysis [35, 77].

of the mixing parameterization [51]. This oscillation channel is of primary importance in current and future proposed accelerator and atmospheric neutrino oscillation experiments.

Current and next generation experiments aim to improve knowledge of the mixing parameters. There are a couple of degeneracies to unravel as well as precise measurement of δ_{CP} . While the two defined mass-squared splittings $\Delta m_{21}^2 = \Delta m_{\text{sol}}^2$ and $\Delta m_{32}^2 = \Delta m_{\text{atm}}^2$ are known, it is unknown which eigenstates are more massive. This problem is known as the mass hierarchy problem and is illustrated in Figure 1.9a on page 22. Normal hierarchy refers to the case where $m_3 > m_2 > m_1$ whereas the inverted hierarchy has $m_2 > m_1 > m_3$. Also distinguishing if θ_{23} is in the first octant $\theta \in (0, \pi/2)$ or second octant $\theta \in (\pi/2, \pi/4)$ of the unit circle requires large statistics. Finally the value of δ_{CP} is quite uncertain with values in the 3rd and 4th quadrants. Best fit measurements of the oscillations parameters are given in Table 1.2 on page 23.

1.1.2.3 Matter Effects

Traveling through matter has the potential to increase the sensitivity of neutrino oscillation measurements if the baseline is long enough. Known as the Mikheyev-Smirnov-Wolfenstein (MSW) effect [82], all oscillations are affected by coherent forward scattering of

neutrinos with electrons in the media. Taking the example of $\overset{(-)}{\nu}_\mu \rightarrow \overset{(-)}{\nu}_e$ from (1.41), the MSW effect to first order is

$$\begin{aligned} \mathcal{P}\left(\overset{(-)}{\nu}_\mu \rightarrow \overset{(-)}{\nu}_e\right) &\rightarrow \mathcal{P}\left(\overset{(-)}{\nu}_\mu \rightarrow \overset{(-)}{\nu}_e\right) + \frac{8\alpha}{\Delta m_{31}^2} \left(c_{13}^2 s_{13}^2 s_{23}^2\right) \left(1 - 2s_{13}^2\right) \\ &\times \left(\sin^2 \phi_{31} \overset{(+) \text{ under } \phi_{31}}{-} \underbrace{\left(\frac{\Delta m_{31}^2 c^3}{4\hbar} \frac{L}{E_\nu}\right)}_{\phi_{31}} \cos \phi_{32} \sin \phi_{31}\right), \end{aligned} \quad (1.47)$$

where

$$\alpha = 2\sqrt{2}G_F n_e E_\nu, \quad (1.48)$$

and n_e is the average electron density of the Earth through which the neutrinos travel [16]. Carefully studying (1.47) reveals that the MSW effect alters the oscillation probability as a function of the electron density and increases in magnitude with baseline.

1.1.3 CP Violation: Origins of Matter

The observation of CP violation in the lepton sector might provide critical insight into the origins of the matter. CP violation dictates that certain interactions behave differently between matter or antimatter like $\mathcal{P}(\nu_\mu \rightarrow \nu_e) \neq \mathcal{P}(\bar{\nu}_\mu \rightarrow \bar{\nu}_e)$. The Big Bang Theory suggests that in the first fractions of a second of the Universe, equal amounts of matter and antimatter were created. However, observational evidence shows the Universe consists of only 4.5% baryonic matter (i.e. protons and neutrons) from cosmological models as shown in Figure 1.10 on page 25. The anti-baryonic fraction of the baryonic matter is infinitesimally low from external constraints on data from gamma-ray telescopes like Fermi-GLAST [80]. This problem is known as the Baryon Asymmetry of the Universe (BAU).

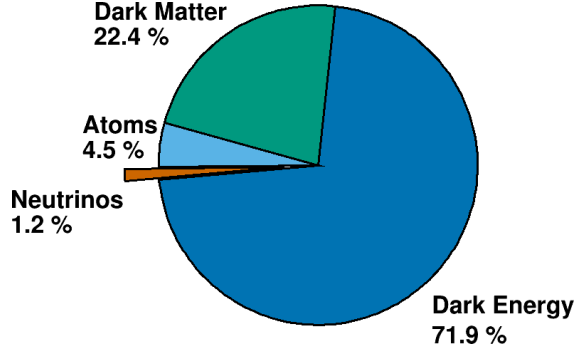


Figure 1.10: The matter and energy content of the Universe. The observable Universe contains about 4.5% of atoms (baryons and electrons) and an estimated neutrino content less than 1.2%. The rest of the Universe consists of Dark Matter at 22.4% and a form of energy called Dark Energy at 71.9%. These inferred parameters are taken from the Λ CDM model, the simplest model that describes the cosmos [53].

The process of Baryogenesis⁵ is a favored model to explain the BAU and lacks a necessary precursor mechanism. One of the necessary conditions for Baryogenesis [68] is C symmetry violation and CP violation. Evidence of CP violation has been experimentally confirmed in the quarks, but not to the level which resolves the BAU. Baryogenesis can be achieved by having Leptogenesis⁶ occur first through the decay of very heavy, right handed Majorana neutrino ($\nu = \bar{\nu}$) through the *see-saw* mechanism. Detailed discussions on Leptogenesis and the *see-saw* mechanism can be found in the following reference [13].

1.1.4 Long-Baseline Neutrino Oscillation Experiments

The KEK to Kamioka (K2K) experiment was the first neutrino oscillation experiment where researchers controlled the production and observation of neutrinos. In K2K, a beam of muon neutrinos were directed from the 12 GeV proton synchrotron at KEK to the Kamioka Observatory at a distance of 250 km. While traveling through the Earth, the neutrinos

⁵Baryogenesis is the mechanism by which matter and antimatter baryons are created in the early Universe.

⁶Leptogenesis is the mechanism by which leptons and anti-leptons are created in the early Universe.

oscillate before they are observed at Kamioka. Prior to K2K, neutrino sources included the atmosphere, the Sun, and one supernova.

The K2K experiment established the experimental methods for current and planned next generation long-baseline neutrino oscillation experiments from accelerators. The accelerator neutrinos are produced when a high energy proton beam hits a target. The secondary particles are then forward focused using electrically pulsed magnets and allowed to decay in a large decay volume. This generates a highly pure muon neutrino beam with order 1% electron neutrino contamination. Prior to any oscillations, a “near” detector is used to measure the neutrino flux as function of neutrino energy and study detector systematic uncertainties associated at the “far” detector at Kamioka. The successor experiment to K2K called Tokai to Kamioka (T2K), closely followed this design methodology. Other notable accelerator-based long-baseline experiments include MINOS [87] and NO ν A [12], both in the United States.

1.2 Tokai to Kamioka Experiment

The Tokai to Kamioka (T2K) experiment is a long-baseline, neutrino oscillation experiment hosted in Japan [1] as shown in Figure 1.11 on page 27. It is the successor experiment to the K2K neutrino oscillation experiment also hosted in Japan. The T2K experiment produces a high intensity, relatively pure muon neutrino beam at the Japan Proton Accelerator Complex (J-PARC) which is a world class particle accelerator facility. The beam is directed at the Super-Kamiokande (SK) [40] detector, which is 295 km away from the source. Additionally, the beam is designed to maximize the $\nu_\mu \rightarrow \nu_e$ probability at the far detector $L = 295$ km baseline using a neutrino energy spectrum sharply peaked at $E_\nu = 0.6$ GeV as shown in Figure 1.12 on page 28. This spectrum is achieved by directing the center of the beam axis 2.5 degrees off center from SK. Along the beamline at 280 m from the beam source is the near detector facility called ND280 [37], whose data is used in thesis. The ND280 fa-

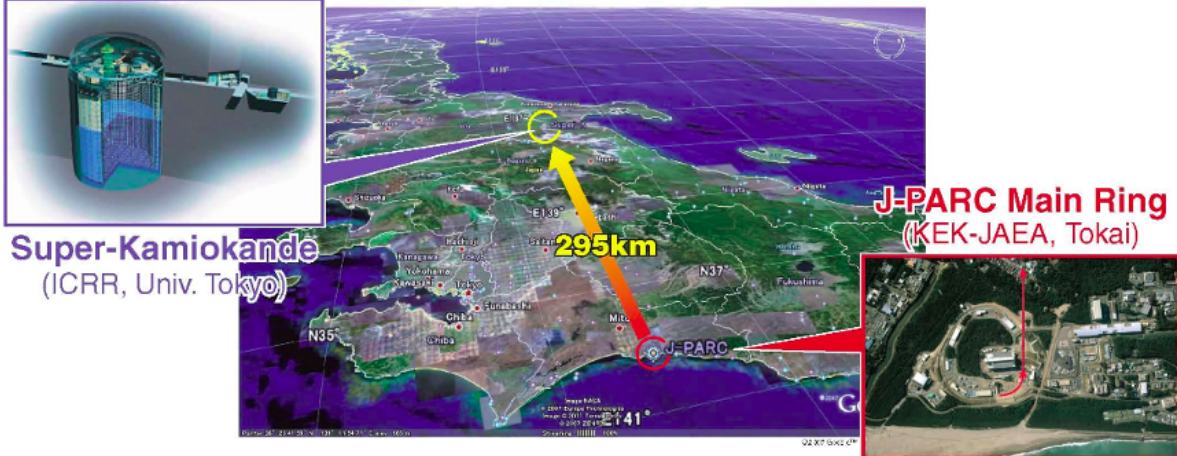


Figure 1.11: Birds eye view of the T2K experiment on the Japanese archipelago. An intense beam of neutrinos is produced at the J-PARC site (bottom right red box) using high energy protons. The beam is directed towards the Super-Kamiokande detector (top left blue box) at a distance of 295 km away from J-PARC.

cility is designed to observe and characterize the unoscillated neutrino beam. There are two detectors at ND280: the primary, off-axis detector and on-axis detector. The measurement in this thesis uses data collected from the off-axis near detector.

The T2K experiment was primarily designed to measure the last unknown MNSP mixing angle θ_{13} , which was thought to be nearly zero, via the $\nu_\mu \rightarrow \nu_e$ channel. In addition it aims to make a precision measurement the atmospheric mixing parameters, θ_{23} and Δm_{23}^2 via the $\nu_\mu \rightarrow \nu_\mu$ channel. An early landmark for the T2K experiment was a 7.3σ measurement excluding non-zero θ_{13} in 2013 [3]. It continues to be a world leader in oscillation physics and as of 2018 rejects CP conserving values ($\delta_{\text{CP}} = 0, \pi$) at the 2σ level [9].

The following topics will be discussed in the following order. First a look how neutrinos are produced at J-PARC. Next a detailed look at the T2K near detectors which are used in this thesis. This is followed by a discussion on Super-Kamiokande, the T2K far detector. The final topic is an examination of the near detector constraint and its importance in the oscillation analysis.

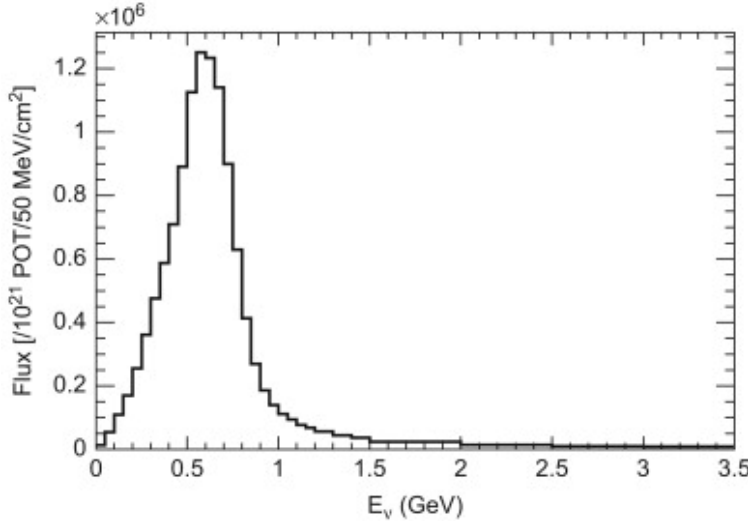


Figure 1.12: The T2K experiment’s unoscillated ν_μ flux at Super-Kamiokande at the off-axis angle of 2.5° .

1.2.1 Neutrino Production at J-PARC

To facilitate the high intensity neutrino beam requirements for T2K, the J-PARC site generates a high intensity proton beam through a series of particle accelerators. A bird’s eye view of J-PARC can be seen in Figure 1.13 on page 29 which highlights its accelerators and other facilities. For this section, note that all beam energies are kinetic energies.

Protons for the T2K beamline are first accelerated in the J-PARC linear accelerator⁷ (linac) and then the rapid cycle synchrotron⁸ (RCS). Hydrogen ions (${}_1^1\text{H}^-$) are extracted from plasma in a electrical discharge chamber and fed through a series of linac elements as shown in Figure 1.14a on page 30. Each linac element, except for the initial quadrupole magnet, accelerates the ions using carefully synchronized oscillating electric fields generated by radio frequency pulses. After traveling 240 m along the linac, the ions have been boosted to 181 MeV of kinetic energy and transported into the RCS. While in transit to the RCS, the

⁷A linear accelerator accelerates particles using time varying electric fields along a one direction, terminal beamline. Linear accelerators are also used in the medical field to generate X-rays.

⁸A synchrotron is cyclic particle accelerator that relies on time varying magnetic fields to accelerate particles. Since they require many magnets and large spaces to operate, they are usually operated at national laboratories for others uses like material and life sciences.

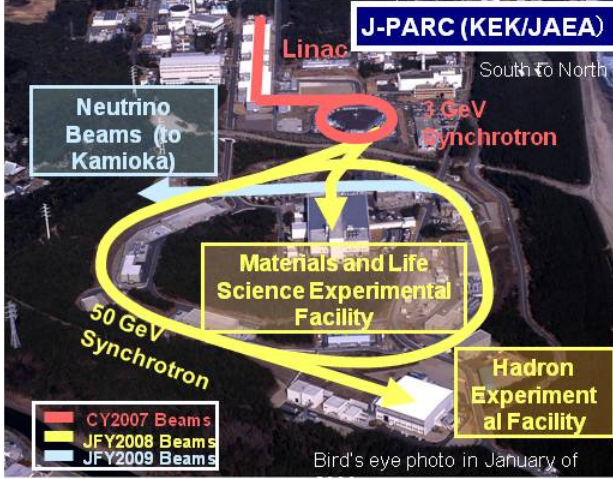
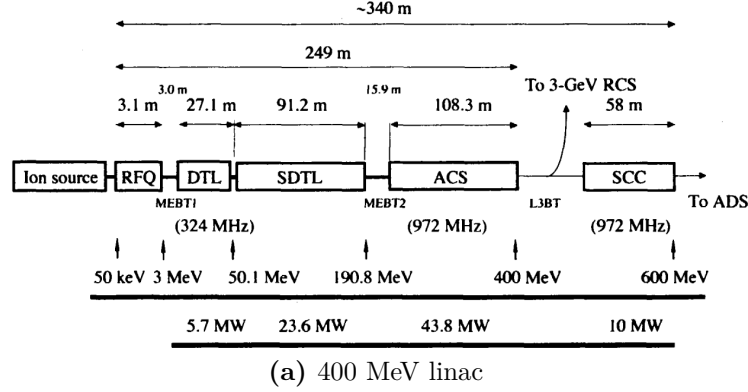


Figure 1.13: Bird's eye view of the J-PARC laboratory showing the primary components of its accelerator programs. To generate the high intensity neutrino beam, first the linear accelerator (Linac, red) accelerates protons into the 3 GeV Synchrotron (also red) called the rapid-cycle synchrotron (RCS). The RCS then injects some of its protons into the 50 GeV Synchrotron (yellow) called the main ring (MR), which currently runs at 30 GeV. Finally the MR protons are directed into a target material along the neutrino beamline (teal) [27].

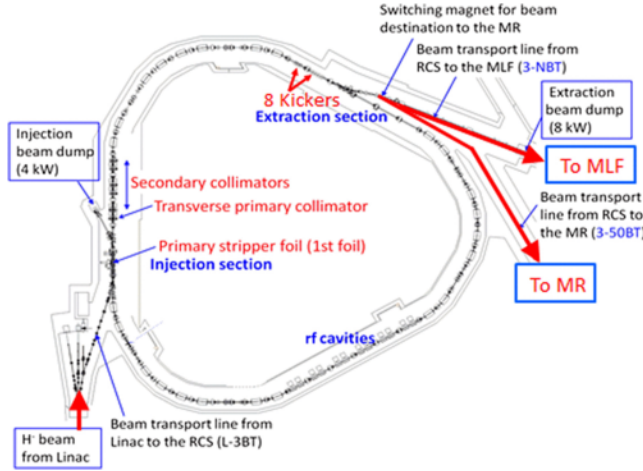
ions are stripped of their electrons via charge stripping foils. The 348 m circumference RCS then further boosts the protons to 3 GeV at an operating frequency of 25 Hz. While being accelerated, protons are aggregated into two bunches and focused using particle collimators as shown in Figure 1.14b on page 30.

The next stage for the protons intended for the neutrino beamline is the much larger main ring (MR) synchrotron as shown in Figure 1.14c on page 30 which has a circumference of 1567 m. While nominally designed to boost protons to 50 GeV, it currently operates at 30 GeV. Protons are injected into the MR to form eight proton bunches (spill), initially six when T2K first ran, before entering the neutrino beamline. The total temporal width of the spill is approximately $0.5 \mu\text{s}$ [1]. At a spill cycle frequency of 0.5Hz, the bunches are extracted from the MR into the neutrino beamline.

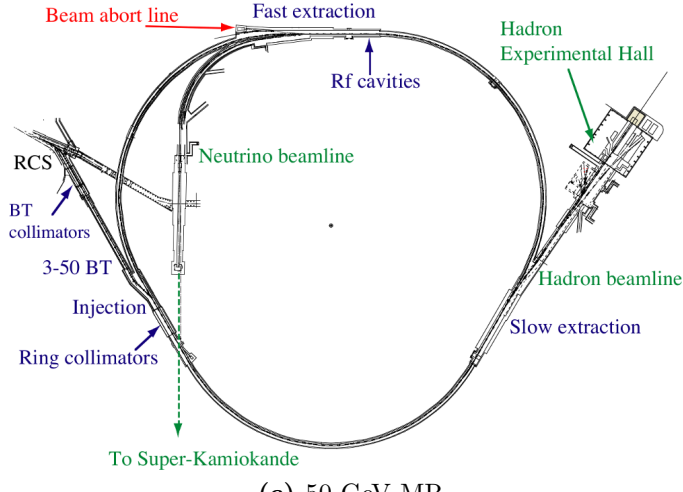
The neutrino beamline is designed to direct the protons toward SK and generate neutrinos by striking them into the end of a cylindrical target. Figure 1.15a on page 31 shows the process of proton extraction from the MR for both primary and secondary neutrino beamlines. In the primary beamline, a series of normal and superconducting magnets steer the



(a) 400 MeV linac

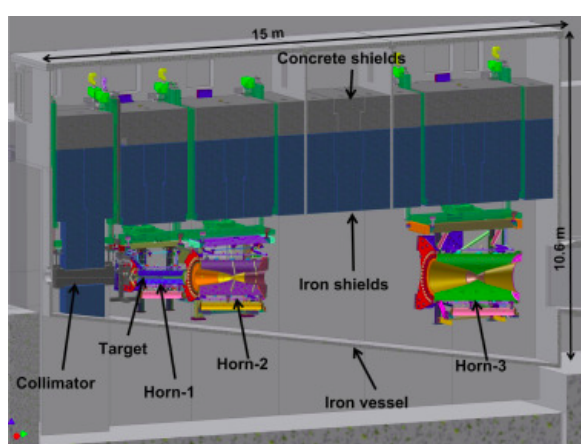
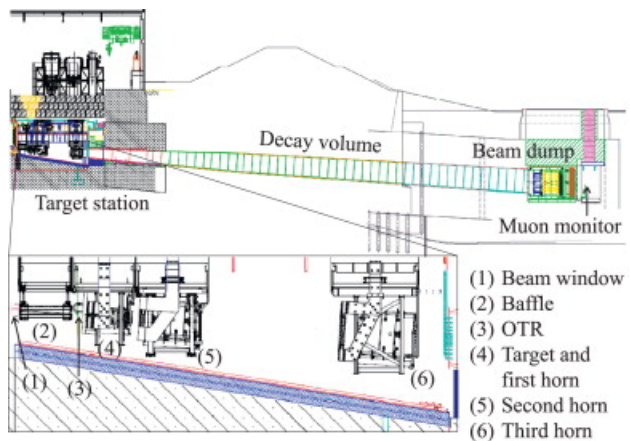
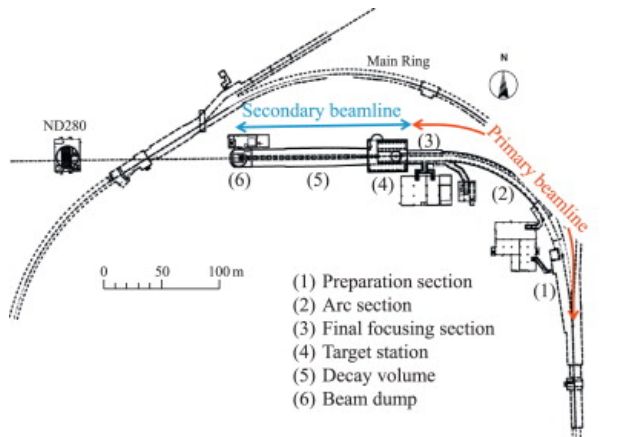


(b) 3 GeV RCS



(c) 50 GeV MR

Figure 1.14: Schematics of the J-PARC accelerators. (a) The linac accelerates hydrogen ions to 181 MeV of kinetic energy, designed for 400 MeV, from the ion source [84]. (b) Protons from the linac are collected into the RCS and accelerated to 3 GeV [67]. (c) Protons from the RCS are injected into the MR synchrotron. While the MR is designed for 50 GeV, it currently operates at 30 GeV.



(c) Beamlne horns

Figure 1.15: The neutrino beamline at J-PARC consists of a primary and secondary beamline. (a) The primary beamline redirects the protons towards the secondary beamline [1]. (b) In the secondary beamline, the protons are impinged on a cylindrical target producing mostly pions. The pions are focused using in sequence horns and decay in a long decay volume. Any non-decayed particles are stopped at the beam dump. (c) A further zoomed in cross section of the target station showing the target and focusing horns [74].



(a) A graphite target at the target station



(b) A magnetic focusing horn

Figure 1.16: Photographs of the T2K target station. (a) The graphite rod being extracted from the target station is shown in the black-dashed box. (b) One focusing horn in T2K.

proton beam away from the MR first along a 54 m preparation section and then a 147 m arc section to bend the beam towards SK. A final focusing section in the primary beamline focuses the protons into the secondary beam while directing it downwards 3.637° with respect to the local horizontal. Since a well-tuned and stable proton beam is necessary for neutrino production, numerous beam monitors are installed along the primary beamline to measure any losses.

The secondary beamline marks the end of the proton beam and production of a neutrino beam as shown in Figure 1.15b on page 31. It consists of a target station, a decay volume for the outgoing particles from the target station, and a beam dump for any remaining particles. The target station houses a 91.4 cm long, 2.6 cm diameter, and 1.8 g/cm^3 graphite rod, which corresponds to 1.9 radiation lengths. When the protons strike the target, strong (nuclear) interactions produce $\pi(\pi)$ -mesons (pions) and K-mesons (kaons) like those produced from cosmic ray collisions in the upper atmosphere. To enhance the flux of neutrinos, a series of three current pulsed, focusing magnets called horns⁹ as shown in Figure 1.15c on page 31 are used to focus the mesons of the correct charge towards SK. Photographs of a graphite

⁹The name horn derives from the fact that the focusing magnets are shaped like brass horns in a music ensemble or marching band. One can think of these horns like a focusing lens for charged particles.

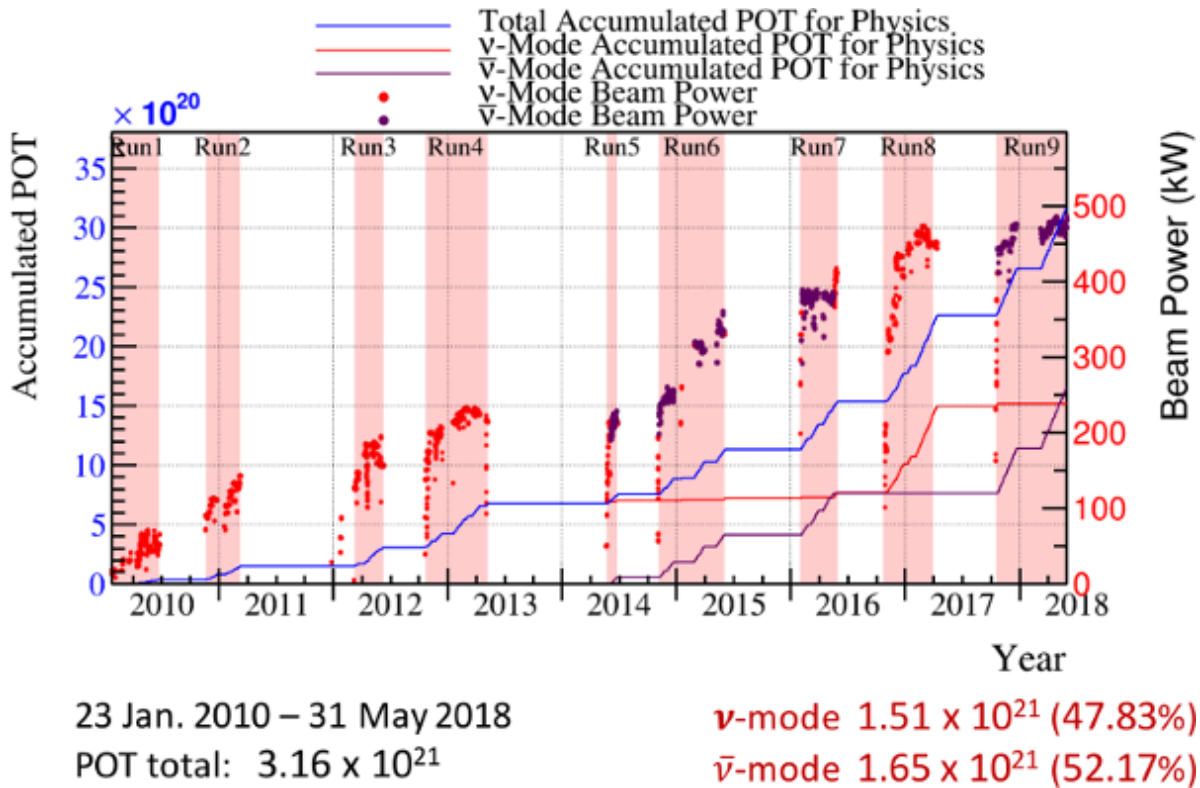


Figure 1.17: The accumulated protons on target for the T2K experiment since 2010 shows a steady increase in beam power over time.

target and focusing horn are shown in Figure 1.16 on page 32. The horns are pulsed at +250 kA (-250 kA) to select positively (negatively) charged pions. The focused pions then decay in the 96 m long decay volume creating a neutrino beam boosted along the secondary beamline direction. For safety reasons, the decay volume is filled with gaseous helium at 1 atm of pressure which has a low pion absorption rate. A beam dump is placed at the end of the decay volume to stop particles like muons that have not yet decayed from contaminating the beam with their decay neutrinos.

Along both beamlines are numerous monitors and timing systems to ensure stable production of neutrinos. Proton beam monitors are placed along the primary beamline to ensure the proton beam is properly steered into the secondary beamline. An optical transition radiation monitor is situated around the target to observe any protons not intersecting with the target region itself. The last monitor along the secondary beamline is the a muon mon-

itor (MUMON), which is placed downstream of the beam dump to characterize the flux of daughter muons of > 5 GeV/c momentum [1].

In order to provide timing information for the neutrino beam at SK, a global positioning system (GPS) is used to synchronize clocks at SK and J-PARC. Any event outside the beam timing window is rejected in the T2K oscillation analysis, and so having precise timing information for the neutrino beam is critical for the experiment. The GPS has an internal accuracy of 50 ns, or about ~ 150 m assuming that the neutrinos are traveling near the speed of light. This is well within the time it takes for a neutrino to travel the 295 km between J-PARC and SK.

J-PARC continues to improve the proton delivery and neutrino flux intensity since T2K began in 2010. The T2K experiment has run in two horn current modes: ν -mode and $\bar{\nu}_\mu$ -mode. Focusing positively charged pions with +250 kA horn current is called forward horn current (FHC) mode. Similarly, using -250 kA horn current is called reverse horn current (RHC) mode. The aggregate running of T2K for both FHC and RHC modes is shown in Figure 1.17 on page 33 in units of protons on target (POT).

In addition the proton beam intensity, as measured in kW, has been increased over time which increases the number of neutrino interactions observed at SK. Note that while ± 250 kA is the preferred horn current in both FHC and RHC modes, the horns were run briefly at +205 kA when operations resumed after 2011 Tohoku earthquake.

1.2.2 Neutrino Near Detectors: ND280

The T2K experiment has a near detector (ND) site at J-PARC that is designed specifically to observe the neutrino beam in flight aimed at Super-K. The primary purpose of a ND site is to *constrain the neutrino flux and interaction rate* at SK in order to reduce the impact of their systematic uncertainties on the oscillation analysis. The analysis in this thesis uses the data collected by the off-axis ND. The site is called ND280 and is located 280 m away from the production target. The primary detector is an off-axis, magnetized tracking

detector consisting of different subdetectors. A separate detector array called the Interactive Neutrino Grid (INGRID) measures the neutrino beam profile.

The following subsections begin with a description of INGRID and its purpose at ND280. This is followed by a general description primary off-axis, magnetized detector. The last two subsections are descriptions of two primary subdetectors in the off axis detector. The first and second being the pi-zero detector (PØD) and time projection chamber (TPC), respectively.

From here on, unless specified, INGRID will refer only to the on-axis ND and ND280 will refer only to off-axis ND.

1.2.2.1 On-Axis Detector

The on-axis near detector called the Interactive Neutrino Grid (INGRID) is a tracking scintillator detector designed to directly measure the neutrino beam profile. As shown in Figure 1.18 on page 36, it is a grid of tracking modules in the shape of a cross centered at the designed neutrino beam center ($\theta = 0$). The INGRID detector is capable of measuring the on-axis neutrino beam in a $10\text{ m} \times 10\text{ m}$ transverse area. Each module consists of alternating layers of iron plates and scintillator bars except for the two most downstream scintillating layers which lack iron plates. To monitor any beam asymmetry, two separate modules are placed off the grid axis.

Each scintillating bar consists of scintillator-doped polystyrene, which emits light when a charged particle deposits energy in the medium. Each bar contains a single wavelength-shifting (WLS) fiber to collect and shift the light to a different wavelength. The light trapped in the fiber is then collected by a device called a multipixel photon counter (MPPC) and converted into an electrical signal. A MPPC is a compact device containing many sensitive avalanche photodiode pixels that act as Geiger micro-counters as shown in Figure 1.19 on page 37. The MPPCs are well matched with the spectral emission of the WLS fibers and operate in a strong magnetic fields, unlike traditional photomultiplier tubes. In order to enhance the collection efficiency, a reflective TiO_2 doped polystyrene shell surrounds each

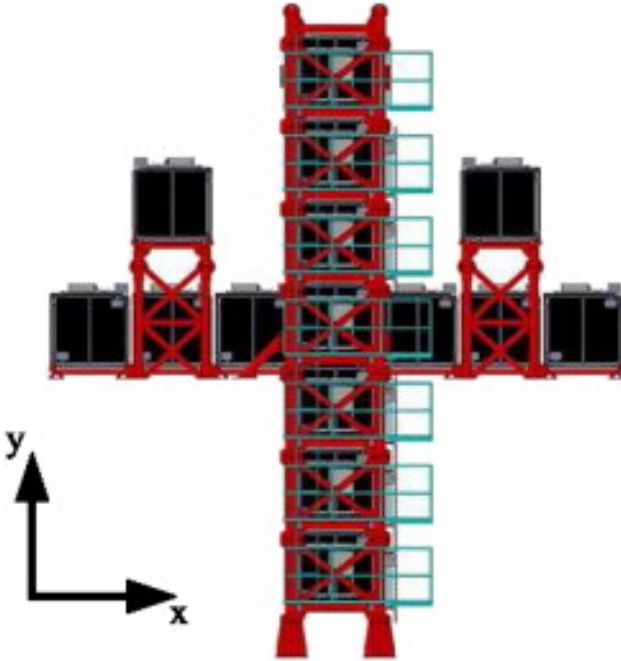


Figure 1.18: A schematic of the INGRID detector showing the arrangement of the tracking scintillating modules. There are 16 identical modules total with seven in the vertical row, seven in the horizontal row, and two at off-axis positions. With the vertical row upstream of the horizontal row, the designed beam center intersects each row's center module [2].

bar. The bars are assembled into planes to provide tracking capabilities. Veto planes also surround each module to prevent false signals to trigger.

The INGRID detector is continuously operated to check that the neutrino beam center was properly aligned at its designed center. Diagnostic plots such as Figure 1.20 on page 37 are collected on a monthly basis to ensure that the neutrino flux at Super-Kamiokande (SK) is consistent with T2K’s requirements. A history of the beam profile and event rate on INGRID between January 2010 and October 2016 is shown in Figure 1.21 on page 38.

1.2.2.2 Off-Axis Detector

The primary ND used for T2K is ND280, which is an off-axis, magnetized tracking detector. It is a collection of different detector technologies designed to facilitate three primary measurements:

1. The flux of ν_μ at SK,

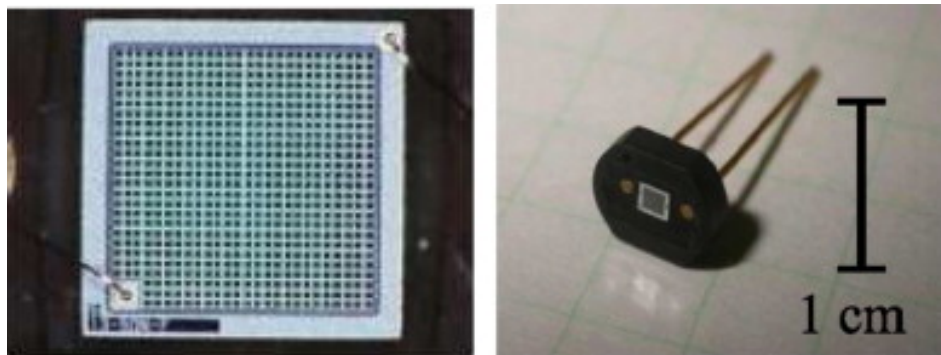


Figure 1.19: Photographs of the specially designed MPPC in T2K. A magnified face view is shown on the left with an entire unit shown on the right. Each device has 667-pixel sensors with an effective area of $1.3 \text{ mm} \times 1.3 \text{ mm}$ [1].

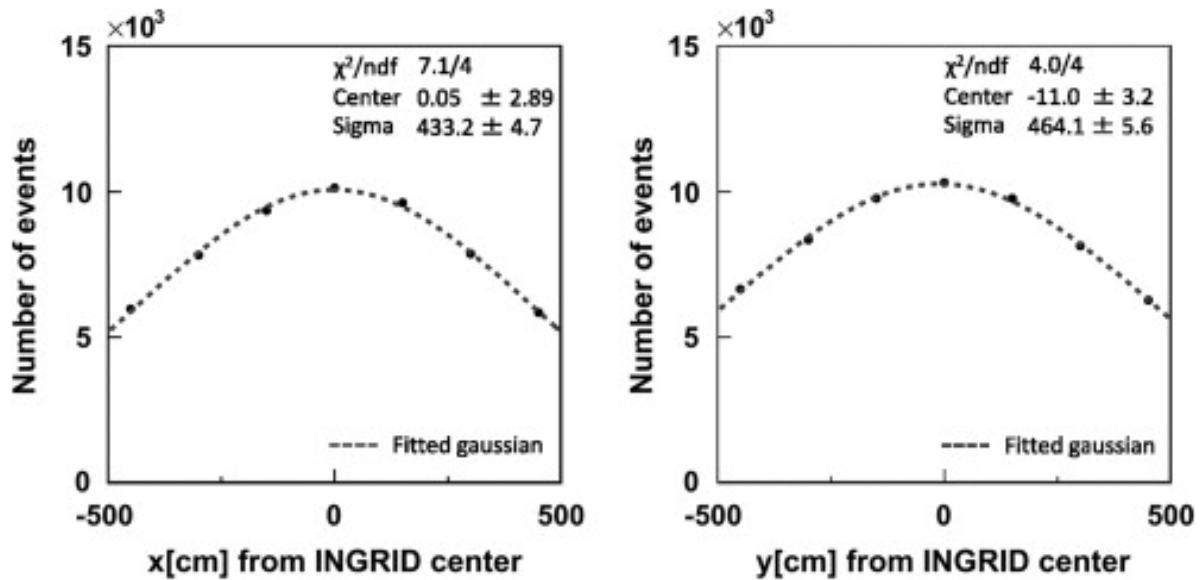


Figure 1.20: A beam profile taken with INGRID in April 2010 shows the Gaussian nature of the beam. The errors on the data points are about 1%. [2]

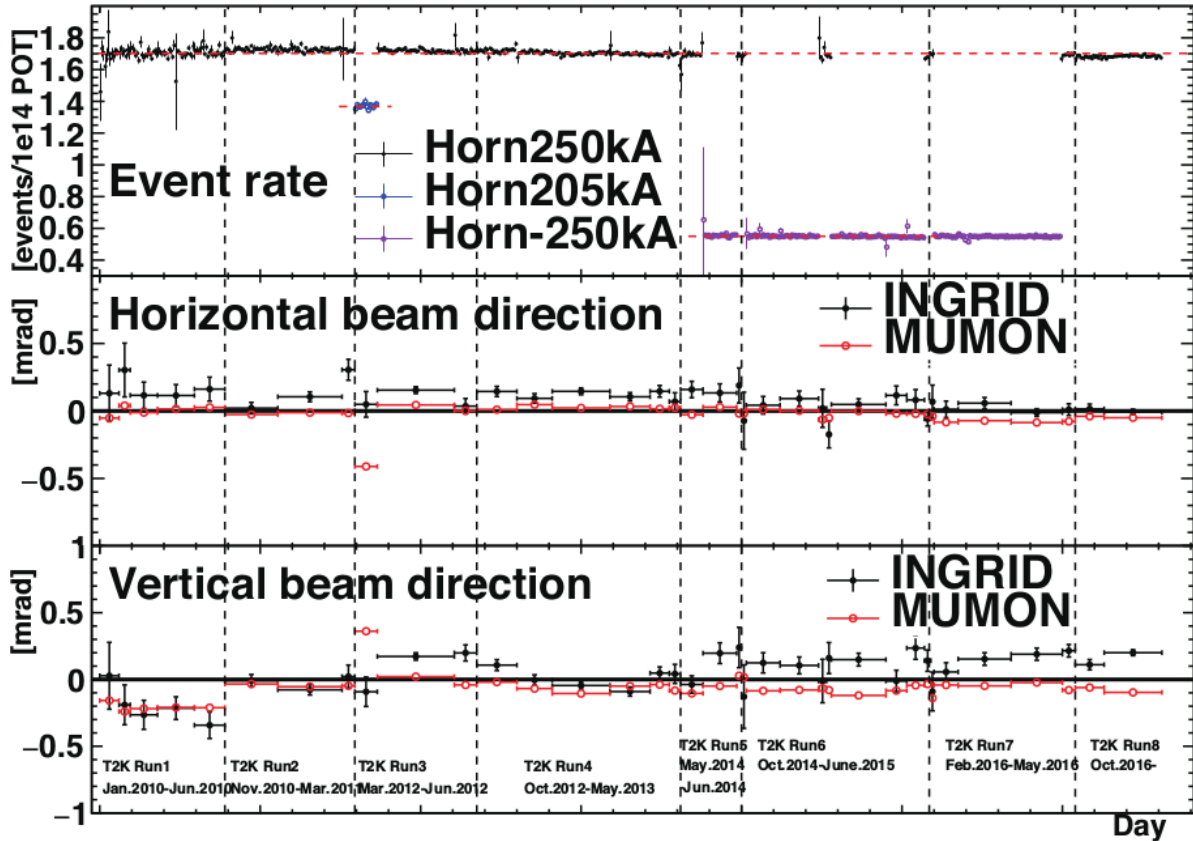


Figure 1.21: The INGRID detector interaction event rate and beam profiles are shown. The top panel shows the event rate for the three different horn currents. The middle and bottom panels show the horizontal and vertical beam directions with respect to the beam center, respectively. A deviation of 1 mrad corresponds to a little under 30 cm. The error bars shown are the statistical errors on the mean.

2. The irreducible ν_e background flux at SK, and
3. The rate of background ν_μ interactions and cross sections for the $\nu_\mu \rightarrow \nu_e$ search.

The ND280 detector consists of a pi-zero detector (PØD), a tracker region consisting of a fine grain detector (FGD) and a time projection chamber (TPC), an electromagnetic calorimeter (ECal), and a side muon range detector (SMRD). The ND280 subdetectors are instrumented inside the recycled UA1/NOMAD magnet with the SMRD in the magnetic field return yoke itself. All but the FGD are instrumented with the same MPPC technology mentioned above. A schematic of the different detector components of ND280 is shown in Figure 1.22 on page 40.

The analysis in this thesis uses measurements from the PØD and the TPC subdetectors. The PØD serves as a massive target for the incident neutrino beam and the TPC serves to measure the charge and momentum of the outgoing particles.

The ND280 magnetic field is generated using electrical current fed through solenoid coils to generate a dipole field of strength 0.2 T^{10} in the x direction. The field is highly uniform near the center of the detector which is where the majority of the TPC system is located. However, it has significant deviations from 0.2 T near the solenoid edges. In order to fully understand the field inside ND280, a precise 3D model was generated using a machine controlled Hall probe. The operating field strength during the mapping process was 0.07 T due to power restrictions at the time. The model was then compared with measurements in the TPC region as shown in Figure 1.23 on page 41. After scaling the model to the nominal operating strength of 0.2 T, a fractional uncertainty of 10^{-3} or uncertainty of 2 Gauss in each direction was obtained.

The ND280 magnetic field permits the measurements of particle charge and momentum. A particle of charge q , rest mass m_0 , and velocity \mathbf{v} under the influence of an external electric

¹⁰This is a powerful magnetic field. According to the The US/UK World Magnetic Model for 2015-2020, the magnetic field strength on the surface of the Earth is about 0.294385 Gauss or $2.94385 \times 10^{-5}\text{ T}$. So the field inside ND280 is about 6800 times more forceful than the Earth's influence [29].

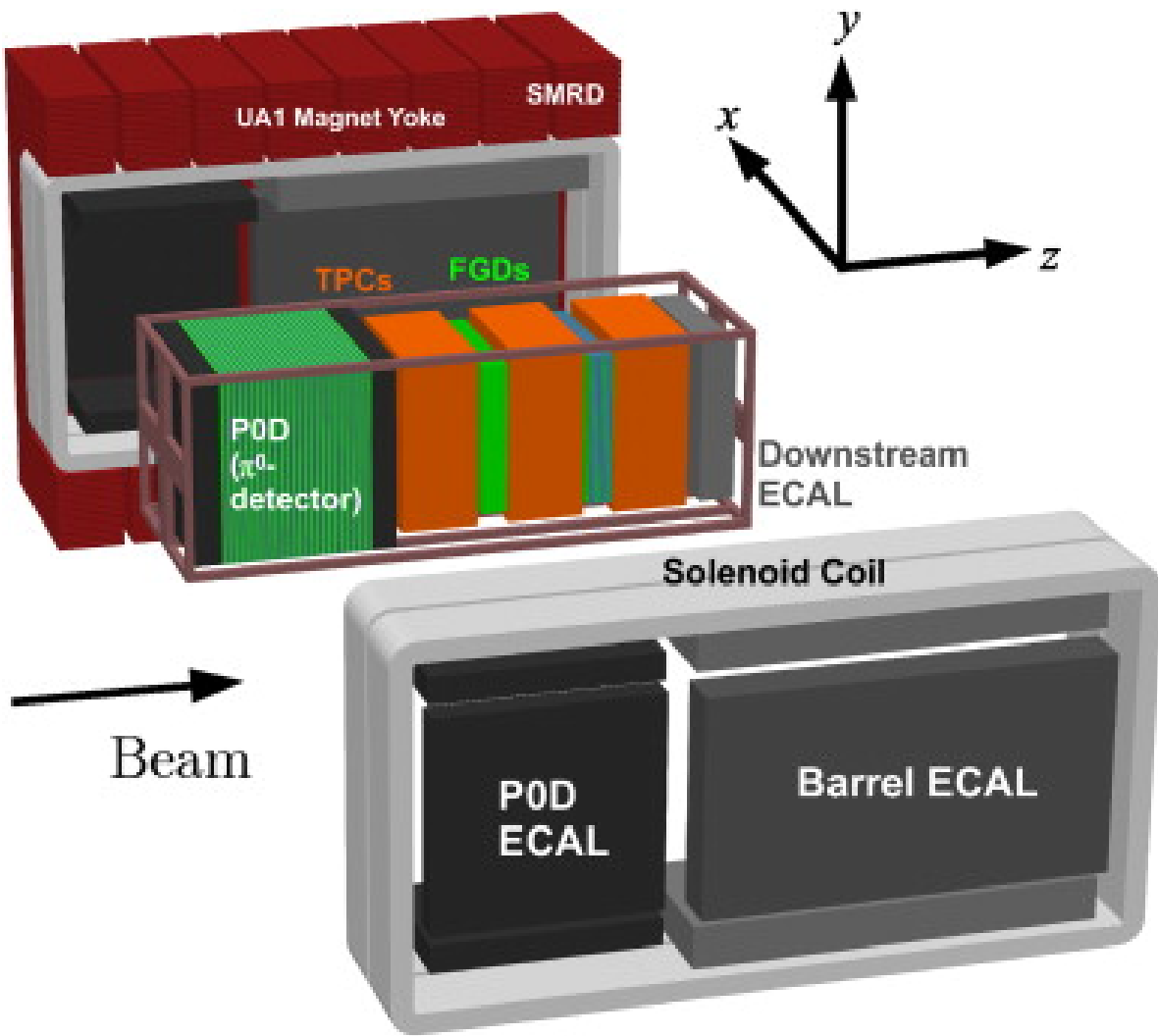


Figure 1.22: An exploded view of the ND280 off-axis detector. The magnetic field is generated from the Solenoid Coil via an electrical current which produces a dipole magnetic field of strength 0.2 T. The field is designed to return to the Magnetic Yoke.

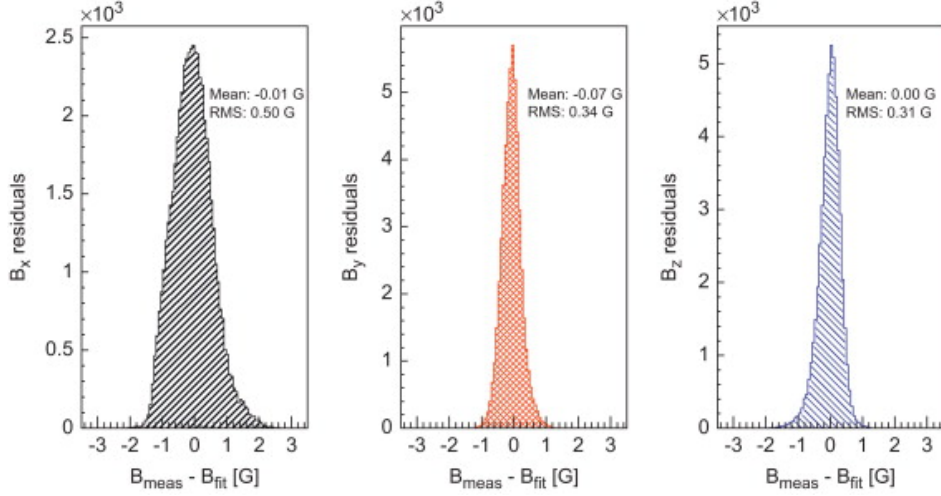


Figure 1.23: The ND280 detector magnetic field measurement in all three directions. Each of the magnetic field components are compared between a fit of the data and the actual measurements near the center of ND280. The systematic uncertainty on the field is extracted from the RMS of the mapping [1].

and magnetic fields, \mathbf{E} and \mathbf{B} , respectively, experiences a force \mathbf{F} given by the Lorentz force equation

$$\mathbf{F} = q(\mathbf{E} + \mathbf{v} \times \mathbf{B}). \quad (1.49)$$

Assuming for now that there is no external electric field, the force on the particle is

$$\mathbf{F} = q\mathbf{v} \times \mathbf{B}, \quad (1.50)$$

which is both orthogonal to \mathbf{v} and \mathbf{B} . Since the mechanical work performed on a particle in a magnetic field is zero, the particle's energy is unchanged ($|\mathbf{v}| = v = \text{constant}$). Newton's Second Law allows us to rewrite the force as an change in momentum \mathbf{P}

$$\begin{aligned}
\mathbf{F} &= \frac{d\mathbf{P}}{dt} \\
&= \frac{d}{dt} (\gamma(v)m_0\mathbf{v}) \\
&= m_0\mathbf{v} \left(\frac{d\gamma(v)}{dt} \right) + \gamma(v)m_0 \left(\frac{d\mathbf{v}}{dt} \right) \\
&= m_0\mathbf{v} \left(\frac{d\gamma(v)}{dv} \right) \cancel{\left(\frac{dv}{dt} \right)}^0 + \gamma(v)m_0\mathbf{a} \\
&= \gamma(v)m_0\mathbf{a},
\end{aligned} \tag{1.51}$$

where $\mathbf{P} = \gamma(v)m_0\mathbf{v}$ is the relativistic momentum and $\gamma(v) = (1 - (v/c)^2)^{-1/2}$ is the Lorentz factor. For uniform circular motion, the magnitude of the acceleration is given by

$$|\mathbf{a}| = v^2/R, \tag{1.52}$$

where R is the radius of curvature for the circle. Combining (1.52) and (1.51) with some algebra yields

$$R = \frac{\gamma(v)m_0v}{q|\mathbf{B}|\sin\theta_{\mathbf{v}\mathbf{B}}}, \tag{1.53}$$

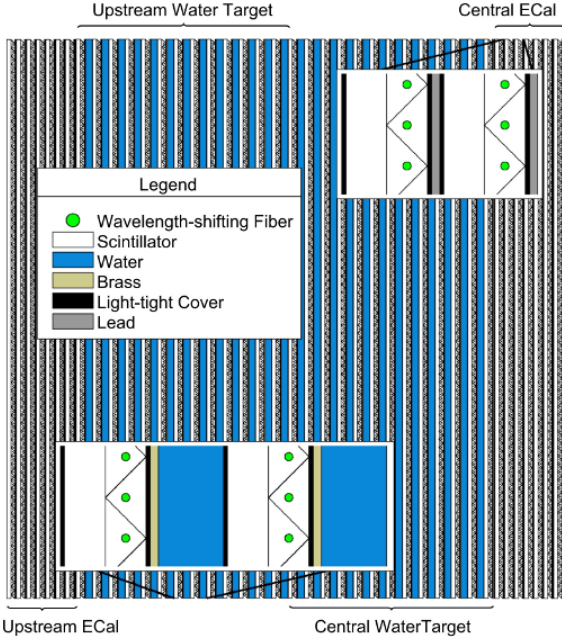
where $\theta_{\mathbf{v}\mathbf{B}}$ is the angle between \mathbf{v} and \mathbf{B} . The numerator of (1.53) is recognized as the magnitude of the momentum $|\mathbf{P}|$. Some further rearrangement yields

$$|\mathbf{P}| = q|\mathbf{B}|R\sin\theta_{\mathbf{v}\mathbf{B}}, \tag{1.54}$$

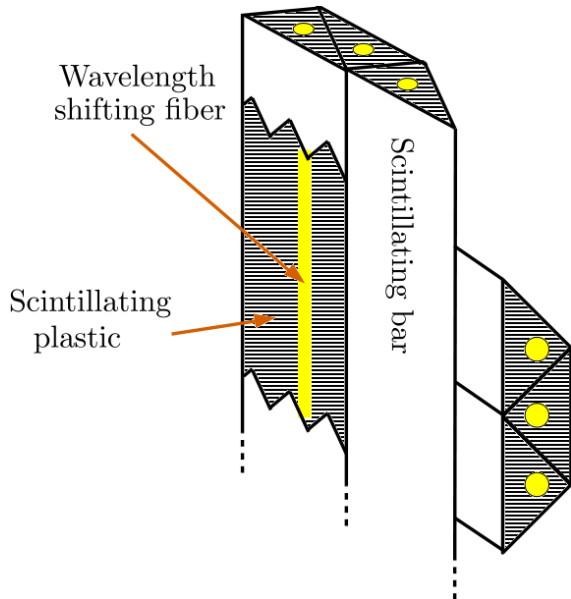
and thus measuring the direction and radius of curvature inside the field provides the charge and momentum, respectively, as desired.

1.2.2.3 Off Axis pi-zero detector (PØD)

The PØD is the primary detector used as the neutrino target in this thesis. It is a plastic scintillator-based tracking calorimeter inside the ND280 magnet region. It was designed to measure the neutral current (NC) process $\nu_\mu + N \rightarrow \nu_\mu + N + \pi^0 + X$ on water, where N is



(a) Schematic of the PØD



(b) Schematic of a PØD module

Figure 1.24: Schematics of the PØD. Left: insets detail the Water Target and ECal layers. Right: A view of a PØD module illustrating the orthogonal layout of the scintillating planes. Both: the neutrino beam is coming from the left.

a nucleus and X is any set of final state particles. The NC π^0 process was expected to be a significant background in the ν_e appearance search in the likelihood that $\theta_{13} \approx 0$ since a pi-zero decay can mimic a ν_e -like signal. The PØD can be operated with or without water, enabling the determination of water target (WT) cross sections by comparing water-in data with water-out data.

A representation of the PØD is shown in Figure 1.24 on page 43. The active detector components are very similar to INGRID's design with the primary difference being that each bar is triangular in shape as shown in Figure 1.25 on page 44. A plane of 134 horizontal and 129 vertical bars together form a PØD module (PØDule) as shown in 1.24b. The purpose of the triangular bar design is that particle tracks (muons and pions) are less likely to deposit energy in only two bars for each layer crossed. This would not be true for electromagnetic shower events which would deposit energy in many bars. These differences provide a discriminant between particle tracks and electromagnetic showers.

Element	Symbol	Fraction [%]
Carbon	C	45.0
Oxygen	O	29.9
Copper	Cu	14.3
Hydrogen	H	8.0
Zinc	Zn	1.6
Chlorine	Cl	1.1
Titanium	Ti	0.1

Table 1.3: Elemental composition of PØD water target region. The table is sorted from top to bottom by fraction of mass. This table was originally produced in reference [7].

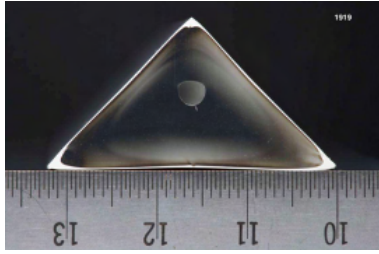


Figure 1.25: A cross section of a PØD scintillating bar. The base and height is 33 mm long and 17 mm high. The wavelength shifting fiber is inserted in the bored hole which is half-way between the base and tip.

The PØD dimensions are $2.298 \times 2.468 \times 2.350 \text{ m}^3$, in XYZ respectively, with a fiducial mass of $\sim 1900 \text{ kg}$ for water and 3570 kg for other materials. The total mass of the PØD is approximately 15,800 kg when the bags are full of water. The PØD is arranged into three regions: a water target (WT) region and two ECals. The WT region contains 26 PØDules interleaved between bags of water 2.8 cm thick when filled and a 1.3 mm thick brass sheets designed to help contain π^0 decay photons. The last two regions are the upstream ECal and central ECal, each with seven PØDules interleaved with steel sheets clad with lead between them [7]. An elemental composition of the WT is shown in Table 1.3 on page 44.

The readout electronics for the PØD is based on the Trip-T application specific integrated circuit (ASIC) shared among the SMRD, ECals, and INGRID. Signals from 64 MPPCs are routed to Trip-T front end boards (TFB) that each house four Trip-T ASICs. Each Trip-T collects the MPPC charge in 23 programmable integration cycles.

The TFBs are readout to back-end electronics which control the TFBs and synchronize clocks. A total of six readout merger module (RMM) electronics receive the TFB data and control each TFB ASIC. The RMM internal timing clocks are synchronized with a cosmic trigger module and a slave clock module (SCM), both of which are synchronized with a master clock module from the beamline. Synchronizing the RMMs with the SCM allows for the Trip-T ASIC integration windows to match with the beam. The RMMs are responsible for distributing the TFB data to the data acquisition (DAQ) system for storage.

The ND280 DAQ consists of a MIDAS framework to monitor and control data collection. The primary purpose of the DAQ system is to merge data and package it for long term storage. In conjunction with the DAQ system is the Global Slow Control (GSC) system which measures temperatures, voltages, and other physical quantities. Together the DAQ and GSC help scientists consistently produce high quality data and maintain the overall stability of the detector [1].

1.2.2.4 Off Axis Time Projection Chamber (TPC)

The ND280 TPC is designed to provide momentum measurements of charged particle tracks and high resolution particle counting capabilities. The TPC is divided into three volumes separated by the two FGD volumes. Each volume ($2.3 \times 2.4 \times 1.0 \text{ m}^3$) consists of an inner box that holds an argon-based gas and an outer box that holds an insulating CO_2 gas. The inner gas mixture is 3000 L of $\text{Ar:CF}_4:\text{C}_4\text{H}_{10}$ (95:3:2) gas. It was selected for its high speed, low diffusion, and good performance with a bulk micromegas detector [1]. A simplified schematic of the TPC is shown in Figure 1.26 on page 46.

A TPC works by measuring the ionization electrons left in the gaseous medium as charged particles through it. The electron drift acceleration is rapid due to the strong 5 kV/cm electric field present. Drift electrons are multiplied and sampled by micromegas detectors that line the sides of the TPC, providing nearly 3 m^2 of active surface coverage. Arrival times of the electrons provide timing information to give a full three dimensional portrait of the events.

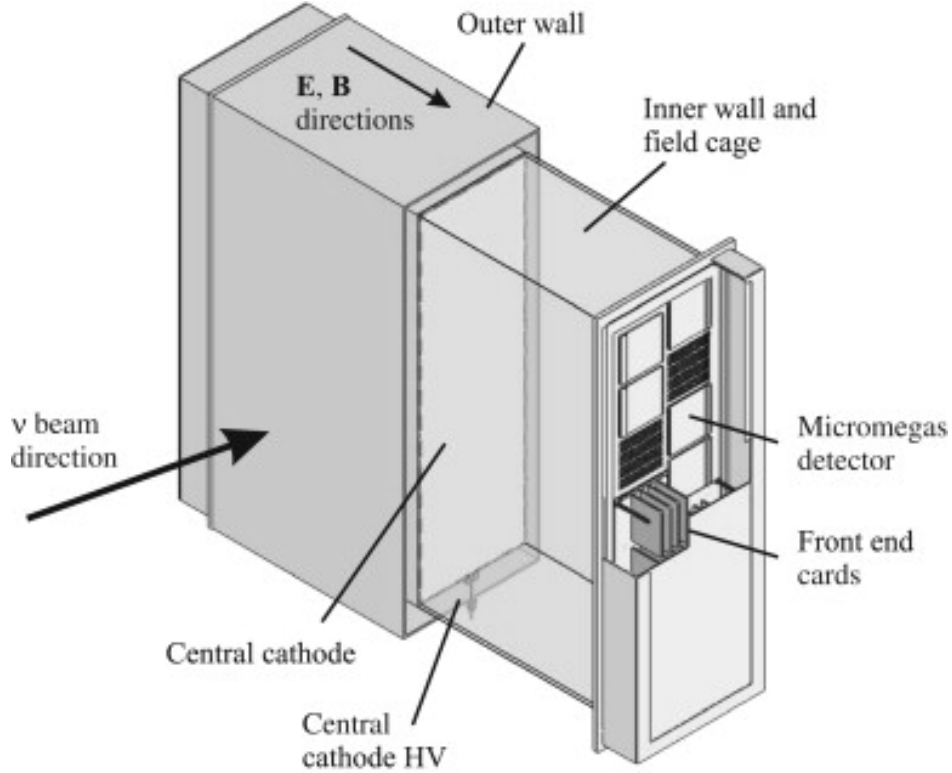


Figure 1.26: Cut-away drawing of a TPC volume in ND280 [1].

1.2.2.5 Track Reconstruction in ND280

The goal of track reconstruction software is to capture the shape and history of energy deposited in the detector. Since ND280 is collection of different technologies, highly specific algorithms and models are used to identify track-like patterns. Since this analysis uses neutrino events incident in the PØD and cross into the TPC, a unified and coherent reconstruction model is needed. A reconstruction package called “Global” is designed to combine all ND280 information for this purpose.

1.2.3 Neutrino Far Detector: Super-Kamiokande

The Super-Kamioka neutrino detection experiment, abbreviated as Super-Kamiokande (SK), is the dedicated far detector for the T2K experiment. Positioned at 295 km away from the neutrino source with a 1 km overburden, it is well designed to detect the elusive neutrino.

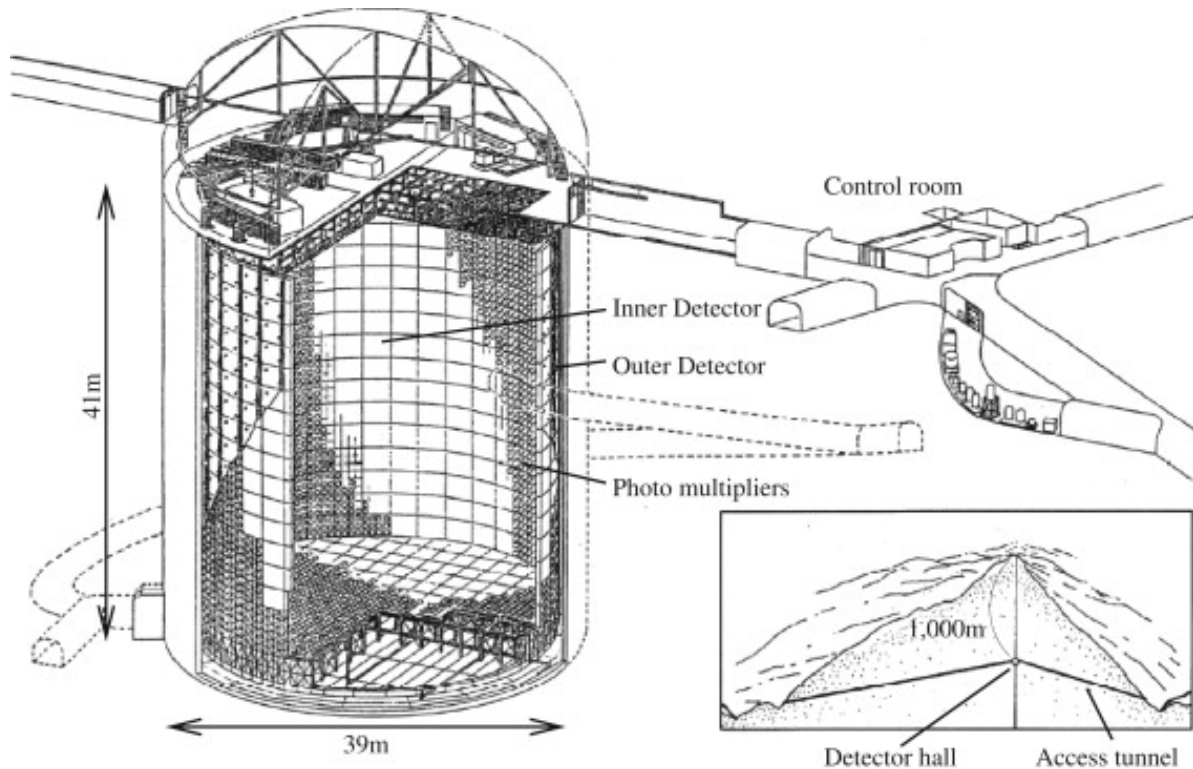


Figure 1.27: Diagram of the Super-Kamiokande detector consisting mainly of the inner and outer detector segments. The boundary between the two segments is cylindrical scaffolding used to mount the PMTs and optically isolate the segments.

Containing about 50 kt of pure water, it is lined with photomultiplier tubes (PMTs) in both an inner and outer detector as shown in Figure 1.27 on page 47.

When charged particles travel through the water, a Cherenkov radiation cone is produced. The sharpness of the cone edge is a unique identifier for the particle species that produced it. An electron produces a fuzzy edge since it experiences many large multiple scatterings off the water molecules. A muon on the other hand produces a sharp edge since it is much more massive and thus is less perturbed by the water molecules. Both types of events are shown in Figure 1.28 on page 48. By identifying the sharpness of the cone, the particle species is deduced. If a cone is coincident with the T2K neutrino beam, it can be used to infer the neutrino flavor.

While events from SK are not used in this analysis, the goal is to try to improve T2K's oscillations parameters which depend on comparing the ND neutrino measurements to the

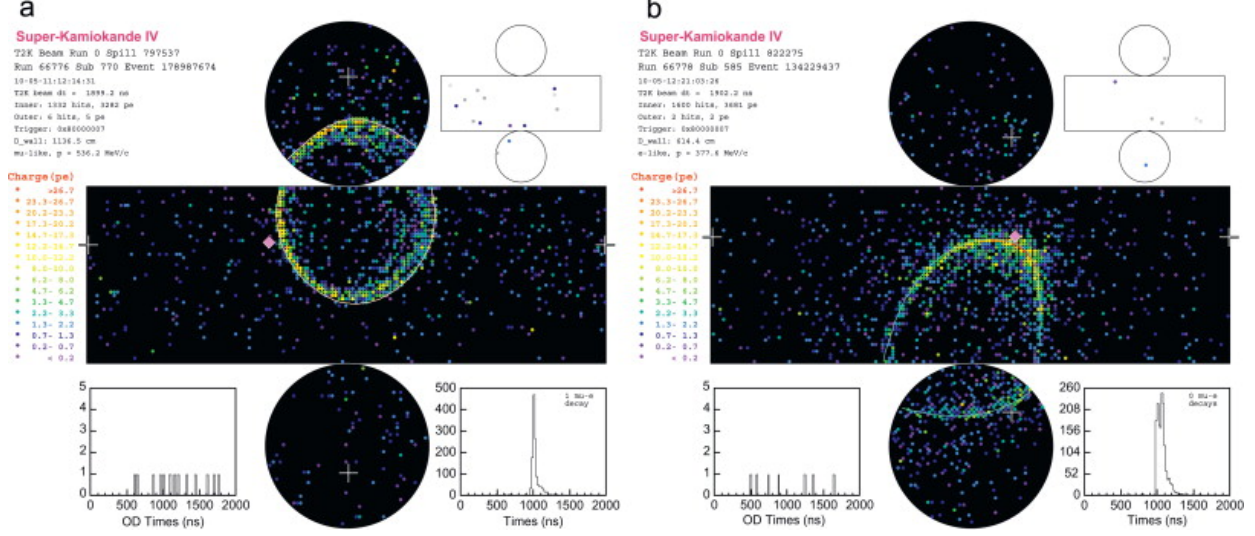


Figure 1.28: Representative T2K events in Super-Kamiokande for (a) a muon-like ring and (b) an electron-like ring. Both figures show Super-Kamiokande unrolled onto a plane with each colored point representing a PMT. The color of each PMT corresponds to the amount of charge collected. In upper right corner shows the same unrolled hit map for the veto outer detector. White crosses indicate the location of the reconstructed vertex. A solid diamond marks the location where a ray parallel to the beam would intersect the detector wall starting from the vertex.

far detector neutrino measurements. Therefore a discussion on the T2K ND constraint on the oscillation analysis is warranted.

1.2.4 Oscillation Analysis ND Constraint

As started before, the primary goals of T2K are measure to measure the oscillation parameters θ_{13} , θ_{23} , Δm_{23}^2 , and nonzero δ_{CP} . This is performed by fitting the oscillation parameters to the number of observed flavored neutrinos at SK. The number of observed neutrino events, N_{ν_α} , of flavor ν_α is

$$N_{\nu_\alpha} = B + S_{\nu_\alpha} \quad (1.55)$$

where B is the number of all misidentified ν_α events and S_{ν_α} is the number of true events.

The expected neutrino appearance rate is given by

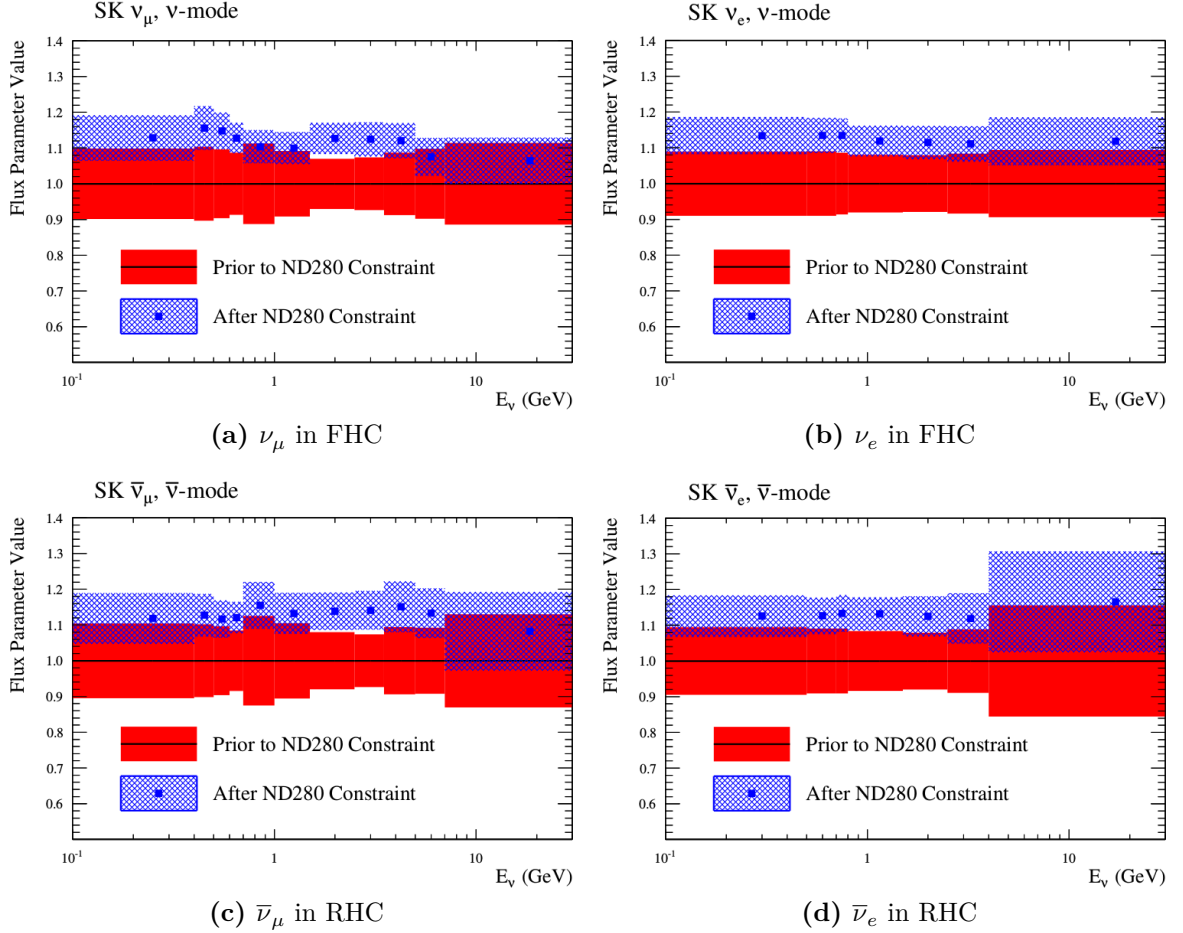


Figure 1.29: Predicted and best fit measurements for the T2K flux at Super-Kamiokande. The horizontal axes are the neutrino energy and the vertical axes are the fractional change in the flux normalization. These figures were taken from the 2017 T2K oscillation analysis [6]. A value 1.1 corresponds to a 10% increase in the number of predicted events.

$$S_{\nu_\alpha} = \sum_{\lambda=e,\mu} \left[\mathcal{P}_{\nu_\lambda \rightarrow \nu_\alpha} (E_\nu; \vec{o}) \right] \times \sum_t \left[\sigma_{\nu_\alpha}^t (E_\nu) \cdot t_N \right] \\ \times \Phi_{\nu_\alpha} (E_\nu) \times \epsilon(p_\alpha, \theta_\alpha), \quad (1.56)$$

where \vec{o} is a vector of the oscillation parameters from (1.38), $\sigma_{\nu_\alpha}^t$ is the cross section for ν_α on target t , t_N is the number of targets of type t , Φ_{ν_α} is the flux of neutrinos, and $\epsilon(p_\alpha, \cos \theta_\alpha)$ is the efficiency of reconstructing and correctly categorizing the event as a function of momentum p and angle θ .

Having a large, sensitive off-axis ND like ND280 provides a tool to determine the oscillation analysis constraints. This includes the oscillation channel $\nu_\mu \rightarrow \nu_e$, but also the

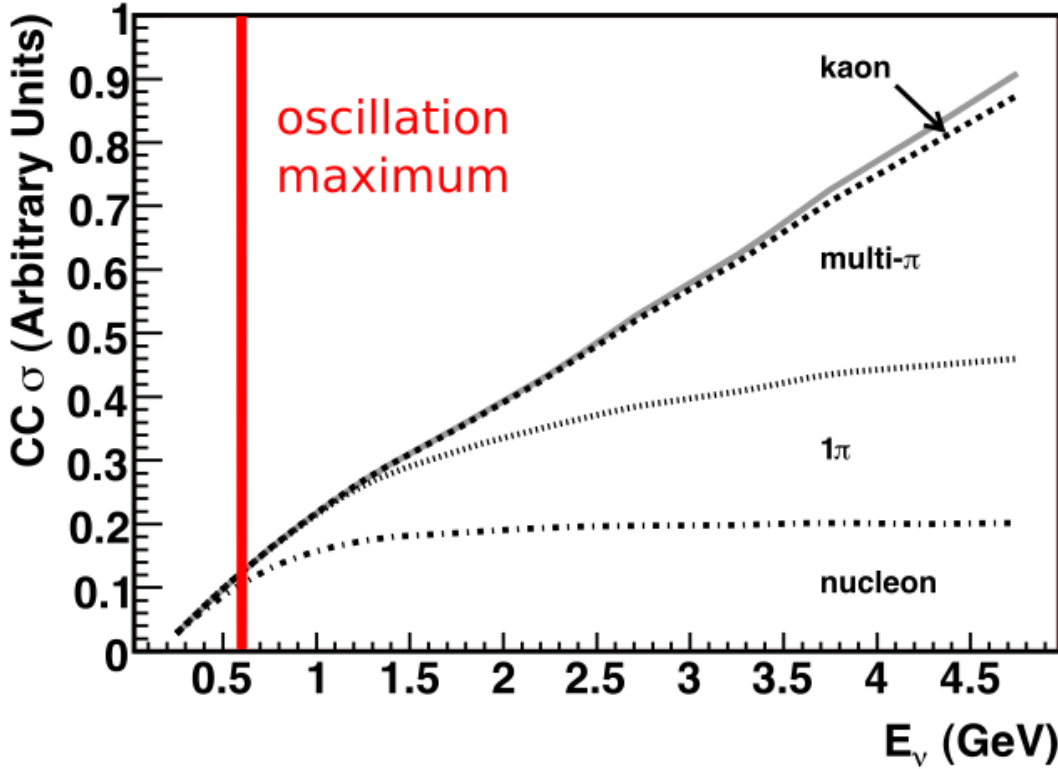


Figure 1.30: Predicted CC inclusive scattering cross section at T2K relevant energies. Only the most common final state modes are shown. A thick, red line indicates the T2K ν_e appearance probability maximum. For CCQE-like interactions (nucleon), a single nucleon is struck. Higher energy interactions like resonance (1π) and DIS (multi- π) interactions produce pion and kaon final states as well. All combined, the inclusive cross section increases linearly with energy. This image was edited and originally produced by Formaggio and Zeller [38].

intrinsic ν_e background in the T2K beam. These neutrinos interact the same way an oscillated neutrino would at SK. Without ND280, the fractional uncertainty on the flux rate is about $\sim 10\%$ per energy bin. These constraints are obtained from the MUMON detector discussed above and the NA61/SHINE experiment [11]. Adding the ND constraint reduces the uncertainty to about $\sim 5\%$ as seen in fig. 1.29 on the preceding page.

T2K uses the NEUT¹¹ [49] program library to simulate neutrino interactions with nucleons and the nucleus. It was originally designed to simulate atmospheric neutrinos for the Kamioka Nucleon Decay Experiment (Kamiokande), the predecessor to the Super-

¹¹NEUT is neither an initialism nor acronym

Kamiokande experiment. Included in NEUT are numerous models for neutrino interactions on matter and intra-medium hadron spatial transport within the nucleus.

Using the ND280 constraint tunes the NEUT cross section model to best match the T2K data. The canonical T2K cross section model in NEUT is problematic due to dependence on effective models describing neutrino-nucleus scattering. In particular, large model and data disparities exist within recent, high statistics CCQE measurements [38]. This forces T2K to constantly explore other physics models, some of which are employed in this analysis.

1.2.5 Contributions to the T2K Experiment

Since joining the T2K experiment five years ago, I have played a critical role in an analysis that is currently in preparation for publication [72]. This analysis was a second generation measurement of the ν_μ CC single pion production cross section on water in the PØD. I am a co-author of that paper and its internal T2K technical document that outlines the analysis procedure and studies. In particular, I helped develop the momentum calibration and event selection using machine learning. Further details on my contributions are found in Appendix A.

In addition to analysis work, the majority of my contributions to the experiment include on-site expertise for the ND280 detector. I was involved in the 2015 work to replace two PØD water bags when they showed evidence of leaking. Additionally, I helped measure the PØD water mass and deformations in the PØD structure due to the internal stresses from the water mass. I am certified as a Trip-T ASIC expert, PØD water system and calibration expert, and experienced DAQ shifter. As an expert in these areas, I was solely responsible for daily reporting and monitoring for the SMRD, ECal, and PØD detectors during beam taking periods. This included being the first point-of-contact, 24/7 for those electronic systems and the PØD water target whenever problems arose.

My most recent contribution was participating in the 2018 SK open tank work at the Kamioka Observatory. My work had three primarily goals:

- Cleaning the support structures, walls, and PMTs of non-water contaminants. This includes using clean wipes to remove diesel fume residue on the support structures from the initial construction and rust removal using electrolysis,
- Collecting glass shards remaining in the tank after a major multi-PMT implosion in 2001, and
- Replacing the light-tight insulation that separates the inner and outer detectors.

These tasks helped the Kamioka Observatory identify external water leaks and remove contaminants in the SK detector. This is all in preparation for adding gadolinium (Gd), a rare earth metal, to the pure water in the detector which will enhance the antineutrino capture cross section.

1.3 Summary

The neutrino is an elusive particle to detect. The relatively new neutrino oscillation phenomenon has opened up the further possibilities of exploring fundamental questions of the Universe like CP violation. In the T2K experiment, some of the uncertainties associated with neutrino oscillations are being explored. To facilitate these goals, constraining all forms of uncertainty in neutrino-nuclear interactions and flux help improve its sensitivity to the oscillation predictions.

The next chapters in this thesis are presented in the following order. First is the ND280 constraint on the flux and cross section models using the beam and near detector flux task force (BANFF) maximum likelihood fit. Next is the description of the analysis samples that are used in the BANFF fit. With the samples defined, the parameterization of the fit bins and penalty terms are defined for this analysis. This is followed by the validation of the BANFF fit in a few scenarios. Then the BANFF postfit results are analyzed in relation to previous analyses. The final chapter is a discussion of the results and prospects for the future.

Chapter 2

BANFF Likelihood

The T2K experiment has organized a task force dedicated to provide the near detector constraint for the oscillation analysis. This task force is called the “Beam And Near detector Flux task Force (BANFF)¹². The BANFF group has implemented a binned likelihood maximization fit of the ND280 data for the oscillation analysis [4].

The BANFF near detector (ND) constraint fit is done separately from fitting the Super-Kamiokande (SK) data. In a joint fit, the measurements from both detectors are considered to estimate the oscillation parameters. This joint-fit approach is more computationally expensive since it must include all parameters that affect the both the ND and SK systematic uncertainties, also called nuisance parameters. Also the time to perform a fit increases non-linearly with increasing the number of fit parameters. Therefore the separate BANFF likelihood maximization, hitherto referred to as the “BANFF fit”, must include parameters that affect the measurement of the oscillation parameters. Then those fit parameters and their respective covariances are used as inputs in the oscillation analysis. This “divide-and-conquer” approach allows for more rapidly completed studies on the effects of model parameters and biases present. However, information encoded in the ND280 measurements for shared nuisances like the neutrino flux is inevitably lost in the BANFF fit.

¹²BANFF is a Canadian national park.

The modern BANFF fit is described in detail in the following reference [6]. To summarize the details, the BANFF fit uses a frequentist approach to find the best parameter set to maximize a binned likelihood. Subsequent updates to the BANFF fit have increased the sample sizes and systematic uncertainty parameterizations.

This chapter describes the BANFF fit and overview of the fitting procedure. First we introduce the concept of likelihood functions. Then we examine the use of likelihood functions to extract model parameters from histogram fits. The final topic is a basic description of the fitting procedure and uncertainty calculation.

2.1 Introduction to Conditional PDFs and Likelihoods

Consider the problem of extracting physics parameters \vec{y} given some data vector \vec{N} . The conditional probability density function (PDF) \mathcal{P} to measure these parameters is given as

$$\mathcal{P}(\vec{y}|\vec{N}) = \frac{\mathcal{L}(\vec{N}|\vec{y})\mathcal{P}(\vec{y})}{\int \mathcal{L}(\vec{N}|\vec{x})\mathcal{P}(\vec{x})d\vec{x}}, \quad (2.1)$$

where anything right of the vertical lines represents a condition on the probability. $\mathcal{L}(\vec{N}|\vec{y})$ is the likelihood of the model with parameters \vec{y} , $\mathcal{P}(\vec{y})$ is the probability for the model, and the denominator is the normalization. A frequentist interpretation of the PDF is a proportion of outcomes of repeated trials or experiments. A likelihood function is an expression of the probability of observing data as a function of the model parameters in their appropriate ranges.

One arrives at (2.1) by using the definition of compound probabilities

$$\mathcal{P}(A, B) = \mathcal{P}(B|A)\mathcal{P}(A), \quad (2.2)$$

to evaluate $\mathcal{P}(\vec{y}|\vec{N})$ as

$$\mathcal{P} \left(\underbrace{\vec{y}}_B \middle| \underbrace{\vec{N}}_A \right) = \frac{\mathcal{P}(\vec{N}, \vec{y})}{\mathcal{P}(\vec{N})}, \quad (2.3)$$

where the denominator is the normalization of the PDF. The compound PDF $\mathcal{P}(\vec{N}, \vec{y})$ can be expanded using Bayes' theorem which states

$$\mathcal{P}(A|B)\mathcal{P}(B) = \mathcal{P}(B|A)\mathcal{P}(A), \quad (2.4)$$

and combined with (2.2) yields

$$\mathcal{P} \left(\underbrace{\vec{N}}_A, \underbrace{\vec{y}}_B \right) = \mathcal{P}(\vec{N}|\vec{y}) \times \mathcal{P}(\vec{y}), \quad (2.5)$$

where the PDFs to the left and right of the \times operator are the likelihoods and priors, respectively. Combining resulting in (2.3) and (2.5) reproduces the original expression of (2.1).

2.2 BANFF Fit Test Statistic

Curve fitting is commonly used in particle physics in order to constrain unknown model parameters using histograms. This procedure seeks to find the “best” set of the model predictions, θ , that match the data, as is the case for the BANFF fit. This analysis uses a chi-squared test to provide a goodness of fit metric, a parameter estimation (also referred to as “best fit parameters”), and a error estimation for the BANFF fit.

The BANFF fit is an attempt to maximize the agreement between the measured and predicted data curves at the ND280 detector. This is equivalent to maximizing a binned likelihood function \mathcal{L} of the ND280 data given a set of parameters in the likelihood function that predict the measured rate. The use of likelihood functions in fits to histograms is explained further in reference [19] and the PDG review on statistics. By invoking Wilks’ theorem, also known as the likelihood ratio theorem, the likelihood maximization procedure

is converted into a minimization problem involving a test statistic denoted as a chi-squared. Below is an explanation of the BANFF test statistic and the model terms.

2.2.1 Log-Likelihood Ratio

Consider many binned samples that select different charged current topologies. A convenient choice of observables for all the samples is the outgoing charged lepton l momentum P_l and angle $\cos \theta_l$ as measured in the ND280 detector [46]. For each $(P_l, \cos \theta_l)$ analysis bin $i = 1, 2, \dots, M - 1, M$, the likelihood is given by

$$\mathcal{L}(\vec{N}^d | \vec{N}^p) = \prod_{i=1}^M \left(\vec{N}_i^p \right)^{\vec{N}_i^d} \frac{e^{-\vec{N}_i^p}}{\vec{N}_i^d!} \quad (2.6)$$

where \vec{N}_i^d is the number of observed data events in the i th bin and \vec{N}_i^p is the number of predicted events as a function of the fit parameters in the same bin. One recognizes the likelihood function in (2.6) as a product of Poisson distributions, since this is counting data measured in M analysis bins. The parameters that affect the predicted event rate are:

- The cross section physics models, labeled as “xsec”,
- The neutrino flux, and
- The detector biases and inefficiencies.

We use these parameters to calculate the number of predicted charged current (CC) events N^{ν_l} from any neutrino flavor ν_l at ND280 as

$$N^{\nu_l} = \underbrace{\Phi_{\nu_l}}_{\text{Flux}} \times \left[\sum_t \underbrace{(\sigma_{\nu_l}^t M^t)}_{\text{Effective area}} \right] \times \underbrace{\epsilon_{\nu_l}}_{\text{Efficiency}} , \quad (2.7)$$

where Φ_{ν_l} is the flux of l flavor neutrinos, $\sigma_{\nu_l}^t$ is the cross section of the interaction for neutrino flavor l on target t , M^t is the number of t targets, and ϵ_{ν_l} is the total efficiency to reconstruct and properly identify the event as ν_l CC interactions. Since the cross section

Description	Symbol	Fit?
Fit bin normalizations	\vec{d}	Yes
Flux normalizations	\vec{b}	Yes
Cross section weights and norms.	$w(\vec{x})$	Yes
POT weight for the MC	w^{POT}	No
Flux bin selector	$\delta_{j,k}^{\text{Flux}}$	No
Number of flux parameters	N^{Flux}	No
Number of cross section parameters	N^{xsec}	No
Number of MC events	N^{MC}	No

Table 2.1: Parameters that affect the analysis bins. The top three parameters are fit while the others are constants set by the input data and bookkeeping.

is a measure of interaction probability in units of area, multiplication of M_t represents the effective cross sectional area of material t in the detector. Each term in (2.7) is modeled carefully using Monte Carlo (MC) simulations. For the efficiency term, control samples are used to constrain detector systematic uncertainties effects.

The number of events in a given analysis bin is varied in the BANFF fit using weight functions. The total number of predicted events in the i th analysis bin is given by

$$\vec{N}_i^p(\vec{b}, \vec{x}, \vec{d}) = \sum_{j=1}^{N_i^{\text{MC}}} \left\{ w_i^{\text{POT}} \sum_{k=1}^{N^{\text{Flux}}} (\delta_{j,k}^{\text{Flux}} \vec{b}_k) \times \left[\prod_{l=1}^{N^{\text{xsec}}} w_{j,l}(\vec{x}_l) \right] \times \vec{d}_i \right\}, \quad (2.8)$$

where the parameters are described in Table 2.1 on page 57. While (2.8) looks complicated as expressed in the T2K model, it is functionally the same as (2.7). Since the flux bins are categorized by neutrino energy, neutrino flavor, and horn current mode, the $\delta_{j,k}^{\text{Flux}}$ term is needed to select the correct flux normalization bin for the j th MC event. Also the number of neutrino targets M in the detector is treated as a detector systematic uncertainty.

Using the likelihood ratio test theorem, a test statistic is defined as taking -2 times the natural logarithm of the ratio of predicted to observed likelihoods from (2.6). This test statistic is given as

$$\begin{aligned}\chi_{\text{LLR}}^2 &= -2 \log \frac{\mathcal{L}(\vec{N}^d | \vec{N}^p)}{\mathcal{L}(\vec{N}^d | \vec{N}^d)} \\ &= 2 \sum_{i=1}^M \left[\vec{N}_i^p - \vec{N}_i^d + \vec{N}_i^d \log \left(\frac{\vec{N}_i^d}{\vec{N}_i^p} \right) \right],\end{aligned}\tag{2.9}$$

where this obeys a true chi-squared distribution for asymptotically large sample sizes. The denominator in (2.9) is the MC predicted probability, which assumes the best maximum likelihood estimate is the number of observed events.

2.2.2 External Constraints on the Fit

Since the BANFF ND constraint is a predictive model fit to data, it is subject to the bias-variance problem. This problem basically states that for a set of samples $s \in \mathcal{S}$, a predictive model $f_1 \in \mathcal{F}$ would have larger variance and smaller bias compared to a constrained or shrunken model $f_2 \subseteq f_1$ of which has larger bias but smaller variance. We wish to have a ND constraint measurement with as little variance as possible, which is achieved by introducing one or more constraints, also called “penalty” terms, to the test statistic (2.9). These penalty terms will introduce the T2K experiment’s model on the flux, cross section, and detector inefficiencies into the fit.

The new test statistic that includes the constraints, χ_{ND280}^2 , is given by

$$\begin{aligned}\chi_{\text{ND280}}^2 &= \chi_{\text{LLR}}^2 + \underbrace{\chi_{\text{xsec}}^2 + \chi_{\text{Flux}}^2 + \chi_{\text{Det}}^2}_{\text{Penalty terms}} \\ &= \chi_{\text{LLR}}^2 - 2 \left(\underbrace{\log \pi(\vec{x})}_{\text{xsec}} + \underbrace{\log \pi(\vec{b})}_{\text{Flux}} + \underbrace{\log \pi(\vec{d})}_{\text{Det}} \right),\end{aligned}\tag{2.10}$$

where each of the PDFs $\pi(\vec{y} = \{\vec{x}, \vec{b}, \vec{d}\})$ is an assumed multivariate normal distribution

$$\pi(\vec{y}) = C_y \exp \left(-\frac{1}{2} (\vec{y} - \vec{y}_0)^T V_y^{-1} (\vec{y} - \vec{y}_0) \right),\tag{2.11}$$

\vec{y}_0 is a vector of the initial parameter values, T corresponds to the transpose operator, C_y is the normalization, and V_y is the covariance matrix for vector \vec{y} . The full form of the test statistic χ^2_{ND280} is given by

$$\chi^2_{\text{ND280}} = 2 \sum_{i=1}^M \left[\vec{N}_i^p - \vec{N}_i^d + \vec{N}_i^d \log \left(\frac{\vec{N}_i^d}{\vec{N}_i^p} \right) \right] + (\Delta \vec{y})^T (V_y^{-1}) (\Delta \vec{y}) \quad (2.12)$$

where $\Delta \vec{y} = \vec{y} - \vec{y}_0$. It must be stated that the test statistic (2.12) purposefully excludes normalization terms since they are constants that do not affect the minimization. Further details on the penalty terms and covariance matrix in (2.12) will be discussed in Chapter 4.

The best fit parameters are those that minimizes the chi-squared statistic, $\hat{\chi}^2_{\text{ND280}}$, given by

$$\hat{\chi}^2_{\text{ND280}} = \underset{\vec{y} \in \mathbb{R}^d}{\operatorname{argmin}} \left\{ \chi^2_{\text{LLR}} (\vec{N}^d, \vec{N}^p) + \chi^2_{\text{Penalty}} (\vec{y}) \right\}, \quad (2.13)$$

where

$$\chi^2_{\text{Penalty}} (\vec{y}) = (\Delta \vec{y})^T (V_y^{-1}) (\Delta \vec{y})$$

and we recall that \vec{N}^p is a function of $\vec{y} = \{\vec{x}, \vec{b}, \vec{d}\}$ as well.

2.2.3 Postfit Covariance

Once the global minimum is found, the postfit covariance matrix needs to be calculated. Consider how the chi-squared varies around the global minimum, or also called the maximum likelihood estimate, $\hat{\vec{y}}$. The test statistic is given analytically by a Taylor series

$$\chi^2 (\vec{y}) = \sum_{n=0}^{\infty} \frac{1}{n!} \left[(\vec{y} - \hat{\vec{y}})^T \nabla_{\vec{y}} \chi^2 \Big|_{\vec{y}=\hat{\vec{y}}} \right]^n.$$

Since the gradient at $\hat{\vec{y}}$ is zero, the first non-zero \vec{y} -dependent term is quadratic in \vec{y}

$$\begin{aligned} \chi^2 (\vec{y}) &\approx \chi^2 (\hat{\vec{y}}) + \frac{1}{2} (\vec{y} - \hat{\vec{y}})^T \left(\nabla_{\vec{y}} \nabla_{\vec{y}}^T \chi^2 (\vec{y}) \Big|_{\vec{y}=\hat{\vec{y}}} \right) (\vec{y} - \hat{\vec{y}}) \\ &\approx \chi^2 (\hat{\vec{y}}) + \frac{1}{2} (\vec{y} - \hat{\vec{y}})^T \mathcal{H} (\vec{y} - \hat{\vec{y}}). \end{aligned}$$

where \mathcal{H} is a square matrix called the Hessian matrix

$$\mathcal{H}_{i,j} = \left. \frac{\partial^2 \chi^2}{\partial y_i \partial y_j} \right|_{\vec{y}=\hat{y}}, \quad (2.14)$$

and $y_i, y_j \in \vec{y}$. Assuming that our test statistic is distributed according to a multivariate normal distribution of the form (2.11), we find that the inverse of the Hessian matrix is the covariance matrix.

Chapter 3

The PØD Selections and Samples

This chapter describes the development of PØD ν_μ and $\bar{\nu}_\mu$ charged current (CC) inclusive¹³ selections in both FHC and RHC beam configurations for the BANFF fit. These selections are in continuation of previous works that developed ν_μ CC-inclusive selections between the PØD and the TPC. The first such analysis was the ν_μ CC-inclusive cross section using the previous ND280 simulation and reconstruction software release called “Production 5”¹⁴ [33]. That analysis relied on each subdetector’s reconstruction software and developed a track matching algorithm since the ND280 “Global” reconstruction matching was not available in that software production. Another cross section analysis measuring the cross section ratio of $\bar{\nu}_\mu/\nu_\mu$ also used this “pre-Global” technique with the modern ND280 “Production 6” software¹⁵ [7]. As the inter-detector matching reconstruction became available in Global, two cross section analyzes, ν_μ CC-0 π [8] and $\bar{\nu}_\mu$ CC-0 π [10, 24], were developed that also used the CC-inclusive selection as pre-selection cuts. A “cut” refers to one or more criteria to select reconstructed events that have desired properties. The pre-selection cuts are designed

¹³A CC-inclusive selection is a set of criteria that select all CC neutrino interaction events as opposed to an CC-exclusive selection like CC-0 π .

¹⁴The ND280 detector reconstruction and monte carlo official software updates are given a “Production” designation. The Production 5 software was actively used between 2012 and early 2014 until it was replaced by Production 6. However, physics analyzers are not as rapid to adopt the software updates.

¹⁵The ND280 “Production 6” software was released in 2014 and is still in active use.

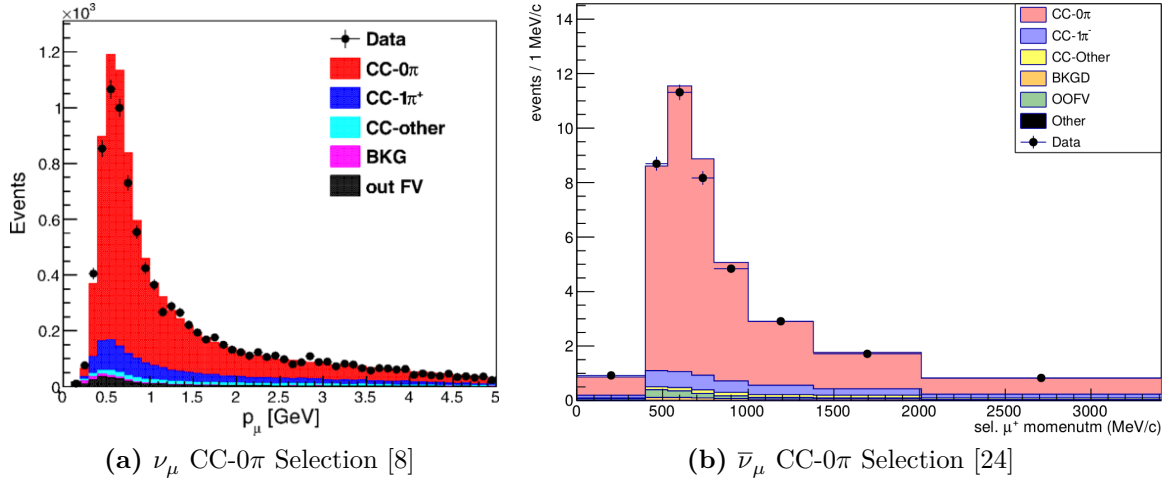


Figure 3.1: The PØD ν_μ and $\bar{\nu}_\mu$ CC- 0π selection kinematics. They importantly share the same pre-selection cuts as this analysis. The error bars are statistical only with the prediction sorted into various truth topologies.

in particular to filter out poor data quality events. They are well validated with results using these cuts are published as shown in Figure 3.1 on page 62. The selections described in this thesis also employ the same pre-selection cuts with the latest stable Global reconstruction software, Production 6.

This paragraph is a layout of the topics in the chapter. The first topic is the event reconstruction using the “Global” reconstruction software. Next is the pre-selection cut flow. With the pre-selection cuts established, three CC-inclusive selection are described in the following order: the ν_μ in foreword horn current (FHC) mode selection, $\bar{\nu}_\mu$ in reverse horn current (RHC) mode selection, and ν_μ background in RHC mode selection. Concluding this section is a discussion of the collected samples and their kinematic properties.

3.1 Global Reconstruction

The task of the Global reconstruction is to combine all of the ND280 information into a combined reconstructed object. It was originally designed to identify CC- 0π events in the Tracker, FGD+TPC, region and has been extended to operate with all of ND280.

The Global reconstruction is a software package that attempts to recognize patterns of deposited energy in ND280 and categorize it accordingly. Particles that deposit energy in long, linear segments are categorized as tracks. If multiple tracks originate from a common origin (vertex), it is likely that a true neutrino interaction event occurred near the reconstructed vertex. Particle cascade or shower reconstruction in Global will not be discussed since they are not selected in this thesis.

Each subdetector reconstruction algorithm is run separately as the seed to Global’s track matching algorithms. This includes the PØD’s track-finding algorithm, which defines a PØD track as a linear sequence of “nodes” with one node at each bar layer. Each node represents the approximate position where the particle intersected the bar layer. To facilitate inter-detector matching, Global attempts to “re-fit” the PØD track using a Kalman filter [81]. The re-fit procedure also corrects for particle energy loss as a function of length and multiple scattering processes. A PØD vertex, which is the assumed location of the neutrino interaction, is then associated with the re-fit track using another Kalman filter algorithm. Matching tracks between the PØD and the TPC is done automatically in the ND280 Global fit.

3.2 The PØD Selection Cuts

The selection of CC-inclusive events uses a series of cuts to select the muon track. Prior to any cuts and after the reconstruction, corrections are applied first to both data and MC events to correct for well known residual differences between them. This includes correcting the MC flux prediction using the secondary beamline data and reconstruction efficiency corrections. A complete list of the corrections applied are given in the following reference [4]. The pre-selection cuts (“precuts”) are then applied to extract events that start in the PØD water target (WT) fiducial volume (FV).

The following sections will describe the precuts common to all CC-inclusive selections. The next section describes the specific selections and their cuts to select the main track associated as the lepton candidate. Finally the lepton candidate and event kinematics for all the samples are described.

3.2.1 Precuts

The precuts were initially developed to select ν_μ CC-inclusive events using the PØD and TPC subdetector reconstruction algorithms separately [7, 33]. They were then used with the Global reconstruction software for the ν_μ CC- 0π selection in the FHC beam configuration [8]. All cuts were implemented in psyche [76] which is the software interface that BANFF uses to select events.

Prior to the precuts, neutrino interaction data event must be collected and reconstructed for each T2K beam spill. Each T2K beam spill has eight bunches that are 58 ns long and temporally separated by 581 ns. When the beam spill occurs, the PØD’s Trip-T electronics are triggered to collect data in preset integration cycles aligned with the bunches. Each integration cycle is 480 ns long and is followed by a 100 ns dead-time to prepare for the next cycle [33]. The data collected in each cycle is used to reconstruct neutrino interaction events using the ND280 subdetector and Global software packages.

Each reconstructed event must pass the following cuts before being assigned to a selection:

1. The event has a “good” data quality flag.
 - An event is rejected if any electronics element or subdetector in ND280 is reported as “bad” during the corresponding bunch.
2. There is at least one (1) track reconstructed in the TPC.
 - There are no restrictions on the number of tracks fully contained in the PØD or exiting into other subdetectors.

3. The track in the TPC must have more than 18 nodes.
 - The TPC reconstruction gathers the vertical and horizontal micromegas that registered collected charge into clusters of “hits”. Each cluster’s charge distribution is used to get a vertical (horizontal) position that is more accurate than the individual readout micromegas. A node is constructed out of each cluster with associated track state information. The set of nodes are used to fit a helix shaped track.

4. The reconstructed vertex is within the PØD WT FV.
 - The PØD FV is defined to include as much of the WT regions as possible. Its X and Y borders are 25 cm away from the PØDule edges while the Z borders intersect the last and first half downstream PØDule in the upstream ECal and central ECal, respectively. The FV edges are listed in Table 3.1 on page 66. This volume, while used for track-based analyzes in the past, was optimized for π^0 and ν_e analyses.

5. All tracks that enter the TPC pass the veto cut
 - An event is rejected if any PØD track enters the TPC from outside the “corridor” volume. This cut was designed to eliminate broken tracks when the pre-Global separate subdetector reconstruction was used [25]. In practice, this cut ensures that Global tracks entering the TPC are away from its X and Y edges. The corridor definition is the same as defined in the $\bar{\nu}_\mu/\nu_\mu$ cross section ratio analysis technical note [26] and shown in Table 3.1 on page 66.

PØD WT FV	Corridor Volume
$-836 < X < 764$	$-988 < X < 910$
$-871 < Y < 869$	$-1020 < Y < 1010$
$-2969 < Z < -1264$	$-3139 < Z < -900$

Table 3.1: The PØD WT FV (left) and veto corridor volume (right) in the ND280 coordinate system. The corridor spans from the 5th (8th) to 40th (80th) PØDule (scintillator layer). All the units are given in millimeters.

After passing of all the precuts, a single, global track, which is observed in the TPC, is assigned as the lepton candidate or “main track” of a selected event. While the main track is different for each selected event, the momentum reconstruction is the same. The momentum of the main track, P , is sum of its measured momentum in the TPC, P_{TPC} , with the estimate momentum lost in the PØD, $\Delta P_{\text{PØD}}$

$$P = P_{\text{TPC}} + \Delta P_{\text{PØD}}. \quad (3.1)$$

The momentum lost in the PØD is estimated by summing the total momentum loss along the track path \mathcal{C}

$$\Delta P = \int_{\mathcal{C}} \left(\frac{dP}{dx} \right) dx, \quad (3.2)$$

where dP/dx is the momentum loss function. The momentum loss function is related to the energy loss function, dE/dx via the chain rule

$$\begin{aligned}
\frac{dE}{dx} &= \left(\frac{dE}{dP} \right) \left(\frac{dP}{dx} \right) \\
&= \frac{d}{dP} \left(\sqrt{P^2 c^2 + m^2 c^4} \right) \left(\frac{dP}{dx} \right) \\
&= \left(\frac{P c^2}{E} \right) \left(\frac{dP}{dx} \right) \\
&= \beta c \left(\frac{dP}{dx} \right),
\end{aligned} \tag{3.3}$$

where β is the particle velocity as a ratio of the speed of light c . Since the reconstructed track's path \mathcal{C} is not infinitesimally precise due to inherent detector resolution, we must replace the integral with a sum and differential $dx \rightarrow \Delta x$. We then arrive at the expression of the momentum loss estimate in the PØD as

$$\Delta P_{\text{PØD}} = \frac{1}{c} \sum_t \left[\left(\frac{dE}{dx} \right) \left(\frac{\Delta x}{\beta} \right) \right]_t, \tag{3.4}$$

where t is a discrete step in x connecting the track nodes. For most tracks entering the TPC, they will be highly relativistic in the PØD ($\beta \approx 1$), and (3.4) simplifies to

$$\Delta P_{\text{PØD}} = \frac{1}{c} \sum_t \left[\left(\frac{dE}{dx} \right) \Delta x \right]_t. \tag{3.5}$$

The next sections describe the selection cuts, first in FHC mode and then RHC mode.

3.2.2 The ν_μ in FHC Mode CC-Inclusive Selection

As discussed in Section 3.2.1, this selection is the basis for the PØD ν_μ CC-0 π analysis [8]. In FHC mode, the vast majority of neutrino interactions are ν_μ CC events that produce an outgoing, negatively charged muon. If there is no negatively charged track in the TPC, the event is likely not a ν_μ -induced interaction. Therefore, the ν_μ in FHC mode CC-inclusive selection in FHC mode has one final cut after the precuts:

1. At least one negatively charged track is reconstructed in the TPC.

- An event is rejected if none of the TPC tracks have a reported negative curvature.

If the event passes this cut, the highest momentum negative (curvature) track, or HMNT, is selected as the lepton candidate. This selection and all subsequent selections are branched into two categories based on the number of tracks counted in the PØD. If there is only one PØD track, and hence only one track in the TPC as required by the precuts, the event is categorized as a “ ν_μ in FHC Mode CC 1-Track” event. Otherwise, the event is categorized as a “ ν_μ in FHC Mode CC N-Tracks” event.

3.2.3 The $\bar{\nu}_\mu$ in RHC Mode CC-Inclusive Selection

In RHC mode, the majority of the beam neutrinos are $\bar{\nu}_\mu$ since the horn focuses negatively charged pions and deflects positively charged pions. However, the ν_μ background interaction rate in RHC mode is larger than the $\bar{\nu}_\mu$ background in FHC mode. The reason for this is two fold. Firstly, the antineutrino-nuclear scattering cross section is suppressed by $\sim 1/3$ compared to the neutrino-nuclear scattering cross section as explained in Section 1.1.1.3. Secondly, the ν_μ flux in RHC is relatively large due to the excess of positively charged pions generated at the target. Therefore there is a non-negligible “wrong-sign” background in RHC mode that we need to reject.

Prior to this analysis, a $\bar{\nu}_\mu$ CC-0 π selection was developed for the PØD [24]. The $\bar{\nu}_\mu$ CC-0 π selection is quite similar to the ν_μ CC-inclusive selection in FHC mode, but relied on the PØD local reconstruction for a particle identification cut. The PØD local reconstruction is, however, unavailable in the event selection software used in the BANFF fit called psyche. So a new selection was developed specifically for this analysis to select $\bar{\nu}_\mu$ interactions in RHC mode.

The $\bar{\nu}_\mu$ in RHC mode CC-inclusive selection uses the precuts described in Section 3.2.1 and the has two cuts:

1. At least one positively charged track is reconstructed in the TPC.

- An event is rejected if none of the TPC tracks have a reported positive curvature.
2. The highest momentum positive (curvature) track, or HMPT, must be the highest momentum track.
 - If the highest momentum track has negative curvature, then the event is rejected.

If the event passes these two cuts, the HMPT is the lepton candidate. If there is only one PØD track, the event is categorized as a “ $\bar{\nu}_\mu$ in RHC Mode CC 1-Track” event. Otherwise, the event is categorized as a “ $\bar{\nu}_\mu$ in RHC Mode CC N-Tracks” event.

3.2.4 The ν_μ in RHC Mode CC-Inclusive Selection

As explained in the previous subsection, the ν_μ background interaction rate in RHC mode is relatively large compared to the $\bar{\nu}_\mu$ interaction rate. Having a measurement of this background is critical for the oscillation analysis due to the small number of expected $\bar{\nu}_\mu \rightarrow \bar{\nu}_e$ counts. To date, there is no PØD measurement of ν_μ background in RHC mode, nor any PØD selection to do so. So like the $\bar{\nu}_\mu$ CC-inclusive selection, a new PØD selection was developed exclusively for this analysis to select ν_μ background events in RHC mode.

The ν_μ background in RHC mode CC-inclusive selection uses the precuts described in Subsection 3.2.1 and has two cuts:

1. At least one negatively charged track is reconstructed in the TPC.
 - An event is rejected if none of the TPC tracks have a reported negative curvature.
2. The HMNT must be the highest momentum track.
 - If the highest momentum track has positive curvature, then the event is rejected.

If the event passes these two cuts, the HMNT is the lepton candidate. If there is only one PØD track, the event is categorized as a “ ν_μ Background in RHC Mode CC 1-Track” event. Otherwise, the event is categorized as a “ ν_μ Background in RHC CC N-Tracks” event.

Run period	Horn current [kA]	PØD status	Data POT ($\times 10^{20}$)	MC POT ($\times 10^{20}$)
2	+250	Water	0.433934	12.0341
		Air	0.359149	9.23937
3b	+205		0.217273	4.47864
3c	+250		1.36447	26.3227
4			1.78271	34.996
		Water	1.64277	34.9712
5c	-250		0.43468	22.7766
6b		Air	1.28838	14.174
6c			0.505895	5.27562
6d			0.775302	6.884
6e			0.847902	8.59439
7b		Water	2.43682	33.7046
8	+250		1.58053	26.4664
		Air	4.14897	36.0694
Sand	+250		-	11.1988
Sand	-250		-	12.9201
2, 3b, 3c, 4, 8		FHC	Air	7.872757
2, 4, 8			Water	3.656589
6b, 6c, 6d, 6e		RHC	Air	3.382490
5c, 7b			Water	2.852340
				54.53

Table 3.2: T2K data-taking periods and collected POT used in the analysis. The bottom four rows are the aggregated periods grouped by horn current and PØD status, which is how the data analysis is performed. Note that the horns were run briefly at +205 kA for Run 3b when operations resumed after 2011 Tōhoku earthquake.

3.3 Selection Kinematics

This section examines the kinematics for each of selections and their respective branches while differentiating between water-in and water-out mode. The data sets used in this analysis are runs 2-8 in both PØD water-in and water-out (air) modes as shown in Table 3.2 on page 70. There will be no data events shown to prevent any potential analysis biases. Simulated events will be arranged into various true categories to study selection kinematics, efficiencies, and purities.

True interactions for these selections are generally divided into four classes:

- A neutrino-induced CCQE interaction (ν CCQE):
 - Only NEUT generated neutrino-induced CCQE event at the interaction vertex.
- A neutrino-induced non-CCQE interaction (ν non-CCQE):
 - Any NEUT generated neutrino-induced CC and NC event *except* neutrino-induced CCQE at the interaction vertex.
- An antineutrino-induced CCQE interaction ($\bar{\nu}$ CCQE):
 - Only NEUT generated antineutrino-induced CCQE event at the interaction vertex.
- An antineutrino-induced non-CCQE interaction ($\bar{\nu}$ non-CCQE):
 - Any NEUT generated antineutrino-induced CC and NC event *except* antineutrino-induced CCQE at the interaction vertex.

These signal classes must occur in the PØD WT FV in order to be selected. The non-CCQE category can be further divided among the dominant T2K CC and all NC interactions modes as enumerated in Table 3.3 on page 72. An out of FV (OOFV) event is any true event that occurs in ND280, but is falsely reconstructed in the PØD FV. Another important ND280 background are true neutrino and antineutrino CC interactions occurring in the sand surrounding the ND280 pit with the muon track falsely reconstructed in the FV. These events are referred to as “sand muon” events and are accounted for accordingly. Since these categories are used frequently in this chapter, the legends used in the histograms are enlarged for the reader’s convenience in Figure 3.2 on page 72.

The ND280 MC uses the GEANT4 software toolkit [14] to simulate the passage of particles through matter. A GEANT4 particle is assigned to a reconstructed track if it contributed the most to the track’s reconstructed hits. The most likely truth matched particles include protons (p), both negatively and positively charged muons (μ^\pm), pions (π^\pm), and

Interaction mode		ν ($\bar{\nu}$) NEUT enumeration
CCQE		1 (-1)
2p2h		2 (-2)
CC-1 π		11 → 16 (-11 → -16)
non-CCQE	CC-N π	21 (-21)
	CC-DIS	26 (-26)
CC-Other		17, 22, 23 (-17, -22, -23)
NC		31 → 100 (-31 → -100)

Table 3.3: Enumeration of the NEUT interaction modes which are also used in Figure 3.2 on page 72. An arrow indicates a sequence of integer steps from left to right of the arrow.

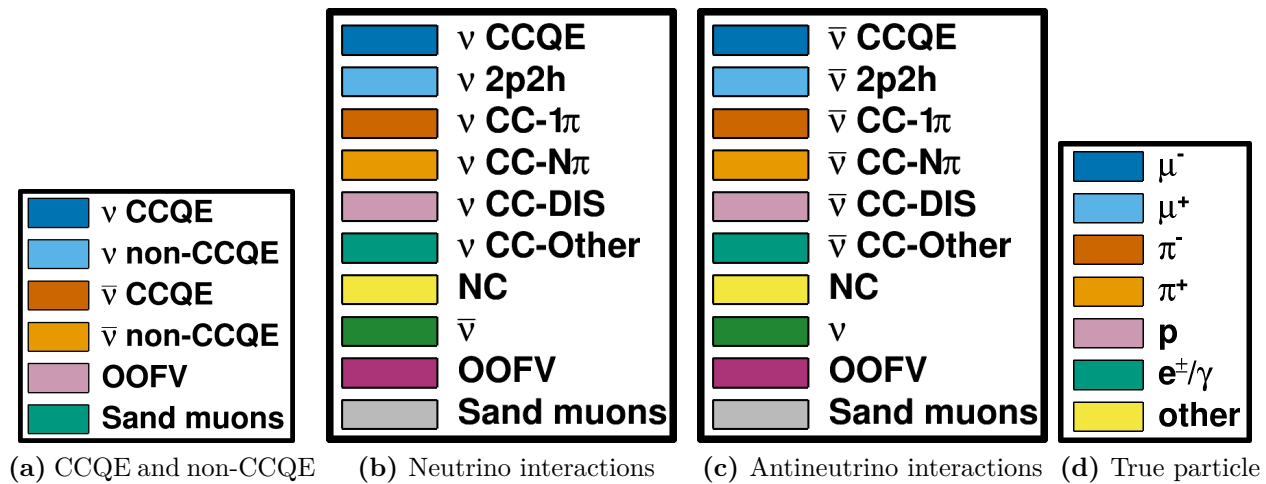


Figure 3.2: Frequently used legends that are enlarged for the reader's convenience.

electrons/positrons (e^\pm). In addition, any electron and positron generated from pair production are grouped together as “ e^\pm/γ ”. Particles that do not match any of these categories is labeled as “other”.

3.3.1 The ν_μ in FHC Mode CC 1-Track Sample

This selection provides the CCQE-like samples in FHC mode. Figure 3.3 on page 74 and Figure 3.4 on page 75 displays the momentum and angular distributions that are inputs to BANFF. Comparing between water-in and water-out modes, we see that the reconstructed

kinematics are nearly identical. In the majority of cases, the lepton candidate is the true muon, making this a very pure ν_μ sample. We also see that there are non-CCQE events, which without a particle identification cut, are an irreducible background. Following this paragraph and the following sections, only the PØD water-in mode kinematics will be shown.

The target nuclei between water-in and water-out modes is shown in Figure 3.5 on page 76. Scattering on the carbon nucleus is the dominant interaction in both modes since the scintillating bars are constructed of polyethylene $[(\text{CH}_2\text{CH}_2)_n]$ plastic. In water-in mode, the oxygen nucleus is a significant target with hydrogen having a small contribution as well. The brass layers between the PØDules and the water bags introduce copper and zinc nuclei scattering events too. The events on lead nuclei are true OOFV and primarily occur in the last PØDule.

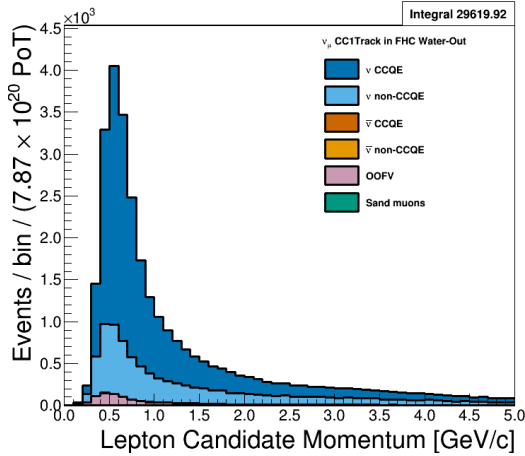
We can examine the efficiencies and purities differentially for true ν_μ CCQE interactions in Figure 3.6 on page 76. The efficiency, ϵ , and purity, ρ , are defined as

$$\epsilon = \frac{N_{\text{Selected}}^{\text{True}}}{N^{\text{True}}} \quad \rho = \frac{N_{\text{Selected}}^{\text{True}}}{N_{\text{Selected}}}, \quad (3.6)$$

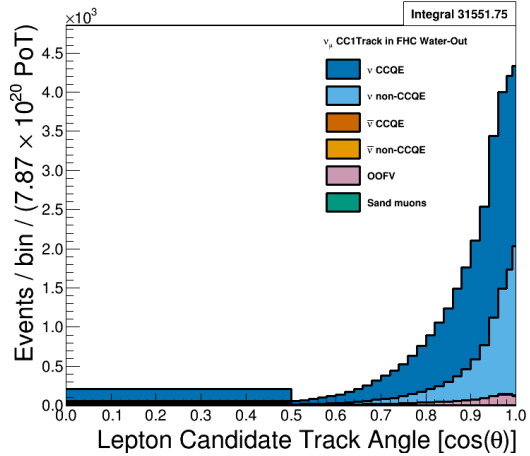
where $N_{\text{Selected}}^{\text{True}}$ is the number of true, selected events, N^{True} is the number of true events, and N_{Selected} is the number of selected events. They demonstrate that the purity is highest near 0.5 GeV/c with the efficiency highly dependent on the track angle.

The underlying true kinematics of the interactions are shown in Figure 3.7 on page 77. Using Figure 1.5 on page 12 as reference, the kinematics shown are the true neutrino energy $E_\nu = k_0$ and 4-momentum transfer $Q^2 = -q^2$. These two variables are of theoretical importance since they are used to generate events using NEUT and are used in the BANFF fit. An interesting CCQE-like final state in this selection are correlated nucleon pair scattering called “2 particle, 2 hole” (2p2h)¹⁶ events [58]. Interaction model parameters for 2p2h have

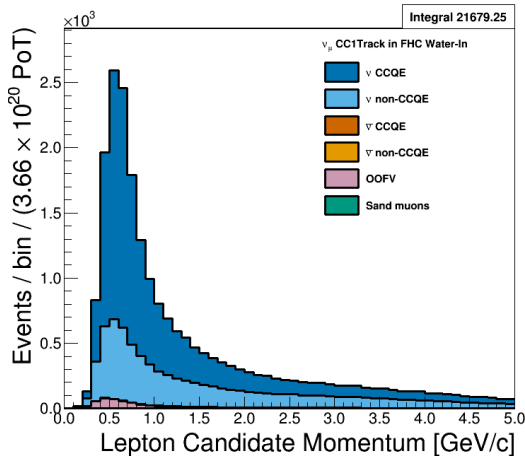
¹⁶The name 2p2h originates from Condensed Matter Physics which motivated the model. In solid state matter, a “hole” refers to the absence of an electron in a valence band. In the High Energy Physics context, 2p2h considers neighboring and interacting nucleon pairs (2p) scattering from an incoming neutrino. The imparted energy on the pair excites them to higher energy states leaving two “hole” states (2h) behind.



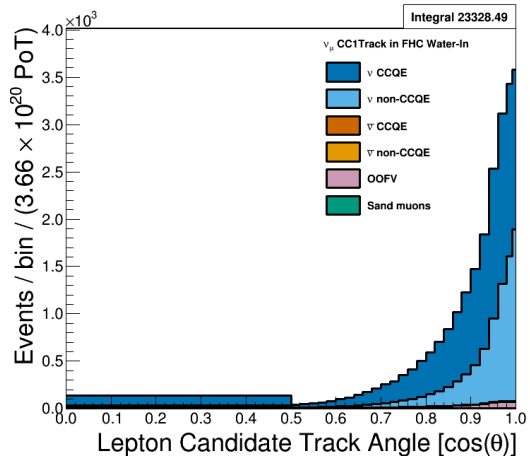
(a) Water-out Momentum



(b) Water-out cos theta

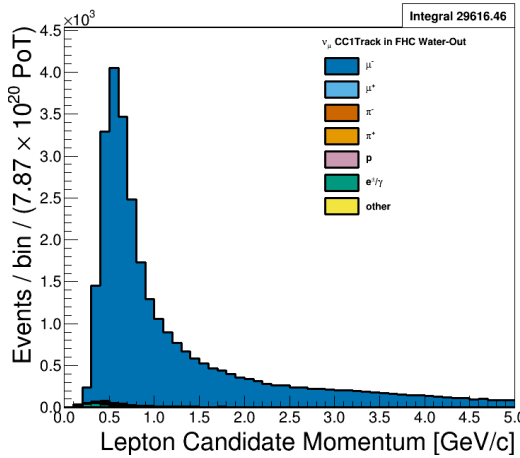


(c) Water-in Momentum

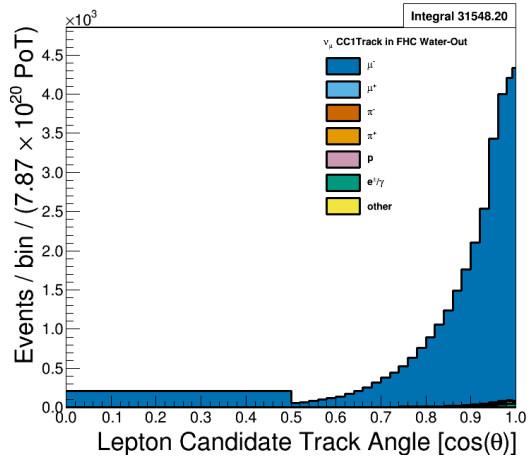


(d) Water-in cos theta

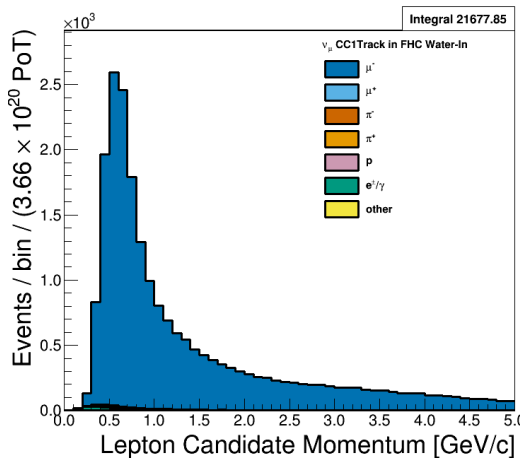
Figure 3.3: Reconstructed kinematics of the ν_μ in FHC Mode CC 1-Track selection categorized by CCQE and non-CCQE interactions. The top figures, (a) and (b), use the PØD water-out MC and are normalized to the FHC water-out mode POT. The bottom figures, (c) and (d), use the PØD water-in MC and are normalized to the FHC water-in mode POT. Also a single bin is used in the range of $0 \leq \cos \theta < 0.5$ in figures (b) and (d).



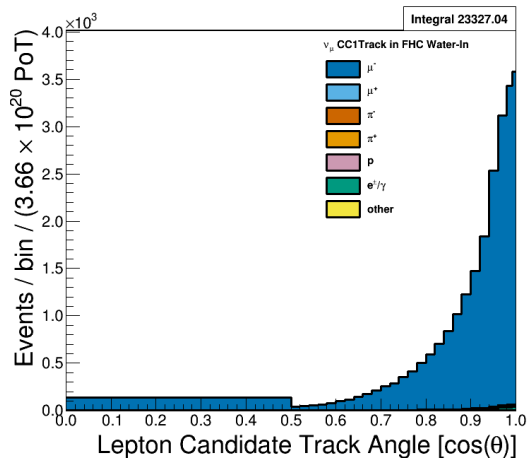
(a) Water-out Momentum



(b) Water-out $\cos \theta$



(c) Water-in Momentum



(d) Water-in $\cos \theta$

Figure 3.4: Reconstructed kinematics of the ν_μ in FHC Mode CC 1-Track selection categorized by the true particle matched to the main track. The top figures, (a) and (b), use the PØD water-out MC and are normalized to the FHC water-out mode POT. The bottom figures, (c) and (d), use the PØD water-in MC and are normalized to the FHC water-in mode POT. Also a single bin is used in the range of $0 \leq \cos \theta < 0.5$ in figures (b) and (d).

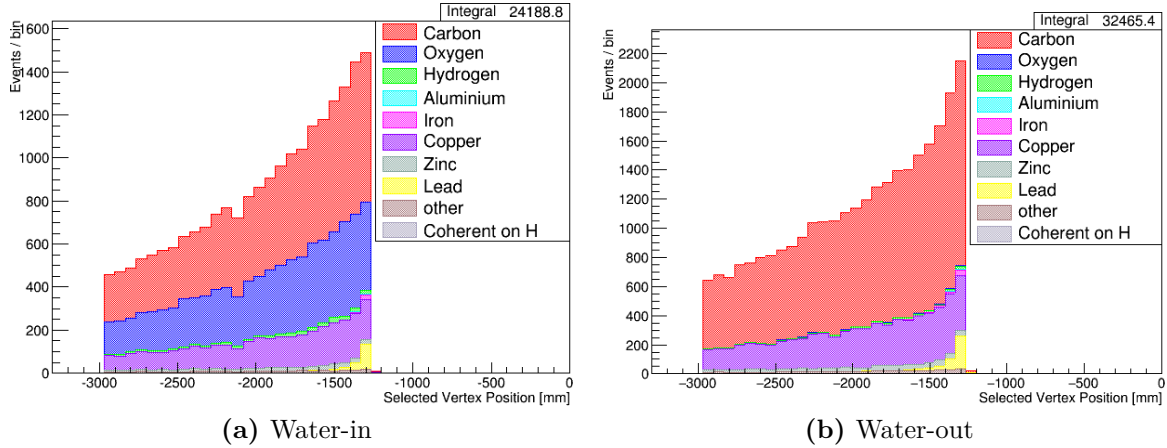


Figure 3.5: Reconstructed vertex Z position of the ν_μ in FHC Mode CC 1-Track selection. The events are categorized by the true target nucleus. The number of selected events increases with increasing Z since the probability of an interaction increases as the neutrino crosses more media in the PØD. Due to a software bug in the MC, coherent events on hydrogen (Coherent on H) are a unique category.

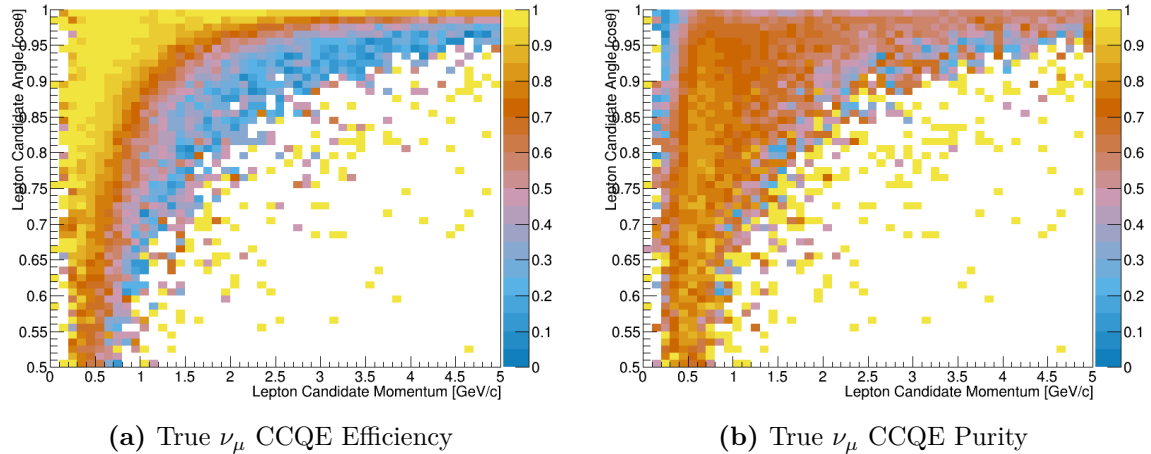


Figure 3.6: Efficiency and purity of the ν_μ in FHC Mode CC 1-Track selection. True events are defined as correctly matched μ^- tracks from ν_μ -induced CCQE interactions at the vertex.

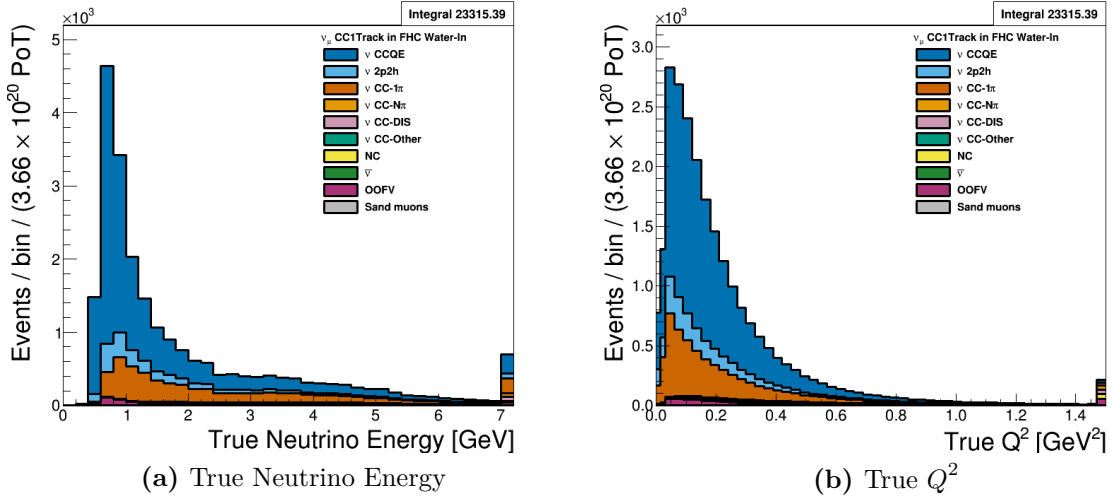


Figure 3.7: True kinematics of the ν_μ in FHC Mode CC 1-Track selection. Water-in mode is displayed here only with the last bin shown is used as overflow. The figures use the PØD water-in MC and are normalized to the FHC water-in mode POT.

large systematic uncertainties in T2K and are included the BANFF fit. Therefore these events could help reduce the 2p2h model uncertainties.

This selection contains a modest fraction of non-CCQE interactions. The largest contamination is 1π interactions, which can happen primarily for a couple of reasons. Firstly, when the final state pion is produced, it is subject to final state interactions (FSI) where a pion can be absorbed or scattered in the nucleus. Secondly, and more importantly, a pion might not be reconstructed as a track in the PØD if its energy is below reconstruction threshold. Together, the large 1π background affects the sensitivity to CC- 0π and CC- 1π model parameters in the BANFF fit.

3.3.2 The ν_μ in FHC Mode CC N-Tracks Sample

This selection provides non-CCQE-like samples in FHC mode inputs to the BANFF fit. The reconstructed momentum and angular distributions are shown in Figure 3.8 on page 78 and Figure 3.9 on page 79. Since this selection is not optimized for any particular CC topology, there are a variety of interaction modes present including 1π , multiple pion ($N\pi$)

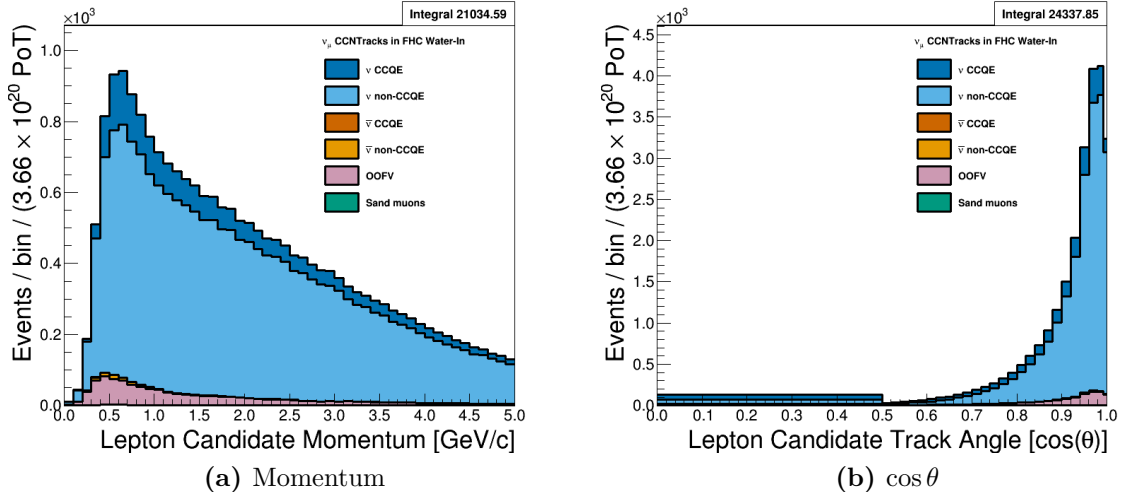


Figure 3.8: Reconstructed kinematics of the ν_μ in FHC Mode CC N-Tracks selection categorized by CCQE and non-CCQE interactions. The figures use the PØD water-in MC and are normalized to the FHC water-in mode POT. Also a single bin is used in the range of $0 \leq \cos \theta < 0.5$ in figure (b).

and deep inelastic scattering (DIS). There are a number of events with a mis-identified main track that are matched to electrons and pions. There is also a relatively larger OOFV contamination compared with the 1-Track selection with some events originating in the upstream ECal as seen in Figure 3.10 on page 79. Otherwise, the vertex position and target materials are quite similar between the 1-Track and N-Tracks selections.

We can examine the efficiencies and purities differentially for the selection in Figure 3.11 on page 80. For the efficiency and purity only, the true signal is any ν_μ CC interaction except ν_μ CCQE (CC non-QE), which the CC 1-Track topology selection is designed to select. The efficiency is high for the higher momenta and higher angle tracks suggesting this is a high Q^2 selection. In addition, the purity is around $\sim 70\%$ in this region.

The fundamental kinematics of the selection are shown in Figure 3.12 on page 81. The selection is relatively ν_μ -pure and captures the high energy tail of the neutrino flux. True kinematics that describe the 1π , $N\pi$, and DIS models are parameterized in Q^2 and the hadronic system mass W . Using Figure 1.5 on page 12, we can define the invariant mass of hadronic system as

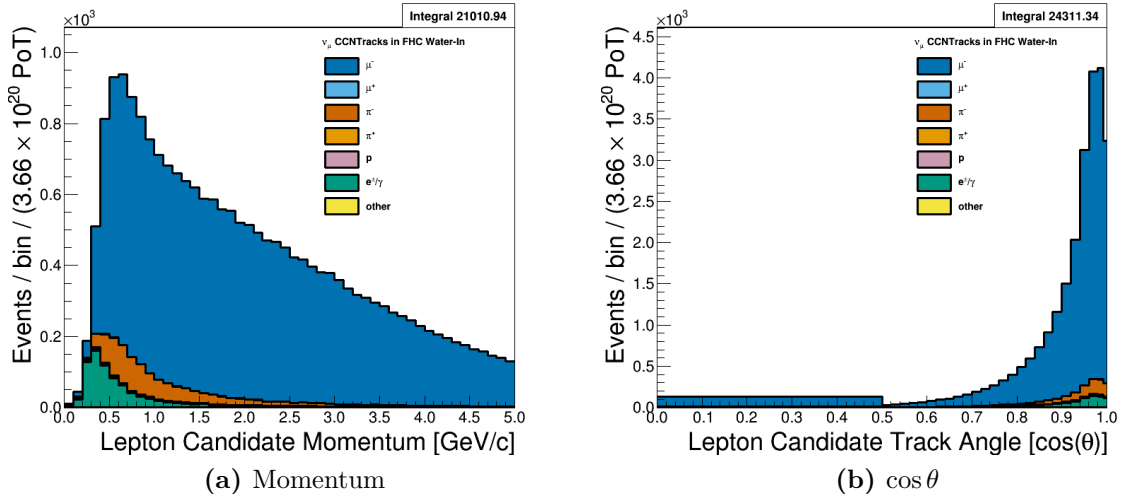


Figure 3.9: Reconstructed kinematics of the ν_μ in FHC Mode CC N-Tracks selection categorized by the true particle matched to the main track. The figures use the PØD water-in MC and are normalized to the FHC water-in mode POT. Also a single bin is used in the range of $0 \leq \cos \theta < 0.5$ in figures (b) and (d).

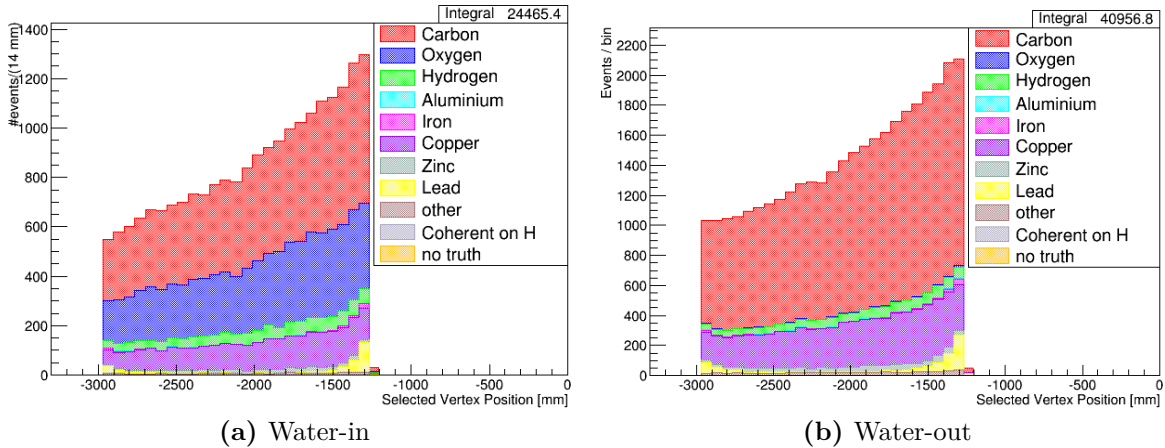


Figure 3.10: Reconstructed vertex Z position of the ν_μ in FHC Mode CC N-Tracks selection categorized by the true target nucleus. The number of events increases with increasing Z since the probability of an interaction increases as the neutrino crosses more media in the PØD. Due to a software bug in the MC, coherent events on hydrogen (Coherent on H) are a unique category.

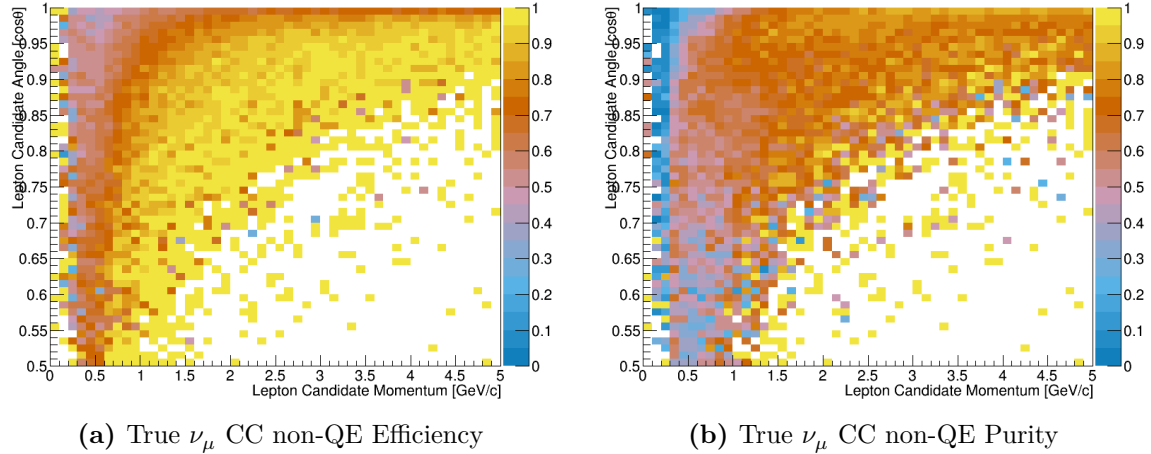


Figure 3.11: Efficiency and purity of the ν_μ in FHC Mode CC N-Tracks selection. True events are defined as correctly matched μ^- tracks from ν_μ -induced CC non-QE interactions at the vertex.

$$\begin{aligned}
 W^2 c^4 &= (p+q)^2 = p^2 + 2p \cdot q + q^2 \\
 &= M_N^2 c^4 + 2M_N c^2 (k_0 - k'_0) - Q^2,
 \end{aligned} \tag{3.7}$$

where M_N is the mass of the struck nucleon and k_0/k'_0 is the energy of the neutrino/outgoing lepton. A dominant mode in the selection is from the 1π interaction from a Δ resonance. A resonance is clearly seen in the W distribution in Figure 3.12 on page 81, which comes from the Δ baryon which has a rest mass of 1.232 GeV/c².

The origin of the mis-identified tracks, in particular the pion matched tracks, becomes more clear since this is a high Q^2 selection. The $N\pi$ and DIS events, which are high Q^2 events, can yield a post-FSI charged pion track. These pions could have more energy than the outgoing muon or could be the only particle observed in the TPC.

3.3.3 The $\bar{\nu}_\mu$ in RHC Mode CC 1-Track Sample

This selection provides the $\bar{\nu}_\mu$ CCQE-like samples in RHC mode that are inputs to the BANFF fit. In Figure 3.13 on page 82 and Figure 3.14 on page 83 display the momentum and angular distributions for this selection. The selection is highly $\bar{\nu}_\mu$ -pure with the selected lepton candidate being positively charged muons. There is a large OOFV background from

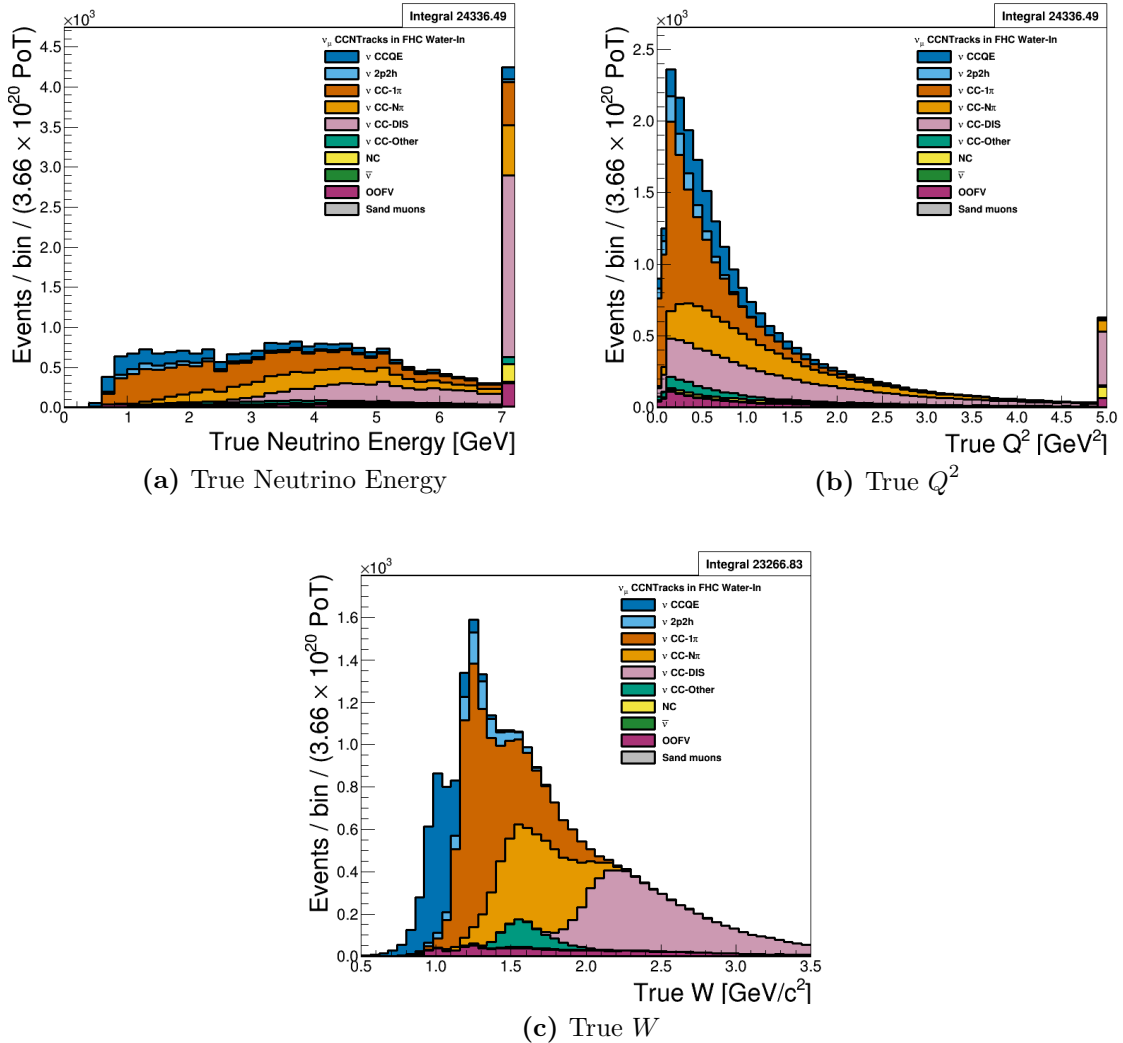


Figure 3.12: True kinematics of the ν_μ in FHC Mode CC N-Tracks selection. The last bin shown in (a) and (b) is used as overflow. The figures use the PØD water-in MC and are normalized to the FHC water-in mode POT. In figure (c), the largest resonance comes from the Δ baryon. There are higher order resonances in (c) as well.

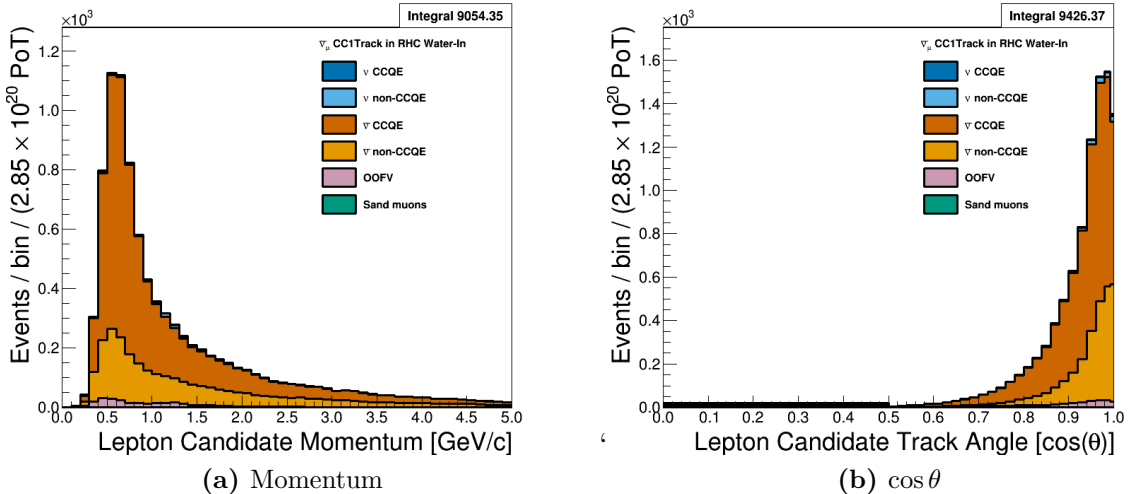


Figure 3.13: Reconstructed kinematics of the $\bar{\nu}_\mu$ in RHC Mode CC 1-Track selection categorized by CCQE and non-CCQE interactions. The figures use the PØD water-in MC and are normalized to the RHC water-in mode POT. Also a single bin is used in the range of $0 \leq \cos \theta < 0.5$ in figure (b).

proton tracks. They are high momentum (> 1 GeV/c) tracks which, at these energies, are minimum ionizing and can reach into the TPC.

We can examine the efficiencies and purities differentially for the selection in Figure 3.15 on page 83. For the efficiency and purity only, the true signal is a true $\bar{\nu}_\mu$ CCQE interaction. The two distributions are very similar to the efficiency and purity observed in the ν_μ in FHC Mode CC 1-Track sample, with the efficiency being relatively high (90%) for high statistics regions.

The underlying true kinematics, E_ν and Q^2 , of the interactions are shown in Figure 3.16 on page 84. We see a similar true reaction composition with that of the ν_μ in FHC Mode sample in Section 3.3.1. Most reactions are true CCQE with a mixture of 2p2h and 1 π events. As previously seen in Section 3.3.1, the significant 1 π contamination may reduce the sensitivity to both CC-0 π and CC-1 π model parameters in the BANFF fit.

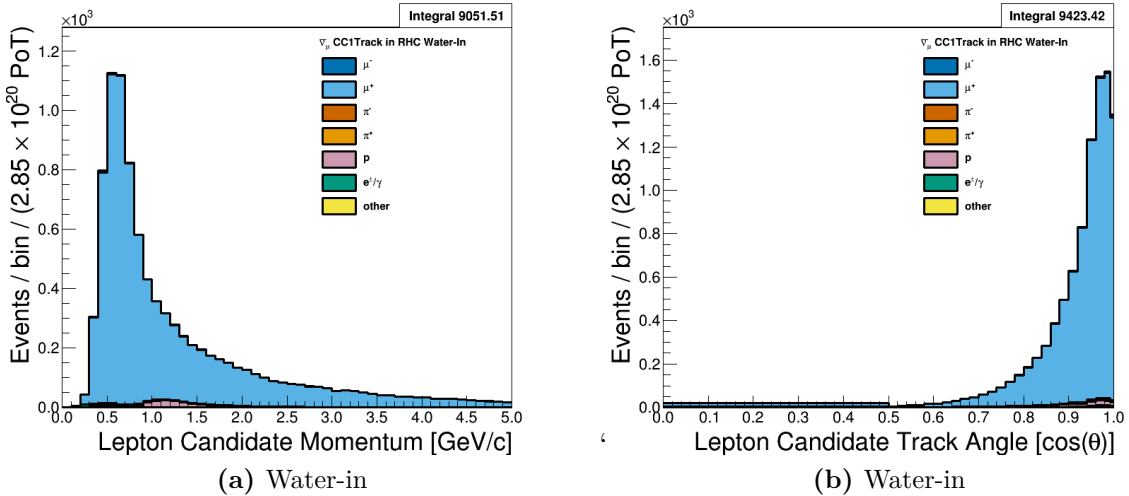


Figure 3.14: Reconstructed kinematics of the $\bar{\nu}_\mu$ in RHC Mode CC 1-Track selection categorized by the true particle matched to the main track. The figures use the PØD water-in MC and are normalized to the RHC water-in mode POT. Also a single bin is used in the range of $0 \leq \cos \theta < 0.5$ in figure (b).

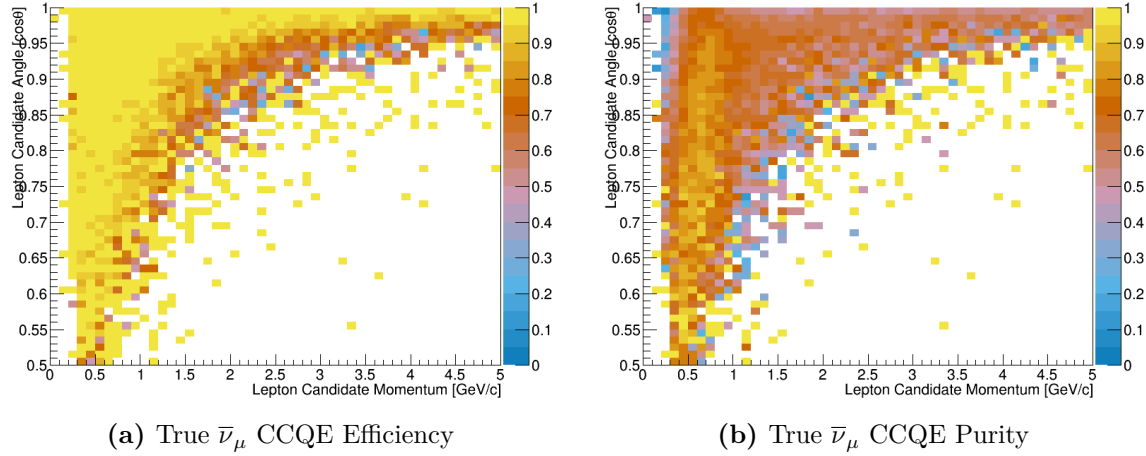


Figure 3.15: Efficiency and purity of the $\bar{\nu}_\mu$ in RHC Mode CC 1-Track selection. The true events are $\bar{\nu}_\mu$ CCQE at the vertex and the selected lepton candidate is the true μ^+ .

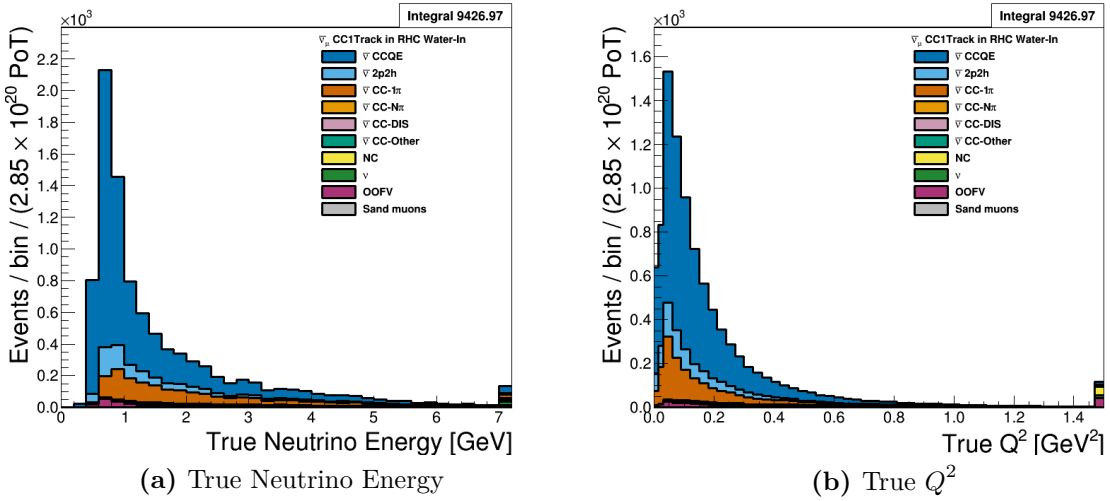


Figure 3.16: True kinematics of the $\bar{\nu}_\mu$ in RHC Mode CC 1-Track selection. Water-in mode is displayed here only with the last bin shown as overflow. The figures use the PØD water-in MC and are normalized to the RHC water-in mode POT.

3.3.4 The $\bar{\nu}_\mu$ in RHC Mode CC N-Tracks Sample

This selection provides the $\bar{\nu}_\mu$ non-CCQE-like samples in RHC mode. Figure 3.17 on page 85 and Figure 3.18 on page 85 display the momentum and angular distributions that are inputs to BANFF. The most striking feature of this selection is the number of mis-identified events. In particular tracks matched to protons are selected as the HMPT when the protons are minimum ionizing particles themselves, which is about 1.3 GeV/c. In addition, the intrinsic ν_μ background contribution is comparable to the desired $\bar{\nu}_\mu$ flavor. These two features should be addressed to increase the utility of the selection for the next iteration of the analysis.

We can examine the efficiencies and purities differentially for the selection in Figure 3.11 on page 80. For the efficiency and purity only, the true signal is any $\bar{\nu}_\mu$ CC interaction except $\bar{\nu}_\mu$ CCQE which the CC 1-Track selection is designed to select. Both the efficiency and purity are low where statistics are high due to the wrong sign background.

The underlying true kinematics, E_ν , Q^2 , and W , of the interactions are shown in Figure 3.20 on page 87. Here we see in better detail the origin of the ν_μ contamination. As

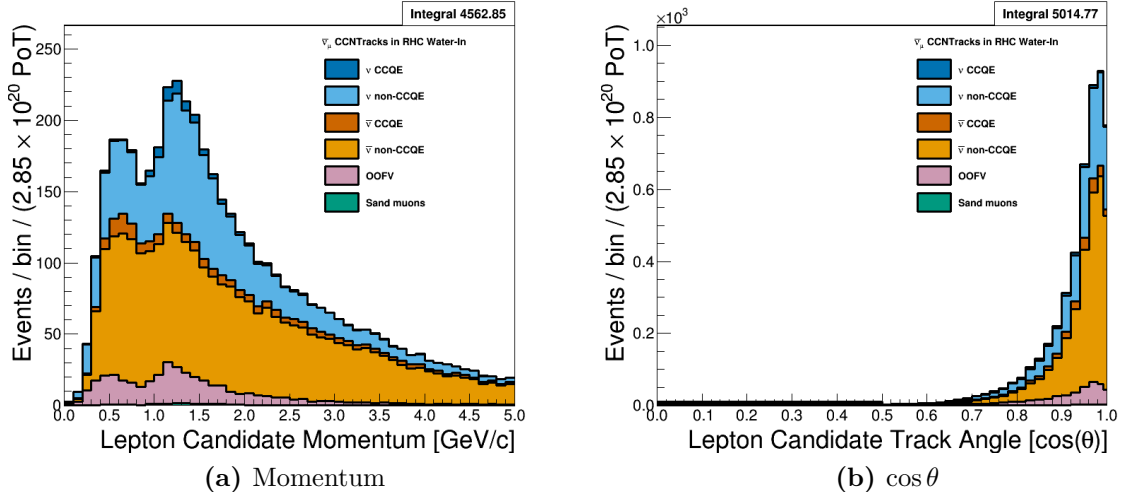


Figure 3.17: Reconstructed kinematics of the $\bar{\nu}_\mu$ in RHC Mode CC N-Tracks selection categorized by CCQE and non-CCQE interactions. The figures use the PØD water-in MC and are normalized to the RHC water-in mode POT. Also a single bin is used in the range of $0 \leq \cos \theta < 0.5$ in figure (b).

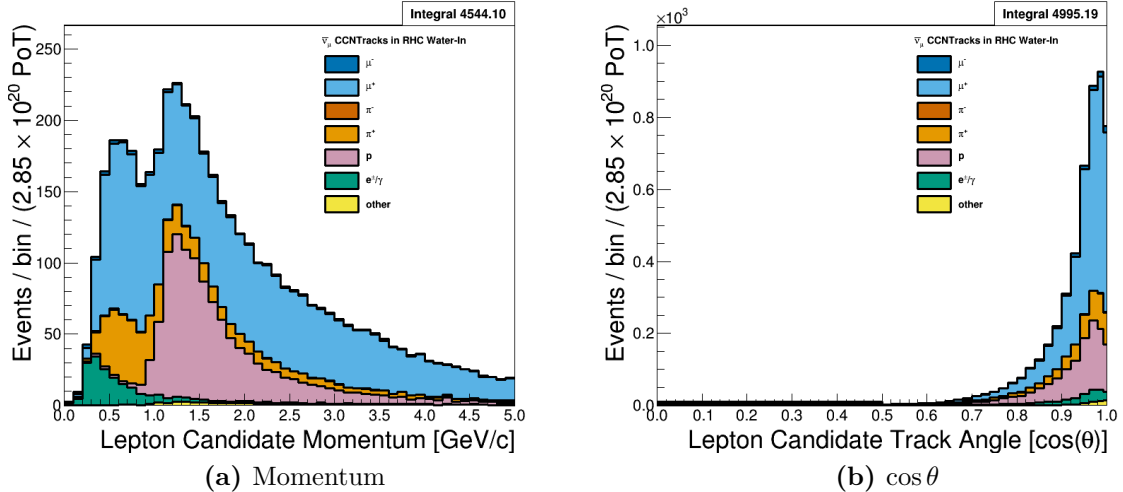


Figure 3.18: Reconstructed kinematics of the $\bar{\nu}_\mu$ in RHC Mode CC N-Tracks selection categorized by the true particle matched to the main track. The figures use the PØD water-in MC and are normalized to the RHC water-in mode POT. Also a single bin is used in the range of $0 \leq \cos \theta < 0.5$ in figure (b).

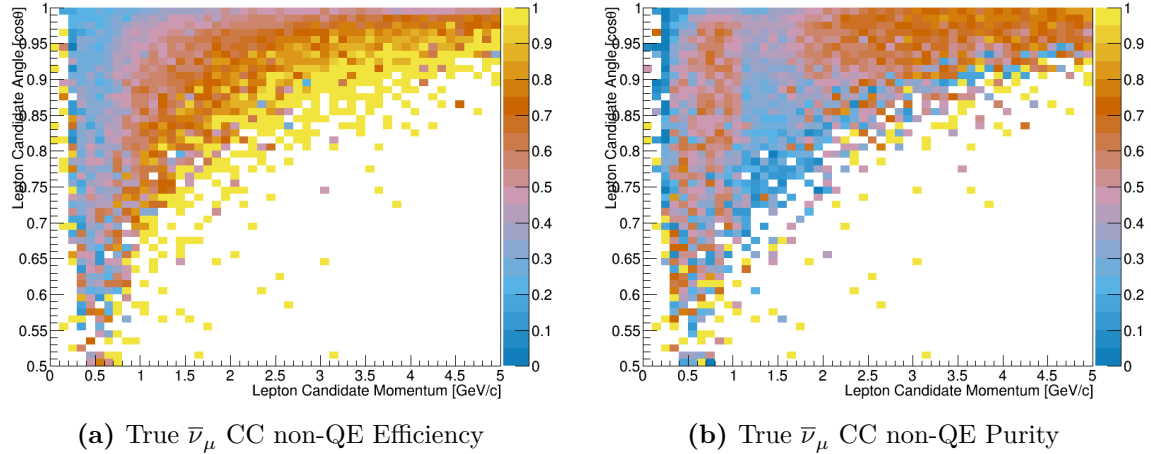


Figure 3.19: Efficiency and purity of the $\bar{\nu}_\mu$ in RHC Mode CC N-Tracks selection. True events are defined as correctly matched μ^+ tracks from $\bar{\nu}_\mu$ -induced CC non-QE interactions at the vertex.

a function of increasing energy, the $\bar{\nu}_\mu$ content is decreasing while the relative ν_μ contribution is increasing. The ν_μ events also have high Q^2 which explains the significant number of misidentified proton main track events. For the hadronic final states, the shape of the $\bar{\nu}_\mu$ -induced resonances is similar to what we saw in Figure 3.12 on page 81. Interestingly, the ν_μ background hadronic mass distribution does not peak in any one region.

3.3.5 The ν_μ Background in RHC Mode CC 1-Track Sample

This selection provides the ν_μ in RHC, also called wrong-sign background, CCQE-like samples . Figure 3.21 on page 88 and Figure 3.22 on page 88 display the momentum and angular distributions inputs to the BANFF fit. We can see this is a relatively low-angle selection compared to previous selections. Importantly the selection is relatively ν_μ -pure which should help constrain the wrong-sign background in the fit. However, the CCQE purity is modest given number of correctly identified lepton candidates. This feature needs to be addressed in the next iteration of the analysis.

We can examine the efficiencies and purities differentially for the selection in Figure 3.23 on page 89. For the efficiency and purity only, the true signal is a true ν_μ CCQE interaction.

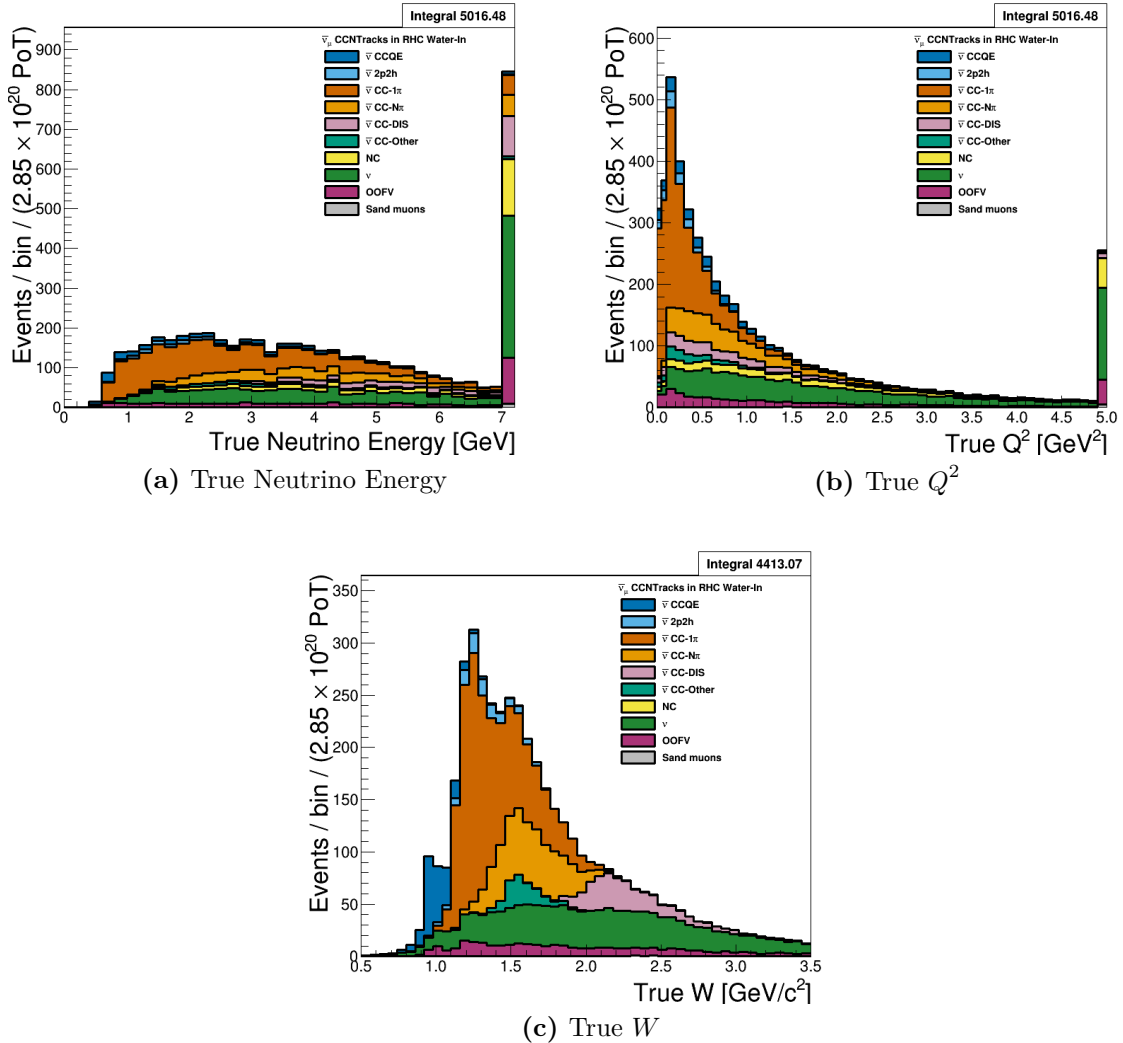


Figure 3.20: True kinematics of the $\bar{\nu}_\mu$ in RHC Mode CC N-Tracks selection. The last bin shown in (a) and (b) is used as overflow. The figures use the PØD water-in MC and are normalized to the RHC water-in mode POT.

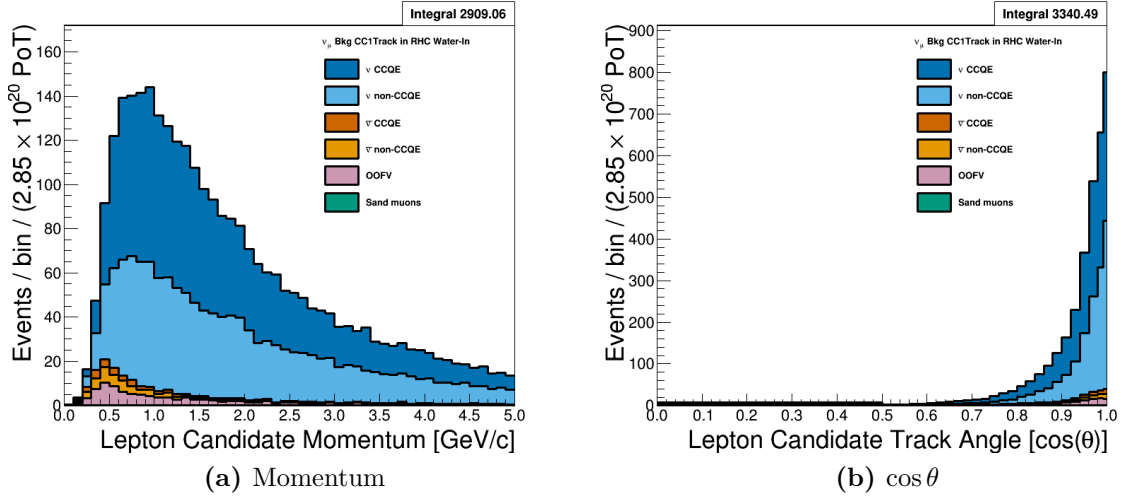


Figure 3.21: Reconstructed kinematics of the ν_μ Background in RHC Mode CC 1-Track selection categorized by CCQE and non-CCQE interactions. The figures use the PØD water-in MC and are normalized to the RHC water-in mode POT. Also a single bin is used in the range of $0 \leq \cos \theta < 0.5$ in figure (b).

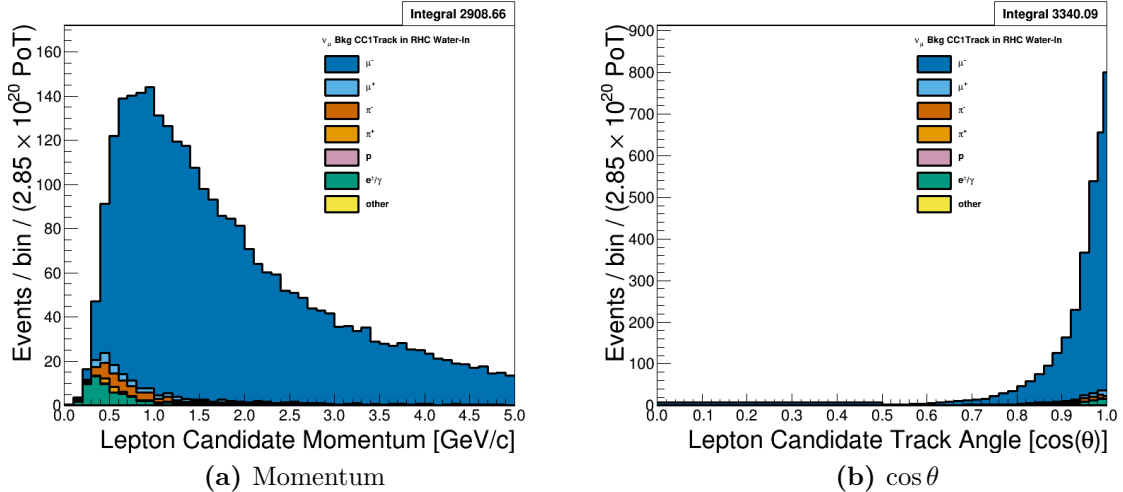


Figure 3.22: Reconstructed kinematics of the ν_μ Background in RHC Mode CC 1-Track selection categorized by the true particle matched to the main track. The figures use the PØD water-in MC and are normalized to the RHC water-in mode POT. Also a single bin is used in the range of $0 \leq \cos \theta < 0.5$ in figure (b).

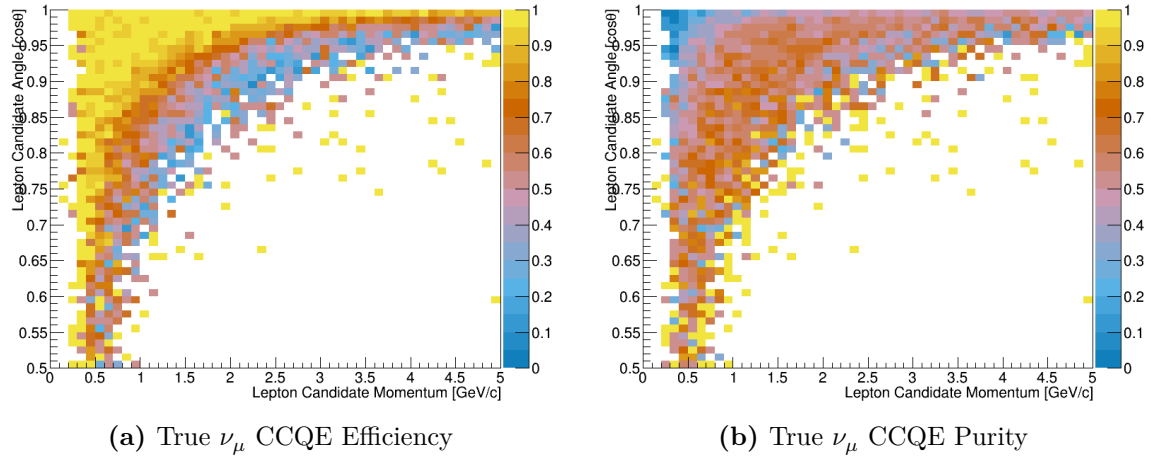


Figure 3.23: Efficiency and purity of the ν_μ Background in RHC Mode CC 1-Track selection. The true events are ν_μ CCQE at the vertex and the selected lepton candidate is the true μ^- .

The efficiency is similar to the ν_μ in FHC CC 1-Track topology efficiency with banded $p - \theta$ regions. As for the purity, it is roughly 70% in a banded region between low momenta, low angle and high momenta, high angle tracks.

The underlying true kinematics, E_ν and Q^2 , of the selection are shown in Figure 3.24 on page 90. The number of the wrong-sign background events peaks at 1 GeV and is a broad peak compared to the designed sharp $\bar{\nu}_\mu$ peak at 0.6 GeV as shown in Figure 3.16 on page 84. Since these are higher energy events, there is more available energy to produce resonance states that produce 1π topologies. This explains the significant non-CCQE event contamination.

3.3.6 The ν_μ Background in RHC Mode CC N-Tracks Sample

This selection provides the non-CCQE-like samples for the ν_μ background in RHC mode. Figure 3.25 on page 90 and Figure 3.26 on page 91 show the momentum and angular distributions that are inputs to the BANFF fit. We can see the selection is relatively ν_μ -pure with a significant mis-identified track rate. Interestingly, the misidentified pion main tracks have a high momentum tail.

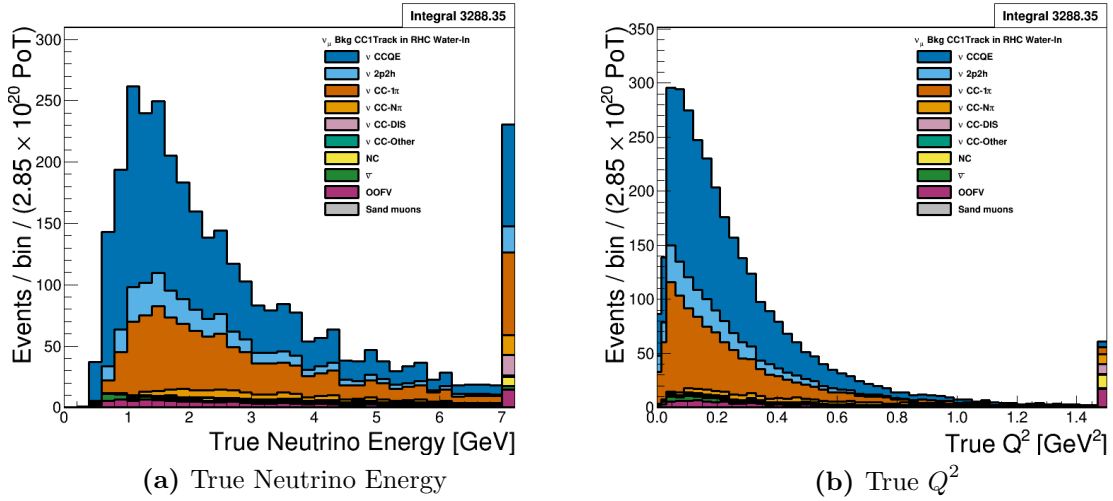


Figure 3.24: True kinematics of the ν_μ Background in RHC Mode CC 1-Track selection. Water-in mode is displayed here only with the last bin shown is used as overflow. The figures use the PØD water-in MC and are normalized to the RHC water-in mode POT.

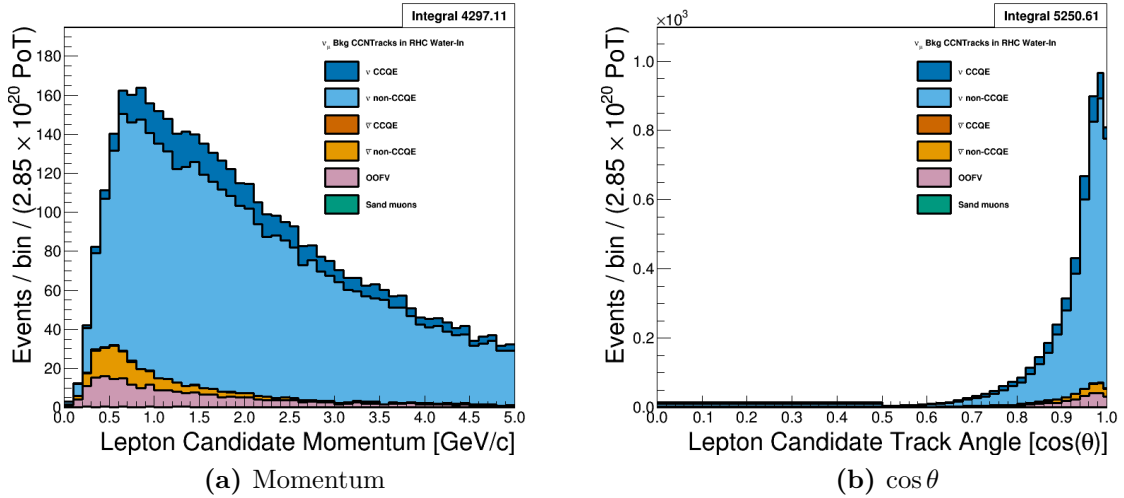


Figure 3.25: Reconstructed kinematics of the ν_μ Background in RHC Mode CC 1-Track selection categorized by CCQE and non-CCQE interactions. The figures use the PØD water-in MC and are normalized to the RHC water-in mode POT. Also a single bin is used in the range of $0 \leq \cos \theta < 0.5$ in figure (b).

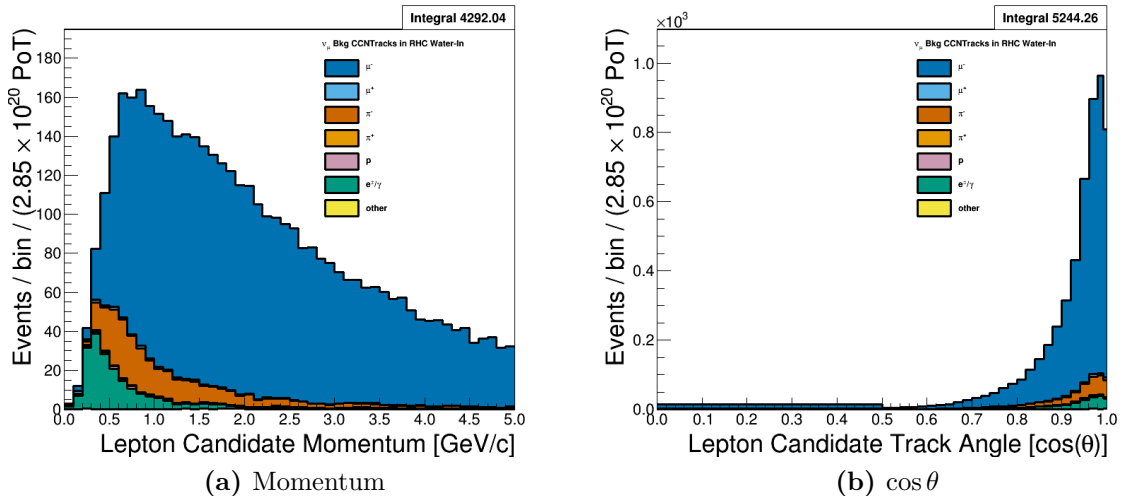


Figure 3.26: Reconstructed kinematics of the ν_μ Background in RHC Mode CC 1-Track selection categorized by the true particle matched to the main track. The figures use the PØD water-in MC and are normalized to the RHC water-in mode POT. Also a single bin is used in the range of $0 \leq \cos \theta < 0.5$ in figure (b).

We can examine the ν_μ CC non-QE efficiency and purity of the selection in Figure 3.27 on page 92. There is a reduction in the purity below 1.5 GeV/c due to the the $\bar{\nu}_\mu$ selections occupying the same phase space. Fortunately, the efficiency and purity are relatively high above 1.5 GeV/c.

The underlying true kinematics, E_ν , Q^2 , and W , of the interactions are shown in Figure 3.28 on page 93. As we have seen before with the CC N-Tracks samples, these are high E_ν events with large Q^2 exchanges. The invariant hadronic system displays the previously seen resonances, with the largest still being from the Δ baryon.

3.4 Summary of Selections

In this chapter we have examined the selection true and reconstruction kinematics that will be used in the BANFF fit. We see the 1-Track selections yield some reasonably pure CCQE samples. By inverting that cut, we obtain some information on the rate of other topologies like CC-1 π and high Q^2 CCDIS events. Importantly is the ability of these samples to

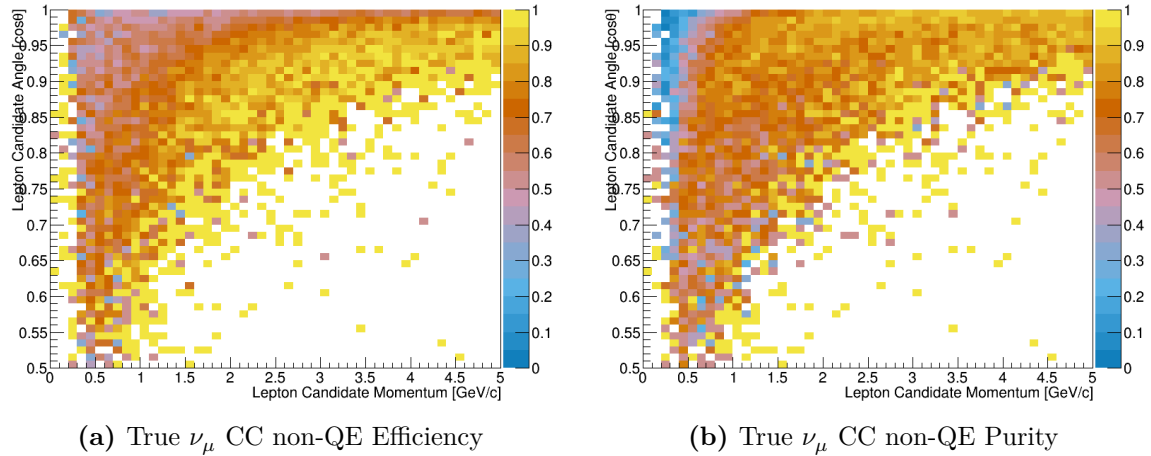


Figure 3.27: Efficiency and purity of the ν_μ Background in RHC Mode CC N-Tracks selection. True events are defined as correctly matched μ^- tracks from ν_μ -induced CC non-QE interactions at the vertex.

constrain the correct sign ($\bar{\nu}_\mu$) and wrong sign (ν_μ) backgrounds in RHC mode, which are very important in the oscillation analysis. We can now move forward to the next chapter to describe the fit parameters and the systematic uncertainties present in the analysis.

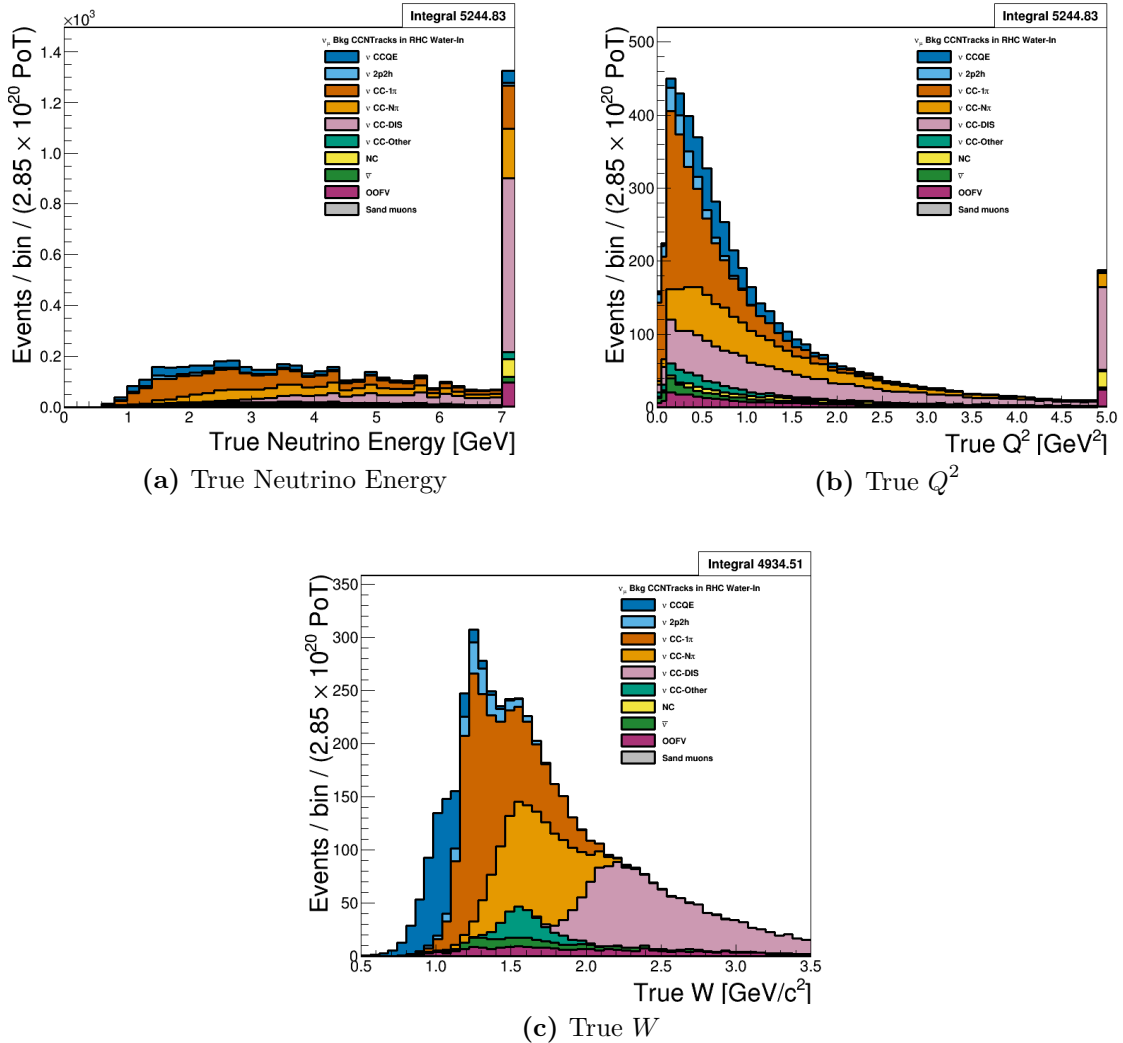


Figure 3.28: True kinematics of the ν_μ Background in RHC Mode CC N-Tracks selection. The last bin shown in (a) and (b) is used as overflow. The figures use the PØD water-in MC and are normalized to the RHC water-in mode POT.

Chapter 4

The BANFF Fit Model Parameters

This chapter explores the fit binning and penalty terms in the test statistic used for this analysis. The BANFF fit includes three sources of systematic uncertainties: neutrino flux, cross section model, and detector inefficiencies. The sources of systematic uncertainty, also referred to just as systematics, will be defined and their effect on the analysis. These three terms directly affect the flux of neutrinos, efficiency of reconstruction, and the cross section for ν_α terms, respectively, in the predicted rate equation given in (1.56).

This chapter is presented in the following order. The first section explores the method to define histogram fit bins in the likelihood ratio. The second section describes the parameterization of each penalty term in the test statistic. The penalty terms, discussed in order, are the neutrino flux model, the detector inefficiencies, and lastly the cross section model.

4.1 Fit Binning

The PØD-only BANFF fit uses the samples described in Chapter 3 to evaluate the log-likelihood ratio term, χ^2_{LLR} . Since this is a binned likelihood in $(p, \cos \theta)$, the bin edges need to be defined first.

The BANFF fit binning is optimized to ensure at least 1 predicted Monte Carlo (MC) event in each bin for every PØD sample when scaled to the collected data POT. The fit

bins must also account for detector smearing effects. In order to mitigate smearing and event migration, the reconstructed muon track kinematics were examined against correctly identified tracks in one-dimensional kinematic slices. The kinematics are scanned across their full phase spaces in order to understand the required width for a fit bin. The first fit bin is always defined starting from the kinematic maximum.

To determine the optimal momentum fit bins, the momentum resolution with the MC truth matched muon is analyzed. The momentum resolution is defined as

$$R(r, t) = \frac{r - t}{t},$$

where r is the reconstructed momentum and t is the true muon momentum. The mean (bias) and standard deviation (stddev) of R are used as proxies for the true bias and resolution for the prediction. Both quantities and prediction errors were extracted using a bootstrapping algorithm [47] in very fine bins of reconstructed momentum. The bootstrapping algorithm works by random sampling with replacement of the true muon momentum. For each bias and stddev prediction, at least 1000 bootstrapping samples were generated. Each bootstrap bias and stddev value were saved to calculate a prediction mean and error. In the case of relatively “large” prediction errors, additional 10000 bootstrapping samples were generated. The main track momentum resolution for the ν_μ in FHC Mode CC 1-Track sample is shown in Figure 4.1 on page 96 to illustrate the results.

The optimal $\cos\theta$ fit bins were determined in a very similar manner with the momentum fit bins. While the fit bins and physics are dictated in $\cos\theta$ space, the detector smearing is a function θ . In addition, since the angle can be nearly zero for the most forward-going tracks, the resolution was not used to characterize the angular uncertainties. Instead, the difference (“residual”) between the true and reconstructed angle θ with respect to (wrt) the ND280 Z-axis was analyzed. The same bootstrapping algorithm described above was used to determine the mean and stddev of the θ residuals. The main track angular residuals for

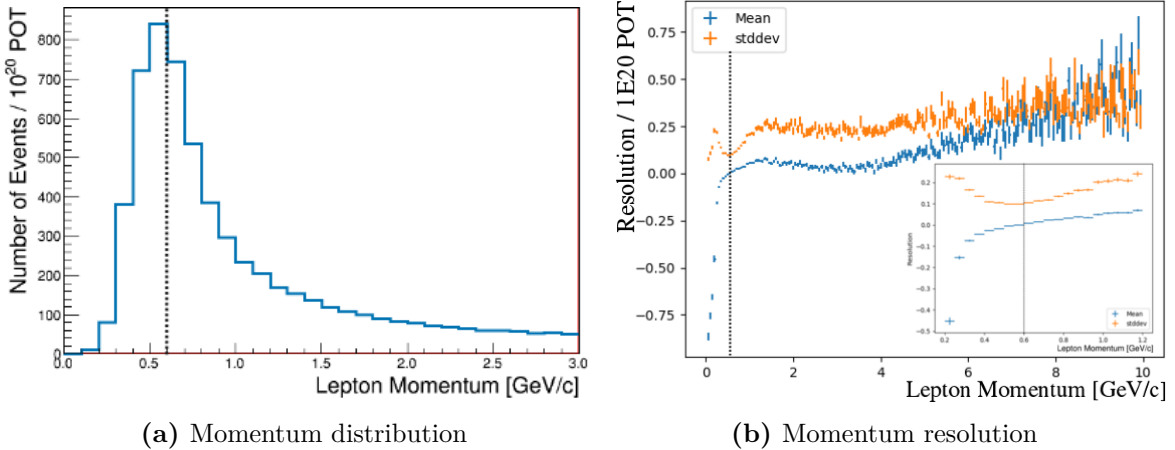


Figure 4.1: Main track momentum resolution for the ν_μ in FHC Mode CC 1-Track sample. Only correctly identified muons are used. The number of events is scaled to 10^{20} POT, which is the approximate scale for all the samples in this analysis. A dashed line indicates the maximum of the distribution peak from figure (a). The resolution of the momentum measurement is shown in figure (b) whose error bars are estimated using bootstrapping. In the inset is the momentum resolution zoomed near the momentum distribution maximum.

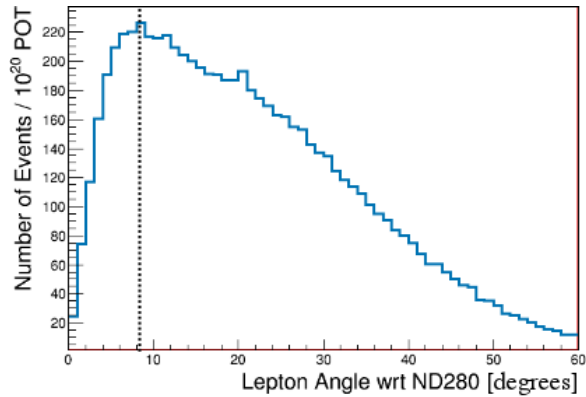
the ν_μ in FHC Mode CC 1-Track sample are shown in Figure 4.2 on page 97 to illustrate the results.

This procedure to define fit bin edges emphasizes regions of high statistics and mitigates regions with low statistics. Since the MC provides about $10\times$ the data statistics, the statistical uncertainty for each bin should be negligible in high statistics regions. However, this does not account for the low statistics regions predicted by the nominal MC. We tackle this problem and other systematic uncertainties for the fit bins using bin normalizations as explained in Chapter 2.

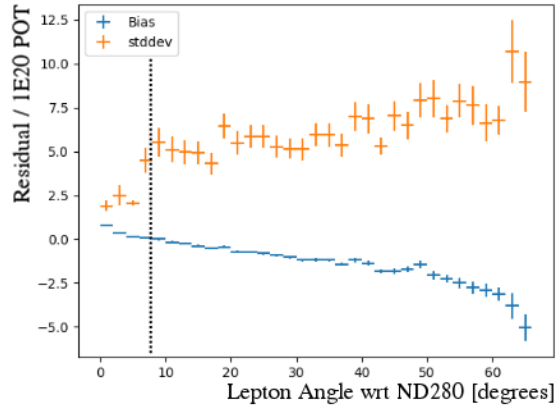
4.1.1 Fit Bin Edges

There are a total 988 fit bins with water-in and water-out modes sharing the same bin edges. The finalized fit bins are tabulated below.

- The ν_μ in FHC Mode CC 1-Track water-in and water-out samples:
 - p [GeV/c]: 0, 0.3, 0.4, 0.5, 0.6, 0.7, 0.8, 1, 1.25, 1.5, 2, 3, 4, 5.5, 30



(a) Angular distribution



(b) Angular residuals

Figure 4.2: Main track angular residuals for the ν_μ in FHC Mode CC 1-Track sample. Only correctly identified muons are used. The number of events is scaled to 10^{20} POT, which is the approximate scale for all the samples in this analysis. A dashed line indicates the maximum of the distribution peak from figure (a). The residual of the angular measurement is shown in figure (b) whose error bars are estimated using bootstrapping.

- $\cos \theta$: -1, 0.7, 0.8 , 0.88, 0.94, 0.96, 0.975, 0.99, 1
- The ν_μ in FHC Mode CC N-Tracks water-in and water-out samples:
 - p [GeV/c]: 0, 0.4, 0.5, 0.6, 0.7, 0.8, 1, 1.2, 1.5, 1.8, 2.2, 2.7, 3.5, 5, 10, 30
 - $\cos \theta$: -1, 0.65, 0.77, 0.85, 0.9, 0.94, 0.97, 0.99, 1
- The $\bar{\nu}_\mu$ in RHC Mode CC 1-Track water-in and water-out samples:
 - p [GeV/c]: 0, 0.4, 0.5, 0.6, 0.7, 0.8, 1, 1.25, 1.5, 2, 3, 30
 - $\cos \theta$: -1, 0.82, 0.87, 0.9, 0.93, 0.95, 0.97, 0.99, 1
- The $\bar{\nu}_\mu$ in RHC Mode CC N-Tracks water-in and water-out samples:
 - p [GeV/c]: 0, 0.5, 0.9, 1.25, 1.6, 2, 3, 8, 30
 - $\cos \theta$: -1, 0.8, 0.89, 0.95, 0.97, 0.99, 1
- The ν_μ in RHC CC 1-Track water-in and water-out samples:
 - p [GeV/c]: 0, 0.4, 0.6, 0.8, 1.1, 2, 10

- $\cos \theta$: -1, 0.78, 0.84, 0.89, 0.92, 0.95, 0.97, 0.98, 0.99, 1
- The ν_μ in RHC CC N-Tracks water-in and water-out samples:
 - p [GeV/c]: 0, 0.4, 0.6, 0.8, 1, 1.5, 2, 3, 10
 - $\cos \theta$: -1, 0.7, 0.8, 0.85, 0.9, 0.94, 0.965, 0.98, 0.99, 1

4.2 Penalty Terms and Systematic Uncertainties

This section expands on the penalty terms, and hence fit parameters, in the BANFF fit. The cross section and flux penalty terms in this analysis are identical to the previous near detector constraint studies [22, 83]. This provides a one-to-one comparison between the PØD-only and FGD-only flux and cross section predictions. However, due to the different detector technologies between the PØD and FGD, different bin normalization parameters are necessary.

The fit parameters are described in the following order. The first set of parameters are the flux terms. This is followed by a description of the fit bin normalization parameters. The final topic is a description of the cross section parameters.

4.2.1 Flux Model Parameters

The T2K neutrino flux model is a description of the neutrino beam energy spectrum for each run period and flavor. This model includes simulations of the proton beam interactions and subsequent hadron production at the target. The predicted hadron production rate, including inside and outside the graphite target, is tuned to the results from the replica target¹⁷ experiment NA61/SHINE [11] and other hadron production experiments. The uncertainties in the unoscillated flux tuning are dominated by hadron production. Smaller effects on the unoscillated flux uncertainty include the proton beam profile, off-axis angle, horn current,

¹⁷The NA61/SHINE experiment has two graphite targets. A thin 2 cm target and a thick 90 cm target. The thick target is a replica of the T2K graphite target.

and horn alignment. Further details about the flux model and uncertainties can be found in the following reference [6]. The flux parameters are especially important since they are used as inputs to the oscillation analysis.

The flux penalty term in the BANFF fit is defined as

$$\chi^2_{\text{Flux}} = (\vec{b} - \vec{b}_0)^T (V^{-1}) (\vec{b} - \vec{b}_0), \quad (4.1)$$

where \vec{b} is the vector of flux parameter values, \vec{b}_0 is the vector of the initial parameter values, and V is the flux covariance matrix. As a remainder, all penalty terms in this analysis have the form of (4.1). Each flux parameter is a neutrino energy bin normalization starting at one (1). Formally, a flux bin is defined as

$$b_i = \frac{N'_{\nu_\alpha,i}}{N_{\nu_\alpha,i}}, \quad (4.2)$$

where $N_{\nu_\alpha,i}$ and $N'_{\nu_\alpha,i}$ are the predicted and ND constrained ν_α event rates, respectively, in the i th energy bin. In other words, *each flux term is a ratio of rates. Further, all penalty terms and covariance terms are dimensionless.* A postfit value of 1.1 indicates that all events in that energy bin have an additional weight of 1.1, signaling that the postfit prefers to increase that neutrino flux by 10%. Equivalently, this means $N'_{\nu_\alpha,i}$ is 10% greater than $N_{\nu_\alpha,i}$.

In the BANFF fit, both ND280 and SK flux parameters are estimated simultaneously. This is achieved using correlations between ND280 and SK flux parameters in the covariance matrix. The covariance matrix is provided by the T2K flux group and is shown in Figure 4.3 on page 100. Also shown in Figure 4.3 on page 100 is the Pearson linear correlation coefficient matrix which is defined as

$$\rho_{i,j} = \frac{V_{i,j}}{\sqrt{V_{i,i}V_{j,j}}}, \quad (4.3)$$

where i and j are bins in V .

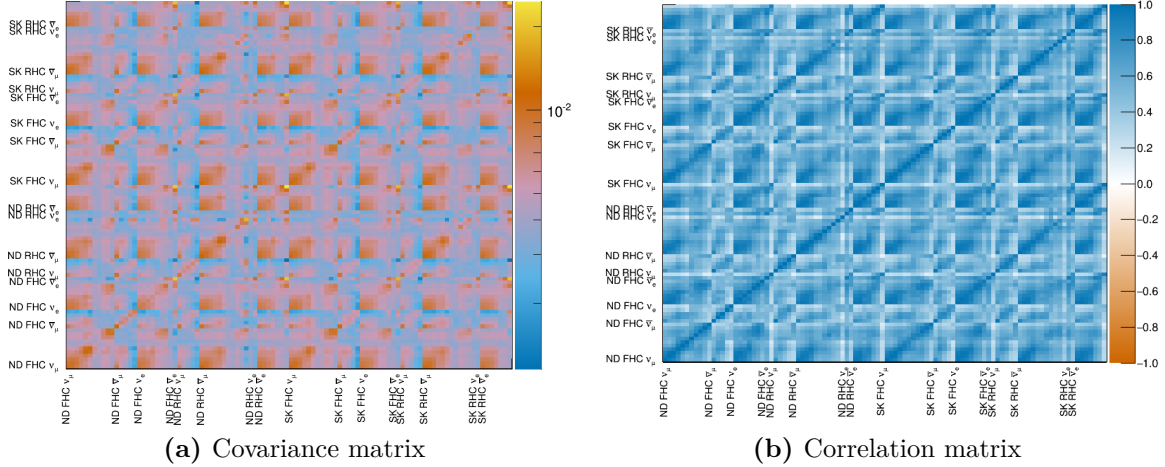


Figure 4.3: The BANFF prefit flux covariance matrix. Figure (a) shows the covariance matrix which is the uncertainty of the normalization for the neutrino flux at both ND280 and SK. The covariance matrix is divided into submatrices in groups by detector, beam mode, and neutrino flavor. Figure (b) is the linear correlation coefficient for each covariance term.

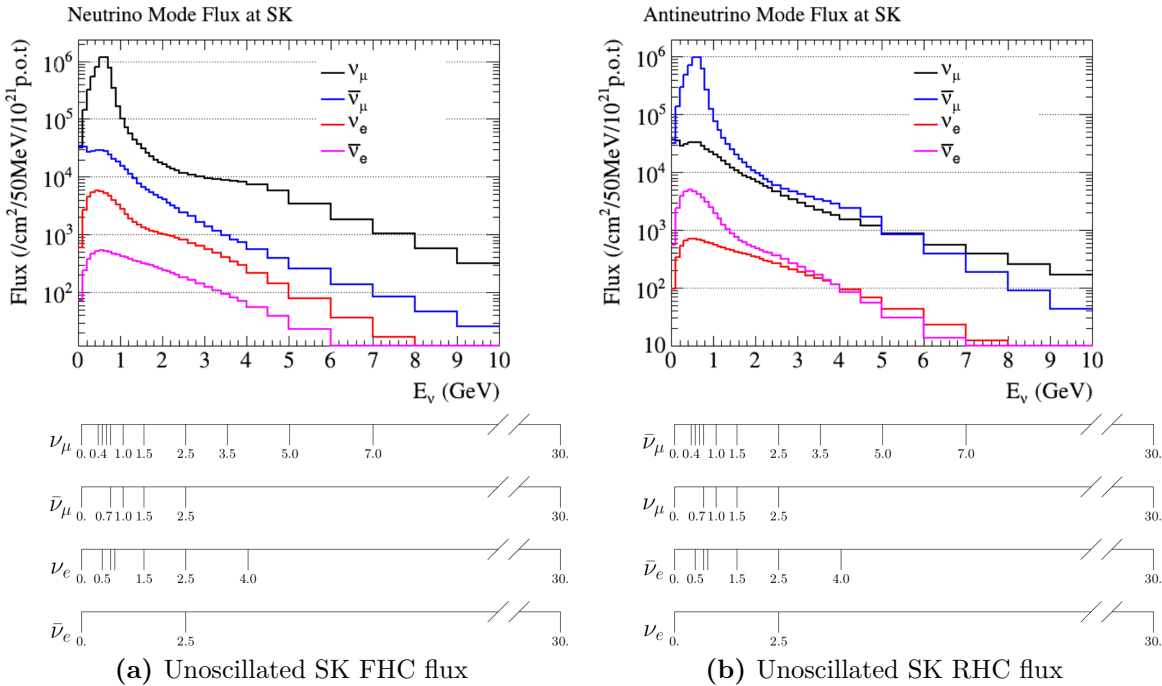


Figure 4.4: Neutrino flux prediction at SK and flux bin edges. The flux prediction for FHC (RHC) mode is shown in figure on the left (right). The flux normalization parameters have an assigned energy range and are the same for both the SK and ND280 detectors. The energy binning used is shown below the plots.

The tabulated flux parameters/bins and uncertainties in this analysis are given in Table 4.1 on page 101. These are the first set of parameters in the fit. The flux parameters are differentiated by neutrino energy, horn current/polarity (FHC mode and RHC mode), neutrino flavor (ν_μ , $\bar{\nu}_\mu$, ν_e , and $\bar{\nu}_e$), and detector (ND280 and SK). There are 50 ND280 and 50 SK flux parameters to yield a total of 100 flux normalizations. In addition, the bin edges are shared between the ND280 and SK. The SK neutrino flux and the flux bin edges are shown in Figure 4.4 on page 100.

Table 4.1: Flux binning and uncertainties used in the BANFF fit.

Fit index	Beam mode	Bin edges [GeV]	Prefit
0	ND280 ν_μ FHC	0.0 - 0.4	1 ± 0.100909
1		0.4 - 0.5	1 ± 0.099431
2		0.5 - 0.6	1 ± 0.092025
3		0.6 - 0.7	1 ± 0.085239
4		0.7 - 1.0	1 ± 0.105356
5		1.0 - 1.5	1 ± 0.104375
6		1.5 - 2.5	1 ± 0.073612
7		2.5 - 3.5	1 ± 0.068993
8		3.5 - 5.0	1 ± 0.082334
9		5.0 - 7.0	1 ± 0.097308
10		7.0 - 30	1 ± 0.114706
11	ND280 $\bar{\nu}_\mu$ FHC	0.0 - 0.7	1 ± 0.103804
12		0.7 - 1.0	1 ± 0.084158
13		1.0 - 1.5	1 ± 0.081349
14		1.5 - 2.5	1 ± 0.085208
15		2.5 - 30	1 ± 0.087735

Fit index	Beam mode	Bin edges [GeV]	Prefit
16	ND280 ν_e FHC	0.0 - 0.5	1 ± 0.091336
17		0.5 - 0.7	1 ± 0.089699
18		0.7 - 0.8	1 ± 0.084648
19		0.8 - 1.5	1 ± 0.079722
20		1.5 - 2.5	1 ± 0.079766
21		2.5 - 4.0	1 ± 0.081399
22		4.0 - 30	1 ± 0.095795
23	ND280 $\bar{\nu}_e$ FHC	0.0 - 2.5	1 ± 0.072069
24		2.5 - 30	1 ± 0.142921
25	ND280 ν_μ RHC	0.0 - 0.7	1 ± 0.094066
26		0.7 - 1.0	1 ± 0.079866
27		1.0 - 1.5	1 ± 0.080948
28		1.5 - 2.5	1 ± 0.083251
29		2.5 - 30	1 ± 0.082653
30	ND280 $\bar{\nu}_\mu$ RHC	0.0 - 0.4	1 ± 0.107277
31		0.4 - 0.5	1 ± 0.098851
32		0.5 - 0.6	1 ± 0.089710
33		0.6 - 0.7	1 ± 0.084692
34		0.7 - 1.0	1 ± 0.106871
35		1.0 - 1.5	1 ± 0.098711
36		1.5 - 2.5	1 ± 0.073350
37		2.5 - 3.5	1 ± 0.070520
38		3.5 - 5.0	1 ± 0.092905
39		5.0 - 7.0	1 ± 0.089083
40		7.0 - 30	1 ± 0.134911

Fit index	Beam mode	Bin edges [GeV]	Prefit
41	ND280 ν_e RHC	0.0 - 2.5	1 ± 0.066214
42		2.5 - 30	1 ± 0.086977
43	ND280 $\bar{\nu}_e$ RHC	0.0 - 0.5	1 ± 0.095575
44		0.5 - 0.7	1 ± 0.089033
45		0.7 - 0.8	1 ± 0.088406
46		0.8 - 1.5	1 ± 0.081472
47		1.5 - 2.5	1 ± 0.078353
48		2.5 - 4.0	1 ± 0.089427
49		4.0 - 30	1 ± 0.156972
50	SK ν_μ FHC	0.0 - 0.4	1 ± 0.102555
51		0.4 - 0.5	1 ± 0.101771
52		0.5 - 0.6	1 ± 0.092573
53		0.6 - 0.7	1 ± 0.084265
54		0.7 - 1.0	1 ± 0.102271
55		1.0 - 1.5	1 ± 0.084528
56		1.5 - 2.5	1 ± 0.066909
57		2.5 - 3.5	1 ± 0.072355
58		3.5 - 5.0	1 ± 0.085299
59		5.0 - 7.0	1 ± 0.096725
60		7.0 - 30	1 ± 0.114112
61	SK $\bar{\nu}_\mu$ FHC	0.0 - 0.7	1 ± 0.103129
62		0.7 - 1.0	1 ± 0.078327
63		1.0 - 1.5	1 ± 0.082367
64		1.5 - 2.5	1 ± 0.082121
65		2.5 - 30	1 ± 0.085123

Fit index	Beam mode	Bin edges [GeV]	Prefit
66	SK ν_e FHC	0.0 - 0.5	1 ± 0.090918
67		0.5 - 0.7	1 ± 0.087065
68		0.7 - 0.8	1 ± 0.082527
69		0.8 - 1.5	1 ± 0.076514
70		1.5 - 2.5	1 ± 0.075773
71		2.5 - 4.0	1 ± 0.082078
72		4.0 - 30	1 ± 0.092882
73	SK $\bar{\nu}_e$ FHC	0.0 - 2.5	1 ± 0.071921
74		2.5 - 30	1 ± 0.128982
75	SK ν_μ RHC	0.0 - 0.7	1 ± 0.093954
76		0.7 - 1.0	1 ± 0.076369
77		1.0 - 1.5	1 ± 0.074900
78		1.5 - 2.5	1 ± 0.078108
79		2.5 - 30	1 ± 0.077505
80	SK $\bar{\nu}_\mu$ RHC	0.0 - 0.4	1 ± 0.108593
81		0.4 - 0.5	1 ± 0.101912
82		0.5 - 0.6	1 ± 0.092787
83		0.6 - 0.7	1 ± 0.082669
84		0.7 - 1.0	1 ± 0.102090
85		1.0 - 1.5	1 ± 0.087732
86		1.5 - 2.5	1 ± 0.068117
87		2.5 - 3.5	1 ± 0.069902
88		3.5 - 5.0	1 ± 0.091711
89		5.0 - 7.0	1 ± 0.084736
90		7.0 - 30	1 ± 0.115488

Fit index	Beam mode	Bin edges [GeV]	Prefit
91	SK ν_e RHC	0.0 - 2.5	1 ± 0.066204
92		2.5 - 30	1 ± 0.082645
93	SK $\bar{\nu}_e$ RHC	0.0 - 0.5	1 ± 0.095453
94		0.5 - 0.7	1 ± 0.088889
95		0.7 - 0.8	1 ± 0.085644
96		0.8 - 1.5	1 ± 0.078536
97		1.5 - 2.5	1 ± 0.075246
98		2.5 - 4.0	1 ± 0.086384
99		4.0 - 30	1 ± 0.152507

4.2.2 Detector Inefficiencies And Bins Normalization Parameters

In the BANFF fit, fit bin normalization parameters are used to penalize variations in the fit bins. Varying fit bins without constraint is nonphysical due to known detector inefficiencies and their systematic uncertainties. This information is incorporated into the penalty term, χ^2_{Det} . Since improperly modeled inefficiencies can cause events to migrate from bin-to-bin, numerous fake “toy experiments” are performed to evaluate the systematic uncertainties in detector inefficiencies. When all toy experiments are analyzed together, correlated variations among fit bins become apparent. These correlations provide the constraints on freely changing bin normalizations. We will see the result of running such toy experiment variations in the coming pages. Hitherto in this thesis, detector inefficiency uncertainties will be referred to as detector systematics.

All the detector systematics are evaluated either as observable variations or weights. An observable variation affects the physical observables of selected events like the calculated

energy loss of a track in the PØD. A weight is a multiplicative factor that alters the normalization of a single event in a bin. There are detector systematics that affect the PØD-only, TPC-only, or both.

This section is organized as follows. The systematics treatment model for the detector systematics developed to evaluate their effects on the analysis is described in Section 4.2.2.1. The specific systematic uncertainties relevant to this analysis are described in Section 4.2.2.2. The detector systematics penalty term used in the BANFF fit is described in Section 4.2.2.3. Finally, the procedure to determine the initial bin normalization is presented in Section 4.2.2.4.

4.2.2.1 Systematic Treatment Models

The BANFF fit analysis uses toy experiment variations to evaluate the effect of detector systematics on the analysis samples. Each toy experiment loops over all the predicted events and varies the known detector systematic effects. Each systematic effect either varies the event’s efficiency weight or event observables. Both the observable variation and efficiency-like weight treatments rely on data-driven studies by comparing data and MC predictions in a control sample¹⁸ (CS). By using a large ensemble of toy experiments, the effect of the detector systematics on the samples is evaluated.

Efficiency-like corrections alter the number of predicted events in a fit bin. The model used to evaluate efficiency-like systematics is given by

$$\epsilon_{\text{Data}}(o) = \left(\frac{\epsilon_{\text{Data}}(o)}{\epsilon_{\text{MC}}(o)} \right)_{\text{CS}} \epsilon_{\text{MC}}(o), \quad (4.4)$$

where $\epsilon_{\text{MC}}/\epsilon_{\text{Data}}$ denotes the mean selection efficiency of the MC/data as a function of some observable kinematic o , and $()_{\text{CS}}$ refers to the selection efficiency measured in a CS. We need to update this model to account for statistical uncertainties in the CS. The updated model, with o dependence assumed, is now

¹⁸Each control sample is validated in T2K prior to introduction to the BANFF analysis.

$$\epsilon'_{\text{Data}} = \left(\frac{\epsilon_{\text{Data}} + x_{\text{Data}} \cdot \sigma_{\epsilon_{\text{Data}}}}{\epsilon_{\text{MC}} + x_{\text{MC}} \cdot \sigma_{\epsilon_{\text{MC}}}} \right)_{\text{CS}} \epsilon_{\text{MC}} \quad (4.5)$$

where $\sigma_{\epsilon_{\text{MC}}} / \sigma_{\epsilon_{\text{Data}}}$ is the standard deviation of the efficiency of the MC/Data and x_{Data} and x_{MC} are uncorrelated, random normally distributed numbers from $\mathcal{N}(\mu = 0, \sigma^2 = 1)$. All the variations are applied to the event, simultaneously affecting all observables, and the event selection is rerun. A weight is derived depending if the event is selected, w_{eff} , or not selected, w_{ineff} . These weights are given below

$$w_{\text{eff}} = \frac{\epsilon'_{\text{Data}}}{\epsilon_{\text{MC}}} \quad (4.6)$$

$$w_{\text{ineff}} = \frac{1 - \epsilon'_{\text{Data}}}{1 - \epsilon_{\text{MC}}}.$$

Observable variation systematics are evaluated as shifts to physically measured quantities like particle track momentum and track length. The systematic can be evaluated in two different ways:

1. If the reconstructed observable, o_{reco} , has a known true value, o_{true} , then the difference between those two is used as scaling. The varied observable is given by

$$o' = o_{\text{true}} + (o_{\text{reco}} - o_{\text{true}})(s + x\sigma_s), \quad (4.7)$$

where s is the mean scaling parameter used to match the true value, σ_s is the uncertainty on s , and x is a random number from $\mathcal{N}(\mu = 0, \sigma^2 = 1)$. The mean scaling parameter and its uncertainty are determined from the standard deviations observed in the data and MC by

$$s = \frac{\delta^{\text{data}}}{\delta^{\text{MC}}} \quad \sigma_s = s \left| \frac{\sigma_{\delta^{\text{data}}}}{\delta^{\text{data}}} - \frac{\sigma_{\delta^{\text{MC}}}}{\delta^{\text{MC}}} \right|. \quad (4.8)$$

2. If the MC reconstructed observable is corrected to match the mean from some CS reconstructed observable. The varied observable in this case is given by

$$o' = o_{\text{Nom}} + \Delta o + x\sigma_{\Delta o}, \quad (4.9)$$

where o' is the varied observable value, o_{Nom} is the nominal MC value, Δo is the average correction to the observable, $\sigma_{\Delta o}$ is the uncertainty on the correction, and x is a random, normal number from $\mathcal{N}(\mu = 0, \sigma^2 = 1)$.

Additional uncertainties from the magnetic field are also special cases of the 2nd observable variation method specifically for the TPC momentum [83]. They are:

- The TPC laser calibration corrections are applied after the magnetic field (B-field) mapping corrections. The B-field corrections are applied at event reconstruction while the calibration corrections are treated as a systematic uncertainty. The varied momentum is given by

$$p' = p_{\text{Nom}} + x(p_{\text{Map}} - p_{\text{Nom}}), \quad (4.10)$$

where p_{Nom} is the nominal MC prediction using the B-field corrections and p_{Map} is the updated momentum using the additional laser calibration mapping.

- The momentum depends on some scale parameter s . The varied momentum due to the scale uncertainty is given by

$$p' = p_{\text{Nom}}(1 + x\sigma_s), \quad (4.11)$$

where σ_s is the uncertainty on the scale. In this parameterization, s is the scale of the ND280 solenoid current.

After all observables are varied and applied to the event, the event selection cuts are applied again. By doing so after all variations are applied, the full impact of the systematic on the sample and analysis bins can be evaluated.

Systematic effect	Affected detector	Treatment
TPC cluster eff.	TPC	efficiency
TPC tracking eff.	TPC	efficiency
TPC charge misassignment	TPC	efficiency
TPC momentum resol.	TPC	observable variation
TPC momentum scale	TPC	observable variation
B field distortion	TPC	observable variation
Pion secondary interactions	All	efficiency
Proton secondary interactions	All	efficiency
TPC Particle ID	TPC	observable variation
TPC track quality eff.	TPC	efficiency
<hr/>		
PØD energy loss scale	PØD	observable variation
PØD energy loss resol.	PØD	observable variation
PØD mass	PØD	(see text)
PØD-TPC matching eff.	PØD+TPC	(see text)

Table 4.2: List of detector systematics in the analysis. The systematics listed above the horizontal line are discussed in the following reference [6]. The PØD mass and track matching systematics were not available in the BANFF framework and treated as uncorrelated additions to the total covariance matrix.

4.2.2.2 Detector Systematics

Since this analysis uses the PØD and TPC detectors, systematics that affect both must be included in the toy experiments. The complete set of detector systematics and their treatment in the analysis are listed in Table 4.2 on page 109. The TPC-only systematics that have been used in previous BANFF fit analysis are included in this analysis. Details on the TPC-only systematics are discussed in the following references [6,83]. There are four PØD-only detector systematics that are considered for this BANFF fit analysis:

- The PØD detector energy loss scale,
- The PØD detector energy loss resolution,
- The PØD-TPC inter-detector matching efficiency, and
- The PØD detector fiducial mass.

The PØD energy loss scale and resolution affect the measured momentum in the PØD and are very significant sources of uncertainty. In the ν_μ CC- 0π cross section analysis [8], the same selection as the ν_μ in FHC Mode CC 1-Track selection, the scale and resolution contributed 1.3% and 6.7%, respectively, to the cross section uncertainty. Those large uncertainties can be attributed to the design of the PØD. It is optimized for π^0 detection as opposed to a dedicated tracking detector like the FGD. Slight variations in the track reconstruction can significantly alter the energy loss as measured in (3.4).

The remaining systematics, the PØD mass and the PØD-TPC matching efficiency, were not available to analyze in toy experiments variations. They were not implemented in the BANFF framework and unavailable to implement due to time constraints on this author. Instead, they were treated as additional uncorrelated systematics on each bin normalization uncertainty with the normalization value remaining fixed.

The PØD mass uncertainty is a normalization systematic which affects the event rate. This is a challenging systematic for analyses of recent T2K data due to increasingly faulty sensors to measure the water content. The procedure to fill the water bags required filling them in unison to prevent uneven bulging. However, faulty sensors would provide poor quality data, hence bags were under and overfilled. This effect alters the expected event rate as a function of position.

Another problem with the mass uncertainty is due to structure deformations in the PØD. To understand how the PØD has deformed, it is important to understand how the PØD is mounted in the ND280 detector. Each corner of the PØD is mounted to the ND280 basket leaving the those corners spatially fixed. When the water bags are filled, the WT volume expands or “bulges” from the middle. The upstream end of the PØD, the Upstream ECal, resists deformations since it is physically against the ND280 support structure and magnet yoke. The downstream end of the PØD, or the Central ECal (CECal), is free to deform, however, since there is a few centimeters air gap between it and the TPC. The CECal, which

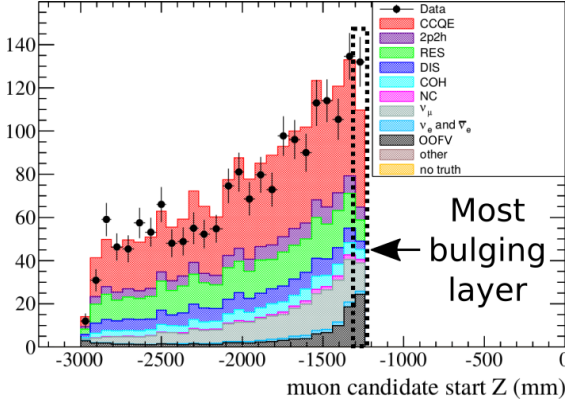


Figure 4.5: Vertex distribution showing evidence of bulging. In the $\bar{\nu}_\mu/\nu_\mu$ cross section ratio analysis, a significant excess of events in the most downstream layer of the PØD (black, dashed line box) was observed. Initially thought to be OOFV events, the analyzers removed the most downstream and upstream layers in their analysis. This distribution was produced using the run 5, RHC period using selection precuts 1 through 4 and a having a positive track in the TPC. Each event is categorized by true interaction mode according to NEUT. This figure was altered for clarity from the following reference [26].

has a design thickness of 304 mm [18], was observed to bulge about 7-8 mm from its center due to WT bulging as well [79].

This left more water volume, and importantly more mass, in the most downstream water bags compared to the upstream bags. This additional mass or bulging effect is evident in the vertex distribution as a function of the Z-position as shown in Figure 4.5 on page 111.

Prior PØD analyses have estimated the mass uncertainty using similar toy experiment techniques, but did not integrate them into the BANFF framework. In particular in the ν_μ in CC- 0π analysis [8], the PØD mass had an 1.5% systematic effect on the cross section. Since the PØD mass uncertainty estimate was determined using the same toy experiment variation method, a conservative estimate of 2% on the mass uncertainty is included in this analysis.

The PØD and TPC (PØD-TPC) inter-detector track matching efficiency is estimated to have a small systematic effect on the analysis. It was analyzed to have over a 99.8% data and MC efficiency in the single track ν_μ CC- 0π analysis and thus was neglected. However, since this analysis includes > 1 track samples, the matching efficiency for non-single track samples is unknown. The best constraint on multiple track inter-detector matching is from the private

T2K technical note on the single bin $\bar{\nu}_\mu/\nu_\mu$ cross section analysis [26]. The analysis estimated the uncertainty at less than 0.14%, albeit using the “pre-Global” technique mentioned in Chapter 3. Because their track matching algorithm is different than Global’s algorithm, the uncertainty is not guaranteed to remain constant across the fit bins. A conservative estimate of 1% for the PØD-TPC matching efficiency was chosen in order to account for the inherent uncertainty in this systematic.

Now that we know the systematics that affect the analysis, we can now begin to understand how the detector systematic penalty term χ^2_{Det} is modeled in the BANFF fit.

4.2.2.3 Toy Experiments and the Detector Systematics Penalty

The bin normalization penalty parameters are restrictions on freely varying fit bins. To determine the correlations between bins, a large ensemble of toy experiments is generated. As described in Section 4.2.2.1, each toy experiment varies event observables, the momentum and angle of the main track, and number of events in a fit bin. The bin normalization parameter for the i th bin, or d_i , is defined as

$$d_i = \frac{\langle N_i \rangle_{\text{toys}}}{N_i}, \quad (4.12)$$

where N_i predicted number of events in fit bin i and $\langle N_i \rangle_{\text{toys}}$ is the average number of events in fit bin i evaluated over all toy experiments (toys). The predicted event rate for bin i is given by

$$N_i = \sum_k^{N_{\text{MC}}} \delta_{i,k}^{\text{bin}} w_k, \quad (4.13)$$

where N_{MC} being the number of unweighted MC events, $\delta_{i,k}^{\text{bin}}$ determines if the k th event goes into analysis bin i as a function of $(p, \cos \theta)$, and w_k is the product of all of the weights applied to the k th event. The weights used in (4.13) are

$$w_k = w_k^{\text{POT}} \times w_k^{\text{Flux}} \times w_k^{\text{xsec}} \times w_k^{\text{Det}}, \quad (4.14)$$

(see (2.8) for all possible weights). The number of events in fit bin i , averaged over all toy experiments (toys), is given by

$$\begin{aligned}\langle N_i \rangle_{\text{toys}} &= \frac{1}{N_{\text{toys}}} \sum_{t=1}^{N_{\text{toys}}} (N_i)_t \\ &= \frac{1}{N_{\text{toys}}} \sum_{t=1}^{N_{\text{toys}}} \left(\sum_k^{N_{\text{MC}}} [\delta_{i,k}^{\text{bin}} w_k] \right)_t,\end{aligned}\quad (4.15)$$

where now each MC event has a toy variation out of N_{toys} total toys. We average the results of the toys to smooth out variations among all toy experiments. In this analysis, and in previous BANFF analyses as well, $N_{\text{toys}} = 2000$ toys were generated as to have a small sample size uncertainty.

As stated before, all the penalty parameters are dimensionless and the detector systematics covariance matrix must be constructed carefully. The bin-to-bin event rate covariance, $V_{i,j}^{\text{Cov}}$, between bins i and j is

$$V_{i,j}^{\text{Cov}} = \frac{1}{N_{\text{toys}}} \sum_{t=1}^{N_{\text{toys}}} ((N_i)_t - \langle N_i \rangle_{\text{toys}}) ((N_j)_t - \langle N_j \rangle_{\text{toys}}), \quad (4.16)$$

where $(N_i)_t$ is defined in (4.15). We also need to account for statistical uncertainties in the fit bins, and so let us define $V_{i,j}^{\text{Stat}}$ as

$$V_{i,j}^{\text{Stat}} = \delta_{i,j} \sum_k^{N_{\text{MC}}} \delta_{i,k}^{\text{bin}} w_k^2, \quad (4.17)$$

where $\delta_{i,j}$ is the Kronecker delta function. In order to incorporate $V_{i,j}^{\text{Cov}}$ and $V_{i,j}^{\text{Stat}}$ uncertainties, the total detector covariance matrix, $V_{i,j}^{\text{Det}}$, in the BANFF fit is defined as

$$V_{i,j}^{\text{Det}} = \frac{V_{i,j}^{\text{Cov}} + V_{i,j}^{\text{Stat}}}{N_i N_j}, \quad (4.18)$$

which is indeed dimensionless as required by (4.12) since we divided out the predicted event rate in bins i and j .

As stated before, the PØD mass and track matching efficiency systematics are treated as uncorrelated systematics. In order to propagate their systematic uncertainties into the analysis, the detector covariance matrix given in (4.18) needs to be updated. The updated covariance matrix is given by

$$V_{i,j}^{\text{Det}} \leftarrow \left(\tilde{V}_{i,j}^{\text{Det}} + \tilde{\sigma}_{\text{Mass}}^2 + \tilde{\sigma}_{\text{Match}}^2 \right) d_i d_j, \quad (4.19)$$

where $\tilde{V}_{i,j}^{\text{Det}}$ is the fractional covariance

$$\tilde{V}_{i,j}^{\text{Det}} = \frac{V_{i,j}^{\text{Det}}}{d_i d_j}, \quad (4.20)$$

d_i/d_j are the bin normalization parameters, and $\tilde{\sigma}_{\text{Mass}}^2 = 2\%$ and $\tilde{\sigma}_{\text{Match}}^2 = 1\%$ are the PØD mass and PØD-TPC matching efficiency systematic uncertainties, respectively, estimated in Section 4.2.2.2. Together, the two additional sources of uncertainty increase each term in the covariance matrix by $0.0005 d_i d_j$. Specifically, the uncertainty in all the bin normalization parameters (square-root of the diagonal terms in the covariance matrix) increases by about 2.23%. The updated detector covariance matrix now accounts for the PØD mass and TPC matching inefficiency systematics.

The penalty term, χ_{Det}^2 , in the fit is given by

$$\chi_{\text{Det}}^2 = \left(\vec{d} - \vec{d}_0 \right)^T \left(V^{\text{Det}} \right)^{-1} \left(\vec{d} - \vec{d}_0 \right)^T, \quad (4.21)$$

where \vec{d}_0 is the initial set values of the parameters and V^{Det} is given by (4.19).

4.2.2.4 Bin Normalization Parameters

While there could be one observable normalization for each analysis bin, a single normalization can be assigned to multiple analysis bins. The purpose is to reduce the number of fit parameters since the time to fit increases non-linearly with the number of fit parameters

and events. Previously, the observable normalization edges were determined by combining fit bins with “similar” covariance. This method proved problematic since the fit bins with relatively higher statistics were shared with the same observable normalization parameter. This left the remaining low statistics regions of $(p, \cos \theta)$ phase space more susceptible to systematic variations in the toy experiments.

A new procedure was developed to improve the shortcomings of old procedure which required careful consideration of the statistical uncertainties and variations between observable normalization prefit values. This procedure can be imagined as reducing the number of contours in a topographic map while considering external constraints from other sensing data. The first step in the procedure is to initialize all of the observable normalization bin edges to be the same as the fit bin edges. All steps after this are performed iteratively.

Starting with observable normalization bin with the highest statistics, a decision is made to merge it with all immediate adjacent bins. If the individual fractional errors differ significantly before the merge, do not merge them. In this analysis, a factor of 10 in fractional uncertainty was determined to sufficiently describe bin similarity by using values larger and smaller than 10 and observing no significant differences in the end result. Additionally if the two unmerged bin normalizations differ by more than 10%, perform the bin merging. This step serves to smooth out the observable normalization prefit space. The procedure is also written in pseudocode in Algorithm 1.

The results of the procedure are shown visually in Figure 4.6 on page 118, Figure 4.7 on page 119, and Figure 4.8 on page 120. While the problem of the highest statistics bins being assigned to a single observable normalization parameter is still present, fluctuations between adjacent observable normalization parameters is iteratively minimized.

A considerable drawback to using toy experiments to estimate the bin normalization values and covariance matrix is that not all detector systematics affect the fit observables $(p, \cos \theta)$ in the same way. There are non-symmetric systematics and they are especially non-Gaussian in their effects. Therefore, the covariance matrix from (4.18) is not an exact

```

repeat
    redo  $\leftarrow$  False;
    for each normalization bin d do //sorted from min to max  $\delta\%$ 
        for each neighboring analysis bin f do
            d'  $\leftarrow$  normalization bin assigned to f;
            if d' is same as d then
                Continue to next analysis bin;
            end
            if  $\delta\%(d) \geq 10 \times \delta\%(d')$  then
                d is assigned as normalization bin for f;
                redo  $\leftarrow$  True;
                Continue to next analysis bin;
            end
            max_norm  $\leftarrow$  max(norm(d), norm(d'));
            min_norm  $\leftarrow$  min(norm(d), norm(d'));
            if max_norm  $\geq 1.1 \times$  min_norm then
                d is assigned as normalization bin for f;
                redo  $\leftarrow$  True;
            end
        end
    end
    Recalculate bin normalizations;
    until redo is False;

```

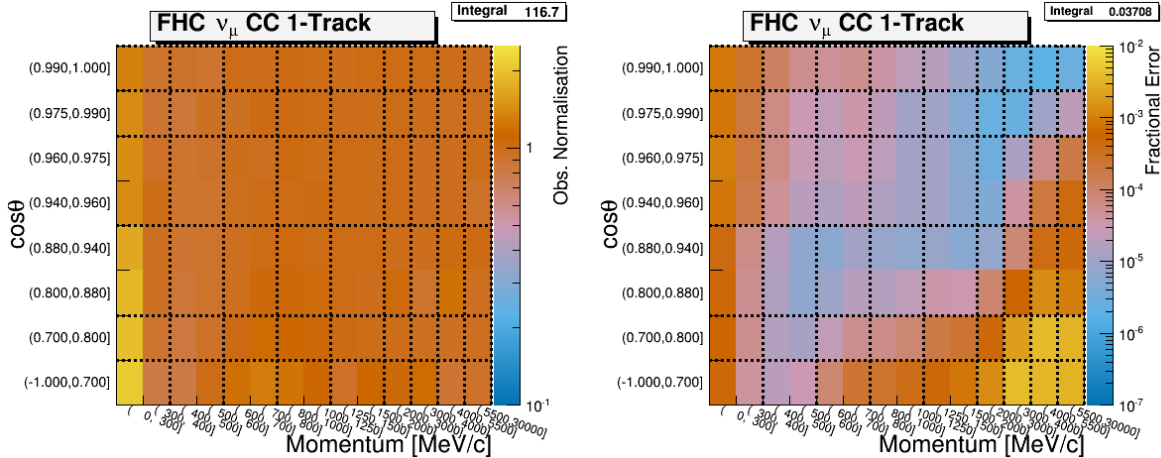
Algorithm 1: Algorithm to merge normalization bins. The “ $\delta\%$ ” operator returns the fractional statistical uncertainty for the bin. Since multiple fit bins can be assigned to a single normalization bin, the statistics of all fits bins are included. The “norm” operator returns the normalization value for a normalization bin determined by (4.13). Finally, the min/max functions return the minimum/maximum element in a tuple, respectively.

representation of the detector systematics. To demonstrate this, results of varied number of events are shown in Figure 4.9 on page 121. However, the bin normalization standard deviations are very wide and able to effectively cover the range of possible bin normalizations, which minimizes the non-Gaussian effects of the systematic. All the varied toy experiment results are provided in Appendix D.

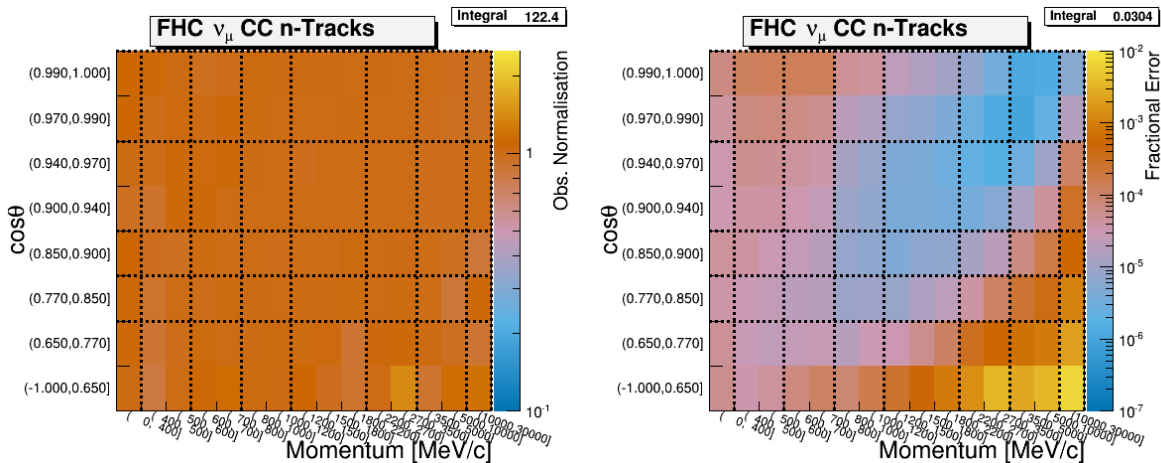
The detector systematic that had the largest effect on the observable normalization prediction was the PØD energy loss resolution (ELossRes) which alters the amount of particle energy deposited in the PØD. This systematic was developed for the ν_μ CC-0 π cross section analysis, it was identified as the largest detector systematic uncertainty in the cross section measurement [86]. When the deposited energy in the PØD is varied, it also changes the distance the truth matched particle travels in the PØD. Hence, this systematic changes the likelihood of a particle being reconstructed as a track. The observed effect is that for bins with relatively low muon momentum, the number of predicted events can vary in a non-Gaussian manner as shown in Figure 4.9 on page 121.

An unexpected phenomenon was observed when comparing the toy experiments with and without the ELossRes variation applied. With the ELossRes variation disabled in the toy experiments, a relatively large shift in the bin prediction was observed compared to the nominal prediction. This shift was expected, but what was not expected was the direction of the shift as shown in Figure 4.9 on page 121. In most cases, the shift is below the nominal MC value. However, in many of the bins, that the shape location of the prediction is above the expectation. This behavior was unexpected prior to running the toy experiment variations.

A relationship between the prediction shape location and selection purity as a function of $(p, \cos \theta)$ was discovered. In high purity $(p, \cos \theta)$ -regions of the 1-Track samples, the shape location of the prediction in the disabled ELossRes toy experiments was below the nominal MC prediction. When the 1-Track sample purity was lower, however, the shape location was above it. This effect is likely due to events migrating from the 1-Track samples into the N-Tracks samples due to multiple particles in the event.

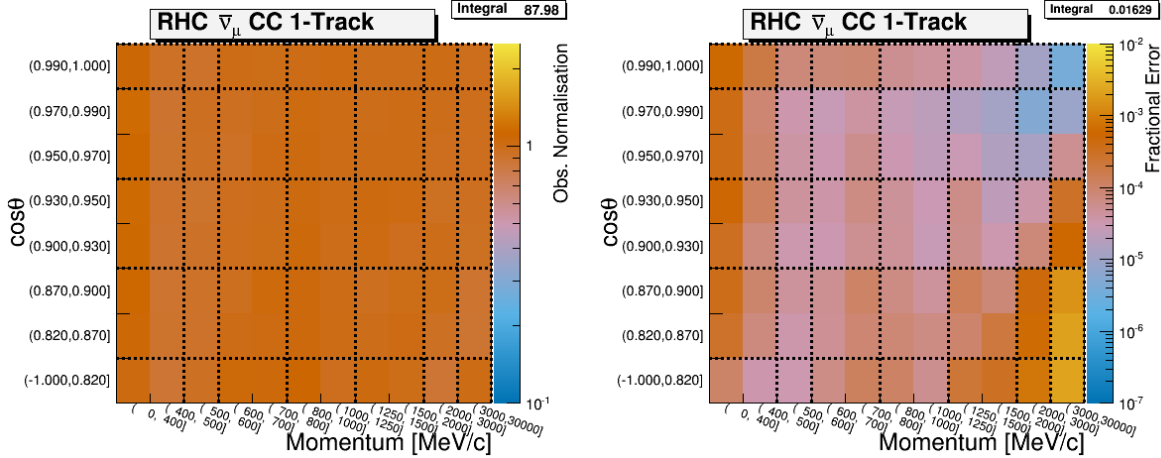


(a) The ν_μ in FHC Mode CC 1-Track sample

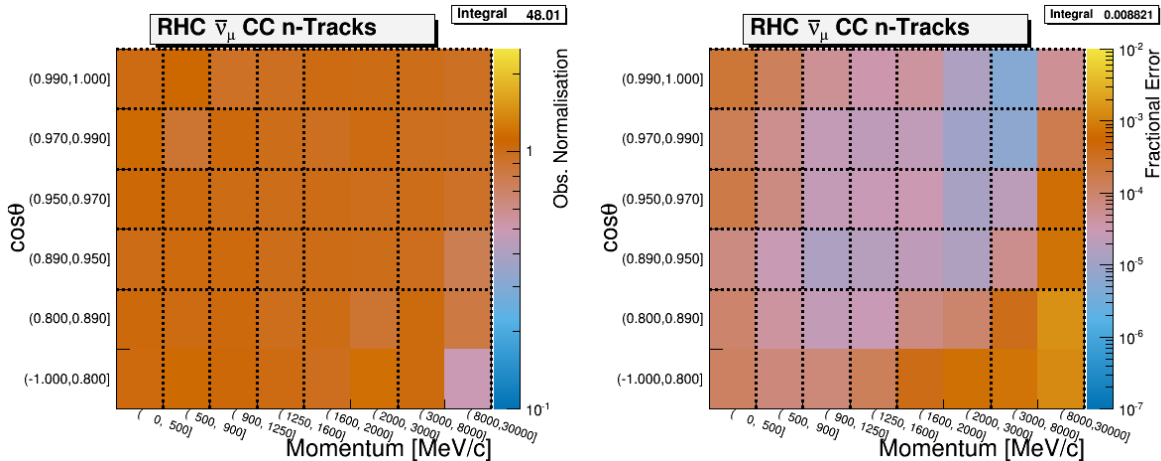


(b) The ν_μ in FHC Mode CC N-Tracks sample

Figure 4.6: Bin normalization edges for the ν_μ in FHC Mode samples. The left and right plots show the bin normalization and the bin statistical fractional error, respectively, if each fit bin had a single bin normalization. The dashed lines indicate the edges of the bin normalization parameters finalized for this analysis. Water-in and water-out modes are qualitatively the same.

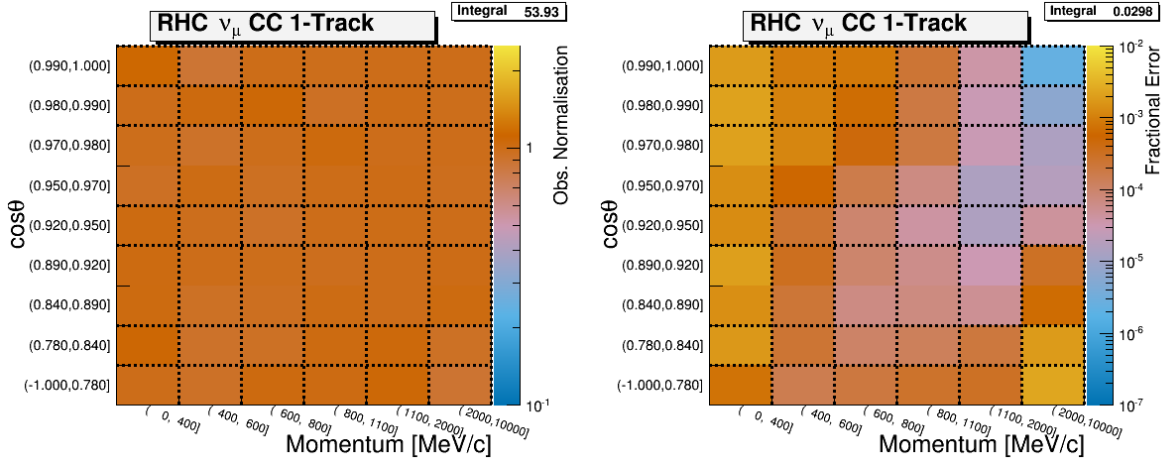


(a) The $\bar{\nu}_\mu$ in RHC Mode CC 1-Track sample

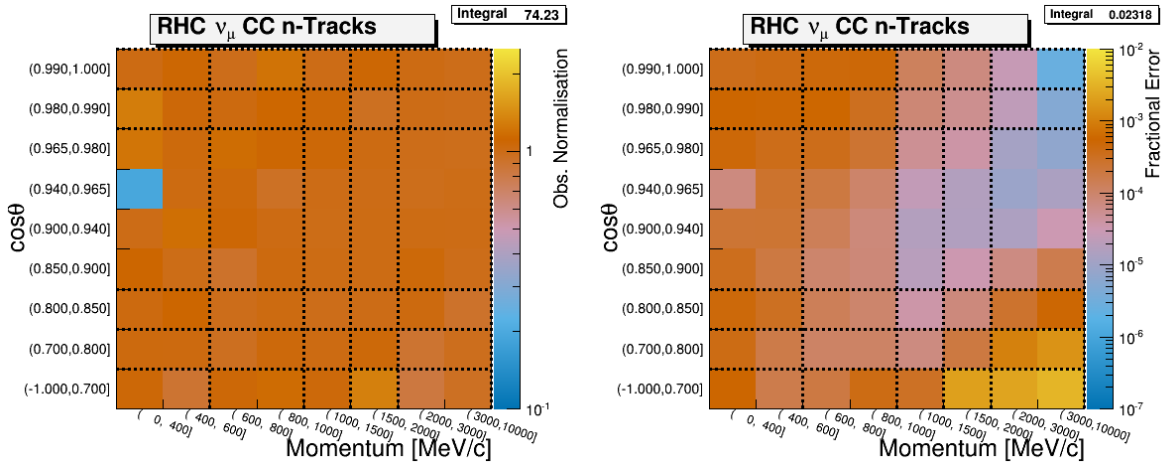


(b) The $\bar{\nu}_\mu$ in RHC Mode CC N-Tracks sample

Figure 4.7: Bin normalization edges for the $\bar{\nu}_\mu$ in RHC Mode samples. The left and right plots show the bin normalization and the bin statistical fractional error, respectively, if each fit bin had a single bin normalization. The dashed lines indicate the edges of the bin normalization parameters finalized for this analysis. Water-in and water-out modes are qualitatively the same.



(a) The ν_μ in RHC CC 1-Track sample



(b) The ν_μ in RHC CC N-Tracks sample

Figure 4.8: Bin normalization edges for the ν_μ Background in RHC Mode samples. The left and right plots show the bin normalization and the bin statistical fractional error, respectively, if each fit bin had a single bin normalization. The dashed lines indicate the edges of the bin normalization parameters finalized for this analysis. Water-in and water-out modes are qualitatively the same.

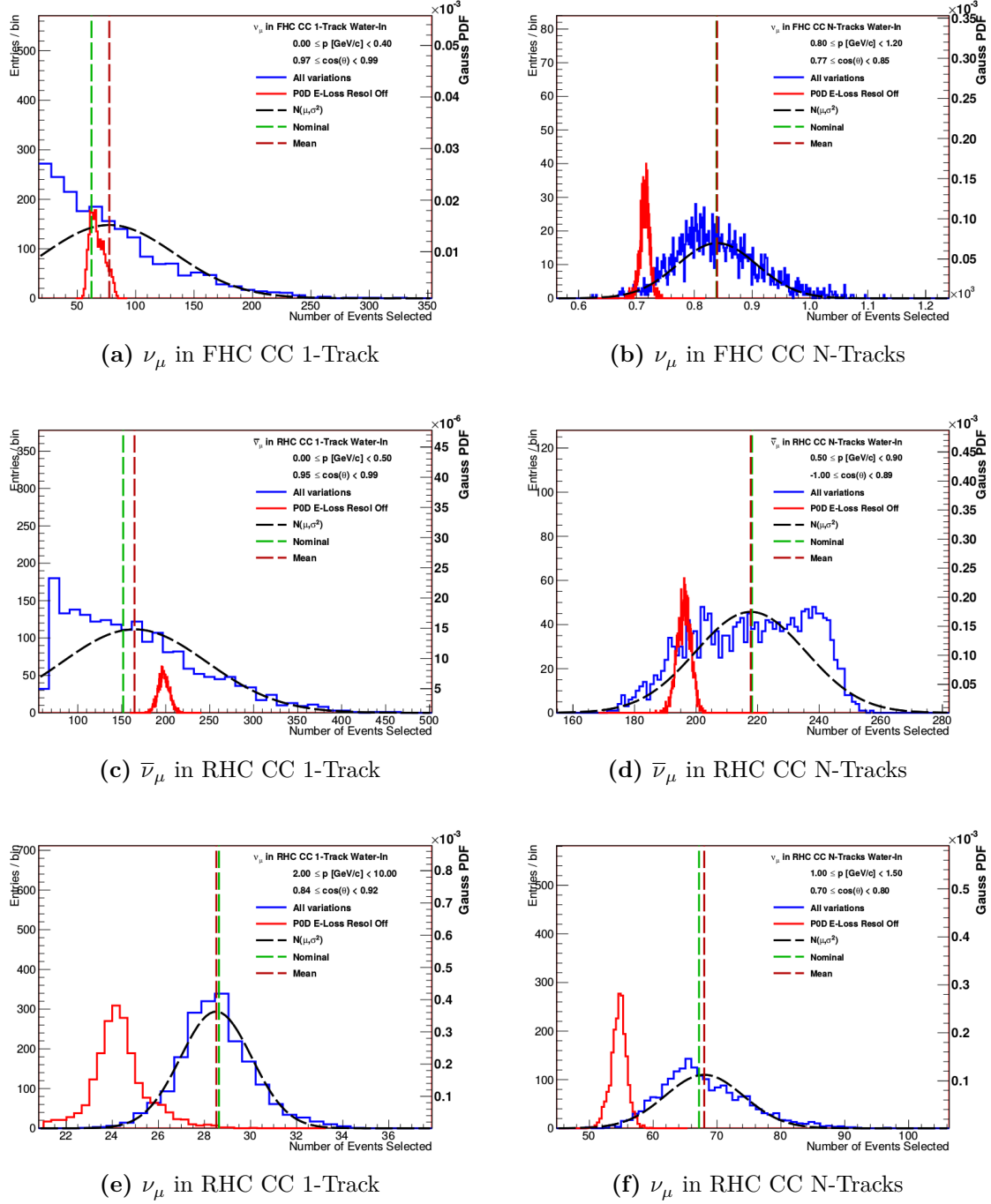
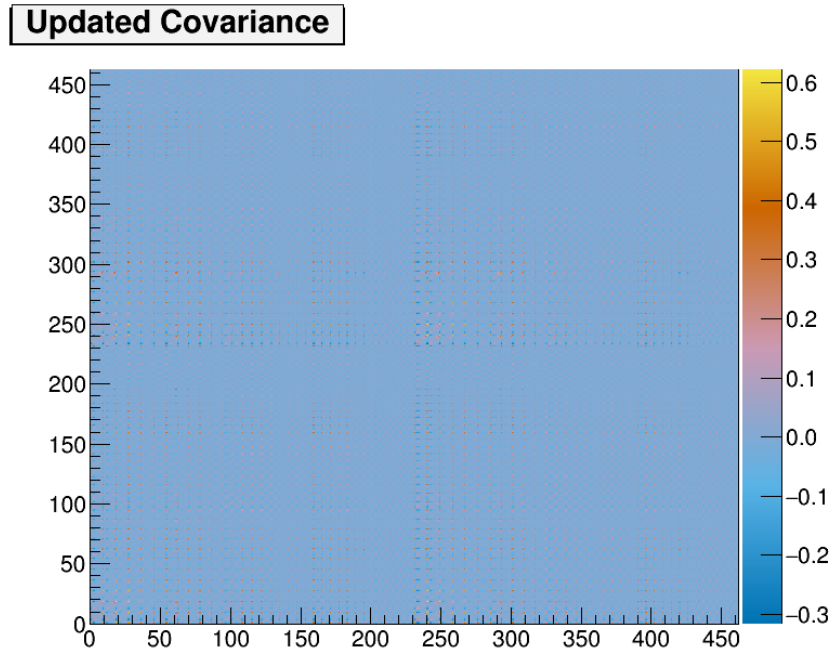


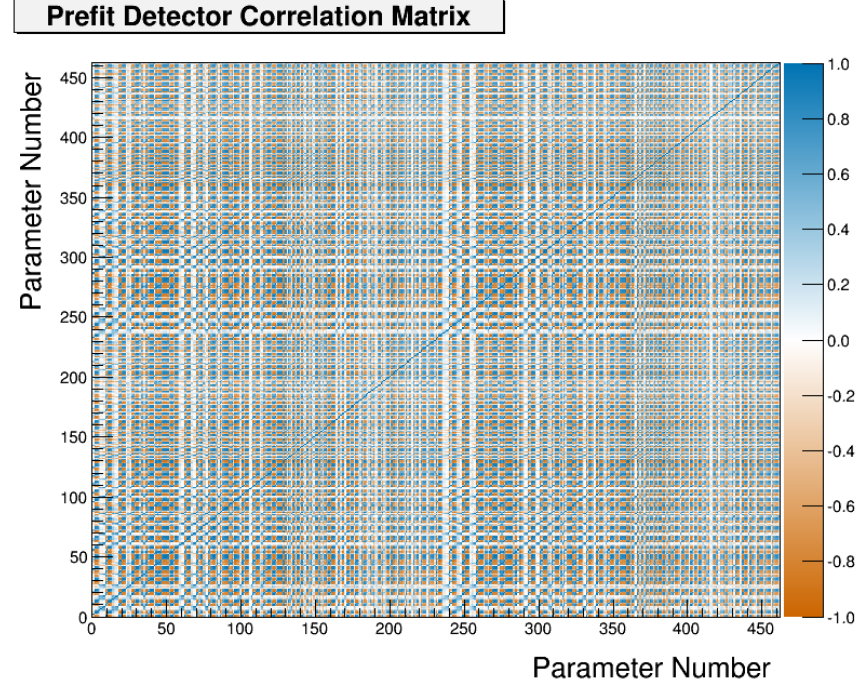
Figure 4.9: Event variations in representative observable normalization bins. Shown in each sub-figure the varied event rate from all toy experiments in a particular observable normalization bin. The blue curve has all the systematics enabled while the red curve has the ELossRes systematic disabled. Vertical dashed lines show the unvaried, weighted MC prediction and varied mean of all toy experiments. The ratio of the horizontal positions of each vertical line is the prefit normalization value for that bin. A Gaussian with variance extracted from the covariance matrix is shown to illustrate the bin's estimate on the normalization uncertainty.

The finalized observable normalization bins are listed below. There are in total $N_d = 461$ bin normalization parameters. The covariance matrix used in the BANFF fit is shown in Figure 4.10 on page 123. Their respective fit index, prefit value, and prefit standard deviation are tabulated in Appendix B.

- The ν_μ in FHC Mode CC 1-Track samples bin normalization edges:
 - p [GeV/c]: 0, 0.4, 0.6, 0.8, 1.25, 2, 3, 4, 5.5, 30
 - $\cos \theta$: -1, 0.7, 0.8, 0.94, 0.975, 0.99, 1
- The ν_μ in FHC Mode CC N-Tracks samples bin normalization edges:
 - p [GeV/c]: 0, 0.4, 0.6, 0.8, 1.2, 2.2, 3.5, 10, 30
 - $\cos \theta$: -1, 0.77, 0.85, 0.9, 0.97, 1
- The $\bar{\nu}_\mu$ in RHC Mode CC 1-Track samples bin normalization edges:
 - p [GeV/c]: 0, 0.5, 0.6, 0.8, 1.25, 2, 3, 30
 - $\cos \theta$: -1, 0.82, 0.9, 0.95, 0.99, 1
- The $\bar{\nu}_\mu$ in RHC Mode CC N-Tracks samples bin normalization edges:
 - p [GeV/c]: 0, 0.5, 0.9, 1.25, 1.6, 3, 30
 - $\cos \theta$: -1, 0.89, 0.95, 0.97, 0.99, 1
- The ν_μ in RHC Mode CC 1-Track samples bin normalization edges:
 - p [GeV/c]: 0, 0.4, 0.6, 0.8, 1.1, 2, 10
 - $\cos \theta$: -1, 0.78, 0.84, 0.92, 0.95, 0.98, 0.99, 1
- The ν_μ in RHC Mode CC N-Tracks samples bin normalization edges:
 - p [GeV/c]: 0, 0.6, 1, 1.5, 2, 10



(a) Covariance matrix



(b) Correlation matrix

Figure 4.10: Detector penalty covariance matrix. Shown in figure (a) is covariance matrix and (b) is the correlation matrix. Note that the parameter indices, which represent the bin normalization indices, are offset from their fit indices value by 99.

- $\cos \theta$: -1, 0.7, 0.8, 0.85, 0.98, 0.99, 1

To better understand how effective the choice of bin normalizations parameters are at characterizing the data variance, principal component analysis was performed using all the available toy experiments. Principal component analysis is the process of a eigenvalue decomposition of a square matrix, M . The principal components of M , which describe the data variance, are the eigenvectors. The relative importance of each eigenvector is set by the magnitude of the associated eigenvalue.

Using this prescription, we define the sample variance, S , as

$$S = \frac{1}{N_{\text{toys}}} X^T X,$$

where X is a $N_{\text{toys}} \times N_d$ matrix of the predicted number of events (not the normalization!) in each normalization bin. The eigenvalue decomposition of S is given by

$$S = U^T V' U,$$

where U is the eigenvector matrix of S and V' is a diagonal matrix of the S matrix eigenvalues. What is useful using principal component analysis is that the eigenvalues and eigenvectors are sorted from largest to smallest magnitude. The sample variance eigenvalues are shown in Table 4.3 on page 125. The first, and hence largest, eigenvalue is two orders of magnitude larger than the next largest eigenvalue, which means that the majority of the bin-to-bin variance can be explained by the first eigenvector. The first eigenvector's coefficients are shown in Figure 4.11 on page 125. We see that all the components are negative and clustered. This result is interpreted to mean we can expect the bins normalizations postfit values to shift all together uniformly.

Additionally, we can estimate the effective degrees of freedom for the bin normalization parameters. The effective degrees of freedom is given by

Index	0	1	2	3	...	458	459	460	461
Eigenvalue	2029	16.45	12.87	11.10	...	0.05325	0.05129	0.04955	0.03992

Table 4.3: Eigenvalues of the sample covariance. The values are sorted from largest to smallest in magnitude. Note that the parameter indices, which represent the bin normalization indices, are offset from their fit indices value by 99.

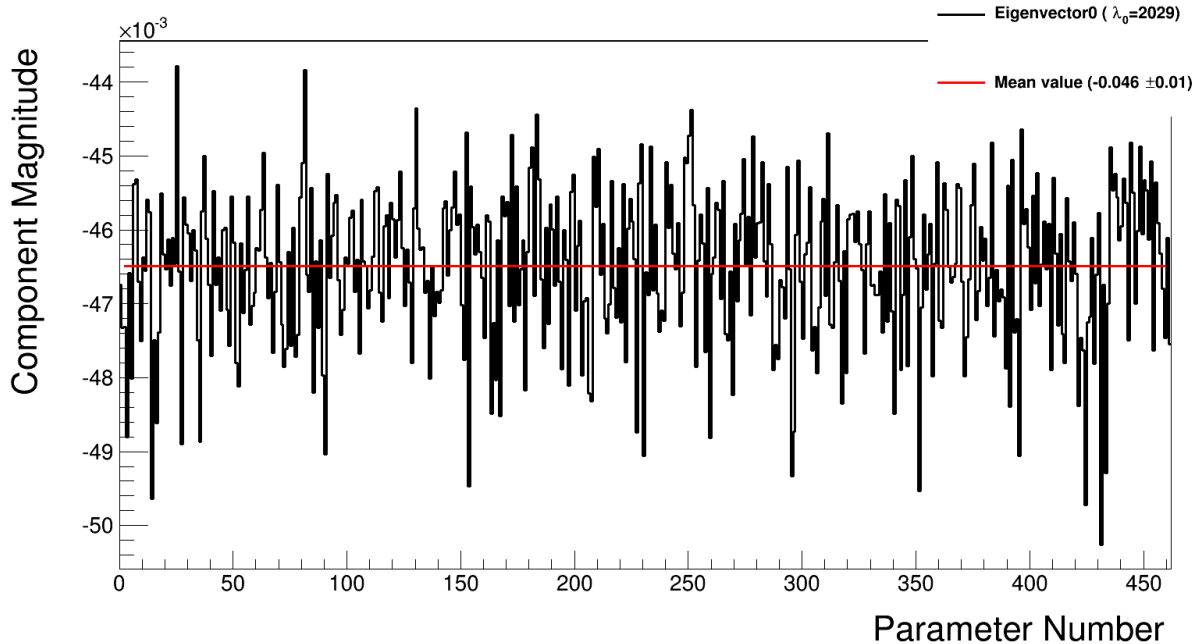


Figure 4.11: Principal component for the sample variance. This is the eigenvector associated with the largest eigenvalue of magnitude. Each parameter coefficient refers to the slope of the axis that describes most of the variance in the sample. The coefficients are all negative and are of similar magnitude. Together, they suggest all the normalization parameters respond linearly and uniformly. Note that the parameter indices, which represent the bin normalization indices, are offset from their fit indices value by 99.

$$df(\lambda) = \sum_{i=0}^{N_d} \frac{v_i}{v_i + \lambda}, \quad (4.22)$$

where v_i are the eigenvalues of V' and λ is a tunable parameter [47]. The idea behind (4.22) is that although all N_d coefficients will be non-zero, they are restricted to vary by the magnitude of λ . In particular, λ represents the regularization strength for the detector systematics penalty, which is set to one ($\lambda = 1$) in the BANFF fit. If there was no (regularization) penalty, or $\lambda = 0$, then the number of degrees of freedom is $df(0)=N_d$. It is found that there are about 137 effective degrees of freedom for the bin normalization parameters, or 29% of N_d . This suggests that a much smaller number bin normalization parameters can effectively describe the sample variance. This is particularly important to consider for a future BANFF fit analysis since this can provide a computational performance while maintaining predictability power in the ND constraint measurement. No further reduction in the number of bin normalization parameters were pursued due to time constraints.

4.2.3 Cross Section Model

There are a number of neutrino-nucleus interaction model parameters implemented in the BANFF fit to account for the uncertainties in cross section measurements. They are frequently updated to account for new models and constraints from external data. The cross section models used in this analysis use the T2K 2017 parameterization, which is a canonical set of parameters shared among all analyses in T2K. A gross description of the cross section model is provided here with a full description in the following reference [9].

There are three types of cross section parameters: shape, normalization, and functional. A cross section shape parameter, x^{Shape} , is defined as a shift in the location of a certain feature in the cross section. The shape parameters are stored in one dimensional splines

$$w(x^{\text{Shape}}) = \frac{d^n \sigma(x^{\text{Shape}})}{dz^n} / \frac{d^n \sigma(x_0^{\text{Shape}})}{dz^n},$$

where $d^n\sigma/dz^n$ is a n dimensional cross section of z dependent parameters, and x_0^{Shape} is the nominal value of the shape parameter. As a design choice, the shape location parameters all start with a prefit value of zero (0). A cross section normalization parameter, x_i^{Norm} , is defined as

$$x^{\text{Norm}} = \frac{p'}{p}, \quad (4.23)$$

where p and p' are NEUT nominal and ND constrained parameters, respectively. And finally functional parameters are scalars to model a cross section function of a true kinematic. For example, if a cross section is by $\sigma(Q^2) = A Q^2 + B$, A and B are the functional parameters in the model.

The next sections deal with the model parameterizations and systematic uncertainties in the NEUT version 5.3.3 [83] interaction library which is used in T2K MC and oscillation analysis.

4.2.3.1 The CC-0 π Model

The cross section models with the largest impact on T2K’s oscillation sensitivity are CCQE and CCQE-like interactions, collectively called CC-0 π . At energies near the ν_e appearance maximum, $E_\nu = 0.6$ GeV, the CCQE interaction is the largest contributor to the neutrino cross section as shown in Figure 1.30 on page 50. The nominal CCQE model in NEUT is a Spectral Function (SF) from Benhar et al [20]. An alternative CCQE model incorporates the Llewellyn-Smith dipole axial form factor¹⁹ [28, 54] and BBBA05 vector form factors coupled to a Smith-Miniz Relativistic Fermi Gas [23, 60, 75] (RFG). A CCQE-like excitation mode involves correlated nucleon pair scattering called “2 particle, 2 hole” [58] (2p2h). An additional nuclear model called the “Random Phase Approximation” (RPA) [31, 59] is used to modify single nucleon scattering by accounting for nucleon correlations inside the nucleus. The default CC-0 π model for T2K analyses is the combination of the Llewellyn-

¹⁹A form factor is a measure of scattering amplitude in the form of the Fourier transform of some charge distribution.

Smith+RFG model, 2p2h excitation, and RPA nuclear model. This combination was selected due to poor data matching with the SF model [83].

The CC- π model has three CCQE parameters: the dipole axial form factor mass M_A^{QE} from the Llewellyn-Smith model, and two Fermi momentum parameters p_F , one for ^{12}C and one for ^{16}O that describe the momentum of nucleons on the surface of a RFG. In the past, using these parameters has been shown to work as effective parameters in T2K when unconstrained. In this analysis, these three parameter are unconstrained. In other words, a flat prior is used for M_A^{QE} , p_F^C , and p_F^O .

For the 2p2h excitation, there are a total of five parameters to describe the model. Three are normalization terms: the ν interaction on ^{12}C , the $\bar{\nu}$ interaction on ^{12}C , and the scaling for $^{12}\text{C} \rightarrow ^{16}\text{O}$. The remaining two systematic parameters in the 2p2h excitation are shape parameters, one for ^{12}C and one for ^{16}O . They are used constrain the interplay of the contributing modes in 2p2h. One contributing mode is the Meson Exchange Current (MEC) which involves a virtual meson exchange between the nucleons. The other mode is nucleon-nucleon (NN) correlations which involves virtual particle exchange. A shape value of -1 determines 2p2h is completely due to MEC, 0 is the nominal MC 2p2h model, and +1 determines 2p2h is completely due to NN. Any differences in the event rate in the region between ± 1 is absorbed by a interference term. However, since no existing T2K nor external neutrino data can constrain the neutrino-induced 2p2h interaction, a flat prior is set for all 2p2h parameters.

The other nuclear interaction in the CC- π model uses the Nieves RPA model [59] to describe nucleon correlations. The RPA model primarily alters the single nucleon cross section and has dependence on both E_ν and Q^2 . A functional weighting scheme called “BeRPA” having only Q^2 dependence was found to work well to mimic the inherent uncertainties in the Nieves RPA model. The BeRPA functional is given by

$$w(Q^2) = \begin{cases} A\beta_0^3(x) + B\beta_1^3(x) + p_1\beta_2^3(x) + D\beta_3^3(x) & Q^2 \leq U \\ 1 + p_2 \exp(-E [Q^2 - U]), & Q^2 > U \end{cases} \quad (4.24)$$

where $x = Q^2/U$, $\beta_i^n(x)$ are the Bernstein polynomials [36]

$$\beta_i^n(x) = \binom{n}{i} x^i (1-x)^{n-i} \quad x \in [0, 1], \quad (4.25)$$

p_1 and p_2 absorb the continuity conditions,

$$p_1 = D + \frac{UE(D-1)}{3}, \quad p_2 = D-1, \quad (4.26)$$

and A , B , D , E , and U are the functional parameters. The parameter U is fixed to prevent unwieldy correlations from appearing.

4.2.3.2 The CC-1 π Model

Another important exclusive channel in NEUT is resonance states that produce a single pion or CC-1 π . The CC-1 π model incorporates the Rein-Seghal model of neutrino-induced Δ resonance decay [42–44, 64] with lepton mass corrections [21, 45]. There are just three tunable parameters in the model. They are resonant axial mass M_A^{Res} , the axial form factor normalization C_A^5 , and the isospin=1/2 background. These three parameters are known to effectively describe neutrino-induced single pion production data from Brookhaven National Laboratory [52] and Argonne National Laboratory [63]. It is important to know that M_A^{Res} and C_A^5 are strongly anticorrelated due to the parameterization of the form factor

$$f(Q^2) = C_A^5 \left(1 + \frac{Q^2}{(M_A^{\text{Res}} c^2)^2} \right)^{-2}. \quad (4.27)$$

4.2.3.3 Coherent Pion Production

Coherent scattering refers to scattering where the wavelength of the incoming particle is larger than the target. In the case of coherent neutrino-nucleus scattering, the neutrino's de Broglie wavelength is larger than the size of the nucleus. In the scattering, no quantum numbers are exchanged, but the nucleus experiences a momentum boost. In coherent pion production, the in-flight virtual boson is converted into a pion with that pion exchanging a Pomeron [5] with the nucleus. The coherent scattering model is described by Rein-Sehgal [65]. Lookup tables are used to scale the cross section to external data [83] and the Berger-Sehgal model [21]. Three tunable normalization parameters are used describe the coherent production model: CC on ^{12}C , CC on ^{16}O , and NC on all nuclei. As a design choice, both CC parameters are 100% correlated with one another, meaning that any change in one parameter changes the other identically.

4.2.3.4 High Energy Scattering Model

There are two parameters that describe high energy neutrino scattering. One is a CC deep inelastic scattering (DIS) interaction shape parameter called “CC DIS”. The other is a normalization for NC interactions called “NC Other”. The CC DIS parameter, which also includes multiple pion production, is modeled as a function of E_ν with a simple uncertainty relation of

$$\frac{0.4}{E_\nu \text{ [GeV]}} (\%),$$

where the uncertainty at 4.0 GeV is 10%. The NC Other parameter is a normalization on NC DIS, single kaon production, single η -meson production, and NC elastic processes with a flat 30% fractional uncertainty [83].

4.2.3.5 Final State Interactions (FSI)

Final state interactions [41] are effects that alter final state pions from neutrino-nucleus events before the pion exits the nucleus. The microscopic model in NEUT is a cascade implementation of the Salcedo-Oset model [69] which describes interactions in the nucleus as probabilities of position and momentum tuned to the world data [66]. These processes are divided into six classes with one parameter for each. These classes are the low energy inelastic scattering (INEL), high energy INEL, pion absorption (ABS), pion production (PROD), low energy charge exchange (CEX), and high energy CEX. The low and high energy transition for both the inelastic scattering and charge exchange processes occurs at $p_\pi = 500$ MeV/c.

4.2.3.6 Fixed Parameters

As mentioned in the CC- 0π model, the BeRPA U parameter is fixed to minimize correlations with the other BeRPA scale parameters. However, there are four other fixed normalization parameters in the BANFF fit since they correspond to SK only parameters. They are included in the fit in order to maintain consistency between the ND280 constraint and oscillation analysis parameterizations. In other words, they are spectators in the BANFF fit. These parameters are the CC ν_e/ν_μ event rate ratio, CC $\bar{\nu}_e/\bar{\nu}_\mu$ event rate ratio, NC- 1γ event rate, and NC other far detector event rate.

4.2.3.7 Fit Parameters

There are a total of 31 cross section parameters in the BANFF fit, five of which are fixed. The fit parameters are listed in Table 4.4 on page 132 with the associated covariance matrix shown in Figure 4.12 on page 134. Following the definition of the flux and bin normalization parameters, cross section parameters are defined as fractional differences either in shape, scale, or normalization. If no prefit uncertainty is shown in Table 4.4 on page 132, and emphasized using red font, then the parameter had a flat prior assigned. A model parameter with an asterisk (*) next to it is fixed in the fit. Abbreviations used in this table are “dim.-

“less” for dimensionless, “norm.” for normalization, “Near” for ND280, “Far” for Super-Kamiokande, and “bkg” for background. Parameters with physical units are shown in both dimensionless and dimensional values for comparison. Prefit values are relative to the NEUT nominal value.

Table 4.4: Cross section model parameters in the fit. See the text for a full description.

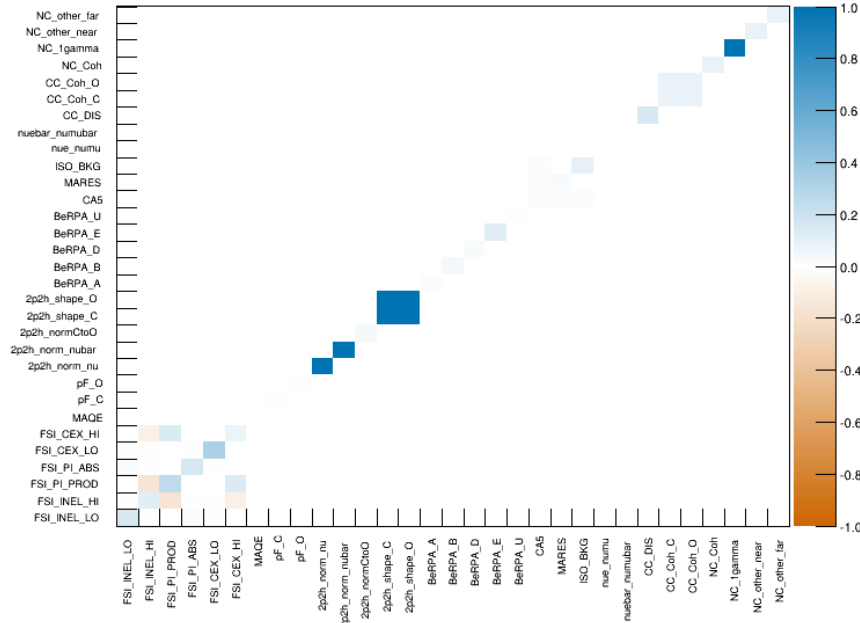
Fit index	Topology	Model	Parameter	Prefit
562	All	FSI	Low energy INEL	0 ± 0.41
563			High energy INEL	0 ± 0.34
564			PROD	0 ± 0.41
565			ABS	0 ± 0.5
566			Low energy CEX	0 ± 0.57
567			High energy CEX	0 ± 0.28
568	CC-0 π	Llewellyn-Smith	M_A^{QE} (dim.-less)	1
			M_A^{QE} (GeV/c 2)	1.20
569		RFG	p_F^C (dim.-less)	1
			p_F^C (MeV/c)	217
570			p_F^O (dim.-less)	1
			p_F^O (MeV/c)	225
571		Nieves 2p2h	ν norm. on ^{12}C	1
572			$\bar{\nu}$ norm. on ^{12}C	1
573			$^{12}\text{C}/^{16}\text{O}$ norm.	1
574			^{16}C shape location	0
575			^{12}O shape location	0
576	BeRPA	A		0.59 ± 0.118
577			B	1.05 ± 0.21
578			D	1.13 ± 0.1695

Fit index	Topology	Model	Parameter	Prefit
579			E	0.88 ± 0.352
580			U*	1.2 ± 0.1
581	CC-1 π	Rein-Seghal resonant 1 π prodction	C_A^5	0.96 ± 0.148
582			M_A^{Res} (dim.-less)	1.1263 ± 0.157
			M_A^{Res} (GeV/c^2)	1.07 ± 0.15
583			I= $^{1/2}$ bkg. norm.	0.74 ± 0.307
584	Other	Event rate at SK	CC- ν_e/ν_μ *	1 ± 0.0282
585			CC- $\bar{\nu}_e/\bar{\nu}_\mu$ *	1 ± 0.0282
586		Coherent pion production	CC-DIS shape location	0 ± 0.4
587			CC norm. on ^{12}C	1 ± 0.3
588			CC norm. on ^{16}O	1 ± 0.3
589			NC norm.	1 ± 0.3
590		Event rate	NC- 1γ *	1 ± 1
591			NC Other Near	1 ± 0.3
592			NC Other Far*	1 ± 0.3

4.3 Chapter Summary

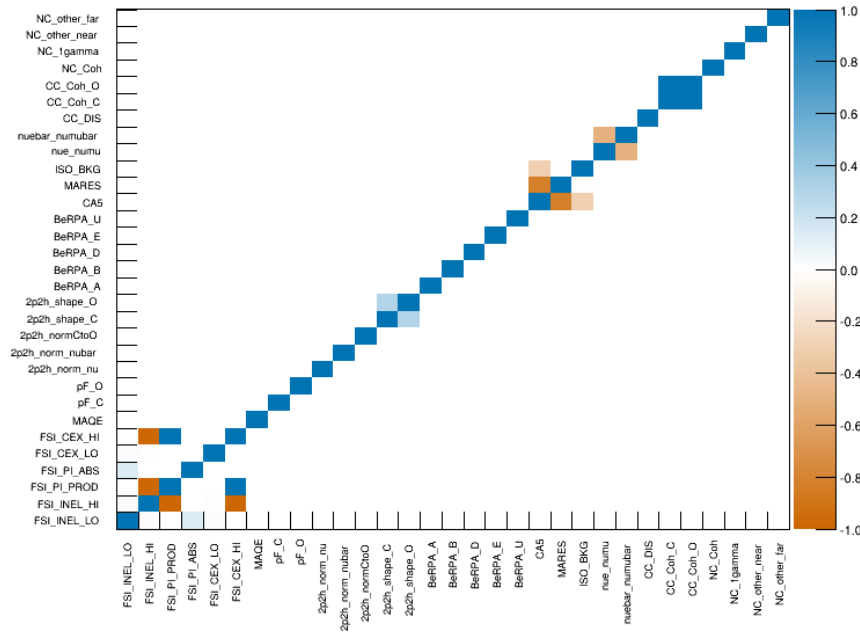
This chapter has described all the fit bins and parameters that go into the BANFF fit. For the fit bins, they are used in the LLR term to model the best possible fit between data and MC without any constraints. However, since there are known systematic uncertainties in the flux, detector inefficiencies, and cross sections, we have described their parameterizations to force the fit work within those constraints. The flux model is constrained by T2K primary and secondary beamline data while the cross sections are constrained by external data.

Prefit XSec Covariance Matrix



(a) Covariance matrix

Prefit XSec Correlation Matrix



(b) Correlation matrix

Figure 4.12: Cross section parameters prefit covariance and correlation matrices.

Finally, the detector systematics are determined via an ensemble of toy experiments based on well established control samples in the ND280 detector.

The next chapter describe the set of validation studies used to examine how the BANFF fit performs.

Chapter 5

Fitter Validation

This chapter will present the checks, tests and validations of the BANFF fit using the MC as input. The first such test is using the weighted MC as the data, referred to as an Asimov data fit. The next are two validation tests using two different data sets that have altered event weights compared to the MC. These are referred to as "fake data" sets. One fake data set alters the flux prediction and is referred to as the "High Energy Neutrino Flux Variation" fake data set. The other is the "Single Pion Event Rate Variation" fake data set.

5.1 Asimov Data Fit

Asimov data refers replacing the ensemble of simulated data sets by a single representative one [32]. In this analysis, this involves fitting the MC data set to itself for the primary purpose of checking the closure of the fitting framework. The Asimov set is produced with the same models as is implemented in the fitter and has all parameters set to their prior central values as defined in Chapter 4. Instead of statistically sampling from the MC, which can insert statistical variations in the fit, the Asimov data set is created by scaling the set down to the full T2K POT with additional finer corrections like flux and cross section weights. The prefit correlation matrix is shown in Figure 5.1 on page 137.

Prefit Correlation Matrix

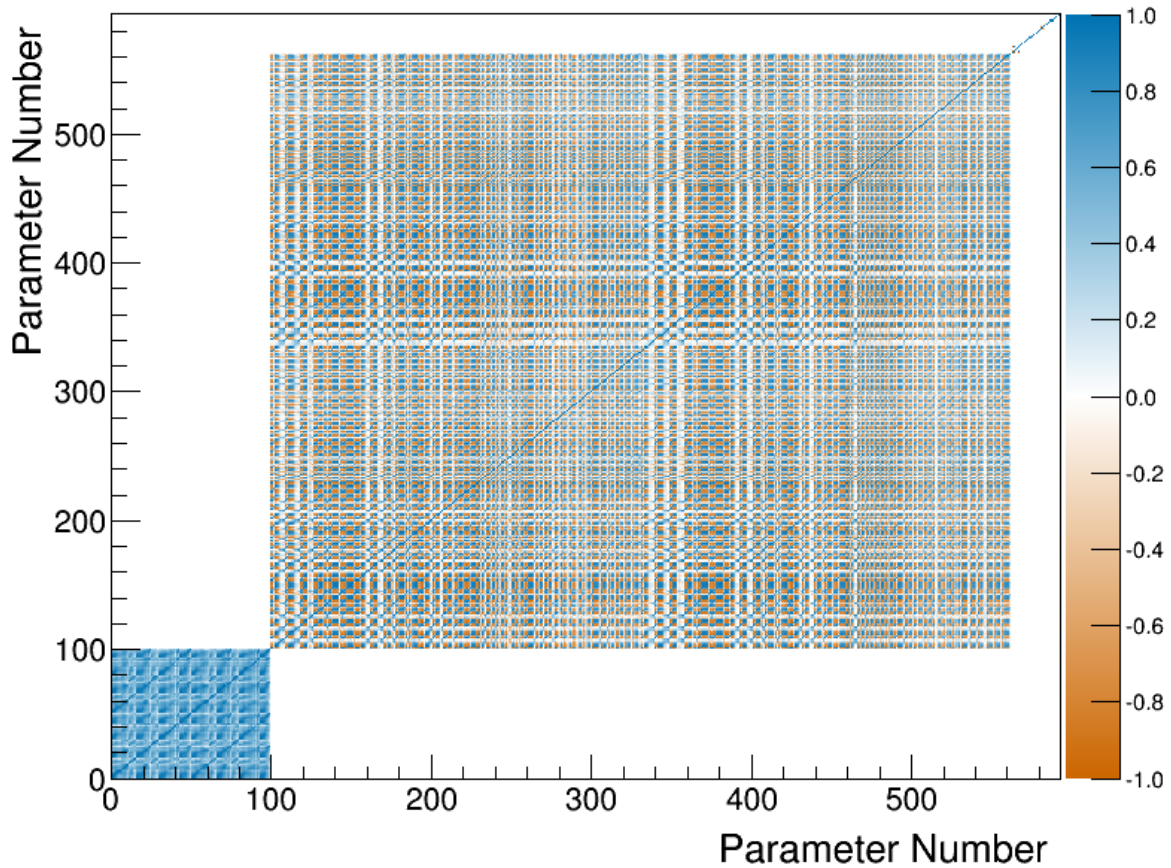


Figure 5.1: Complete prefit correlation matrix for the BANFF fit. The first 100 parameters are the flux bins. Between 100 and 561 are the bin normalization parameters. Finally 562 through 592 are the cross section parameters.

In addition to running an Asimov fit, other metrics were examined in the Asimov set. Shown first is a comparison of the event rates before and after applying weights to the MC. Next is an examination of the cross section weight functions. Finally is a set of scans of the test statistic space to ensure the sample and penalty terms are behaving as expected. Then the Asimov data set fit is explored.

5.1.1 Event Rate

Shown in Table 5.1 on page 139 is the event rates for the various samples for the Asimov fit. The data events column refers to real T2K data collected in the sample with the rest are MC events. There are a weights that correct differences between the data and MC. The POT weight normalizes the MC event rate to data rate. The other weights, which where discussed in Chapter 2, are the flux, cross section, and detector corrections. We see that applying the POT weight scales the MC event rate close to that of the data. The other weights are fine tuning corrections to the rate from known systematics like flux and cross sections. Application of all the weights is the prefit event rate and is collectively referred to as Asimov data set.

Sample name	Data events	Raw MC events	POT only	Application of weights			Prefit	
				POT+Flux	POT+xsec	POT+Det	POT+flux+xsec+Det	
ν_μ 1-Trk Wtr	27151.00	526226.00	26270.98	28766.86	24222.45	26286.14	27327.94	
ν_μ N-Trks	31013.00	529538.00	26708.61	31464.27	26267.19	26708.74	31098.20	
$\bar{\nu}_\mu$ RHC 1-Trk	8779.00	176007.00	9152.04	9365.78	8321.76	9161.91	8461.37	
$\bar{\nu}_\mu$ RHC N-Trks	4613.00	93132.00	4876.93	5014.74	4652.01	4876.81	4802.12	
ν_μ RHC 1-Trk	3502.00	56861.00	2933.20	3182.20	2747.29	2938.29	3025.76	
ν_μ RHC N-Trks	5424.00	85599.00	4460.10	4988.89	4413.01	4464.45	4956.19	
ν_μ 1-Trk Air	23504.00	309373.00	23383.39	25319.17	21594.49	23402.63	23603.03	
ν_μ N-Trks	32736.00	371986.00	28495.10	33255.58	27822.42	28505.66	32302.08	
$\bar{\nu}_\mu$ RHC 1-Trk	6681.00	75374.00	7374.13	7512.47	6732.25	7381.37	6767.79	
$\bar{\nu}_\mu$ RHC N-Trks	4437.00	47951.00	4689.16	4820.43	4446.52	4690.57	4544.72	
ν_μ RHC 1-Trk	2324.00	20943.00	2049.01	2198.46	1916.33	2052.56	2067.12	
ν_μ RHC N-Trks	4801.00	42098.00	4119.63	4586.22	4050.71	4122.39	4567.72	
Total	154965.00	2335088.00	144512.28	160475.06	137186.41	144591.53	153524.03	

Table 5.1: Event rate table for Asimov set. The “Raw MC” column refers the number of events in the sample from the nominal MC prediction without any weights applied. From left to right, applications of weights are applied to understand their affect on the samples. The “POT only” column refers to applying the POT weight to all events. Columns with “POT+Flux”, “POT+xsec”, and “POT+Det” refer to applying the POT weight together with the flux, cross section, and detector weights, respectively. The “Prefit” column has the POT, flux, cross section, and detector (POT+Flux+xsec+Det) weights all multiplied together.

5.1.2 One Sigma Variation of Cross Section Parameters

To ensure the cross section spline weight functions were functioning properly, the samples were analyzed when the parameters were set to their $\pm 1\sigma$ values. The results of the variations are shown in Appendix D, which show the samples are indeed affected by the weight functions.

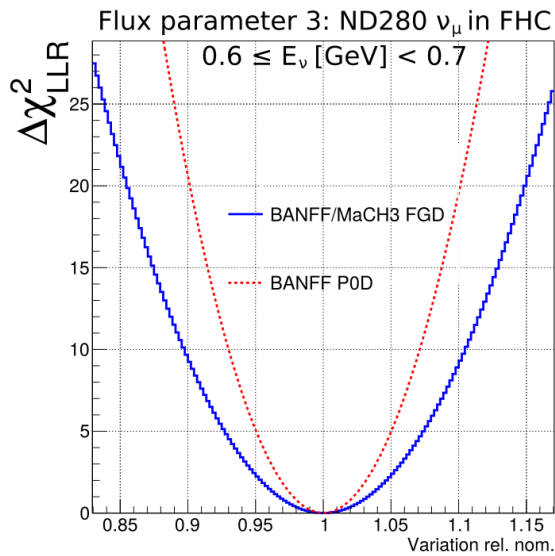
5.1.3 Log-Likelihood Scans

Log-likelihood scans of the sample and penalty terms were examined in the Asimov data set. The results of the scans are shown in Figure 5.2 on page 141 with comparisons between the PØD-only samples and FGD-only samples shown. It demonstrates that same penalties are applied between the PØD-only and FGD-only analyses. Also observed is that the PØD-only data has similar sensitivity and shape dependence on the flux parameters with that of the FGD-only data. The complete set of scans are shown in Appendix E and Appendix F.

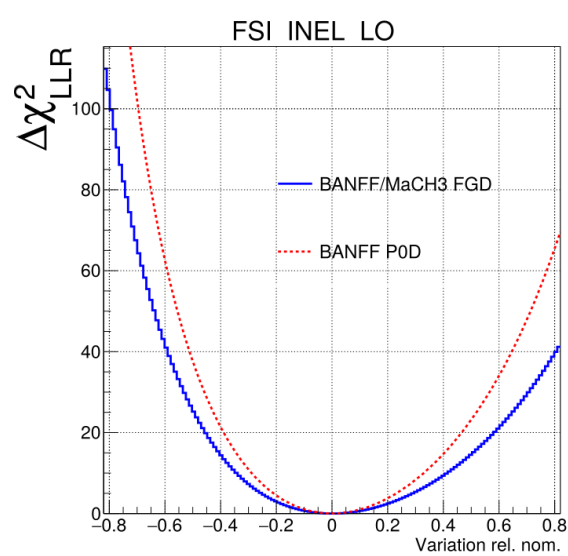
5.1.4 Fit Results

The postfit results of the Asimov data fit are shown in Figure 5.3 on page 142 to Figure 5.6 on page 145. In order to provide a unified graphical representation for all the parameters, the prefit and postfit cross section shape parameters are adjusted to be relative to one (1).

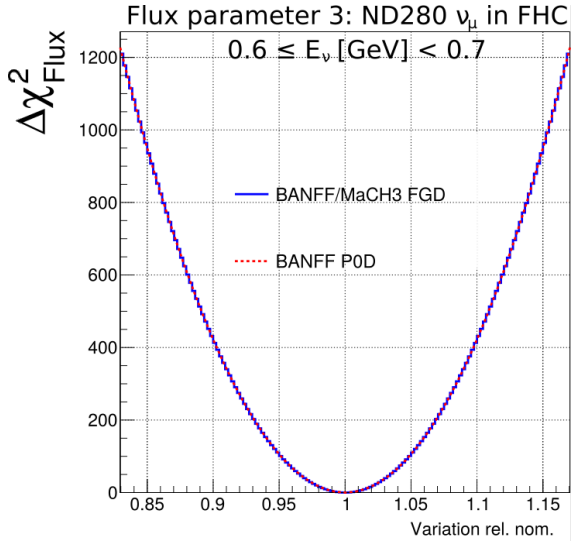
We see that the postfit parameters have uncertainties that are different compared to their prefit values. This is expected since correlations between the sub-matrices in the covariance matrix, which were assumed uncorrelated to start, have been calculated. The complete postfit correlation matrix is shown in Figure 5.7 on page 146 and the flux and cross section only correlation matrix is shown in Figure 5.8 on page 146. We observe significant anti-correlations between each of the sub-matrices which is predicted from (2.7) since any increase in one parameter weight forces a decrease in the others.



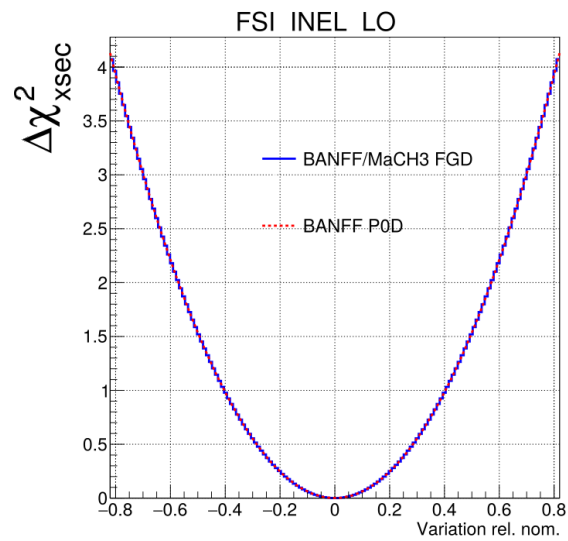
(a) Flux normalization b_3 $\Delta\chi^2_{\text{LLR}}$ scan



(b) FSI low energy inelastic shape location $\Delta\chi^2_{\text{LLR}}$ scan



(c) Flux normalization b_3 $\Delta\chi^2_{\text{Flux}}$ scan



(d) FSI low energy inelastic shape location $\Delta\chi^2_{\text{xsec}}$ scan

Figure 5.2: Comparison of $\Delta\chi^2$ scans for variations in fit parameters in the Asimov set. Two parameters are varied: parameter 3 (left) corresponding to a flux bin normalization and 562 (right) corresponding to a FSI shape location parameter. The top panel shows the change in the LLR test statistic $\Delta\chi^2_{\text{LLR}}$ while the bottom panel shows the penalty terms. In all sub-figures are comparisons between the BANFF/MaCH3 FGD 2017 results [6] against the BANFF P0D-only results. Special thanks goes to Clarence Wret (c.wret@rochester.edu) of the University of Rochester for generating the plots.

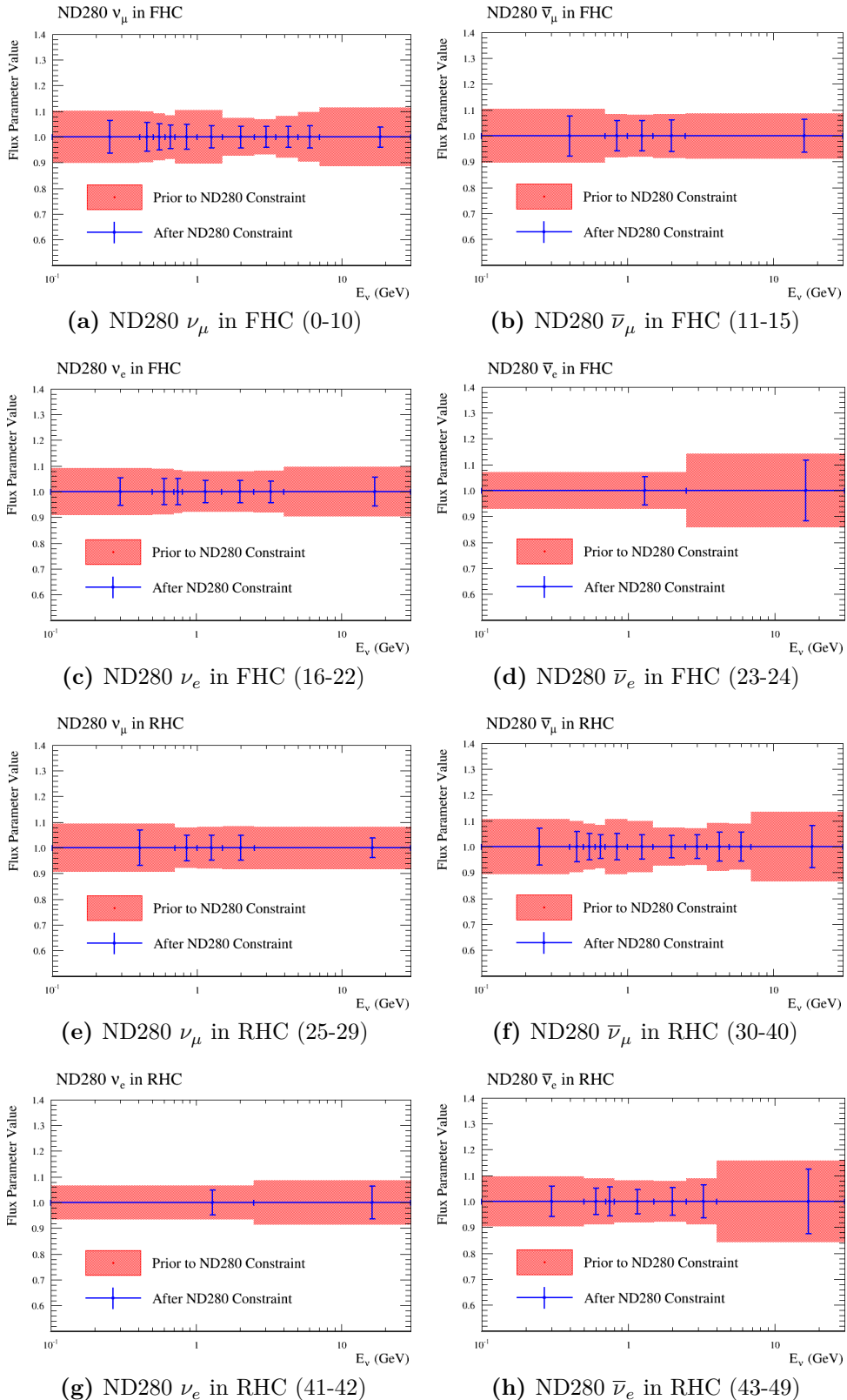


Figure 5.3: Asimov fit results for the Flux at ND280. The numbers in parentheses indicate the fit indices.

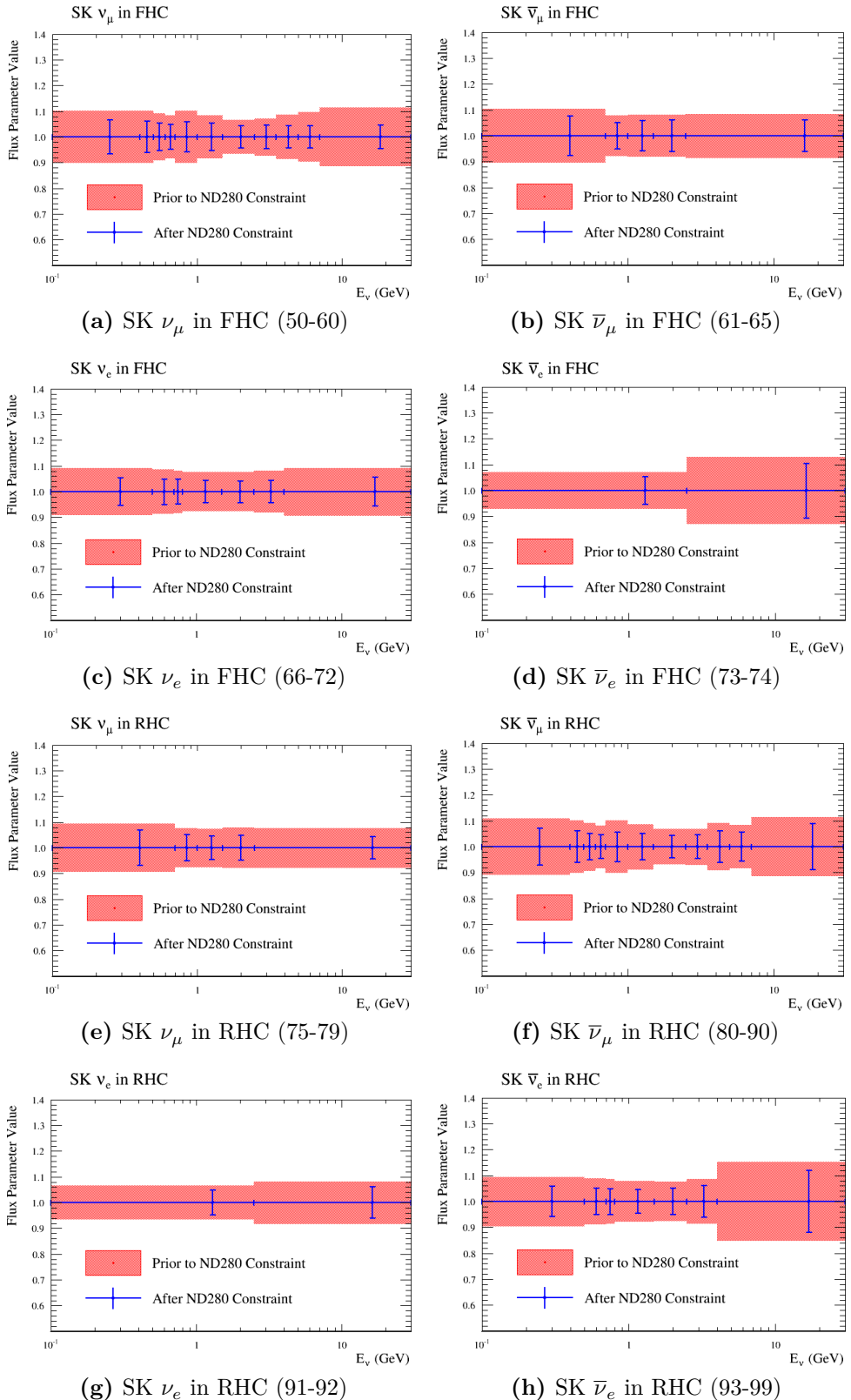


Figure 5.4: Asimov fit results for the Flux at Super-K. The numbers in parentheses indicate the fit indices .

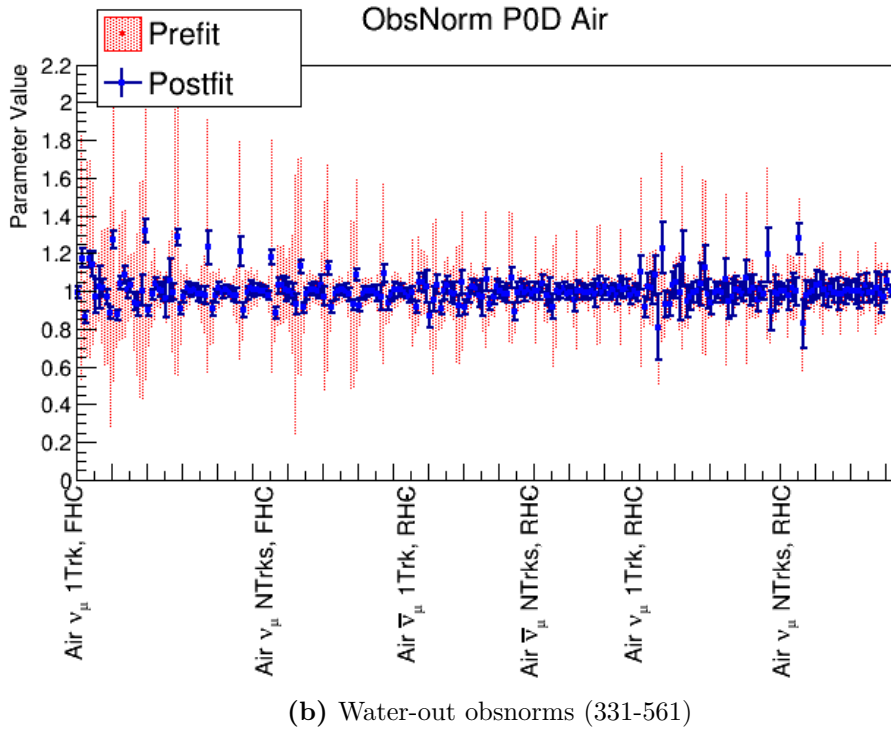
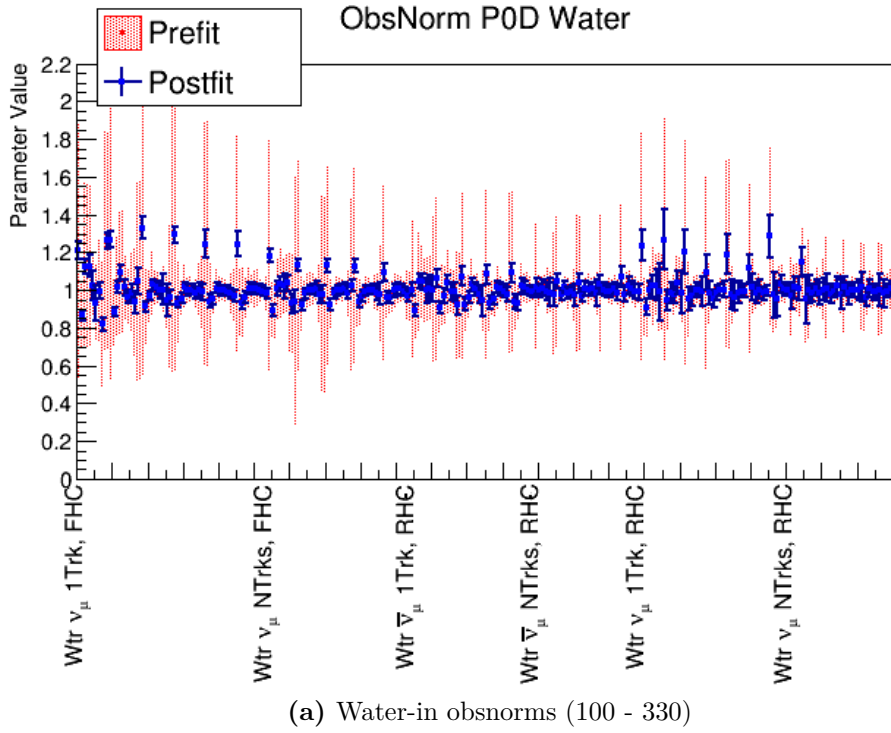
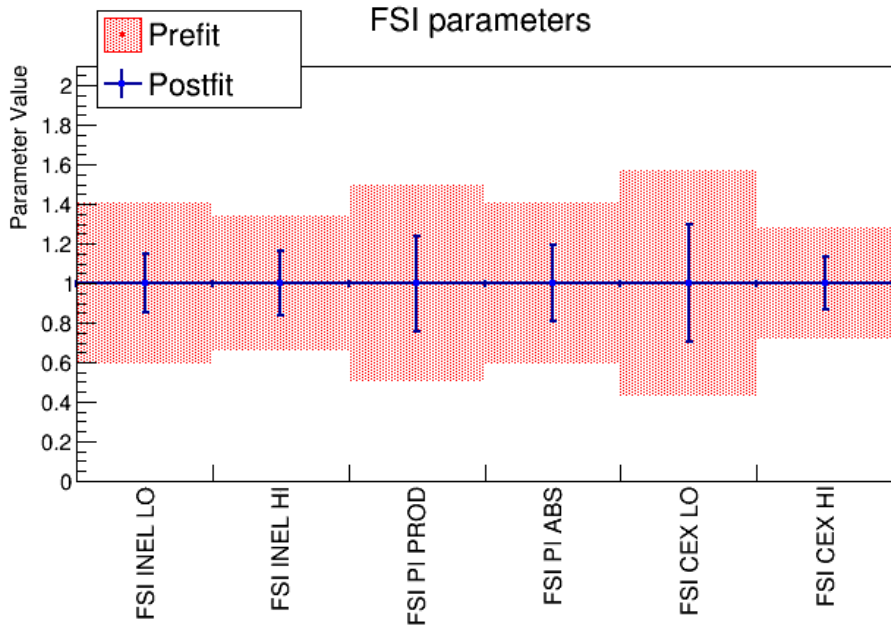
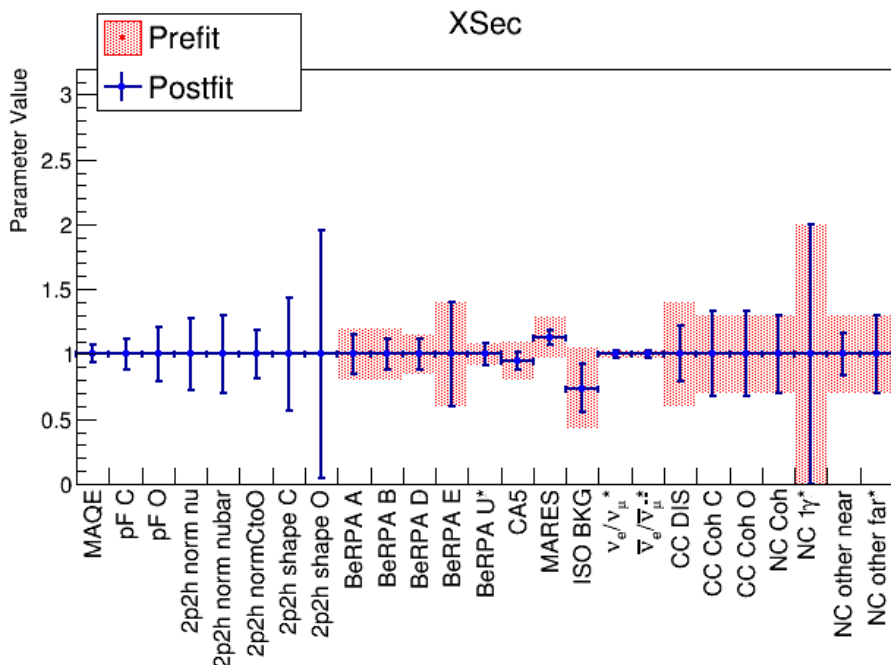


Figure 5.5: Asimov fit results for the obsnorm parameters. The numbers in parentheses indicate the fit indices. The large jumps in the bin normalization parameters is an artifact of the indexing choice with the indices increasing in increasing momentum in constant angular slices. Compare the changes in the bin normalizations in the ν_μ in FHC CC 1-Track in Figure 4.6 on page 118.



(a) FSI (562-567)



(b) Cross Section (568-592)

Figure 5.6: Asimov fit results for the FSI and cross section parameters. The numbers in parentheses indicate the fit indices. In order to provide a consistent presentation of parameter changes between prefit and postfit among all parameters, shape location and scale parameters are adjusted to prefits of one (1). In effect, the value and uncertainties for all parameters are fractional changes.

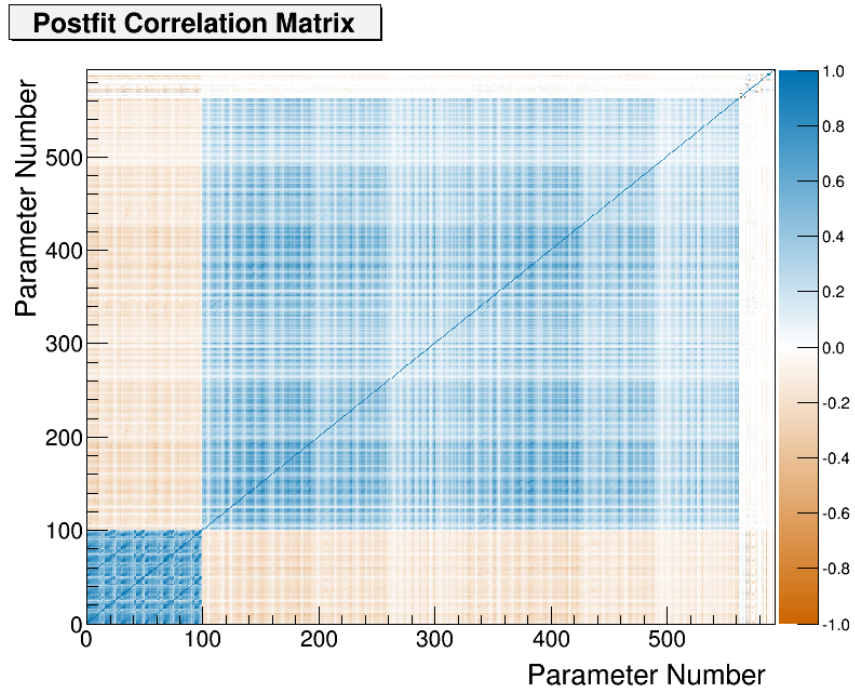


Figure 5.7: Complete postfit correlation matrix for the Asimov data fit.

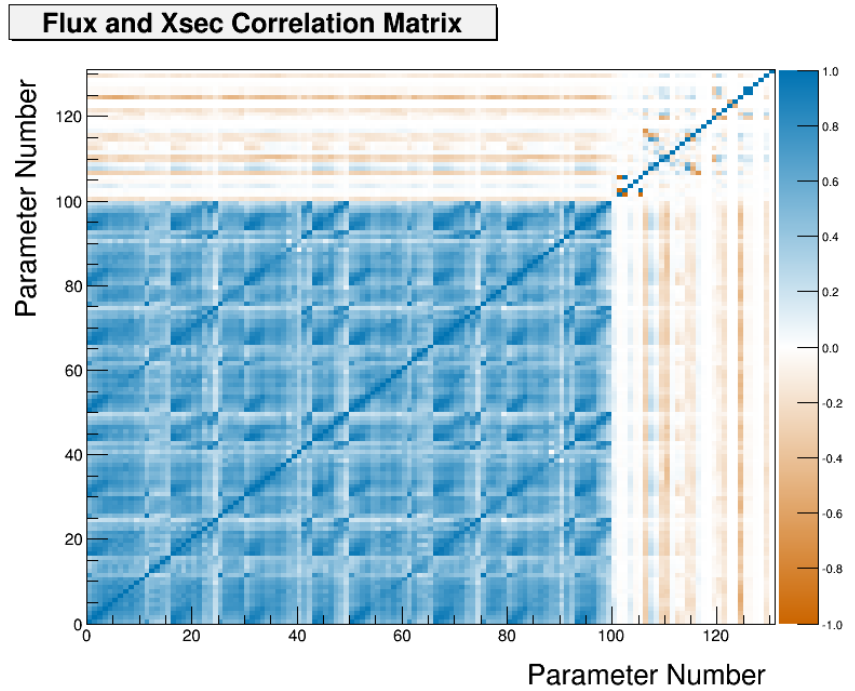


Figure 5.8: Flux and cross section postfit correlation matrix for the Asimov data fit. The parameters from 1-100 are the flux parameters and all parameters after are the cross section.

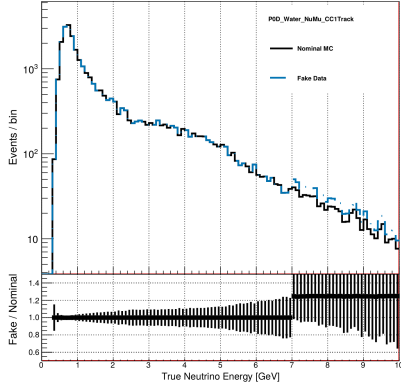
5.2 Fake Data

In this section, we examine the results of BANFF fits when given data sets with non-physical alterations. As stated earlier, these are called “fake data” sets since we are treating these as data in the fit, but they are in fact generated starting with the MC. These data sets initially start with the Asimov data set and have variations applied to it. Here we are only interested in the results of the flux and cross section parameters since they are the parameters that are propagated to the oscillation analysis. The first fake data set is a variation of the high energy ν_μ in FHC neutrino flux. The other test is a variation of the Single Pion Event Rate Variation.

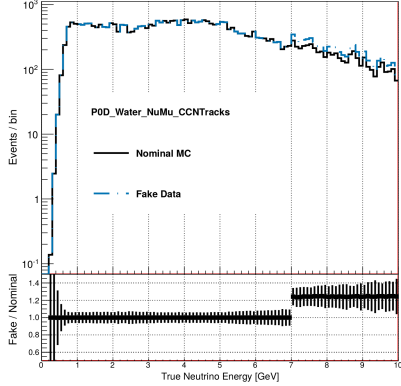
While other fake data sets could be generated that are more or less similar to the Asimov data set, that is not the purpose of fitting to fake data sets. *The purpose of these tests is to show the fit can converge when provided with non-Asimov data sets and we can understand the results.* The fitting software MINUIT in the BANFF fit is known to not converge on a global minimum when using altered Asimov data. In particular, fitting FGD-only data generated from random and uncorrelated variations of all fit flux, cross section, and bin normalization parameters, 127 out of 500 fits ($\sim 25\%$) reported fit convergence problems. So convergence is not assured in all situations, but is possible. The information it does provide is possible biases in the fit results for given systematic parameters. By demonstrating the BANFF fit converges with PØD-only fake data and we can sensibly understand the results, we establish that a credible PØD-only real data fit result is possible.

5.2.1 High Energy ν_μ in FHC Flux Variation

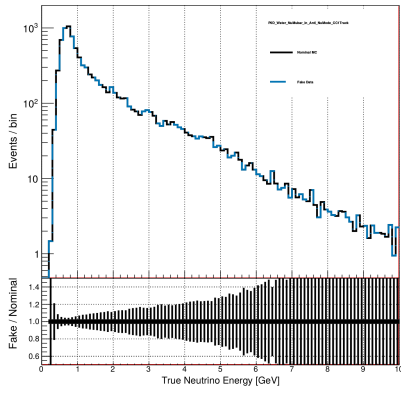
This fake data set arbitrarily increases the ν_μ in FHC flux between 7 and 30 GeV by +25%. This variation was chosen since this energy range corresponds precisely to flux parameter b_{10} and it could affect all analysis bins. The input fake data in true neutrino energy is shown in Figure 5.9 on page 148.



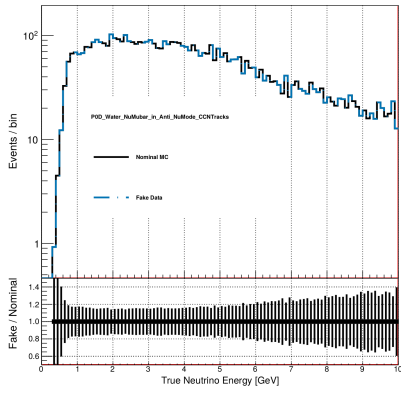
(a) ν_μ in FHC CC 1-Track



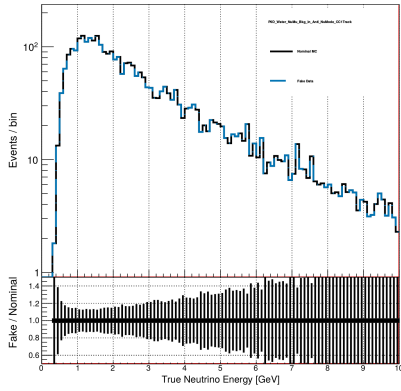
(b) ν_μ in FHC CC N-Tracks



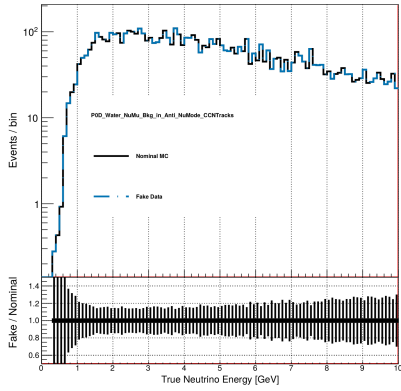
(c) $\bar{\nu}_\mu$ in RHC CC 1-Track



(d) $\bar{\nu}_\mu$ in RHC CC N-Tracks



(e) ν_μ in RHC CC 1-Track



(f) ν_μ in RHC CC N-Tracks

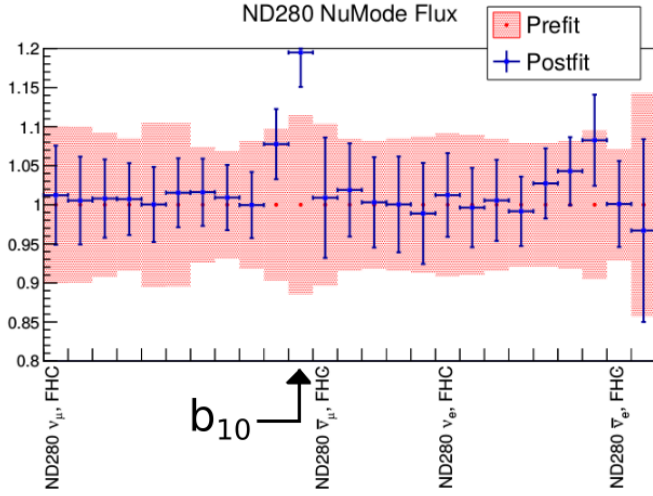
Figure 5.9: Neutrino flux before and after applying the +25% increase to ν_μ in FHC flux in the High Energy Neutrino Flux Variation data set. In the figures, “Nominal MC” refers to the Asimov prediction and “Fake Data” is the altered data set. A ratio of the fake data to nominal MC is shown below each histogram to show the variation was applied correctly. The flux of neutrinos, both ν_μ and $\bar{\nu}_\mu$, in RHC are not affected.

The postfit parameter plots are shown in Figure 5.10 on page 150. We see that the target flux parameter b_{10} has significantly increased from its prefit value by almost +20%. However, due to correlations in the flux covariance matrix, other flux parameters have changed. The BANFF fit prefers to increase the previous energy flux parameter and the high energy ν_e flux parameters as well. While we saw that the flux and hence event rate was not changed in the RHC samples, the RHC flux parameters are also slightly affected. However, the RHC flux parameters are still well within prefit uncertainties. The statement is true for the cross section and FSI parameters. Therefore we can conclude that the fit prefers to resolve nonphysical changes large, singular changes with many correlated parameter variations.

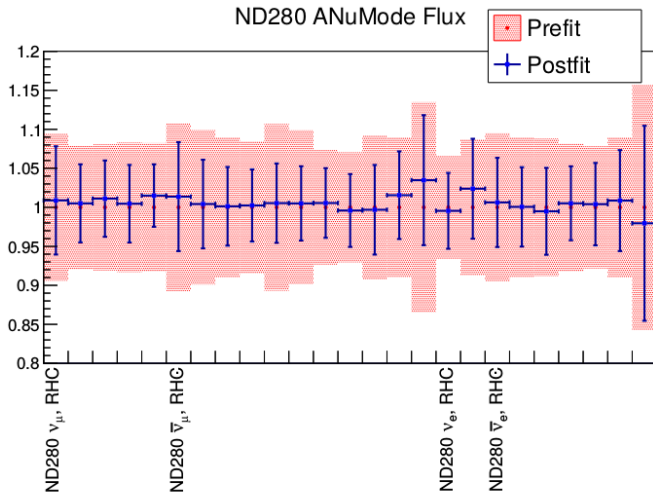
5.2.2 Single Pion Event Rate Variation

This fake data set arbitrarily increases the number of resonant single pion events by +25%. This was implemented by taking all true NEUT CC- 1π events, extracting the event weight, and increasing it by +25%. This is what is observed in the lepton candidate momentum distributions as shown in Figure 5.11 on page 151. According to the CC- 1π model, the event rate can be singly absorbed in C_A^5 . However as seen in Appendix D, increases in any CC- 1π parameter will increase the event rate. Additionally, C_A^5 and M_A^{Res} are anticorrelated with one another meaning that these parameters will be forced to shift in opposite directions together. Given the postfit results from the previous fake data fit, we should expect to see more than just the CC- 1π parameters to vary.

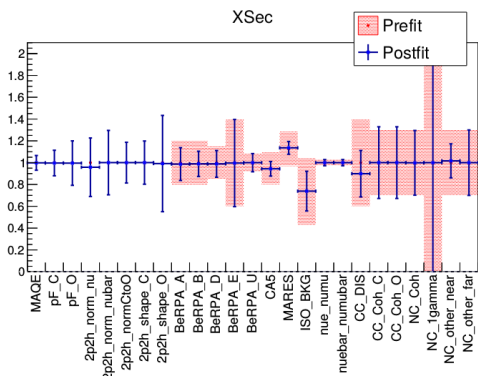
The postfit results for this fake data set are shown in Figure 5.12 on page 153. We observe that the CC- 1π parameter C_A^5 increased by $\sim 10\%$, but this is not enough to account for the input fake data shift. We also notice that due to anticorrelations, M_A^{Res} was decreased by about several percent. What the fit prefers is to increase the isospin= $1/2$ background, 2p2h normalization, and all the flux parameters. Like the first fake data set, we see that in the presence of nonphysical variations to the Physics, the fit prefers to spread out variations



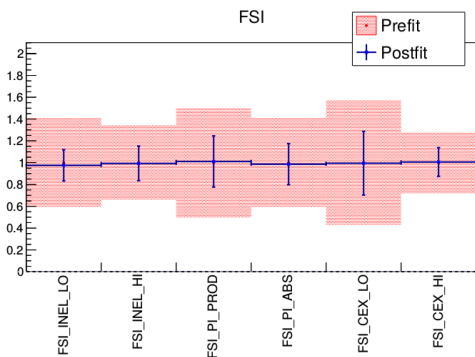
(a) ND280 FHC Flux



(b) ND280 RHC Flux



(c) Cross section parameters



(d) FSI parameters

Figure 5.10: Postfit parameters for the high energy ν_μ in FHC flux variation fake data fit. All the flux parameters in FHC are shown together and ordered sequentially from left to right. The same is true the RHC flux.

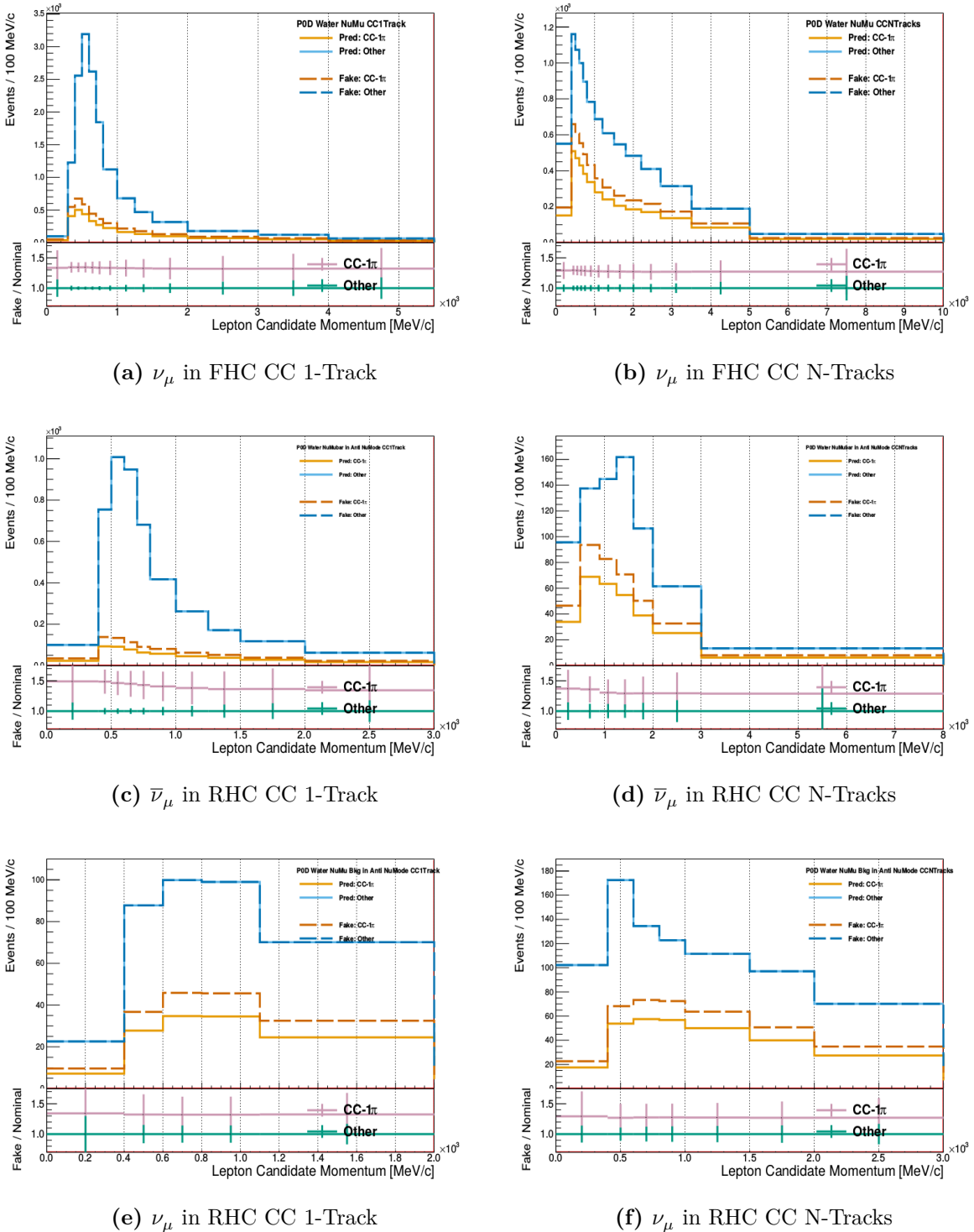


Figure 5.11: Lepton candidate momentum for the Single Pion Event Rate Variation fake data set. The nominal MC and fake data predictions are shown as solid and dashed lines, respectively. True CC-1 π events are differentiated from all other interactions to illustrate the event scaling applied. A ratio plot of CC-1 π events to all other interaction events shown beneath each main histogram.

among the other parameters. However, this time the variations are shared among flux and cross section parameters.

5.3 Validation Summary

We have validated the BANFF fit indeed works and tested its robustness in a variety of scenarios. We learned from the Asimov data set, which is the T2K nominal MC corrected to data POT with fine tuning corrections, in particular how the flux and cross section parameters affect the samples. In the fake data sets, we saw the effect of the penalty terms and how their correlations influence the fit. While more rigorous tests could establish where biases exist, these limitations are beyond the scope of this thesis. What has been established is that sensible fit results using the PØD selections are possible. We can now examine the PØD-only data and be assured the BANFF can fit can converge with PØD-only data.

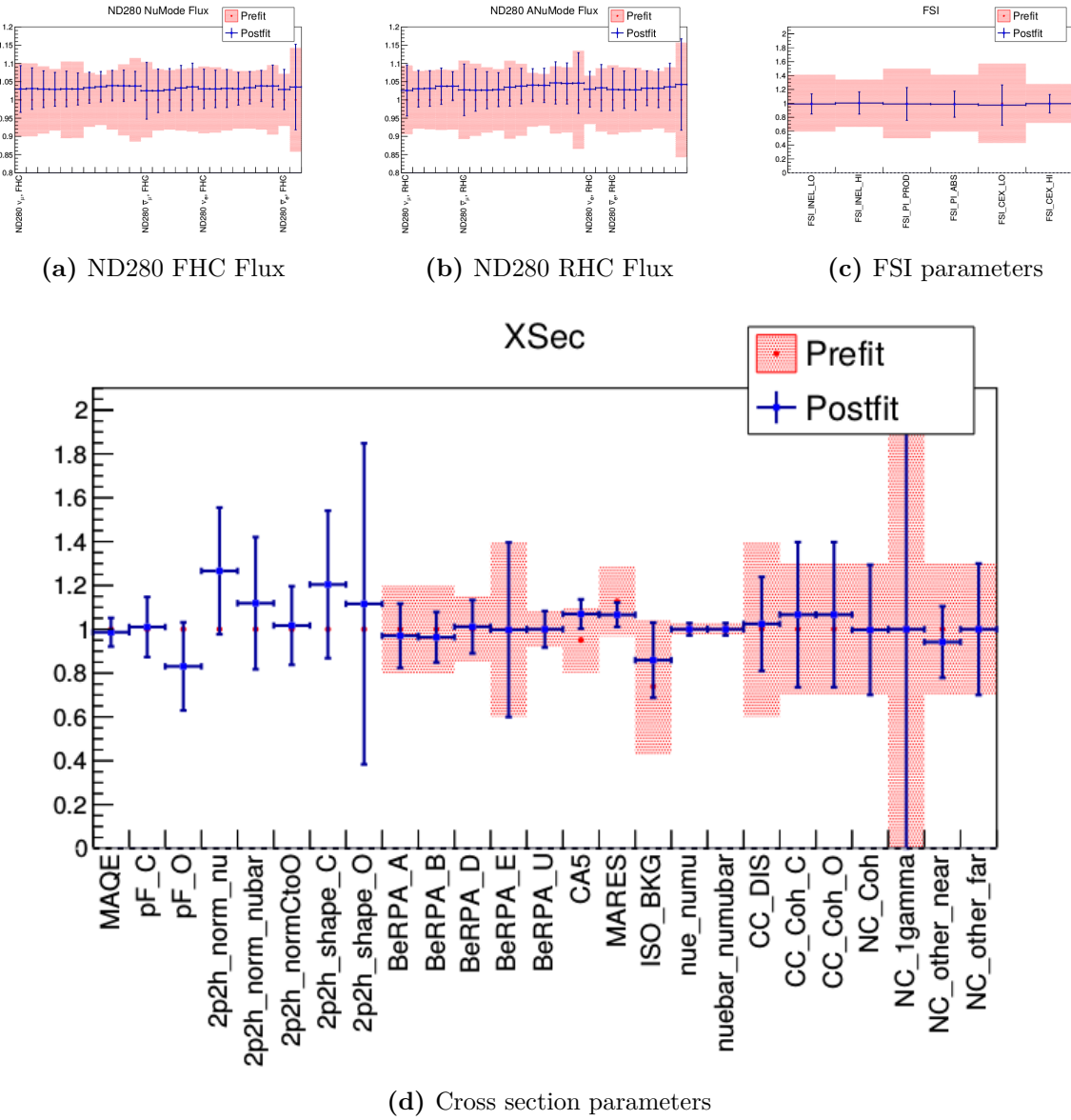


Figure 5.12: Postfit parameters for the Single Pion Event Rate Variation fake data fit. All the flux parameters in FHC are shown together and ordered sequentially from left to right. The same is true the RHC flux.

Chapter 6

Fitter Results

This chapter explores the results of performing the BANFF fit using the PØD-only samples. We have confirmed the fit machinery is working and the samples demonstrate sensitivity to flux and cross section parameters. The focus in this chapter is to examine the results of the PØD-only data fit and compare it against the FGD-only result.

The chapter will proceed in the following order. First the data will be examined since we have remained purposefully and mostly blind up to this state. Next the postfit results will be carefully examined and compared with that of the FGD-only fit. Finally, a hypothesis test will be performed to test the level of agreement between the two fits.

6.1 Prefit Sample Distributions

This section presents the first look at the data for the 12 samples according to the fit bins set in Chapter 4. The samples are categorized, as before seen, into four true interaction modes: ν CCQE, ν non-CCQE, $\bar{\nu}$ CCQE, and $\bar{\nu}$ non-CCQE. However, true fiducial volume (FV) and out of FV events are not differentiated in this case. The legend used to classify the data and prefit events is shown in Figure 6.1 on page 155. The prefit samples with the data shown are presented between Figure 6.2 on page 156 and Figure 6.13 on page 167. First

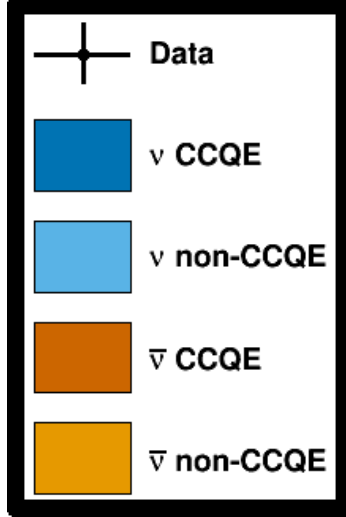


Figure 6.1: Data and prefit legend

the water-in samples are displayed, and then the water-out samples are shown. As we saw before, the water-in and water-out samples are qualitatively the same.

In general, we notice good agreement between the data and prefit distributions. Their agreement is represented in one-dimensional profiles with the data to prefit ratio shown below the histograms. Evidence of the PØD bulging effect in the most downstream layers can be seen in all water-in samples. In particular, since there is more true mass in the most downstream layers, particles with lower momenta are more likely to enter the TPC than predicted by the MC using the as-built mass. Better agreement is observed in the water-out periods, but there is some initial tension in the samples.

6.2 Postfit Results

The results of the PØD-only BANFF fit are presented here. MINUIT reported that it took between 149000 and 150000 iterations to find the $\Delta\chi^2_{ND280}$ minimum with an additional 176000 iterations to calculate the Hessian matrix. The total time to load all the data and complete the Hessian calculation was 27.5 hours using OpenMP with 16 cores, which is not unreasonable in terms of large scale computational work. However, a significant fraction of

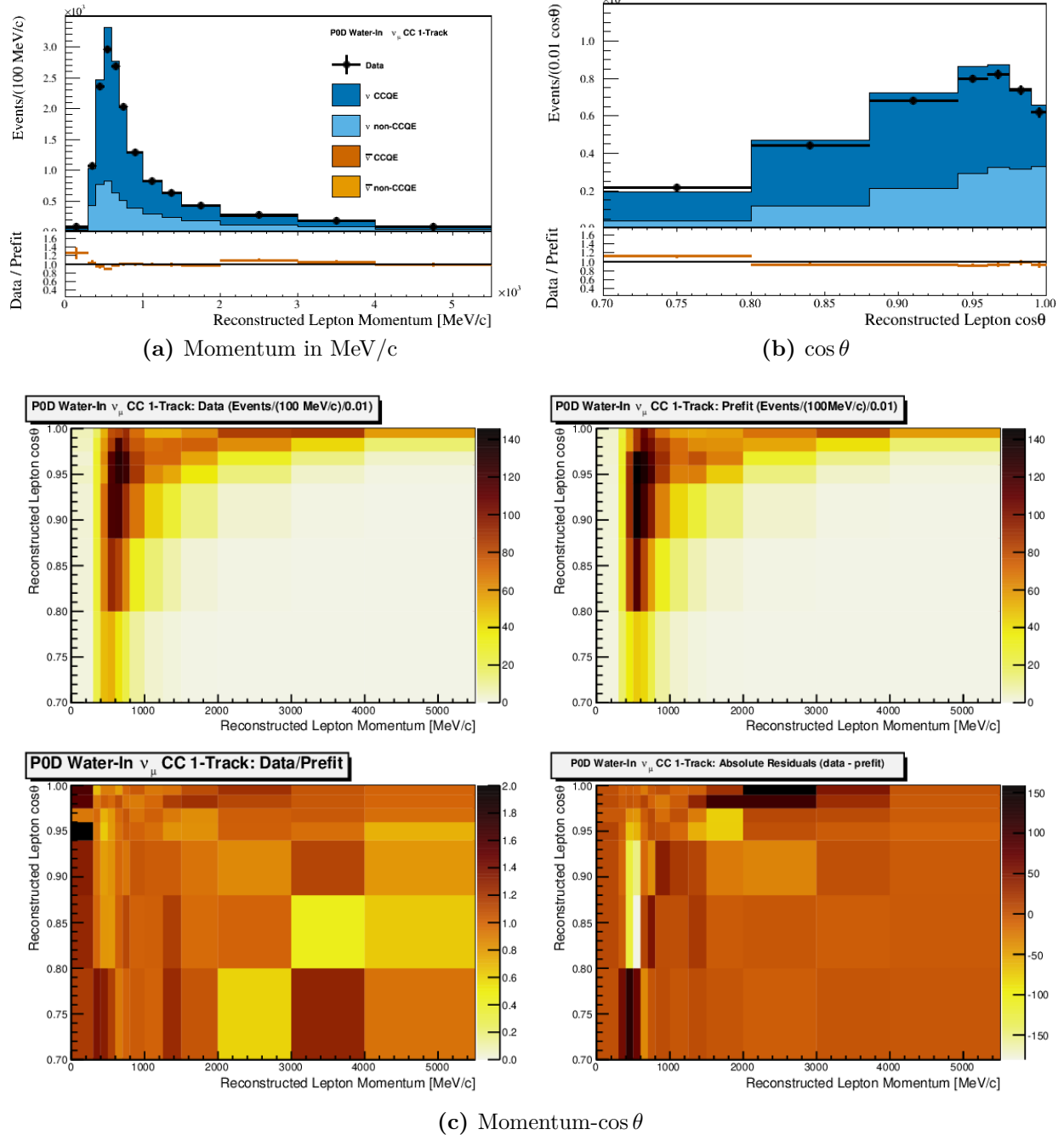


Figure 6.2: Data and prefit expectation for the PØD Water-In ν_μ in FHC CC 1-Track sample. Sub-figure (a) shows the momentum one-dimensional profile in all but the highest momentum fit bin. Sub-figure (b) shows the $\cos\theta$ one-dimensional profile in all but the highest angle fit bin. Shown in both (a) and (b) is the ratio between data and the prefit value. Sub-figure (c) shows a grid of two-dimensional data and prefit distributions in the same phase space as (a) and (b). Moving from top-left to bottom-right in (c) is the data, prefit, data to prefit ratio, and data to prefit difference.

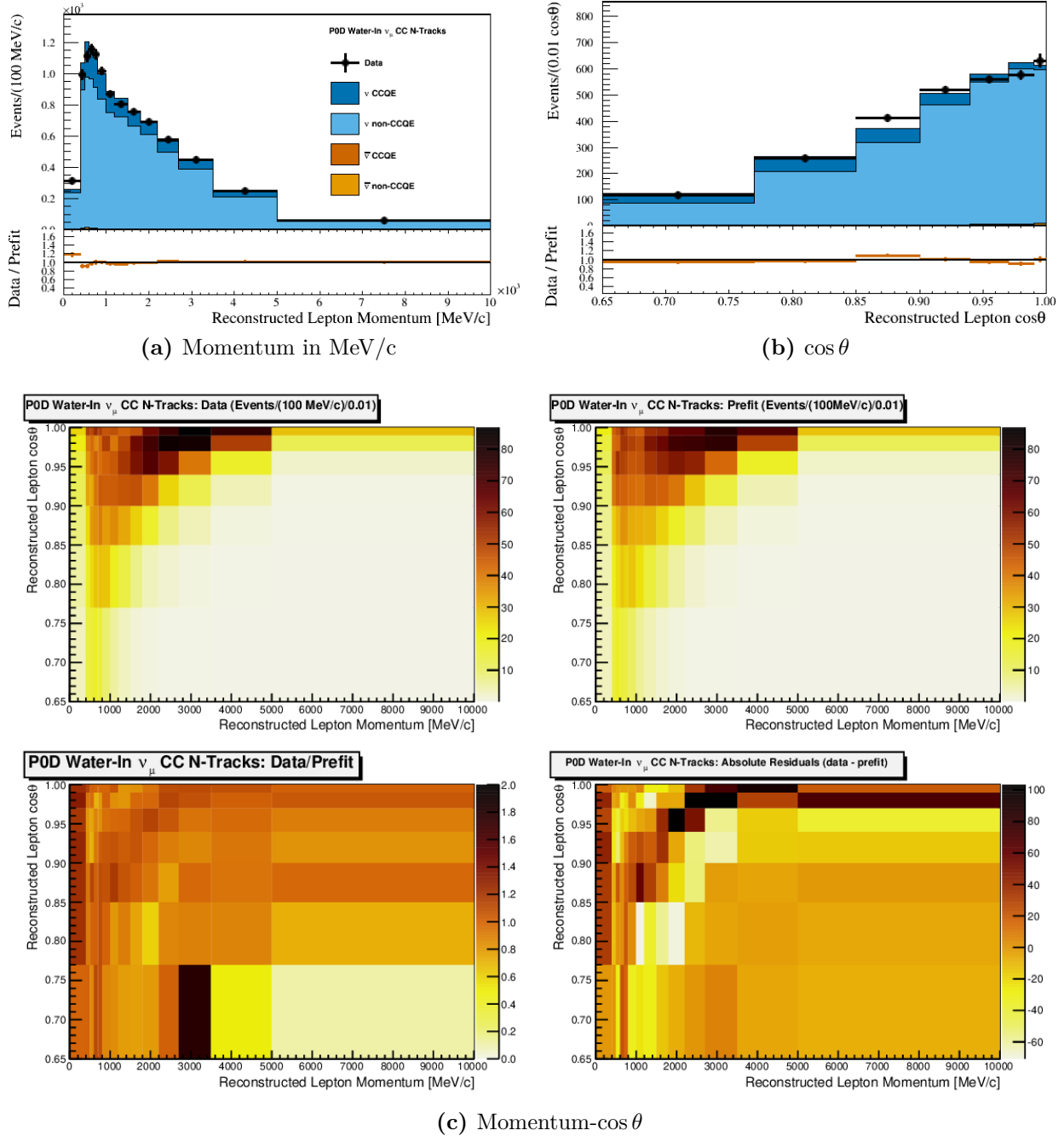


Figure 6.3: Data and prefit expectation for the PØD Water-In ν_μ in FHC CC N-Tracks sample. Sub-figure (a) shows the momentum one-dimensional profile in all but the highest momentum fit bin. Sub-figure (b) shows the $\cos\theta$ one-dimensional profile in all but the highest angle fit bin. Shown in both (a) and (b) is the ratio between data and the prefit value. Sub-figure (c) shows a grid of two-dimensional data and prefit distributions in the same phase space as (a) and (b). Moving from top-left to bottom-right in (c) is the data, prefit, data to prefit ratio, and data to prefit difference.

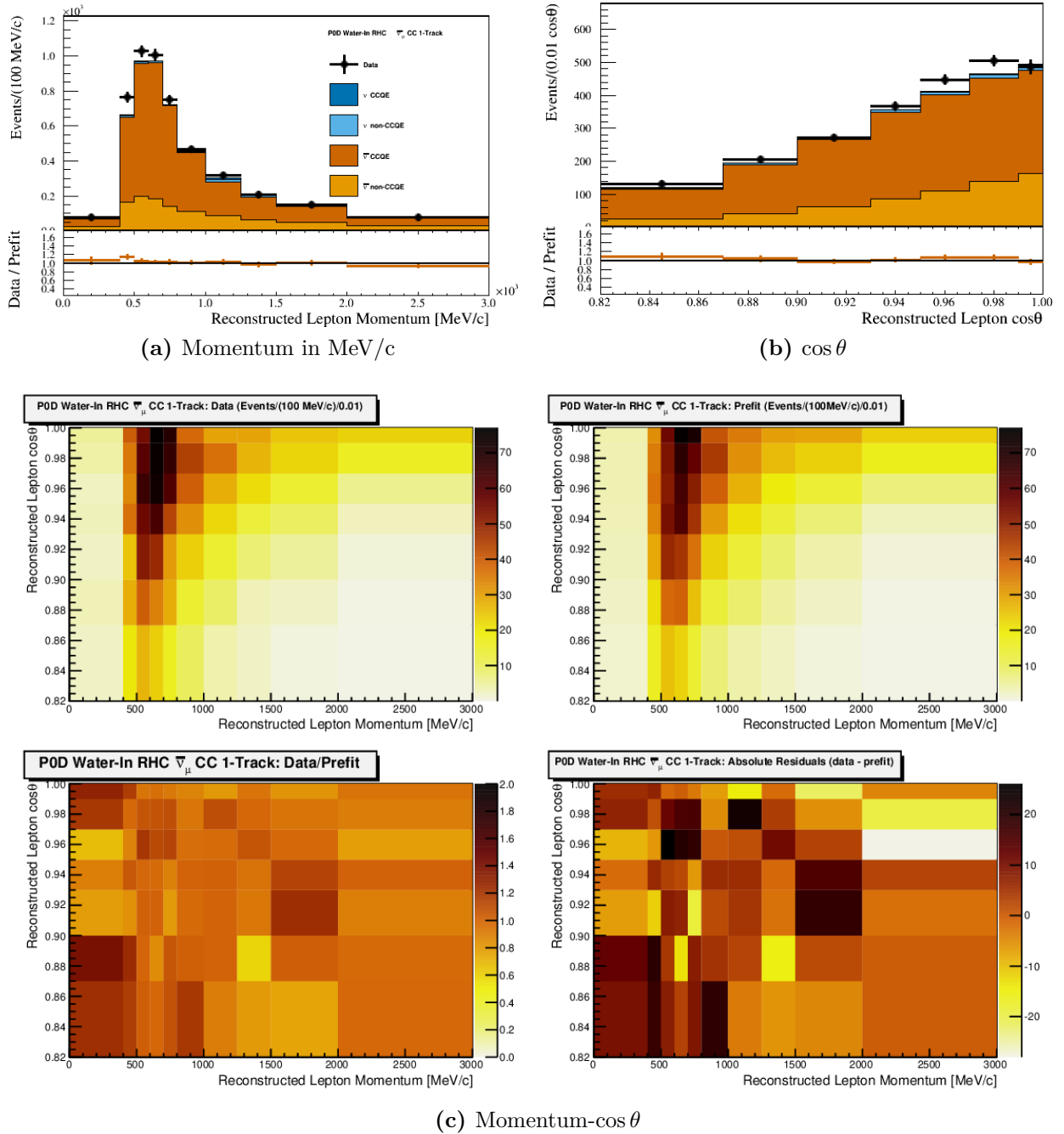


Figure 6.4: Data and prefit expectation for the PØD Water-In $\bar{\nu}_\mu$ in RHC CC 1-Track sample. Sub-figure (a) shows the momentum one-dimensional profile in all but the highest momentum fit bin. Sub-figure (b) shows the $\cos \theta$ one-dimensional profile in all but the highest angle fit bin. Shown in both (a) and (b) is the ratio between data and the prefit value. Sub-figure (c) shows a grid of two-dimensional data and prefit distributions in the same phase space as (a) and (b). Moving from top-left to bottom-right in (c) is the data, prefit, data to prefit ratio, and data to prefit difference.

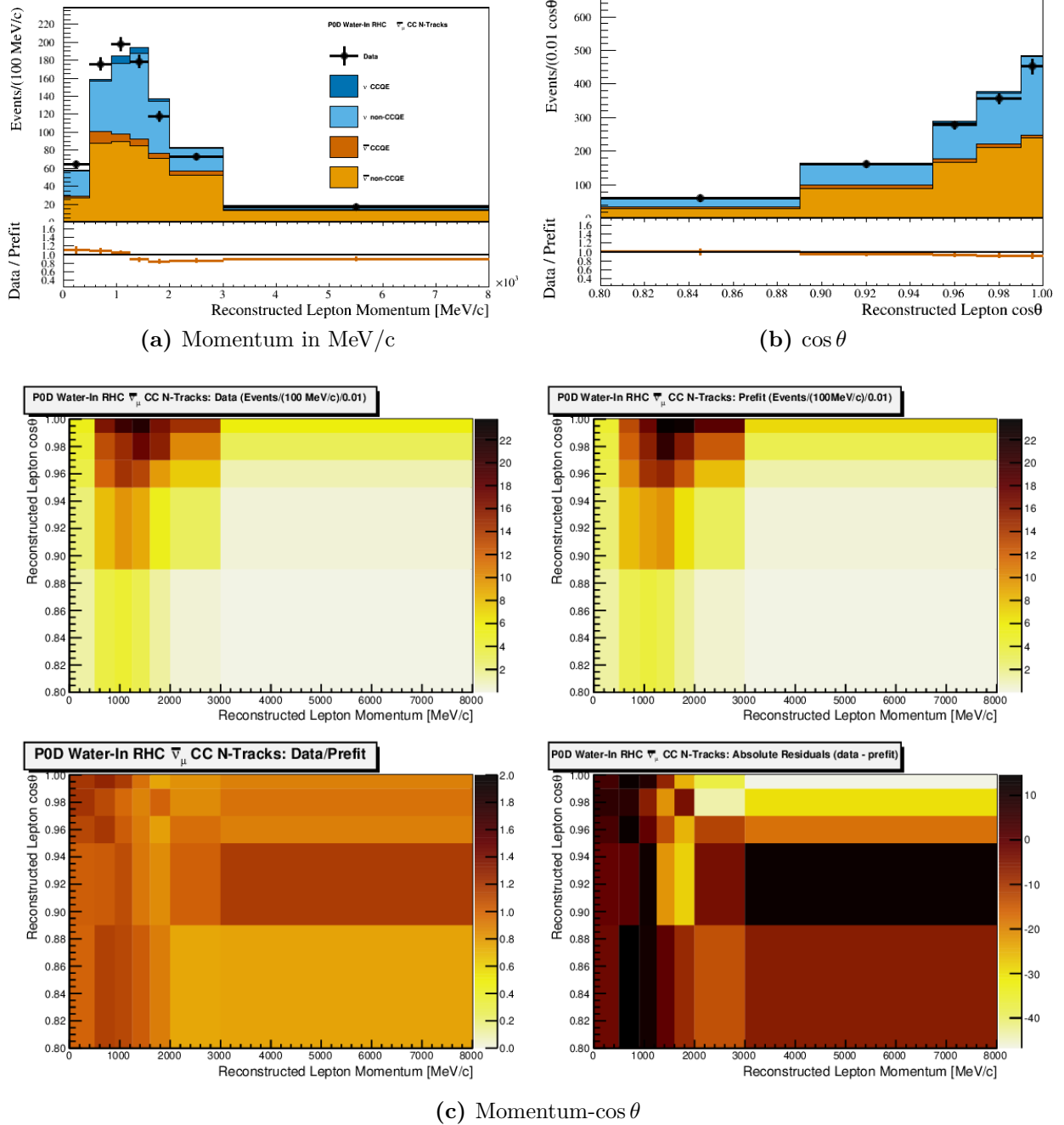


Figure 6.5: Data and prefit expectation for the PØD Water-In $\bar{\nu}_\mu$ in RHC CC N-Tracks sample. Sub-figure (a) shows the momentum one-dimensional profile in all but the highest momentum fit bin. Sub-figure (b) shows the $\cos \theta$ one-dimensional profile in all but the highest angle fit bin. Shown in both (a) and (b) is the ratio between data and the prefit value. Sub-figure (c) shows a grid of two-dimensional data and prefit distributions in the same phase space as (a) and (b). Moving from top-left to bottom-right in (c) is the data, prefit, data to prefit ratio, and data to prefit difference.

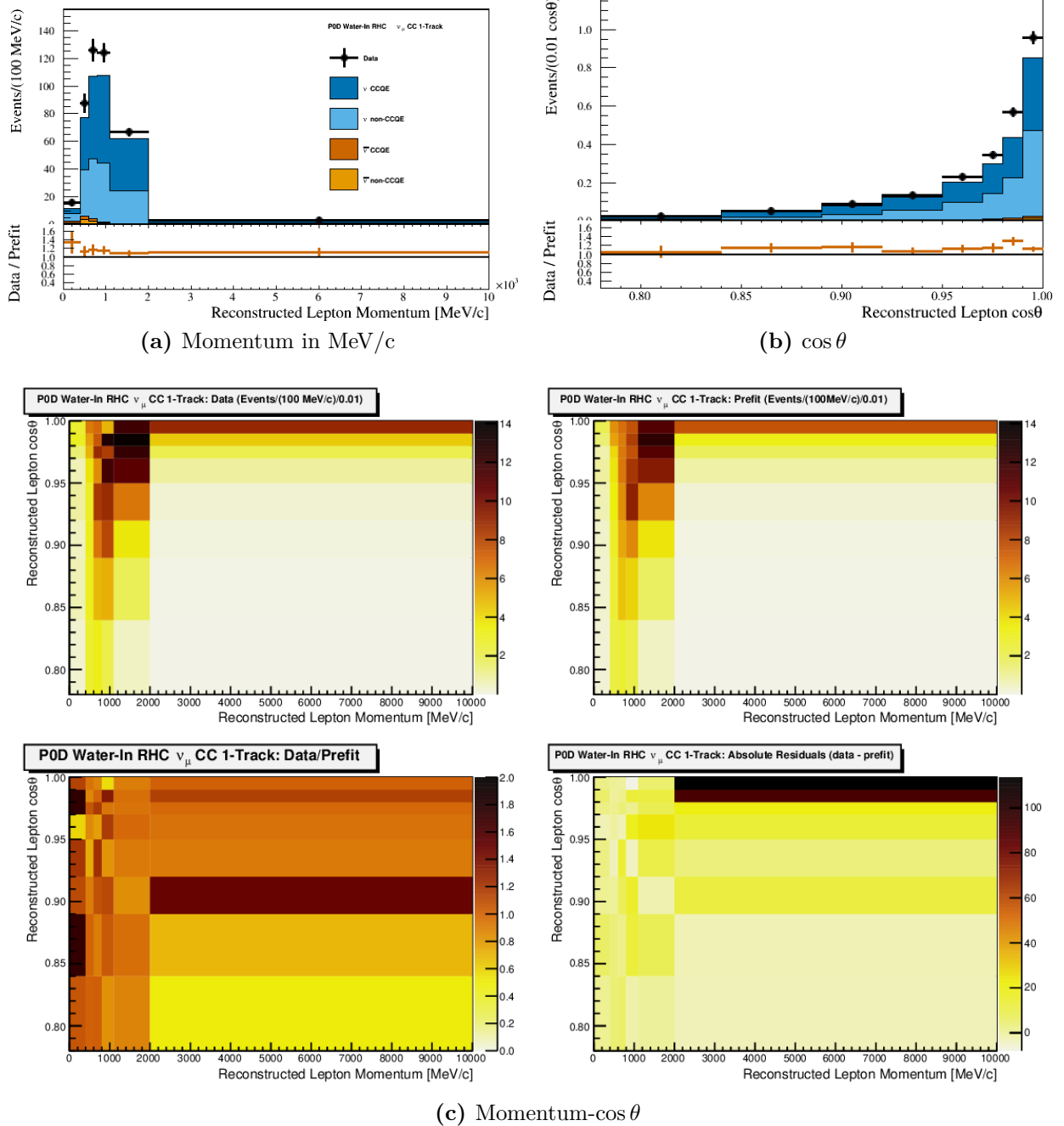


Figure 6.6: Data and prefit expectation for the PØD Water-In ν_μ in RHC CC 1-Track sample. Sub-figure (a) shows the momentum one-dimensional profile in all but the highest momentum fit bin. Sub-figure (b) shows the $\cos\theta$ one-dimensional profile in all but the highest angle fit bin. Shown in both (a) and (b) is the ratio between data and the prefit value. Sub-figure (c) shows a grid of two-dimensional data and prefit distributions in the same phase space as (a) and (b). Moving from top-left to bottom-right in (c) is the data, prefit, data to prefit ratio, and data to prefit difference.

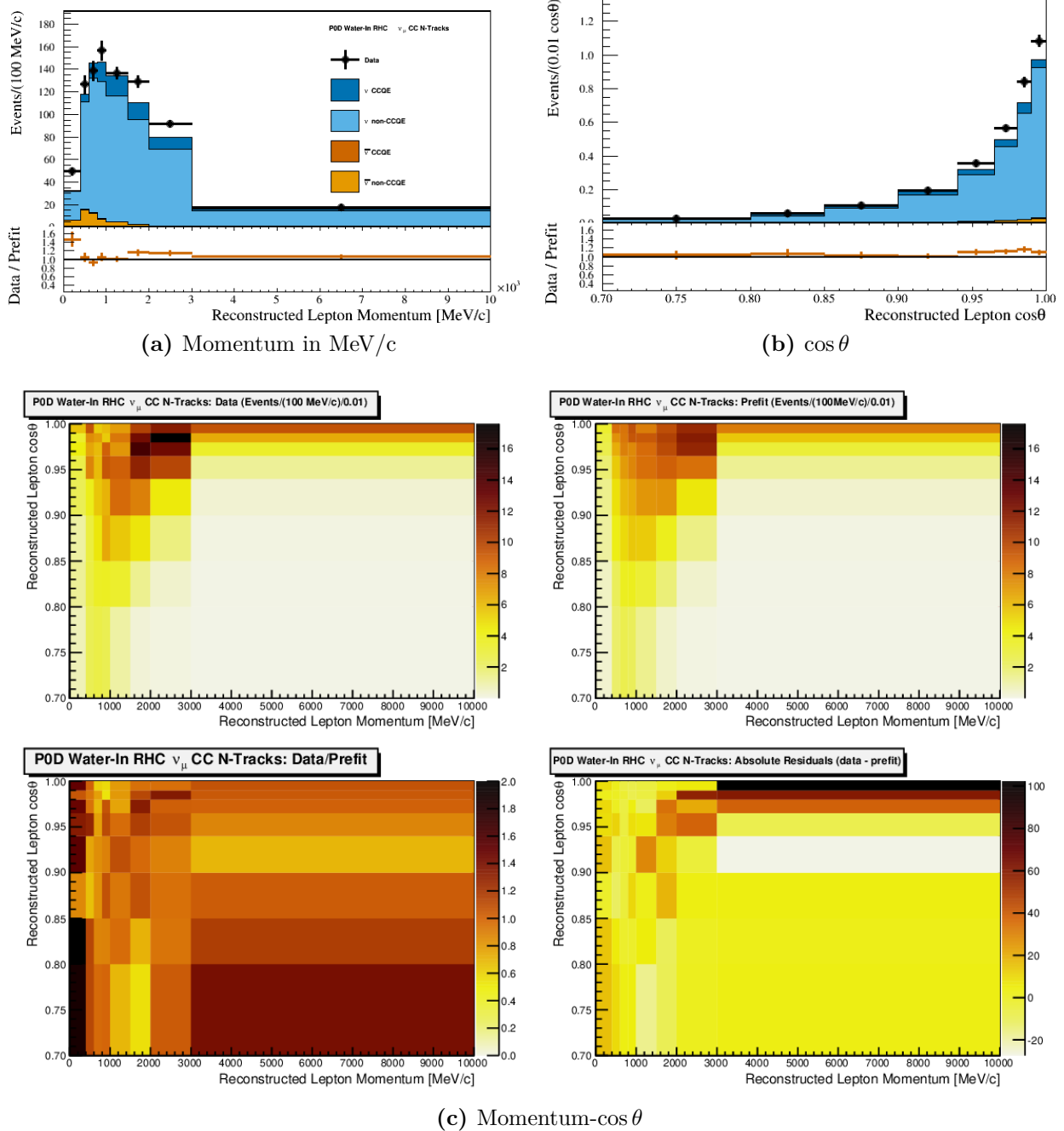


Figure 6.7: Data and prefit expectation for the PØD Water-In ν_μ in RHC CC N-Tracks sample. Sub-figure (a) shows the momentum one-dimensional profile in all but the highest momentum fit bin. Sub-figure (b) shows the $\cos\theta$ one-dimensional profile in all but the highest angle fit bin. Shown in both (a) and (b) is the ratio between data and the prefit value. Sub-figure (c) shows a grid of two-dimensional data and prefit distributions in the same phase space as (a) and (b). Moving from top-left to bottom-right in (c) is the data, prefit, data to prefit ratio, and data to prefit difference.

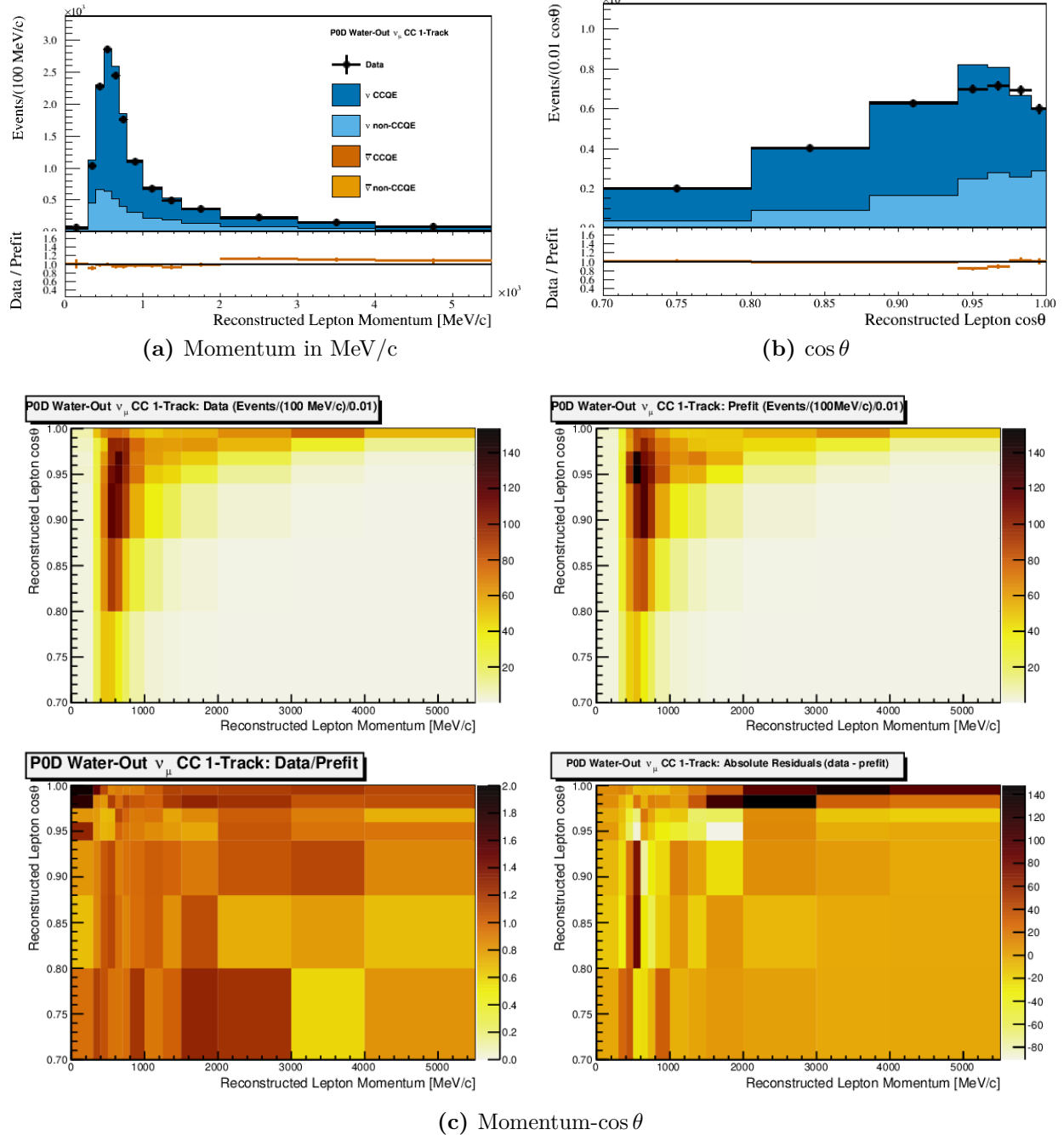


Figure 6.8: Data and prefit expectation for the PØD Water-Out ν_μ in FHC CC 1-Track sample. Sub-figure (a) shows the momentum one-dimensional profile in all but the highest momentum fit bin. Sub-figure (b) shows the $\cos\theta$ one-dimensional profile in all but the highest angle fit bin. Shown in both (a) and (b) is the ratio between data and the prefit value. Sub-figure (c) shows a grid of two-dimensional data and prefit distributions in the same phase space as (a) and (b). Moving from top-left to bottom-right in (c) is the data, prefit, data to prefit ratio, and data to prefit difference.

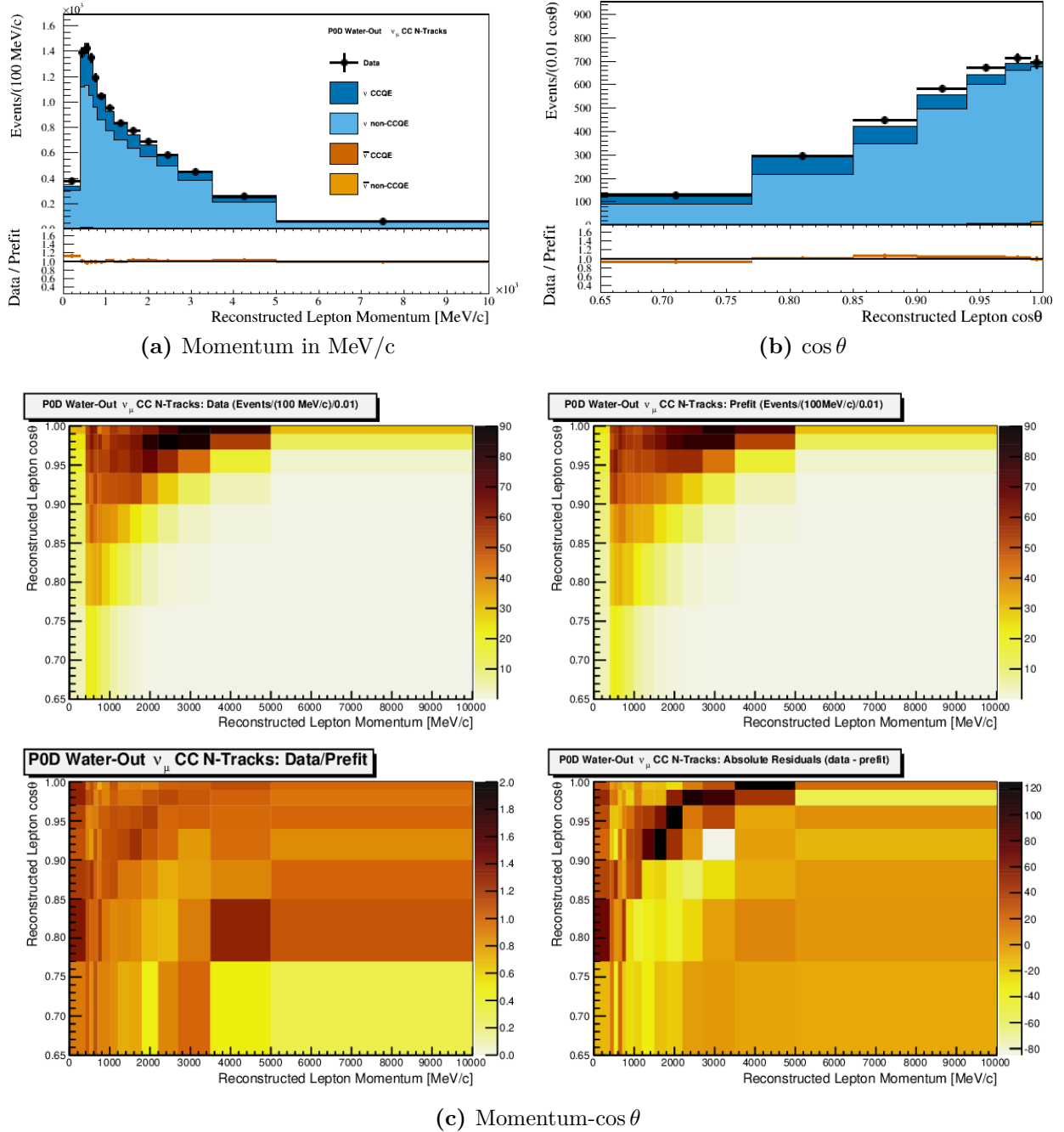


Figure 6.9: Data and prefit expectation for the PØD Water-Out ν_μ in FHC CC N-Tracks sample. Sub-figure (a) shows the momentum one-dimensional profile in all but the highest momentum fit bin. Sub-figure (b) shows the $\cos\theta$ one-dimensional profile in all but the highest angle fit bin. Shown in both (a) and (b) is the ratio between data and the prefit value. Sub-figure (c) shows a grid of two-dimensional data and prefit distributions in the same phase space as (a) and (b). Moving from top-left to bottom-right in (c) is the data, prefit, data to prefit ratio, and data to prefit difference.

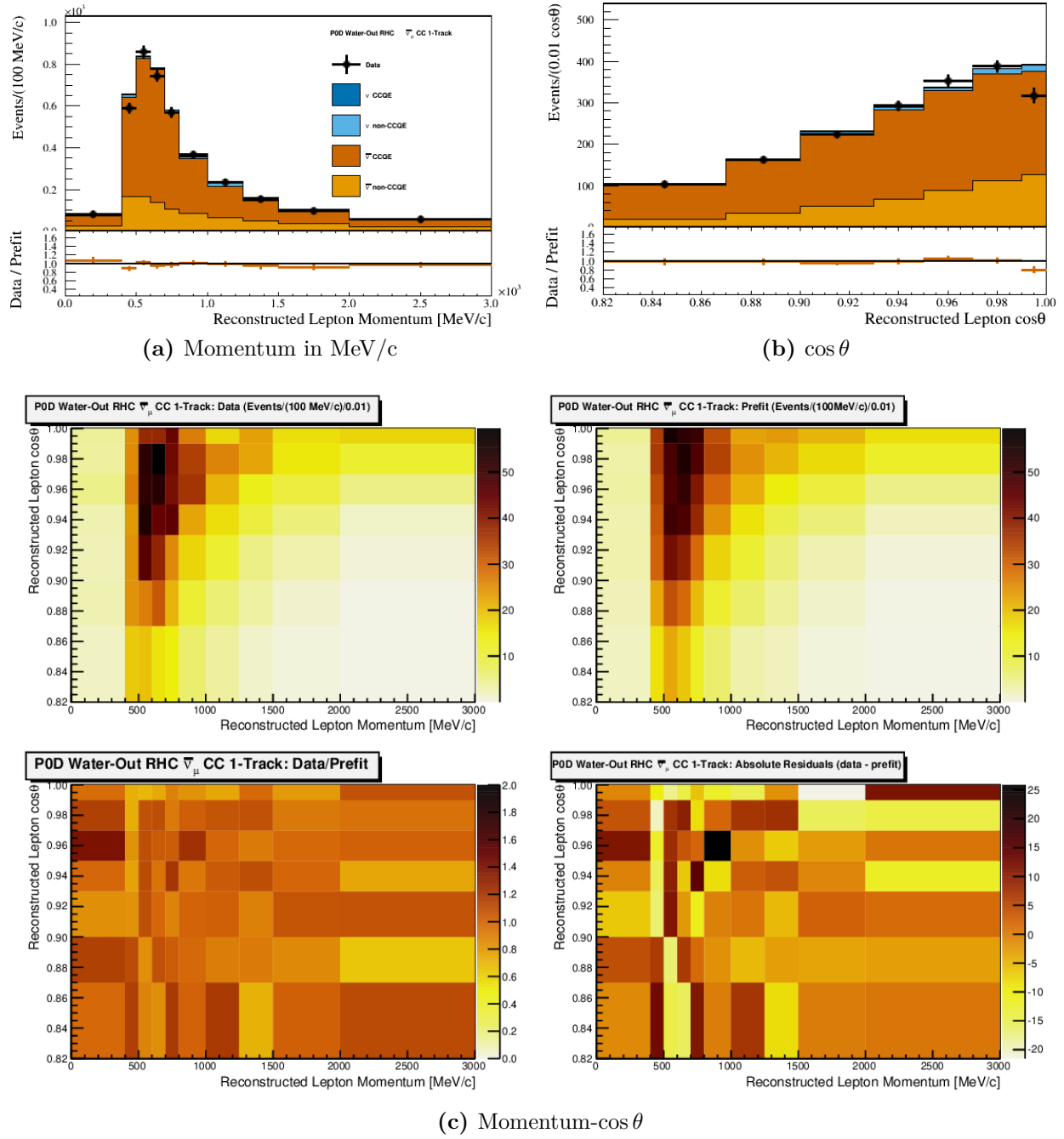


Figure 6.10: Data and prefit expectation for the PØD Water-Out $\bar{\nu}_\mu$ in RHC CC 1-Track sample. Sub-figure (a) shows the momentum one-dimensional profile in all but the highest momentum fit bin. Sub-figure (b) shows the $\cos \theta$ one-dimensional profile in all but the highest angle fit bin. Shown in both (a) and (b) is the ratio between data and the prefit value. Sub-figure (c) shows a grid of two-dimensional data and prefit distributions in the same phase space as (a) and (b). Moving from top-left to bottom-right in (c) is the data, prefit, data to prefit ratio, and data to prefit difference.

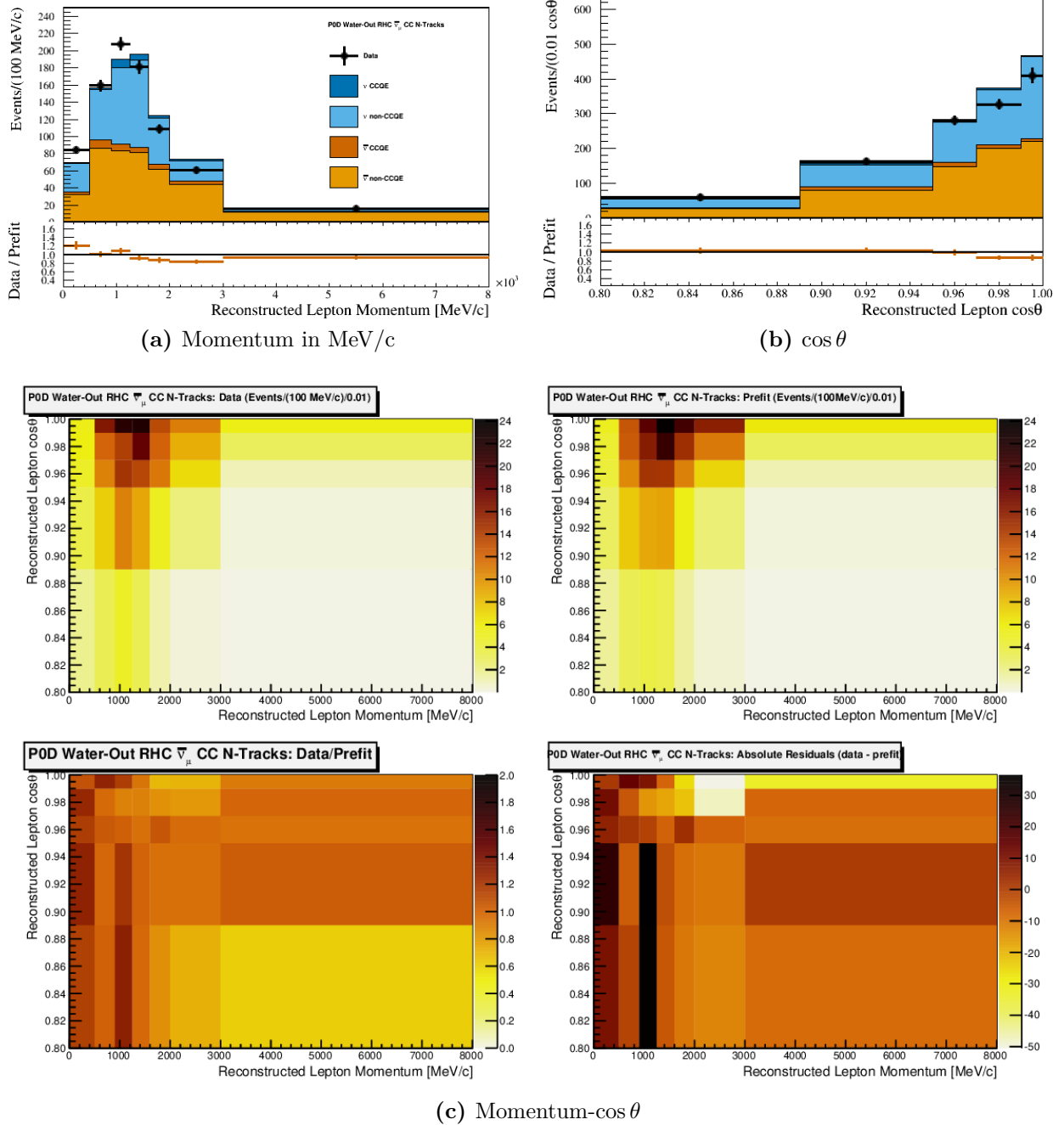


Figure 6.11: Data and prefit expectation for the PØD Water-Out $\bar{\nu}_\mu$ in RHC CC N-Tracks sample. Sub-figure (a) shows the momentum one-dimensional profile in all but the highest momentum fit bin. Sub-figure (b) shows the $\cos \theta$ one-dimensional profile in all but the highest angle fit bin. Shown in both (a) and (b) is the ratio between data and the prefit value. Sub-figure (c) shows a grid of two-dimensional data and prefit distributions in the same phase space as (a) and (b). Moving from top-left to bottom-right in (c) is the data, prefit, data to prefit ratio, and data to prefit difference.

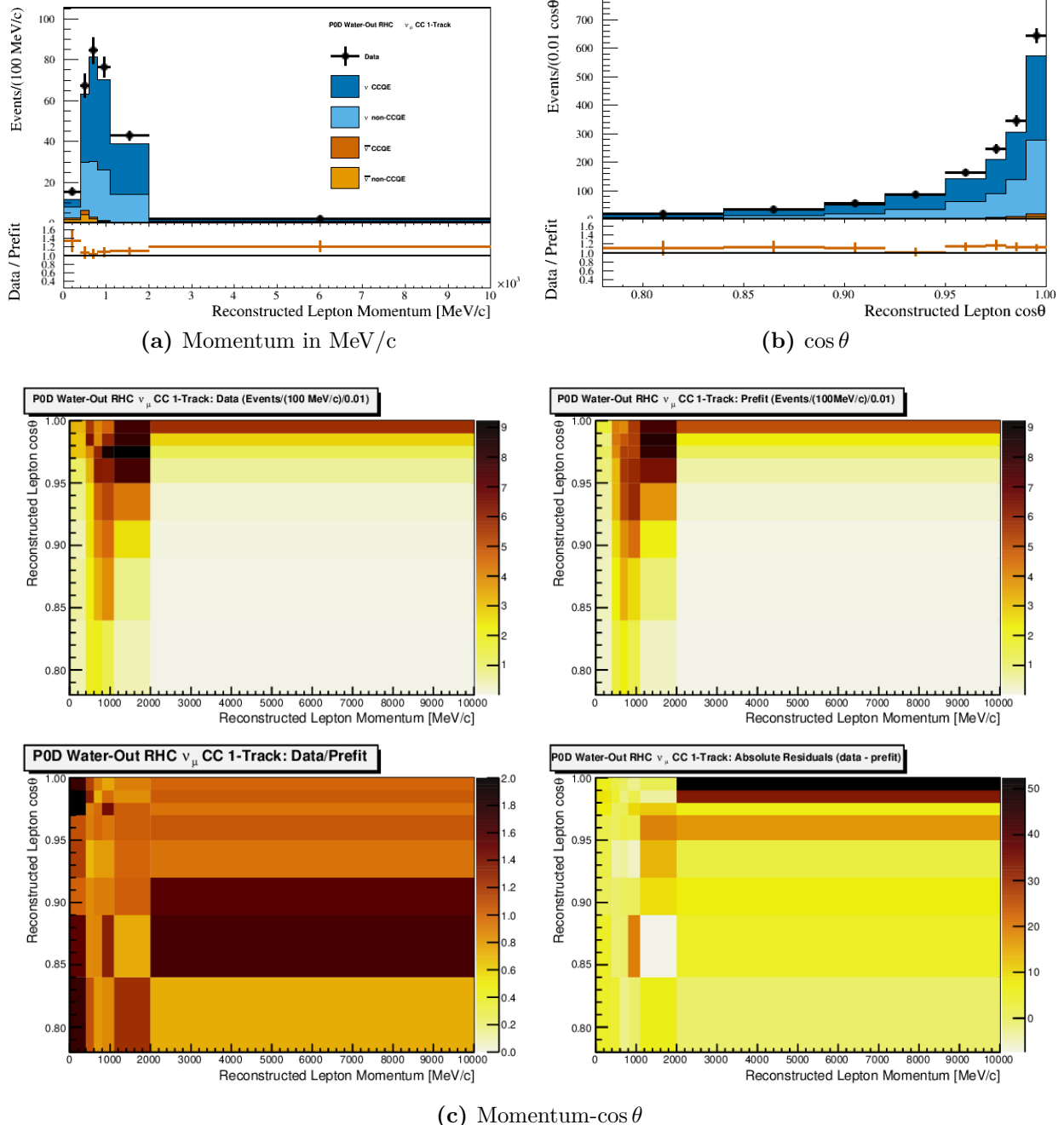


Figure 6.12: Data and prefit expectation for the PØD Water-Out ν_μ in RHC CC 1-Track sample. Sub-figure (a) shows the momentum one-dimensional profile in all but the highest momentum fit bin. Sub-figure (b) shows the $\cos\theta$ one-dimensional profile in all but the highest angle fit bin. Shown in both (a) and (b) is the ratio between data and the prefit value. Sub-figure (c) shows a grid of two-dimensional data and prefit distributions in the same phase space as (a) and (b). Moving from top-left to bottom-right in (c) is the data, prefit, data to prefit ratio, and data to prefit difference.

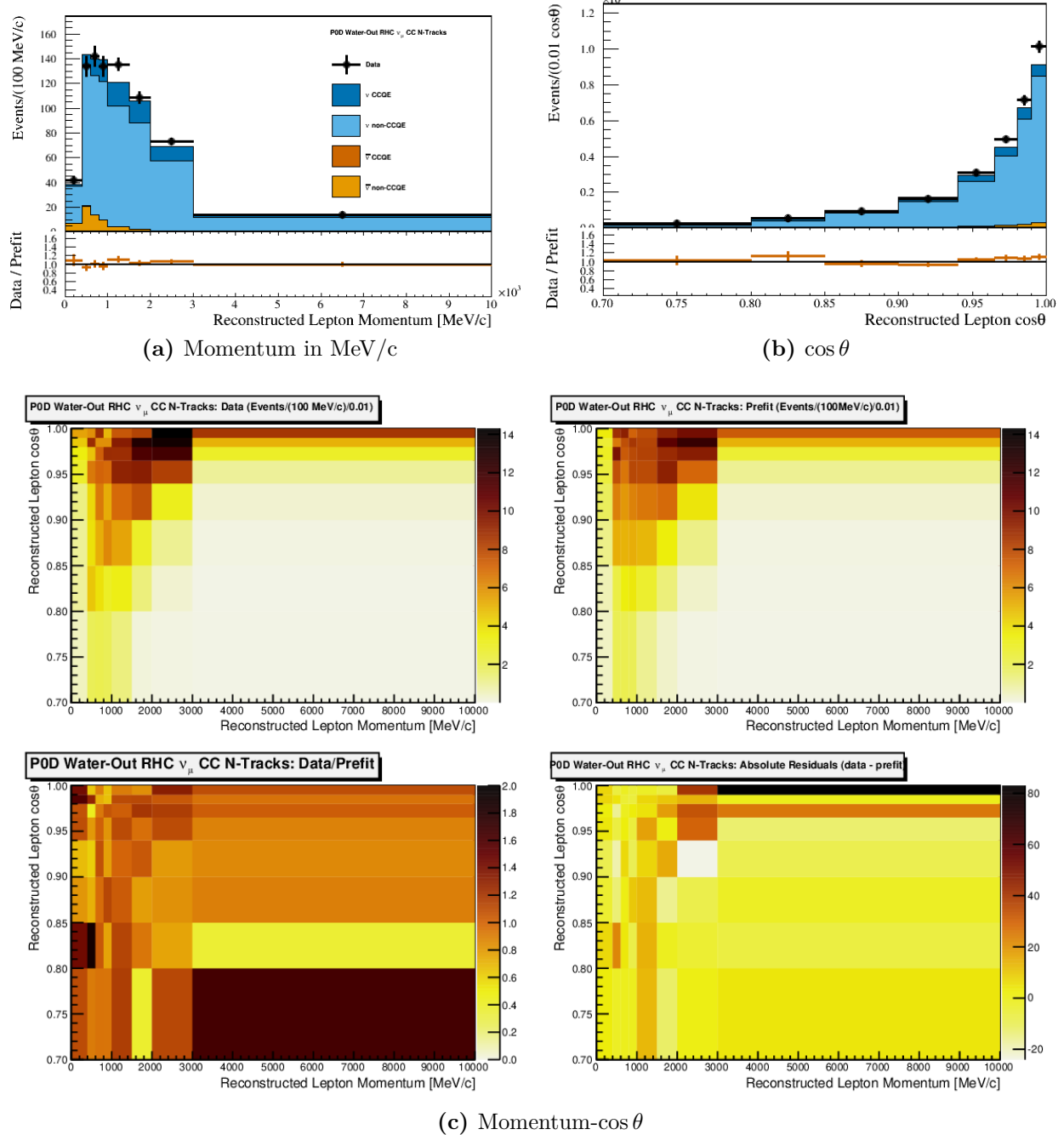


Figure 6.13: Data and prefit expectation for the PØD Water-Out ν_μ in RHC CC N-Tracks sample. Sub-figure (a) shows the momentum one-dimensional profile in all but the highest momentum fit bin. Sub-figure (b) shows the $\cos\theta$ one-dimensional profile in all but the highest angle fit bin. Shown in both (a) and (b) is the ratio between data and the prefit value. Sub-figure (c) shows a grid of two-dimensional data and prefit distributions in the same phase space as (a) and (b). Moving from top-left to bottom-right in (c) is the data, prefit, data to prefit ratio, and data to prefit difference.

the time, about 6.2 hours hours, was spent loading the data and cross section splines into memory which consumed about 40 GB of RAM.

Specific topics on the postfit results are presented in the following order. First is an examination of the postfit samples in one-dimensional profiles and two-dimensional spaces. Next is a comparison of the parameter values among the prefit, PØD-only, and FGD-only results. And finally is a hypothesis test on the level of agreement between the PØD-only and FGD-only BANFF fit results.

6.2.1 Postfit Sample Distributions

Presented below are the 12 samples again, but with the postfit parameters applied to the fit bins. This ensures we have not altered the data and the data to tuned prediction (postfit) ratios have improved as a result of the fit. The samples are shown in Figure 6.14 on page 170 to Figure 6.25 on page 181 in the same order as presented in the previous section.

We see an improved agreement between the postfit prediction and the data. There still is tension, in particular, in the lowest momentum bins which could of been mitigated by having more bin normalization parameters. Between the water-in and water-out modes, disagreement between them is balanced since the flux affects them the same way. Given there still is tension in those lowest momentum bins, perhaps the water mass varied between T2K runs more than what could be accounted for using the static detector model in the BANFF fit.

To further explore this idea, a visual search was conducted of data to postfit ratio improvement in the water-in sample’s lowest momentum bins with decreasing $\cos \theta$, or equivalently increasing angle. If this trend is observed, it could indicate the mass variability and additional bulging were problematic in the fit. The higher angle tracks are more likely to originate upstream of the most bulging layer due to geometric considerations. If better agreement is observed in higher angle bins compared to lower, more forward-going track bins, this would support the mass variability idea. There was a weak observed trend in the water-in samples

and such a weak one could be coincidental. Therefore, it is difficult to draw any conclusions at this stage about mass uncertainty contribution.

Now that we have examined the postfit samples and seen that the prediction has indeed changed, we can proceed to look at the parameter values.

6.2.2 Parameter Value and Correlation Comparisons

The postfit parameters from the PØD-only BANFF fit are shown in Figure 6.27 on page 186 through Figure 6.30 on page 189. A complete listing of the prefit and postfit values is given in Appendix G. Additionally, a comparison is made between the PØD-only results with that of the FGD-only results. The legend used to compare between the PØD-only and FGD-only fits is shown in Figure 6.26 on page 182. It must be stated that while the PØD-only and FGD-only fits are using the same 2017 canonical cross section parameterization, the analyses had different POT exposures.

This PØD-only analysis fit uses runs 2 - 8 while the FGD-only fit uses runs 2 - 6. In order to understand how the two analyses compare to each other in terms of sensitivity to the flux, and carbon and oxygen cross section parameters, we can examine Table 6.1 on page 183. A proxy for the number of incident neutrinos to certain elements in the detector is the product of the fiducial mass and POT. While the PØD has much more mass, the water-in and water-out modes are mutually exclusive, resulting in a reduced aggregate POT exposure as compared to each static FGD. Also since the FGD2 has a larger water mass fraction compared to the PØD water-in mode, the amount of neutrino-oxygen interactions are very similar. The comparative advantage of the PØD-only data lies in the number of neutrino-carbon events, which is about 10 times greater than the FGD. This is all assuming the comparisons from Table 6.1 on page 183.

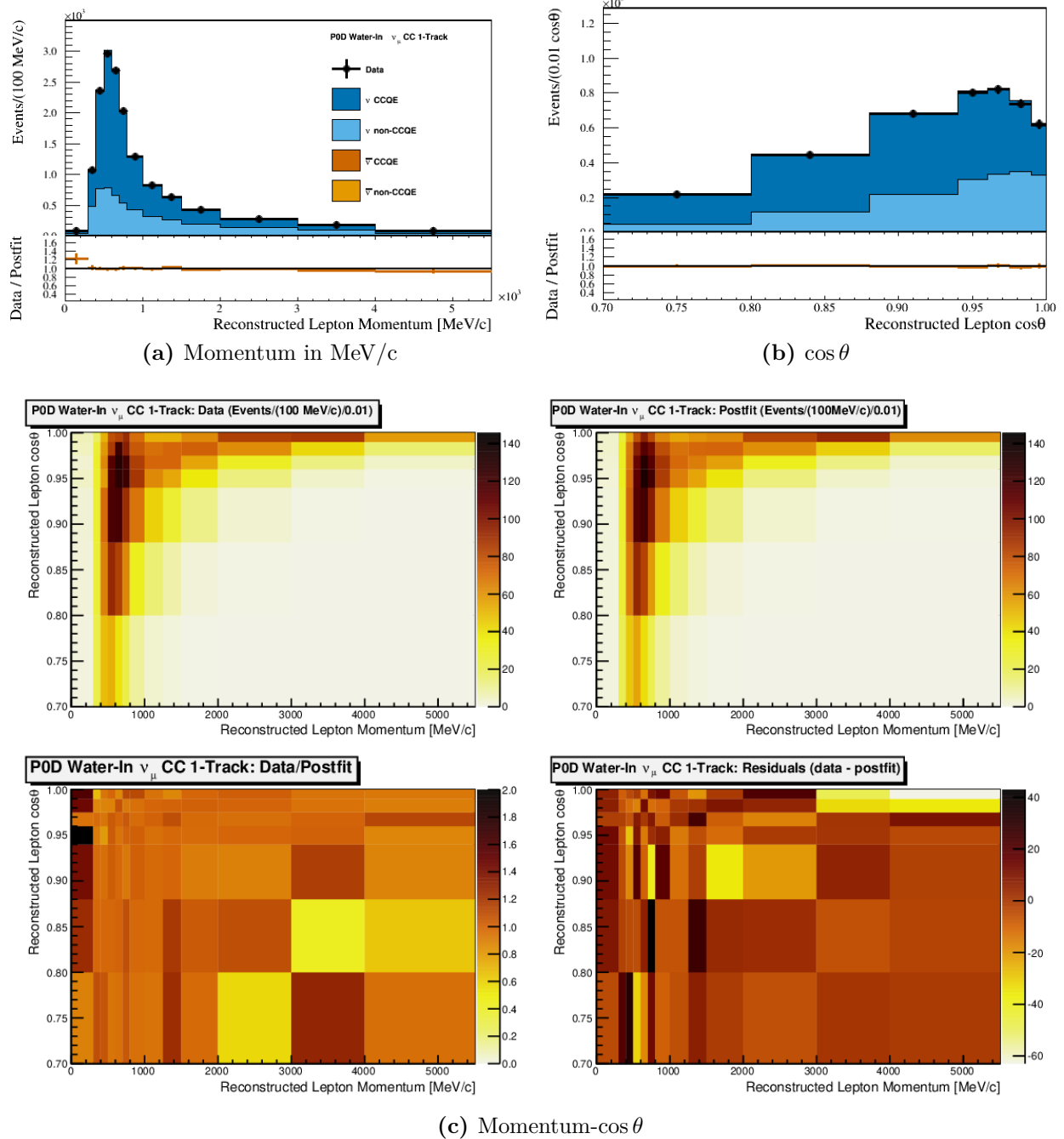


Figure 6.14: Data and postfit for the PØD Water-In ν_μ in FHC CC 1-Track sample. Sub-figure (a) shows the momentum one-dimensional profile in all but the highest momentum fit bin. Sub-figure (b) shows the $\cos\theta$ one-dimensional profile in all but the highest angle fit bin. Shown in both (a) and (b) is the ratio between data and the postfit value. Sub-figure (c) shows a grid of two-dimensional data and postfit distributions in the same phase space as (a) and (b). Moving from top-left to bottom-right in (c) is the data, postfit, data to postfit ratio, and data to postfit difference.

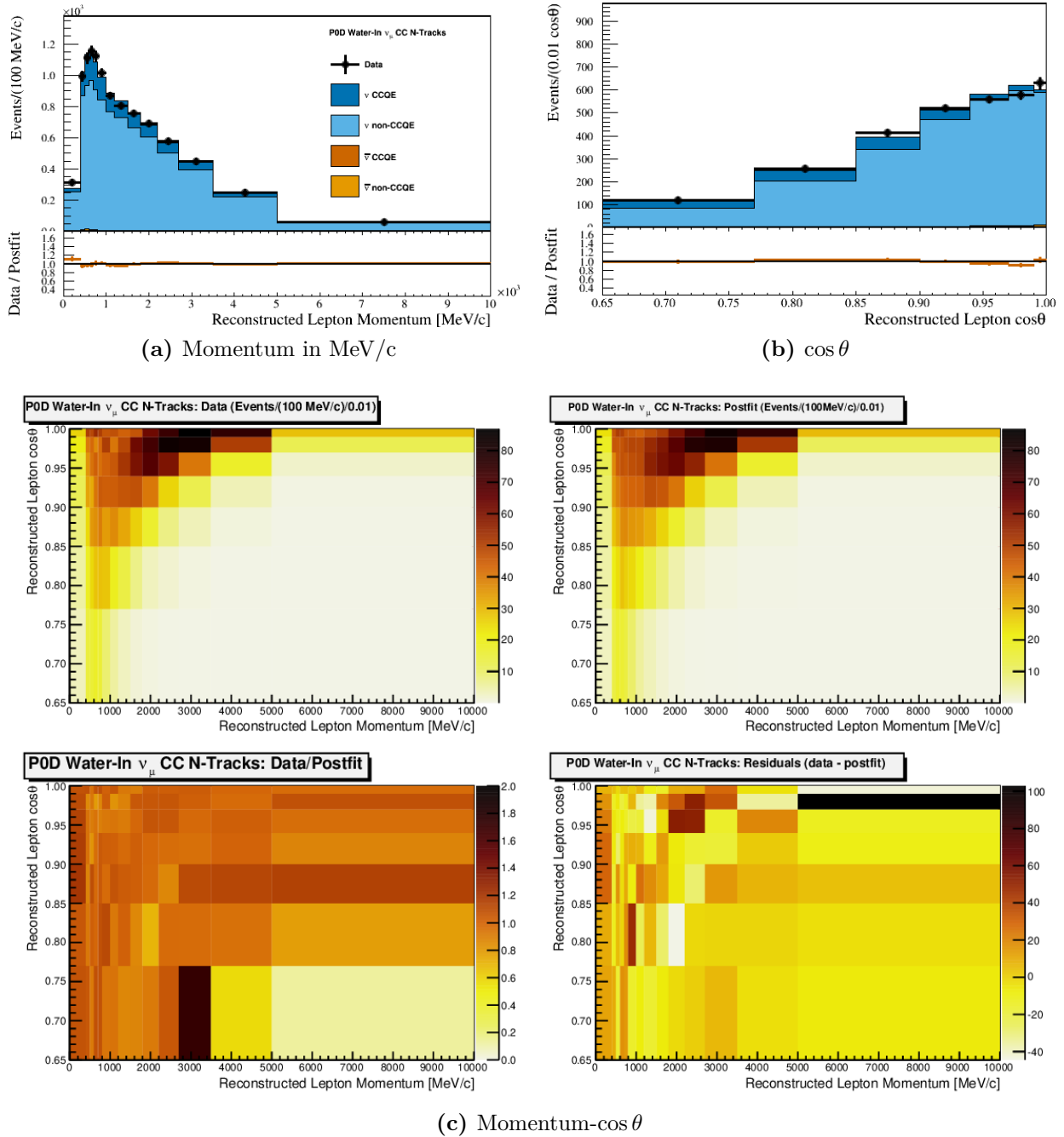


Figure 6.15: Data and postfit for the PØD Water-In ν_μ in FHC CC 1-Track sample. Sub-figure (a) shows the momentum one-dimensional profile in all but the highest momentum fit bin. Sub-figure (b) shows the $\cos\theta$ one-dimensional profile in all but the highest angle fit bin. Shown in both (a) and (b) is the ratio between data and the postfit value. Sub-figure (c) shows a grid of two-dimensional data and postfit distributions in the same phase space as (a) and (b). Moving from top-left to bottom-right in (c) is the data, postfit, data to postfit ratio, and data to postfit difference.

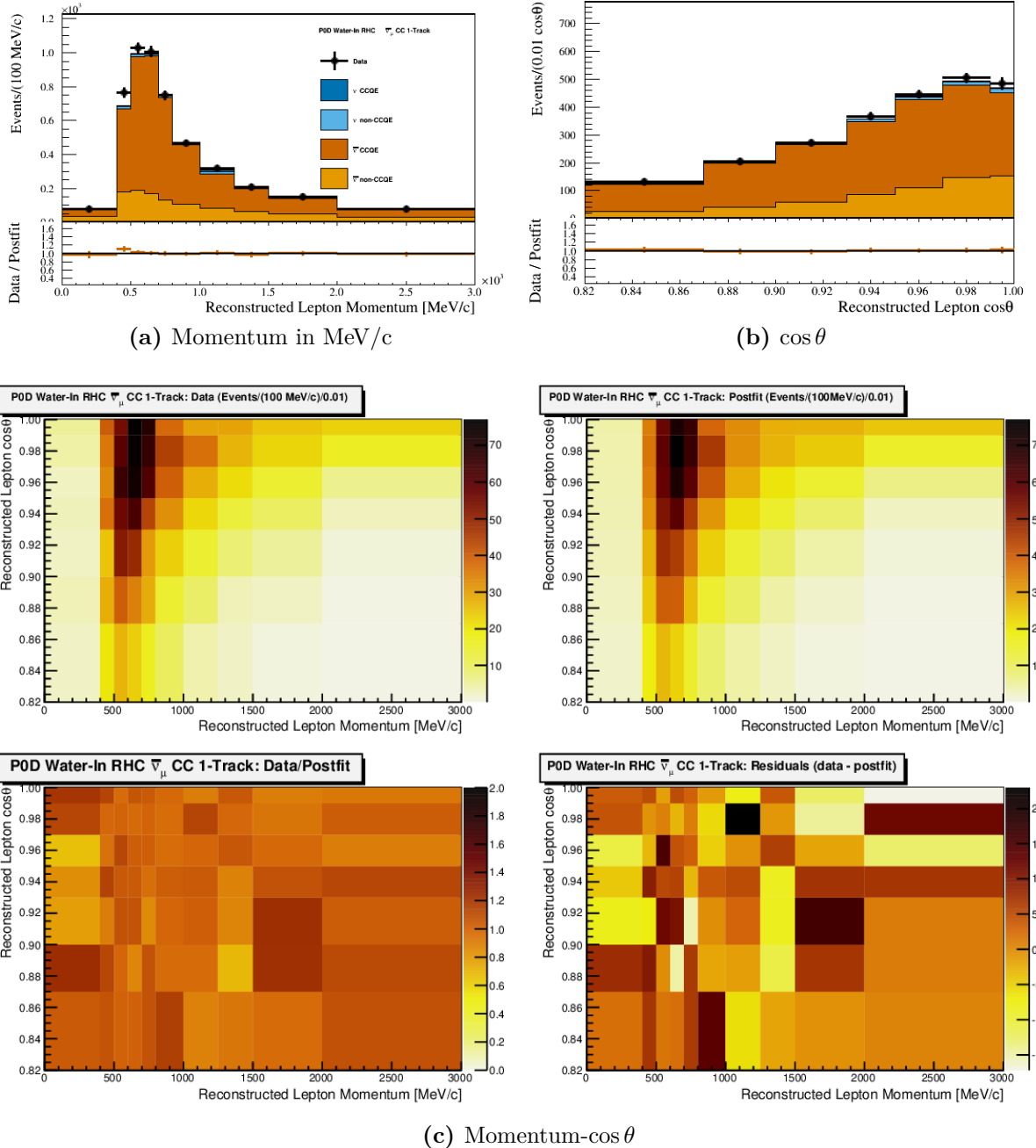


Figure 6.16: Data and postfit for the PØD Water-In $\bar{\nu}_\mu$ in RHC CC 1-Track sample. Sub-figure (a) shows the momentum one-dimensional profile in all but the highest momentum fit bin. Sub-figure (b) shows the $\cos \theta$ one-dimensional profile in all but the highest angle fit bin. Shown in both (a) and (b) is the ratio between data and the postfit value. Sub-figure (c) shows a grid of two-dimensional data and postfit distributions in the same phase space as (a) and (b). Moving from top-left to bottom-right in (c) is the data, postfit, data to postfit ratio, and data to postfit difference.

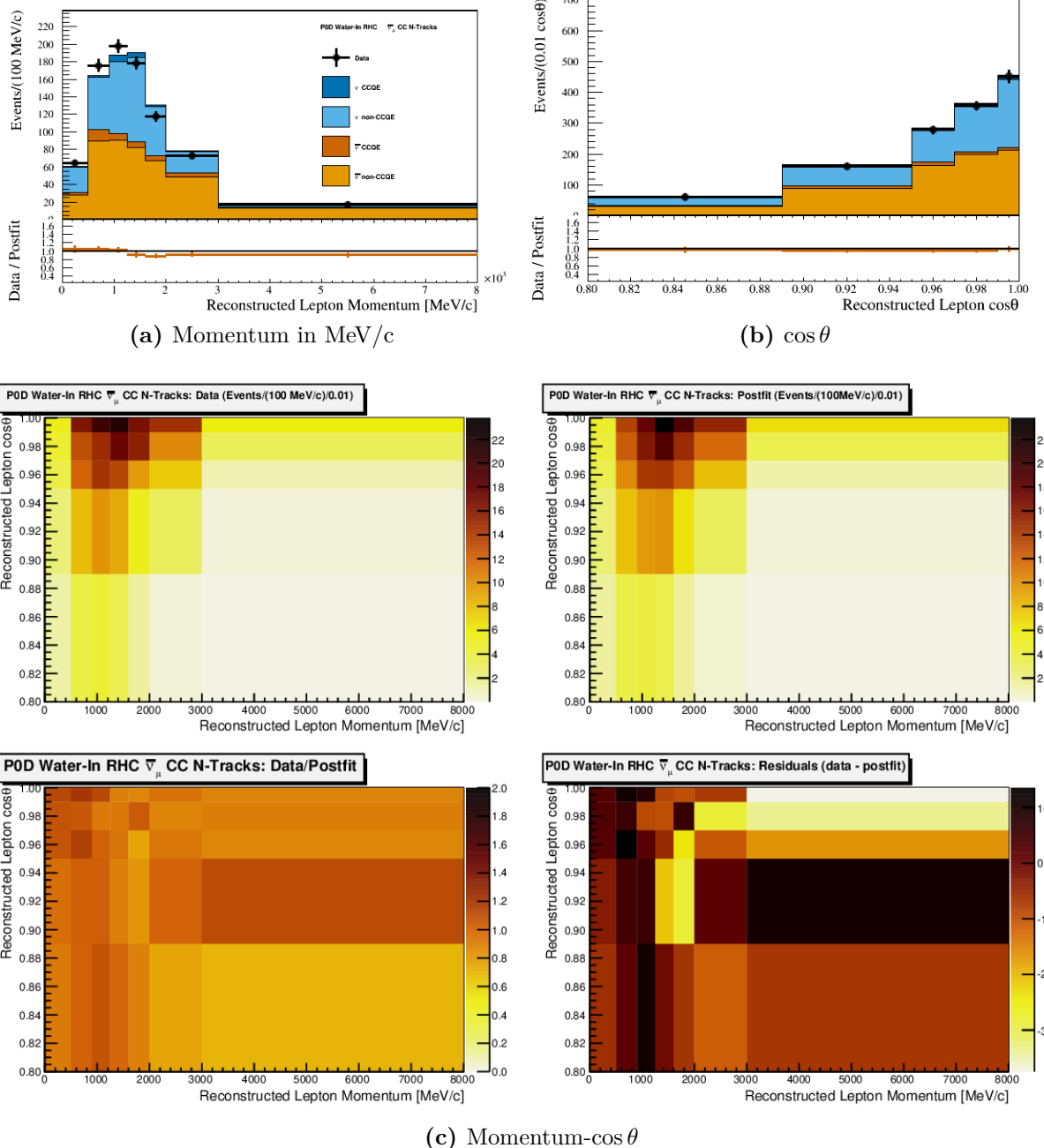


Figure 6.17: Data and postfit for the PØD Water-In $\bar{\nu}_\mu$ in RHC CC N-Tracks sample. Sub-figure (a) shows the momentum one-dimensional profile in all but the highest momentum fit bin. Sub-figure (b) shows the $\cos \theta$ one-dimensional profile in all but the highest angle fit bin. Shown in both (a) and (b) is the ratio between data and the postfit value. Sub-figure (c) shows a grid of two-dimensional data and postfit distributions in the same phase space as (a) and (b). Moving from top-left to bottom-right in (c) is the data, postfit, data to postfit ratio, and data to postfit difference.

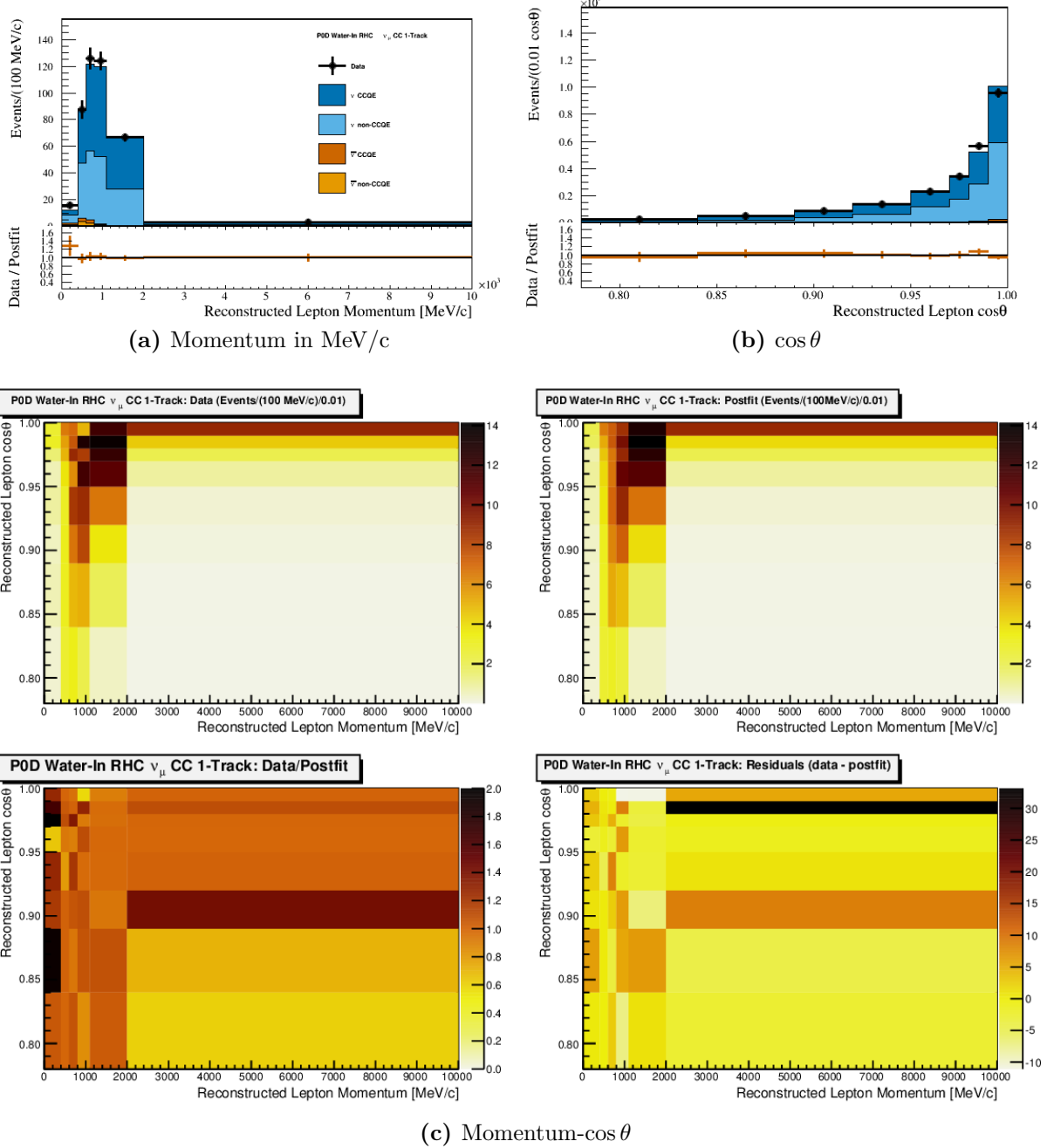


Figure 6.18: Data and postfit for the PØD Water-In ν_μ in RHC CC 1-Track sample. Sub-figure (a) shows the momentum one-dimensional profile in all but the highest momentum fit bin. Sub-figure (b) shows the $\cos \theta$ one-dimensional profile in all but the highest angle fit bin. Shown in both (a) and (b) is the ratio between data and the postfit value. Sub-figure (c) shows a grid of two-dimensional data and postfit distributions in the same phase space as (a) and (b). Moving from top-left to bottom-right in (c) is the data, postfit, data to postfit ratio, and data to postfit difference.

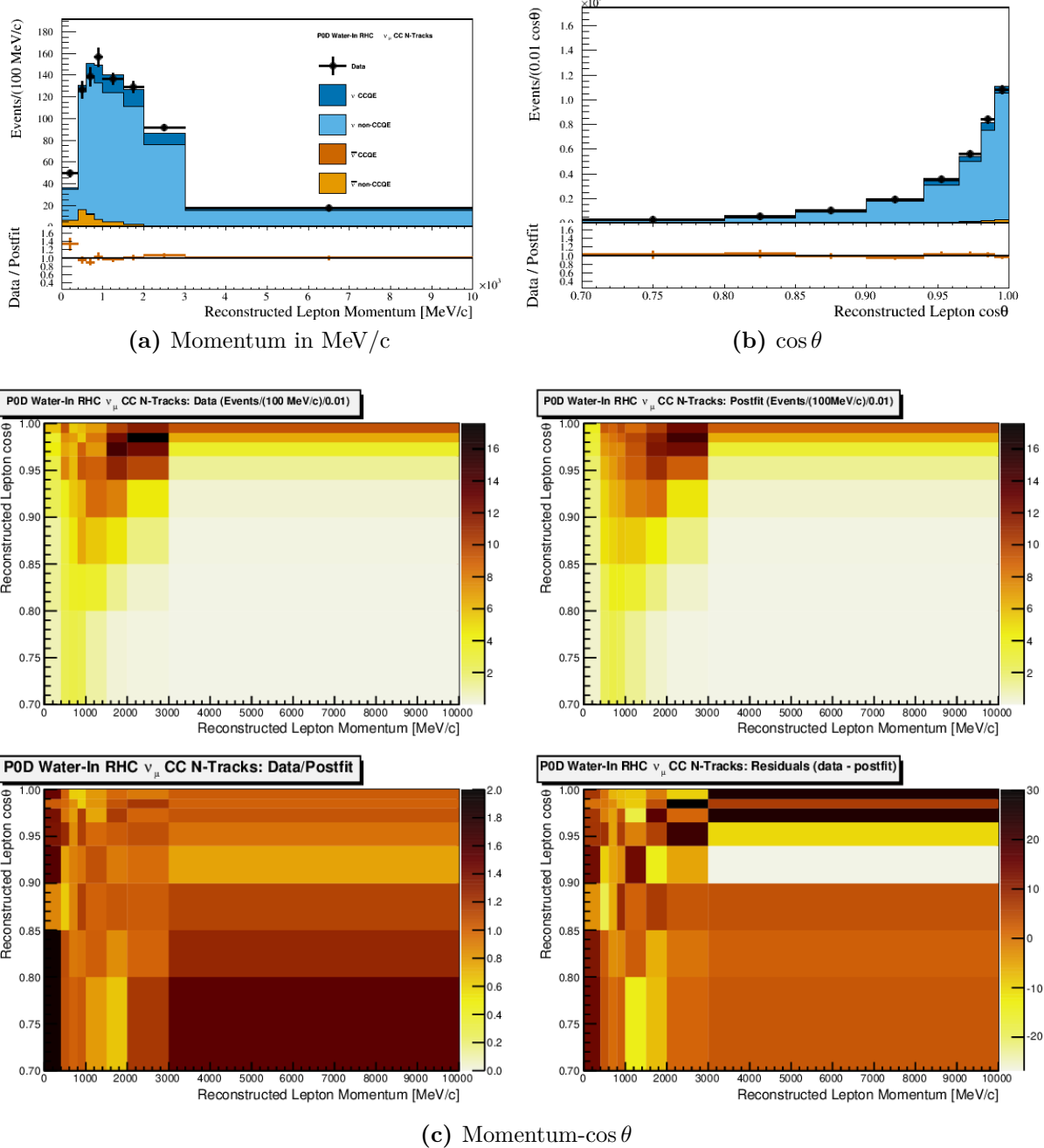


Figure 6.19: Data and postfit for the PØD Water-In ν_μ in RHC CC N-Tracks sample. Sub-figure (a) shows the momentum one-dimensional profile in all but the highest momentum fit bin. Sub-figure (b) shows the $\cos \theta$ one-dimensional profile in all but the highest angle fit bin. Shown in both (a) and (b) is the ratio between data and the postfit value. Sub-figure (c) shows a grid of two-dimensional data and postfit distributions in the same phase space as (a) and (b). Moving from top-left to bottom-right in (c) is the data, postfit, data to postfit ratio, and data to postfit difference.

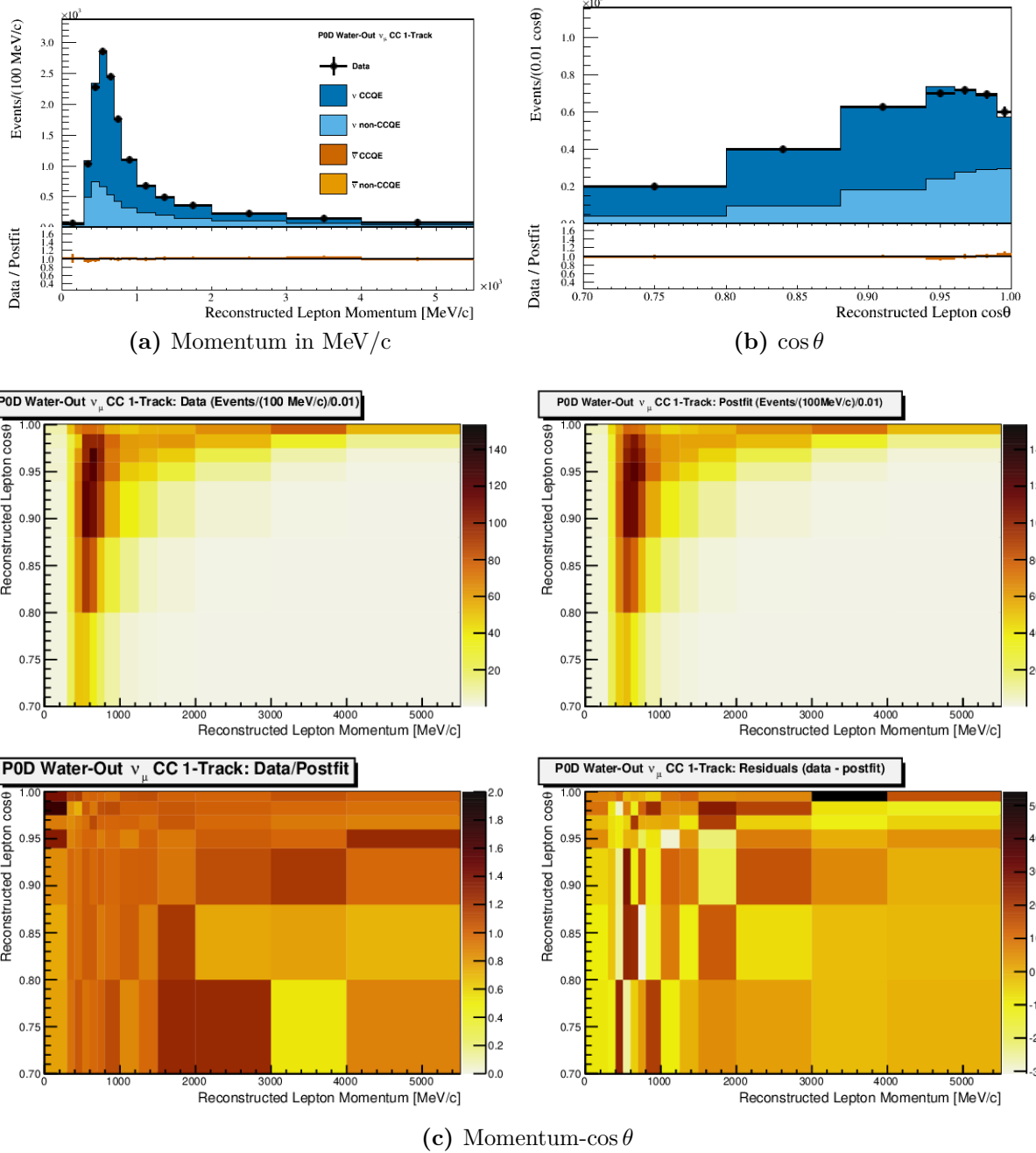


Figure 6.20: Data and postfit for the PØD Water-Out ν_μ in FHC CC 1-Track sample. Sub-figure (a) shows the momentum one-dimensional profile in all but the highest momentum fit bin. Sub-figure (b) shows the $\cos\theta$ one-dimensional profile in all but the highest angle fit bin. Shown in both (a) and (b) is the ratio between data and the postfit value. Sub-figure (c) shows a grid of two-dimensional data and postfit distributions in the same phase space as (a) and (b). Moving from top-left to bottom-right in (c) is the data, postfit, data to postfit ratio, and data to postfit difference.

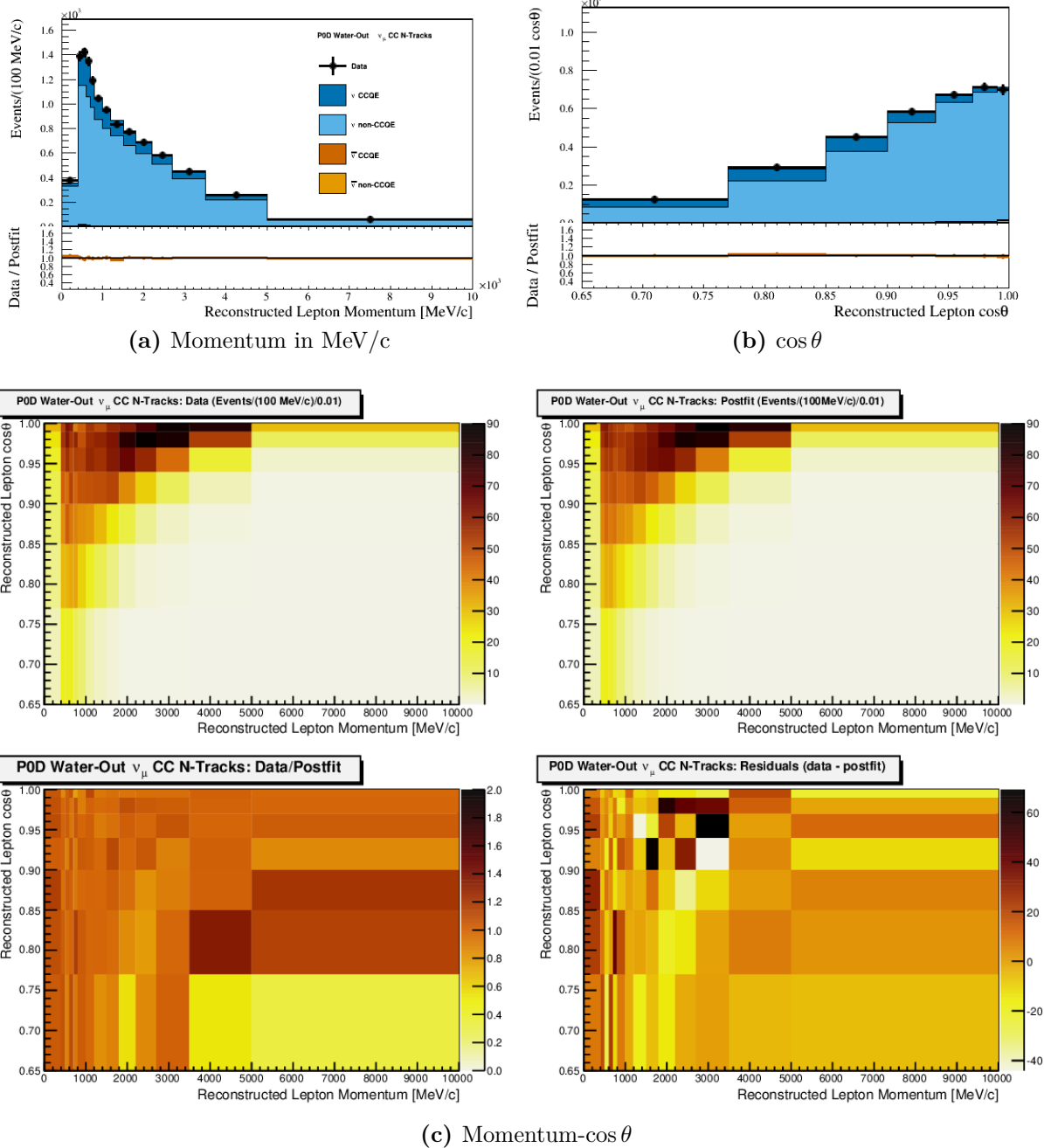


Figure 6.21: Data and postfit for the PØD Water-Out ν_μ in FHC CC N-Tracks sample. Sub-figure (a) shows the momentum one-dimensional profile in all but the highest momentum fit bin. Sub-figure (b) shows the $\cos \theta$ one-dimensional profile in all but the highest angle fit bin. Shown in both (a) and (b) is the ratio between data and the postfit value. Sub-figure (c) shows a grid of two-dimensional data and postfit distributions in the same phase space as (a) and (b). Moving from top-left to bottom-right in (c) is the data, postfit, data to postfit ratio, and data to postfit difference.

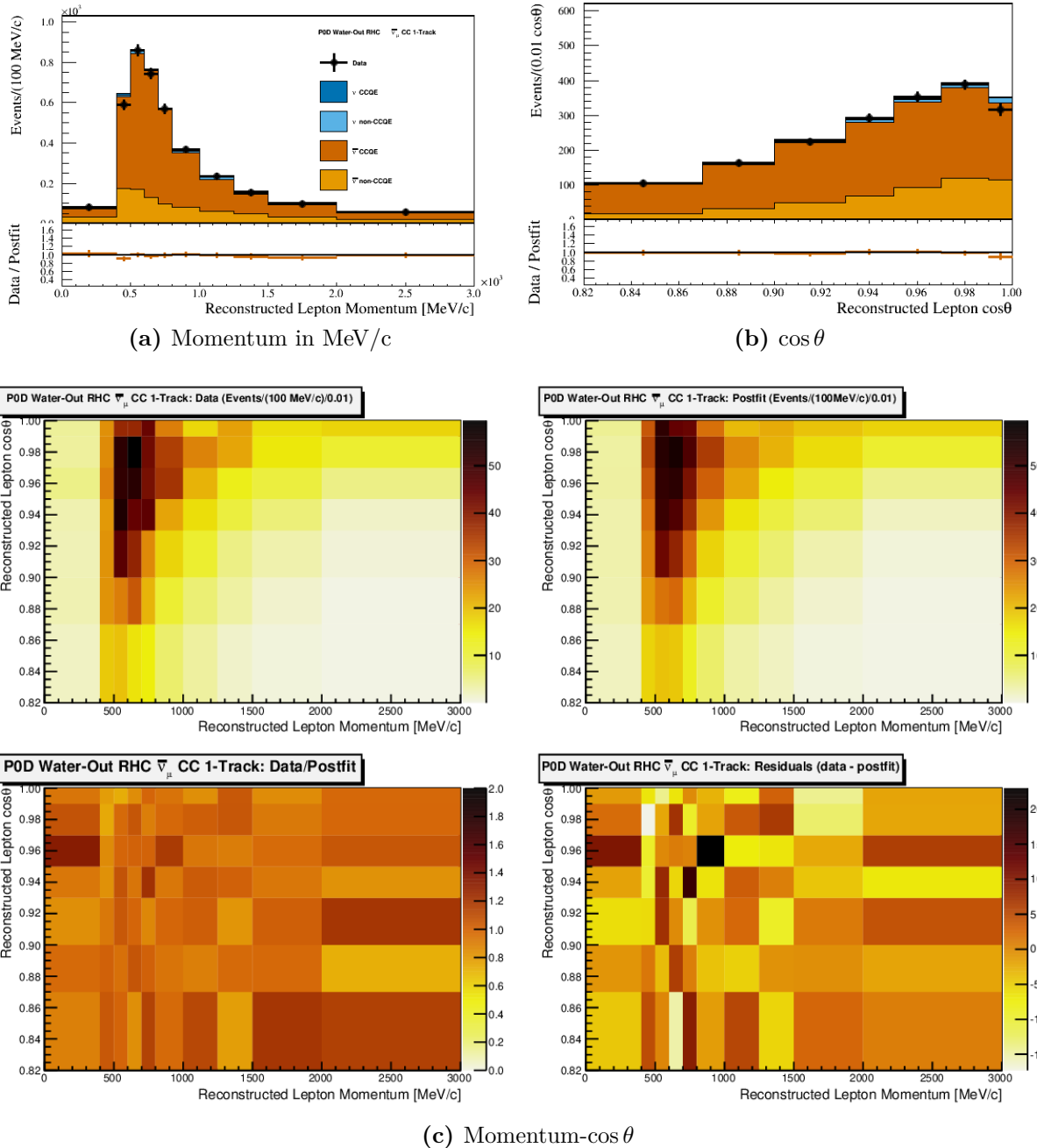


Figure 6.22: Data and postfit for the PØD Water-Out $\bar{\nu}_\mu$ in RHC CC 1-Track sample. Sub-figure (a) shows the momentum one-dimensional profile in all but the highest momentum fit bin. Sub-figure (b) shows the $\cos \theta$ one-dimensional profile in all but the highest angle fit bin. Shown in both (a) and (b) is the ratio between data and the postfit value. Sub-figure (c) shows a grid of two-dimensional data and postfit distributions in the same phase space as (a) and (b). Moving from top-left to bottom-right in (c) is the data, postfit, data to postfit ratio, and data to postfit difference.

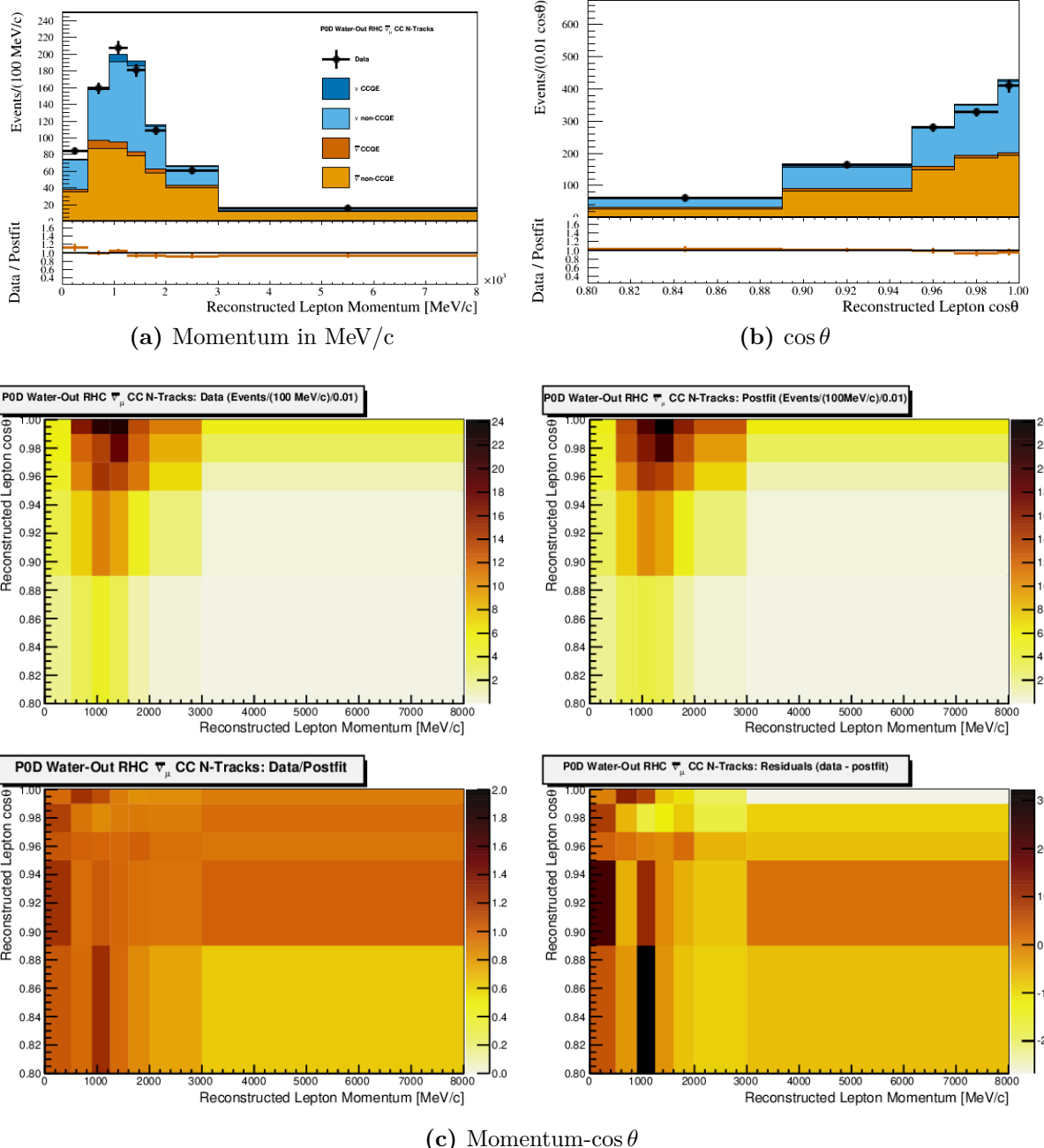


Figure 6.23: Data and postfit for the PØD Water-Out $\bar{\nu}_\mu$ in RHC CC N-Tracks sample. Sub-figure (a) shows the momentum one-dimensional profile in all but the highest momentum fit bin. Sub-figure (b) shows the $\cos \theta$ one-dimensional profile in all but the highest angle fit bin. Shown in both (a) and (b) is the ratio between data and the postfit value. Sub-figure (c) shows a grid of two-dimensional data and postfit distributions in the same phase space as (a) and (b). Moving from top-left to bottom-right in (c) is the data, postfit, data to postfit ratio, and data to postfit difference.

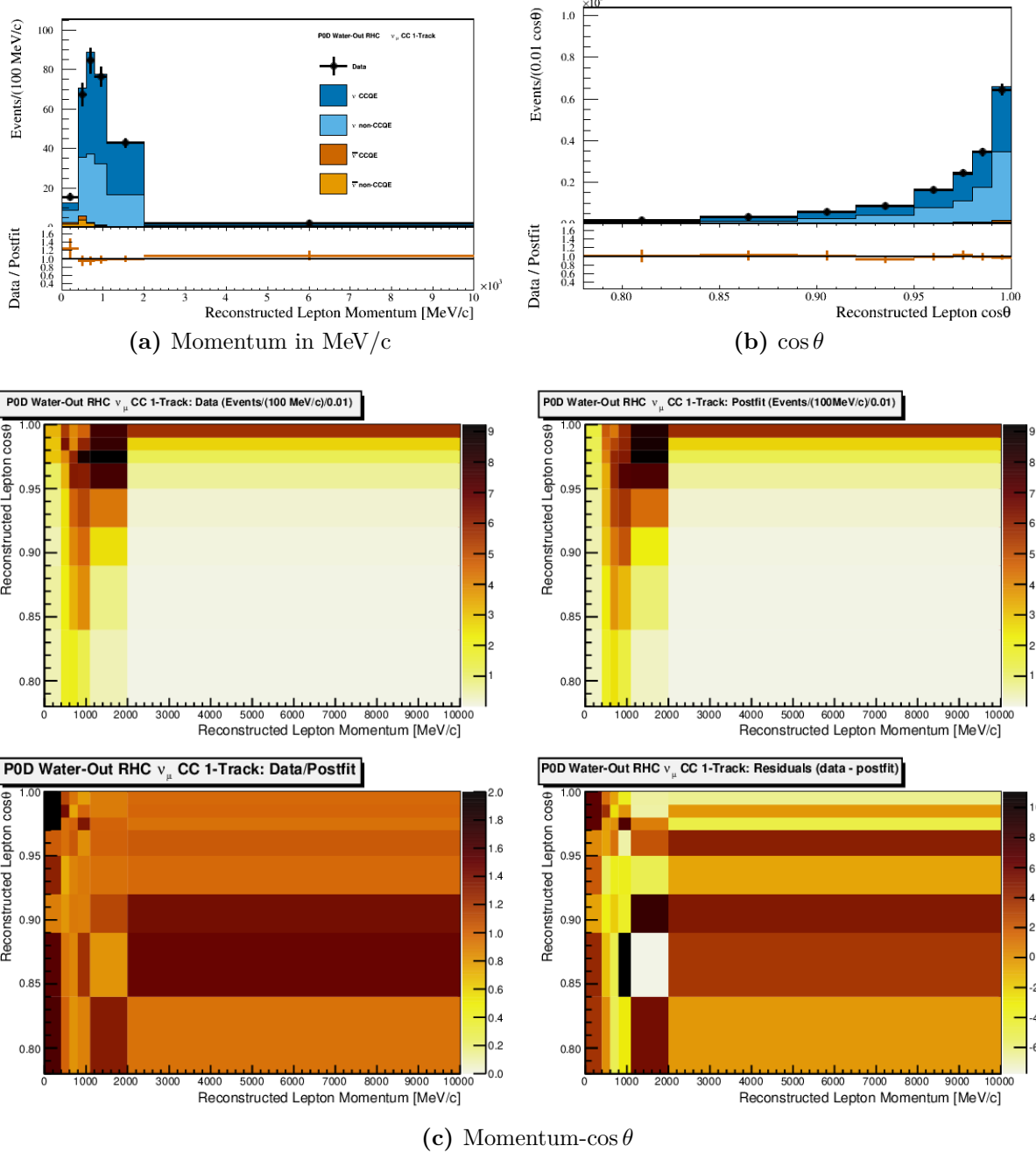


Figure 6.24: Data and postfit for the PØD Water-Out ν_μ in RHC CC 1-Track sample. Sub-figure (a) shows the momentum one-dimensional profile in all but the highest momentum fit bin. Sub-figure (b) shows the $\cos \theta$ one-dimensional profile in all but the highest angle fit bin. Shown in both (a) and (b) is the ratio between data and the postfit value. Sub-figure (c) shows a grid of two-dimensional data and postfit distributions in the same phase space as (a) and (b). Moving from top-left to bottom-right in (c) is the data, postfit, data to postfit ratio, and data to postfit difference.

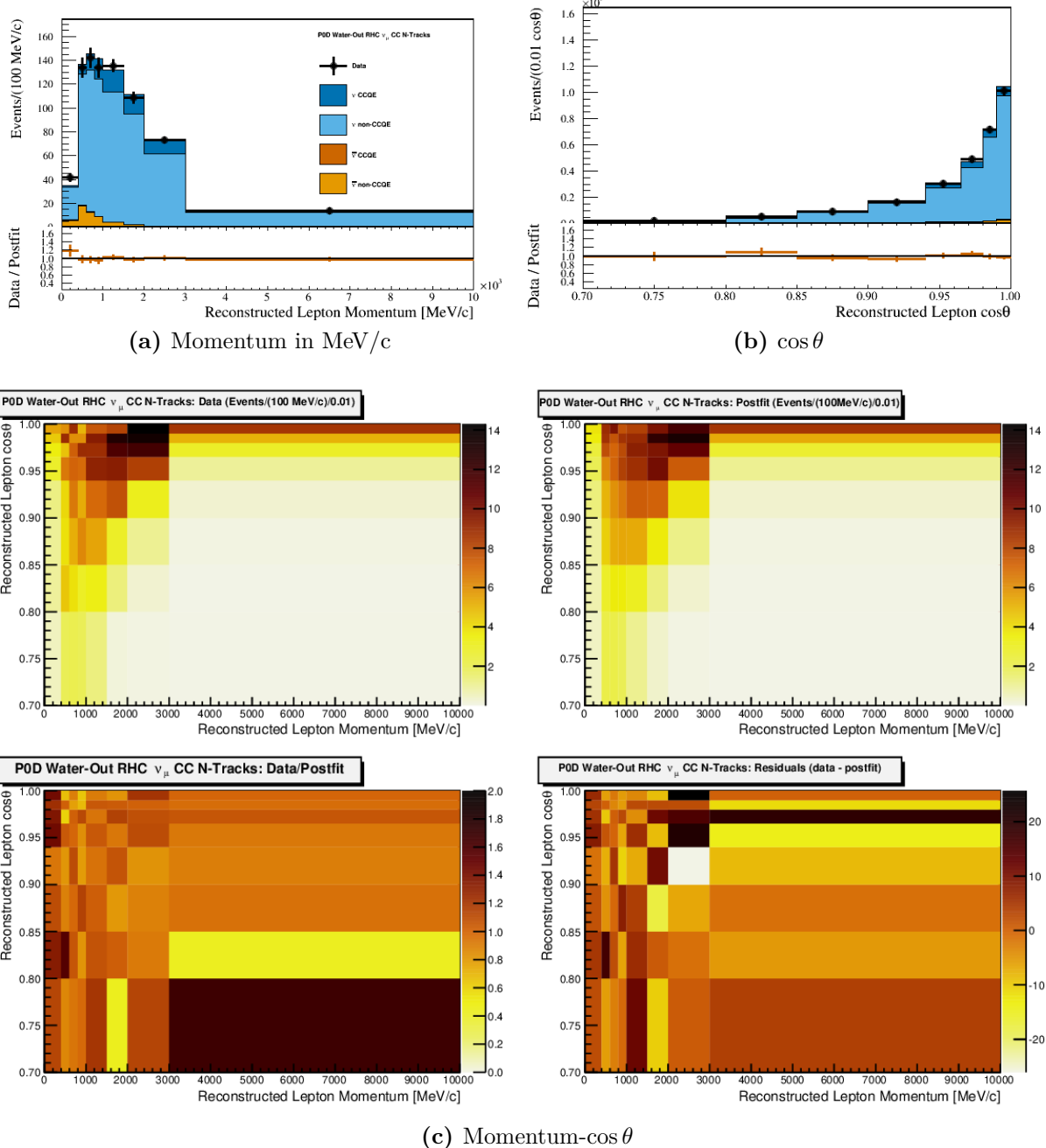


Figure 6.25: Data and postfit for the PØD Water-Out ν_μ in RHC CC N-Tracks sample. Sub-figure (a) shows the momentum one-dimensional profile in all but the highest momentum fit bin. Sub-figure (b) shows the $\cos \theta$ one-dimensional profile in all but the highest angle fit bin. Shown in both (a) and (b) is the ratio between data and the postfit value. Sub-figure (c) shows a grid of two-dimensional data and postfit distributions in the same phase space as (a) and (b). Moving from top-left to bottom-right in (c) is the data, postfit, data to postfit ratio, and data to postfit difference.



Figure 6.26: Legend used to compare PØD-only and FGD-only fit results.

Detector	Fiducial volume mass				POT (10^{20})		kg POT (10^{24})	PØD-to-FGD (kg POT)		
	(kg)	^{12}C (%)	^{16}O (%)	other (%)	FHC	RHC		^{12}C	^{16}O	other
PØD Water-out FGD1	3570	70	0.67	19.33	7.872	-	2.81	3.99	-	9.21
	985	86	3.7	10.3	5.81	-	0.572			
PØD Water-In FGD2	5470	45	30	25	3.657	-	2.00	10.63	1.43	8.05
	972	15	74	11	5.81	-	0.565			
PØD Water-out FGD1	3570	70	0.67	19.33	-	3.382	1.207	3.513	-	8.10
	985	86	3.7	10.3	-	2.84	0.280			
PØD Water-In FGD2	5470	45	30	25	-	2.852	1.56	16.9	2.29	12.8
	972	15	74	11	-	2.84	0.276			

Table 6.1: Neutrino-nucleon exposure on target elements in the PØD-only and FGD-only analyses. The FGD1 and FGD2 masses were calculated using the following sources [15, 55, 56]. The PØD mass was taken from the following source [73]. The other mass elements include hydrogen, copper, and heavier elements.

There is good visual agreement between the PØD-only and FGD-only BANFF parameter values. The flux parameters follow the same shape trends with the PØD-only fit, but with the PØD-only parameters having a higher expectation comparatively. Also, the magnitude of the flux uncertainties is similar between the two, which suggests the two configurations are statistically similar.

If we examine the bin normalization parameters for the PØD-only fit in Figure 6.30 on page 189, they are suggesting a reduction in the event rate across most bins. This high flux, low bin normalization result is likely due to the anticorrelated relationship between them as indicated in the correlation matrix shown in Figure 6.32 on page 191. This has been observed in previous BANFF analyses. Interestingly, the results of the principal components analysis on the bin normalizations in Section 4.2.2.4 are observed here as well. The analysis predicted most of the parameters would shift in unison, and we see that trend largely replicated in the postfit values. This indicates that we can possibly reduce the number of bin normalizations and still obtain a similar postfit result.

The cross section parameters are also quite similar between the two fits, with some larger uncertainties in the PØD-only result. The CCQE and BeRPA parameters are in very good agreement with both fits preferring a significant increase in the BeRPA B scale parameter. There is tension in the fits with the M_A^{Res} parameter which is not currently understood. However, if the difference in the postfit parameters is distributed according to a chi-squared distribution, then a deviation such as this is not unexpected. We will explore this idea further with a hypothesis test in the next section.

A couple of interesting features are observed in the 2p2h parameters. Firstly is the 2p2h ν normalization on carbon which is about two-times larger in the PØD-only fit than the FGD-only fit. This normalization result is currently an unknown phenomenon. It could be explained by the fact that the PØD has nearly twice as much non-carbon and non-oxygen elements, which is mostly brass, by mass fraction as the FGD (see Table 6.1 on page 183). The second feature involves the 2p2h shape parameters, *both of which have postfit values*

at the physical limit of +1, or +2 as shown graphically. This sets the 2p2h model to fully pionless-Delta-decay-like with the same event normalization. This result is also shared with the FGD result and is being addressed in the next generation BANFF analysis. To provide an uncertainty on those shape parameters, even though they are situated at a discontinuity in the derivative, a “mirrored” spline was implemented as shown in Figure 6.31 on page 190. The mirrored spline was shown to not affect the fit result while providing a calculable uncertainty in MINUIT for the Hessian matrix [22].

The postfit correlations are shown in Figure 6.32 on page 191. The full matrix shows large anticorrelations between the systematic parameters sets. Largest in magnitude are the flux and cross section parameters. To better see the correlations for those sets, they are zoomed into on Figure 6.33 on page 192. For the cross section parameters only, they are shown in Figure 6.34 on page 193.

6.2.3 P-Value Between PØD and FGD Fits

We can now provide a quantification of the agreement between the PØD-only BANFF fit and that of the FGD-only BANFF fit. As a starting assumption, let the FGD-only result be the expectation of the result. We wish to test the hypothesis, H_1 , that the PØD-only data and FGD-only data are sampling from two different neutrino interaction populations. We can also call this the alternative hypothesis. The null hypothesis, H_0 , is that PØD-only and FGD-only data are sampled from the same interaction population. For each measurement X_i that is independently and identically distributed from a standard normal $\mathcal{N}(\mu = 0, \sigma^2 = 1)$, then the following function

$$\chi^2 = \sum_i X_i^2, \quad (6.1)$$

is distributed according to a chi-square distribution

$$F(\chi^2, r) = \frac{1}{2^{r/2}\Gamma(r/2)} (\chi^2)^{(r/2-1)/2} e^{-\chi^2/2}, \quad (6.2)$$

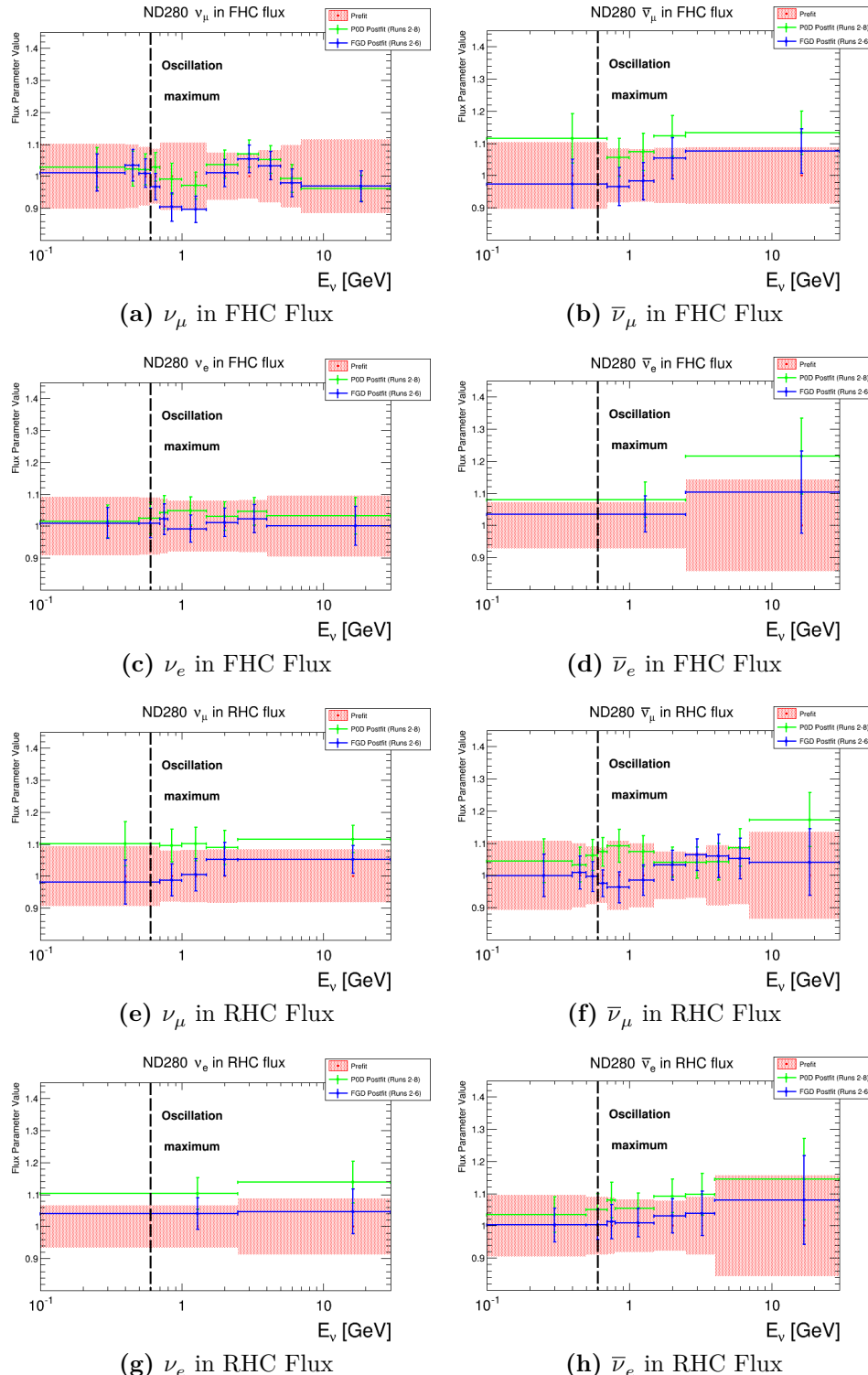


Figure 6.27: Postfit ND280 flux parameters for the PØD-only (green) and FGD-only (blue) BANFF fit as functions of neutrino energy. The energy that maximizes the $\nu_\mu \rightarrow \nu_e$ oscillation (0.6 GeV) is shown with a dashed, black line.

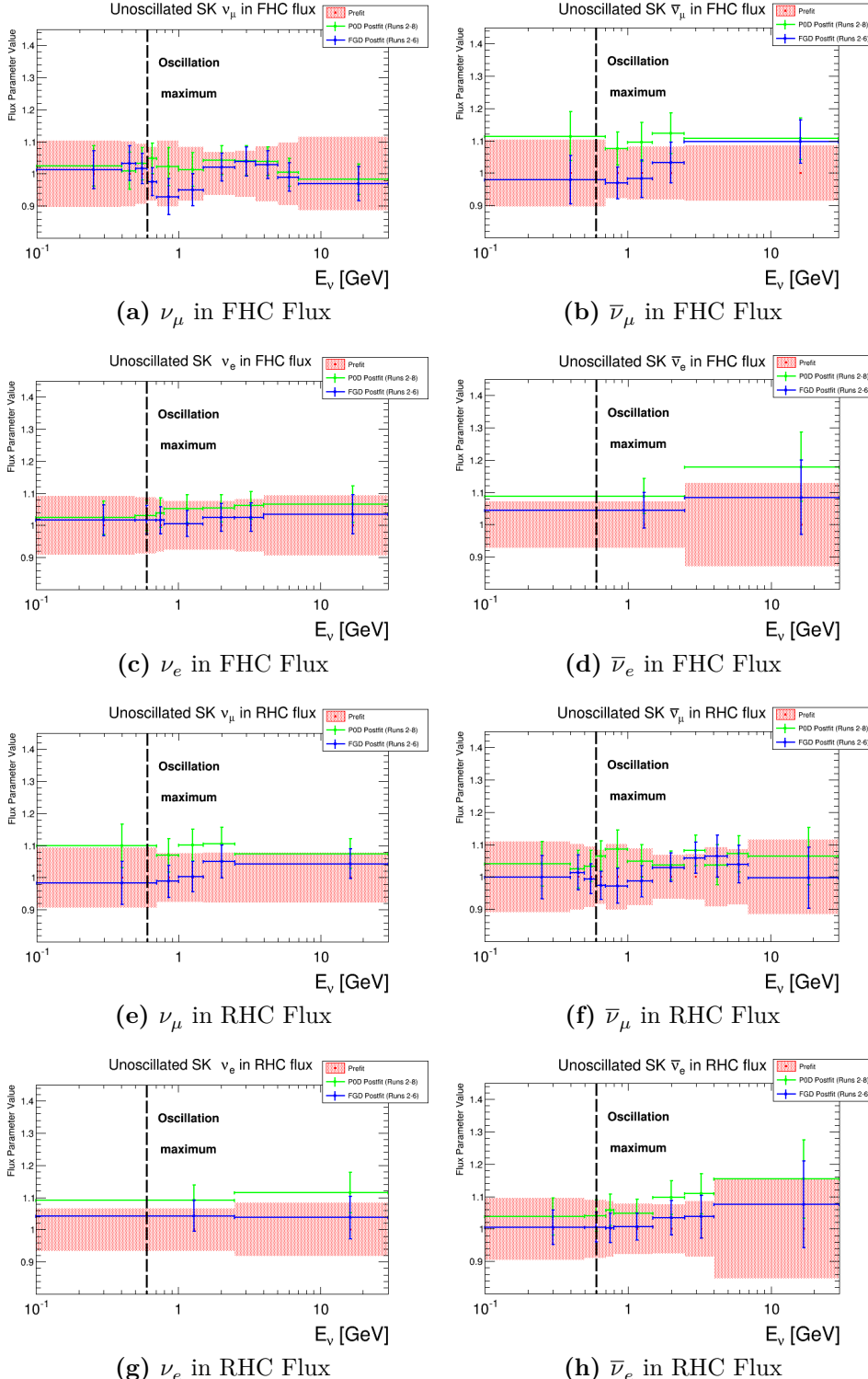
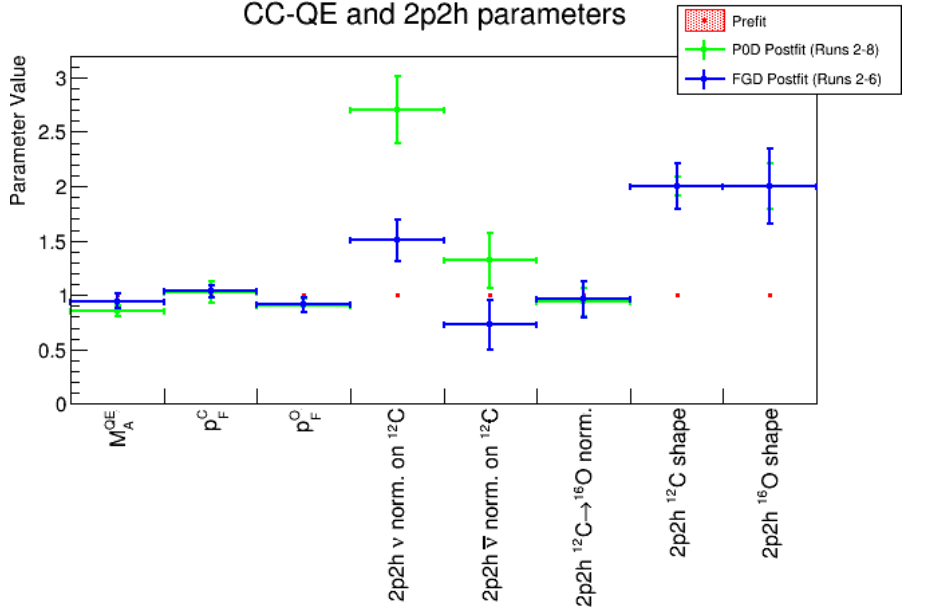
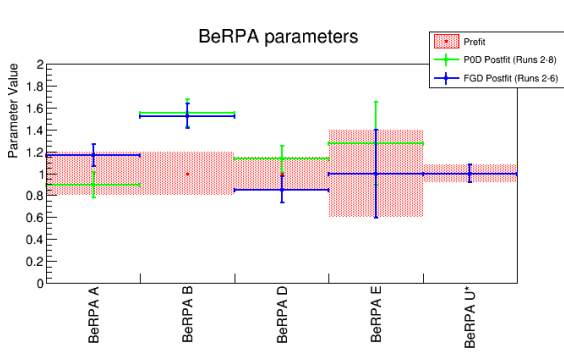


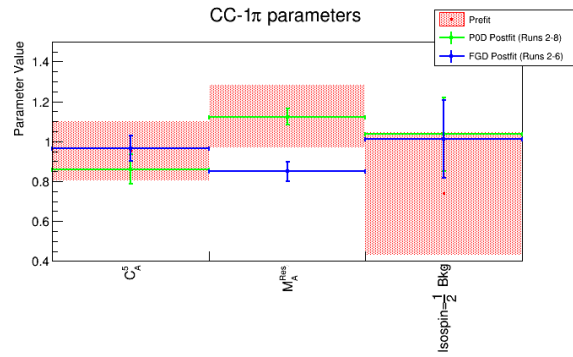
Figure 6.28: Postfit SK flux parameters for the PØD-only (green) and FGD-only (blue) BANFF fit as functions of neutrino energy. The energy that maximizes the $\nu_\mu \rightarrow \nu_e$ oscillation (0.6 GeV) is shown with a dashed, black line.



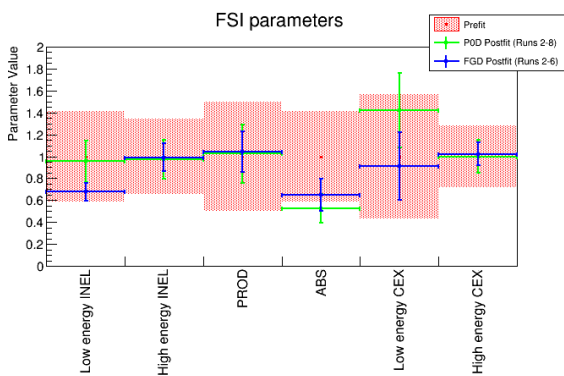
(a) CC- 0π Parameters



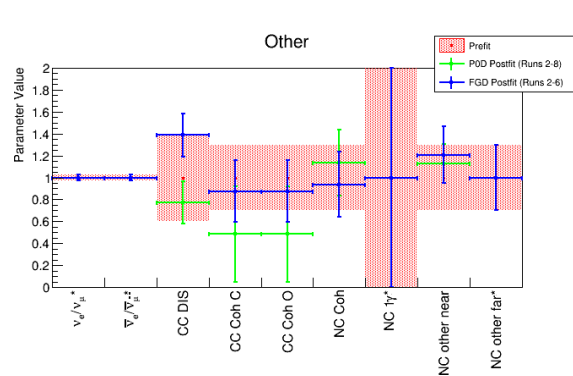
(b) BeRPA Parameters



(c) CC- 1π Parameters

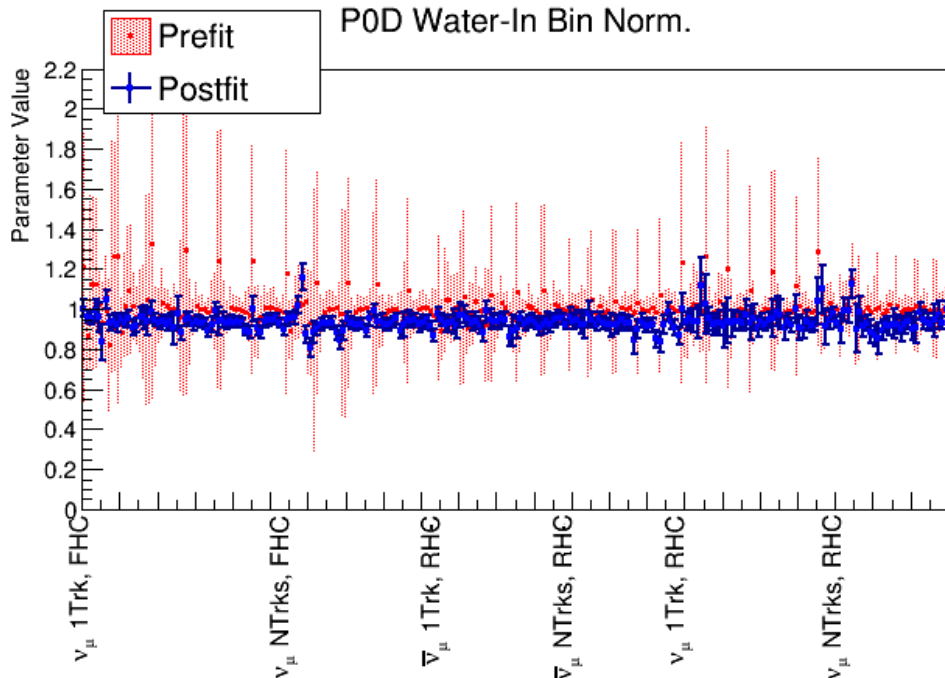


(d) FSI Parameters

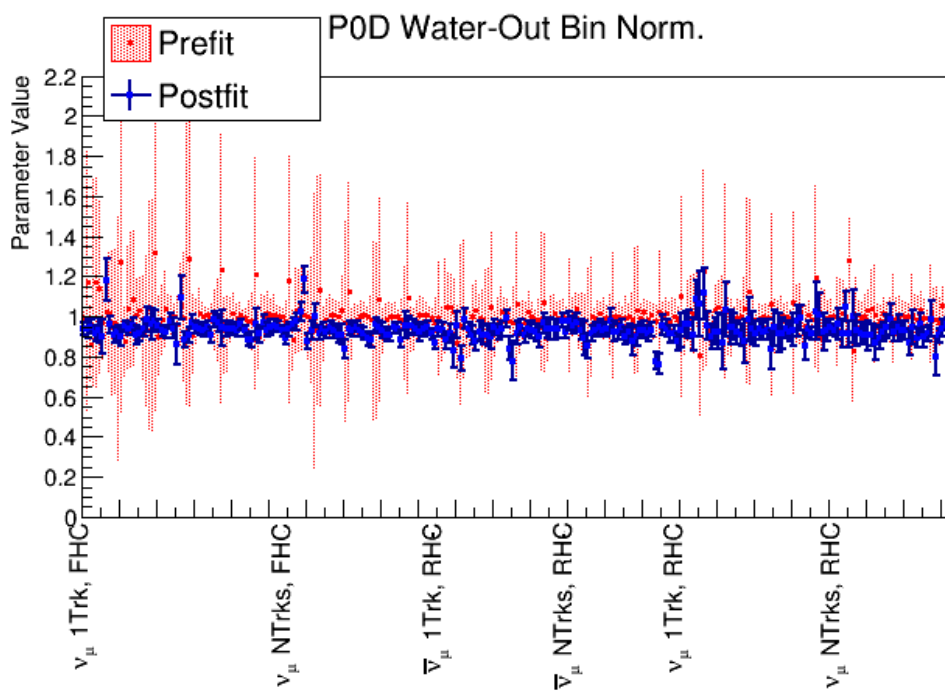


(e) CC-Other and NC-Other Parameters

Figure 6.29: Postfit cross section parameters for the PØD-only (green) and FGD-only (blue) BANFF fit. In these figures, all shape and scale factor parameters are adjusted to 1 to provide a consistent graphical representation of all fit parameters. Shape parameters always have a prefit value of 0. Parameters without prefit uncertainties had a flat prior applied to them and an asterisk (*) represents a fixed parameter.



(a) Water-In



(b) Water-Out

Figure 6.30: Prefit and postfit PØD bin normalization parameters.

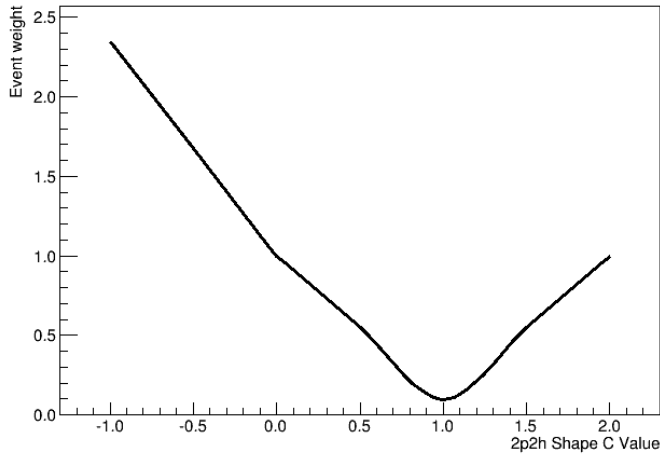


Figure 6.31: The “mirrored” spline for a single event. The spline represents an event weight and variations from the prefit value of 0 alters the event weight. The 2p2h shape splines are mirrored about the value of +1 to provide an uncertainty in the postfit result.

where r is the number of degrees of freedom (NDOF) and $\Gamma(x+1) = x!$ is the Gamma function. We can calculate a p-value to reject the null hypothesis at the α -level.

If we let $p_i^{\text{P}\bar{\text{O}}\text{D}} \left(p_i^{\text{FGD}} \right)$ represent the measurement of the i th parameter for the P $\bar{\text{O}}\text{D}$ -only (FGD-only) BANFF fit, then our test statistic can be formally defined as

$$\chi_{\text{P}\bar{\text{O}}\text{DvsFGD}}^2 = \sum_i \sum_j \frac{\left(p_i^{\text{P}\bar{\text{O}}\text{D}} - p_i^{\text{FGD}} \right) \left(p_j^{\text{P}\bar{\text{O}}\text{D}} - p_j^{\text{FGD}} \right)}{V_{i,j}^{\text{P}\bar{\text{O}}\text{DvsFGD}}} \quad (6.3)$$

where $V_{i,j}^{\text{P}\bar{\text{O}}\text{DvsFGD}}$ is the covariance of measurement i, j . Since the purpose of the BANFF fit is to provide a constraint on the SK flux and cross section models, we will ignore the ND flux bins and $(p, \cos \theta)$ bin normalization parameters. Also assume for simplicity that the P $\bar{\text{O}}\text{D}$ and FGD data are completely uncorrelated. This simplifies the test statistic to

$$\chi_{\text{P}\bar{\text{O}}\text{DvsFGD}}^2 = \sum_i \frac{\left(p_i^{\text{P}\bar{\text{O}}\text{D}} - p_i^{\text{FGD}} \right)^2}{V_{i,i}^{\text{P}\bar{\text{O}}\text{D}} + V_{i,i}^{\text{FGD}}}, \quad (6.4)$$

where $V_{i,i}^{\text{P}\bar{\text{O}}\text{D}}/V_{i,i}^{\text{FGD}}$ is the variance of the i th parameter from the P $\bar{\text{O}}\text{D}$ -/FGD-only BANFF fit measurement. We can calculate a p-value, p , of observing a test statistic at least as extreme

Postfit Correlation Matrix

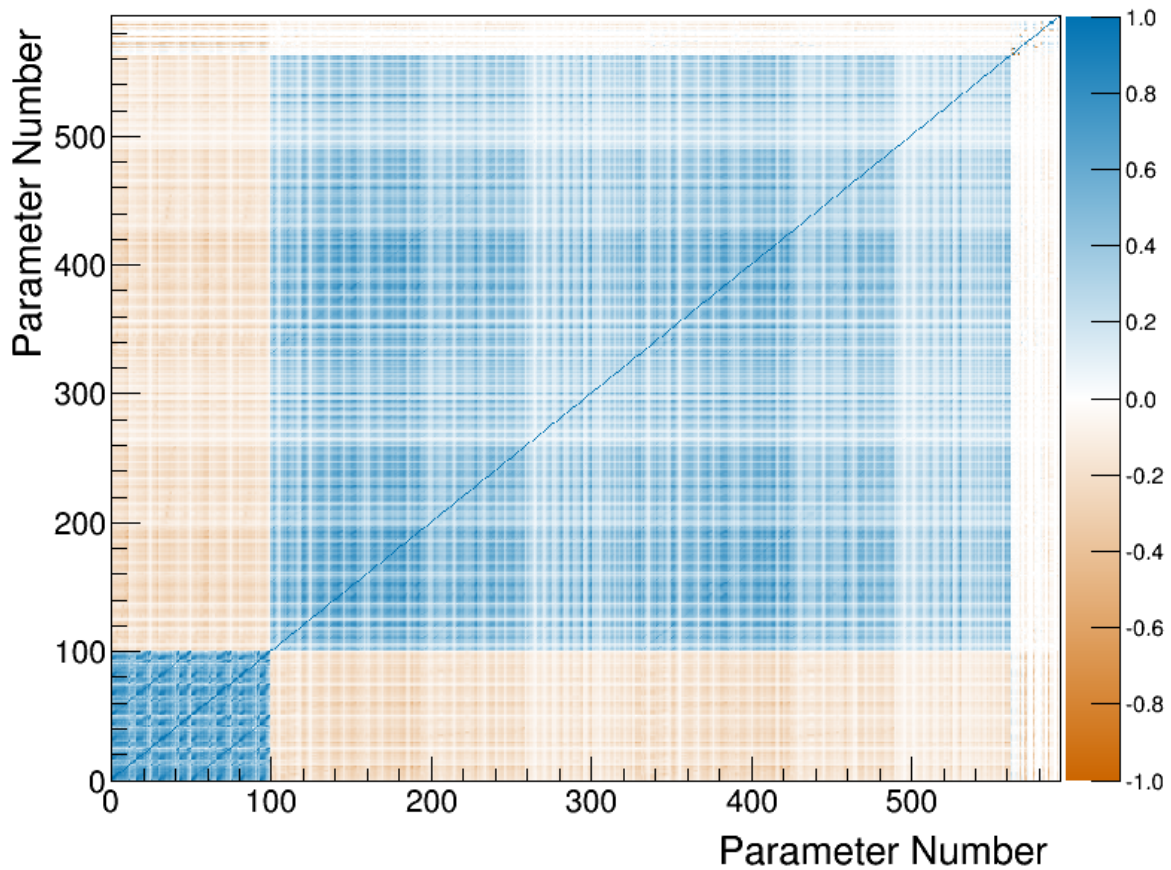
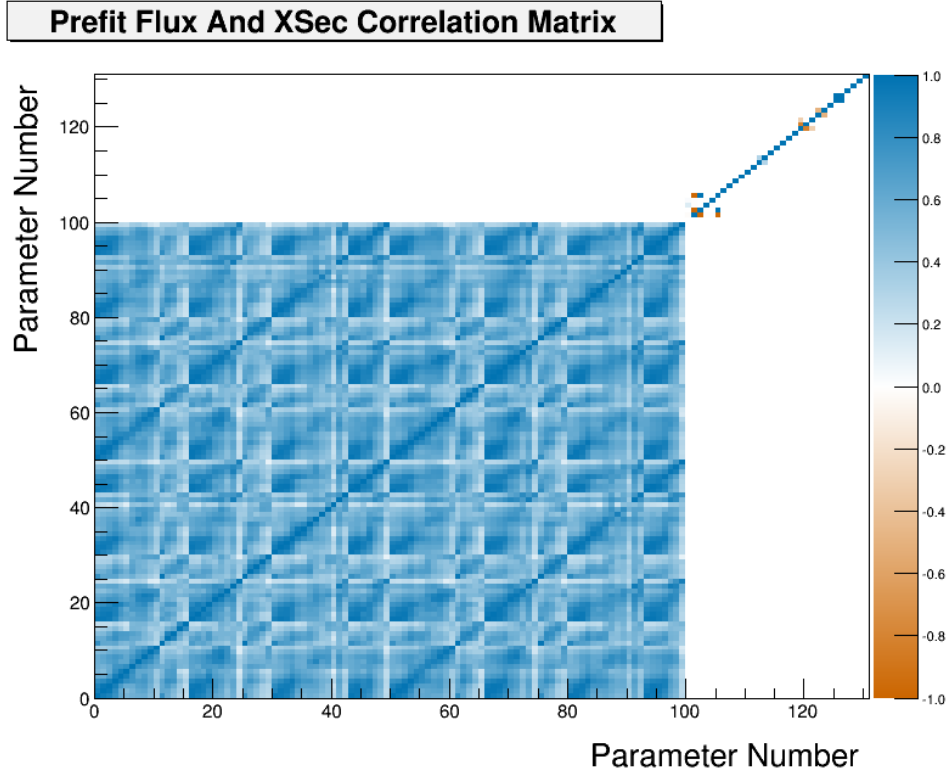
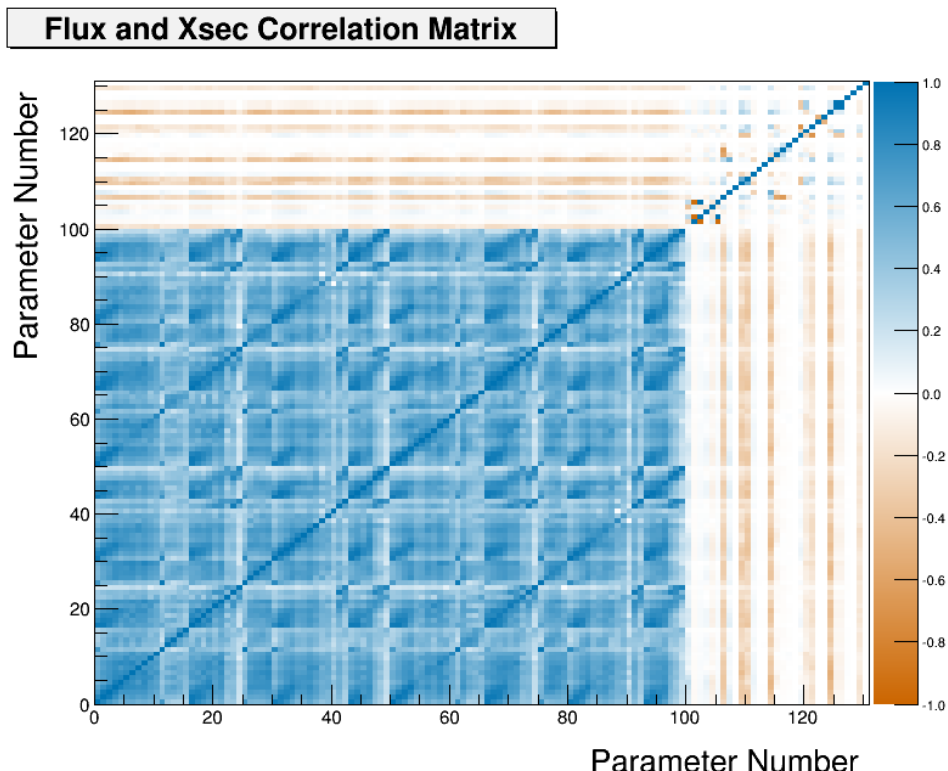


Figure 6.32: Postfit correlation matrix. The first 100 parameters are the flux parameters with the first 50 corresponding to ND280 and the last 50 with Super-K. Between 100 and 561 are the bin normalization parameters. The last 31 are the cross section parameters.



(a) Prefit flux and cross sections correlations



(b) Postfit flux and cross section correlations

Figure 6.33: Prefit and post fit flux and cross section parameter correlations. In sub-figures (a) and (b), the prefit and postfit, respectively, correlation matrices for the flux and cross section parameters are shown. In both (a) and (b), the first 100 parameters are the flux parameters with the first 50 corresponding to ND280 and the last 50 with Super-K. The last 31 are the cross section parameters.

XSec Correlation Matrix

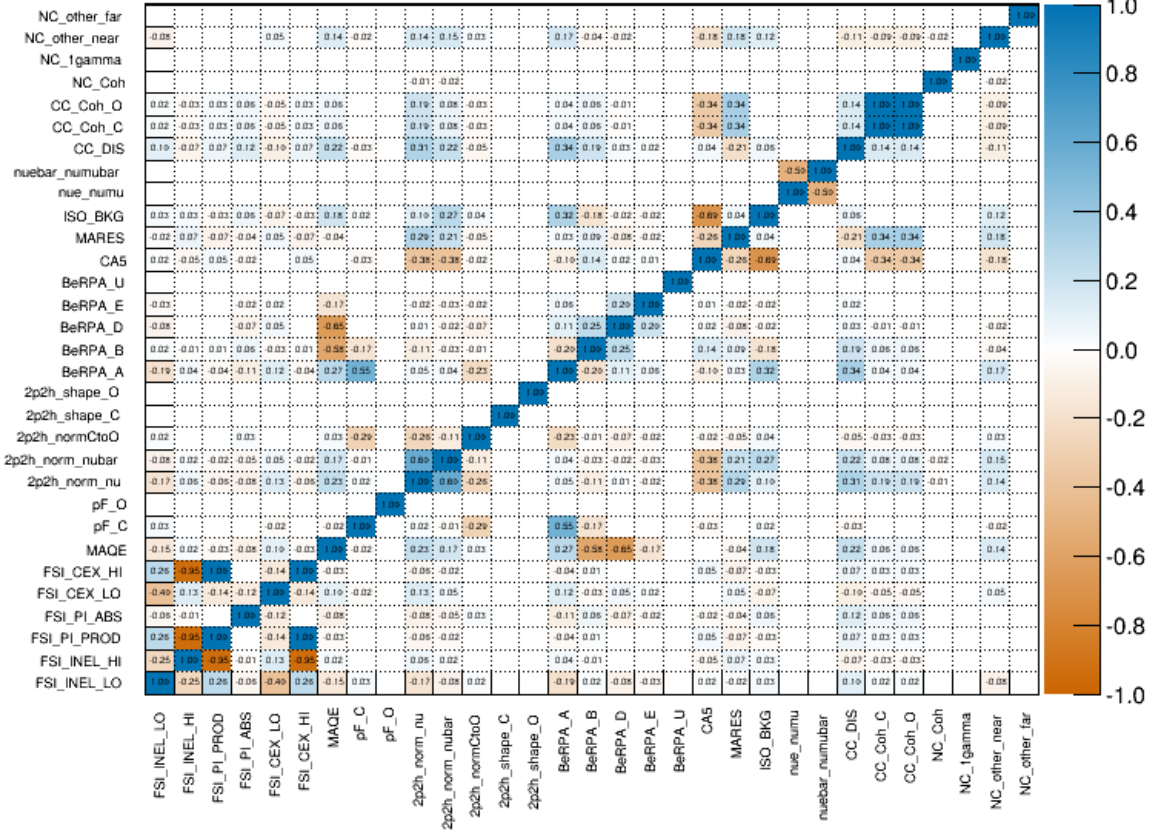


Figure 6.34: Postfit cross section correlation matrix

in a chi-square distribution by integrating the right-hand tail of the chi-square distribution using the inverse cumulative distribution function (ICDF)

$$p(\chi^2, r) = \int_{\chi^2}^{\infty} F(x', r) dx', \quad (6.5)$$

where χ^2 is the test-statistic from 6.4.

Now let us count the NDOF for the p-value calculation. There are 50 SK flux parameters and 31 cross section parameters. However, five of cross section parameters are fixed. Additionally, we have assumed the FGD-only result is our expectation, and so we have one less NDOF. This leaves us with

$$r = \underbrace{50}_{\text{SK Flux}} + \underbrace{(31 - 5)}_{\text{XSec}} - 1 = 75 \text{ NDOF.}$$

If we wish to reject the null hypothesis at the 5% level, this requires a chi-squared value of 96.21 or greater.

If we calculate the test statistic as defined above, we find that

$$\tilde{\chi}_{\text{P}\emptyset\text{DvsFGD}}^2 = \frac{\chi_{\text{P}\emptyset\text{DvsFGD}}^2}{r} = \frac{81.41}{75} \approx 1.085,$$

of which indicates good agreement between the two measurements for the ND constraint since $\tilde{\chi}^2 \sim 1$. This corresponds to a p-value of 0.2865 or a 28.65% probability of obtaining a larger test statistic. This result is visualized in Figure 6.35 on page 195. Since this is not sufficiently close to the 5% level, we fail to reject the null hypothesis. *We can conclude the PØD-only and FGD-only samples and subsequent BANFF fits describe the same data in T2K.*

We must qualify the above conclusion given the flaws of the test statistic definition. The PØD-only flux parameters are clearly skewed above the FGD-only flux parameters, and, therefore, their difference is not normally distributed about zero. This indicates a large, pos-

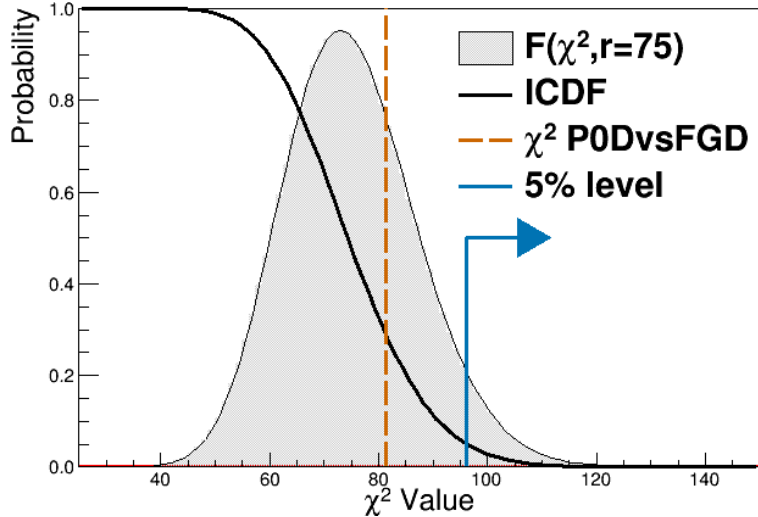


Figure 6.35: P-value for the PØD vs FGD ND constraint. Shown in solid black is the inverse cumulative distribution function (ICDF) with 75 NDOF. The chi-squared PDF is shown in gray with arbitrary normalization. The obtained value of the test statistic, shown as a dashed, red line, is 81.41 which is below the 5% level, shown as a solid, blue arrow.

itive correlation between the two measurements, and breaks the uncorrelated uncertainties assumption. Given this correlated result, we expect better agreement between the PØD-only and FGD-only fits as indicated with the above test statistic using a more accurate covariance matrix.

6.3 Summary

In this chapter, we have explored the postfit results for the PØD-only data set and compared it against the FGD-only fit. While the FGD-only data samples have about twice as many more neutrino-oxygen events than the PØD-only data, which helps with the sensitivity to oxygen cross section parameters that affect SK more, the accumulated neutrino exposures are similar. We observe a good level of agreement between the two fits with moderate differences in some parameters. A hypothesis test was performed to test if the PØD-only and FGD-only data are similar or not. In order to reject the null hypothesis, which is that the two sets are similar, at the 5% level, a χ^2 of 96.21 or greater was needed. A χ^2 of 81.41 was obtained, corresponding to a p-value of 28.65, which is insufficient to reject the

null hypothesis. Therefore, using the BANFF fit method with the current PØD samples and cross section parameterization, the ND280 constraint is expected to be largely similar if propagated to the next stage in the oscillation analysis.

Chapter 7

Discussion

This chapter serves to summarize the methods and results shown in this thesis. The Tokai to Kamioka (T2K) experiment is a long baseline, neutrino oscillation experiment designed to observe a ν_μ beam oscillate into ν_e . With the aid of the world class Japan Proton Accelerator Research Complex (J-PARC), a dedicated near detector called ND280 is located downstream of the neutrino production source to observe the beam before oscillations occur. Since starting operations, the fine grain detector (FGD) in ND280 has provided constraints on the neutrino flux and neutrino-water interaction modes important in the oscillation analysis. This thesis is an analysis of an independent measurement of the ND280 constraint using a maximum likelihood estimate in the Beam and Near Detector Flux Task Flux (BANFF) framework with samples from the Pi-Zero Detector (PØD).

Analysis samples have been developed with the PØD to capture a wide variety of interaction modes in T2K, importantly interactions classified as charged current quasi-elastic (CCQE) which constitute the highest cross section in the T2K neutrino energy spectrum. While the PØD has a larger volume compared to the FGD, which means it has more neutrino interactions to choose from, the PØD is less sensitive to harder to measure phenomena like CC single pion production. This limitation is largely due to the design of the detector and sample cuts which reduce its $(p, \cos \theta)$ sensitivity to the lower energy outgoing muons. The

systematic uncertainties inherent in the samples were controlled for in a similar manner with previous BANFF analyses.

The PØD-only data fit shows very good agreement with the FGD-only result using the same flux and cross section parameters. Trends in the data like shape dependence on the flux and accounting for quantum mechanical correlation effects the observable cross section where observed in both sets of fits. A hypothesis test was conducted to test if the PØD-only and FGD-only data fits are consistent with one another. The test produced

$$\tilde{\chi}^2 = \frac{\chi^2}{\text{NDOF}} = \frac{81.41}{75}, \quad p = 0.2865,$$

which indicates the test failed to reject the null hypothesis. *This is another way of saying the PØD provides a similar ND280 constraint compared to the FGD.*

7.1 Potential Impacts on the T2K Oscillation Analysis

7.2 Analysis Improvements

First is a discussion on applying a different regularization strength. The next topic is a method to reduce the number of effective bin normalization parameters using a different penalty function called the Lasso.

7.2.1 Regularization Strength

Recall that the BANFF ND constraint test statistic is defined as

$$\hat{\chi}_{\text{ND280}}^2 = \underset{\Delta \vec{y} \in \mathbb{R}^d}{\operatorname{argmin}} \left\{ \chi_{\text{LLR}}^2 (\vec{N}^d, \vec{N}^p) + \Delta \chi_{\text{Penalty}}^2 (\Delta \vec{y}) \right\}$$

where \vec{N}^d and \vec{N}^p are the binned data and prediction measurements, respectively, and $\Delta \vec{y}$ is the difference between postfit and prefit parameter values in the fit. This equation is similar

to the general class of parameter regression using regularization [47]

$$\operatorname{argmin}_{f \in \mathcal{F}} \left\{ L(\eta, f(\vec{\beta})) + \lambda J(f) \right\}, \quad (7.1)$$

where L is a loss function of measurements η , $J(f)$ is a penalty function, $f(\vec{\beta})$ is a d -dimensional function of parameters $\vec{\beta}$ in \mathbb{R}^d , λ is the regularization parameter, and \mathcal{F} is a space of function on which $J(f)$ is defined. In regularized regression problems, the penalty term serves to solve an ill posed problem by adding external information. Similarly, the regularization parameter controls the importance of the penalty. We recognize that the loss function L is the log-likelihood ratio term χ_{LLR}^2 , and penalty term is $J = \chi_{\text{Penalty}}^2$ with regularization strength $\lambda = 1$.

In defining the BANFF test statistic in Chapter 2, the regularization term λ was set to 1 without justification. We can test the effectiveness of this choice using cross-validation. Cross-Validation provides an estimate on the prediction error as well as determines the “optimal” choice of regularization. In cross-validation, the input data is randomly split into K equal sized partitions. For the $k \in K$ data partition, we fit the model to the other $K - 1$ parts of the data and calculate a prediction error P .

In this verification of the regularization strength, the test statistic is altered to include a regularization term

$$\begin{aligned} \hat{\chi}_{\text{ND280}}^2 &= \operatorname{argmin}_{\Delta \vec{y} \in \mathbb{R}^d} \left\{ \chi_{\text{LLR}}^2 + \lambda \chi_{\text{Penalty}}^2 \right\} \\ &= \operatorname{argmin}_{\Delta \vec{y} \in \mathbb{R}^d} \left\{ \chi_{\text{LLR}}^2 + \lambda (\Delta \vec{y})^T V^{-1} (\Delta \vec{y}) \right\}, \end{aligned} \quad (7.2)$$

and the data is split into $K = 5$ partitions. The prediction error, P , in this analysis is defined as

$$P_k \left(\left(\chi_{\text{train}}^2 \right)^{-k}, \left(\chi_{\text{test}}^2 \right)^k \right) = \left| \left(\chi_{\text{train}}^2 \right)^{-k} - \left(\chi_{\text{test}}^2 \right)^k \right| \quad (7.3)$$

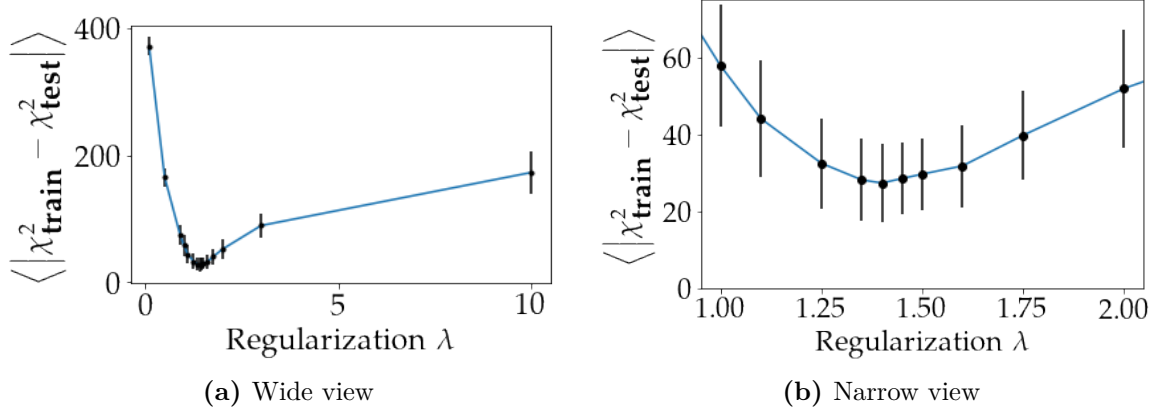


Figure 7.1: Cross-validation curve for the BANFF fit regularization strength. Figure (a) examines the cross-validation error for a wide range of regularization strengths. Figure (b) zooms in on the minimized error. The error bars shown are statistical only.

where $(\chi_{\text{train}}^2)^{-k}$ is the fitted model statistic on all but the k th partition, and $(\chi_{\text{test}}^2)^k$ is prediction from the fitted model on the k th partition. This definition of P is useful since the penalty terms cancel, leaving only the difference in log-likelihood terms. The optimal regularization strength is determined by minimizing the cross-validation error,

$$\begin{aligned} \text{CV}(\lambda) &= \langle |\chi_{\text{train}}^2 - \chi_{\text{test}}^2| \rangle \\ &= \frac{1}{5} \sum_{k=1}^5 P_k \left((\chi_{\text{train}}^2)^{-k}, (\chi_{\text{test}}^2)^k \right), \end{aligned} \tag{7.4}$$

which is the average prediction error.

Results of the cross-validation are shown in Figure 7.1 on page 200. We see that while the penalty strength of $\lambda = 1$ nearly minimizes the cross-validation error, slightly larger penalties are preferred. The cross-validation error curve is minimized at $\lambda = 1.45$, and it is roughly quadratic in the neighborhood around the minimum.

7.2.2 Alternative Penalty

Consider solving the linear regression problem

$$\vec{\eta} = X\vec{\beta} \quad (7.5)$$

where X is a $p \times d$ matrix of d model features from p measurements, $\vec{\beta}$ is a vector of regression weights with p rows, and $\vec{\eta}$ is a response vector. There are many approaches to solving (7.5) using (7.1). A popular solution is the l_2 -regularization constraint [47]

$$\operatorname{argmin}_{\vec{\beta} \in \mathbb{R}^d} \left\{ L(\vec{\eta}, \vec{\beta}) + \lambda \sum_i |\beta_i|^2 \right\} \quad (7.6)$$

where the sum of squares of the weights β_i sets the constraint and L is the loss function. The usual choice of L is using ordinary least squares

$$L(\vec{\eta}, \vec{\beta}) = \sum_j |\vec{\eta} - X\vec{\beta}|^2,$$

which provides the lowest variance in parameter weights.

With some algebra, we can rewrite the BANFF test statistic (2.13) into the form of (7.6). We again recognize χ_{LLR}^2 is the loss function L which leaves the penalty term to be tackled. The (inverse) covariance matrix is symmetric and real and can be decomposed as

$$V^{-1} = U\Lambda U^T$$

where U and V are the matrix of the eigenvectors and eigenvalues, respectively, of V^{-1} . Since the eigenvalues are real and positive, the matrix Λ can be expressed as the square of a diagonal matrix Γ

$$\Lambda = \Gamma^2.$$

We can now rewrite the penalty term as an inner product of two vectors.

$$\begin{aligned}\chi_{\text{Penalty}}^2 &= (\Delta \vec{y})^T V^{-1} (\Delta \vec{y}) \\ &= (\Delta \vec{y})^T U \Gamma^2 U^T (\Delta \vec{y}) \\ &= [\Gamma U^T \Delta \vec{y}]^T [\Gamma U^T \Delta \vec{y}].\end{aligned}$$

If we let $\vec{\psi} = \Gamma U^T \Delta \vec{y}$, then the penalty term becomes

$$\chi_{\text{Penalty}}^2 = \vec{\psi}^T \vec{\psi} = \sum_j |\psi_j|^2$$

and test statistic is now

$$\hat{\chi}_{\text{ND280}}^2 = \underset{\vec{\psi} \in \mathbb{R}^d}{\operatorname{argmin}} \left\{ \chi_{\text{LLR}}^2(N^d, N^p) + \|\psi_j\|_2^2 \right\}, \quad (7.7)$$

where $\|\cdot\|_2^2$ is shorthand for the l_2 -regularization constraint sum of squares. We see that the BANFF test statistic is indeed a l_2 -regularized solution with $\Delta \vec{y}$, recast as $\vec{\psi}$, acting as the parameter weight vector and has the regularization strength $\lambda = 1$.

Consider now another solution to (7.5) using the l_1 -regularization constraint or least absolute shrinkage and selection operator (Lasso)²⁰

$$\underset{\vec{\beta} \in \mathbb{R}^d}{\operatorname{argmin}} \left\{ L(\vec{\eta}, \vec{\beta}) + \lambda \|\beta\|_1 \right\}, \quad (7.8)$$

where $\|\cdot\|_1$ indicates the sum of absolute values of the parameter weight terms. What is unique about the Lasso is its ability to promote model solutions with few nonzero coefficient weights, sometimes called sparse solutions. In other words, predictor parameters with no model impact are excluded in the solution using the l_1 -regularized constraint. Thus the Lasso has the advantage of providing an interpretable model in situations with very high

²⁰The Lasso or l_1 -regularization constraint is commonly employed in parameter estimation problems in linear systems. For example, the method has been used in cancer class prediction with gene expression profiling in the “PAM” package [78]. The Lasso has also been shown to work with generalized linear models [39].

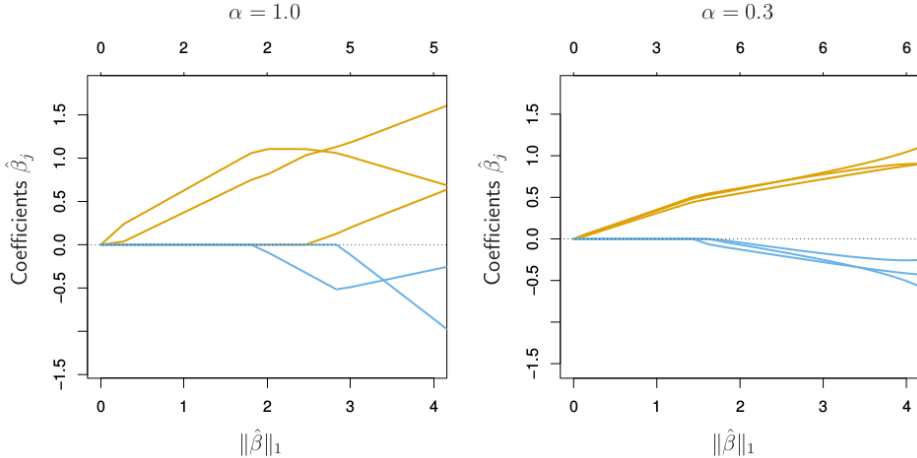


Figure 7.2: The Lasso vs elastic net constraint. Six variables are shown and the highly correlated variables are in groups of three. The Lasso estimate, left, estimate exhibits erratic behavior as the regularization strength λ is varied. The elastic net, right, pulls highly correlated variables together. In both panels, the vertical axis is the magnitude of the parameter weights (coefficients), the bottom horizontal axis is the regularization strength as measured by the estimate $\|\hat{\beta}\|_1$, and top horizontal axis is the count of non-zero parameter weights. This figure was taken directly from the following reference [48].

parameter spaces. However, the Lasso does not handle highly correlated variables very well. This is overcome by combining the Lasso with l_2 -regularization which is called the elastic net constraint

$$\underset{\vec{\beta} \in \mathbb{R}^d}{\operatorname{argmin}} \left\{ L(\vec{\eta}, \vec{\beta}) + \lambda \left[\frac{1}{2} (1 - \alpha) \|\beta_i\|_2^2 + \alpha \|\beta_i\|_1 \right] \right\},$$

where α is the “budget” between the Lasso and l_2 -regularization. The results of using the Lasso and elastic net with highly correlated variables is shown in Figure 7.2 on page 203. The elastic net controls for strong within-group correlations and has a unique solution. Further details about the Lasso and elastic net can be found in the following reference [48].

We can potentially reduce the dimensionality of the ND constraint by utilizing the elastic net. Using the elastic net constraint provides a data-driven method to determine the number of important bin normalizations in the analysis. The method to define the fit binning described in Chapter 4 would be unchanged. What changes is that instead of merging fit bins prior to the fit, the elastic net determines which bin normalizations are important or not important. Along with cross-validation, fit bins with minimal to no impact on the fit can be

excluded or combined with important fit bins. Then the best fit parameters and covariance matrix using the current BANFF machinery can still be found.

Another possibility in the future is for the BANFF fit to use the elastic net to directly estimate the flux and cross section parameters. The challenge with this approach is that using non-Gaussian priors, the covariance matrix is no longer calculable using the Hess matrix. This is a general critique of the BANFF fit postfit error estimates since there are non-Gaussian priors for many of the cross section parameters. Instead, bootstrap methods could be employed to infer the parameter covariances. This is further discussed in the following reference [47].

7.3 Future Prospects

There are potential improvements in a “joint” PØD+FGD BANFF fit for the T2K experiment. As shown in the previous chapter, the number of neutrino-carbon and neutrino-oxygen events can be increased by including the PØD data. However, since the fits were performed on different T2K run periods, an equal POT exposure comparison is useful here. Proposing to run a “joint” PØD+FGD ND constraint using T2K runs 2 - 8, the updated neutrino-nucleus exposures are given in Table 7.1 on page 206. We see that while the number of neutrino-carbon events is still larger in the PØD. However, the PØD has 25% fewer neutrino-oxygen events in FHC mode and 9% more in RHC mode. We can estimate the fractional statistical error (δN) reduction in a joint fit using the data from Table 7.1 on page 206 assuming the FGD fit is the nominal ND constraint. The fractional errors decrease approximately by

$$\begin{aligned}
\delta N_{^{12}C}^{\text{FGD1-FHC}} &= \frac{1}{\sqrt{N_{^{12}C}^{\text{FGD1-FHC}}}} \xrightarrow{+\text{PØD Air}} \frac{1}{\sqrt{(1 + 2.01)N_{^{12}C}^{\text{FGD1-FHC}}}} \sim \frac{1}{\sqrt{3.0}} \\
\delta N_{^{16}O}^{\text{FGD2-FHC}} &= \frac{1}{\sqrt{N_{^{16}O}^{\text{FGD2-FHC}}}} \xrightarrow{+\text{PØD Water}} \frac{1}{\sqrt{(1 + 0.72)N_{^{12}C}^{\text{FGD1-FHC}}}} \sim \frac{1}{\sqrt{1.7}} \\
\delta N_{^{12}C}^{\text{FGD1-RHC}} &= \frac{1}{\sqrt{N_{^{12}C}^{\text{FGD1-RHC}}}} \xrightarrow{+\text{PØD Air}} \frac{1}{\sqrt{(1 + 1.60)N_{^{12}C}^{\text{FGD1-RHC}}}} \sim \frac{1}{\sqrt{2.6}} \\
\delta N_{^{16}O}^{\text{FGD2-RHC}} &= \frac{1}{\sqrt{N_{^{16}O}^{\text{FGD2-RHC}}}} \xrightarrow{+\text{PØD Water}} \frac{1}{\sqrt{(1 + 1.04)N_{^{12}C}^{\text{FGD2-RHC}}}} \sim \frac{1}{\sqrt{2.0}},
\end{aligned}$$

where combinations of FGD1/2 and FHC/RHC represent the FGD in the different beam modes, and an right-point arrow indicates adding the PØD data. These results indicate a fractional statistical error reductions around $1/\sqrt{2}$ for both neutrino-oxygen events and also potentially stronger flux constraint from higher statistics.

Detector	POT (10^{20})		kg POT (10^{24})	PØD-to-FGD (kg POT)		
	FHC	RHC		^{12}C	^{16}O	other
PØD Water-out FGD1	7.872	-	2.81	2.01	-	4.64
	11.529	-	1.14			
PØD Water-In FGD2	3.657	-	2.00	5.36	0.724	4.06
	11.529	-	1.12			
PØD Water-out FGD1	-	3.382	1.207	1.60	-	3.69
	-	6.234	0.614			
PØD Water-In FGD2	-	2.852	1.56	7.72	1.04	5.85
	-	6.234	0.606			

Table 7.1: Neutrino-nucleon exposure on target elements in a joint PØD and FGD analysis using T2K runs 2 - 8. The original numbers can be found in Table 6.1 on page 183.

Employing both the FGD and PØD in a joint BANFF fit has been attempted during the validation of the results. This requires updating to the newer canonical T2K 2018 cross section parameterization which impairs the ability to compare between fits. Also including both detectors more than doubles the number of parameters and events than for a single detector-only fit. The FGD run periods are also expanded to runs 7 and 8. With more events and parameters, computational limits are already occurring. On a modest high performance computing setup, the fit time for the “Asimov” fit which starts at the likelihood minimum already, required two weeks to complete, or about 10 times longer than the PØD-only Asimov fit. *The joint data fit also did not converge since it ran into machine precision limits.* So possible improvements must be considered if both computational speed and maximum statistical power are desired in the BANFF fit.

Looking forward into the future, this analysis can be improved on significantly. Firstly, the selections are simplistic compared to the recent developments in the T2K experiment. The author was a part of the second generation cross section analysis of single pion production in the PØD, which utilized deep learning techniques, to select a relatively pure CC-1 π sample. Additionally, the PØD $\bar{\nu}_\mu$ CC-0 π analysis was able to achieve a high-purity CCQE-like sample using almost identical cuts as presented in this thesis. However, both analyses use cuts not yet available in the BANFF framework due to technical difficulties and lack of expertise in the collaboration.

Secondly, more validation studies could be done to understand the sensitivity of the samples. A test of the biases of the fit parameters require fitting an ensemble of “fake data” sets, which are normal variations of the Asimov set. This requires significant amount of computational time to complete, and not to mention the potential carbon footprint left afterwards.

Bibliography

- [1] K. Abe et al. The T2K Experiment. *Nucl. Instrum. Meth.*, A659:106–135, 2011. 26, 29, 31, 34, 37, 41, 45, 46
- [2] K. Abe et al. Measurements of the T2K neutrino beam properties using the INGRID on-axis near detector. *Nucl. Instrum. Meth.*, A694:211–223, 2012. 36, 37
- [3] K. Abe et al. Observation of Electron Neutrino Appearance in a Muon Neutrino Beam. *Phys. Rev. Lett.*, 112:061802, 2014. 27
- [4] K. Abe et al. Measurements of neutrino oscillation in appearance and disappearance channels by the T2K experiment with 6.6×10^{20} protons on target. *Phys. Rev. D*, 91:072010, April 2015. 53, 63
- [5] K. Abe et al. Measurement of Coherent pi(+) Production in Low Energy Neutrino-Carbon Scattering. *Phys. Rev. Lett.*, 117(19), NOV 4 2016. 130
- [6] K. Abe et al. Measurement of neutrino and antineutrino oscillations by the T2K experiment including a new additional sample of ν_e interactions at the far detector. *Phys. Rev. D*, 96(9), NOV 21 2017. 49, 54, 99, 109, 141
- [7] K. Abe et al. Measurement of ν_μ and $\bar{\nu}_\mu$ charged current inclusive cross sections and their ratio with the T2K off-axis near detector. *Phys. Rev. D*, 96(5), September 2017. 44, 61, 64

- [8] K. Abe et al. First measurement of the ν_μ charged-current cross section on a water target without pions in the final state. *Phys. Rev. D*, 97:012001, January 2018. 61, 62, 64, 67, 110, 111
- [9] K. Abe et al. Search for CP Violation in Neutrino and Antineutrino Oscillations by the T2K Experiment with 2.2×10^{21} Protons on Target. *Phys. Rev. Lett.*, 121:171802, October 2018. 27, 126
- [10] K. Abe et al. First Measurement of the Anti-NuMu Charge Current Double Differential Cross Section on Water without Pions in the Final State. *Phys. Rev. D.*, Forthcoming. 61
- [11] N. Abgrall et al. Measurements of π^\pm , K^\pm , K_S^0 , Λ and proton production in proton-carbon interactions at 31 GeV/c with the NA61/SHINE spectrometer at the CERN SPS. *Eur. Phys. J. C*, 76:84, 2016. 50, 98
- [12] M. A. Acero et al. New constraints on oscillation parameters from ν_e appearance and ν_μ disappearance in the NOvA experiment. *Phys. Rev. D*, 98:032012, Aug 2018. 26
- [13] C. Adams et al. The Long-Baseline Neutrino Experiment: Exploring Fundamental Symmetries of the Universe. 2013. arXiv:1307.7335. 3, 22, 25
- [14] S. Agostinelli et al. GEANT4: A Simulation toolkit. *Nucl. Instrum. Meth.*, A506:250–303, 2003. 71
- [15] P. A. Amaudruz et al. The T2K Fine-Grained Detectors. *Nucl. Instrum. Meth.*, A696:1–31, 2012. 183
- [16] J. Arafune et al. CP violation and matter effect in long baseline neutrino oscillation experiments. *Phys. Rev. D*, 56:3093–3099, September 1997. 24
- [17] S. Assylbekov. *Measurement of ν_μ -induced charged-current single π^+ production on H20*. PhD thesis, Colorado State University, Fort Collins, 2014. 217, 221

- [18] S. Assylbekov et al. The T2K ND280 Off-Axis Pi-Zero Detector. *Nucl. Instrum. Meth.*, A686:48–63, 2012. 111
- [19] S. Baker et al. Clarification of the use of Chi-Square and Likelihood Functions in Fits to Histograms. *Nucl. Instrum. Meth.*, A221:437–442, 1983. 55
- [20] O. Benhar et al. Spectral function of finite nuclei and scattering of GeV electrons. *Nucl. Phys.*, A579:193–517, 1994. 127
- [21] Ch. Berger and L. M. Seghal. Lepton mass effects in single pion production by neutrinos. *Phys. Rev. D*, 76:113004, December 2007. 129, 130
- [22] S. Bienstock et al. Constraining the Flux and Cross Section Models with Data from the ND280 Detector using FGD1 and FGD2 for the 2017 Joint Oscillation Analysis, 2017. T2K-TN-324. 98, 185, 292
- [23] R. Bradford et al. A new parameterization of the nucleon elastic form factors. *Nucl. Phys.*, B159(127), 2006. 127
- [24] T. Campbell. *Measurement of the muon anti-neutrino charged current double differential cross section with no pions in the final state on water using the pi-zero detector at T2K*. PhD thesis, Colorado State University, Fort Collins, Colorado, USA, 2018. 61, 62, 68
- [25] T. Campbell et al. Analysis of ν_μ Charged Current Inclusive Events in the PØD in Runs 1+2+3+4, March 2014. T2K-TN-80 v4. 65
- [26] T. Campbell et al. The ANuMu/NuMu Cross Sections Ratio With the P0D+TPC Samples, 2017. 65, 111, 112
- [27] J-PARC Center. What is J-PARC?, January 2019. <https://j-parc.jp/researcher/en/about/what/index.html>, Accessed on 26 January 2019. 29
- [28] L. H. Chan et al. Nucleon Form Factors and Their Interpretation. *Phys. Rev.*, 141:1298–1307, January 1966. 127

- [29] A. Chulliat et al. The US/UK World Magnetic Model for 2015-2020. Technical report, National Geophysical Data Center, NOAA, 2015. 39
- [30] B. T. Cleveland et al. Measurement of the Solar Electron Neutrino Flux with the Homestake Chlorine Detector. *Astronomical Journal*, 496:505–526, March 1998. 13
- [31] G. Co'. Random phase approximation and neutrino-nucleus cross sections. *Acta Phys. Polon.*, B37:2235–2242, 2006. 127
- [32] G. Cowan et al. Asymptotic formulae for likelihood-based tests of new physics. *Eur. Phys. J.*, C71:1554, 2011. [Erratum: Eur. Phys. J.C73,2501(2013)]. 136
- [33] R. Das. *Measurement of NuMu induced charged current inclusive cross section on water using the near detector of the T2K experiment*. PhD thesis, Colorado State University, Fort Collins, Colorado, USA, 2016. 61, 64
- [34] A. de Gouvea et al. Working Group Report: Neutrinos. In *Proceedings, 2013 Community Summer Study on the Future of U.S. Particle Physics: Snowmass on the Mississippi*, 2013. arXiv:1310.4340. 22
- [35] I. Esteban et al. Global analysis of three-flavour neutrino oscillations: synergies and tensions in the determination of θ_{23} , δ_{CP} , and the mass ordering. 2018. arXiv:1811.05487. 23
- [36] R. T. Farouki. The Bernstein polynomial basis: A centennial retrospective. *Computer Aided Geometric Design*, 29(6):379–419, 2012. 129
- [37] A. Ferrero. The ND280 Near Detector of the T2K Experiment. *AIP Conference Proceedings*, 1189(1):77–82, 2009. 26
- [38] J. A. Formaggio and G. P. Zeller. From eV to EeV: Neutrino Cross Sections Across Energy Scales. *Rev. Mod. Phys.*, 84:1307–1341, 2012. 50, 51

- [39] Jerome Friedman et al. Regularization Paths for Generalized Linear Models via Coordinate Descent. *Journal of Statistical Software, Articles*, 33(1):1–22, 2010. 202
- [40] S. Fukuda et al. The Super-Kamiokande detector. *Nucl. Instrum. Meth. A*, 501(2):418–462, 2003. 26
- [41] T. Golan et al. Final State Interactions Effects in Neutrino-Nucleus Interactions. *Phys. Rev. C*, 86:015505, 2012. 131
- [42] K. M. Graczyk et al. C_A^5 axial form factor from bubble chamber experiments. *Phys. Rev.*, D80:093001, 2009. 129
- [43] K. M. Graczyk et al. Electroweak form factors of the $\Delta(1232)$ resonance. *Phys. Rev. D*, 90:093001, November 2014. 129
- [44] K. M. Graczyk and J. T. Sobczyk. Form factors in the quark resonance model. *Phys. Rev. D*, 77:053001, March 2008. 129
- [45] K. M. Graczyk and J.T. Sobczyk. Lepton mass effects in weak charged current single pion production. *Phys. Rev. D*, 77:053003, March 2008. 129
- [46] M. Hartz et al. Constraining the Flux and Cross Section Models with Data from the ND280 Detector for the 2014/15 Oscillation Analysis. Technical report, T2K Collaboration, May 2015. T2K-TN-220 v4. 56
- [47] T. Hastie et al. *The Elements of Statistical Learning: Data Mining, Inference, and Prediction*. Springer Series in Statistics. Springer New York, New York, NY, 2009. 95, 126, 199, 201, 204
- [48] T. Hastie et al. *Statistical Learning with Sparsity: The Lasso and Generalizations*. Chapman and Hall/CRC monographs on statistics and applied probability. CRC Press, Taylor and Francis Group, Boca Raton, 2015. 203

- [49] Y. Hayato. A neutrino interaction simulation program library NEUT. *Acta Phys. Polon.*, B40:2477–2489, 2009. 50
- [50] A. Hoecker et al. TMVA: Toolkit for Multivariate Data Analysis. *PoS*, ACAT:040, 2007. 218
- [51] C. Jarlskog. A Basis Independent Formulation of the Connection Between Quark Mass Matrices, CP Violation and Experiment,. *Z. Phys.*, C29:491–497, 1985. 23
- [52] T. Kitagaki et al. Charged-current exclusive pion production in neutrino-deuterium interactions. *Phys. Rev. D*, 34:2554–2565, November 1986. 129
- [53] E. Komatsu et al. Seven-year Wilkinson Microwave Anisotropy Probe (WMAP) Observations: Cosmological Interpretation. *Astrophys. J.*, 192:18, February 2011. 25
- [54] C. H. Llewellyn Smith. Neutrino Reactions at Accelerator Energies. *Phys. Rept.*, 3:261–379, 1972. 127
- [55] F. Lodovico and P. Martins. Measurement of the Charged Current CoherentPion Production Cross-Section on Carbon andOxygen using the ND280 tracker. Technical report, T2K Collaboration, 2017. T2K-TN-290. 183
- [56] A. Longhin et al. Measurement of the inclusive charged-current numu cross section in plastic using the ND280 tracker Run 5c data. Technical report, T2K Collaboration, 2016. T2K-TN-249v8. 183
- [57] Z Maki et al. Remarks on the Unified Model of Elementary Particles. *Progr. Theor. Exp. Phys.*, 28(5), 1962. 18
- [58] M. Martini et al. A Unified approach for nucleon knock-out, coherent and incoherent pion production in neutrino interactions with nuclei. *Phys. Rev.*, C80:065501, 2009. 73, 127

- [59] J. Nieves et al. Inclusive Charged–Current Neutrino–Nucleus Reactions. *Phys. Rev.*, C83:045501, 2011. 127, 128
- [60] K. Niewczas and J.T. Sobczyk. Search for nucleon-nucleon correlations in neutrino-argon scattering. *Phys. Rev.*, C93(3):035502, 2016. 127
- [61] B. Pontecorvo. Inverse Beta Processes and Nonconservation of Lepton Charge. *J. Exp. Theor. Phys.*, 28(5), 1957. 18
- [62] B. Pontecorvo. Mesonium and Anti-Mesonium. *Sov. Phys. JETP*, 6:429, 1957. 14
- [63] G. M. Radecky et al. Study of single-pion production by weak charged currents in low-energy νd interactions. *Phys. Rev. D*, 25:1161–1173, March 1982. 129
- [64] D. Rein and L. M. Sehgal. Neutrino-excitation of baryon resonances and single pion production. *Ann. Phys.*, 133(1):79–153, 1981. 129
- [65] D. Rein and L. M. Sehgal. Coherent π^0 production in neutrino reactions. *Nucl. Phys. B*, 223(1):29–44, 1983. 130
- [66] G. Rowe et al. Energy-dependent phase shift analysis of pion-nucleon scattering below 400 MeV. *Phys. Rev. C*, 18:584–589, July 1978. 131
- [67] P. K. Saha et al. Simulation, measurement, and mitigation of beam instability caused by the kicker impedance in the 3-GeV rapid cycling synchrotron at the Japan Proton Accelerator Research Complex. *Phys. Rev. Accel. Beams*, 21:024203, February 2018. 30
- [68] Andrei D Sakharov. Violation of CP invariance, C asymmetry, and baryon asymmetry of the universe. *Soviet Physics Uspekhi*, 34(5):392, 1991. 25
- [69] L.L. Salcedo et al. Computer simulation of inclusive pion nuclear reactions. *Nucl. Phys. A*, 484(3):557–592, 1988. 131

- [70] J. Schechter and J. W. F. Valle. Neutrinoless double- β decay in $SU(2) \times U(1)$ theories. *Phys. Rev. D*, 25:2951–2954, 1982. 20
- [71] N. Schmitz. *Neutrinophysik*. Teubner, Stuttgart, 1997. 19
- [72] J. Schwehr et al. Measurement of the ν_μ CC1 π^+ Differential Cross Sections in μ Momentum and Angle in the P0D, Ocotober 2018. TN-333. 51
- [73] Jaclyn Schwehr. *Measurement of the Differential Charged Current Single Pion Cross Section Using Muon Momentum and Muon Angle In the Pi Zero Detector of the T2K Experiment*. PhD thesis, Colorado State University, Fort Collins, Colorado, 2018. 183, 217, 218, 221
- [74] T. Sekiguchi et al. Development and operational experience of magnetic horn system for T2K experiment. *Nucl. Instrum. Meth. A*, 789:57–80, 2015. 31
- [75] R.A. Smith and E.J. Moniz. Neutrino reactions on nuclear targets. *Nucl. Phys. B*, 43:605–622, 1972. 127
- [76] Alfonso Andrés García Soto. *Study of the ν_μ interactions via charged current in the T2K near detector*. PhD thesis, Universitat Autònoma de Barcelona, 2017. 64
- [77] M. Tanabashi et al. The Review of Particle Physics. *Phys. Rev. D*, 98(030001), 2018. 20, 23
- [78] R. Tibshirani et al. Diagnosis of multiple cancer types by shrunken centroids of gene expression. *Proceedings of the National Academy of Sciences of the United States of America*, 99(10):6567–6572, MAY 14 2002. 202
- [79] W. Toki. Update of P0D Inspection. Private communication, June 2016. 111
- [80] P. von Ballmoos. Antimatter in the Universe: Constraints from Gamma-Ray Astronomy. *Hyperfine Interact.*, 228(1):91–100, October 2014. 24

- [81] G. Welch and G. Bishop. An Introduction to the Kalman Filter. Technical Report 95041, University of North Carolina at Chapel Hill, Chapel Hill, NC 27599-3175, July 2006. A description of the mathematics involved in the Kalman filer. 63
- [82] L. Wolfenstein. Neutrino oscillations in matter. *Phys. Rev. D*, 17:2369–2374, May 1978. 23
- [83] Carl Vincent Clarence Wret. *Minimising Systematic Uncertainties in the T2K Experiment Using Near-Detector and External Data*. PhD thesis, Imperial College London, 2019. 98, 108, 109, 127, 128, 130
- [84] Y. Yamazaki. Accelerator technical design report for high-intensity proton accelerator facility project, J-PARC. Report 2002-013, KEK, 2003. 30
- [85] T. Yang. *A Study of Muon Neutrino to Electron Neutrino Oscillations in the MINOS Experiment*. PhD thesis, Stanford University, 2009. 219
- [86] T. Yuan et al. Double Differential Measurement of the Flux Averaged ν_μ CC0Pi Cross Section on Water, August 2016. T2K-TN-258 v4.6.1. 117
- [87] Kai Zuber. *Neutrino Physics*. CRC Press, Boca Raton, FL., 2nd edition, 2012. 1, 13, 18, 26

Appendix A

Contributions to the PØD CC- π Analysis

Prior to the work on the near detector constraint, I participated in the PØD ν_μ CC- π cross section on water analysis. This was a second generation analysis designed to make significant improvements to the first generation analysis, which was a single bin measurement [17]. The primary goal of the analysis was to provide a differential measurement in muon kinematics. The challenges now were to identify the muon and pion while measuring their respective momenta. The results of the analysis are given in the following thesis [73] and a publication is in preparation.

My primary contributions to the analysis included developing the particle identification (PID) tools and momentum calibration for muon and pion tracks. Machine learning based selection cuts were added in the analysis chain that were exclusively designed to exploit the PØD local reconstruction since the ND280 global reconstruction was not available during development. These selection cuts provided the means to make PID cuts to select only one muon and one pion in a two track event. To provide a differential cross section measurement in the muon kinematics, a momentum measurement was developed and calibrated for the analysis.

The first section describes my contributions to the development of the machine learning PID tools. The second section includes the description of the momentum measurement and calibration method.

A.1 Particle Identification Tools

Since there are no particle identification (PID) tools in the local PØD reconstruction, the PØD CC- 1π analysis developed a unique set of tools were designed specifically to select muon and pion tracks. These details are explained in further detail in the following thesis [73]. The approach taken by this analysis was to use machine learning techniques for event selection and PID for each track. Only reconstructed topological information were used to minimize interaction vertex model and detector model dependencies.

Machine learning is a rapidly developing field of study in which a computer system can perform a certain task without explicit instructions. For classification based problems, the goal is to assign two or more labels to a set of input vectors. Training a classifier requires a sample of pre-classified data to determine which attributes of each datum can be used to best separate data of unknown classification. Unclassified data are then assigned a classification based on their position in attribute space.

The specific machine learning technique used in this analysis is a random forest method called Boosted Decision Tree (BDT) implemented in the ROOT Toolkit for Multivariate Analysis (TMVA) package [50]. A decision tree is a binary tree classifier that applies rectangular cuts on inputs features until a stop condition is reached. In order to prevent model overfitting to the training set, a set of decision trees (forest) are generated by scaling misclassified events by a “boost” weight. By averaging the results over the forest, an enhancement of the model performance is achieved.

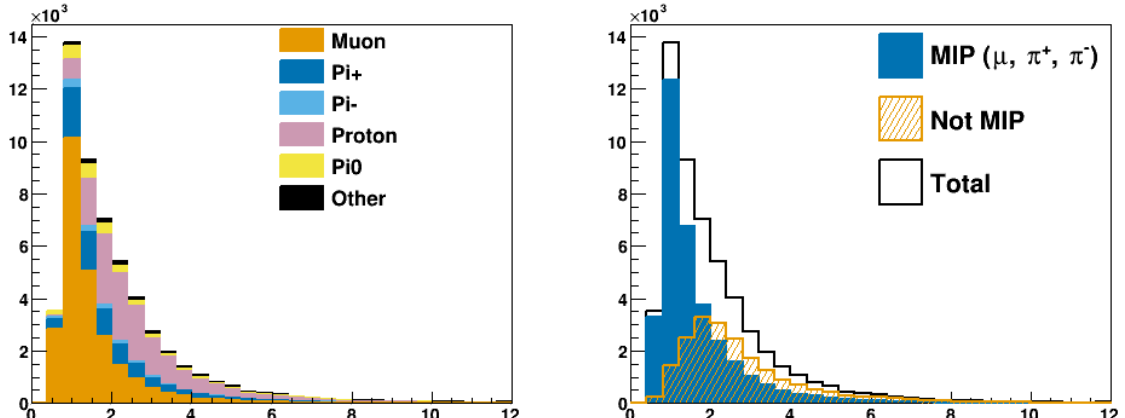
The inputs for the BDTs were developed from topological track information in both the longitudinal and transverse directions of PØD tracks. A traditional longitudinal track mea-

surement is the mean energy deposition in a tracking calorimeter or TPC, or the “ dE/dx ” of the track. The idea behind using topological information is that they reduce neutrino interaction model dependence. This should also minimize the detector model dependence assuming the detector systematics have been studied sufficiently with control samples. The inputs I developed for the BDTs were motivated from the work done at MINOS to select tracks using machine learning classifiers [85]. Many of the input features provided discriminating power for minimizing ionizing particle (MIP) tracks from other non-MIP particle tracks like protons. Examples of the longitudinal and transverse topological features I developed are shown in Figure A.1.

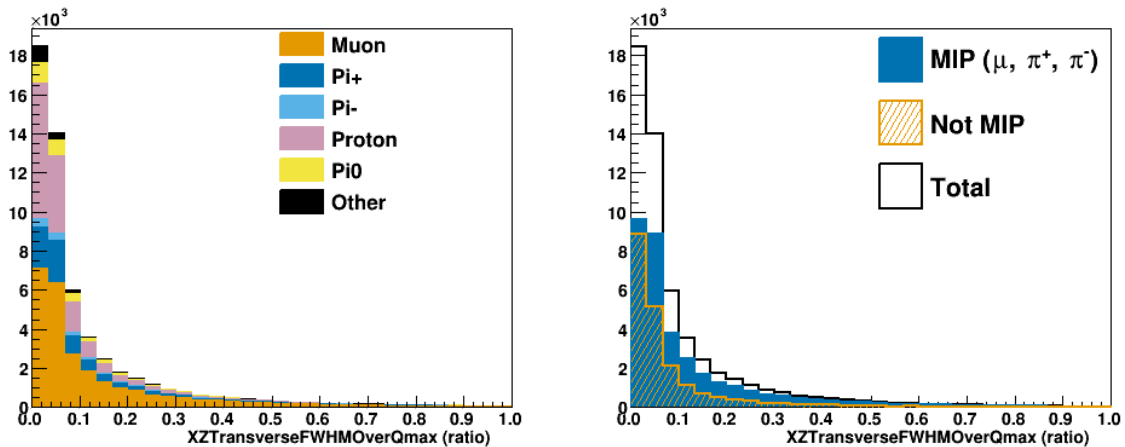
The CC-1 π analysis used two BDTs classifiers to make event selections. The first classifier provided a continuous discriminator to classify tracks as MIP-like or not. Selected events are those that have two MIP tracks. The second BDT classifier helps assign which track is the muon and pion using a likelihood cut describe.

In developing the BDT classifiers, cross validation studies were performed to identify the best input features. Cross validation is a model validation technique that assess how the model generalizes to independent data sets. In particular, the model is trained on a “training” set and it evaluated on a “testing” set to ensure the results are similar between them. The training and testing sets were equally populated using random sampling of the input data. This is especially important since I needed to perform data imputation for any missing information in the training, which can affect the results of the model. The chosen method of data imputation was to assign a handpicked default value based on feature distribution.

Also in the cross validation procedure, variable selection was determined by training models with and without the variable to assess the variable’s importance. A variable was removed from the final BDT model if removing it had minimal impact on the receiver operating characteristic curve, which is a diagnostic on the performance of a binary classifier.



(a) Longitudinal feature



(b) Transverse feature

Figure A.1: Topological track features developed for the machine learning classifier cuts. The top figure shows a longitudinal feature and the bottom shows a transverse feature. The left figures categorize tracks by their particle species while the right figures consider MIP and not-MIP distinctions.

Selection	Total events	Signal events	Purity	Efficiency
After pre-selection	6258.6	1278.2	0.204	0.269
One MIP-like track	3533.3	998.4	0.283	0.210
Selected signal	970.2	598.7	0.617	0.126
“Near” sideband	757.3	255.7	0.338	0.0538
“Far” sideband	1805.8	144.0	0.0798	0.0303

Table A.1: Selection statistics for the CC-1 π analysis. For each event passing the pre-selection cuts, to select ν_μ events, there must be one muon-like track passing the MIP BDT. The result of the second track MIP BDT determined if it was selected as a CC-1 π event or a sideband event. Two sidebands, labeled “near” and “far”, were used to help constrain backgrounds in the analysis [73].

This procedure dramatically reduced the number of input features selected in the BDT models.

The selection purity and efficiency for the analysis are shown in Table A.1 on page 221. Compared to the first generation analysis, the selected signal efficiency increased by a factor of two from around 6% to 12%, and the its purity also increased from 50% to 61% [17].

A.2 Momentum Reconstruction

The algorithm to reconstruct particle momentum in CC- 1π analysis integrates the average energy deposition per unit of areal density along the track through the PØD. The path of the track is determined by the energy depositions in each scintillator plane of the PØD associated with the reconstructed track object. The integration for contained tracks is done starting at the end of the reconstructed track, where the momentum is assumed to be close to zero to the start position of the reconstructed track. In cases where the track exits the PØD into TPC1, the momentum calculated by TPC1 is used as the starting momentum and the integration begins at the point where the track exited the PØD. (For this discussion the downstream ECal is considered to be part of the PØD, and the difference in areal density is taken into consideration.) Events with tracks that exit the PØD but do not enter TPC1 (do not have a matched track in TPC1) are excluded from the analysis.

Relativistic particles will generally deposit energy as Minimum Ionizing Particles (MIPs) as characterized by the Bethe-Bloch curve in (A.1)

$$-\frac{dT}{dx} = K z^2 \frac{Z}{A} \frac{1}{\beta^2} \left[\frac{1}{2} \ln \left(\frac{2m_e c^2 (\beta \gamma)^2 T_{\max}}{I^2} \right) - \beta^2 - \frac{\delta(\beta \gamma)}{2} \right] \quad (\text{A.1})$$

with

$$T_{\max} = \frac{2m_e c^2 (\beta \gamma)^2}{1 + 2\gamma \frac{m_e}{M} + \left(\frac{m_e}{M} \right)^2}$$

where T is the kinetic energy, x is the distance traveled, K is proportional to the material density, I is the mean excitation potential in eV, z is the charge, c is the speed of light, M is the rest mass of the particle, m_e is the rest mass of the electron, β is the velocity as a fraction of c , and γ is the Lorentz relativistic factor $(1 - \beta^2)^{-0.5}$. Both muons ($m_\mu = 105.6 \text{ MeV}/c^2$) and pions ($m_\pi = 139.5 \text{ MeV}/c^2$) are relativistic at the energies required to be detected and reconstructed by the PØD.

A.2.1 Momentum Tool

The Momentum Tool (MT), the collection of functions that estimate a particle's momentum in the PØD, was initially developed to estimate the kinetic energy of protons fully contained in the PØD. The MT estimated the proton's momentum by summing up the assumed ionization energy loss in each material traversed over the range of the track in the PØD. Stopping power data for different materials came from the NIST PSTAR catalog as a function of kinetic energy. The MT was extended to measurements of muon and pion momenta for tracks originating in the PØD and entering TPC1. The extension involved converting kinetic energy to $\beta\gamma = p/(Mc)$, the dimensionless quantity of a particle's momentum divided by its mass.

The starting kinetic energy for the MT is given by (A.2),

$$T_{i,\alpha} = \begin{cases} \sqrt{(p_{\text{TPC1}}c)^2 + (m_\alpha c^2)^2} - m_\alpha c^2 & \text{if } p_{\text{TPC1}} \neq 0 \\ \epsilon_\alpha & \text{otherwise} \end{cases} \quad (\text{A.2})$$

where the index α denotes either a muon, proton, or pion. The starting kinetic energy ϵ for muons and pions is 30 MeV and for protons is 50 MeV. A study showed that the resulting momentum distributions for the muon and pion did not change when using a starting point smaller than 30 MeV.

The MT steps through the PØD along the path defined by a collection of track-nodes. A track-node is a collection of time-correlated hits inside active material with charged-weighted position and direction. The direction vector points to the next node except in the case of the last track-node, in which case, it uses the previous node's direction. The positions of two successive nodes and the associated direction vector determine the angle, θ , of the track w.r.t. the PØD z-axis. The MT numerically integrates the energy loss for each material traversed in the following manner,

$$\Delta T = \left(\frac{dT}{d\rho_A} \right)_{\text{mat}} (\Delta\rho_A)$$

$$T \rightarrow T + \Delta T$$

where the index “mat” represents each material in the path, ρ_A is the areal density, and $\Delta\rho_A$ is a small step of 0.05 gram/cm² in areal density. Each $\Delta\rho_A$ step in $dT/d\rho_A$ is evaluated at the point $\beta\gamma = (\beta\gamma)_0 + \Delta(\beta\gamma)/2$ where $(\beta\gamma)_0$ is the value of $\beta\gamma$ for a single particle of kinetic energy T and $\Delta(\beta\gamma)$ is the density correction term from (A.1).

A.2.2 Momentum Calibration

The muon and pion track momenta were calibrated for all the track topologies in the analysis. To not bias the calibration to NEUT generator kinematics, the muon and pion tracks were selected from true events passing the particle identification cuts. Additionally, calibration training samples were extracted using subsets of the monte carlo (MC). Specifically, about 1.16×10^{21} POT from both water-in and water-out MC were used. This is about $5\times$ and $3\times$ the data statistics for water-in and water-out modes, respectively, in the measurement.

A bias subtraction method is applied on each track to calibrate to the true momentum. To characterize the momentum bias, a two-dimensional histogram of the true-vs-reconstructed momenta over the full particle’s phase-space is created and used to generate a profile histogram of the momentum bias as a function of the reconstructed momentum. This profile histogram is also constructed with each bin to have approximately equal statistics so as to minimize the impact of statistical fluctuations. The profile is then carefully examined for features, such as tails, maxima, or minima, in order to characterize the shape with a function. Next a closed form function that reasonably describes the shape of the bias is identified. The metric for a determining if the chosen function is “adequate” is to require at least four bins in the profile and that a chi-squared fit value is similar to the number of

degrees of freedom. Once the suitable functional form, R , is fitted to the profile histogram, the calibrated momentum, p_c is calculating using (A.3)

$$p_c = [1 - R(p_r)] \times p_r \quad (\text{A.3})$$

where p_r is the uncalibrated, raw momentum.

To illustrate the method of calibration, the calibration method for true CC-1 π muon tracks fully contained in the PØD is shown in Figure A.2. There is better agreement between the true and reconstructed momenta, but additional variance is introduced. The increase in the variance is expected since a bias corrections will introduce a larger spread to the momentum distribution. The calibration function for this set is given by

$$R(p_r [\text{GeV}/c]) = 0.02955 + \frac{0.045662}{1 + \exp[-24.61(p_r - 0.4415)]}$$

and is shown in Figure A.3.

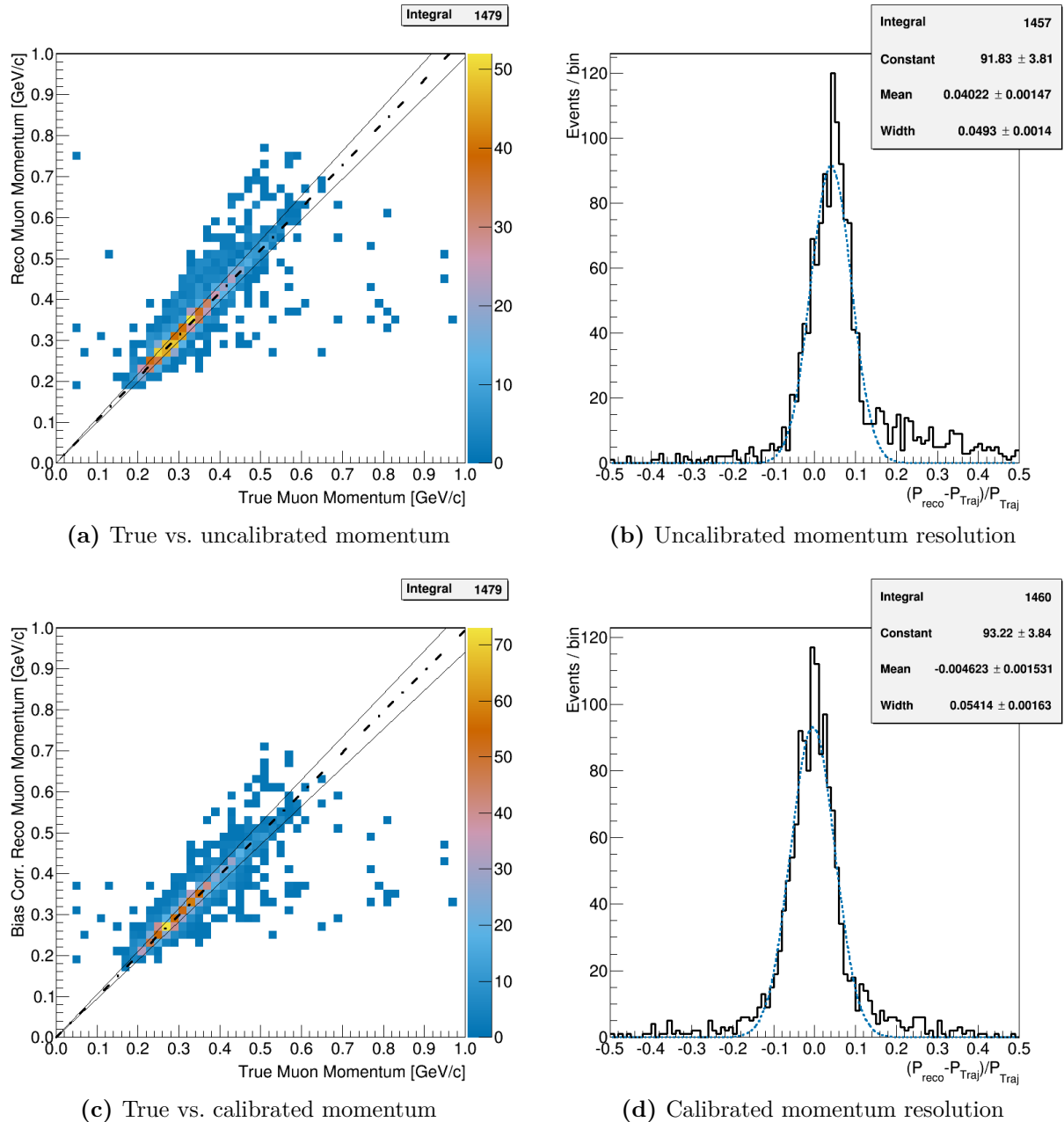


Figure A.2: The momentum for true muon tracks events before (top) and after (bottom) the calibration. These muon tracks are fully contained in the PØD and are fitted using an algorithm aided by a Kalman filter in the PØD reconstruction. The plots on the left are scatter plots of the true vs. reconstructed momentum while the right plots show the resolution of the momentum. After the calibration, the muon tracks have nearly no bias, but at the cost of some additional variance as indicated by the Gaussian fits in (b) and (d). The extracted Gaussian fit mean and standard deviation are shown as dashed-dot and solid lines, respectively, in (a) and (c).

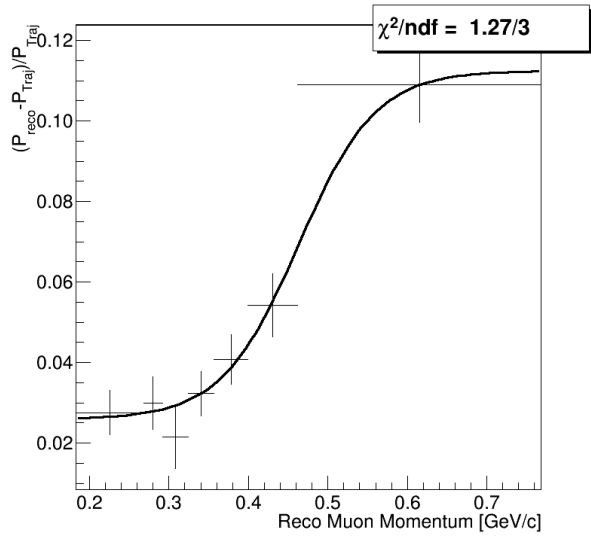


Figure A.3: The profile histogram for the momentum resolution as function of the reconstructed momentum for PØD water-in contained muons. The smooth black curve is a characterization using a logistic function. Each bin in the profile has equal statistics to minimize statistical fluctuations.

Appendix B

The PØD-Only Bin Normalization Parameters

The observable normalizations used in the PØD-only BANFF fit are tabulated here.

Table B.1: Observable normalization fit bins.

Fit Index	Sample	p [GeV/c]	$\cos\theta$	Prefit
100	ν_μ 1-Trk Wtr	$0 \leq p < 0.40$	$-1 \leq \cos\theta < 0.70$	1.21 ± 0.67
101		$0.40 \leq p < 0.60$	$-1 \leq \cos\theta < 0.70$	0.87 ± 0.18
102		$0.60 \leq p < 0.80$	$-1 \leq \cos\theta < 0.70$	1.12 ± 0.44
103		$0.80 \leq p < 1.25$	$-1 \leq \cos\theta < 0.70$	1.13 ± 0.43
104		$1.25 \leq p < 2.00$	$-1 \leq \cos\theta < 0.70$	1.02 ± 0.17
105		$2.00 \leq p < 3.00$	$-1 \leq \cos\theta < 0.70$	0.93 ± 0.20
106		$3.00 \leq p < 4.00$	$-1 \leq \cos\theta < 0.70$	1.00 ± 0.28
107		$4.00 \leq p < 5.50$	$-1 \leq \cos\theta < 0.70$	0.82 ± 0.33
108		$5.50 \leq p < 30$	$-1 \leq \cos\theta < 0.70$	1.26 ± 0.58
109		$0 \leq p < 0.40$	$0.70 \leq \cos\theta < 0.80$	1.27 ± 0.74
110	ν_μ 1-Trk Wtr	$0.40 \leq p < 0.60$	$0.70 \leq \cos\theta < 0.80$	0.89 ± 0.18
111		$0.60 \leq p < 0.80$	$0.70 \leq \cos\theta < 0.80$	1.02 ± 0.27

Fit Index	Sample	p [GeV/c]	$\cos\theta$	Prefit
112		$0.80 \leq p < 1.25$	$0.70 \leq \cos\theta < 0.80$	1.09 ± 0.33
113		$1.25 \leq p < 2.00$	$0.70 \leq \cos\theta < 0.80$	1.02 ± 0.17
114		$2.00 \leq p < 3.00$	$0.70 \leq \cos\theta < 0.80$	0.96 ± 0.15
115		$3.00 \leq p < 4.00$	$0.70 \leq \cos\theta < 0.80$	0.99 ± 0.21
116		$4.00 \leq p < 5.50$	$0.70 \leq \cos\theta < 0.80$	0.94 ± 0.29
117		$5.50 \leq p < 30$	$0.70 \leq \cos\theta < 0.80$	1.05 ± 0.53
118		$0 \leq p < 0.40$	$0.80 \leq \cos\theta < 0.94$	1.33 ± 0.78
119		$0.40 \leq p < 0.60$	$0.80 \leq \cos\theta < 0.94$	0.91 ± 0.21
120	ν_μ 1-Trk Wtr	$0.60 \leq p < 0.80$	$0.80 \leq \cos\theta < 0.94$	0.97 ± 0.14
121		$0.80 \leq p < 1.25$	$0.80 \leq \cos\theta < 0.94$	1.03 ± 0.17
122		$1.25 \leq p < 2.00$	$0.80 \leq \cos\theta < 0.94$	1.01 ± 0.09
123		$2.00 \leq p < 3.00$	$0.80 \leq \cos\theta < 0.94$	1.00 ± 0.05
124		$3.00 \leq p < 4.00$	$0.80 \leq \cos\theta < 0.94$	1.00 ± 0.12
125		$4.00 \leq p < 5.50$	$0.80 \leq \cos\theta < 0.94$	0.95 ± 0.15
126		$5.50 \leq p < 30$	$0.80 \leq \cos\theta < 0.94$	0.96 ± 0.38
127		$0 \leq p < 0.40$	$0.94 \leq \cos\theta < 0.97$	1.29 ± 0.73
128		$0.40 \leq p < 0.60$	$0.94 \leq \cos\theta < 0.97$	0.93 ± 0.22
129		$0.60 \leq p < 0.80$	$0.94 \leq \cos\theta < 0.97$	0.96 ± 0.09
130	ν_μ 1-Trk Wtr	$0.80 \leq p < 1.25$	$0.94 \leq \cos\theta < 0.97$	1.02 ± 0.11
131		$1.25 \leq p < 2.00$	$0.94 \leq \cos\theta < 0.97$	1.00 ± 0.07
132		$2.00 \leq p < 3.00$	$0.94 \leq \cos\theta < 0.97$	1.00 ± 0.03
133		$3.00 \leq p < 4.00$	$0.94 \leq \cos\theta < 0.97$	0.99 ± 0.08
134		$4.00 \leq p < 5.50$	$0.94 \leq \cos\theta < 0.97$	1.00 ± 0.14
135		$5.50 \leq p < 30$	$0.94 \leq \cos\theta < 0.97$	0.99 ± 0.20
136		$0 \leq p < 0.40$	$0.97 \leq \cos\theta < 0.99$	1.25 ± 0.65
137		$0.40 \leq p < 0.60$	$0.97 \leq \cos\theta < 0.99$	0.94 ± 0.20

Fit Index	Sample	p [GeV/c]	$\cos\theta$	Prefit
138		$0.60 \leq p < 0.80$	$0.97 \leq \cos\theta < 0.99$	0.95 ± 0.08
139		$0.80 \leq p < 1.25$	$0.97 \leq \cos\theta < 0.99$	1.01 ± 0.11
140	ν_μ 1-Trk Wtr	$1.25 \leq p < 2.00$	$0.97 \leq \cos\theta < 0.99$	1.00 ± 0.07
141		$2.00 \leq p < 3.00$	$0.97 \leq \cos\theta < 0.99$	1.00 ± 0.06
142		$3.00 \leq p < 4.00$	$0.97 \leq \cos\theta < 0.99$	1.00 ± 0.03
143		$4.00 \leq p < 5.50$	$0.97 \leq \cos\theta < 0.99$	0.98 ± 0.10
144		$5.50 \leq p < 30$	$0.97 \leq \cos\theta < 0.99$	0.97 ± 0.14
145		$0 \leq p < 0.40$	$0.99 \leq \cos\theta < 1$	1.25 ± 0.58
146		$0.40 \leq p < 0.60$	$0.99 \leq \cos\theta < 1$	0.93 ± 0.18
147		$0.60 \leq p < 0.80$	$0.99 \leq \cos\theta < 1$	0.96 ± 0.11
148		$0.80 \leq p < 1.25$	$0.99 \leq \cos\theta < 1$	1.01 ± 0.11
149		$1.25 \leq p < 2.00$	$0.99 \leq \cos\theta < 1$	1.01 ± 0.08
150	ν_μ 1-Trk Wtr	$2.00 \leq p < 3.00$	$0.99 \leq \cos\theta < 1$	1.01 ± 0.10
151		$3.00 \leq p < 4.00$	$0.99 \leq \cos\theta < 1$	1.00 ± 0.06
152		$4.00 \leq p < 5.50$	$0.99 \leq \cos\theta < 1$	1.00 ± 0.05
153		$5.50 \leq p < 30$	$0.99 \leq \cos\theta < 1$	0.98 ± 0.10
154	ν_μ N-Trks Wtr	$0 \leq p < 0.40$	$-1 \leq \cos\theta < 0.77$	1.18 ± 0.61
155		$0.40 \leq p < 0.60$	$-1 \leq \cos\theta < 0.77$	0.89 ± 0.15
156		$0.60 \leq p < 0.80$	$-1 \leq \cos\theta < 0.77$	1.01 ± 0.16
157		$0.80 \leq p < 1.20$	$-1 \leq \cos\theta < 0.77$	1.03 ± 0.19
158		$1.20 \leq p < 2.20$	$-1 \leq \cos\theta < 0.77$	1.02 ± 0.15
159		$2.20 \leq p < 3.50$	$-1 \leq \cos\theta < 0.77$	1.04 ± 0.16
160	ν_μ N-Trks Wtr	$3.50 \leq p < 10.0$	$-1 \leq \cos\theta < 0.77$	0.93 ± 0.26
161		$10.0 \leq p < 30$	$-1 \leq \cos\theta < 0.77$	0.94 ± 0.67
162		$0 \leq p < 0.40$	$0.77 \leq \cos\theta < 0.85$	1.13 ± 0.56
163		$0.40 \leq p < 0.60$	$0.77 \leq \cos\theta < 0.85$	0.92 ± 0.15

Fit Index	Sample	p [GeV/c]	$\cos\theta$	Prefit
164		$0.60 \leq p < 0.80$	$0.77 \leq \cos\theta < 0.85$	0.98 ± 0.07
165		$0.80 \leq p < 1.20$	$0.77 \leq \cos\theta < 0.85$	1.00 ± 0.09
166		$1.20 \leq p < 2.20$	$0.77 \leq \cos\theta < 0.85$	1.01 ± 0.08
167		$2.20 \leq p < 3.50$	$0.77 \leq \cos\theta < 0.85$	1.01 ± 0.06
168		$3.50 \leq p < 10.0$	$0.77 \leq \cos\theta < 0.85$	0.98 ± 0.16
169		$10.0 \leq p < 30$	$0.77 \leq \cos\theta < 0.85$	0.98 ± 0.52
170	ν_μ N-Trks Wtr	$0 \leq p < 0.40$	$0.85 \leq \cos\theta < 0.90$	1.13 ± 0.53
171		$0.40 \leq p < 0.60$	$0.85 \leq \cos\theta < 0.90$	0.92 ± 0.14
172		$0.60 \leq p < 0.80$	$0.85 \leq \cos\theta < 0.90$	0.98 ± 0.05
173		$0.80 \leq p < 1.20$	$0.85 \leq \cos\theta < 0.90$	1.00 ± 0.07
174		$1.20 \leq p < 2.20$	$0.85 \leq \cos\theta < 0.90$	1.00 ± 0.06
175		$2.20 \leq p < 3.50$	$0.85 \leq \cos\theta < 0.90$	1.01 ± 0.05
176		$3.50 \leq p < 10.0$	$0.85 \leq \cos\theta < 0.90$	0.99 ± 0.12
177		$10.0 \leq p < 30$	$0.85 \leq \cos\theta < 0.90$	1.03 ± 0.46
178		$0 \leq p < 0.40$	$0.90 \leq \cos\theta < 0.97$	1.13 ± 0.52
179		$0.40 \leq p < 0.60$	$0.90 \leq \cos\theta < 0.97$	0.94 ± 0.13
180	ν_μ N-Trks Wtr	$0.60 \leq p < 0.80$	$0.90 \leq \cos\theta < 0.97$	0.97 ± 0.06
181		$0.80 \leq p < 1.20$	$0.90 \leq \cos\theta < 0.97$	0.99 ± 0.08
182		$1.20 \leq p < 2.20$	$0.90 \leq \cos\theta < 0.97$	1.00 ± 0.07
183		$2.20 \leq p < 3.50$	$0.90 \leq \cos\theta < 0.97$	1.00 ± 0.03
184		$3.50 \leq p < 10.0$	$0.90 \leq \cos\theta < 0.97$	0.99 ± 0.10
185		$10.0 \leq p < 30$	$0.90 \leq \cos\theta < 0.97$	0.98 ± 0.25
186		$0 \leq p < 0.40$	$0.97 \leq \cos\theta < 1$	1.09 ± 0.47
187		$0.40 \leq p < 0.60$	$0.97 \leq \cos\theta < 1$	0.96 ± 0.11
188		$0.60 \leq p < 0.80$	$0.97 \leq \cos\theta < 1$	0.96 ± 0.09
189		$0.80 \leq p < 1.20$	$0.97 \leq \cos\theta < 1$	1.00 ± 0.09

Fit Index	Sample	p [GeV/c]	$\cos\theta$	Prefit
190	ν_μ N-Trks Wtr	$1.20 \leq p < 2.20$	$0.97 \leq \cos\theta < 1$	1.01 ± 0.09
191		$2.20 \leq p < 3.50$	$0.97 \leq \cos\theta < 1$	1.01 ± 0.08
192		$3.50 \leq p < 10.0$	$0.97 \leq \cos\theta < 1$	0.99 ± 0.05
193		$10.0 \leq p < 30$	$0.97 \leq \cos\theta < 1$	0.97 ± 0.13
194	$\bar{\nu}_\mu$ RHC 1-Trk Wtr	$0 \leq p < 0.50$	$-1 \leq \cos\theta < 0.82$	1.00 ± 0.36
195		$0.50 \leq p < 0.60$	$-1 \leq \cos\theta < 0.82$	0.90 ± 0.15
196		$0.60 \leq p < 0.80$	$-1 \leq \cos\theta < 0.82$	1.05 ± 0.26
197		$0.80 \leq p < 1.25$	$-1 \leq \cos\theta < 0.82$	1.04 ± 0.20
198		$1.25 \leq p < 2.00$	$-1 \leq \cos\theta < 0.82$	1.00 ± 0.17
199		$2.00 \leq p < 3.00$	$-1 \leq \cos\theta < 0.82$	1.01 ± 0.17
200	$\bar{\nu}_\mu$ RHC 1-Trk Wtr	$3.00 \leq p < 30$	$-1 \leq \cos\theta < 0.82$	1.00 ± 0.39
201		$0 \leq p < 0.50$	$0.82 \leq \cos\theta < 0.90$	1.06 ± 0.43
202		$0.50 \leq p < 0.60$	$0.82 \leq \cos\theta < 0.90$	0.91 ± 0.13
203		$0.60 \leq p < 0.80$	$0.82 \leq \cos\theta < 0.90$	0.97 ± 0.16
204		$0.80 \leq p < 1.25$	$0.82 \leq \cos\theta < 0.90$	1.04 ± 0.17
205		$1.25 \leq p < 2.00$	$0.82 \leq \cos\theta < 0.90$	1.00 ± 0.11
206		$2.00 \leq p < 3.00$	$0.82 \leq \cos\theta < 0.90$	0.99 ± 0.11
207		$3.00 \leq p < 30$	$0.82 \leq \cos\theta < 0.90$	0.92 ± 0.28
208		$0 \leq p < 0.50$	$0.90 \leq \cos\theta < 0.95$	1.07 ± 0.44
209		$0.50 \leq p < 0.60$	$0.90 \leq \cos\theta < 0.95$	0.93 ± 0.14
210	$\bar{\nu}_\mu$ RHC 1-Trk Wtr	$0.60 \leq p < 0.80$	$0.90 \leq \cos\theta < 0.95$	0.96 ± 0.11
211		$0.80 \leq p < 1.25$	$0.90 \leq \cos\theta < 0.95$	1.03 ± 0.14
212		$1.25 \leq p < 2.00$	$0.90 \leq \cos\theta < 0.95$	1.01 ± 0.08
213		$2.00 \leq p < 3.00$	$0.90 \leq \cos\theta < 0.95$	0.98 ± 0.06
214		$3.00 \leq p < 30$	$0.90 \leq \cos\theta < 0.95$	0.95 ± 0.17
215		$0 \leq p < 0.50$	$0.95 \leq \cos\theta < 0.99$	1.08 ± 0.45

Fit Index	Sample	p [GeV/c]	$\cos\theta$	Prefit
216		$0.50 \leq p < 0.60$	$0.95 \leq \cos\theta < 0.99$	0.93 ± 0.16
217		$0.60 \leq p < 0.80$	$0.95 \leq \cos\theta < 0.99$	0.96 ± 0.09
218		$0.80 \leq p < 1.25$	$0.95 \leq \cos\theta < 0.99$	1.02 ± 0.12
219		$1.25 \leq p < 2.00$	$0.95 \leq \cos\theta < 0.99$	1.01 ± 0.07
220	$\bar{\nu}_\mu$ RHC 1-Trk Wtr	$2.00 \leq p < 3.00$	$0.95 \leq \cos\theta < 0.99$	1.00 ± 0.04
221		$3.00 \leq p < 30$	$0.95 \leq \cos\theta < 0.99$	0.98 ± 0.09
222		$0 \leq p < 0.50$	$0.99 \leq \cos\theta < 1$	1.09 ± 0.43
223		$0.50 \leq p < 0.60$	$0.99 \leq \cos\theta < 1$	0.94 ± 0.15
224		$0.60 \leq p < 0.80$	$0.99 \leq \cos\theta < 1$	0.93 ± 0.10
225		$0.80 \leq p < 1.25$	$0.99 \leq \cos\theta < 1$	1.02 ± 0.12
226		$1.25 \leq p < 2.00$	$0.99 \leq \cos\theta < 1$	1.01 ± 0.08
227		$2.00 \leq p < 3.00$	$0.99 \leq \cos\theta < 1$	1.00 ± 0.07
228		$3.00 \leq p < 30$	$0.99 \leq \cos\theta < 1$	0.99 ± 0.05
229	$\bar{\nu}_\mu$ RHC N-Trks Wtr	$0 \leq p < 0.50$	$-1 \leq \cos\theta < 0.89$	1.02 ± 0.34
230		$0.50 \leq p < 0.90$	$-1 \leq \cos\theta < 0.89$	1.00 ± 0.09
231		$0.90 \leq p < 1.25$	$-1 \leq \cos\theta < 0.89$	1.01 ± 0.07
232		$1.25 \leq p < 1.60$	$-1 \leq \cos\theta < 0.89$	0.99 ± 0.13
233		$1.60 \leq p < 3.00$	$-1 \leq \cos\theta < 0.89$	0.99 ± 0.11
234		$3.00 \leq p < 30$	$-1 \leq \cos\theta < 0.89$	0.98 ± 0.33
235		$0 \leq p < 0.50$	$0.89 \leq \cos\theta < 0.95$	1.05 ± 0.34
236		$0.50 \leq p < 0.90$	$0.89 \leq \cos\theta < 0.95$	0.97 ± 0.05
237		$0.90 \leq p < 1.25$	$0.89 \leq \cos\theta < 0.95$	1.02 ± 0.06
238		$1.25 \leq p < 1.60$	$0.89 \leq \cos\theta < 0.95$	0.98 ± 0.09
239		$1.60 \leq p < 3.00$	$0.89 \leq \cos\theta < 0.95$	0.99 ± 0.06
240	$\bar{\nu}_\mu$ RHC N-Trks Wtr	$3.00 \leq p < 30$	$0.89 \leq \cos\theta < 0.95$	0.98 ± 0.14
241		$0 \leq p < 0.50$	$0.95 \leq \cos\theta < 0.97$	1.04 ± 0.36

Fit Index	Sample	p [GeV/c]	$\cos\theta$	Prefit
242		$0.50 \leq p < 0.90$	$0.95 \leq \cos\theta < 0.97$	0.97 ± 0.05
243		$0.90 \leq p < 1.25$	$0.95 \leq \cos\theta < 0.97$	1.01 ± 0.05
244		$1.25 \leq p < 1.60$	$0.95 \leq \cos\theta < 0.97$	1.00 ± 0.09
245		$1.60 \leq p < 3.00$	$0.95 \leq \cos\theta < 0.97$	1.01 ± 0.06
246		$3.00 \leq p < 30$	$0.95 \leq \cos\theta < 0.97$	0.98 ± 0.12
247		$0 \leq p < 0.50$	$0.97 \leq \cos\theta < 0.99$	1.03 ± 0.37
248		$0.50 \leq p < 0.90$	$0.97 \leq \cos\theta < 0.99$	1.01 ± 0.05
249		$0.90 \leq p < 1.25$	$0.97 \leq \cos\theta < 0.99$	1.00 ± 0.05
250	$\bar{\nu}_\mu$ RHC N-Trks Wtr	$1.25 \leq p < 1.60$	$0.97 \leq \cos\theta < 0.99$	0.99 ± 0.07
251		$1.60 \leq p < 3.00$	$0.97 \leq \cos\theta < 0.99$	1.01 ± 0.07
252		$3.00 \leq p < 30$	$0.97 \leq \cos\theta < 0.99$	0.99 ± 0.07
253		$0 \leq p < 0.50$	$0.99 \leq \cos\theta < 1$	1.07 ± 0.39
254		$0.50 \leq p < 0.90$	$0.99 \leq \cos\theta < 1$	0.98 ± 0.07
255		$0.90 \leq p < 1.25$	$0.99 \leq \cos\theta < 1$	1.02 ± 0.08
256		$1.25 \leq p < 1.60$	$0.99 \leq \cos\theta < 1$	1.01 ± 0.08
257		$1.60 \leq p < 3.00$	$0.99 \leq \cos\theta < 1$	0.99 ± 0.09
258		$3.00 \leq p < 30$	$0.99 \leq \cos\theta < 1$	0.99 ± 0.06
259	ν_μ RHC 1-Trk Wtr	$0 \leq p < 0.40$	$-1 \leq \cos\theta < 0.78$	1.24 ± 0.60
260		$0.40 \leq p < 0.60$	$-1 \leq \cos\theta < 0.78$	0.91 ± 0.16
261		$0.60 \leq p < 0.80$	$-1 \leq \cos\theta < 0.78$	1.00 ± 0.13
262		$0.80 \leq p < 1.10$	$-1 \leq \cos\theta < 0.78$	1.02 ± 0.21
263		$1.10 \leq p < 2.00$	$-1 \leq \cos\theta < 0.78$	1.03 ± 0.17
264		$2.00 \leq p < 10.0$	$-1 \leq \cos\theta < 0.78$	0.99 ± 0.21
265		$0 \leq p < 0.40$	$0.78 \leq \cos\theta < 0.84$	1.27 ± 0.64
266		$0.40 \leq p < 0.60$	$0.78 \leq \cos\theta < 0.84$	0.95 ± 0.16
267		$0.60 \leq p < 0.80$	$0.78 \leq \cos\theta < 0.84$	0.99 ± 0.06

Fit Index	Sample	p [GeV/c]	cosθ	Prefit
268		$0.80 \leq p < 1.10$	$0.78 \leq \cos \theta < 0.84$	0.98 ± 0.11
269		$1.10 \leq p < 2.00$	$0.78 \leq \cos \theta < 0.84$	1.04 ± 0.14
270	ν_μ RHC 1-Trk Wtr	$2.00 \leq p < 10.0$	$0.78 \leq \cos \theta < 0.84$	0.99 ± 0.16
271		$0 \leq p < 0.40$	$0.84 \leq \cos \theta < 0.92$	1.20 ± 0.60
272		$0.40 \leq p < 0.60$	$0.84 \leq \cos \theta < 0.92$	0.95 ± 0.20
273		$0.60 \leq p < 0.80$	$0.84 \leq \cos \theta < 0.92$	0.97 ± 0.07
274		$0.80 \leq p < 1.10$	$0.84 \leq \cos \theta < 0.92$	1.00 ± 0.08
275		$1.10 \leq p < 2.00$	$0.84 \leq \cos \theta < 0.92$	1.00 ± 0.08
276		$2.00 \leq p < 10.0$	$0.84 \leq \cos \theta < 0.92$	1.00 ± 0.10
277		$0 \leq p < 0.40$	$0.92 \leq \cos \theta < 0.95$	1.10 ± 0.52
278		$0.40 \leq p < 0.60$	$0.92 \leq \cos \theta < 0.95$	0.99 ± 0.16
279		$0.60 \leq p < 0.80$	$0.92 \leq \cos \theta < 0.95$	0.95 ± 0.06
280	ν_μ RHC 1-Trk Wtr	$0.80 \leq p < 1.10$	$0.92 \leq \cos \theta < 0.95$	0.99 ± 0.04
281		$1.10 \leq p < 2.00$	$0.92 \leq \cos \theta < 0.95$	1.00 ± 0.07
282		$2.00 \leq p < 10.0$	$0.92 \leq \cos \theta < 0.95$	1.00 ± 0.06
283		$0 \leq p < 0.40$	$0.95 \leq \cos \theta < 0.98$	1.19 ± 0.50
284		$0.40 \leq p < 0.60$	$0.95 \leq \cos \theta < 0.98$	0.98 ± 0.15
285		$0.60 \leq p < 0.80$	$0.95 \leq \cos \theta < 0.98$	0.96 ± 0.09
286		$0.80 \leq p < 1.10$	$0.95 \leq \cos \theta < 0.98$	0.99 ± 0.07
287		$1.10 \leq p < 2.00$	$0.95 \leq \cos \theta < 0.98$	1.00 ± 0.06
288		$2.00 \leq p < 10.0$	$0.95 \leq \cos \theta < 0.98$	1.00 ± 0.04
289		$0 \leq p < 0.40$	$0.98 \leq \cos \theta < 0.99$	1.12 ± 0.46
290	ν_μ RHC 1-Trk Wtr	$0.40 \leq p < 0.60$	$0.98 \leq \cos \theta < 0.99$	1.01 ± 0.15
291		$0.60 \leq p < 0.80$	$0.98 \leq \cos \theta < 0.99$	0.98 ± 0.09
292		$0.80 \leq p < 1.10$	$0.98 \leq \cos \theta < 0.99$	1.00 ± 0.09
293		$1.10 \leq p < 2.00$	$0.98 \leq \cos \theta < 0.99$	0.98 ± 0.07

Fit Index	Sample	p [GeV/c]	$\cos\theta$	Prefit
294		$2.00 \leq p < 10.0$	$0.98 \leq \cos\theta < 0.99$	1.00 ± 0.03
295		$0 \leq p < 0.40$	$0.99 \leq \cos\theta < 1$	1.29 ± 0.47
296		$0.40 \leq p < 0.60$	$0.99 \leq \cos\theta < 1$	0.98 ± 0.20
297		$0.60 \leq p < 0.80$	$0.99 \leq \cos\theta < 1$	0.95 ± 0.16
298		$0.80 \leq p < 1.10$	$0.99 \leq \cos\theta < 1$	1.03 ± 0.10
299		$1.10 \leq p < 2.00$	$0.99 \leq \cos\theta < 1$	1.01 ± 0.08
300	ν_μ RHC 1-Trk Wtr	$2.00 \leq p < 10.0$	$0.99 \leq \cos\theta < 1$	1.00 ± 0.03
301	ν_μ RHC N-Trks Wtr	$0 \leq p < 0.60$	$-1 \leq \cos\theta < 0.70$	0.97 ± 0.21
302		$0.60 \leq p < 1.00$	$-1 \leq \cos\theta < 0.70$	1.01 ± 0.13
303		$1.00 \leq p < 1.50$	$-1 \leq \cos\theta < 0.70$	1.01 ± 0.15
304		$1.50 \leq p < 2.00$	$-1 \leq \cos\theta < 0.70$	1.15 ± 0.19
305		$2.00 \leq p < 10.0$	$-1 \leq \cos\theta < 0.70$	0.95 ± 0.23
306		$0 \leq p < 0.60$	$0.70 \leq \cos\theta < 0.80$	1.00 ± 0.26
307		$0.60 \leq p < 1.00$	$0.70 \leq \cos\theta < 0.80$	0.99 ± 0.08
308		$1.00 \leq p < 1.50$	$0.70 \leq \cos\theta < 0.80$	1.01 ± 0.11
309		$1.50 \leq p < 2.00$	$0.70 \leq \cos\theta < 0.80$	0.98 ± 0.09
310	ν_μ RHC N-Trks Wtr	$2.00 \leq p < 10.0$	$0.70 \leq \cos\theta < 0.80$	1.00 ± 0.16
311		$0 \leq p < 0.60$	$0.80 \leq \cos\theta < 0.85$	1.01 ± 0.28
312		$0.60 \leq p < 1.00$	$0.80 \leq \cos\theta < 0.85$	0.98 ± 0.06
313		$1.00 \leq p < 1.50$	$0.80 \leq \cos\theta < 0.85$	1.00 ± 0.08
314		$1.50 \leq p < 2.00$	$0.80 \leq \cos\theta < 0.85$	1.02 ± 0.08
315		$2.00 \leq p < 10.0$	$0.80 \leq \cos\theta < 0.85$	0.98 ± 0.11
316		$0 \leq p < 0.60$	$0.85 \leq \cos\theta < 0.98$	1.02 ± 0.25
317		$0.60 \leq p < 1.00$	$0.85 \leq \cos\theta < 0.98$	0.98 ± 0.07
318		$1.00 \leq p < 1.50$	$0.85 \leq \cos\theta < 0.98$	1.00 ± 0.07
319		$1.50 \leq p < 2.00$	$0.85 \leq \cos\theta < 0.98$	1.00 ± 0.07

Fit Index	Sample	p [GeV/c]	cosθ	Prefit
320	ν_μ RHC N-Trks Wtr	$2.00 \leq p < 10.0$	$0.85 \leq \cos \theta < 0.98$	1.00 ± 0.06
321		$0 \leq p < 0.60$	$0.98 \leq \cos \theta < 0.99$	1.02 ± 0.24
322		$0.60 \leq p < 1.00$	$0.98 \leq \cos \theta < 0.99$	0.96 ± 0.10
323		$1.00 \leq p < 1.50$	$0.98 \leq \cos \theta < 0.99$	1.01 ± 0.09
324		$1.50 \leq p < 2.00$	$0.98 \leq \cos \theta < 0.99$	0.99 ± 0.09
325		$2.00 \leq p < 10.0$	$0.98 \leq \cos \theta < 0.99$	0.99 ± 0.04
326		$0 \leq p < 0.60$	$0.99 \leq \cos \theta < 1$	1.00 ± 0.25
327		$0.60 \leq p < 1.00$	$0.99 \leq \cos \theta < 1$	0.98 ± 0.11
328		$1.00 \leq p < 1.50$	$0.99 \leq \cos \theta < 1$	1.00 ± 0.09
329		$1.50 \leq p < 2.00$	$0.99 \leq \cos \theta < 1$	1.01 ± 0.10
330	ν_μ RHC N-Trks Wtr	$2.00 \leq p < 10.0$	$0.99 \leq \cos \theta < 1$	1.00 ± 0.04
331	ν_μ 1-Trk Air	$0 \leq p < 0.40$	$-1 \leq \cos \theta < 0.70$	1.17 ± 0.66
332		$0.40 \leq p < 0.60$	$-1 \leq \cos \theta < 0.70$	0.86 ± 0.19
333		$0.60 \leq p < 0.80$	$-1 \leq \cos \theta < 0.70$	1.17 ± 0.53
334		$0.80 \leq p < 1.25$	$-1 \leq \cos \theta < 0.70$	1.15 ± 0.44
335		$1.25 \leq p < 2.00$	$-1 \leq \cos \theta < 0.70$	0.97 ± 0.19
336		$2.00 \leq p < 3.00$	$-1 \leq \cos \theta < 0.70$	1.02 ± 0.19
337		$3.00 \leq p < 4.00$	$-1 \leq \cos \theta < 0.70$	1.02 ± 0.31
338		$4.00 \leq p < 5.50$	$-1 \leq \cos \theta < 0.70$	0.97 ± 0.37
339		$5.50 \leq p < 30$	$-1 \leq \cos \theta < 0.70$	0.88 ± 0.62
340	ν_μ 1-Trk Air	$0 \leq p < 0.40$	$0.70 \leq \cos \theta < 0.80$	1.27 ± 0.75
341		$0.40 \leq p < 0.60$	$0.70 \leq \cos \theta < 0.80$	0.87 ± 0.17
342		$0.60 \leq p < 0.80$	$0.70 \leq \cos \theta < 0.80$	1.04 ± 0.31
343		$0.80 \leq p < 1.25$	$0.70 \leq \cos \theta < 0.80$	1.09 ± 0.34
344		$1.25 \leq p < 2.00$	$0.70 \leq \cos \theta < 0.80$	1.01 ± 0.18
345		$2.00 \leq p < 3.00$	$0.70 \leq \cos \theta < 0.80$	1.03 ± 0.17

Fit Index	Sample	p [GeV/c]	$\cos\theta$	Prefit
346		$3.00 \leq p < 4.00$	$0.70 \leq \cos\theta < 0.80$	0.94 ± 0.27
347		$4.00 \leq p < 5.50$	$0.70 \leq \cos\theta < 0.80$	0.93 ± 0.38
348		$5.50 \leq p < 30$	$0.70 \leq \cos\theta < 0.80$	1.00 ± 0.58
349		$0 \leq p < 0.40$	$0.80 \leq \cos\theta < 0.94$	1.32 ± 0.79
350	ν_μ 1-Trk Air	$0.40 \leq p < 0.60$	$0.80 \leq \cos\theta < 0.94$	0.90 ± 0.20
351		$0.60 \leq p < 0.80$	$0.80 \leq \cos\theta < 0.94$	0.98 ± 0.17
352		$0.80 \leq p < 1.25$	$0.80 \leq \cos\theta < 0.94$	1.04 ± 0.19
353		$1.25 \leq p < 2.00$	$0.80 \leq \cos\theta < 0.94$	1.01 ± 0.10
354		$2.00 \leq p < 3.00$	$0.80 \leq \cos\theta < 0.94$	1.00 ± 0.07
355		$3.00 \leq p < 4.00$	$0.80 \leq \cos\theta < 0.94$	0.97 ± 0.14
356		$4.00 \leq p < 5.50$	$0.80 \leq \cos\theta < 0.94$	1.06 ± 0.22
357		$5.50 \leq p < 30$	$0.80 \leq \cos\theta < 0.94$	1.00 ± 0.33
358		$0 \leq p < 0.40$	$0.94 \leq \cos\theta < 0.97$	1.29 ± 0.73
359		$0.40 \leq p < 0.60$	$0.94 \leq \cos\theta < 0.97$	0.91 ± 0.20
360	ν_μ 1-Trk Air	$0.60 \leq p < 0.80$	$0.94 \leq \cos\theta < 0.97$	0.97 ± 0.11
361		$0.80 \leq p < 1.25$	$0.94 \leq \cos\theta < 0.97$	1.02 ± 0.12
362		$1.25 \leq p < 2.00$	$0.94 \leq \cos\theta < 0.97$	1.00 ± 0.07
363		$2.00 \leq p < 3.00$	$0.94 \leq \cos\theta < 0.97$	1.01 ± 0.04
364		$3.00 \leq p < 4.00$	$0.94 \leq \cos\theta < 0.97$	0.98 ± 0.09
365		$4.00 \leq p < 5.50$	$0.94 \leq \cos\theta < 0.97$	0.98 ± 0.15
366		$5.50 \leq p < 30$	$0.94 \leq \cos\theta < 0.97$	0.98 ± 0.21
367		$0 \leq p < 0.40$	$0.97 \leq \cos\theta < 0.99$	1.23 ± 0.68
368		$0.40 \leq p < 0.60$	$0.97 \leq \cos\theta < 0.99$	0.91 ± 0.20
369		$0.60 \leq p < 0.80$	$0.97 \leq \cos\theta < 0.99$	0.98 ± 0.12
370	ν_μ 1-Trk Air	$0.80 \leq p < 1.25$	$0.97 \leq \cos\theta < 0.99$	1.02 ± 0.11
371		$1.25 \leq p < 2.00$	$0.97 \leq \cos\theta < 0.99$	0.99 ± 0.08

Fit Index	Sample	p [GeV/c]	$\cos\theta$	Prefit
372		$2.00 \leq p < 3.00$	$0.97 \leq \cos\theta < 0.99$	1.01 ± 0.06
373		$3.00 \leq p < 4.00$	$0.97 \leq \cos\theta < 0.99$	1.00 ± 0.04
374		$4.00 \leq p < 5.50$	$0.97 \leq \cos\theta < 0.99$	0.98 ± 0.11
375		$5.50 \leq p < 30$	$0.97 \leq \cos\theta < 0.99$	0.98 ± 0.15
376		$0 \leq p < 0.40$	$0.99 \leq \cos\theta < 1$	1.21 ± 0.58
377		$0.40 \leq p < 0.60$	$0.99 \leq \cos\theta < 1$	0.90 ± 0.16
378		$0.60 \leq p < 0.80$	$0.99 \leq \cos\theta < 1$	0.99 ± 0.12
379		$0.80 \leq p < 1.25$	$0.99 \leq \cos\theta < 1$	1.02 ± 0.12
380	ν_μ 1-Trk Air	$1.25 \leq p < 2.00$	$0.99 \leq \cos\theta < 1$	1.01 ± 0.09
381		$2.00 \leq p < 3.00$	$0.99 \leq \cos\theta < 1$	1.01 ± 0.10
382		$3.00 \leq p < 4.00$	$0.99 \leq \cos\theta < 1$	1.00 ± 0.06
383		$4.00 \leq p < 5.50$	$0.99 \leq \cos\theta < 1$	1.00 ± 0.05
384		$5.50 \leq p < 30$	$0.99 \leq \cos\theta < 1$	0.98 ± 0.10
385	ν_μ N-Trks Air	$0 \leq p < 0.40$	$-1 \leq \cos\theta < 0.77$	1.18 ± 0.62
386		$0.40 \leq p < 0.60$	$-1 \leq \cos\theta < 0.77$	0.88 ± 0.15
387		$0.60 \leq p < 0.80$	$-1 \leq \cos\theta < 0.77$	1.03 ± 0.21
388		$0.80 \leq p < 1.20$	$-1 \leq \cos\theta < 0.77$	1.03 ± 0.21
389		$1.20 \leq p < 2.20$	$-1 \leq \cos\theta < 0.77$	1.01 ± 0.16
390	ν_μ N-Trks Air	$2.20 \leq p < 3.50$	$-1 \leq \cos\theta < 0.77$	1.00 ± 0.22
391		$3.50 \leq p < 10.0$	$-1 \leq \cos\theta < 0.77$	0.99 ± 0.32
392		$10.0 \leq p < 30$	$-1 \leq \cos\theta < 0.77$	0.93 ± 0.69
393		$0 \leq p < 0.40$	$0.77 \leq \cos\theta < 0.85$	1.13 ± 0.58
394		$0.40 \leq p < 0.60$	$0.77 \leq \cos\theta < 0.85$	0.91 ± 0.14
395		$0.60 \leq p < 0.80$	$0.77 \leq \cos\theta < 0.85$	0.99 ± 0.10
396		$0.80 \leq p < 1.20$	$0.77 \leq \cos\theta < 0.85$	1.01 ± 0.11
397		$1.20 \leq p < 2.20$	$0.77 \leq \cos\theta < 0.85$	1.01 ± 0.08

Fit Index	Sample	p [GeV/c]	$\cos\theta$	Prefit
398		$2.20 \leq p < 3.50$	$0.77 \leq \cos\theta < 0.85$	1.00 ± 0.08
399		$3.50 \leq p < 10.0$	$0.77 \leq \cos\theta < 0.85$	1.03 ± 0.18
400	ν_μ N-Trks Air	$10.0 \leq p < 30$	$0.77 \leq \cos\theta < 0.85$	0.97 ± 0.51
401		$0 \leq p < 0.40$	$0.85 \leq \cos\theta < 0.90$	1.12 ± 0.55
402		$0.40 \leq p < 0.60$	$0.85 \leq \cos\theta < 0.90$	0.92 ± 0.13
403		$0.60 \leq p < 0.80$	$0.85 \leq \cos\theta < 0.90$	0.99 ± 0.08
404		$0.80 \leq p < 1.20$	$0.85 \leq \cos\theta < 0.90$	1.00 ± 0.08
405		$1.20 \leq p < 2.20$	$0.85 \leq \cos\theta < 0.90$	1.01 ± 0.07
406		$2.20 \leq p < 3.50$	$0.85 \leq \cos\theta < 0.90$	1.00 ± 0.06
407		$3.50 \leq p < 10.0$	$0.85 \leq \cos\theta < 0.90$	0.98 ± 0.13
408		$10.0 \leq p < 30$	$0.85 \leq \cos\theta < 0.90$	0.93 ± 0.45
409		$0 \leq p < 0.40$	$0.90 \leq \cos\theta < 0.97$	1.09 ± 0.51
410	ν_μ N-Trks Air	$0.40 \leq p < 0.60$	$0.90 \leq \cos\theta < 0.97$	0.93 ± 0.11
411		$0.60 \leq p < 0.80$	$0.90 \leq \cos\theta < 0.97$	0.99 ± 0.08
412		$0.80 \leq p < 1.20$	$0.90 \leq \cos\theta < 0.97$	1.00 ± 0.08
413		$1.20 \leq p < 2.20$	$0.90 \leq \cos\theta < 0.97$	1.00 ± 0.07
414		$2.20 \leq p < 3.50$	$0.90 \leq \cos\theta < 0.97$	1.00 ± 0.03
415		$3.50 \leq p < 10.0$	$0.90 \leq \cos\theta < 0.97$	0.99 ± 0.10
416		$10.0 \leq p < 30$	$0.90 \leq \cos\theta < 0.97$	0.97 ± 0.28
417		$0 \leq p < 0.40$	$0.97 \leq \cos\theta < 1$	1.09 ± 0.48
418		$0.40 \leq p < 0.60$	$0.97 \leq \cos\theta < 1$	0.94 ± 0.12
419		$0.60 \leq p < 0.80$	$0.97 \leq \cos\theta < 1$	0.98 ± 0.11
420	ν_μ N-Trks Air	$0.80 \leq p < 1.20$	$0.97 \leq \cos\theta < 1$	1.01 ± 0.10
421		$1.20 \leq p < 2.20$	$0.97 \leq \cos\theta < 1$	1.01 ± 0.09
422		$2.20 \leq p < 3.50$	$0.97 \leq \cos\theta < 1$	1.01 ± 0.07
423		$3.50 \leq p < 10.0$	$0.97 \leq \cos\theta < 1$	0.99 ± 0.06

Fit Index	Sample	p [GeV/c]	$\cos\theta$	Prefit
424		$10.0 \leq p < 30$	$0.97 \leq \cos\theta < 1$	0.97 ± 0.13
425	$\bar{\nu}_\mu$ RHC 1-Trk Air	$0 \leq p < 0.50$	$-1 \leq \cos\theta < 0.82$	0.99 ± 0.29
426		$0.50 \leq p < 0.60$	$-1 \leq \cos\theta < 0.82$	0.92 ± 0.14
427		$0.60 \leq p < 0.80$	$-1 \leq \cos\theta < 0.82$	1.05 ± 0.24
428		$0.80 \leq p < 1.25$	$-1 \leq \cos\theta < 0.82$	1.05 ± 0.18
429		$1.25 \leq p < 2.00$	$-1 \leq \cos\theta < 0.82$	1.02 ± 0.17
430	$\bar{\nu}_\mu$ RHC 1-Trk Air	$2.00 \leq p < 3.00$	$-1 \leq \cos\theta < 0.82$	0.87 ± 0.19
431		$3.00 \leq p < 30$	$-1 \leq \cos\theta < 0.82$	0.96 ± 0.41
432		$0 \leq p < 0.50$	$0.82 \leq \cos\theta < 0.90$	1.03 ± 0.35
433		$0.50 \leq p < 0.60$	$0.82 \leq \cos\theta < 0.90$	0.91 ± 0.12
434		$0.60 \leq p < 0.80$	$0.82 \leq \cos\theta < 0.90$	1.00 ± 0.16
435		$0.80 \leq p < 1.25$	$0.82 \leq \cos\theta < 0.90$	1.03 ± 0.15
436		$1.25 \leq p < 2.00$	$0.82 \leq \cos\theta < 0.90$	0.99 ± 0.12
437		$2.00 \leq p < 3.00$	$0.82 \leq \cos\theta < 0.90$	0.99 ± 0.15
438		$3.00 \leq p < 30$	$0.82 \leq \cos\theta < 0.90$	0.93 ± 0.31
439		$0 \leq p < 0.50$	$0.90 \leq \cos\theta < 0.95$	1.05 ± 0.37
440	$\bar{\nu}_\mu$ RHC 1-Trk Air	$0.50 \leq p < 0.60$	$0.90 \leq \cos\theta < 0.95$	0.92 ± 0.11
441		$0.60 \leq p < 0.80$	$0.90 \leq \cos\theta < 0.95$	0.98 ± 0.12
442		$0.80 \leq p < 1.25$	$0.90 \leq \cos\theta < 0.95$	1.03 ± 0.12
443		$1.25 \leq p < 2.00$	$0.90 \leq \cos\theta < 0.95$	1.02 ± 0.08
444		$2.00 \leq p < 3.00$	$0.90 \leq \cos\theta < 0.95$	0.97 ± 0.08
445		$3.00 \leq p < 30$	$0.90 \leq \cos\theta < 0.95$	0.97 ± 0.19
446		$0 \leq p < 0.50$	$0.95 \leq \cos\theta < 0.99$	1.06 ± 0.37
447		$0.50 \leq p < 0.60$	$0.95 \leq \cos\theta < 0.99$	0.93 ± 0.12
448		$0.60 \leq p < 0.80$	$0.95 \leq \cos\theta < 0.99$	0.97 ± 0.11
449		$0.80 \leq p < 1.25$	$0.95 \leq \cos\theta < 0.99$	1.02 ± 0.10

Fit Index	Sample	p [GeV/c]	cosθ	Prefit
450	$\bar{\nu}_\mu$ RHC 1-Trk Air	$1.25 \leq p < 2.00$	$0.95 \leq \cos \theta < 0.99$	1.00 ± 0.07
451		$2.00 \leq p < 3.00$	$0.95 \leq \cos \theta < 0.99$	0.99 ± 0.04
452		$3.00 \leq p < 30$	$0.95 \leq \cos \theta < 0.99$	0.99 ± 0.10
453		$0 \leq p < 0.50$	$0.99 \leq \cos \theta < 1$	1.07 ± 0.35
454		$0.50 \leq p < 0.60$	$0.99 \leq \cos \theta < 1$	0.89 ± 0.12
455		$0.60 \leq p < 0.80$	$0.99 \leq \cos \theta < 1$	0.99 ± 0.11
456		$0.80 \leq p < 1.25$	$0.99 \leq \cos \theta < 1$	1.02 ± 0.11
457		$1.25 \leq p < 2.00$	$0.99 \leq \cos \theta < 1$	0.99 ± 0.09
458		$2.00 \leq p < 3.00$	$0.99 \leq \cos \theta < 1$	1.01 ± 0.07
459		$3.00 \leq p < 30$	$0.99 \leq \cos \theta < 1$	0.99 ± 0.06
460	$\bar{\nu}_\mu$ RHC N-Trks Air	$0 \leq p < 0.50$	$-1 \leq \cos \theta < 0.89$	1.00 ± 0.29
461		$0.50 \leq p < 0.90$	$-1 \leq \cos \theta < 0.89$	1.00 ± 0.10
462		$0.90 \leq p < 1.25$	$-1 \leq \cos \theta < 0.89$	1.04 ± 0.09
463		$1.25 \leq p < 1.60$	$-1 \leq \cos \theta < 0.89$	0.98 ± 0.14
464		$1.60 \leq p < 3.00$	$-1 \leq \cos \theta < 0.89$	0.98 ± 0.13
465		$3.00 \leq p < 30$	$-1 \leq \cos \theta < 0.89$	0.92 ± 0.33
466		$0 \leq p < 0.50$	$0.89 \leq \cos \theta < 0.95$	1.00 ± 0.31
467		$0.50 \leq p < 0.90$	$0.89 \leq \cos \theta < 0.95$	0.99 ± 0.06
468		$0.90 \leq p < 1.25$	$0.89 \leq \cos \theta < 0.95$	1.02 ± 0.06
469		$1.25 \leq p < 1.60$	$0.89 \leq \cos \theta < 0.95$	0.99 ± 0.11
470	$\bar{\nu}_\mu$ RHC N-Trks Air	$1.60 \leq p < 3.00$	$0.89 \leq \cos \theta < 0.95$	0.99 ± 0.06
471		$3.00 \leq p < 30$	$0.89 \leq \cos \theta < 0.95$	0.96 ± 0.16
472		$0 \leq p < 0.50$	$0.95 \leq \cos \theta < 0.97$	1.00 ± 0.32
473		$0.50 \leq p < 0.90$	$0.95 \leq \cos \theta < 0.97$	1.00 ± 0.07
474		$0.90 \leq p < 1.25$	$0.95 \leq \cos \theta < 0.97$	1.00 ± 0.06
475		$1.25 \leq p < 1.60$	$0.95 \leq \cos \theta < 0.97$	1.00 ± 0.11

Fit Index	Sample	p [GeV/c]	$\cos\theta$	Prefit
476		$1.60 \leq p < 3.00$	$0.95 \leq \cos\theta < 0.97$	1.00 ± 0.06
477		$3.00 \leq p < 30$	$0.95 \leq \cos\theta < 0.97$	0.99 ± 0.13
478		$0 \leq p < 0.50$	$0.97 \leq \cos\theta < 0.99$	1.03 ± 0.32
479		$0.50 \leq p < 0.90$	$0.97 \leq \cos\theta < 0.99$	0.99 ± 0.07
480	$\bar{\nu}_\mu$ RHC N-Trks Air	$0.90 \leq p < 1.25$	$0.97 \leq \cos\theta < 0.99$	1.02 ± 0.07
481		$1.25 \leq p < 1.60$	$0.97 \leq \cos\theta < 0.99$	0.99 ± 0.10
482		$1.60 \leq p < 3.00$	$0.97 \leq \cos\theta < 0.99$	1.01 ± 0.08
483		$3.00 \leq p < 30$	$0.97 \leq \cos\theta < 0.99$	0.98 ± 0.09
484		$0 \leq p < 0.50$	$0.99 \leq \cos\theta < 1$	1.02 ± 0.31
485		$0.50 \leq p < 0.90$	$0.99 \leq \cos\theta < 1$	1.01 ± 0.07
486		$0.90 \leq p < 1.25$	$0.99 \leq \cos\theta < 1$	1.02 ± 0.08
487		$1.25 \leq p < 1.60$	$0.99 \leq \cos\theta < 1$	0.98 ± 0.10
488		$1.60 \leq p < 3.00$	$0.99 \leq \cos\theta < 1$	1.00 ± 0.09
489		$3.00 \leq p < 30$	$0.99 \leq \cos\theta < 1$	0.99 ± 0.07
490	ν_μ RHC 1-Trk Air	$0 \leq p < 0.40$	$-1 \leq \cos\theta < 0.78$	1.10 ± 0.50
491		$0.40 \leq p < 0.60$	$-1 \leq \cos\theta < 0.78$	0.92 ± 0.12
492		$0.60 \leq p < 0.80$	$-1 \leq \cos\theta < 0.78$	1.03 ± 0.16
493		$0.80 \leq p < 1.10$	$-1 \leq \cos\theta < 0.78$	1.02 ± 0.20
494		$1.10 \leq p < 2.00$	$-1 \leq \cos\theta < 0.78$	1.08 ± 0.14
495		$2.00 \leq p < 10.0$	$-1 \leq \cos\theta < 0.78$	0.81 ± 0.31
496		$0 \leq p < 0.40$	$0.78 \leq \cos\theta < 0.84$	1.23 ± 0.50
497		$0.40 \leq p < 0.60$	$0.78 \leq \cos\theta < 0.84$	0.93 ± 0.18
498		$0.60 \leq p < 0.80$	$0.78 \leq \cos\theta < 0.84$	0.93 ± 0.09
499		$0.80 \leq p < 1.10$	$0.78 \leq \cos\theta < 0.84$	1.03 ± 0.12
500	ν_μ RHC 1-Trk Air	$1.10 \leq p < 2.00$	$0.78 \leq \cos\theta < 0.84$	1.05 ± 0.14
501		$2.00 \leq p < 10.0$	$0.78 \leq \cos\theta < 0.84$	1.00 ± 0.21

Fit Index	Sample	p [GeV/c]	$\cos\theta$	Prefit
502		$0 \leq p < 0.40$	$0.84 \leq \cos\theta < 0.92$	1.17 ± 0.49
503		$0.40 \leq p < 0.60$	$0.84 \leq \cos\theta < 0.92$	0.95 ± 0.15
504		$0.60 \leq p < 0.80$	$0.84 \leq \cos\theta < 0.92$	0.97 ± 0.08
505		$0.80 \leq p < 1.10$	$0.84 \leq \cos\theta < 0.92$	1.00 ± 0.10
506		$1.10 \leq p < 2.00$	$0.84 \leq \cos\theta < 0.92$	1.00 ± 0.08
507		$2.00 \leq p < 10.0$	$0.84 \leq \cos\theta < 0.92$	1.04 ± 0.16
508		$0 \leq p < 0.40$	$0.92 \leq \cos\theta < 0.95$	1.13 ± 0.47
509		$0.40 \leq p < 0.60$	$0.92 \leq \cos\theta < 0.95$	0.99 ± 0.13
510	ν_μ RHC 1-Trk Air	$0.60 \leq p < 0.80$	$0.92 \leq \cos\theta < 0.95$	0.94 ± 0.09
511		$0.80 \leq p < 1.10$	$0.92 \leq \cos\theta < 0.95$	0.99 ± 0.07
512		$1.10 \leq p < 2.00$	$0.92 \leq \cos\theta < 0.95$	1.00 ± 0.06
513		$2.00 \leq p < 10.0$	$0.92 \leq \cos\theta < 0.95$	0.99 ± 0.08
514		$0 \leq p < 0.40$	$0.95 \leq \cos\theta < 0.98$	1.06 ± 0.46
515		$0.40 \leq p < 0.60$	$0.95 \leq \cos\theta < 0.98$	0.95 ± 0.14
516		$0.60 \leq p < 0.80$	$0.95 \leq \cos\theta < 0.98$	0.97 ± 0.11
517		$0.80 \leq p < 1.10$	$0.95 \leq \cos\theta < 0.98$	1.01 ± 0.10
518		$1.10 \leq p < 2.00$	$0.95 \leq \cos\theta < 0.98$	1.00 ± 0.07
519		$2.00 \leq p < 10.0$	$0.95 \leq \cos\theta < 0.98$	0.99 ± 0.06
520	ν_μ RHC 1-Trk Air	$0 \leq p < 0.40$	$0.98 \leq \cos\theta < 0.99$	1.07 ± 0.46
521		$0.40 \leq p < 0.60$	$0.98 \leq \cos\theta < 0.99$	1.00 ± 0.15
522		$0.60 \leq p < 0.80$	$0.98 \leq \cos\theta < 0.99$	1.02 ± 0.16
523		$0.80 \leq p < 1.10$	$0.98 \leq \cos\theta < 0.99$	0.96 ± 0.10
524		$1.10 \leq p < 2.00$	$0.98 \leq \cos\theta < 0.99$	1.01 ± 0.08
525		$2.00 \leq p < 10.0$	$0.98 \leq \cos\theta < 0.99$	0.99 ± 0.04
526		$0 \leq p < 0.40$	$0.99 \leq \cos\theta < 1$	1.19 ± 0.46
527		$0.40 \leq p < 0.60$	$0.99 \leq \cos\theta < 1$	0.89 ± 0.17

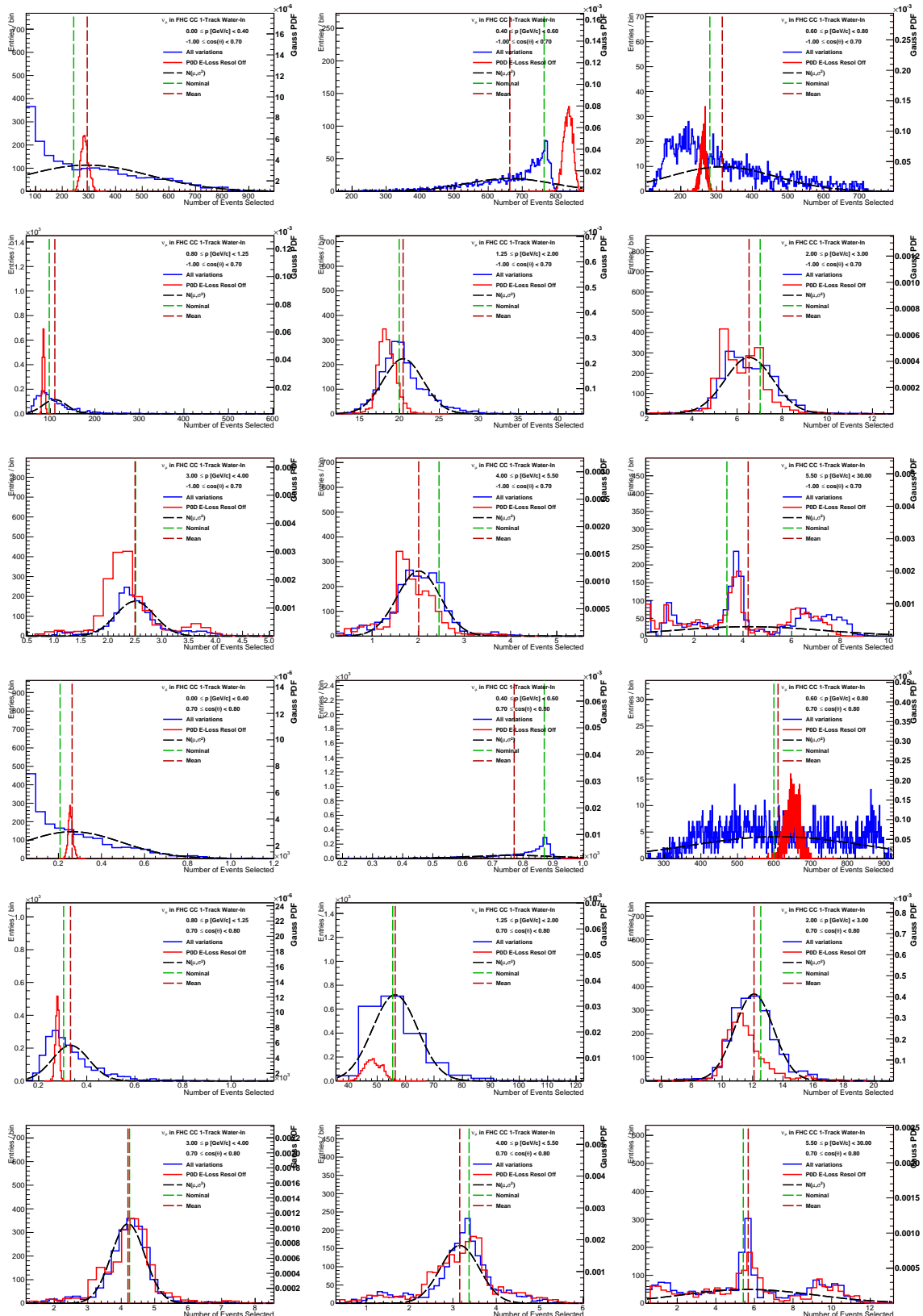
Fit Index	Sample	p [GeV/c]	$\cos\theta$	Prefit
528		$0.60 \leq p < 0.80$	$0.99 \leq \cos\theta < 1$	0.99 ± 0.15
529		$0.80 \leq p < 1.10$	$0.99 \leq \cos\theta < 1$	0.99 ± 0.10
530	ν_μ RHC 1-Trk Air	$1.10 \leq p < 2.00$	$0.99 \leq \cos\theta < 1$	1.00 ± 0.09
531		$2.00 \leq p < 10.0$	$0.99 \leq \cos\theta < 1$	1.00 ± 0.03
532	ν_μ RHC N-Trks Air	$0 \leq p < 0.60$	$-1 \leq \cos\theta < 0.70$	0.97 ± 0.22
533		$0.60 \leq p < 1.00$	$-1 \leq \cos\theta < 0.70$	1.02 ± 0.17
534		$1.00 \leq p < 1.50$	$-1 \leq \cos\theta < 0.70$	1.00 ± 0.14
535		$1.50 \leq p < 2.00$	$-1 \leq \cos\theta < 0.70$	1.28 ± 0.22
536		$2.00 \leq p < 10.0$	$-1 \leq \cos\theta < 0.70$	0.83 ± 0.25
537		$0 \leq p < 0.60$	$0.70 \leq \cos\theta < 0.80$	0.98 ± 0.22
538		$0.60 \leq p < 1.00$	$0.70 \leq \cos\theta < 0.80$	0.99 ± 0.09
539		$1.00 \leq p < 1.50$	$0.70 \leq \cos\theta < 0.80$	1.00 ± 0.11
540	ν_μ RHC N-Trks Air	$1.50 \leq p < 2.00$	$0.70 \leq \cos\theta < 0.80$	1.03 ± 0.11
541		$2.00 \leq p < 10.0$	$0.70 \leq \cos\theta < 0.80$	1.04 ± 0.20
542		$0 \leq p < 0.60$	$0.80 \leq \cos\theta < 0.85$	1.01 ± 0.25
543		$0.60 \leq p < 1.00$	$0.80 \leq \cos\theta < 0.85$	0.98 ± 0.08
544		$1.00 \leq p < 1.50$	$0.80 \leq \cos\theta < 0.85$	1.01 ± 0.08
545		$1.50 \leq p < 2.00$	$0.80 \leq \cos\theta < 0.85$	1.00 ± 0.08
546		$2.00 \leq p < 10.0$	$0.80 \leq \cos\theta < 0.85$	0.99 ± 0.12
547		$0 \leq p < 0.60$	$0.85 \leq \cos\theta < 0.98$	0.99 ± 0.22
548		$0.60 \leq p < 1.00$	$0.85 \leq \cos\theta < 0.98$	1.00 ± 0.10
549		$1.00 \leq p < 1.50$	$0.85 \leq \cos\theta < 0.98$	1.01 ± 0.07
550	ν_μ RHC N-Trks Air	$1.50 \leq p < 2.00$	$0.85 \leq \cos\theta < 0.98$	1.00 ± 0.07
551		$2.00 \leq p < 10.0$	$0.85 \leq \cos\theta < 0.98$	1.00 ± 0.07
552		$0 \leq p < 0.60$	$0.98 \leq \cos\theta < 0.99$	1.00 ± 0.22
553		$0.60 \leq p < 1.00$	$0.98 \leq \cos\theta < 0.99$	0.99 ± 0.12

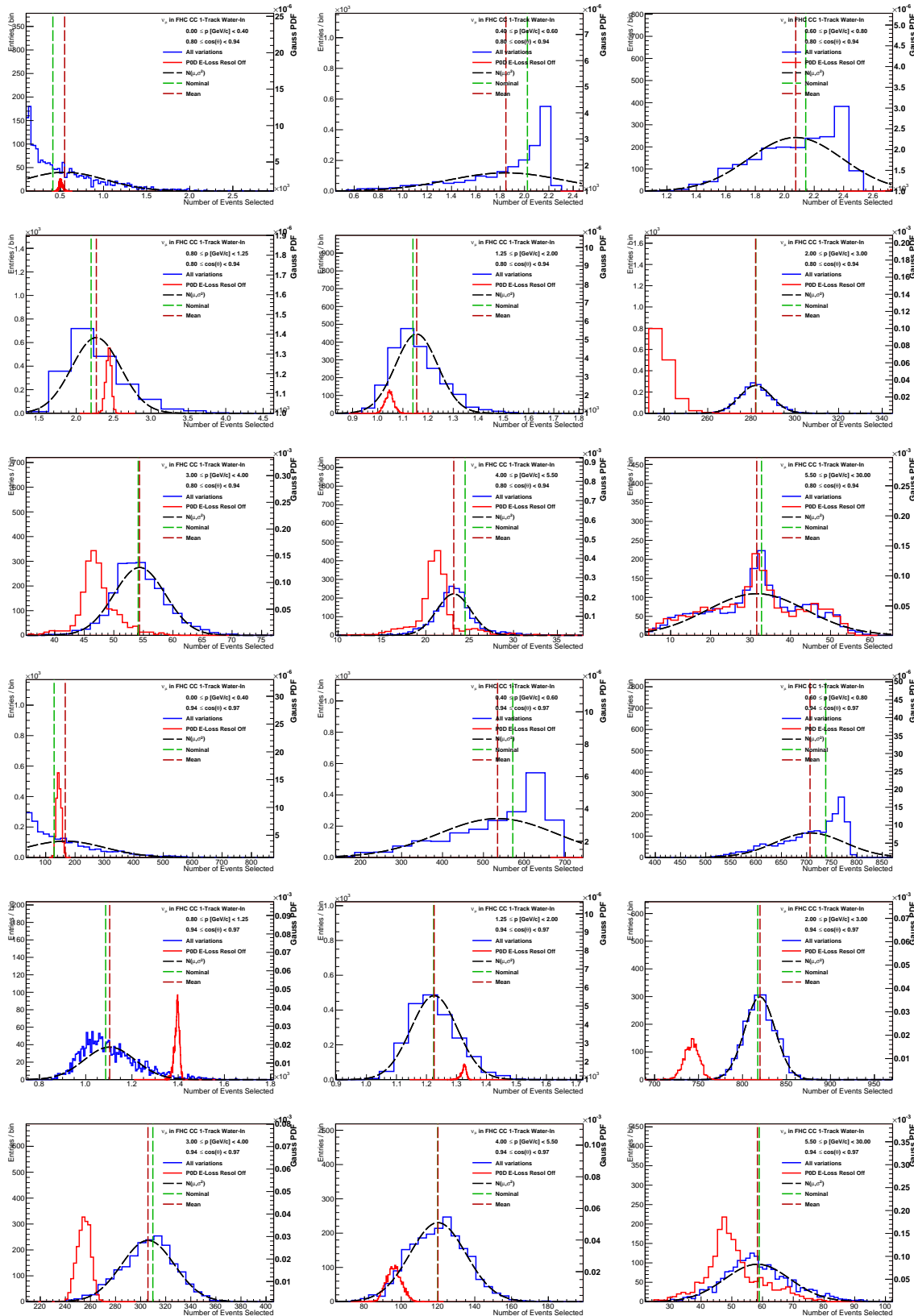
Fit Index	Sample	p [GeV/c]	cosθ	Prefit
554		$1.00 \leq p < 1.50$	$0.98 \leq \cos \theta < 0.99$	1.04 ± 0.10
555		$1.50 \leq p < 2.00$	$0.98 \leq \cos \theta < 0.99$	0.99 ± 0.10
556		$2.00 \leq p < 10.0$	$0.98 \leq \cos \theta < 0.99$	0.99 ± 0.04
557		$0 \leq p < 0.60$	$0.99 \leq \cos \theta < 1$	1.01 ± 0.24
558		$0.60 \leq p < 1.00$	$0.99 \leq \cos \theta < 1$	0.99 ± 0.16
559		$1.00 \leq p < 1.50$	$0.99 \leq \cos \theta < 1$	0.97 ± 0.12
560	ν_μ RHC N-Trks Air	$1.50 \leq p < 2.00$	$0.99 \leq \cos \theta < 1$	1.06 ± 0.10
561		$2.00 \leq p < 10.0$	$0.99 \leq \cos \theta < 1$	1.00 ± 0.04

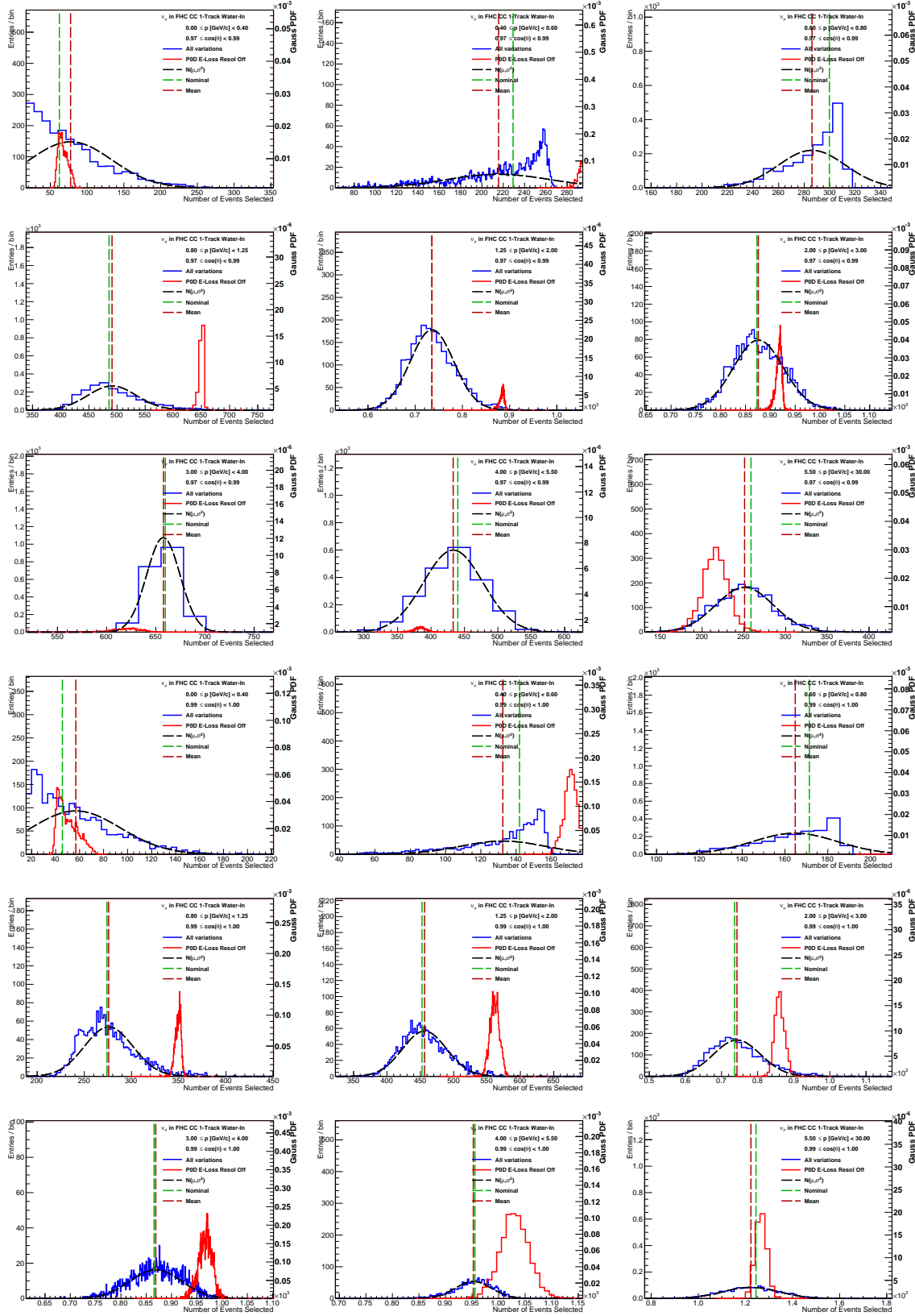
Appendix C

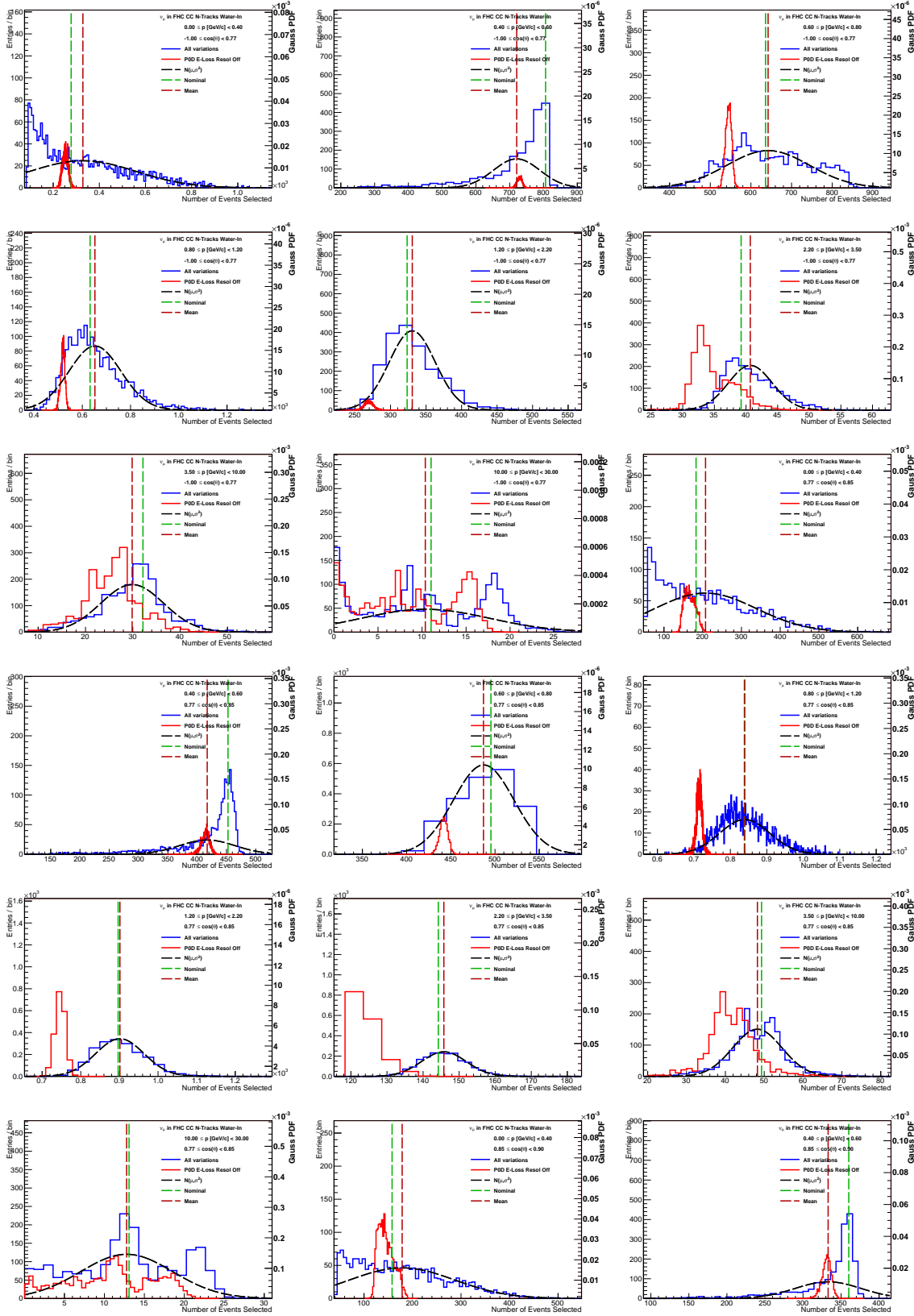
Toy Experiment Variations

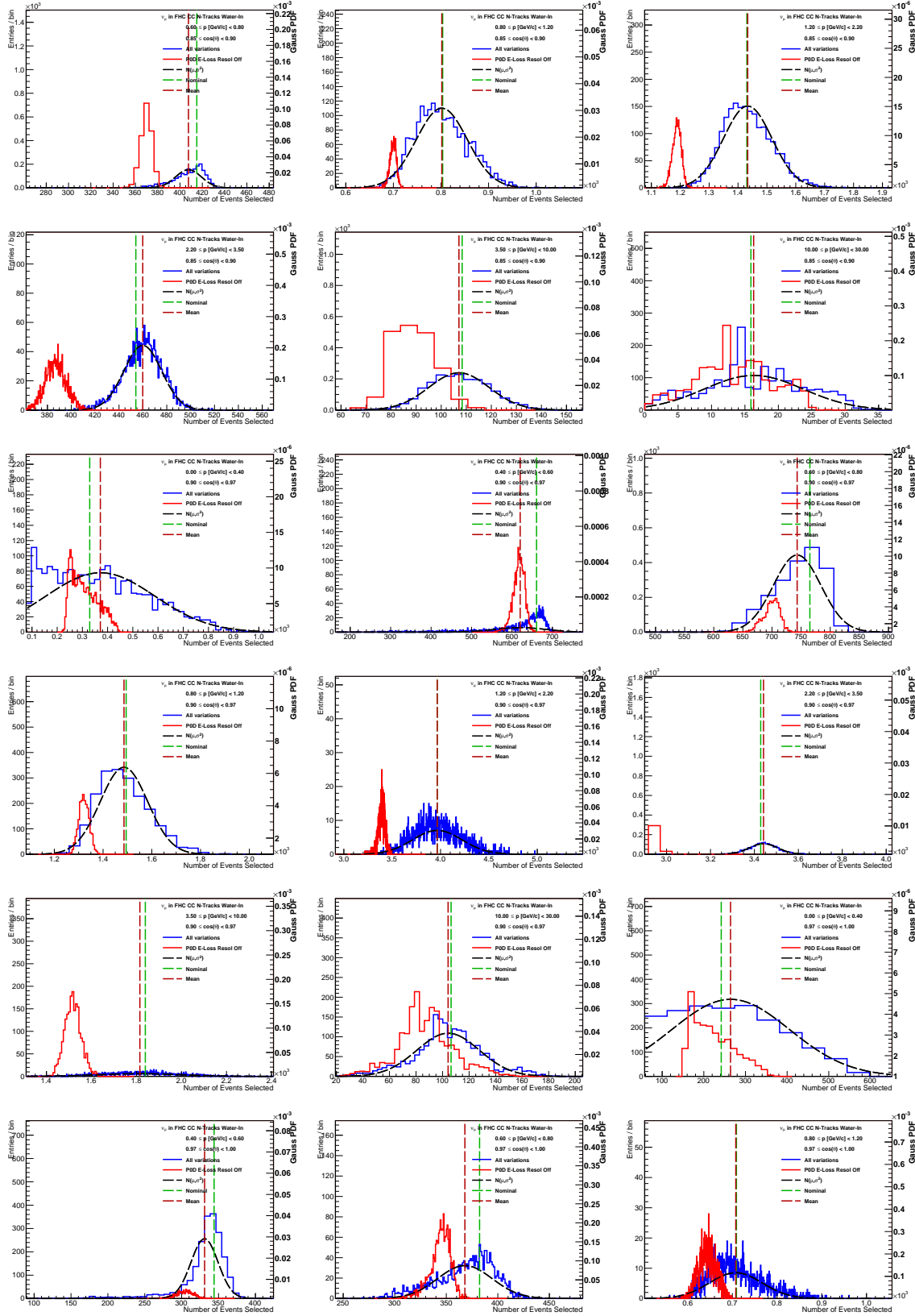
In this appendix is the collection of all toy experiments used to make observable normalization parameters and detector covariance matrix. Each of the observable bin relevant samples and $(p, \cos \theta)$ edges are listed in the plots. The nominal MC (Nominal) predicted value and varied mean are shown as differently dashed lines. A normal curve, whose variance was extracted from the covariance matrix itself, is shown to illustrate the estimate on the bin normalization uncertainty. In addition, toy experiment variations with the PØD energy loss resolution off (E-Loss Resol Off) is shown to demonstrate the absence of the energy correction and its affect on when not varied.

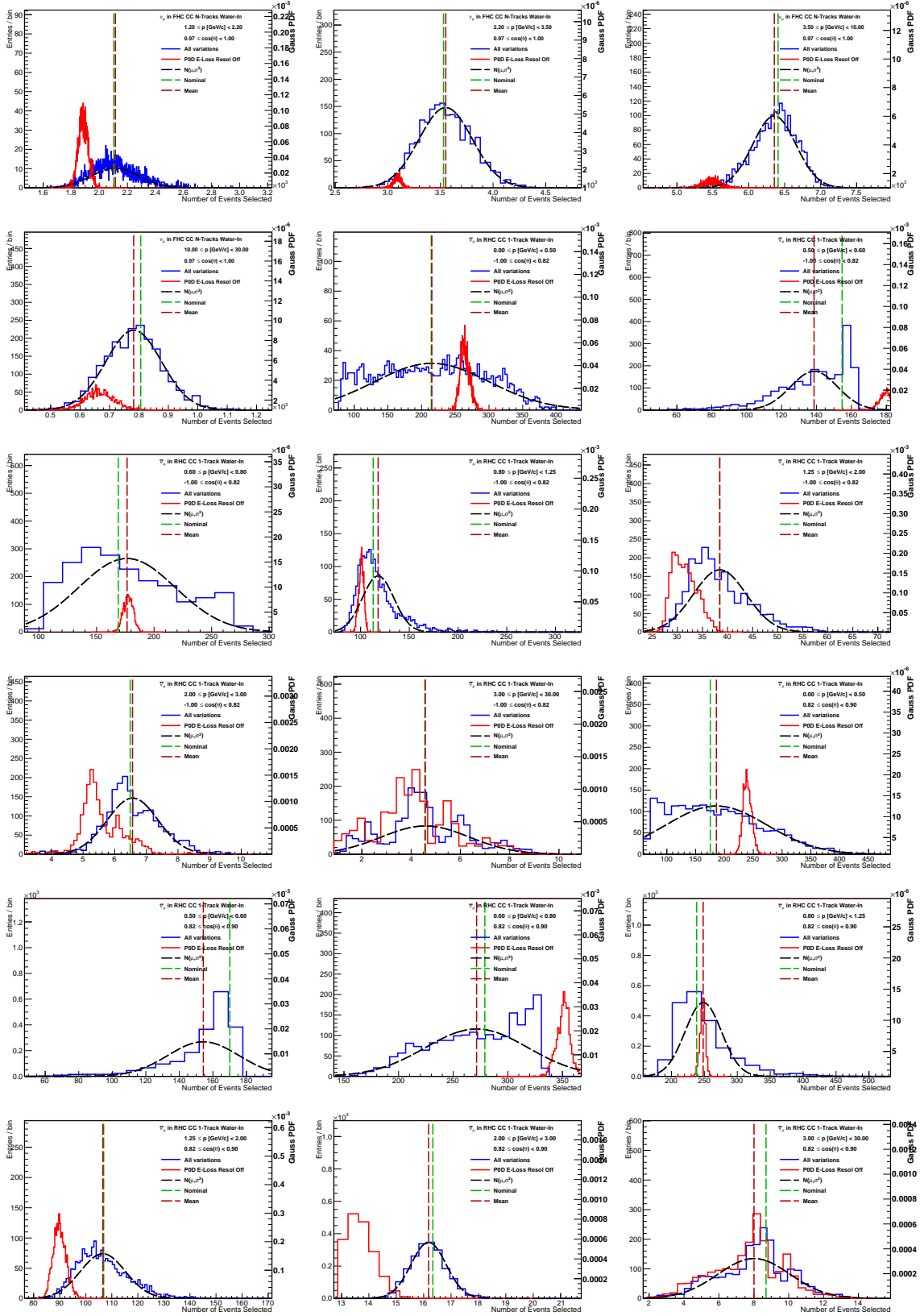


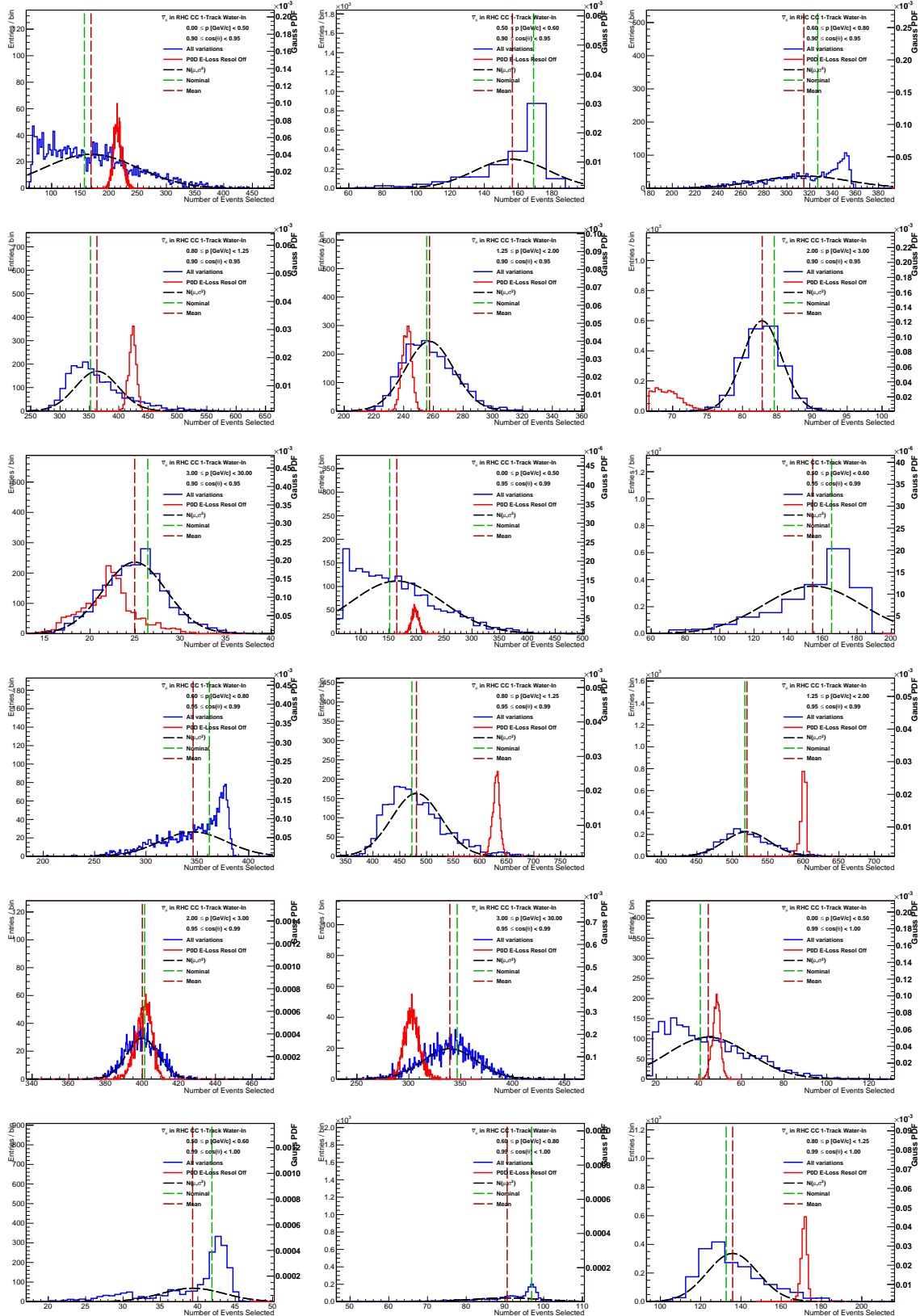


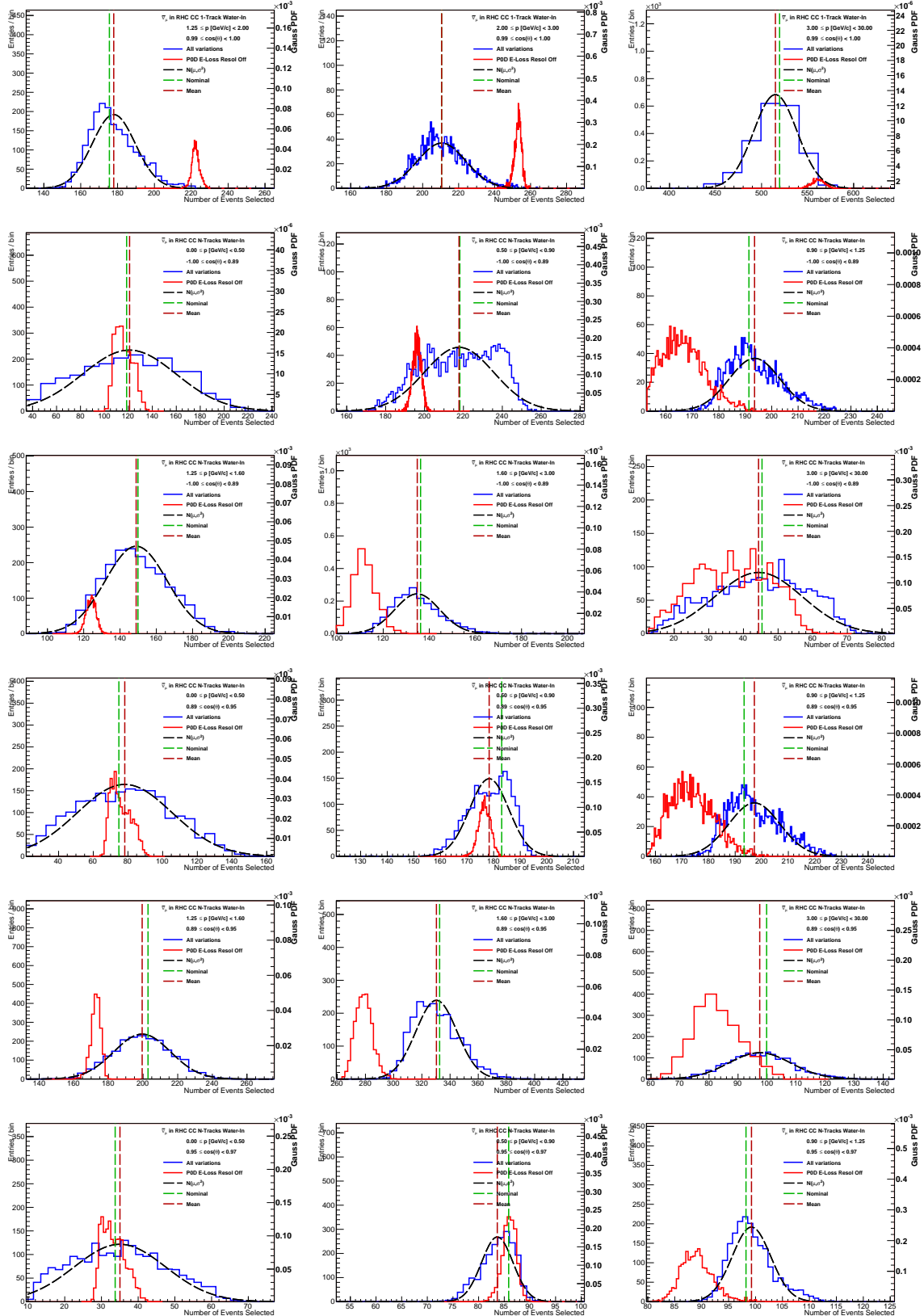


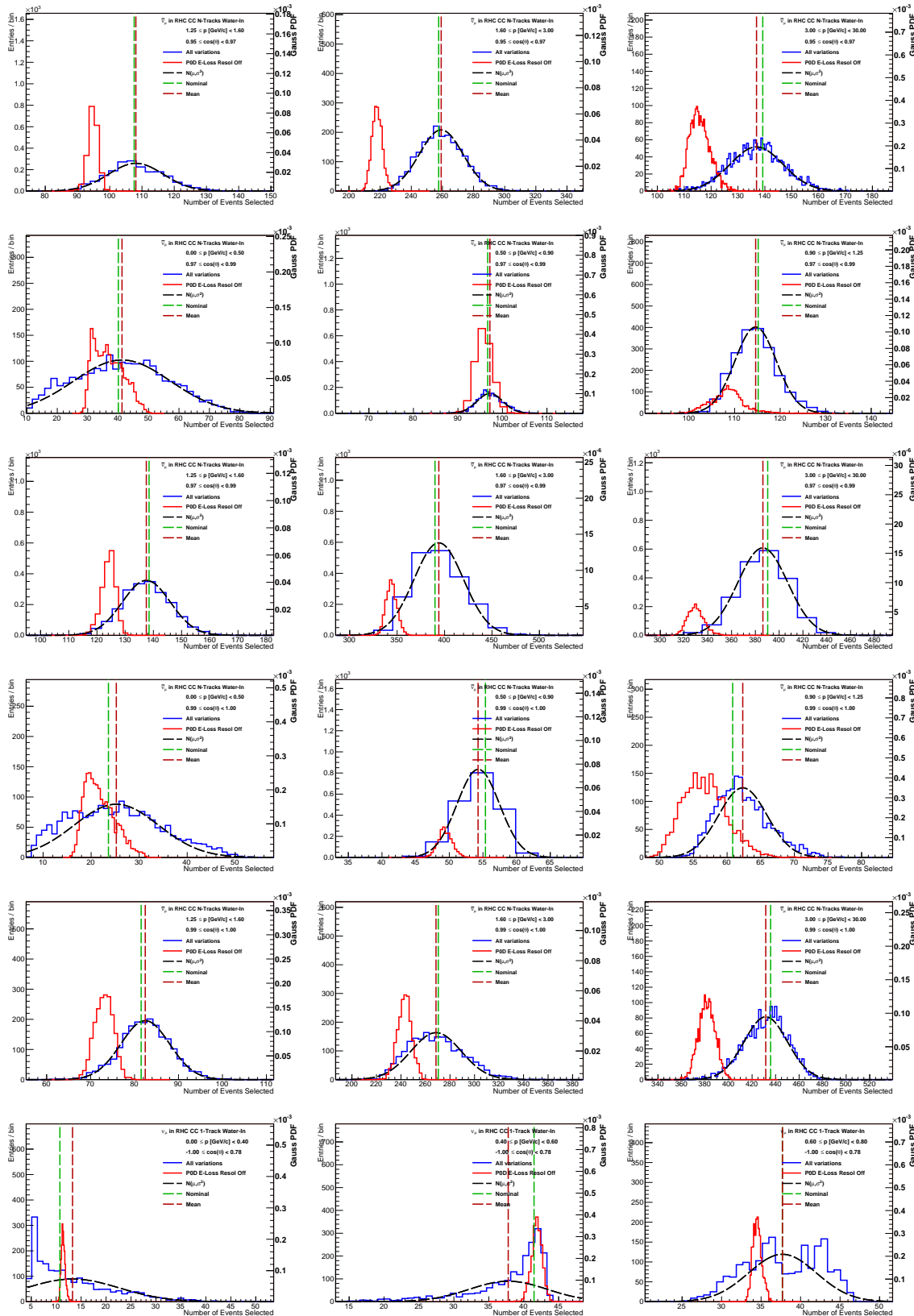


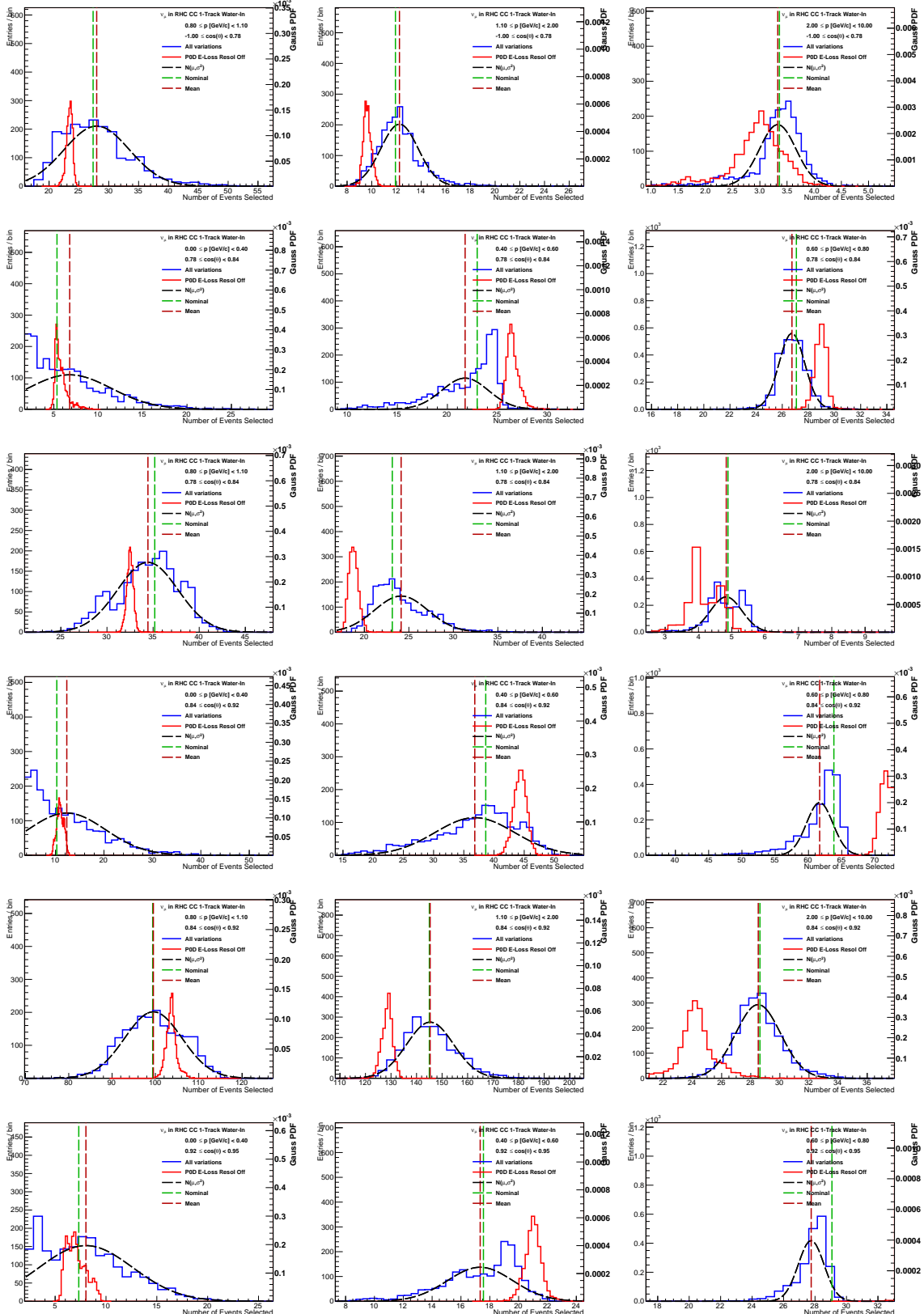


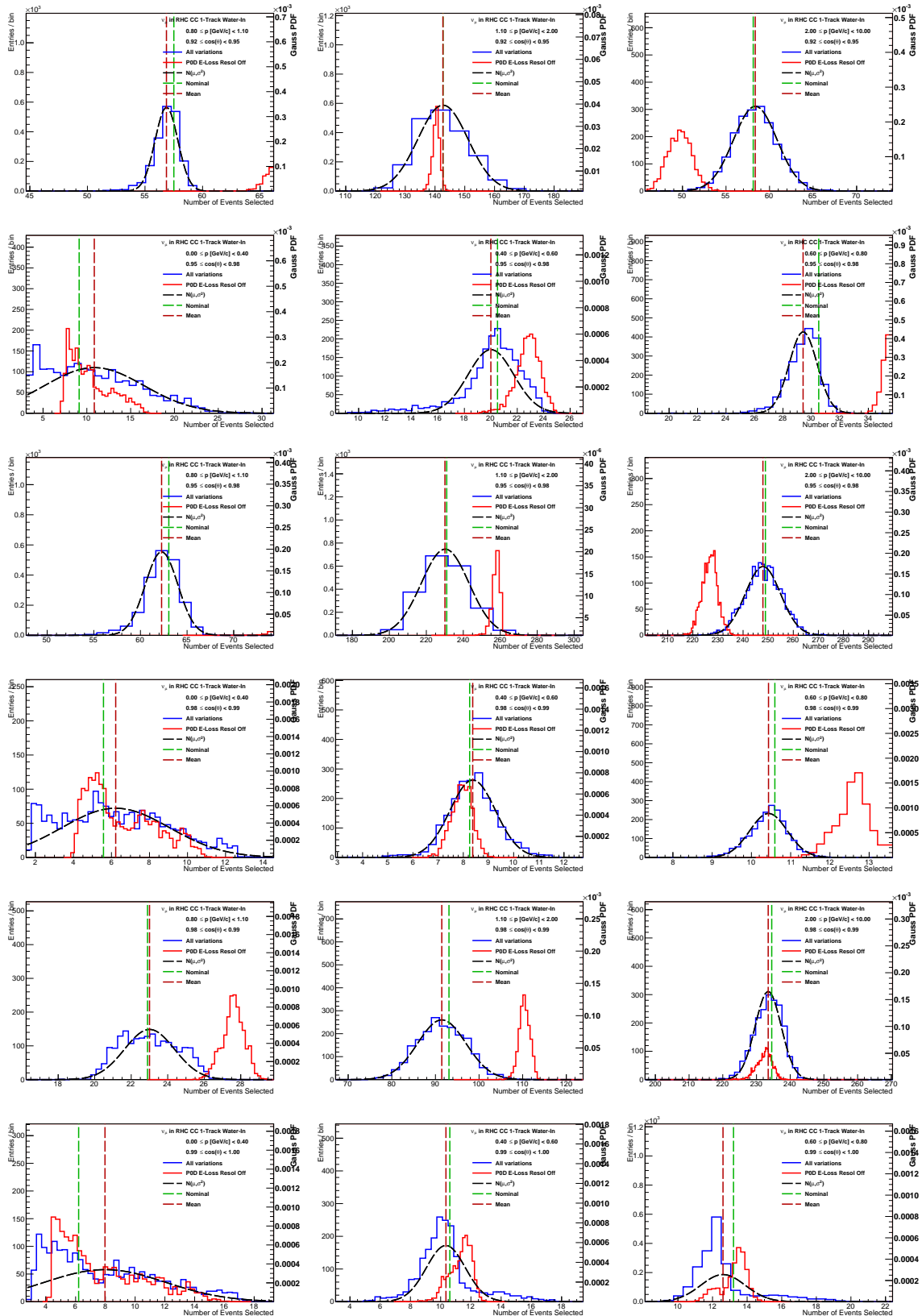


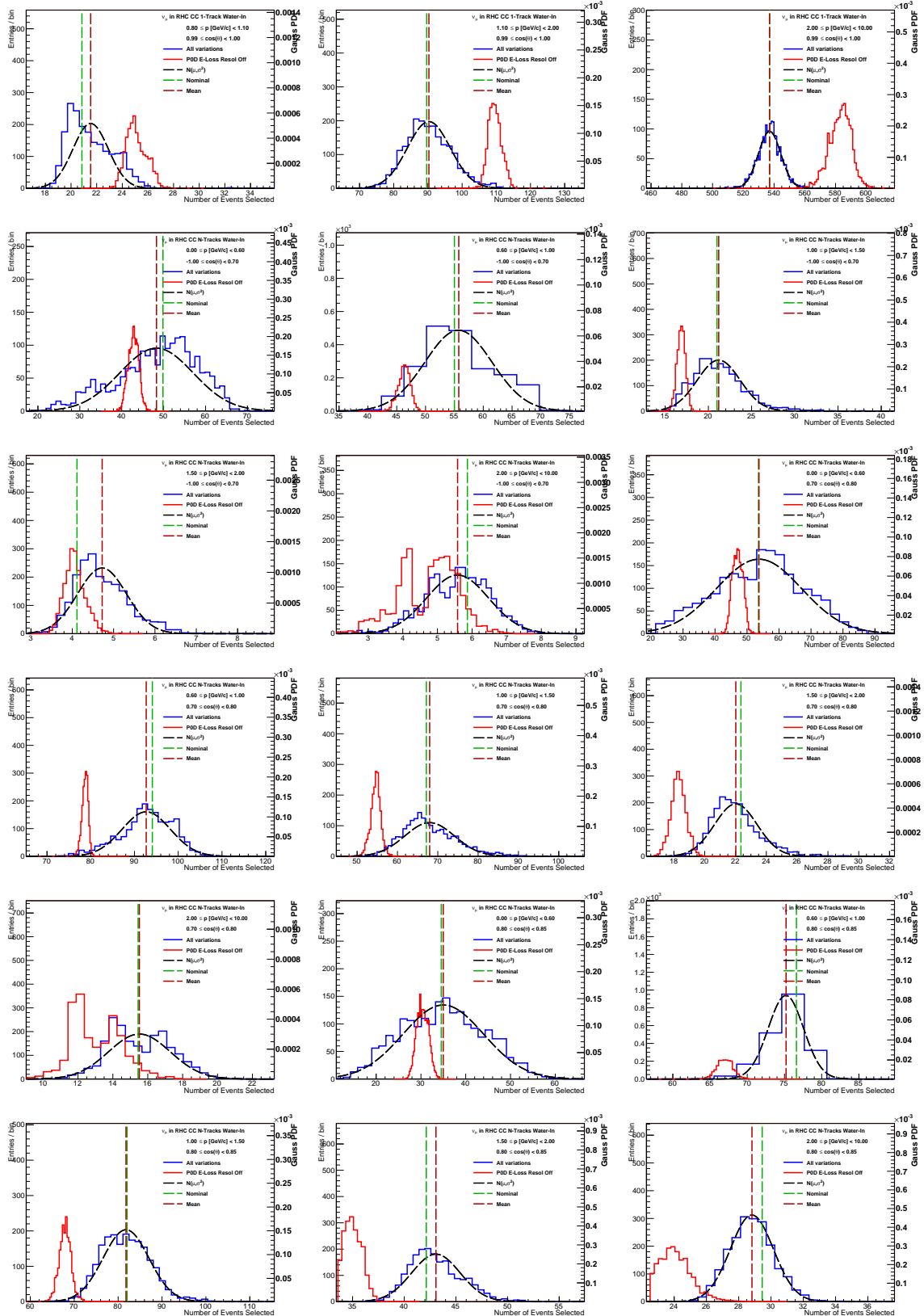


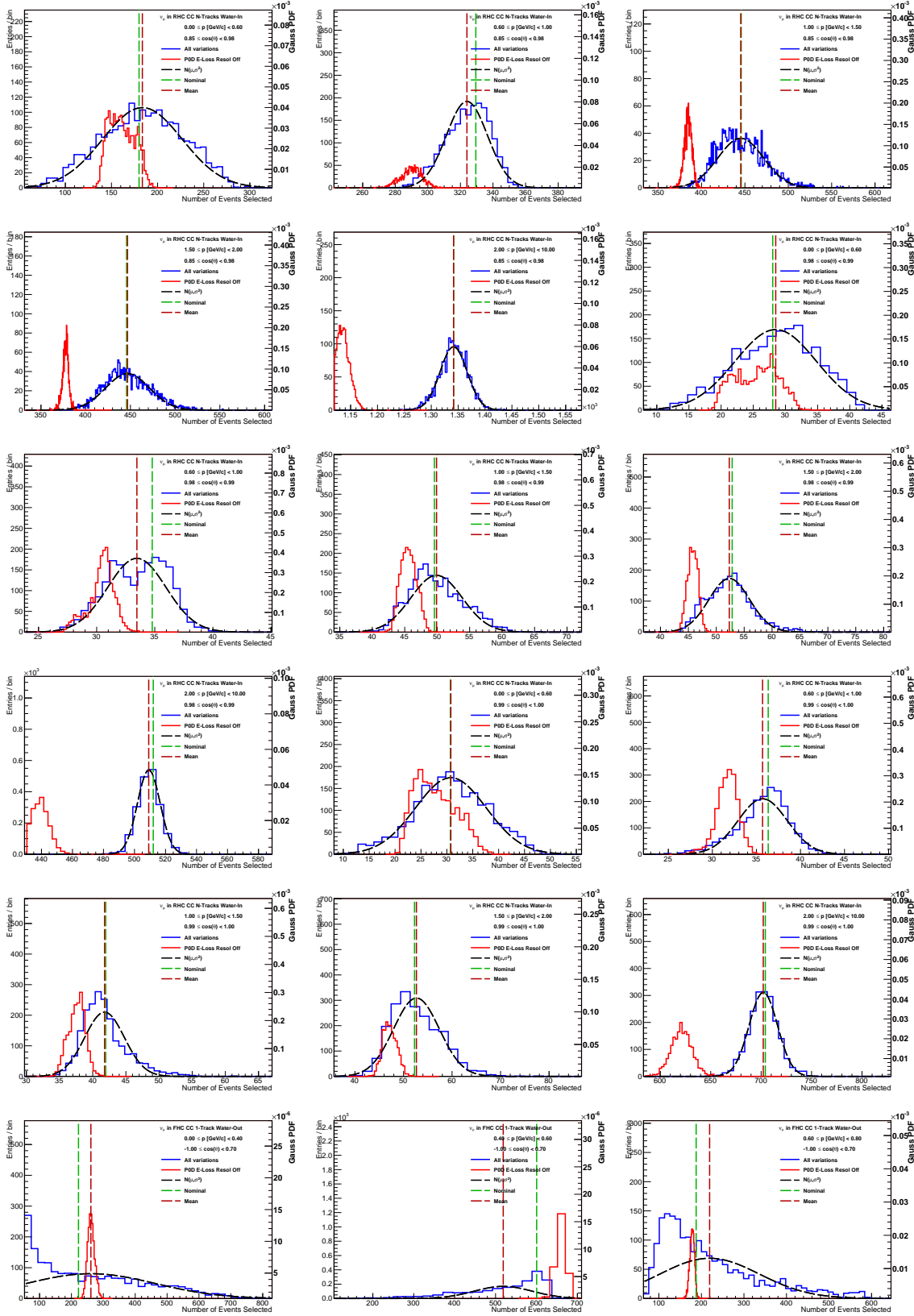


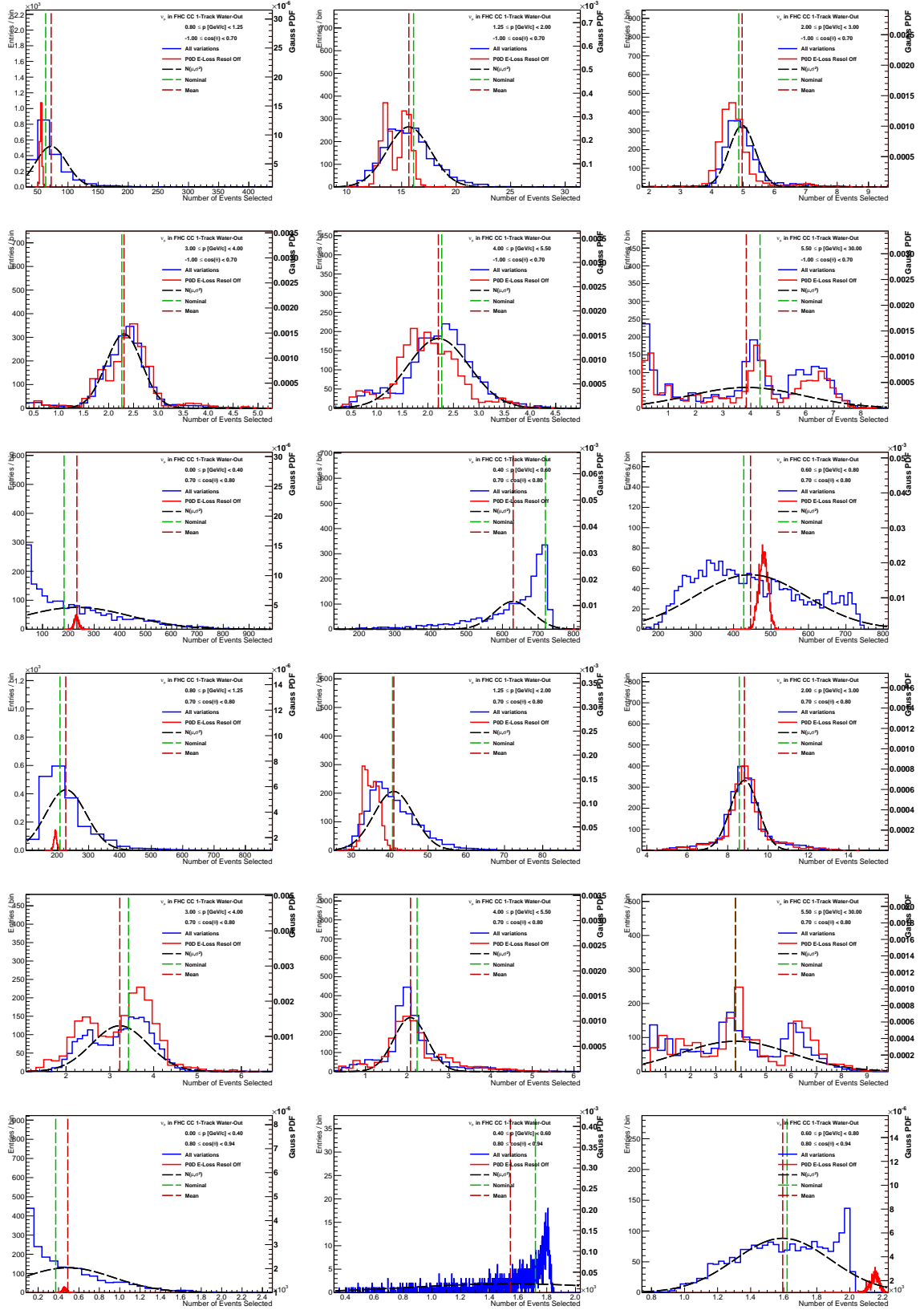


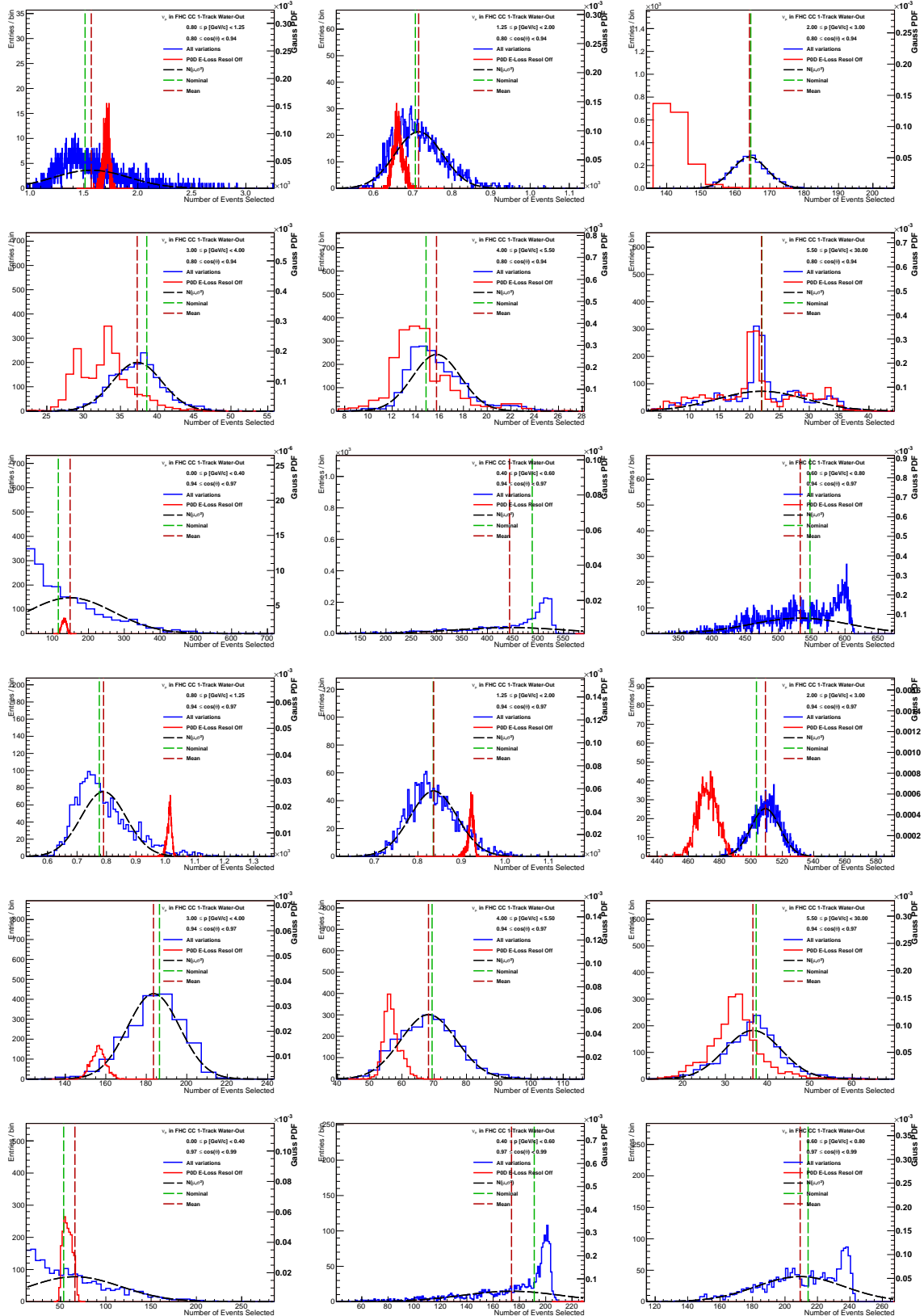


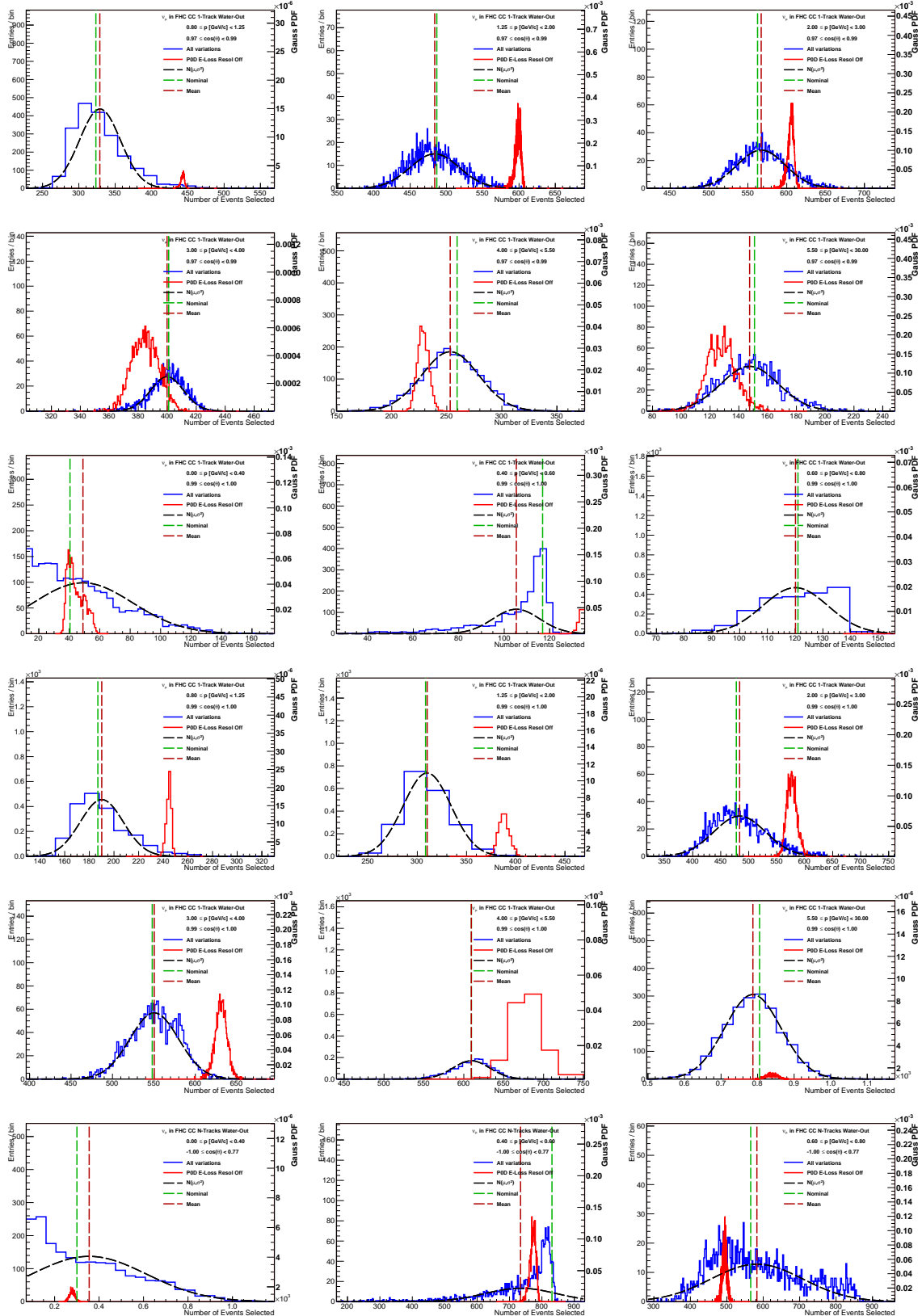


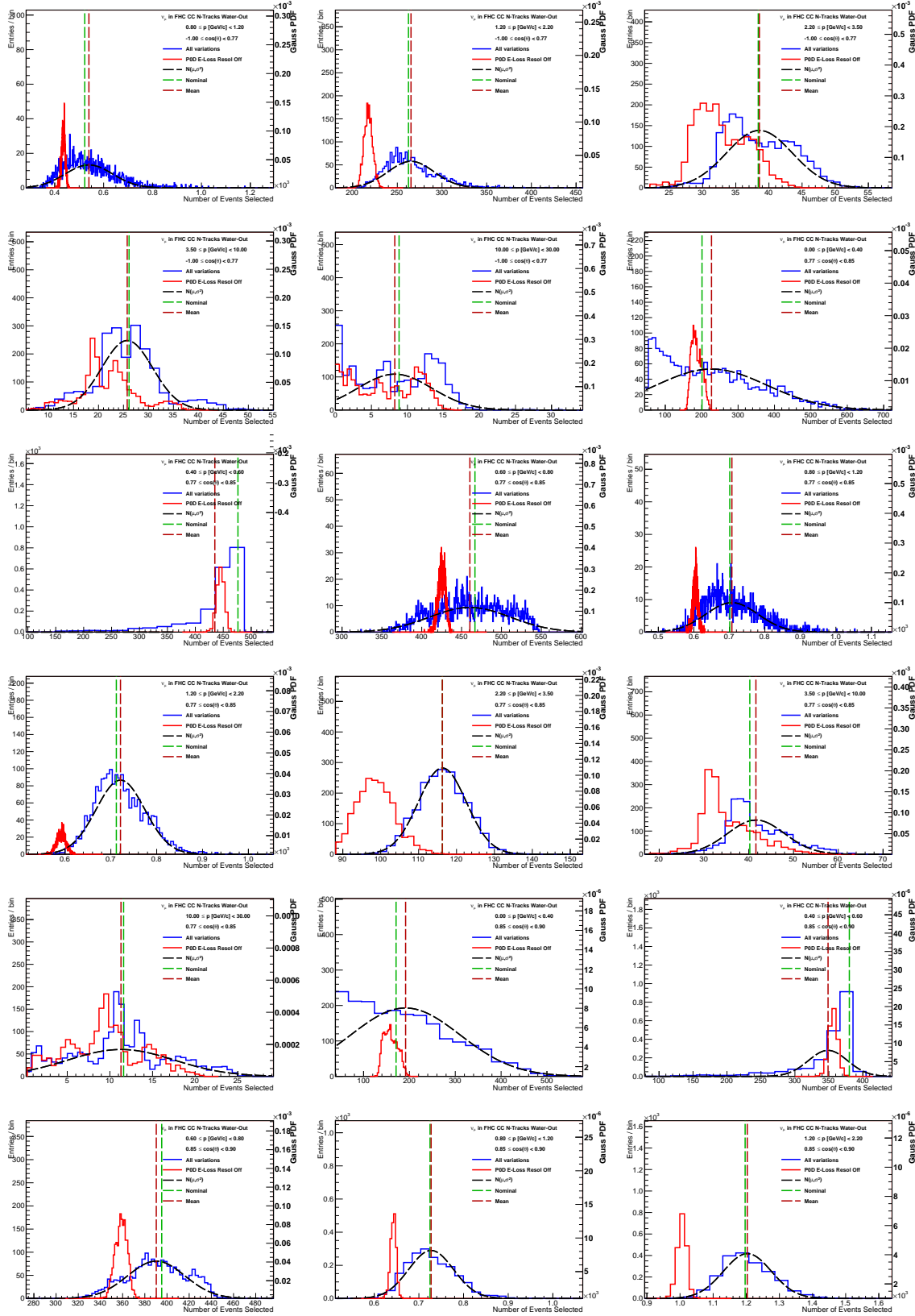


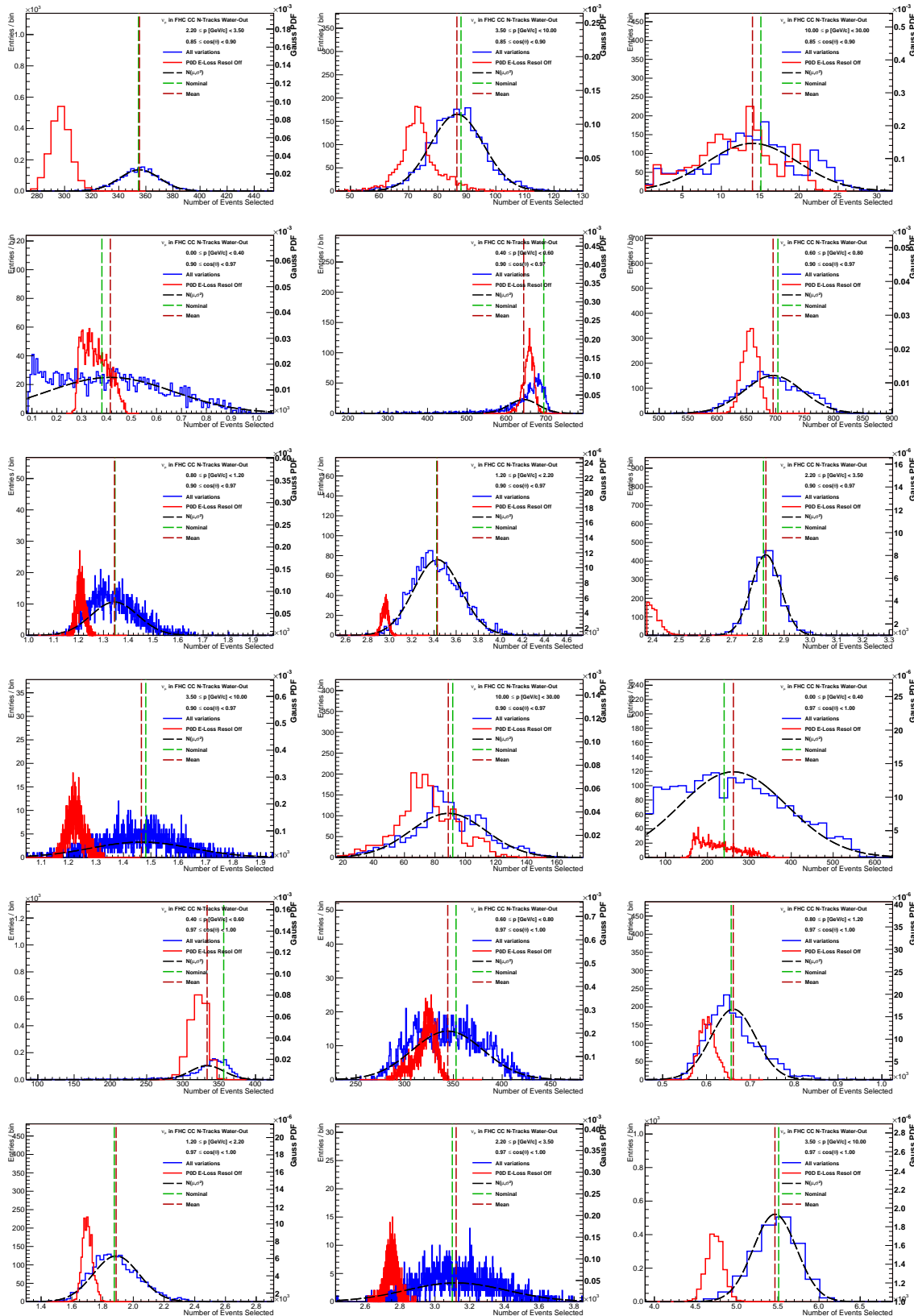


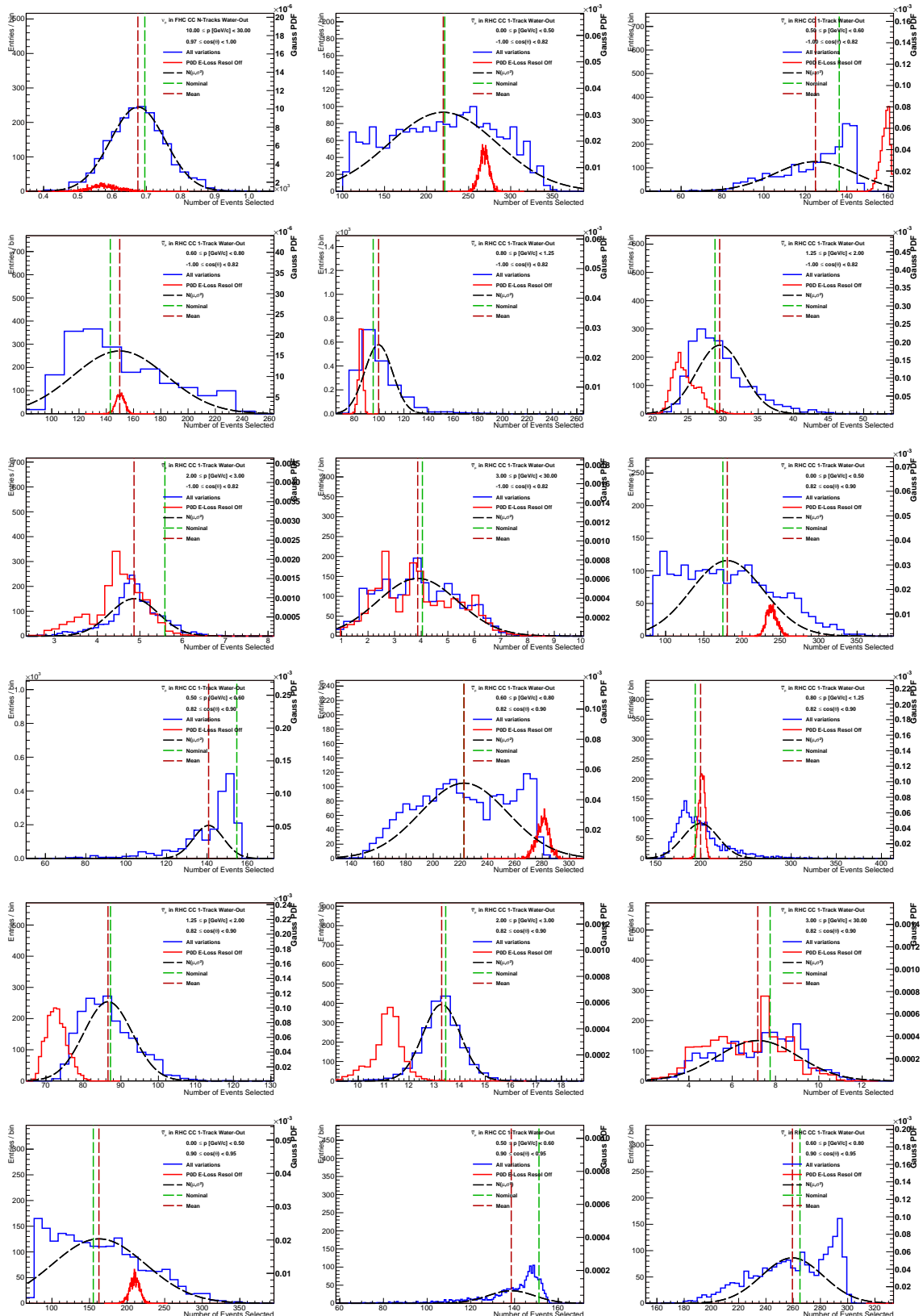


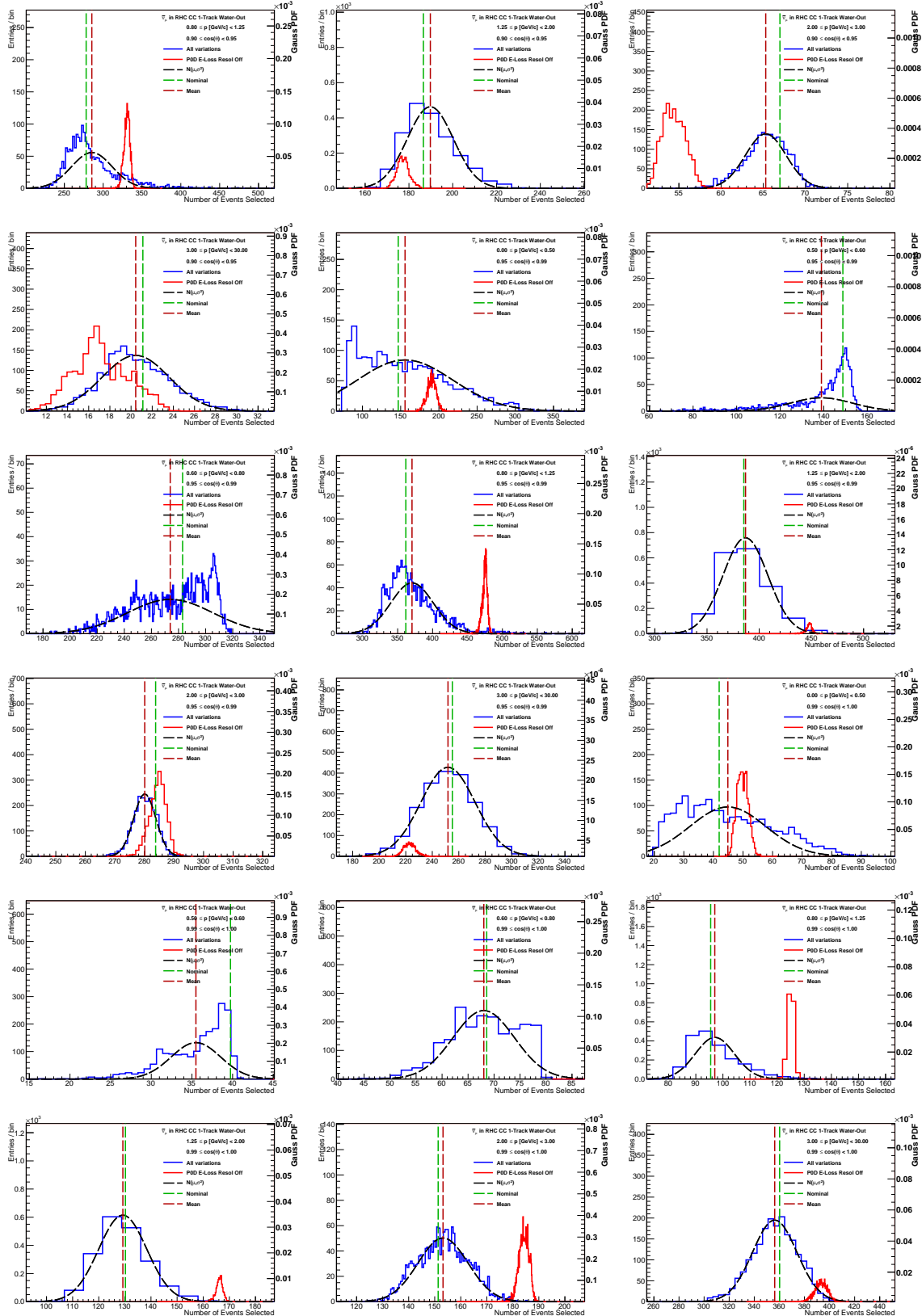


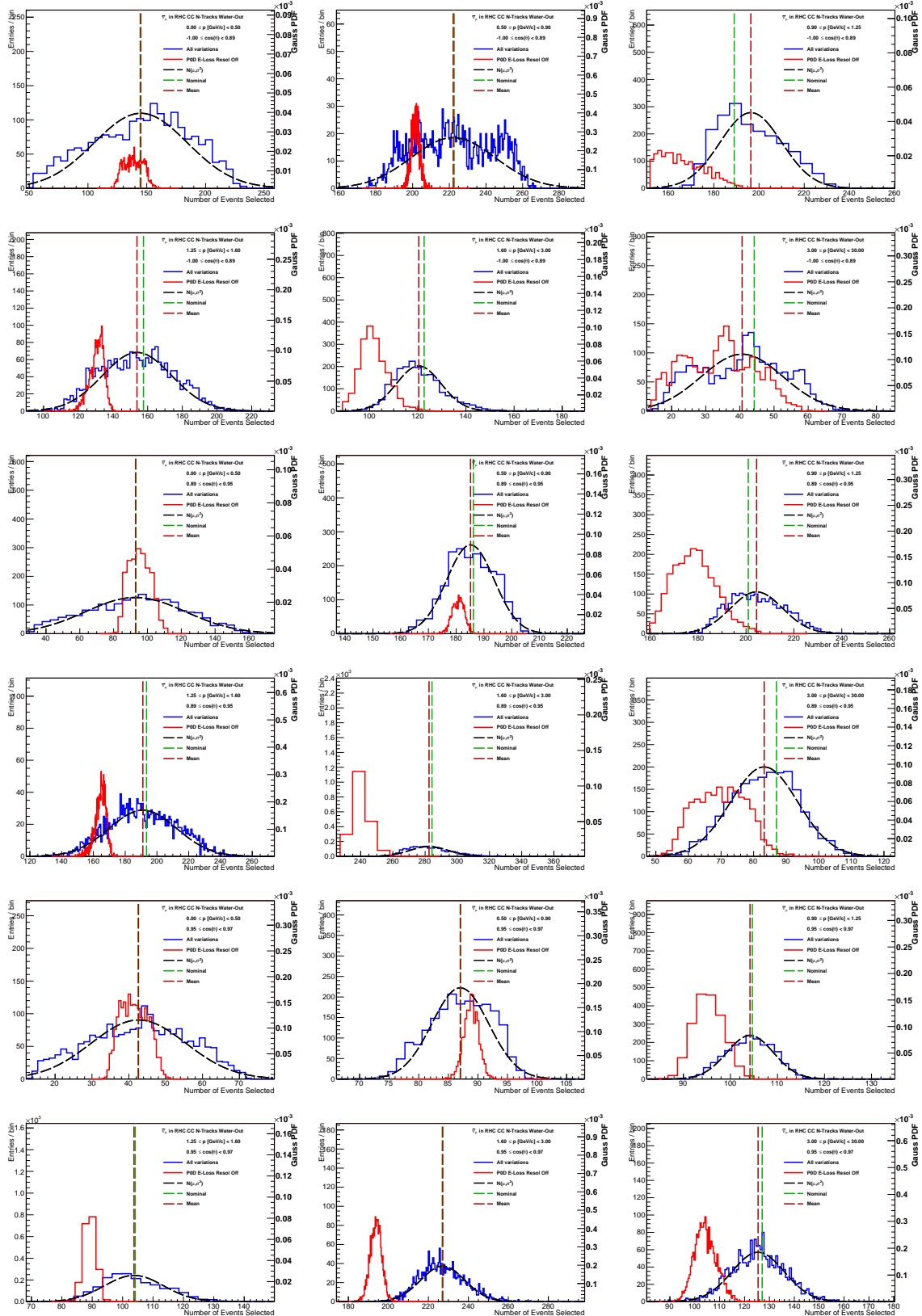


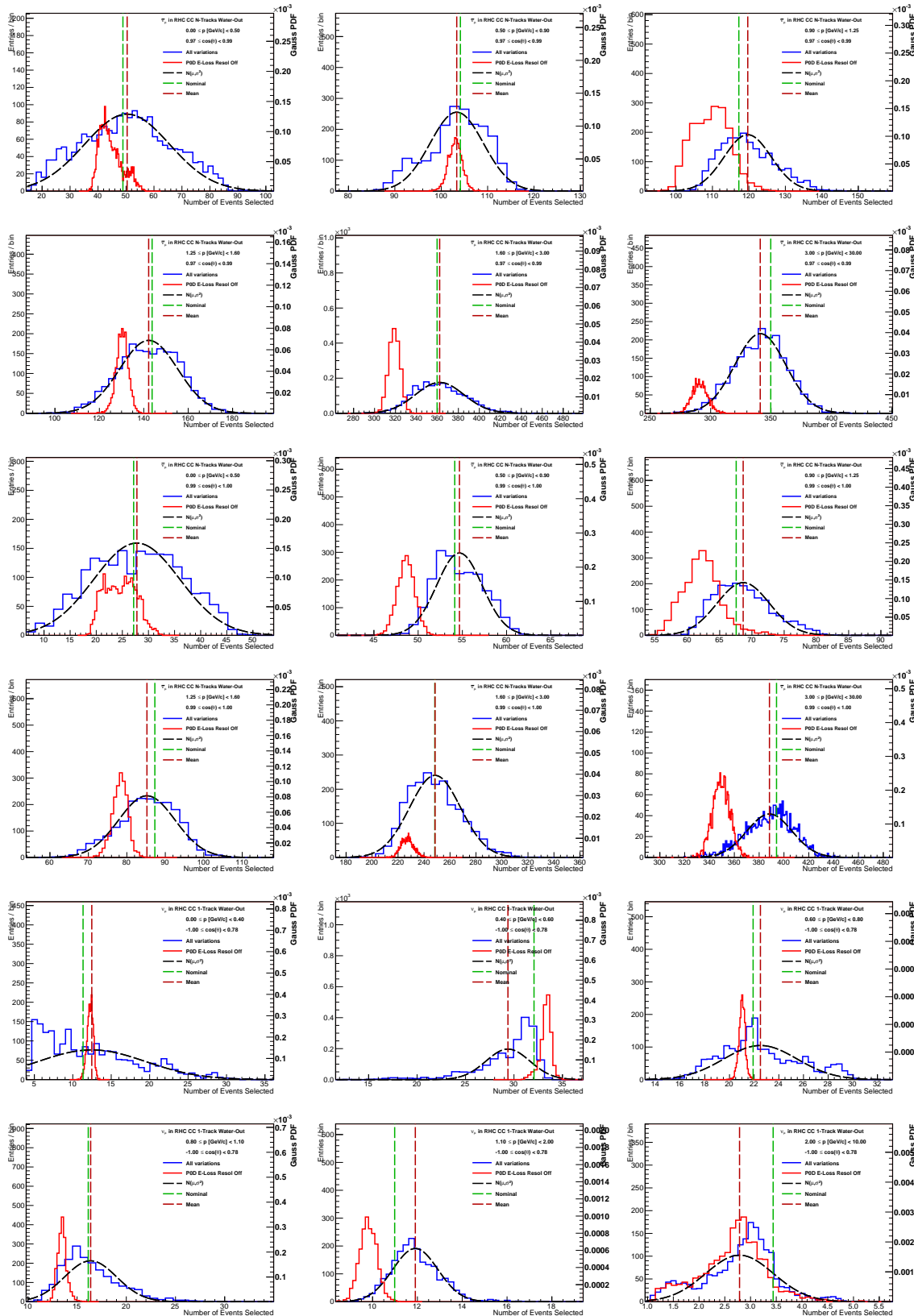


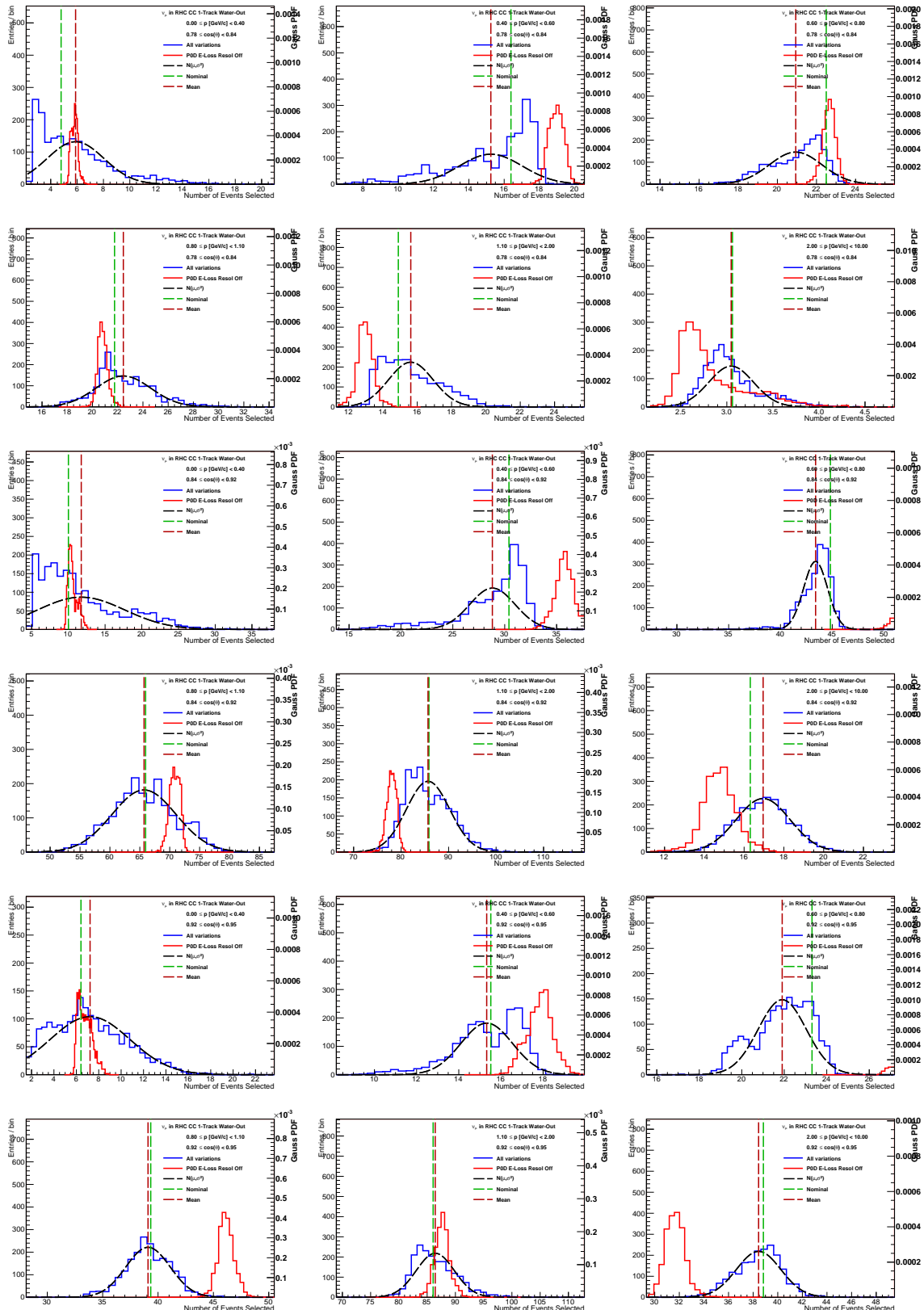


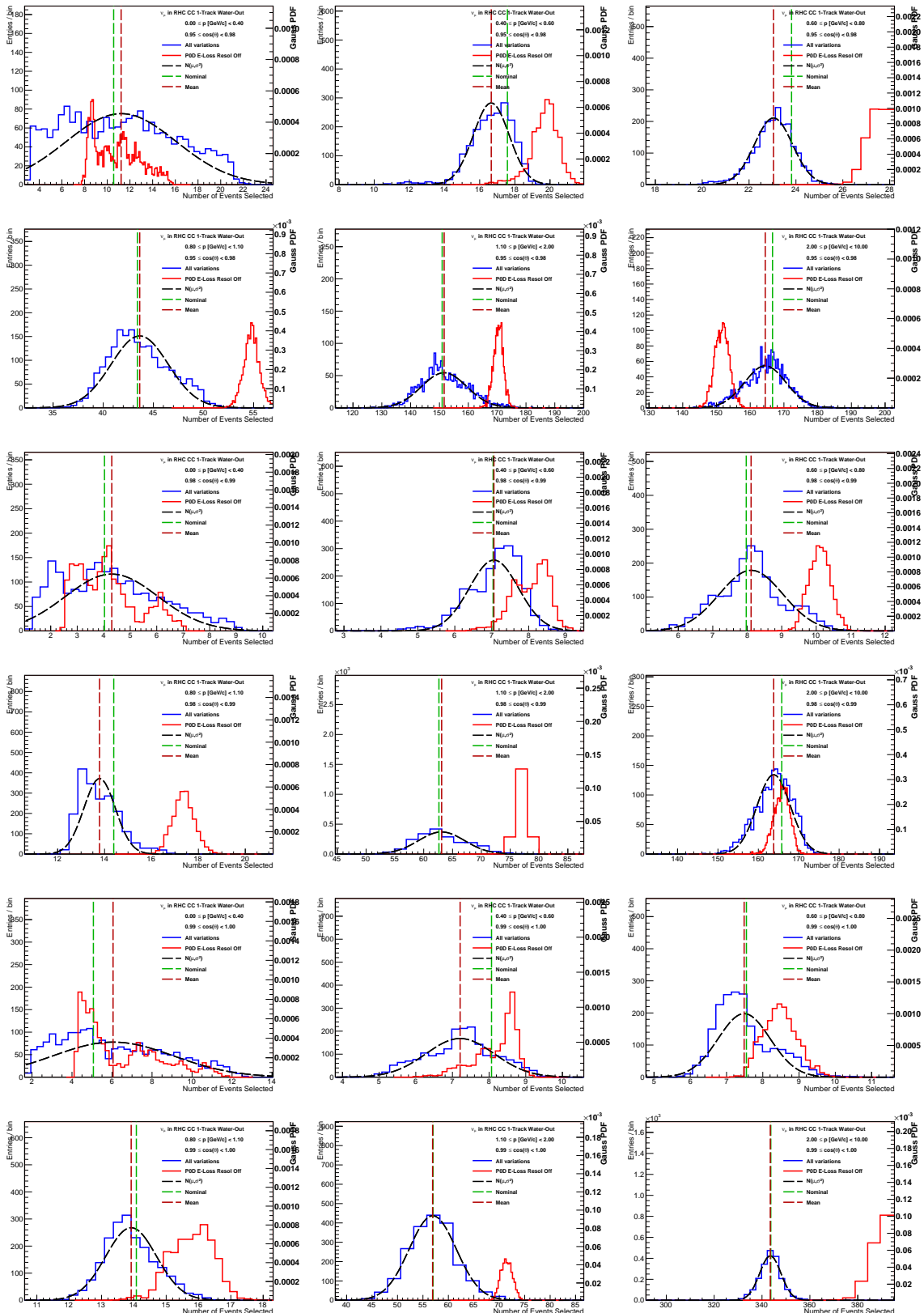


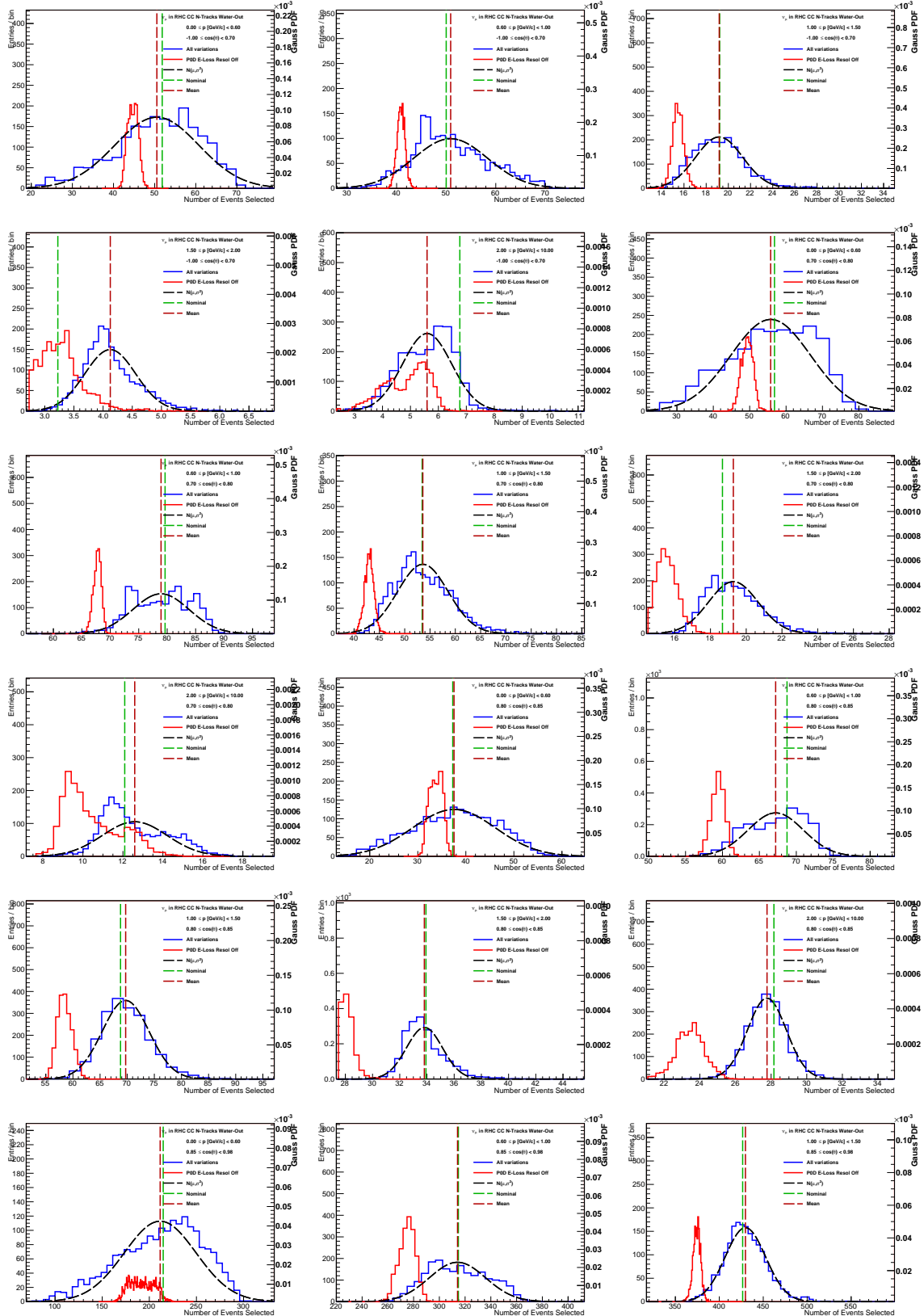


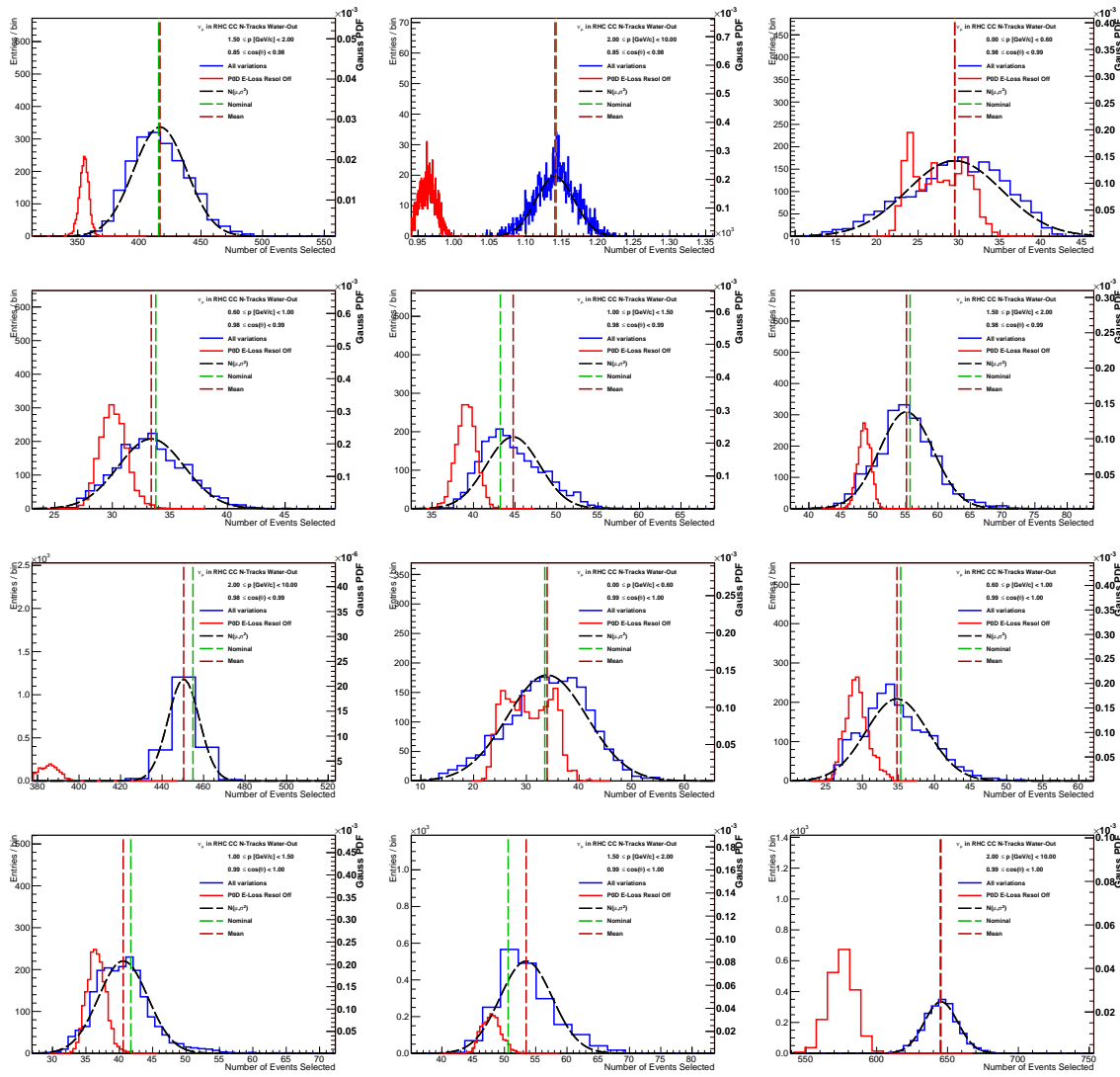












Appendix D

Cross Section Parameters Variations

This appendix is a tabulation of variations of the cross section parameters and their uncorrelated affect on the analysis samples. Note that the “nominal” column refers to all weighted events in the sample. When a “ $\pm 1\sigma$ ” variation is applied, the corresponding fractional change is reported.

Parameter	1σ value	Sample	-1σ (%)	nominal	$+1\sigma$ (%)
562 : FSI Low energy INEL	0.41	ν_μ 1-Trk Wtr	-0.9	27316.74	0.7
		ν_μ N-Trks	0.7	30904.32	-0.5
		$\bar{\nu}_\mu$ RHC 1-Trk	-0.5	8414.09	0.4
		$\bar{\nu}_\mu$ RHC N-Trks	1.0	4724.34	-0.7
		ν_μ RHC 1-Trk	-1.2	3022.10	0.9
		ν_μ RHC N-Trks	0.5	4928.38	-0.4
		ν_μ 1-Trk Air	-0.9	23605.76	0.7
		ν_μ N-Trks	0.5	32304.13	-0.4
		$\bar{\nu}_\mu$ RHC 1-Trk	-0.6	6767.65	0.5
		$\bar{\nu}_\mu$ RHC N-Trks	0.8	4544.65	-0.6
563 : FSI High energy INEL	0.34	ν_μ RHC 1-Trk	-1.5	2067.37	1.4
		ν_μ RHC N-Trks	0.6	4568.13	-0.7
		ν_μ 1-Trk Wtr	-0.2	27316.74	0.2
		ν_μ N-Trks	-0.1	30904.32	0.2
		$\bar{\nu}_\mu$ RHC 1-Trk	-0.1	8414.09	0.1
		$\bar{\nu}_\mu$ RHC N-Trks	-0.0	4724.34	0.1
		ν_μ RHC 1-Trk	-0.4	3022.10	0.4
		ν_μ RHC N-Trks	-0.1	4928.38	0.1
		ν_μ 1-Trk Air	-0.2	23605.76	0.1
		ν_μ N-Trks	-0.2	32304.13	0.2

Table D.1: Event rate variations per cross section parameter variation.

Parameter	1σ value	Sample	-1σ (%)	nominal	$+1\sigma$ (%)
564 : FSI PROD	0.50	ν_μ 1-Trk Wtr	-0.1	27316.74	0.1
		ν_μ N-Trks	-0.0	30904.32	0.1
		$\bar{\nu}_\mu$ RHC 1-Trk	-0.0	8414.09	0.0
		$\bar{\nu}_\mu$ RHC N-Trks	0.1	4724.34	-0.0
		ν_μ RHC 1-Trk	-0.1	3022.10	0.1
		ν_μ RHC N-Trks	-0.1	4928.38	0.1
		ν_μ 1-Trk Air	-0.0	23605.76	0.1
		ν_μ N-Trks	-0.1	32304.13	0.1
		$\bar{\nu}_\mu$ RHC 1-Trk	-0.0	6767.65	0.0
		$\bar{\nu}_\mu$ RHC N-Trks	0.2	4544.65	-0.1
565 : FSI ABS	0.41	ν_μ RHC 1-Trk	-0.1	2067.37	0.1
		ν_μ RHC N-Trks	-0.1	4568.13	0.1
		ν_μ 1-Trk Wtr	-0.7	27316.74	0.5
		ν_μ N-Trks	0.6	30904.32	-0.5
		$\bar{\nu}_\mu$ RHC 1-Trk	-0.6	8414.09	0.5
		$\bar{\nu}_\mu$ RHC N-Trks	1.0	4724.34	-0.8
		ν_μ RHC 1-Trk	-1.0	3022.10	0.8
		ν_μ RHC N-Trks	0.5	4928.38	-0.4
		ν_μ 1-Trk Air	-0.7	23605.76	0.6
		ν_μ N-Trks	0.6	32304.13	-0.4

Event rate variations per cross section parameter variation.

Parameter	1σ value	Sample	-1σ (%)	nominal	$+1\sigma$ (%)
566 : FSI Low energy CEX	0.57	ν_μ 1-Trk Wtr	0.3	27316.74	-0.2
		ν_μ N-Trks	-0.3	30904.32	0.2
		$\bar{\nu}_\mu$ RHC 1-Trk	0.2	8414.09	-0.1
		$\bar{\nu}_\mu$ RHC N-Trks	-0.2	4724.34	0.2
		ν_μ RHC 1-Trk	0.4	3022.10	-0.3
		ν_μ RHC N-Trks	-0.3	4928.38	0.2
		ν_μ 1-Trk Air	0.3	23605.76	-0.2
		ν_μ N-Trks	-0.3	32304.13	0.2
		$\bar{\nu}_\mu$ RHC 1-Trk	0.2	6767.65	-0.1
		$\bar{\nu}_\mu$ RHC N-Trks	-0.3	4544.65	0.3
		ν_μ RHC 1-Trk	0.2	2067.37	-0.2
		ν_μ RHC N-Trks	-0.1	4568.13	0.1
567 : FSI High energy CEX	0.28	ν_μ 1-Trk Wtr	-0.0	27316.74	0.0
		ν_μ N-Trks	-0.0	30904.32	0.0
		$\bar{\nu}_\mu$ RHC 1-Trk	-0.0	8414.09	0.0
		$\bar{\nu}_\mu$ RHC N-Trks	0.0	4724.34	-0.0
		ν_μ RHC 1-Trk	-0.1	3022.10	0.1
		ν_μ RHC N-Trks	-0.0	4928.38	0.0
		ν_μ 1-Trk Air	-0.0	23605.76	0.0
		ν_μ N-Trks	-0.1	32304.13	0.1
		$\bar{\nu}_\mu$ RHC 1-Trk	-0.0	6767.65	0.0
		$\bar{\nu}_\mu$ RHC N-Trks	0.0	4544.65	-0.0
		ν_μ RHC 1-Trk	-0.0	2067.37	0.0
		ν_μ RHC N-Trks	-0.0	4568.13	0.0

Event rate variations per cross section parameter variation.

Parameter	1σ value	Sample	-1σ (%)	nominal	$+1\sigma$ (%)
568 : M_A^{QE}	0.03	ν_μ 1-Trk Wtr	-0.8	27316.74	0.8
		ν_μ N-Trks	-0.4	30904.32	0.4
		$\bar{\nu}_\mu$ RHC 1-Trk	-0.7	8414.09	0.7
		$\bar{\nu}_\mu$ RHC N-Trks	-0.2	4724.34	0.3
		ν_μ RHC 1-Trk	-0.9	3022.10	0.9
		ν_μ RHC N-Trks	-0.4	4928.38	0.4
		ν_μ 1-Trk Air	-0.8	23605.76	0.8
		ν_μ N-Trks	-0.5	32304.13	0.5
		$\bar{\nu}_\mu$ RHC 1-Trk	-0.7	6767.65	0.7
		$\bar{\nu}_\mu$ RHC N-Trks	-0.2	4544.65	0.3
569 : p_F^C	0.06	ν_μ RHC 1-Trk	-0.9	2067.37	0.9
		ν_μ RHC N-Trks	-0.4	4568.13	0.4
		ν_μ 1-Trk Wtr	0.8	27316.74	-0.7
		ν_μ N-Trks	0.0	30904.32	-0.0
		$\bar{\nu}_\mu$ RHC 1-Trk	0.7	8414.09	-0.7
		$\bar{\nu}_\mu$ RHC N-Trks	0.0	4724.34	-0.0
		ν_μ RHC 1-Trk	0.4	3022.10	-0.4
		ν_μ RHC N-Trks	0.0	4928.38	-0.0
		ν_μ 1-Trk Air	1.1	23605.76	-1.0
		ν_μ N-Trks	0.0	32304.13	-0.0

Event rate variations per cross section parameter variation.

Parameter	1σ value	Sample	-1σ (%)	nominal	$+1\sigma$ (%)
570 : p_F^O	0.06	ν_μ 1-Trk Wtr	0.4	27316.74	-0.4
		ν_μ N-Trks	0.0	30904.32	-0.0
		$\bar{\nu}_\mu$ RHC 1-Trk	0.5	8414.09	-0.5
		$\bar{\nu}_\mu$ RHC N-Trks	0.0	4724.34	-0.0
		ν_μ RHC 1-Trk	0.3	3022.10	-0.3
		ν_μ RHC N-Trks	0.0	4928.38	-0.0
		ν_μ 1-Trk Air	0.0	23605.76	-0.0
		ν_μ N-Trks	0.0	32304.13	-0.0
		$\bar{\nu}_\mu$ RHC 1-Trk	0.0	6767.65	-0.0
		$\bar{\nu}_\mu$ RHC N-Trks	-0.0	4544.65	-0.0
		ν_μ RHC 1-Trk	-0.0	2067.37	0.0
		ν_μ RHC N-Trks	0.0	4568.13	-0.0
571 : 2p2h ν norm. on ^{12}C	1.00	ν_μ 1-Trk Wtr	-8.9	27316.74	8.9
		ν_μ N-Trks	-3.0	30904.32	3.0
		$\bar{\nu}_\mu$ RHC 1-Trk	-0.1	8414.09	0.1
		$\bar{\nu}_\mu$ RHC N-Trks	-0.2	4724.34	0.2
		ν_μ RHC 1-Trk	-9.0	3022.10	9.0
		ν_μ RHC N-Trks	-2.6	4928.38	2.6
		ν_μ 1-Trk Air	-8.1	23605.76	8.1
		ν_μ N-Trks	-3.3	32304.13	3.3
		$\bar{\nu}_\mu$ RHC 1-Trk	-0.1	6767.65	0.1
		$\bar{\nu}_\mu$ RHC N-Trks	-0.2	4544.65	0.2
		ν_μ RHC 1-Trk	-8.6	2067.37	8.6
		ν_μ RHC N-Trks	-2.8	4568.13	2.8

Event rate variations per cross section parameter variation.

Parameter	1σ value	Sample	-1σ (%)	nominal	$+1\sigma$ (%)
572 : 2p2h $\bar{\nu}$ norm. on ^{12}C	1.00	ν_μ 1-Trk Wtr	-0.0	27316.74	0.0
		ν_μ N-Trks	-0.0	30904.32	0.0
		$\bar{\nu}_\mu$ RHC 1-Trk	-9.3	8414.09	9.3
		$\bar{\nu}_\mu$ RHC N-Trks	-2.1	4724.34	2.1
		ν_μ RHC 1-Trk	-0.2	3022.10	0.2
		ν_μ RHC N-Trks	-0.0	4928.38	0.0
		ν_μ 1-Trk Air	-0.0	23605.76	0.0
		ν_μ N-Trks	-0.0	32304.13	0.0
		$\bar{\nu}_\mu$ RHC 1-Trk	-8.9	6767.65	8.9
		$\bar{\nu}_\mu$ RHC N-Trks	-2.2	4544.65	2.2
		ν_μ RHC 1-Trk	-0.3	2067.37	0.3
		ν_μ RHC N-Trks	-0.0	4568.13	0.0
573 : 2p2h $^{12}\text{C} \rightarrow ^{16}\text{O}$ norm.	0.20	ν_μ 1-Trk Wtr	-0.6	27316.74	0.6
		ν_μ N-Trks	-0.2	30904.32	0.2
		$\bar{\nu}_\mu$ RHC 1-Trk	-0.8	8414.09	0.8
		$\bar{\nu}_\mu$ RHC N-Trks	-0.2	4724.34	0.2
		ν_μ RHC 1-Trk	-0.8	3022.10	0.8
		ν_μ RHC N-Trks	-0.2	4928.38	0.2
		ν_μ 1-Trk Air	-0.0	23605.76	0.0
		ν_μ N-Trks	-0.0	32304.13	0.0
		$\bar{\nu}_\mu$ RHC 1-Trk	-0.0	6767.65	0.0
		$\bar{\nu}_\mu$ RHC N-Trks	-0.0	4544.65	0.0
		ν_μ RHC 1-Trk	-0.0	2067.37	0.0
		ν_μ RHC N-Trks	-0.0	4568.13	0.0

Event rate variations per cross section parameter variation.

Parameter	1σ value	Sample	-1σ (%)	nominal	$+1\sigma$ (%)
574 : 2p2h ^{12}C shape location	2.00	ν_μ 1-Trk Wtr	3.8	27316.74	0.0
		ν_μ N-Trks	-1.1	30904.32	0.0
		$\bar{\nu}_\mu$ RHC 1-Trk	0.2	8414.09	0.0
		$\bar{\nu}_\mu$ RHC N-Trks	-0.8	4724.34	0.0
		ν_μ RHC 1-Trk	4.3	3022.10	0.0
		ν_μ RHC N-Trks	-0.8	4928.38	0.0
		ν_μ 1-Trk Air	5.7	23605.76	0.0
		ν_μ N-Trks	-1.5	32304.13	0.0
		$\bar{\nu}_\mu$ RHC 1-Trk	0.2	6767.65	0.0
		$\bar{\nu}_\mu$ RHC N-Trks	-1.1	4544.65	0.0
575 : 2p2h ^{16}O shape location	2.00	ν_μ RHC 1-Trk	8.1	2067.37	0.0
		ν_μ RHC N-Trks	-1.4	4568.13	0.0
		ν_μ 1-Trk Wtr	2.1	27316.74	0.0
		ν_μ N-Trks	-0.5	30904.32	0.0
		$\bar{\nu}_\mu$ RHC 1-Trk	0.1	8414.09	0.0
		$\bar{\nu}_\mu$ RHC N-Trks	-0.5	4724.34	0.0
		ν_μ RHC 1-Trk	3.2	3022.10	0.0
		ν_μ RHC N-Trks	-0.6	4928.38	0.0
		ν_μ 1-Trk Air	0.0	23605.76	0.0
		ν_μ N-Trks	-0.0	32304.13	0.0

Event rate variations per cross section parameter variation.

Parameter	1σ value	Sample	-1σ (%)	nominal	$+1\sigma$ (%)
576 : BeRPA A scale	0.12	ν_μ 1-Trk Wtr	-5.1	27316.74	5.1
		ν_μ N-Trks	-0.3	30904.32	0.3
		$\bar{\nu}_\mu$ RHC 1-Trk	-4.7	8414.09	4.7
		$\bar{\nu}_\mu$ RHC N-Trks	-0.2	4724.34	0.2
		ν_μ RHC 1-Trk	-3.5	3022.10	3.5
		ν_μ RHC N-Trks	-0.1	4928.38	0.1
		ν_μ 1-Trk Air	-5.1	23605.76	5.1
		ν_μ N-Trks	-0.3	32304.13	0.3
		$\bar{\nu}_\mu$ RHC 1-Trk	-4.6	6767.65	4.6
		$\bar{\nu}_\mu$ RHC N-Trks	-0.1	4544.65	0.1
577 : BeRPA B scale	0.21	ν_μ RHC 1-Trk	-3.7	2067.37	3.7
		ν_μ RHC N-Trks	-0.2	4568.13	0.2
		ν_μ 1-Trk Wtr	-3.4	27316.74	3.4
		ν_μ N-Trks	-0.6	30904.32	0.6
		$\bar{\nu}_\mu$ RHC 1-Trk	-2.6	8414.09	2.6
		$\bar{\nu}_\mu$ RHC N-Trks	-0.2	4724.34	0.2
		ν_μ RHC 1-Trk	-3.1	3022.10	3.1
		ν_μ RHC N-Trks	-0.4	4928.38	0.4
		ν_μ 1-Trk Air	-3.3	23605.76	3.3
		ν_μ N-Trks	-0.6	32304.13	0.6

Event rate variations per cross section parameter variation.

Parameter	1σ value	Sample	-1σ (%)	nominal	$+1\sigma$ (%)
578 : BeRPA D scale	0.17	ν_μ 1-Trk Wtr	-1.3	27316.74	1.3
		ν_μ N-Trks	-1.0	30904.32	1.0
		$\bar{\nu}_\mu$ RHC 1-Trk	-1.0	8414.09	1.0
		$\bar{\nu}_\mu$ RHC N-Trks	-0.5	4724.34	0.5
		ν_μ RHC 1-Trk	-1.7	3022.10	1.7
		ν_μ RHC N-Trks	-0.9	4928.38	0.9
		ν_μ 1-Trk Air	-1.1	23605.76	1.1
		ν_μ N-Trks	-0.9	32304.13	0.9
		$\bar{\nu}_\mu$ RHC 1-Trk	-0.9	6767.65	0.9
		$\bar{\nu}_\mu$ RHC N-Trks	-0.4	4544.65	0.4
579 : BeRPA E scale	0.35	ν_μ RHC 1-Trk	-1.4	2067.37	1.4
		ν_μ RHC N-Trks	-0.9	4568.13	0.9
		ν_μ 1-Trk Wtr	-0.1	27316.74	0.1
		ν_μ N-Trks	-0.0	30904.32	0.0
		$\bar{\nu}_\mu$ RHC 1-Trk	-0.1	8414.09	0.1
		$\bar{\nu}_\mu$ RHC N-Trks	0.0	4724.34	-0.0
		ν_μ RHC 1-Trk	-0.1	3022.10	0.1
		ν_μ RHC N-Trks	-0.0	4928.38	0.0
		ν_μ 1-Trk Air	-0.1	23605.76	0.1
		ν_μ N-Trks	-0.0	32304.13	0.0

Event rate variations per cross section parameter variation.

Parameter	1σ value	Sample	-1σ (%)	nominal	$+1\sigma$ (%)
580 : BeRPA U scale*	0.10	ν_μ 1-Trk Wtr	0.7	27316.74	-0.7
		ν_μ N-Trks	0.1	30904.32	-0.1
		$\bar{\nu}_\mu$ RHC 1-Trk	0.6	8414.09	-0.5
		$\bar{\nu}_\mu$ RHC N-Trks	0.0	4724.34	-0.0
		ν_μ RHC 1-Trk	0.7	3022.10	-0.6
		ν_μ RHC N-Trks	0.1	4928.38	-0.1
		ν_μ 1-Trk Air	0.7	23605.76	-0.6
		ν_μ N-Trks	0.1	32304.13	-0.1
		$\bar{\nu}_\mu$ RHC 1-Trk	0.5	6767.65	-0.5
		$\bar{\nu}_\mu$ RHC N-Trks	0.0	4544.65	-0.0
581 : C_A^5	0.15	ν_μ RHC 1-Trk	0.7	2067.37	-0.6
		ν_μ RHC N-Trks	0.1	4568.13	-0.1
		ν_μ 1-Trk Wtr	-3.4	27316.74	3.9
		ν_μ N-Trks	-4.4	30904.32	5.0
		$\bar{\nu}_\mu$ RHC 1-Trk	-2.7	8414.09	3.4
		$\bar{\nu}_\mu$ RHC N-Trks	-4.7	4724.34	5.8
		ν_μ RHC 1-Trk	-4.5	3022.10	5.2
		ν_μ RHC N-Trks	-4.1	4928.38	4.7
		ν_μ 1-Trk Air	-2.9	23605.76	3.3
		ν_μ N-Trks	-4.6	32304.13	5.2

Event rate variations per cross section parameter variation.

Parameter	1σ value	Sample	-1σ (%)	nominal	$+1\sigma$ (%)
582 : M_A^{RES}	0.16	ν_μ 1-Trk Wtr	-2.1	27316.74	1.9
		ν_μ N-Trks	-4.8	30904.32	5.1
		$\bar{\nu}_\mu$ RHC 1-Trk	-1.6	8414.09	1.6
		$\bar{\nu}_\mu$ RHC N-Trks	-4.8	4724.34	5.8
		ν_μ RHC 1-Trk	-3.1	3022.10	2.9
		ν_μ RHC N-Trks	-4.8	4928.38	5.3
		ν_μ 1-Trk Air	-1.7	23605.76	1.5
		ν_μ N-Trks	-4.6	32304.13	4.9
		$\bar{\nu}_\mu$ RHC 1-Trk	-1.4	6767.65	1.5
		$\bar{\nu}_\mu$ RHC N-Trks	-4.8	4544.65	5.9
		ν_μ RHC 1-Trk	-2.5	2067.37	2.3
		ν_μ RHC N-Trks	-4.7	4568.13	5.2
583 : $I=^{1/2}$ bkg. norm.	0.31	ν_μ 1-Trk Wtr	-1.1	27316.74	1.8
		ν_μ N-Trks	-2.4	30904.32	3.7
		$\bar{\nu}_\mu$ RHC 1-Trk	-0.8	8414.09	1.3
		$\bar{\nu}_\mu$ RHC N-Trks	-3.1	4724.34	4.8
		ν_μ RHC 1-Trk	-1.7	3022.10	2.5
		ν_μ RHC N-Trks	-2.5	4928.38	3.8
		ν_μ 1-Trk Air	-1.1	23605.76	1.6
		ν_μ N-Trks	-2.4	32304.13	3.6
		$\bar{\nu}_\mu$ RHC 1-Trk	-0.7	6767.65	1.1
		$\bar{\nu}_\mu$ RHC N-Trks	-3.0	4544.65	4.5
		ν_μ RHC 1-Trk	-1.6	2067.37	2.4
		ν_μ RHC N-Trks	-2.4	4568.13	3.7

Event rate variations per cross section parameter variation.

Parameter	1σ value	Sample	-1σ (%)	nominal	$+1\sigma$ (%)
584 : CC-ν_e/ν_μ^*	0.03	ν_μ 1-Trk Wtr	0.0	27316.74	0.0
		ν_μ N-Trks	0.0	30904.32	0.0
		$\bar{\nu}_\mu$ RHC 1-Trk	0.0	8414.09	0.0
		$\bar{\nu}_\mu$ RHC N-Trks	0.0	4724.34	0.0
		ν_μ RHC 1-Trk	0.0	3022.10	0.0
		ν_μ RHC N-Trks	0.0	4928.38	0.0
		ν_μ 1-Trk Air	0.0	23605.76	0.0
		ν_μ N-Trks	0.0	32304.13	0.0
		$\bar{\nu}_\mu$ RHC 1-Trk	0.0	6767.65	0.0
		$\bar{\nu}_\mu$ RHC N-Trks	0.0	4544.65	0.0
585 : CC-$\bar{\nu}_e/\bar{\nu}_\mu^*$	0.03	ν_μ RHC 1-Trk	0.0	2067.37	0.0
		ν_μ RHC N-Trks	0.0	4568.13	0.0
		ν_μ 1-Trk Wtr	0.0	27316.74	0.0
		ν_μ N-Trks	0.0	30904.32	0.0
		$\bar{\nu}_\mu$ RHC 1-Trk	0.0	8414.09	0.0
		$\bar{\nu}_\mu$ RHC N-Trks	0.0	4724.34	0.0
		ν_μ RHC 1-Trk	0.0	3022.10	0.0
		ν_μ RHC N-Trks	0.0	4928.38	0.0
		ν_μ 1-Trk Air	0.0	23605.76	0.0
		ν_μ N-Trks	0.0	32304.13	0.0

Event rate variations per cross section parameter variation.

Parameter	1σ value	Sample	-1σ (%)	nominal	$+1\sigma$ (%)
586 : CC-DIS shape location	0.40	ν_μ 1-Trk Wtr	-0.4	27316.74	0.4
		ν_μ N-Trks	-4.2	30904.32	4.2
		$\bar{\nu}_\mu$ RHC 1-Trk	-0.3	8414.09	0.3
		$\bar{\nu}_\mu$ RHC N-Trks	-4.3	4724.34	4.3
		ν_μ RHC 1-Trk	-0.7	3022.10	0.7
		ν_μ RHC N-Trks	-4.4	4928.38	4.4
		ν_μ 1-Trk Air	-0.3	23605.76	0.3
		ν_μ N-Trks	-3.9	32304.13	3.9
		$\bar{\nu}_\mu$ RHC 1-Trk	-0.2	6767.65	0.2
		$\bar{\nu}_\mu$ RHC N-Trks	-4.2	4544.65	4.2
587 : CC Coherent on ^{12}C norm.	0.30	ν_μ RHC 1-Trk	-0.6	2067.37	0.6
		ν_μ RHC N-Trks	-4.1	4568.13	4.1
		ν_μ 1-Trk Wtr	-0.1	27316.74	0.1
		ν_μ N-Trks	-0.2	30904.32	0.2
		$\bar{\nu}_\mu$ RHC 1-Trk	-0.1	8414.09	0.1
		$\bar{\nu}_\mu$ RHC N-Trks	-0.4	4724.34	0.4
		ν_μ RHC 1-Trk	-0.1	3022.10	0.1
		ν_μ RHC N-Trks	-0.2	4928.38	0.2
		ν_μ 1-Trk Air	-0.1	23605.76	0.1
		ν_μ N-Trks	-0.3	32304.13	0.3

Event rate variations per cross section parameter variation.

Parameter	1σ value	Sample	-1σ (%)	nominal	$+1\sigma$ (%)
588 : CC Coherent on ^{16}O norm.	0.30	ν_μ 1-Trk Wtr	-0.0	27316.74	0.0
		ν_μ N-Trks	-0.1	30904.32	0.1
		$\bar{\nu}_\mu$ RHC 1-Trk	-0.1	8414.09	0.1
		$\bar{\nu}_\mu$ RHC N-Trks	-0.2	4724.34	0.2
		ν_μ RHC 1-Trk	-0.1	3022.10	0.1
		ν_μ RHC N-Trks	-0.1	4928.38	0.1
		ν_μ 1-Trk Air	-0.0	23605.76	0.0
		ν_μ N-Trks	-0.0	32304.13	0.0
		$\bar{\nu}_\mu$ RHC 1-Trk	-0.0	6767.65	0.0
		$\bar{\nu}_\mu$ RHC N-Trks	-0.0	4544.65	0.0
589 : NC Coherent norm.	0.30	ν_μ RHC 1-Trk	-0.0	2067.37	0.0
		ν_μ RHC N-Trks	-0.0	4568.13	0.0
		ν_μ 1-Trk Wtr	-0.0	27316.74	0.0
		ν_μ N-Trks	-0.0	30904.32	0.0
		$\bar{\nu}_\mu$ RHC 1-Trk	-0.0	8414.09	0.0
		$\bar{\nu}_\mu$ RHC N-Trks	-0.0	4724.34	0.0
		ν_μ RHC 1-Trk	-0.0	3022.10	0.0
		ν_μ RHC N-Trks	-0.0	4928.38	0.0
		ν_μ 1-Trk Air	-0.0	23605.76	0.0
		ν_μ N-Trks	-0.0	32304.13	0.0

Event rate variations per cross section parameter variation.

Parameter	1σ value	Sample	-1σ (%)	nominal	$+1\sigma$ (%)
590 : NC-1γ^*	1.00	ν_μ 1-Trk Wtr	-0.0	27316.74	0.0
		ν_μ N-Trks	-0.0	30904.32	0.0
		$\bar{\nu}_\mu$ RHC 1-Trk	0.0	8414.09	0.0
		$\bar{\nu}_\mu$ RHC N-Trks	-0.0	4724.34	0.0
		ν_μ RHC 1-Trk	0.0	3022.10	0.0
		ν_μ RHC N-Trks	0.0	4928.38	0.0
		ν_μ 1-Trk Air	-0.0	23605.76	0.0
		ν_μ N-Trks	0.0	32304.13	0.0
		$\bar{\nu}_\mu$ RHC 1-Trk	0.0	6767.65	0.0
		$\bar{\nu}_\mu$ RHC N-Trks	-0.0	4544.65	0.0
591 : NC Other Near	0.30	ν_μ RHC 1-Trk	0.0	2067.37	0.0
		ν_μ RHC N-Trks	0.0	4568.13	0.0
		ν_μ 1-Trk Wtr	-0.1	27316.74	0.1
		ν_μ N-Trks	-0.6	30904.32	0.6
		$\bar{\nu}_\mu$ RHC 1-Trk	-0.2	8414.09	0.2
		$\bar{\nu}_\mu$ RHC N-Trks	-1.9	4724.34	1.9
		ν_μ RHC 1-Trk	-0.2	3022.10	0.2
		ν_μ RHC N-Trks	-0.8	4928.38	0.8
		ν_μ 1-Trk Air	-0.1	23605.76	0.1
		ν_μ N-Trks	-0.6	32304.13	0.6

Event rate variations per cross section parameter variation.

Parameter	1σ value	Sample	-1σ (%)	nominal	$+1\sigma$ (%)	
591 : NC Other Far*	0.30	ν_μ 1-Trk Wtr	-0.1	27316.74	0.1	
		ν_μ N-Trks	-0.4	30904.32	0.4	
		$\bar{\nu}_\mu$ RHC 1-Trk	-0.1	8414.09	0.1	
		$\bar{\nu}_\mu$ RHC N-Trks	-1.2	4724.34	1.2	
		ν_μ RHC 1-Trk	-0.1	3022.10	0.1	
		ν_μ RHC N-Trks	-0.5	4928.38	0.5	
		ν_μ 1-Trk Air	-0.1	23605.76	0.1	
		ν_μ N-Trks	-0.6	32304.13	0.6	
		$\bar{\nu}_\mu$ RHC 1-Trk	-0.3	6767.65	0.3	
		$\bar{\nu}_\mu$ RHC N-Trks	-1.8	4544.65	1.8	
		ν_μ RHC 1-Trk	-0.2	2067.37	0.2	
		ν_μ RHC N-Trks	-0.8	4568.13	0.8	

Event rate variations per cross section parameter variation.

Appendix E

Log-Likelihood Sample Scans

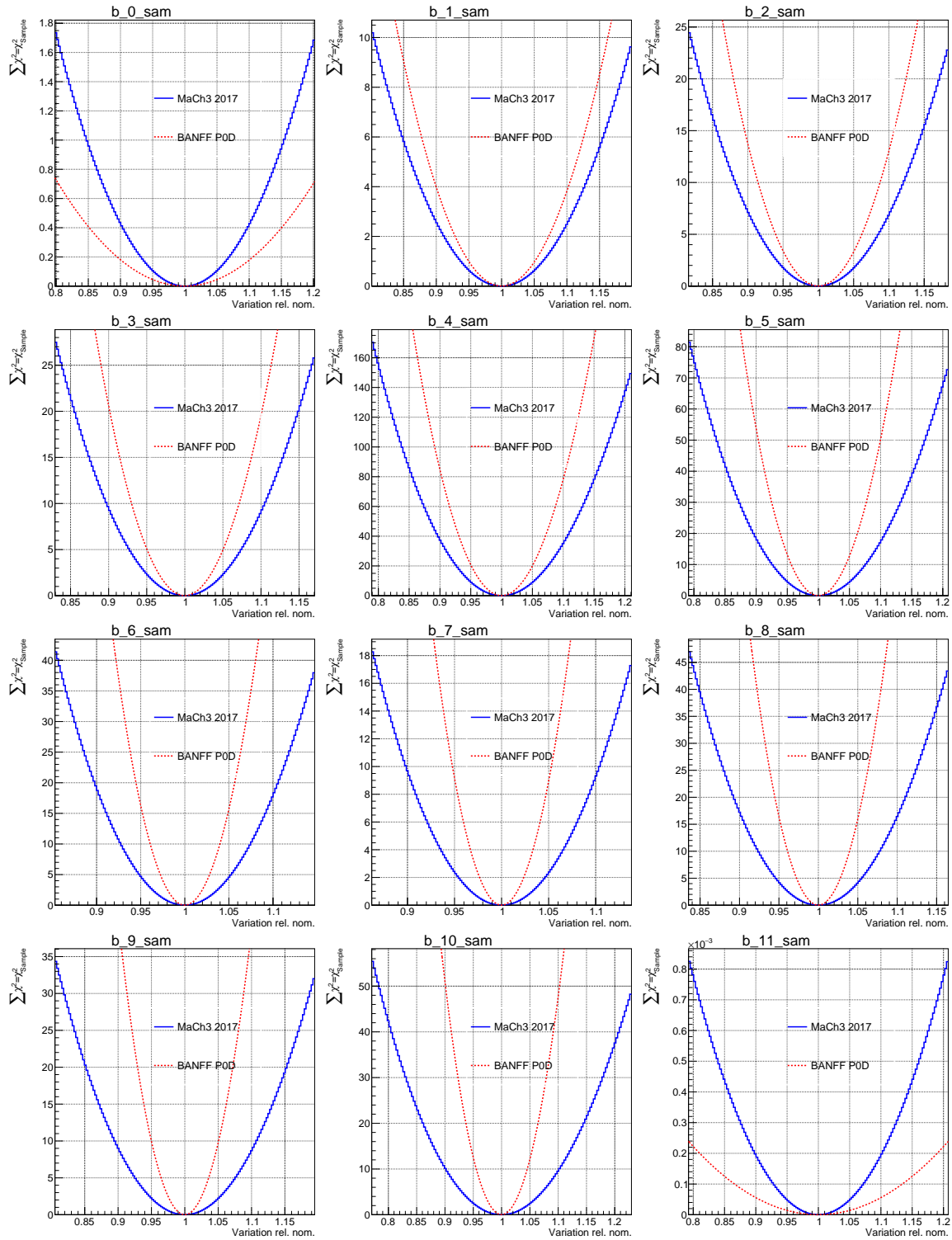
This appendix examines the PØD-only BANFF fit likelihood term $\Delta\chi^2_{\text{LLR}} = \chi^2_{\text{sample}}$ response (scans) to variations in flux and cross section parameters. For the cross section terms, the scans shapes correspond to the shape of the spline weight. In addition, comparison scans are provided for the FGD MaCh3 2017 analysis. Extensive comparisons were made to ensure that the FGD MaCh3 and FGD BANFF analyses have identical splines. So it is an equal comparison with the FGD BANFF as shown in Chapter 4. In some cases, the PØD-only scans indicate higher sensitivity to parameters than the FGD.

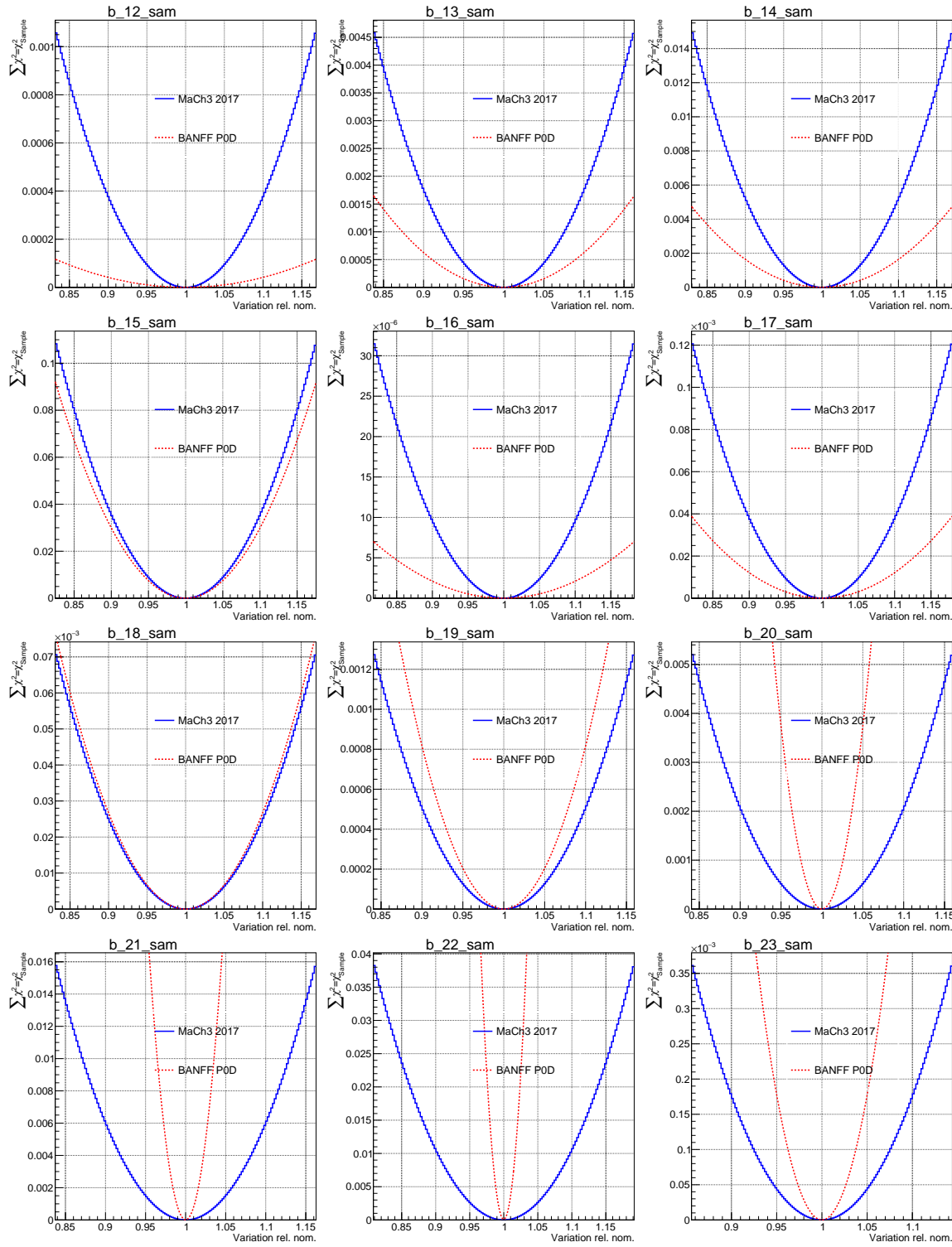
These were generously produced by Clarence Wret (c.wret@rochester.edu) of the University of Rochester. The likelihood scans are ordered as such. The first 50 plots “b_0_sam” through “b_49_sam” are the ND280 flux sample contributions. The next 50 “b_50_sam” through “b_99_sam” are the sample contributions that affect the SK flux. The last scans are variations on the cross section parameters. Due to a bug in plotting script, the scans 2p2h shape location for ^{12}C and ^{16}O were empty for the PØD. The correct PØD scans are shown in Figure E.1 on page 304 with the MaCH3 inputs reproduced as faithfully as possible.

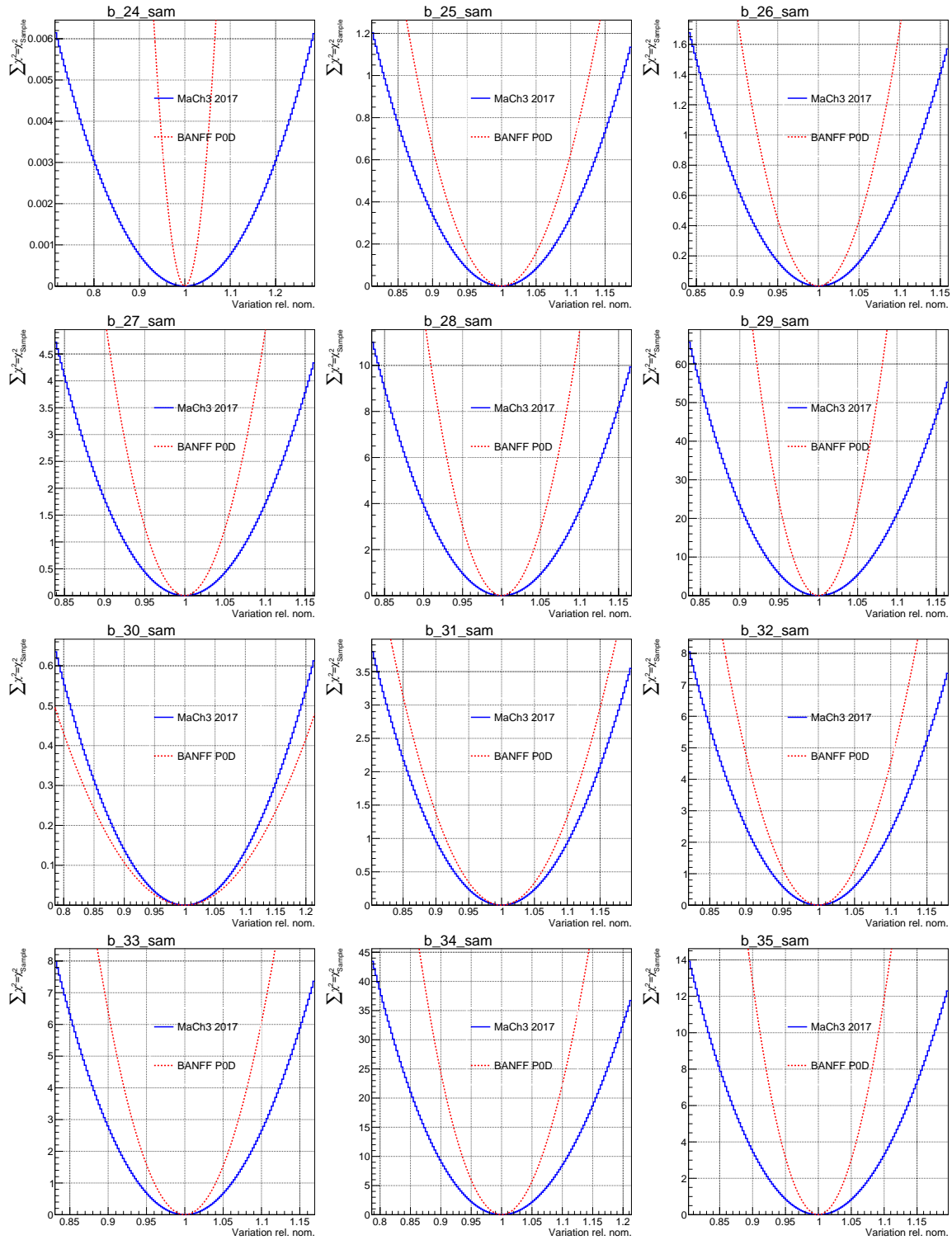
As expected, the SK flux variations are flat with respect to the sample chi-squared. This is due model parameterization in which the ND280 samples only affect the ND280 flux

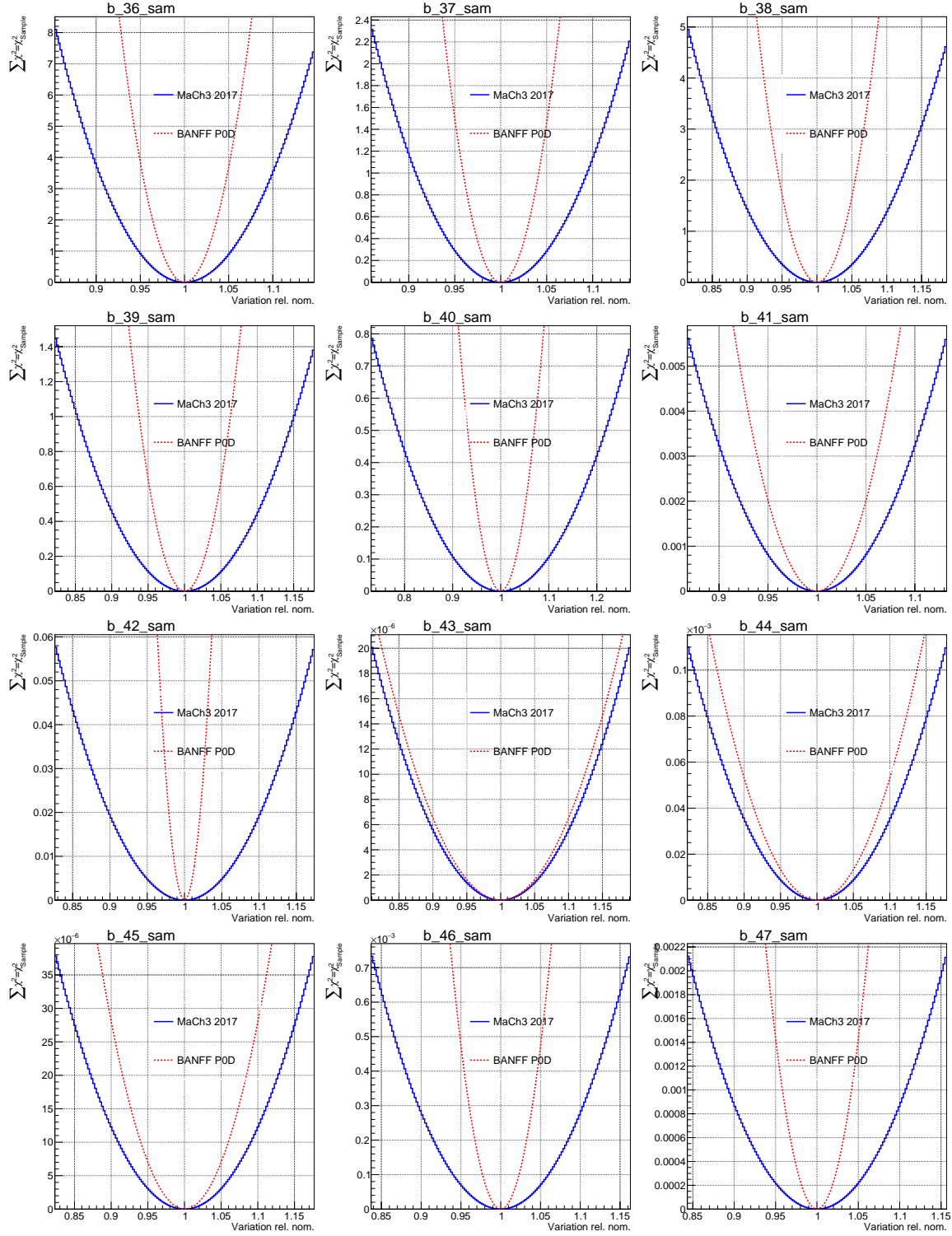
parameters. In other words, the log-likelihood scans for the SK flux parameters have no affect on the ND280 sample events.

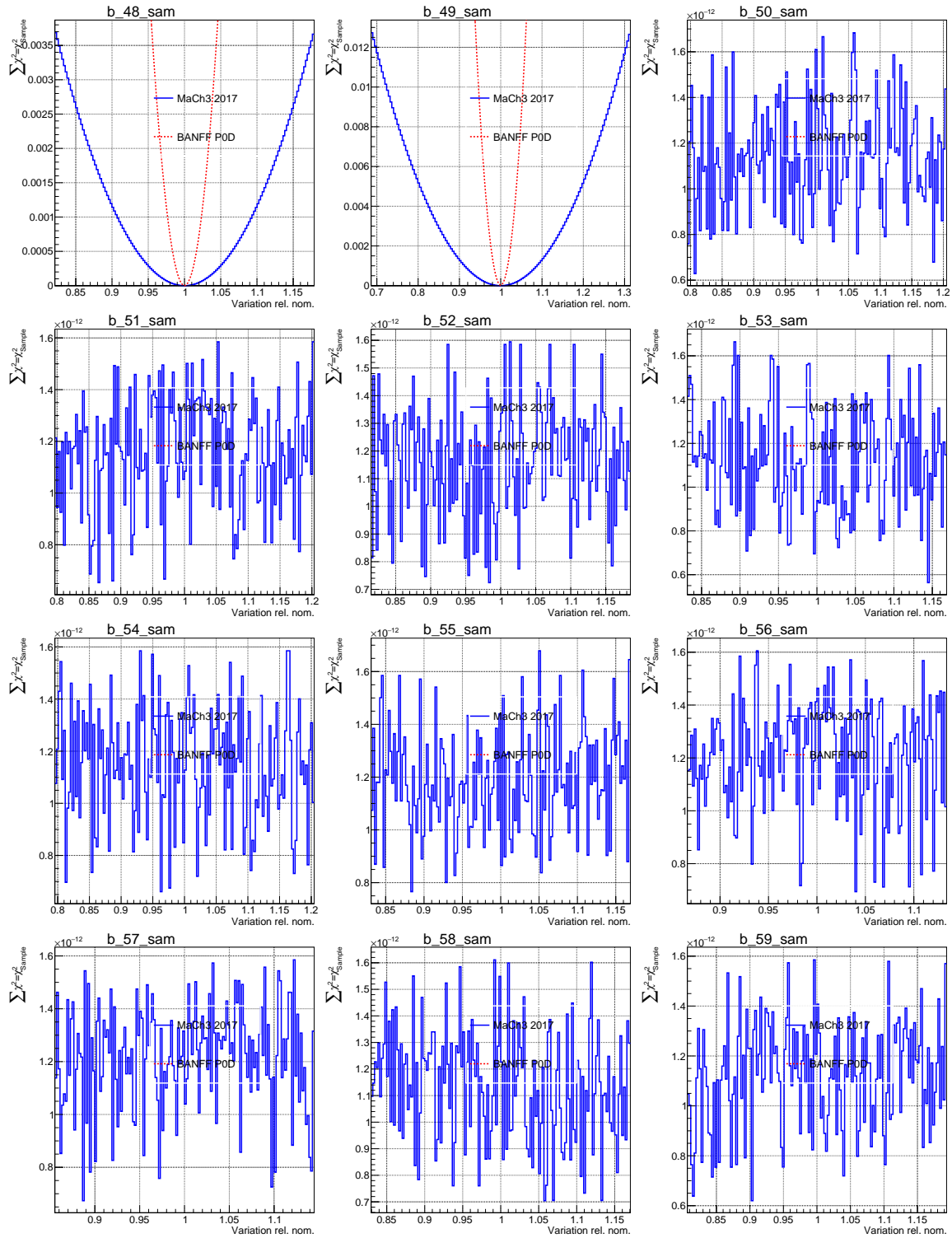
Some of cross section parameter splines are reflected about a point in order to properly calculate correlations between parameters. In previous fits to data, the 2p2h ^{12}C and ^{16}O shape location terms hit their physical boundaries at +1. The result was that the fitter MINUIT inaccurately calculated the Hess matrix. The decision was made to reflect, also called “mirroring”, the splines about a certain point to expand the limit. Tests showed that this did not affect the postfit results for any parameters, but the correlations between all other parameters was calculated to less than 1% [22].

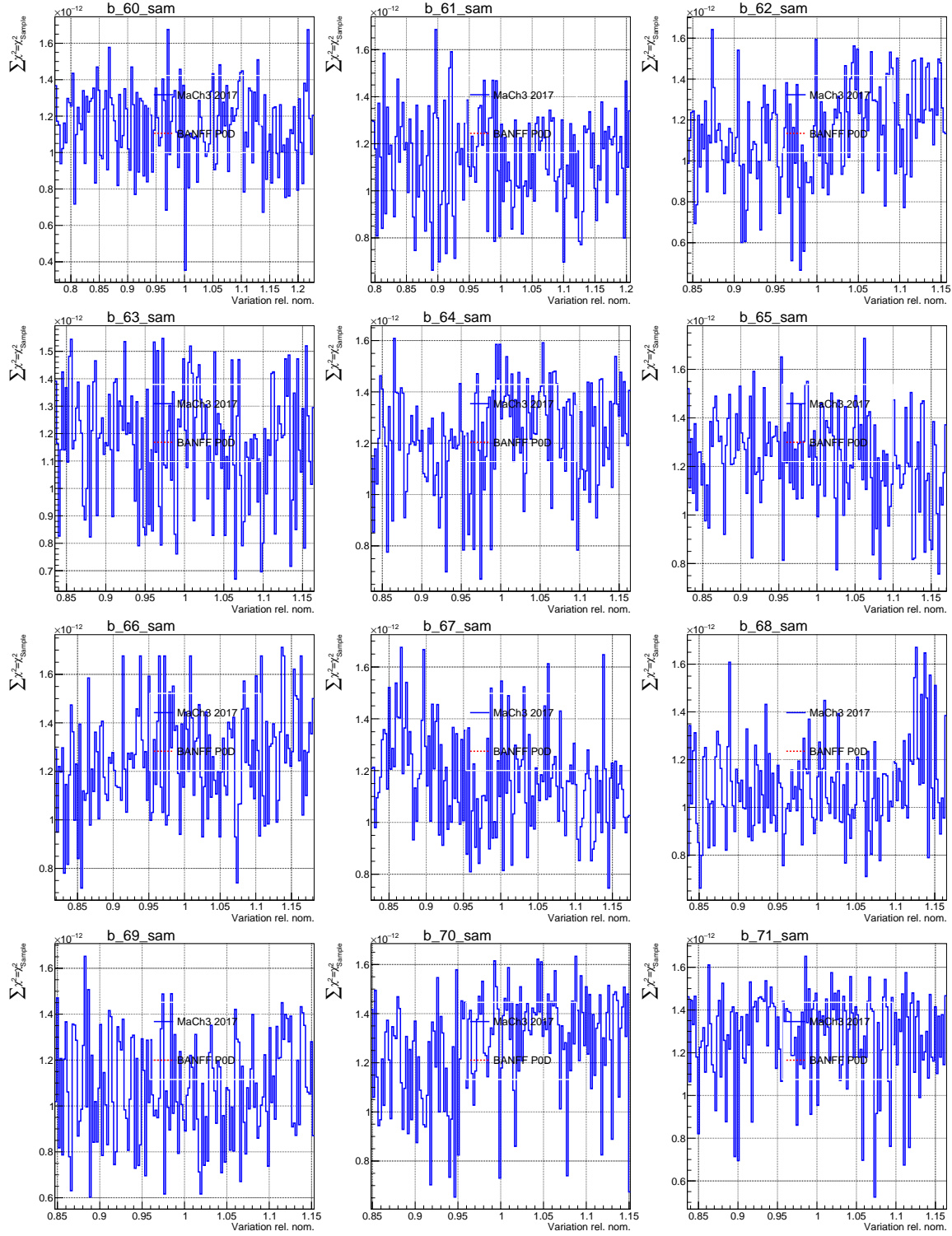


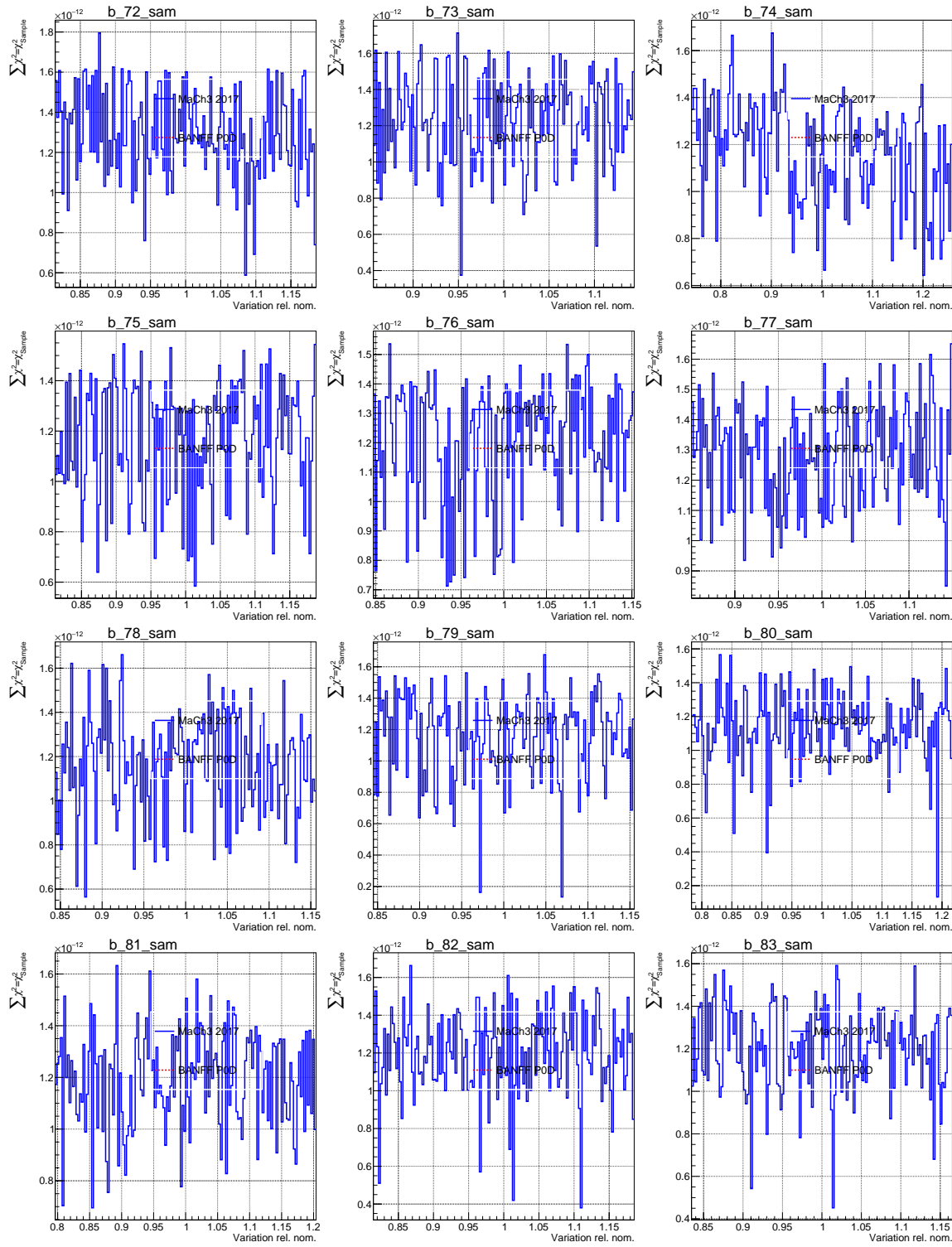


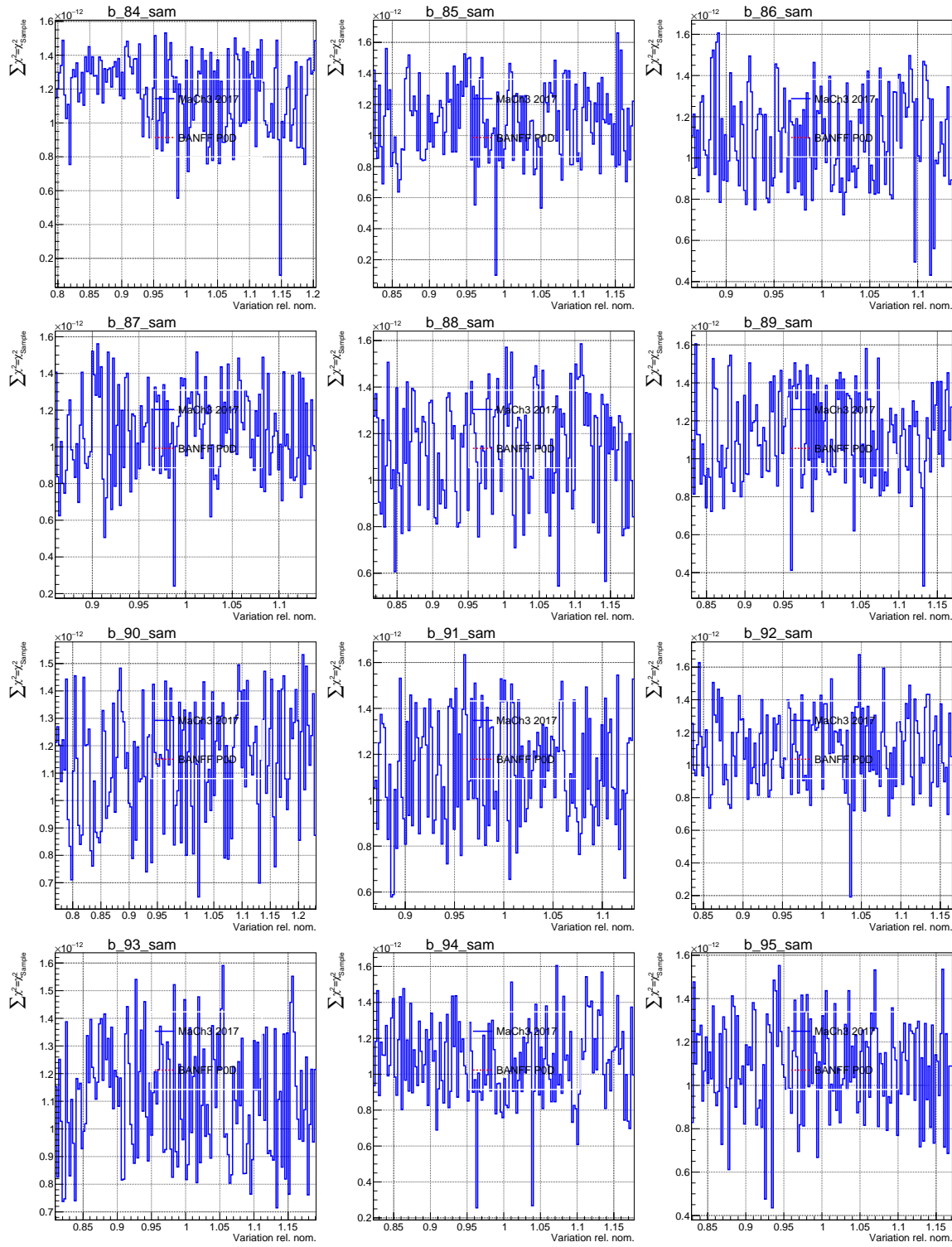


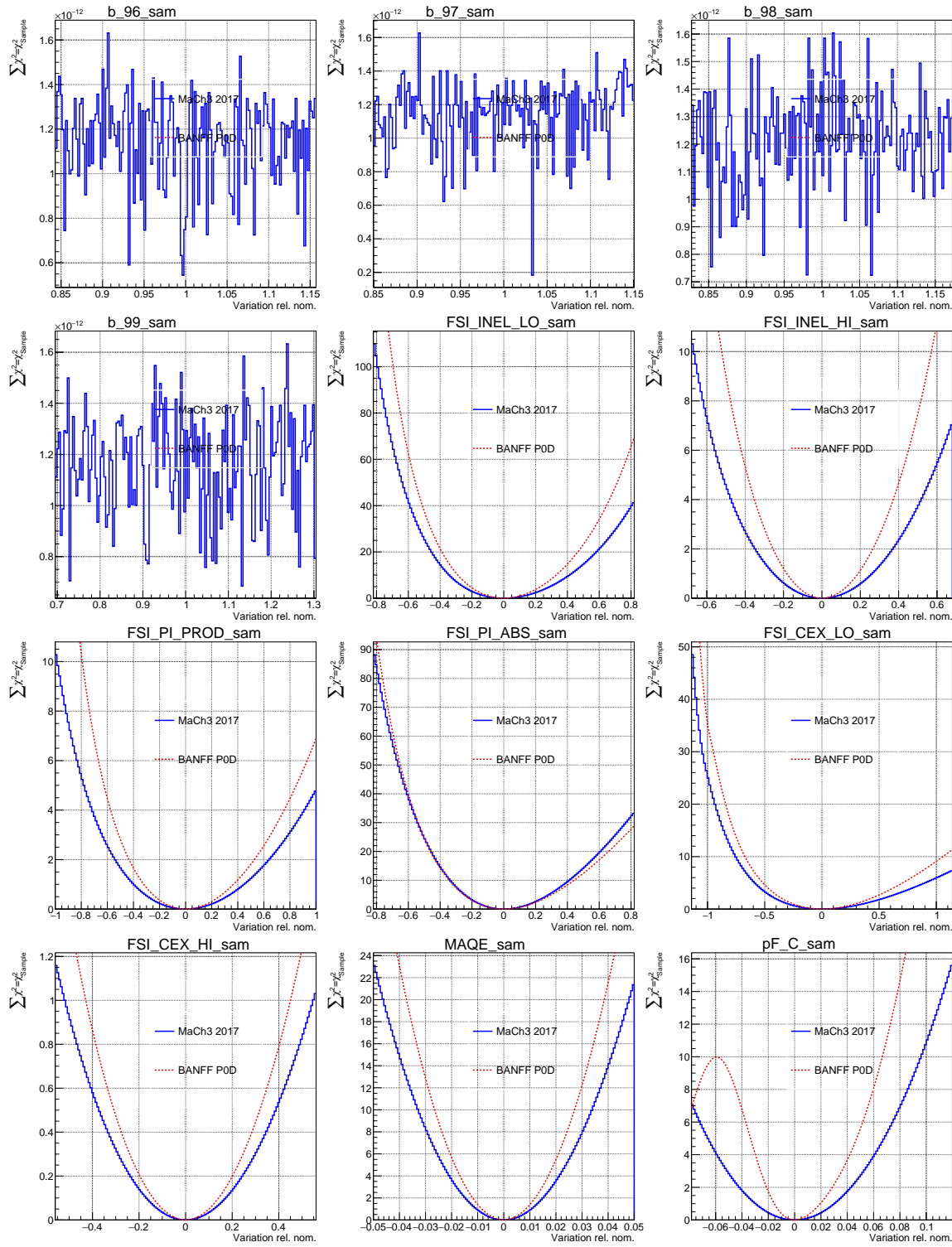


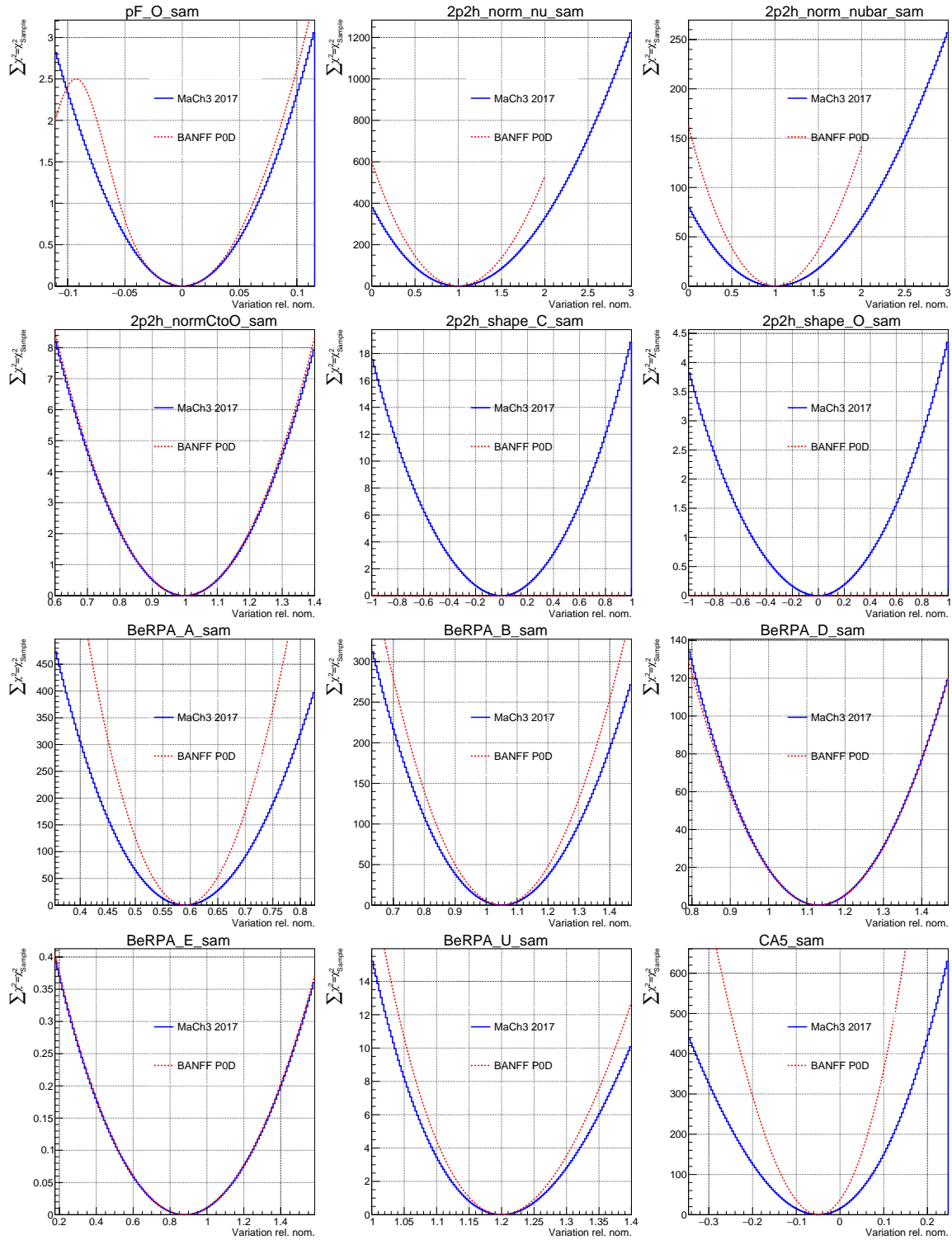


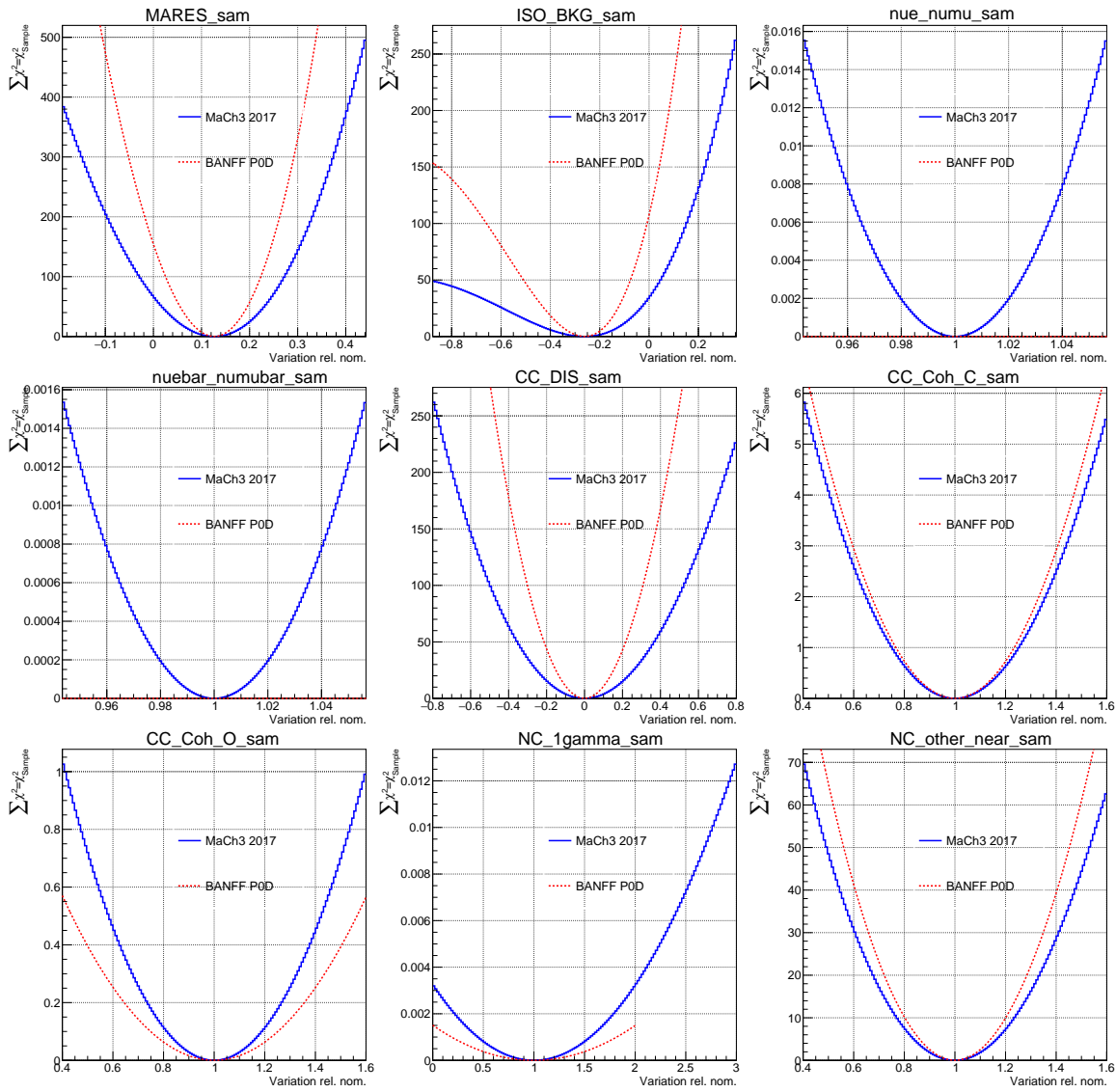












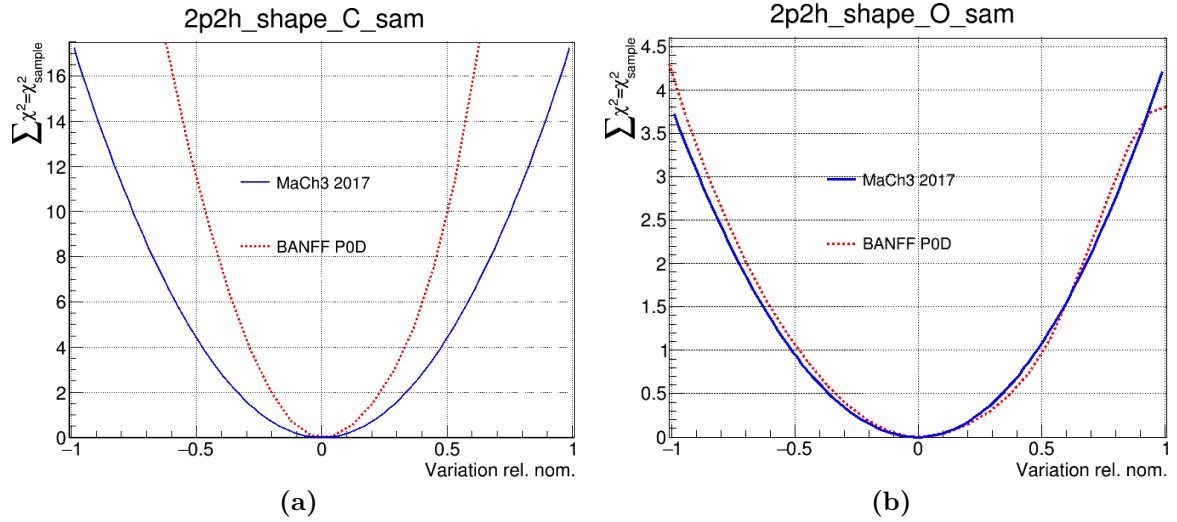
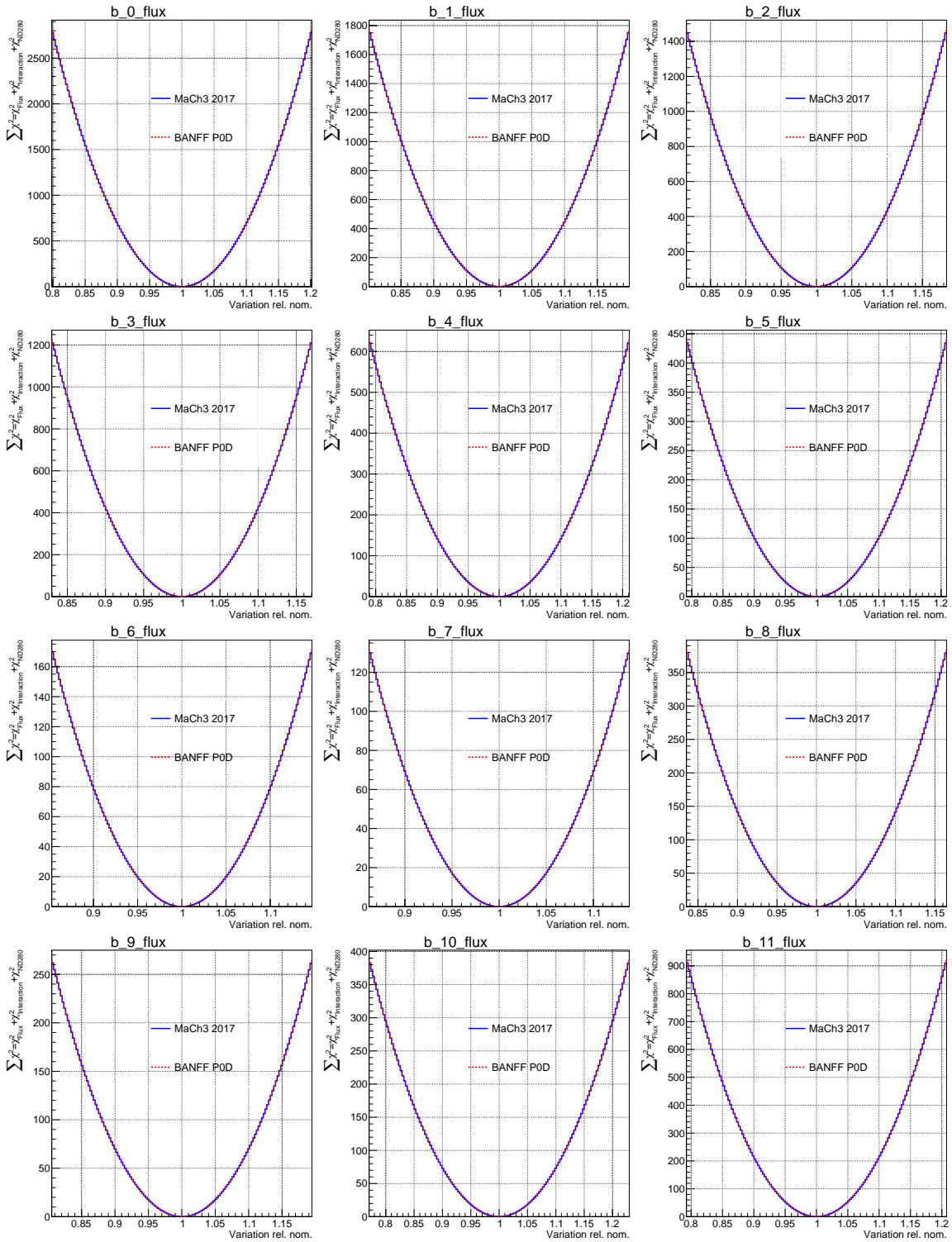


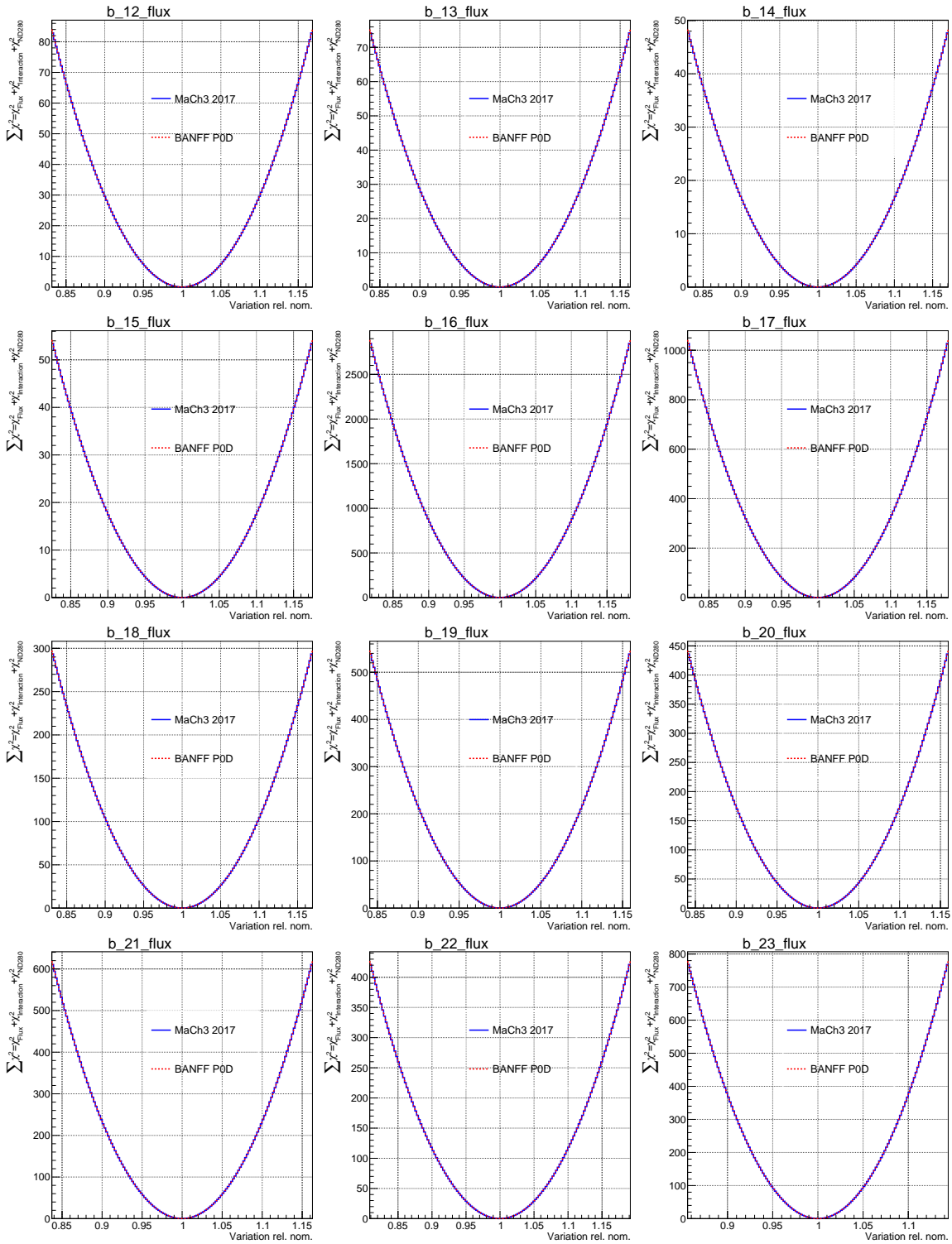
Figure E.1: Correct PØD scans with faithful reproductions of the MaCh3 scans for the 2p2h shape location cross section parameters.

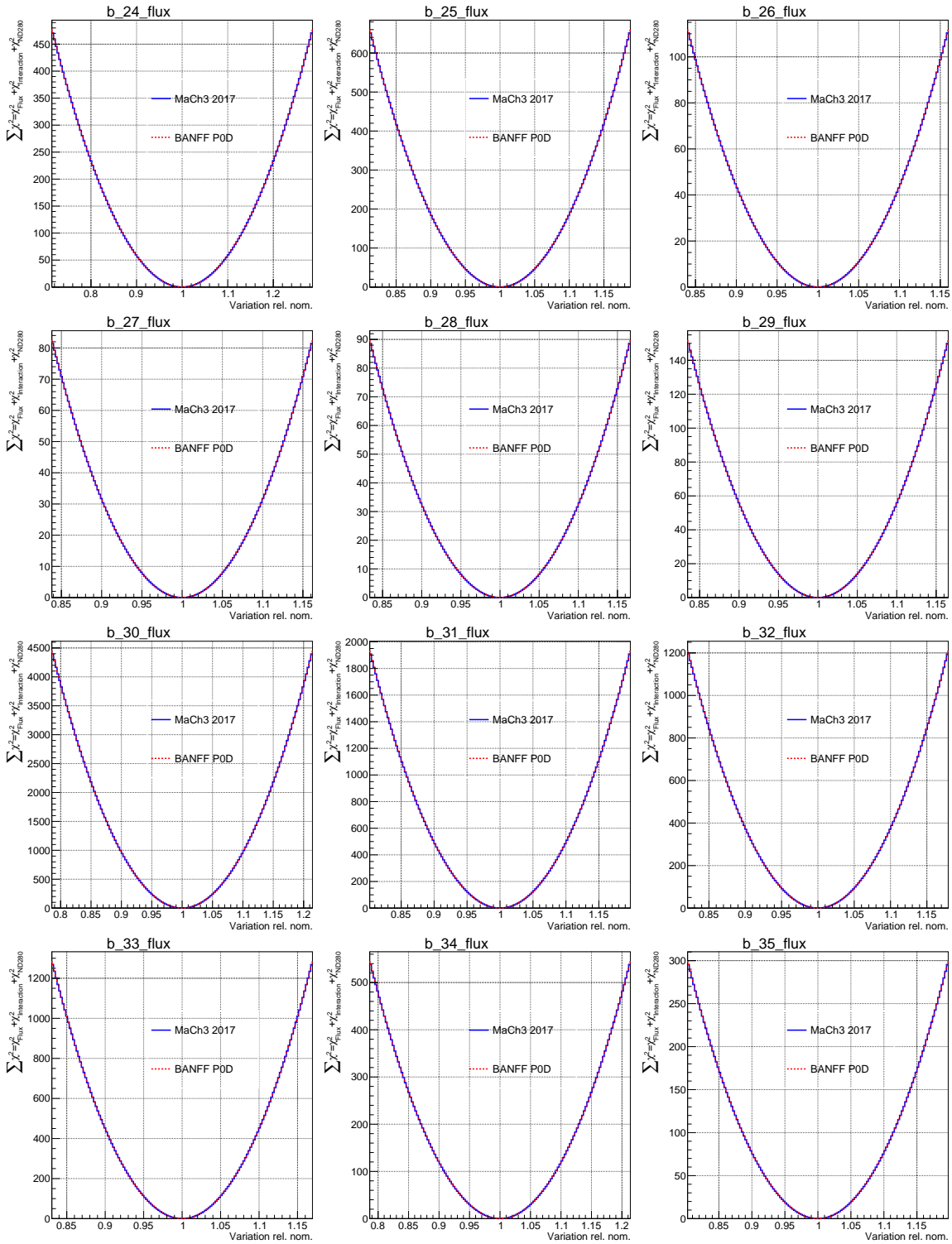
Appendix F

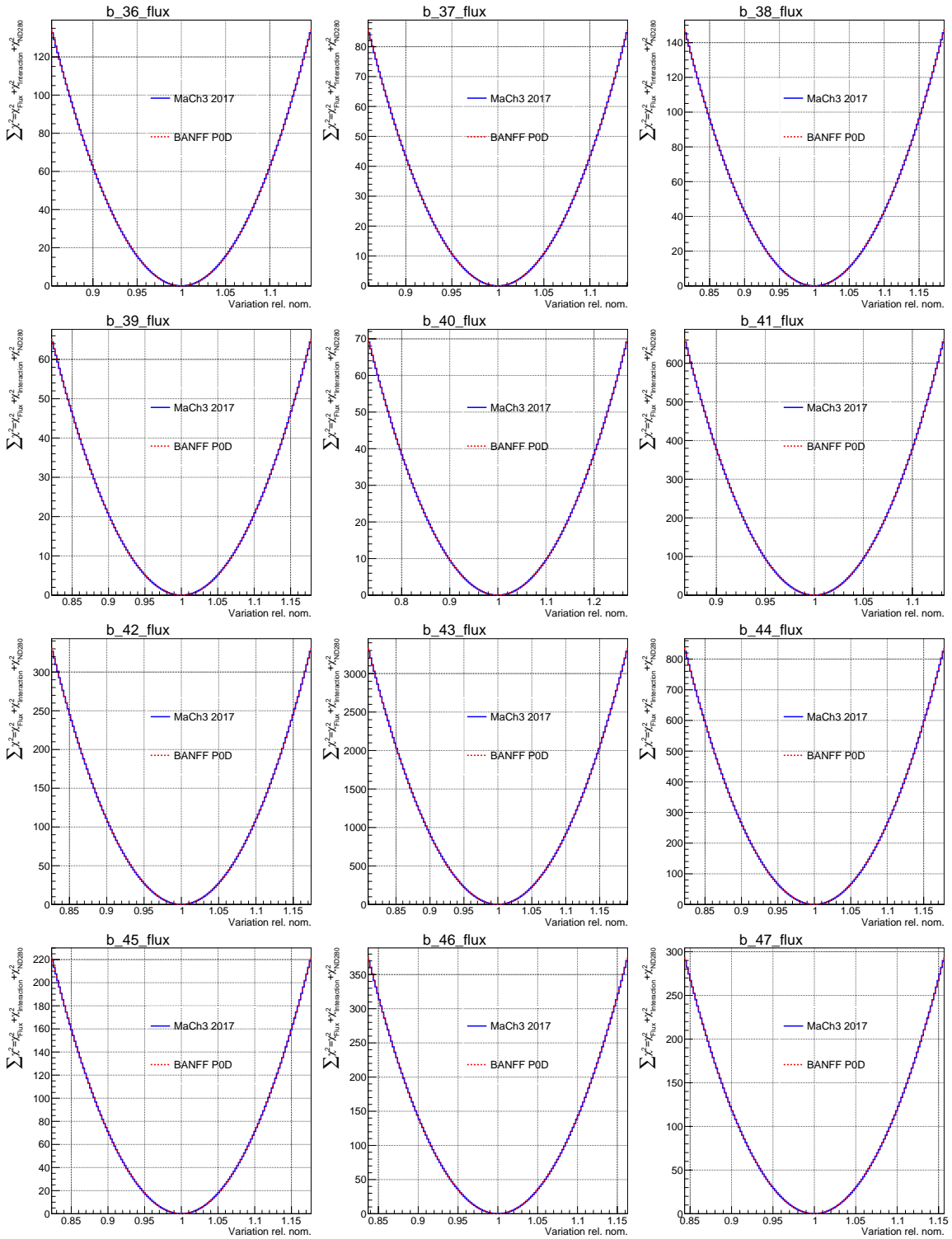
Log-Likelihood Penalty Scans

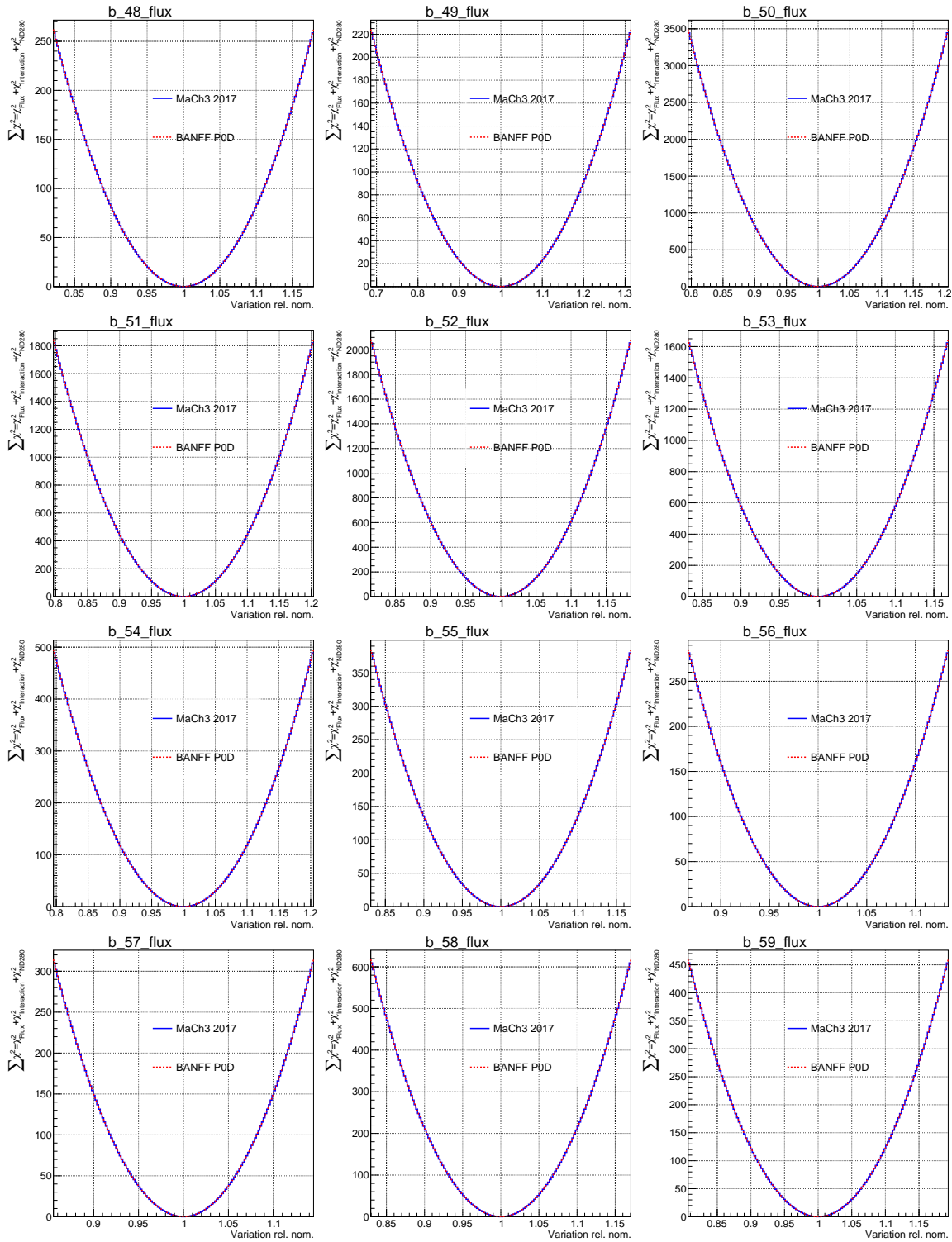
This appendix examines the PØD-only BANFF fit penalty terms $\Delta\chi^2_{\text{Flux}} + \Delta\chi^2_{\text{xsec}} + \Delta\chi^2_{\text{Det}}$ response (scans) to variations in flux and cross section parameters. In addition, comparison scans are provided for the FGD MaCH3/BANFF 2017 analysis. In all cases, the penalty terms overlap indicating the parameters have the same prior constraints between analyses.

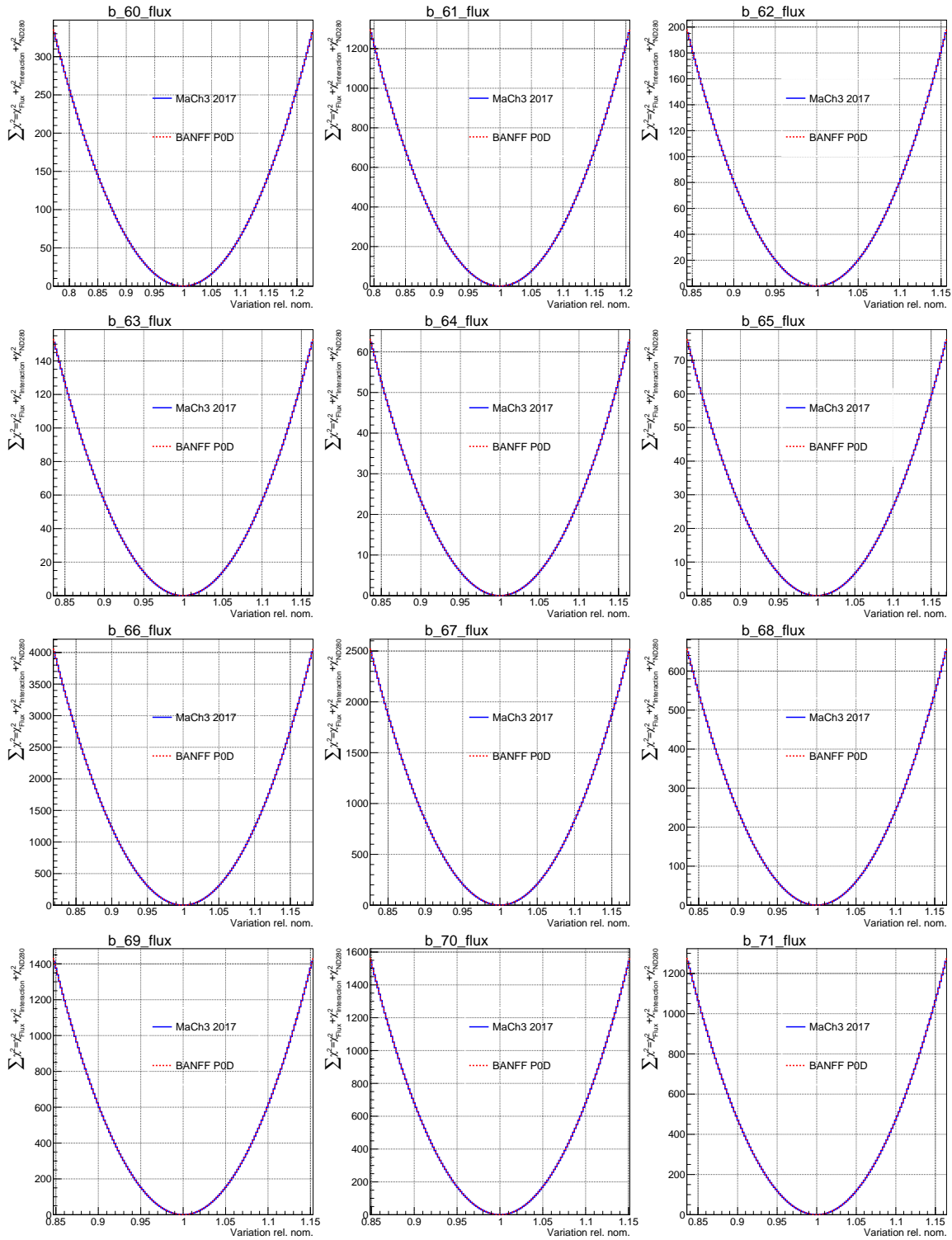


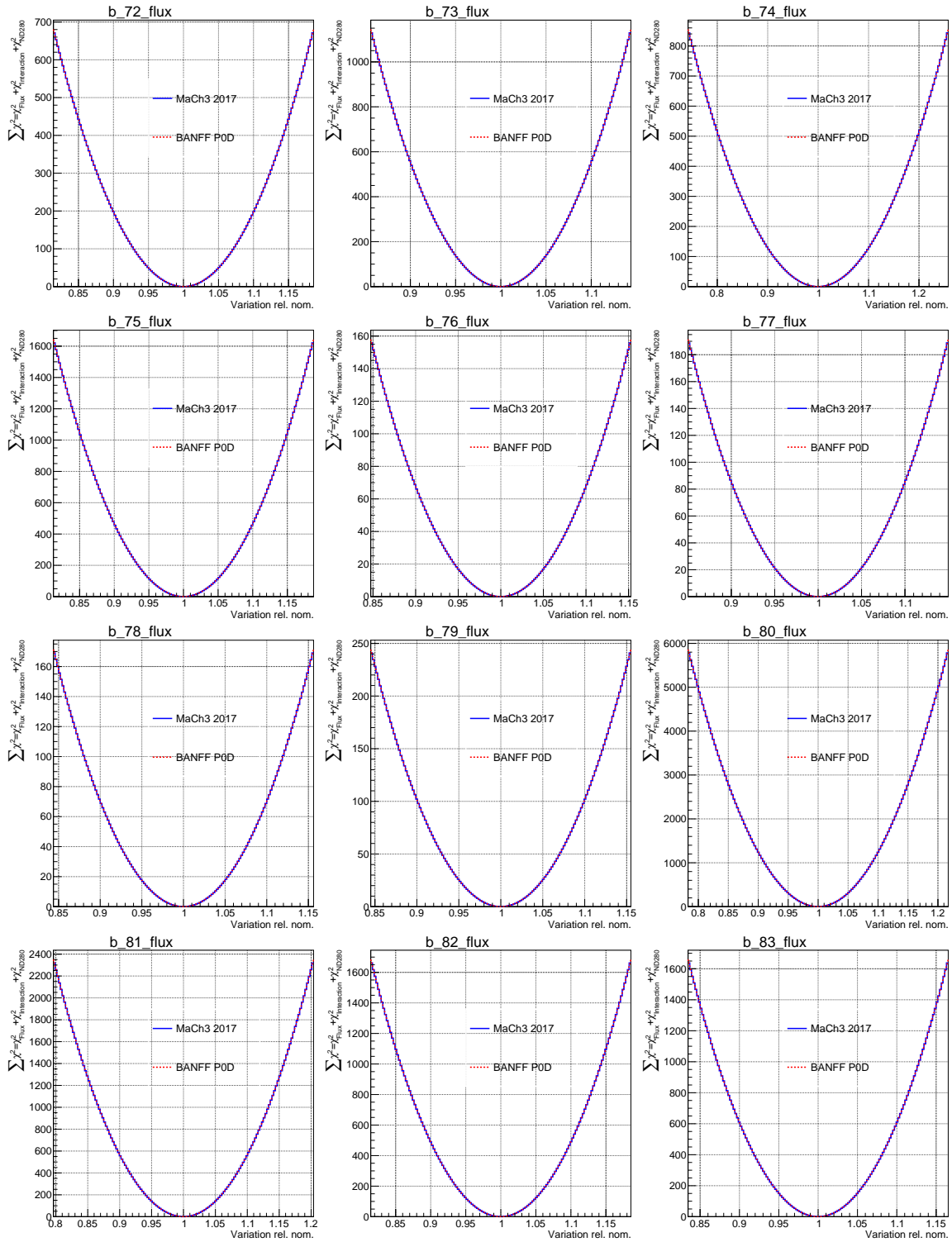


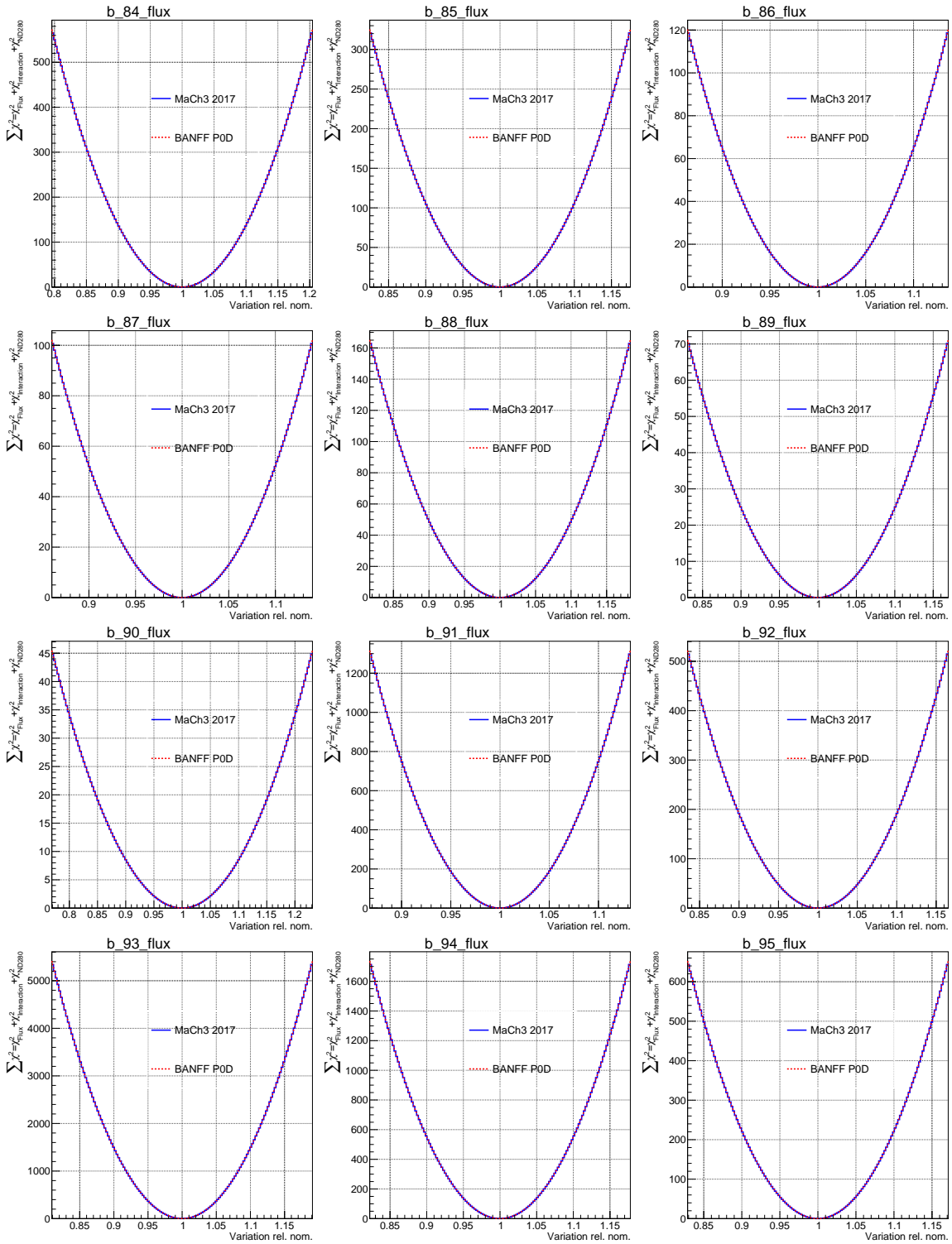


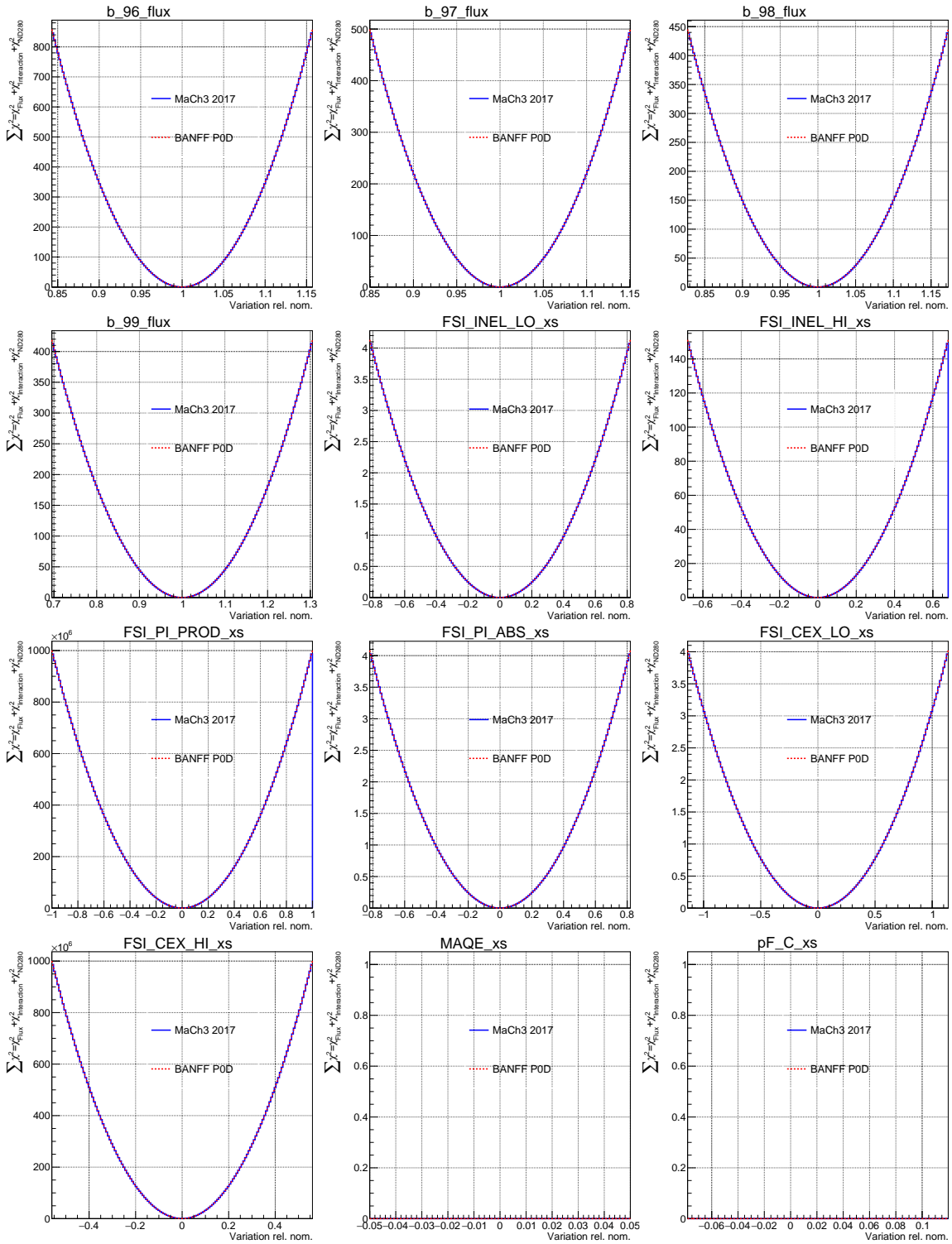


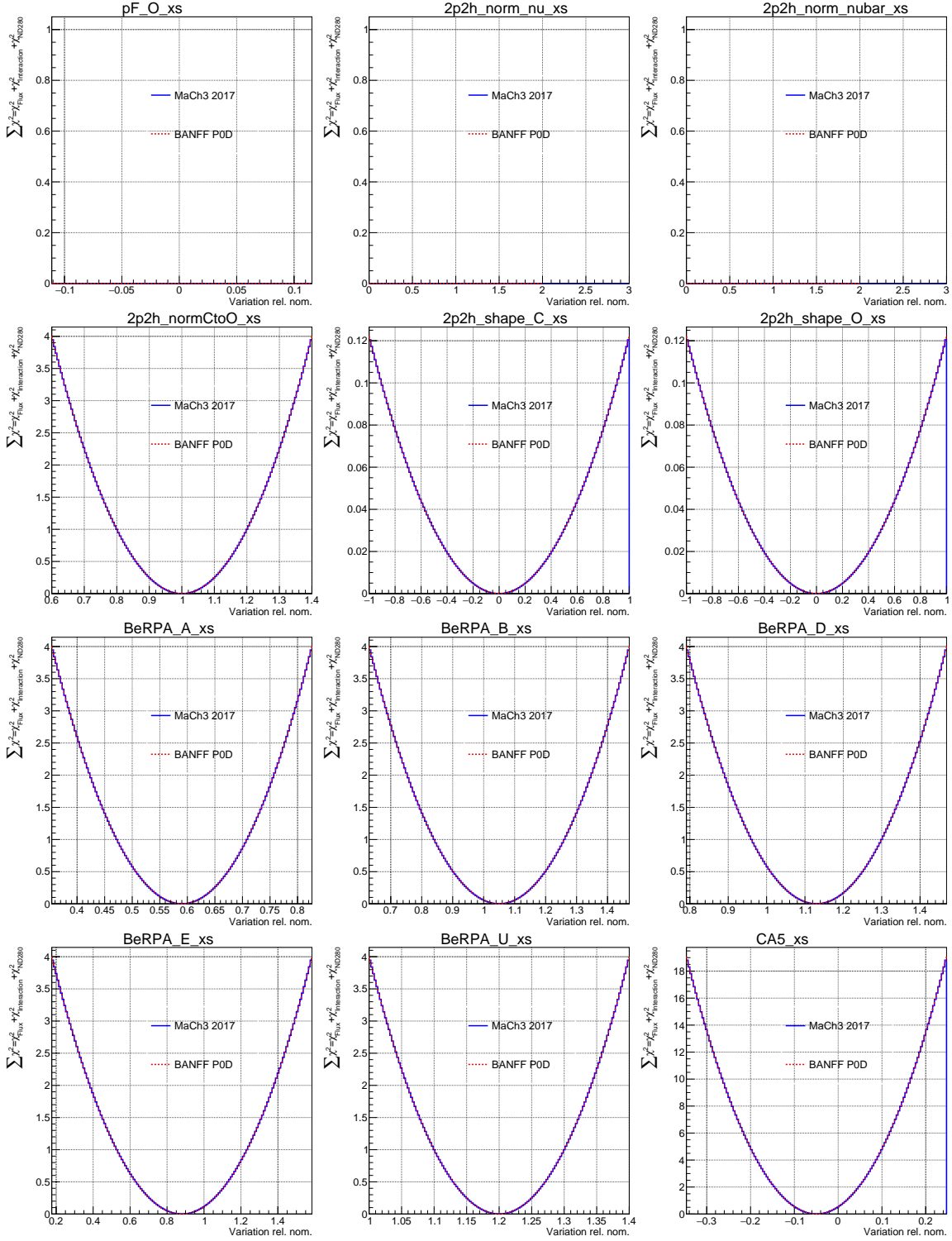


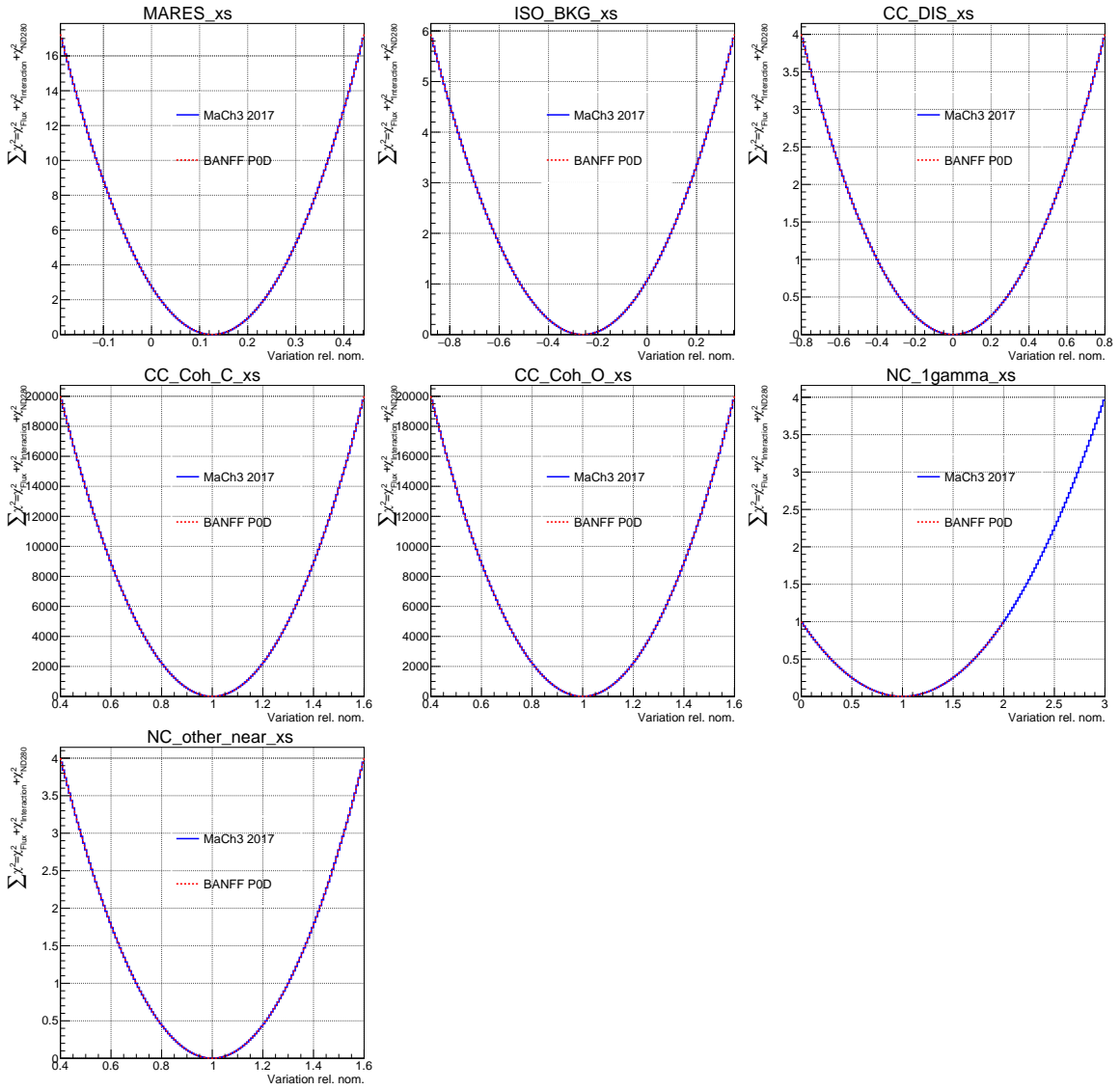












Appendix G

The PØD-Only Postfit Parameters

In this appendix is the complete listing of the fit parameters, both in prefit and postfit values. The first 50 are ND280 flux parameters then followed by 50 SK flux parameters as defined in Table 4.1 on page 101,. Between 100 and 561 are the bin normalization parameters defined in Appendix B. The last 31 are cross section parameters as defined in Table 4.4 on page 132.

Table G.1: Prefit and postfit parameters with errors.

Index	Prefit	\pm error	Postfit	\pm error
0	1.00	0.10	1.03	0.06
1	1.00	0.10	1.02	0.05
2	1.00	0.09	1.02	0.05
3	1.00	0.09	1.03	0.05
4	1.00	0.11	0.99	0.05
5	1.00	0.10	0.97	0.04
6	1.00	0.07	1.04	0.04
7	1.00	0.07	1.07	0.04
8	1.00	0.08	1.05	0.04
9	1.00	0.10	0.99	0.04
10	1.00	0.11	0.96	0.04
11	1.00	0.10	1.11	0.08
12	1.00	0.08	1.06	0.06
13	1.00	0.08	1.07	0.06
14	1.00	0.09	1.12	0.06
15	1.00	0.09	1.13	0.07
16	1.00	0.09	1.01	0.05
17	1.00	0.09	1.02	0.05
18	1.00	0.08	1.04	0.05
19	1.00	0.08	1.05	0.04
20	1.00	0.08	1.03	0.04
21	1.00	0.08	1.05	0.04
22	1.00	0.10	1.03	0.06
23	1.00	0.07	1.08	0.06
24	1.00	0.14	1.22	0.12

Index	Prefit	\pm error	Postfit	\pm error
25	1.00	0.09	1.10	0.07
26	1.00	0.08	1.10	0.05
27	1.00	0.08	1.10	0.05
28	1.00	0.08	1.09	0.05
29	1.00	0.08	1.12	0.04
30	1.00	0.11	1.05	0.07
31	1.00	0.10	1.03	0.05
32	1.00	0.09	1.06	0.05
33	1.00	0.08	1.07	0.04
34	1.00	0.11	1.09	0.05
35	1.00	0.10	1.07	0.05
36	1.00	0.07	1.04	0.05
37	1.00	0.07	1.04	0.05
38	1.00	0.09	1.04	0.06
39	1.00	0.09	1.09	0.06
40	1.00	0.13	1.17	0.08
41	1.00	0.07	1.10	0.05
42	1.00	0.09	1.14	0.07
43	1.00	0.10	1.03	0.06
44	1.00	0.09	1.05	0.05
45	1.00	0.09	1.08	0.06
46	1.00	0.08	1.05	0.05
47	1.00	0.08	1.09	0.05
48	1.00	0.09	1.10	0.06
49	1.00	0.16	1.14	0.13
50	1.00	0.10	1.02	0.06

Index	Prefit	\pm error	Postfit	\pm error
51	1.00	0.10	1.01	0.06
52	1.00	0.09	1.03	0.05
53	1.00	0.08	1.05	0.05
54	1.00	0.10	1.02	0.06
55	1.00	0.08	1.01	0.05
56	1.00	0.07	1.04	0.05
57	1.00	0.07	1.04	0.05
58	1.00	0.09	1.04	0.04
59	1.00	0.10	1.00	0.04
60	1.00	0.11	0.98	0.05
61	1.00	0.10	1.11	0.08
62	1.00	0.08	1.08	0.05
63	1.00	0.08	1.10	0.06
64	1.00	0.08	1.12	0.06
65	1.00	0.09	1.11	0.06
66	1.00	0.09	1.02	0.05
67	1.00	0.09	1.03	0.05
68	1.00	0.08	1.04	0.05
69	1.00	0.08	1.05	0.04
70	1.00	0.08	1.05	0.04
71	1.00	0.08	1.06	0.04
72	1.00	0.09	1.07	0.06
73	1.00	0.07	1.09	0.05
74	1.00	0.13	1.18	0.11
75	1.00	0.09	1.10	0.07
76	1.00	0.08	1.07	0.05

Index	Prefit	\pm error	Postfit	\pm error
77	1.00	0.07	1.10	0.05
78	1.00	0.08	1.10	0.05
79	1.00	0.08	1.07	0.05
80	1.00	0.11	1.04	0.07
81	1.00	0.10	1.02	0.06
82	1.00	0.09	1.03	0.05
83	1.00	0.08	1.06	0.05
84	1.00	0.10	1.09	0.06
85	1.00	0.09	1.05	0.05
86	1.00	0.07	1.04	0.05
87	1.00	0.07	1.08	0.05
88	1.00	0.09	1.04	0.06
89	1.00	0.08	1.07	0.06
90	1.00	0.12	1.06	0.09
91	1.00	0.07	1.09	0.05
92	1.00	0.08	1.11	0.06
93	1.00	0.10	1.04	0.06
94	1.00	0.09	1.04	0.05
95	1.00	0.09	1.06	0.05
96	1.00	0.08	1.05	0.04
97	1.00	0.08	1.10	0.05
98	1.00	0.09	1.11	0.06
99	1.00	0.15	1.15	0.12
100	1.21	0.67	1.00	0.04
101	0.87	0.18	0.96	0.03
102	1.12	0.44	0.96	0.04

Index	Prefit	\pm error	Postfit	\pm error
103	1.13	0.43	0.99	0.05
104	1.02	0.17	0.96	0.08
105	0.93	0.20	0.84	0.09
106	1.00	0.28	1.05	0.05
107	0.82	0.33	0.93	0.04
108	1.26	0.58	0.94	0.03
109	1.27	0.74	0.92	0.04
110	0.89	0.18	0.95	0.03
111	1.02	0.27	0.93	0.03
112	1.09	0.33	0.96	0.04
113	1.02	0.17	0.91	0.04
114	0.96	0.15	0.92	0.03
115	0.99	0.21	0.97	0.04
116	0.94	0.29	0.96	0.06
117	1.05	0.53	0.94	0.07
118	1.33	0.78	0.99	0.05
119	0.91	0.21	0.95	0.03
120	0.97	0.14	0.93	0.03
121	1.03	0.17	0.94	0.03
122	1.01	0.09	0.93	0.03
123	1.00	0.05	0.94	0.04
124	1.00	0.12	0.91	0.08
125	0.95	0.15	0.98	0.08
126	0.96	0.38	0.88	0.04
127	1.29	0.73	0.95	0.04
128	0.93	0.22	0.96	0.03

Index	Prefit	\pm error	Postfit	\pm error
129	0.96	0.09	0.92	0.03
130	1.02	0.11	0.94	0.03
131	1.00	0.07	0.93	0.03
132	1.00	0.03	0.93	0.03
133	0.99	0.08	0.89	0.03
134	1.00	0.14	0.92	0.04
135	0.99	0.20	0.99	0.04
136	1.25	0.65	0.94	0.07
137	0.94	0.20	0.95	0.04
138	0.95	0.08	0.93	0.03
139	1.01	0.11	0.94	0.03
140	1.00	0.07	0.93	0.03
141	1.00	0.06	0.94	0.03
142	1.00	0.03	0.93	0.03
143	0.98	0.10	0.90	0.03
144	0.97	0.14	0.88	0.03
145	1.25	0.58	1.00	0.06
146	0.93	0.18	0.91	0.04
147	0.96	0.11	0.89	0.03
148	1.01	0.11	0.94	0.03
149	1.01	0.08	0.95	0.03
150	1.01	0.10	0.95	0.03
151	1.00	0.06	0.95	0.03
152	1.00	0.05	0.93	0.03
153	0.98	0.10	0.90	0.03
154	1.18	0.61	0.95	0.03

Index	Prefit	\pm error	Postfit	\pm error
155	0.89	0.15	0.95	0.03
156	1.01	0.16	0.96	0.04
157	1.03	0.19	1.02	0.04
158	1.02	0.15	1.16	0.07
159	1.04	0.16	0.87	0.04
160	0.93	0.26	0.81	0.05
161	0.94	0.67	0.89	0.06
162	1.13	0.56	0.90	0.03
163	0.92	0.15	0.93	0.03
164	0.98	0.07	0.93	0.03
165	1.00	0.09	0.93	0.03
166	1.01	0.08	0.93	0.03
167	1.01	0.06	0.88	0.04
168	0.98	0.16	0.84	0.05
169	0.98	0.52	0.89	0.05
170	1.13	0.53	0.95	0.03
171	0.92	0.14	0.93	0.03
172	0.98	0.05	0.92	0.03
173	1.00	0.07	0.92	0.03
174	1.00	0.06	0.92	0.03
175	1.01	0.05	0.89	0.03
176	0.99	0.12	0.95	0.03
177	1.03	0.46	0.99	0.03
178	1.13	0.52	0.94	0.03
179	0.94	0.13	0.94	0.04
180	0.97	0.06	0.92	0.03

Index	Prefit	\pm error	Postfit	\pm error
181	0.99	0.08	0.92	0.03
182	1.00	0.07	0.94	0.03
183	1.00	0.03	0.95	0.03
184	0.99	0.10	0.89	0.04
185	0.98	0.25	0.92	0.06
186	1.09	0.47	0.95	0.04
187	0.96	0.11	0.94	0.03
188	0.96	0.09	0.95	0.03
189	1.00	0.09	0.92	0.04
190	1.01	0.09	0.93	0.03
191	1.01	0.08	0.94	0.03
192	0.99	0.05	0.92	0.03
193	0.97	0.13	0.87	0.03
194	1.00	0.36	0.97	0.03
195	0.90	0.15	0.95	0.03
196	1.05	0.26	0.92	0.04
197	1.04	0.20	0.93	0.04
198	1.00	0.17	0.94	0.06
199	1.01	0.17	0.92	0.06
200	1.00	0.39	0.97	0.06
201	1.06	0.43	0.97	0.04
202	0.91	0.13	0.95	0.03
203	0.97	0.16	0.93	0.04
204	1.04	0.17	0.94	0.04
205	1.00	0.11	0.92	0.05
206	0.99	0.11	0.88	0.05

Index	Prefit	\pm error	Postfit	\pm error
207	0.92	0.28	0.99	0.05
208	1.07	0.44	0.95	0.05
209	0.93	0.14	0.94	0.04
210	0.96	0.11	0.94	0.03
211	1.03	0.14	0.95	0.03
212	1.01	0.08	0.95	0.03
213	0.98	0.06	0.87	0.05
214	0.95	0.17	0.89	0.08
215	1.08	0.45	0.91	0.05
216	0.93	0.16	0.95	0.03
217	0.96	0.09	0.93	0.03
218	1.02	0.12	0.94	0.03
219	1.01	0.07	0.94	0.03
220	1.00	0.04	0.93	0.03
221	0.98	0.09	0.91	0.04
222	1.09	0.43	0.92	0.04
223	0.94	0.15	0.94	0.04
224	0.93	0.10	0.93	0.04
225	1.02	0.12	0.94	0.04
226	1.01	0.08	0.96	0.04
227	1.00	0.07	0.95	0.03
228	0.99	0.05	0.92	0.03
229	1.02	0.34	0.96	0.04
230	1.00	0.09	0.94	0.04
231	1.01	0.07	0.95	0.04
232	0.99	0.13	0.93	0.05

Index	Prefit	\pm error	Postfit	\pm error
233	0.99	0.11	0.92	0.07
234	0.98	0.33	0.97	0.06
235	1.05	0.34	0.95	0.04
236	0.97	0.05	0.93	0.03
237	1.02	0.06	0.95	0.03
238	0.98	0.09	0.93	0.03
239	0.99	0.06	0.92	0.03
240	0.98	0.14	0.92	0.06
241	1.04	0.36	0.92	0.05
242	0.97	0.05	0.93	0.04
243	1.01	0.05	0.94	0.04
244	1.00	0.09	0.93	0.04
245	1.01	0.06	0.93	0.04
246	0.98	0.12	0.84	0.07
247	1.03	0.37	0.90	0.05
248	1.01	0.05	0.94	0.04
249	1.00	0.05	0.92	0.04
250	0.99	0.07	0.92	0.03
251	1.01	0.07	0.92	0.03
252	0.99	0.07	0.85	0.04
253	1.07	0.39	0.84	0.05
254	0.98	0.07	0.93	0.04
255	1.02	0.08	0.99	0.04
256	1.01	0.08	0.94	0.04
257	0.99	0.09	0.91	0.04
258	0.99	0.06	0.87	0.04

Index	Prefit	\pm error	Postfit	\pm error
259	1.24	0.60	1.00	0.08
260	0.91	0.16	0.94	0.05
261	1.00	0.13	0.95	0.05
262	1.02	0.21	0.94	0.06
263	1.03	0.17	0.94	0.08
264	0.99	0.21	1.11	0.14
265	1.27	0.64	1.03	0.15
266	0.95	0.16	0.95	0.06
267	0.99	0.06	0.92	0.05
268	0.98	0.11	0.93	0.05
269	1.04	0.14	0.93	0.06
270	0.99	0.16	0.91	0.11
271	1.20	0.60	0.94	0.11
272	0.95	0.20	0.93	0.06
273	0.97	0.07	0.94	0.05
274	1.00	0.08	0.94	0.04
275	1.00	0.08	0.93	0.04
276	1.00	0.10	0.97	0.07
277	1.10	0.52	0.93	0.09
278	0.99	0.16	0.96	0.06
279	0.95	0.06	0.91	0.05
280	0.99	0.04	0.94	0.04
281	1.00	0.07	0.93	0.03
282	1.00	0.06	0.95	0.04
283	1.19	0.50	0.95	0.09
284	0.98	0.15	0.99	0.07

Index	Prefit	\pm error	Postfit	\pm error
285	0.96	0.09	0.97	0.07
286	0.99	0.07	0.91	0.06
287	1.00	0.06	0.94	0.03
288	1.00	0.04	0.92	0.03
289	1.12	0.46	1.00	0.07
290	1.01	0.15	0.91	0.06
291	0.98	0.09	0.90	0.05
292	1.00	0.09	0.94	0.05
293	0.98	0.07	0.92	0.03
294	1.00	0.03	0.92	0.03
295	1.29	0.47	1.04	0.11
296	0.98	0.20	1.10	0.12
297	0.95	0.16	0.92	0.09
298	1.03	0.10	0.95	0.05
299	1.01	0.08	0.98	0.03
300	1.00	0.03	0.93	0.03
301	0.97	0.21	0.90	0.07
302	1.01	0.13	1.00	0.06
303	1.01	0.15	0.99	0.06
304	1.15	0.19	1.12	0.07
305	0.95	0.23	0.90	0.12
306	1.00	0.26	0.99	0.07
307	0.99	0.08	0.91	0.05
308	1.01	0.11	0.93	0.04
309	0.98	0.09	0.89	0.06
310	1.00	0.16	0.87	0.05

Index	Prefit	\pm error	Postfit	\pm error
311	1.01	0.28	0.86	0.08
312	0.98	0.06	0.90	0.05
313	1.00	0.08	0.93	0.04
314	1.02	0.08	0.92	0.05
315	0.98	0.11	0.93	0.07
316	1.02	0.25	0.92	0.05
317	0.98	0.07	0.90	0.06
318	1.00	0.07	0.92	0.04
319	1.00	0.07	0.94	0.04
320	1.00	0.06	0.90	0.06
321	1.02	0.24	0.91	0.08
322	0.96	0.10	0.99	0.05
323	1.01	0.09	0.95	0.05
324	0.99	0.09	0.93	0.04
325	0.99	0.04	0.92	0.03
326	1.00	0.25	0.94	0.08
327	0.98	0.11	0.97	0.07
328	1.00	0.09	0.93	0.03
329	1.01	0.10	1.00	0.04
330	1.00	0.04	0.94	0.03
331	1.17	0.66	0.94	0.05
332	0.86	0.19	0.95	0.03
333	1.17	0.53	0.92	0.04
334	1.15	0.44	0.93	0.06
335	0.97	0.19	0.90	0.09
336	1.02	0.19	1.18	0.11

Index	Prefit	\pm error	Postfit	\pm error
337	1.02	0.31	0.96	0.04
338	0.97	0.37	0.91	0.04
339	0.88	0.62	0.92	0.03
340	1.27	0.75	0.90	0.04
341	0.87	0.17	0.95	0.03
342	1.04	0.31	0.94	0.03
343	1.09	0.34	0.95	0.04
344	1.01	0.18	0.91	0.04
345	1.03	0.17	0.91	0.03
346	0.94	0.27	0.94	0.04
347	0.93	0.38	0.99	0.06
348	1.00	0.58	0.96	0.08
349	1.32	0.79	0.98	0.06
350	0.90	0.20	0.95	0.03
351	0.98	0.17	0.93	0.03
352	1.04	0.19	0.93	0.03
353	1.01	0.10	0.98	0.04
354	1.00	0.07	0.94	0.05
355	0.97	0.14	0.86	0.10
356	1.06	0.22	1.09	0.11
357	1.00	0.33	0.88	0.04
358	1.29	0.73	0.91	0.04
359	0.91	0.20	0.97	0.03
360	0.97	0.11	0.95	0.03
361	1.02	0.12	0.94	0.03
362	1.00	0.07	0.93	0.03

Index	Prefit	\pm error	Postfit	\pm error
363	1.01	0.04	0.95	0.03
364	0.98	0.09	0.91	0.04
365	0.98	0.15	0.99	0.04
366	0.98	0.21	0.97	0.04
367	1.23	0.68	0.94	0.09
368	0.91	0.20	0.94	0.04
369	0.98	0.12	0.94	0.04
370	1.02	0.11	0.94	0.03
371	0.99	0.08	0.93	0.03
372	1.01	0.06	0.96	0.03
373	1.00	0.04	0.93	0.03
374	0.98	0.11	0.89	0.03
375	0.98	0.15	0.89	0.04
376	1.21	0.58	0.96	0.08
377	0.90	0.16	0.91	0.04
378	0.99	0.12	0.97	0.04
379	1.02	0.12	0.93	0.04
380	1.01	0.09	0.95	0.04
381	1.01	0.10	0.95	0.03
382	1.00	0.06	0.95	0.03
383	1.00	0.05	0.93	0.03
384	0.98	0.10	0.89	0.03
385	1.18	0.62	0.94	0.04
386	0.88	0.15	0.96	0.03
387	1.03	0.21	0.98	0.04
388	1.03	0.21	1.02	0.04

Index	Prefit	\pm error	Postfit	\pm error
389	1.01	0.16	1.18	0.07
390	1.00	0.22	0.88	0.04
391	0.99	0.32	0.93	0.05
392	0.93	0.69	1.00	0.06
393	1.13	0.58	0.92	0.03
394	0.91	0.14	0.94	0.03
395	0.99	0.10	0.92	0.03
396	1.01	0.11	0.95	0.03
397	1.01	0.08	0.93	0.03
398	1.00	0.08	0.91	0.04
399	1.03	0.18	0.91	0.05
400	0.97	0.51	0.84	0.05
401	1.12	0.55	0.94	0.03
402	0.92	0.13	0.93	0.03
403	0.99	0.08	0.95	0.03
404	1.00	0.08	0.93	0.03
405	1.01	0.07	0.91	0.03
406	1.00	0.06	0.89	0.03
407	0.98	0.13	0.88	0.03
408	0.93	0.45	0.96	0.03
409	1.09	0.51	0.95	0.03
410	0.93	0.11	0.93	0.04
411	0.99	0.08	0.91	0.04
412	1.00	0.08	0.91	0.03
413	1.00	0.07	0.95	0.03
414	1.00	0.03	0.94	0.03

Index	Preft	\pm error	Postfit	\pm error
415	0.99	0.10	0.89	0.04
416	0.97	0.28	0.96	0.07
417	1.09	0.48	0.95	0.05
418	0.94	0.12	0.95	0.03
419	0.98	0.11	0.94	0.03
420	1.01	0.10	0.92	0.04
421	1.01	0.09	0.94	0.04
422	1.01	0.07	0.94	0.03
423	0.99	0.06	0.91	0.03
424	0.97	0.13	0.87	0.03
425	0.99	0.29	0.94	0.04
426	0.92	0.14	0.93	0.03
427	1.05	0.24	0.88	0.04
428	1.05	0.18	0.92	0.05
429	1.02	0.17	0.83	0.08
430	0.87	0.19	0.96	0.07
431	0.96	0.41	0.79	0.06
432	1.03	0.35	0.99	0.05
433	0.91	0.12	0.94	0.04
434	1.00	0.16	0.91	0.05
435	1.03	0.15	0.87	0.05
436	0.99	0.12	0.93	0.05
437	0.99	0.15	0.91	0.05
438	0.93	0.31	0.90	0.05
439	1.05	0.37	0.90	0.06
440	0.92	0.11	0.95	0.04

Index	Prefit	\pm error	Postfit	\pm error
441	0.98	0.12	0.93	0.04
442	1.03	0.12	0.94	0.04
443	1.02	0.08	0.99	0.04
444	0.97	0.08	0.84	0.06
445	0.97	0.19	0.78	0.10
446	1.06	0.37	0.92	0.06
447	0.93	0.12	0.95	0.04
448	0.97	0.11	0.91	0.04
449	1.02	0.10	0.94	0.04
450	1.00	0.07	0.93	0.04
451	0.99	0.04	0.92	0.04
452	0.99	0.10	0.90	0.05
453	1.07	0.35	0.97	0.05
454	0.89	0.12	0.94	0.05
455	0.99	0.11	0.94	0.05
456	1.02	0.11	0.94	0.05
457	0.99	0.09	0.94	0.05
458	1.01	0.07	0.98	0.03
459	0.99	0.06	0.92	0.03
460	1.00	0.29	0.98	0.04
461	1.00	0.10	0.96	0.04
462	1.04	0.09	0.97	0.05
463	0.98	0.14	0.93	0.05
464	0.98	0.13	0.89	0.09
465	0.92	0.33	0.85	0.06
466	1.00	0.31	0.92	0.04

Index	Prefit	\pm error	Postfit	\pm error
467	0.99	0.06	0.93	0.03
468	1.02	0.06	0.95	0.03
469	0.99	0.11	0.93	0.03
470	0.99	0.06	0.94	0.04
471	0.96	0.16	0.98	0.06
472	1.00	0.32	0.92	0.05
473	1.00	0.07	0.92	0.04
474	1.00	0.06	0.95	0.04
475	1.00	0.11	0.90	0.04
476	1.00	0.06	0.92	0.04
477	0.99	0.13	0.88	0.07
478	1.03	0.32	0.90	0.05
479	0.99	0.07	0.93	0.04
480	1.02	0.07	0.93	0.04
481	0.99	0.10	0.92	0.04
482	1.01	0.08	0.93	0.04
483	0.98	0.09	0.78	0.04
484	1.02	0.31	0.76	0.05
485	1.01	0.07	0.96	0.05
486	1.02	0.08	0.94	0.05
487	0.98	0.10	0.91	0.04
488	1.00	0.09	0.92	0.04
489	0.99	0.07	0.87	0.04
490	1.10	0.50	0.93	0.09
491	0.92	0.12	0.96	0.06
492	1.03	0.16	0.96	0.07

Index	Prefit	\pm error	Postfit	\pm error
493	1.02	0.20	0.91	0.08
494	1.08	0.14	1.08	0.10
495	0.81	0.31	1.06	0.16
496	1.23	0.50	1.11	0.13
497	0.93	0.18	0.96	0.07
498	0.93	0.09	0.90	0.06
499	1.03	0.12	0.92	0.07
500	1.05	0.14	0.93	0.09
501	1.00	0.21	0.87	0.14
502	1.17	0.49	1.04	0.14
503	0.95	0.15	0.95	0.08
504	0.97	0.08	0.95	0.07
505	1.00	0.10	0.92	0.06
506	1.00	0.08	0.91	0.05
507	1.04	0.16	0.88	0.11
508	1.13	0.47	0.98	0.11
509	0.99	0.13	0.94	0.08
510	0.94	0.09	0.92	0.07
511	0.99	0.07	0.94	0.05
512	1.00	0.06	0.93	0.04
513	0.99	0.08	0.94	0.05
514	1.06	0.46	0.83	0.10
515	0.95	0.14	0.95	0.09
516	0.97	0.11	0.92	0.10
517	1.01	0.10	0.92	0.08
518	1.00	0.07	0.94	0.05

Index	Preft	\pm error	Postfit	\pm error
519	0.99	0.06	0.92	0.04
520	1.07	0.46	0.93	0.08
521	1.00	0.15	0.98	0.08
522	1.02	0.16	0.99	0.06
523	0.96	0.10	0.85	0.07
524	1.01	0.08	0.94	0.04
525	0.99	0.04	0.92	0.03
526	1.19	0.46	1.03	0.14
527	0.89	0.17	1.01	0.10
528	0.99	0.15	0.92	0.09
529	0.99	0.10	0.93	0.06
530	1.00	0.09	0.95	0.04
531	1.00	0.03	0.93	0.03
532	0.97	0.22	0.96	0.08
533	1.02	0.17	0.92	0.07
534	1.00	0.14	1.05	0.07
535	1.28	0.22	0.91	0.07
536	0.83	0.25	1.00	0.13
537	0.98	0.22	0.93	0.08
538	0.99	0.09	0.92	0.06
539	1.00	0.11	0.91	0.05
540	1.03	0.11	0.90	0.07
541	1.04	0.20	0.91	0.05
542	1.01	0.25	0.87	0.08
543	0.98	0.08	0.89	0.06
544	1.01	0.08	0.92	0.05

Index	Prefit	\pm error	Postfit	\pm error
545	1.00	0.08	0.95	0.06
546	0.99	0.12	0.99	0.08
547	0.99	0.22	0.92	0.05
548	1.00	0.10	0.95	0.07
549	1.01	0.07	0.93	0.05
550	1.00	0.07	0.93	0.05
551	1.00	0.07	0.87	0.07
552	1.00	0.22	0.95	0.09
553	0.99	0.12	0.90	0.05
554	1.04	0.10	0.96	0.06
555	0.99	0.10	0.90	0.05
556	0.99	0.04	0.91	0.04
557	1.01	0.24	0.99	0.09
558	0.99	0.16	0.80	0.10
559	0.97	0.12	0.91	0.04
560	1.06	0.10	0.94	0.04
561	1.00	0.04	0.96	0.03
562	0.00	0.41	-0.04	0.19
563	0.00	0.34	-0.03	0.18
564	0.00	0.50	0.03	0.26
565	0.00	0.41	-0.47	0.13
566	0.00	0.57	0.42	0.34
567	0.00	0.28	0.01	0.15
568	1.00	0.03	0.85	0.05
569	1.00	0.06	1.03	0.10
570	1.00	0.06	0.91	0.06

Index	Prefit	\pm error	Postfit	\pm error
571	1.00	1.00	2.71	0.31
572	1.00	1.00	1.32	0.25
573	1.00	0.20	0.94	0.13
574	1.00	3.00	2.00	0.09
575	1.00	3.00	2.00	0.21
576	0.59	0.12	0.53	0.07
577	1.05	0.21	1.63	0.13
578	1.13	0.17	1.28	0.13
579	0.88	0.35	1.12	0.33
580	1.20	0.10	1.20	0.10
581	0.95	0.15	0.86	0.07
582	1.13	0.16	1.12	0.04
583	0.74	0.31	1.04	0.18
584	1.00	0.03	1.00	0.03
585	1.00	0.03	1.00	0.03
586	0.00	0.40	-0.23	0.20
587	1.00	0.30	0.48	0.44
588	1.00	0.30	0.48	0.44
589	1.00	0.30	1.13	0.30
590	1.00	1.00	1.00	1.00
591	1.00	0.30	1.13	0.18
592	1.00	0.30	1.00	0.30